



Acoustic Characteristics of Various Treatment Panel Designs for HSCT Ejector Liner Acoustic Technology Development Program

*M. Salikuddin, R.E. Kraft, A.A. Syed, D.D. Vu, P. Mungur,
L.E. Langenbrunner, and R.K. Majjigi
General Electric Aircraft Engines, Cincinnati, Ohio*

NASA STI Program . . . in Profile

Since its founding, NASA has been dedicated to the advancement of aeronautics and space science. The NASA Scientific and Technical Information (STI) program plays a key part in helping NASA maintain this important role.

The NASA STI Program operates under the auspices of the Agency Chief Information Officer. It collects, organizes, provides for archiving, and disseminates NASA's STI. The NASA STI program provides access to the NASA Aeronautics and Space Database and its public interface, the NASA Technical Reports Server, thus providing one of the largest collections of aeronautical and space science STI in the world. Results are published in both non-NASA channels and by NASA in the NASA STI Report Series, which includes the following report types:

- **TECHNICAL PUBLICATION.** Reports of completed research or a major significant phase of research that present the results of NASA programs and include extensive data or theoretical analysis. Includes compilations of significant scientific and technical data and information deemed to be of continuing reference value. NASA counterpart of peer-reviewed formal professional papers but has less stringent limitations on manuscript length and extent of graphic presentations.
- **TECHNICAL MEMORANDUM.** Scientific and technical findings that are preliminary or of specialized interest, e.g., quick release reports, working papers, and bibliographies that contain minimal annotation. Does not contain extensive analysis.
- **CONTRACTOR REPORT.** Scientific and technical findings by NASA-sponsored contractors and grantees.

- **CONFERENCE PUBLICATION.** Collected papers from scientific and technical conferences, symposia, seminars, or other meetings sponsored or cosponsored by NASA.
- **SPECIAL PUBLICATION.** Scientific, technical, or historical information from NASA programs, projects, and missions, often concerned with subjects having substantial public interest.
- **TECHNICAL TRANSLATION.** English-language translations of foreign scientific and technical material pertinent to NASA's mission.

Specialized services also include creating custom thesauri, building customized databases, organizing and publishing research results.

For more information about the NASA STI program, see the following:

- Access the NASA STI program home page at <http://www.sti.nasa.gov>
- E-mail your question via the Internet to help@sti.nasa.gov
- Fax your question to the NASA STI Help Desk at 301-621-0134
- Telephone the NASA STI Help Desk at 301-621-0390
- Write to:
NASA STI Help Desk
NASA Center for AeroSpace Information
7121 Standard Drive
Hanover, MD 21076-1320



Acoustic Characteristics of Various Treatment Panel Designs for HSCT Ejector Liner Acoustic Technology Development Program

*M. Salikuddin, R.E. Kraft, A.A. Syed, D.D. Vu, P. Mungur,
L.E. Langenbrunner, and R.K. Majjigi
General Electric Aircraft Engines, Cincinnati, Ohio*

Prepared under Contract NAS3-27235

National Aeronautics and
Space Administration

Glenn Research Center
Cleveland, Ohio 44135

Acknowledgments

The authors are thankful to J. Low and Fred Stern of P&W for their advice and contribution in the selection and design process for the liner concepts. The authors recognize the contribution of T. Parrot for providing the design for variable depth 2DOF panels. The authors are also thankful to Jia Yu of BF Goodrich Aerospace (previously Rohr, Inc.) for his help in the process of test sample fabrication. The authors appreciate the contribution made by H.W. Kwan of BF Goodrich Aerospace (previously Rohr, Inc.) in insertion loss measurement of various treatment panels at Rohr's flow duct facility.

Trade names and trademarks are used in this report for identification only. Their usage does not constitute an official endorsement, either expressed or implied, by the National Aeronautics and Space Administration.

This work was sponsored by the Fundamental Aeronautics Program at the NASA Glenn Research Center.

Level of Review: This material has been technically reviewed by NASA technical management.

Available from

NASA Center for Aerospace Information
7121 Standard Drive
Hanover, MD 21076-1320

National Technical Information Service
5285 Port Royal Road
Springfield, VA 22161

Available electronically at <http://gltrs.grc.nasa.gov>

FOREWORD

This report is prepared by GE Aircraft Engines, Cincinnati, Ohio for NASA-Glenn Research Center (previously known as Lewis Research Center), Cleveland, Ohio under HSR Program, Contract NAS3-26617 & NAS3-27235. Mr. Gene Krejsa was the Project Manager for NASA-Glenn Research Center initially and Dr. James Bridges took over his responsibility at a later date. Mr. Fred Krause was the Project Manager for GEAE. GEAE Program Manager was Dr. R. K. Majjigi.

SUMMARY

The objectives of the initial effort (Phase I) of HSR Liner Technology Program, the selection of promising liner concepts, design and fabrication of these concepts for laboratory tests, testing these liners in the laboratory by using impedance tube and flow ducts, and developing empirical impedance/suppression correlation, are successfully completed. Acoustic and aerodynamic criteria for the liner design are established. Based on these criteria several liners are designed. The liner concepts designed and fabricated include Single-Degree-of-Freedom (SDOF), Two-Degree-of-Freedom (2DOF), and Bulk Absorber. Two types of SDOF treatment are fabricated, one with a perforated type face plate and the other with a wiremesh (woven) type faceplate. In addition, special configurations of these concepts are also included in the design. Several treatment panels are designed for parametric study. In these panels the facesheets of different porosity, hole diameter, and sheet thickness are utilized. Several deep panels (i.e., 1 inch deep) are designed and instrumented to measure DC flow resistance and in-situ impedance in the presence of grazing flow. Basic components of these panels (i.e., facesheets, bulk materials, etc.) are also procured and tested. The results include DC flow resistance, normal impedance, and insertion loss.

In addition, the data acquired by testing a Gen 1 mixer-ejector at NASA-Glenn NATR facility is used to extract the acoustic suppression (Δ PWL) due to the variety of treatments used in the ejector. The laboratory test results and the extracted Δ PWL are utilized to develop correlation to predict normal impedance and insertion loss.

Major observations are listed below;

DC Flow and Normal Impedance Tube Test Results:

- The similarity principle to normalize DC flow resistance and the approach velocity with respect to viscosity and temperature is applicable for perforated sheets and silicon Carbide bulk materials.
- DC flow resistance for perforated sheets increases with decreasing porosity and with decreasing thickness.
- Normal impedance for perforated sheets increases with decreasing porosity and with increasing thickness.
- Normal resistance for perforated sheets decreases with decreasing hole diameter. However, the normal reactance decreases with decreasing hole diameter first and then increases by further decrease of hole diameter.

- The nonlinearity of normal impedance due to excitation level for perforated sheets is relatively higher for normal resistance compared to normal reactance. Nonlinearity increases with decreasing porosity, increasing hole diameter, and increasing thickness.
- For SDOF type liner with linear facesheets the normal impedance increases with increasing resistivity of the facesheet.
- DC flow resistance for Silicon Carbide bulk material increases with pores/inch.
- For Silicon Carbide bulk normal resistance increases and normal reactance decreases with increasing pores/inch. For very low pores/inch the cavity influence is dominant on normal impedance levels.

Flow Duct Test Results:

- DC flow resistance increases with increasing grazing flow Mach number for SDOF type liners with perforated facesheets.
- In-situ resistance increases significantly with increasing grazing flow Mach number. In-situ reactance decreases slightly with increasing grazing flow Mach number.
- At measurement location the boundary layer profiles are fully developed and the boundary layer thicknesses are relatively higher for perforated plates than those for hardwall. Boundary layer becomes more turbulent with increasing facesheet porosity.
- Local skin friction coefficient decreases with increasing grazing flow and increases with increasing porosity.
- Insertion loss for every panel increases with increasing flow Mach number, as the panels are designed to give maximum suppression at higher Mach number. However, with further increase of grazing flow Mach number, the insertion loss decreases.
- Insertion loss spectra for different panels, designed for different duct heights, are of same shape when plotted against nondimensional frequency, confirming the scaling principle.
- For SDOF type panels insertion loss peak increases with decreasing porosity at no flow condition. The effect diminishes with flow. Higher hole diameter helps suppress more acoustic energy at no flow condition. The trend is reversed with flow. Acoustic suppression seems to be higher for thick facesheets.
- Insertion loss seems to be higher for the bulk absorber without honeycomb compared to honeycomb filled bulk absorber.
- Insertion loss is highest for 2DOF panel with linear facesheet and septum compared to SDOF and bulk filled panels. However, the insertion loss spectrum for SDOF panel with linear facesheet and bulk absorbers are very close to that of 2DOF panel.

Gen 1 Mixer-Ejector Test Results (Acoustic Suppression, Δ PWL):

- Δ PWL increases with increasing flight velocity at higher nozzle aerothermodynamic conditions. The effect is negligible at lower nozzle aerothermodynamic conditions.
- Δ PWL increases with decreasing nozzle aerothermodynamic condition.

- Δ PWL increases with decreasing ppi for SiC at takeoff condition. Similar effect is also observed with decreasing density for HTP material.
- Δ PWL increases with increasing facesheet porosity for bulk absorber liners.
- Δ PWL increases with increasing facesheet thickness for bulk absorber liners.
- Δ PWL increases with increasing facesheet porosity SDOF type liners.
- Effect of facesheet thickness and hole diameter on acoustic suppression is negligible for SDOF type liners.
- Bulk absorber type liners perform better compared to SDOF type liners with perforated facesheet in acoustic suppression.

Normal Impedance and Acoustic Suppression Correlation:

- Extensive acoustic impedance modeling of several material types is performed. The existing models for acoustic impedance are modified. The models can be improved for higher frequency range and for other parameters when more such data is available.
- The insertion loss modeling of the duct suppressor connecting two reverberation chambers is achieved. The results are reasonably good but could be improved. At present stage of development it would be risky to use this model to predict optimum configurations.
- The acoustic suppression modeling of Gen. 1 mixer-ejector is achieved with reasonably good agreement with the data. The model is very fundamental and probably worth improving.

FOREWORD.....	iii
SUMMARY	v
1.0 INTRODUCTION.....	1
2.0 CONCEPT SELECTION	3
2.1 Concept Selection Process	3
2.2 Liner Preliminary Design Criteria.....	3
2.3 Preliminary Design of Liners.....	18
2.3.1 Assumptions for Impedance Prediction	20
2.3.2 Acoustic Suppression Prediction	21
2.3.3 Optimum Liner Designs	24
2.3.4 Predicted Normal Impedance Spectra.....	25
2.3.5 Empirically Predicted Acoustic Suppression	28
2.3.6 Predicted Acoustic Suppression by Modal Analysis	28
2.3.7 Influence of Design Parameters.....	42
2.3.8 Influence of Grazing Flow.....	49
3.0 TEST FACILITY AND TEST APPROACH.....	59
3.1 Normal Incidence Impedance Measurements	59
3.1.1 Low Frequency Normal Impedance Measurements	59
3.1.2 High Frequency Normal Impedance Measurements.....	61
3.2 DC Flow Resistance Measurements	64
3.2.1 Room Temperature DC Flow Measurements.....	64
3.2.2 High Temperature DC Flow Measurements.....	67

3.3	Flow Duct Facility at GEAE	67
3.3.1	Suppression Measurements	70
3.3.2	Boundary-Layer Profile Measurements	72
3.3.3	In-situ Method of Normal Impedance Measurements	74
3.4	Flow Duct Facility for Insertion Loss Evaluation (Rohr).....	79
4.0	DESIGN AND PROCUREMENT OF TEST SAMPLES	86
4.1	Design of Panels for Flow Duct Test.....	86
4.2	Detail Design of Test Samples	105
5.0	LABORATORY TESTS AND RESULTS	128
5.1	Acoustic Characteristics of Perforated Facesheet	129
5.1.1	DCFlow Resistance.....	129
5.1.2	Normal Impedance.....	141
5.2	Acoustic Characteristics of Perforated Facesheets Mounted on 0.5"-Deep Honeycomb Structures (No Backplate)	159
5.3	Acoustic Characteristics of SDOF Type Panels with Perforated Facesheets	
5.3.1	Boundary Layer Results	168
5.3.2	Insertion Loss Results	176
5.4	Acoustic Characteristics of Instrumented 1"-Deep SDOF Type Panels with Perforated Facesheets	188
5.4.1	DC Flow Results	188
5.4.2	In-situ Impedance Results	197
5.4.3	Boundary Layer Results	208
5.4.4	Insertion Loss Results	217

5.5	Acoustic Characteristics of SDOF Type Panels with Linear Facesheets	223
5.6	Acoustic Characteristics of Bulk-filled SDOF Type and Bulk Only Panels with Linear Facesheets.....	234
5.6.1	Bulk Samples without Facesheet for DC Flow & Normal Impedance Tests.....	234
5.6.2	Bulk Panels with Linear Facesheets for Flow Duct Tests.....	256
5.7	Acoustic Characteristics of 2DOF Type Panels with Linear Facesheets and Septum.....	280
5.7.1	Normal Impedance	280
5.7.2	Boundary Layer Results.....	289
5.7.3	Insertion Loss Results.....	289
6.0	DATA CORRELATION.....	302
6.1	Insertion Loss - Normal Impedance Correlation.....	305
6.2	Validation/Improvement of Insertion Loss - Normal Impedance Correlation.....	305
7.0	CONCLUSIONS, CONCERNS, AND RECOMMENDATIONS.....	307
7.1	Conclusions	307
7.1.1	Conclusions on DC Flow and Normal Impedance Tube Test Results.....	307
7.1.2	Conclusions on Flow Duct Test Results	307
7.1.3	Conclusions on Gen 1 Mixer-Ejector Test Results (Acoustic Suppression, APWL).....	308
7.1.4	Conclusions on Normal Impedance and Acoustic Suppression Correlation.....	308
7.2	Concerns and Recommendations	308

APPENDIX A: ANALYTICAL BACKGROUND FOR MODAL ANALYSIS METHOD.....	310
APPENDIX B: UNDERSTANDING OF INSERTION LOSS RESULTS MEASURED BY GEAE'S FLOW-DUCT FACILITY.....	316
APPENDIX C: A SCREENING STUDY FOR CERAMIC MATRIX COMPOSITE MATERIALS FOR HSCT EJECTOR LINER.....	370
APPENDIX D: ACOUSTIC CHARACTERISTICS OF BULK MATERIALS WITH FACESHEETS.....	395
REFERENCES	411

1.0 INTRODUCTION

Environmental acceptability and economic viability are crucial issues in the development of the next generation High Speed Civil Transport (HSCT) and low noise exhaust nozzle technology has significant impact on both issues. The exhaust system design that meets FAR 36 Stage 3 takeoff acoustic requirements and provides high levels of cruise and transonic performance and adequate takeoff performance at an acceptable weight is essential to the success of any HSCT program.

Acoustic liners are required for HSCT mixer/ejector nozzles to attenuate broadband, high-frequency mixing noise and shock associated noise generated within the confines of the ejector walls and meet FAR 36 Stage 3 noise goals. Research and development of acoustic liners is a critical element of the High Speed Research Program, to ensure timely progress in high-temperature, high grazing flow velocity acoustic liner technology. This effort includes coordinated experimental and theoretical work on a number of technical areas, such as, source definition, duct propagation, liner physics, and testing of liners in impedance tube, flow duct, and scale model ejector nozzles.

The overall objective of the liner technology program is to develop a design methodology for both bulk absorber (with facesheet) and SDOF (honeycomb with facesheet) type liners to obtain needed acoustic suppression with minimum skin friction loss. Currently, both bulk absorber and SDOF liner designs are being pursued to reduce technical risk (i.e., material, weight, and durability considerations). The liner design methodology contains three basic elements, (1) a correlation of the DC flow resistance and physical properties of a liner at room temperature with its normal impedance at a desired temperature and flow condition, (2) a correlation between the normal impedance and the insertion loss (acoustic suppression) of the liner accounting for liner scaling, and (3) a correlation between liner facesheet properties (i.e., porosity, thickness, hole diameter, and shape of holes for perforated facesheets/or resistivity and type of construction for linear facesheets) and its skin friction loss.

The first correlation determines the required properties of a liner design at room temperature with respect to an established impedance goal for the liner at the actual flow and temperature condition. If for some reason the impedance goal does not yield the desired or maximum acoustic suppression and it needs to be altered, then the corresponding liner characteristics at room temperature can easily be determined without any additional test or analysis. The second correlation determines the acoustic suppression capability of a liner design with known normal impedance, accounting for liner scaling. Finally, the third relationship helps selecting the liner

materials, especially the facesheets, which would minimize the friction loss. While the first two elements are achieved as planned, the third element is not pursued as a correlation due to the time constraint. However, the local friction coefficients for several liner configurations are evaluated to select liner designs with minimum possible friction coefficients.

The development process of liner design methodology is described in several reports. This report contains the results of the initial effort (Phase I) of concept development, screening, laboratory testing of various liner concepts, and preliminary correlation (Generic data). The second phase of laboratory test results of more practical concepts and their data correlation are presented in a second report (Product specific). Finally, the detail steps for liner design methodology and the relevant results are presented in a third report. In addition, several elements of the liner technology programs, namely, (1) internal components of farfield acoustic characteristics for various mixer-ejector nozzles in terms of acoustic suppression and (2) data correlation to predict normal impedance and acoustic suppression of various liner designs, are presented in a number of HSR/CPC Program Coordination Memos and informal reports.

Phase I effort is carried out by evolving a liner design approach to screen, evaluate, and scale liner concepts to achieve desired noise suppression levels and liner acoustic impedance values. This report includes the selection of promising liner concepts, design and fabrication of these concepts for laboratory tests, testing these liners in the laboratory by using impedance tube and flow duct, and developing empirical impedance/suppression correlation.

2.0 CONCEPT SELECTION

2.1 Concept Selection Process: The concept selection process involves ranking of various concepts, preliminary design of selected concepts, selection of liner parameters to be varied for each concepts with dominant effect on noise characteristics, decision of the number of liner samples to be fabricated, and finally, development of a test plan for the laboratory test phase. The ranking of the liner concepts was based on acoustic, performance, and producibility criteria. Other criteria, such as weight, maintainability, life, and strength were relatively less important for laboratory test samples at this stage of the program.

2.2 Liner Preliminary Design Criteria: Frequency range, noise levels at which the liner will be effective in noise suppression, and the flow conditions which will be experienced by the liner during the takeoff, are the major criteria for the liner design process. In addition, the normal impedance goals are established for suppression maximization. All these criteria and goals were established in 1992 on the basis of the data existed at that time and was relevant to the ejector nozzles. The database utilized in this study was mostly for axisymmetric ejector/suppressor configurations tested in the past. Parameters like farfield spectral shapes, noise levels, pressure, and temperature distributions on the ejector surface, etc. for axisymmetric configurations may be similar for the HSCT two-dimensional mixer-ejector nozzles. Later (not included in this section), some of the criteria, especially the internal noise levels, temperature, and pressure, are slightly modified on the basis of the more realistic database, generated from 2D mixer-ejector model tests.

Under a NASA contract, acoustic characteristics of treated ejectors on mechanical suppressors were studied (Refs. 1-2) in 1986. A coannular inverted-velocity-profile plug nozzle with 20-shallow chute outer stream suppressor with hardwall plug with and without an ejector were the nominal configurations. Additional configurations tested were the combinations of plug and ejector treatments of the nominal nozzle configurations. In this study farfield noise data was acquired for a number of configurations with and without ejector treatment. In addition, temperature and pressure distributions on the ejector surfaces were measured for different aerothermodynamic conditions. Similar results are also obtained for an axisymmetric 24-chute ejector/suppressor nozzle tested under GEAE IR&D program. Data from these two programs and other related studies were utilized to establish the design criteria for HSCT liner.

1. Basis for Frequency Range Criteria: Typical farfield results from reference 1 for the nozzles scaled to 1400 square inch size, are shown in Figures 1 and 2. A 20-chute axisymmetric suppressor was used in these configurations. Noise levels are substantial up to a

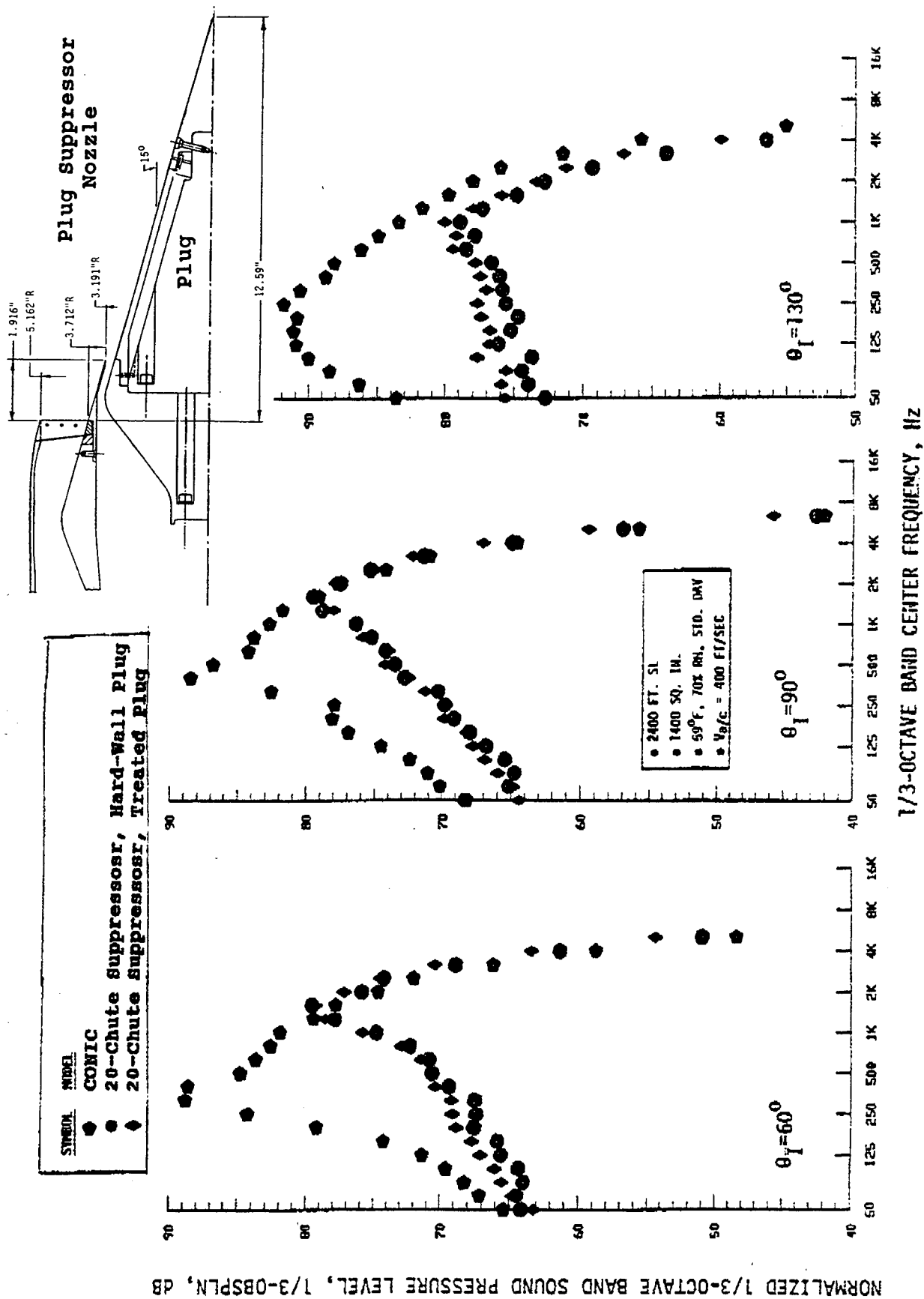


Figure 1. Typical farfield spectra showing the effect of treated plug for conannular inverted-velocity-profile plug nozzle with 20-shallow chute outer stream suppressor at takeoff conditions (Ref. 1).

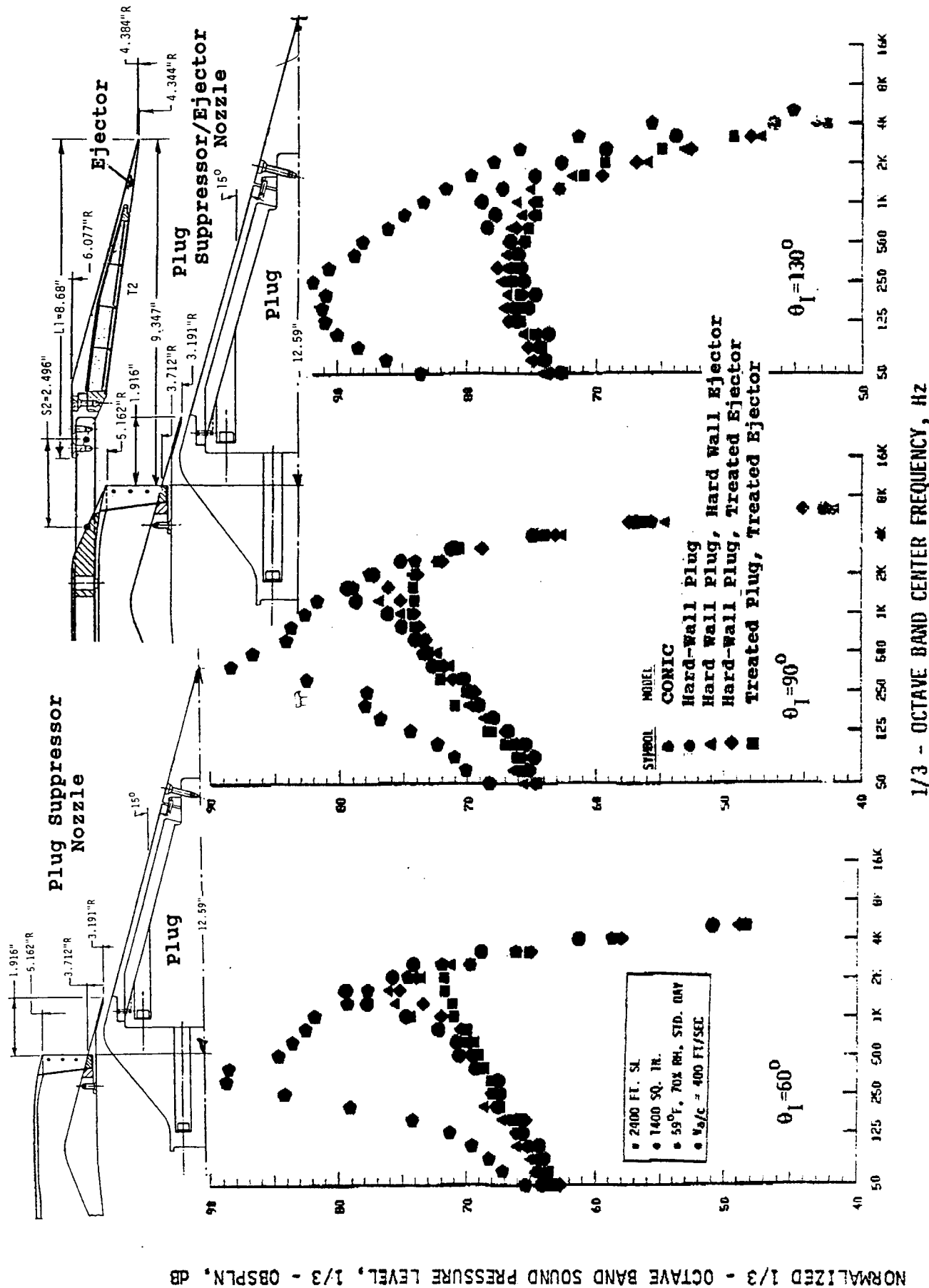
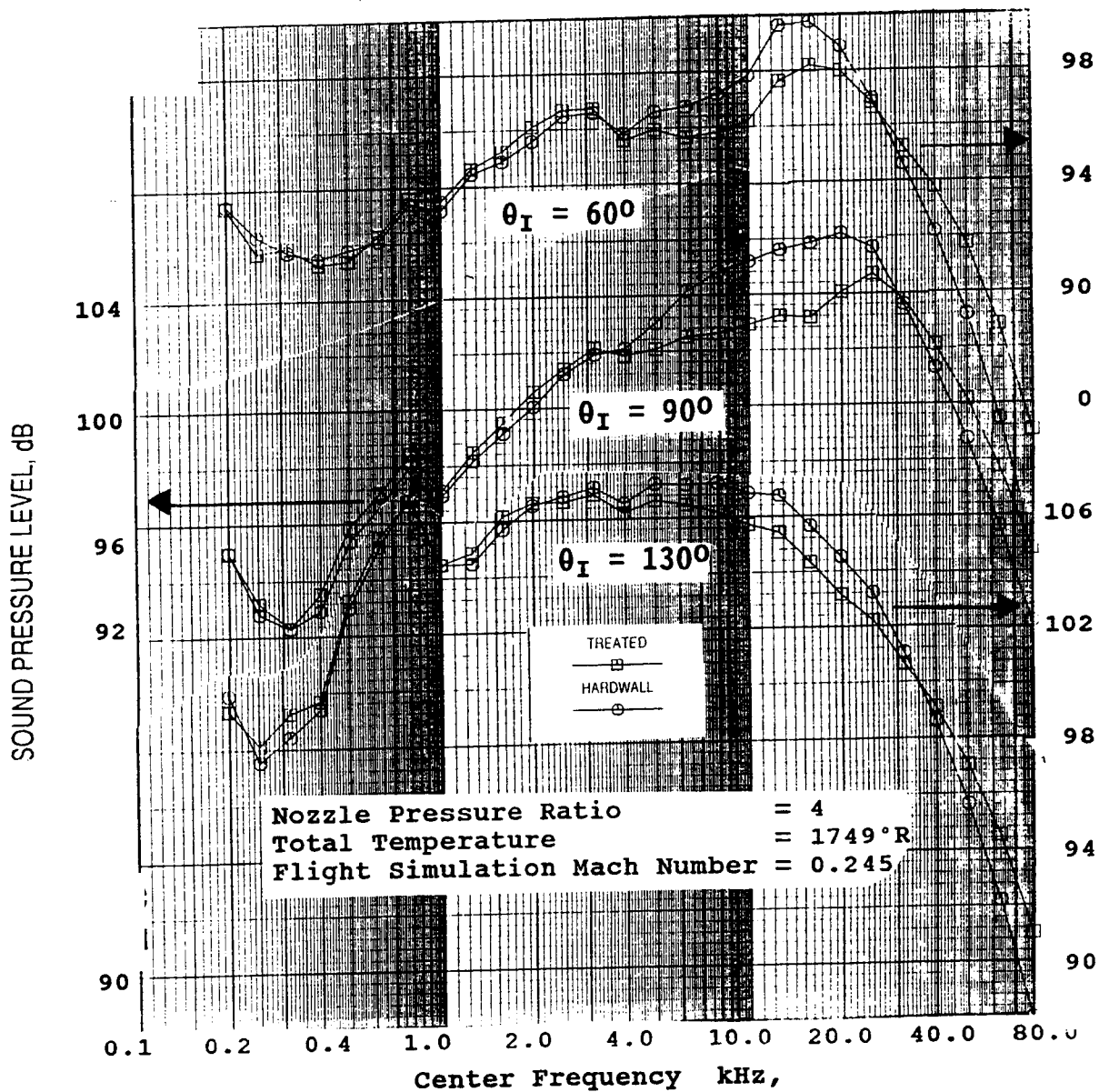


Figure 2. Typical farfield spectra showing the effect of treated plug and treated ejector for coannular inverted-velocity-profile plug nozzle with 20-shallow chute outer stream suppressor and the similar plug nozzle ejector at takeoff conditions (Ref. 1).

frequency of about 4 kHz with a peak at around 2 kHz. Considering 1086 square inch be the full scale area of HSCT nozzle the corresponding frequencies become 4.5 kHz and about 2.25 kHz. Similar results for the 24-chute nozzle of area 13.2 square inches (tested under IR&D and LET programs), shown in Figure 3, indicate frequency for dominant noise up to about 45 kHz with the peak occurring at about 18 kHz. For HSCT nozzle area these frequencies scaled down to about 4.5 kHz and 2 kHz, respectively. Both these configurations indicate that the frequency for dominant noise extends up to about 4.5 kHz and the peak level occurs at about 2 kHz. Based on the annoyance weighting procedure utilized in FAR 36 regulation the impact of low frequency noise up to about 1 kHz is small. Therefore, the liner effectiveness should be sought for a frequency range of 1 to 5 kHz with peak suppression capability at about 2 kHz.

2. Basis for Acoustic Load Criteria: At GEAE full-scale nozzle tests were performed in the past at various realistic aerothermodynamic conditions. In these tests acoustic measurements were made close to the nozzle exit in a manner where the ejector surface would be for ejector/nozzle configuration. Typical spectral data measured by microphones slightly downstream of the nozzle exit for two different nozzles are shown in Figures 4 and 5. Results shown in Figure 4 for the 443 square inch conical nozzle indicate SPL levels as high as 150 dB for nozzle pressure ratio of 2.779 and total temperature of 1306°R. The nozzle pressure ratio and total temperature for HSCT takeoff conditions are about 4.0 and 2000°R, which are relatively higher than the case indicated in Figure 4. Results shown in Figure 5 cover the aerothermodynamic conditions similar to HSCT takeoff case and higher than that. Based on Figure 5, an SPL of as high as 151 dB and an OASPL of 161 dB are expected on HSCT ejector surfaces. Model scale 2D-CD nozzles were tested in another study, in which, flush-mounted transducers were used to measure unsteady pressures inside the nozzles on divergent flap skin surfaces for various nozzle pressure ratios in room temperature. These results indicated OASPLs of 140 to 150 dB in regions before the formation of any shock in the nozzle and OASPLs of 150 to 170 dB after a strong shock. Based on these results 1/3-octave band internal SPLs of 150 to 155 dB and OASPLs of 160 to 170 dB are expected on the HSCT ejector surfaces.

3. Basis for Static Temperature Criteria: Figure 6 shows typical static temperature distributions along the ejector inner-flow surface at different nozzle total temperature, T_{t8} °R for a coannular 20-chute suppressor/ejector plug nozzle (Ref. 2). Similar results for the single stream 24-chute suppressor/ejector plug nozzle tested under GEAE IR&D program are shown in Figure 7. Maximum ejector surface temperatures corresponding to the nozzle total temperatures for both the nozzle tests are plotted in Figure 8 with respect to the nozzle total



7

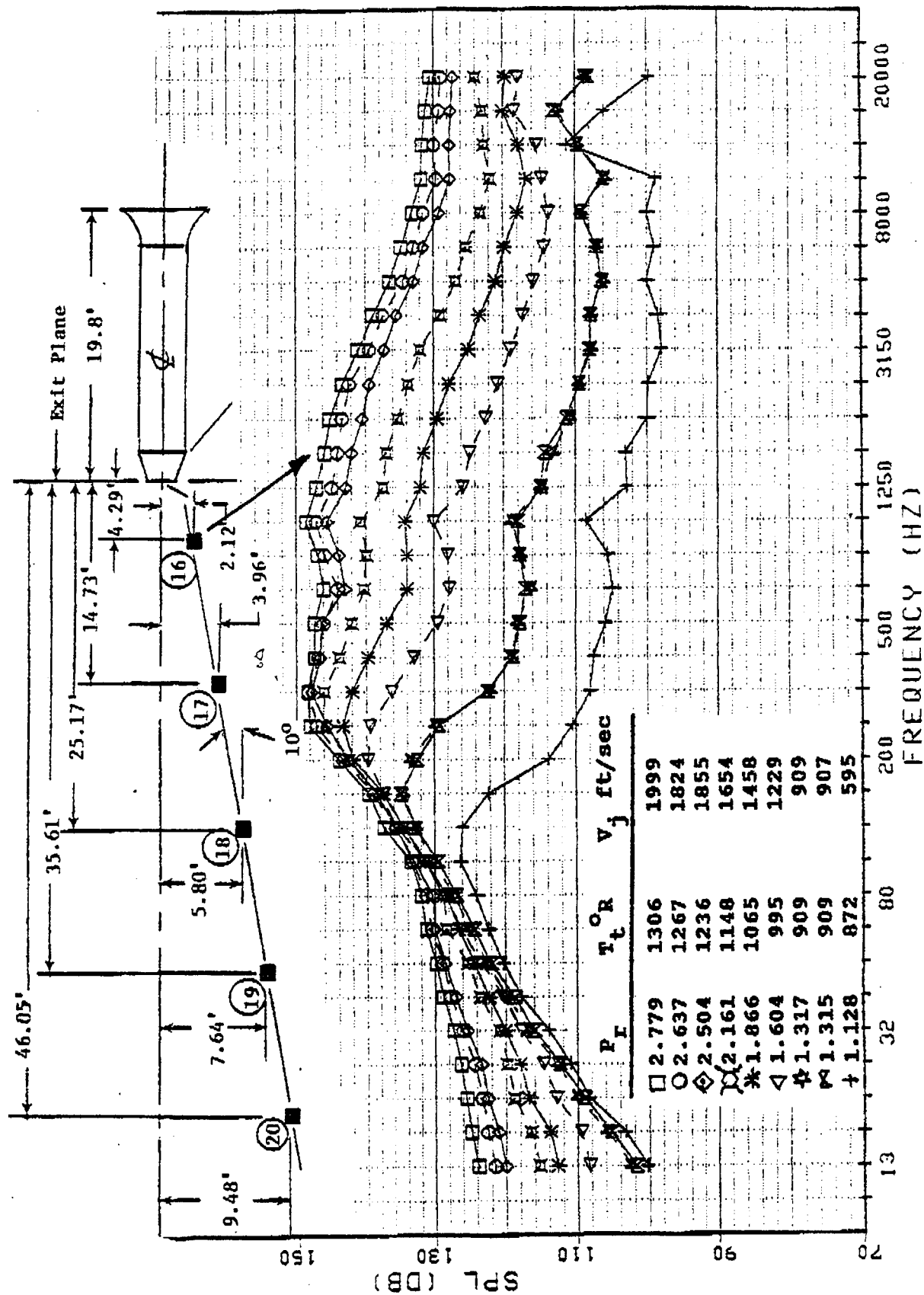


Figure 4. Jet proximity sound pressure level spectra for a 443 in' conical nozzle at different aerodynamic conditions.

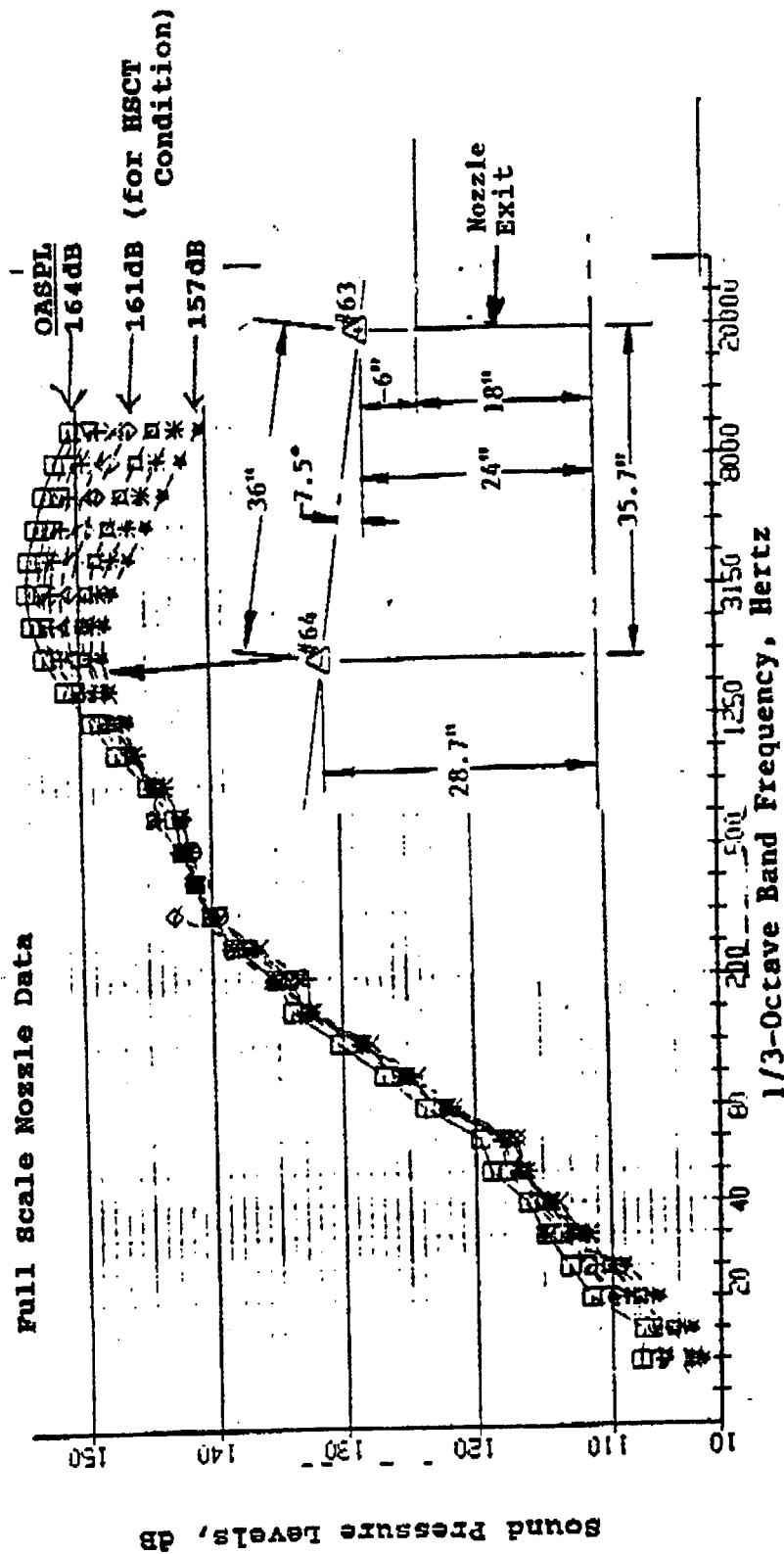


Figure 5. Jet proximity sound pressure level spectra for a full scale nozzle at different aerothermodynamic conditions.

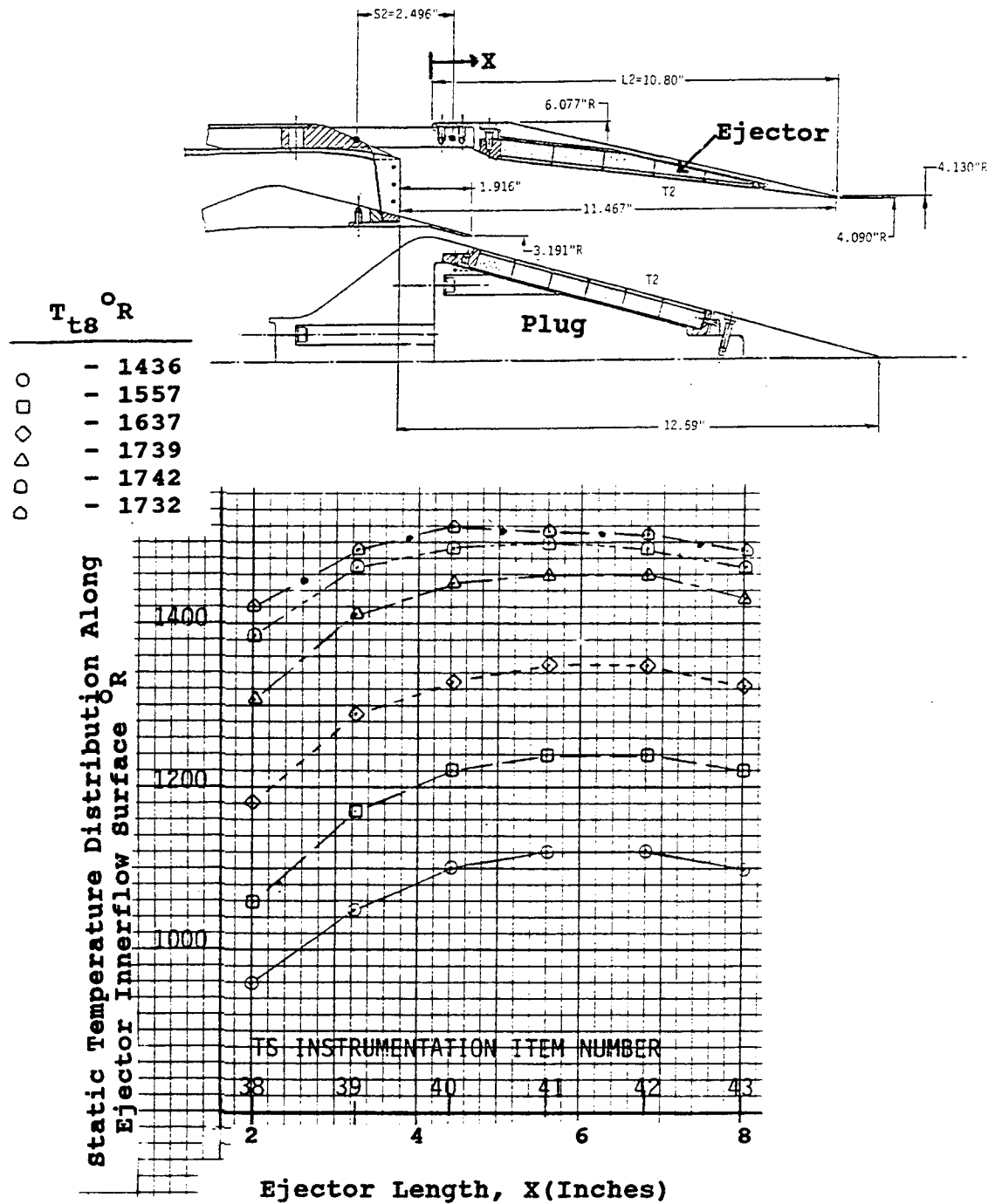


Figure 6. Typical static temperature distribution along the ejector inner flow surface for coannular inverted-velocity-profile plug nozzle with 20-shallow chute outer stream suppressor and with treated plug and treated ejector (Ref. 2)

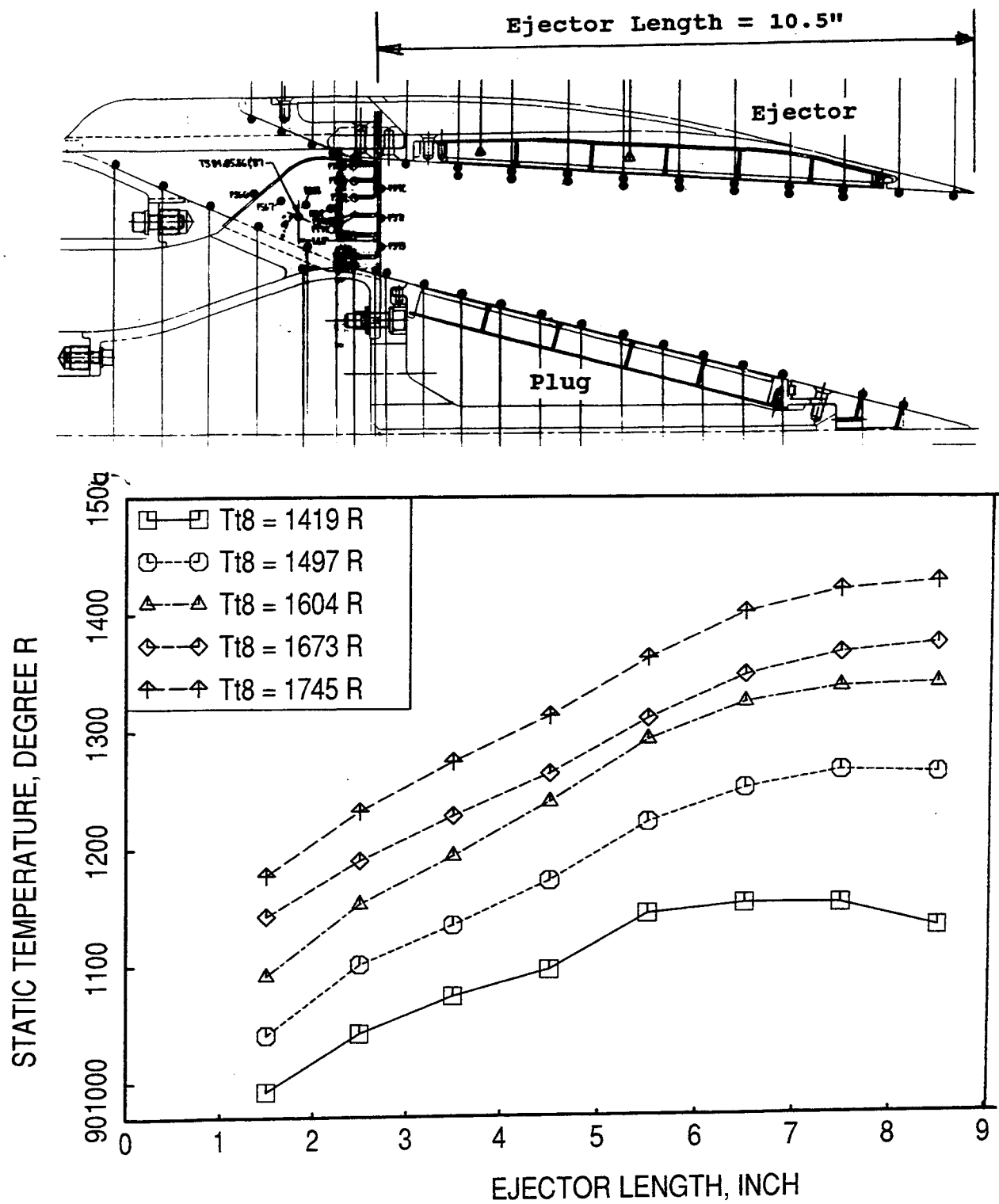


Figure 7. Typical static temperature distribution along the ejector inner flow surface for a 13.2 in² model scale plug nozzle with 24-chute suppressor and ejector.

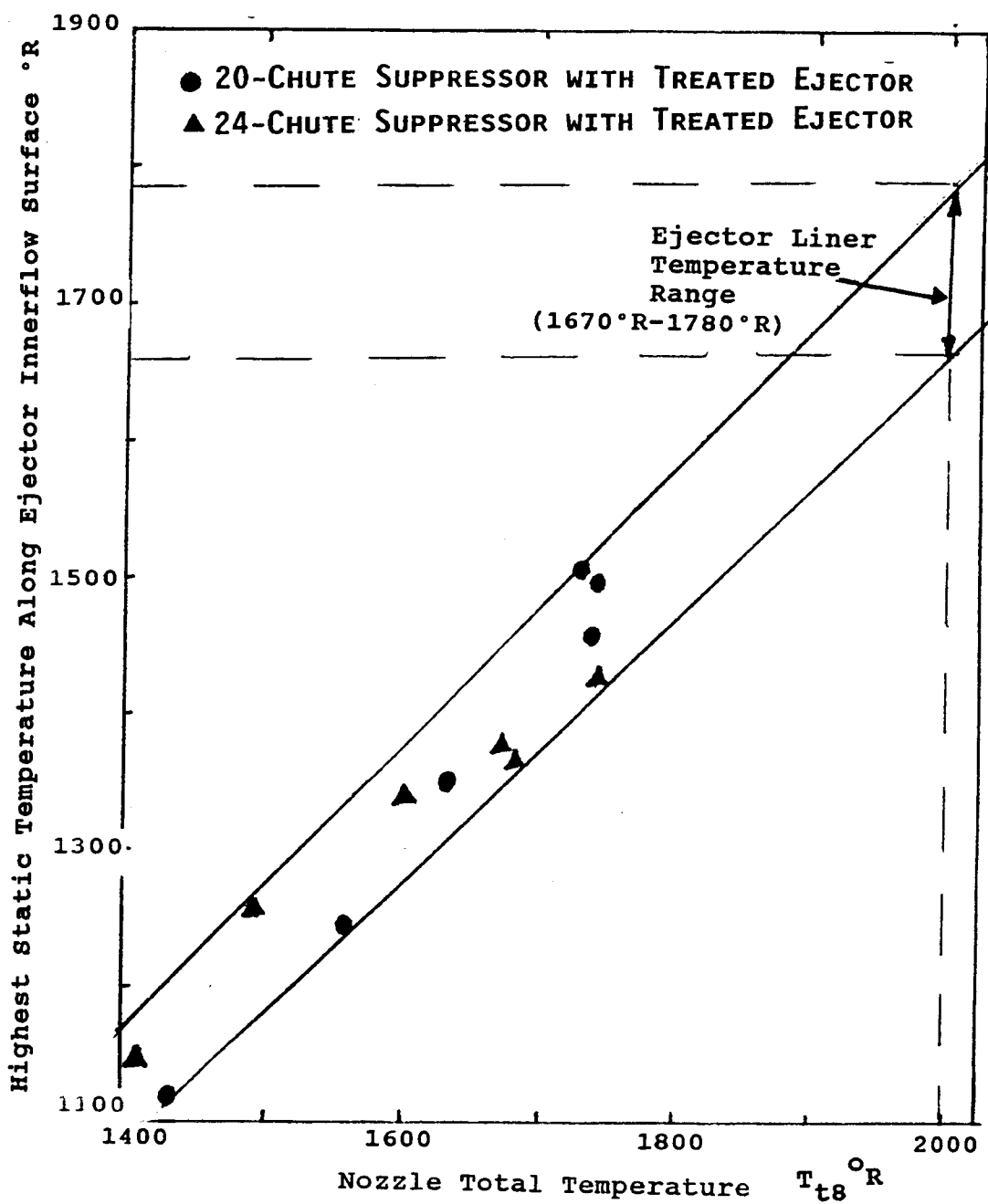


Figure 8. Expected range of ejector surface temperature for takeoff conditions evaluated from axisymmetric suppressor/ejector nozzle data.

temperature T_{18} . Extrapolation of these data gives the range of static temperature (i.e., 1670°R to 1780°R) at $T_{18} = 2000^\circ\text{R}$, which is expected to be the ejector surface maximum temperature for the HSCT ejector nozzle at takeoff. Thus, the liner design would be such that its acoustic effectiveness must be retained at this temperature range.

4. Basis for Static Pressure and Mach Number Criteria: Typical static pressure distributions along the ejector inner-flow surface at different nozzle total pressures for the coannular 20-chute suppressor/ejector nozzle (Ref. 2) are shown in Figure 9. The maximum static pressure on the ejector surface with respect to the corresponding nozzle total pressure, shown in Figure 10, indicates a possible maximum static pressure of about 30 psi (i.e., 2.08 times P_{amb}) on the ejector for a nozzle total pressure of about 59 psi (i.e., for nozzle pressure ratio of 4). Based on these results a pressure variation of 16 to 30 psi is expected on the major portion of the HSCT ejector surface. The isentropic Mach numbers corresponding to this pressure range are about 1.5 and 1.05 (assuming specific heat ratio of 1.3 at 2000°R).

The 24-chute suppressor/ejector data (i.e., tested under IR&D program), plotted in Figure 11, shows a pressure variation of about 13 to 17 psi on ejector surface for nozzle pressure ratio of 4, which is considerably lower than the coannular nozzle data. The corresponding isentropic Mach numbers of 1.67 to 1.49 are much higher compared to those for coannular 20-chute suppressor/ejector nozzle.

In 1992, model scale 2D ejector nozzles were tested at NASA Langley's 16-foot transonic tunnel for performance estimation under the ongoing NASA Contract, NAS3-25415. The test configuration consisted of 2D suppressor nozzle with CD chutes and with variable mixing area divergence (MAD) ejector flaps. Figure 12 shows typical axial pressure distributions on the ejector surface, aligned with the inner flow (primary flow), for three different MAD values. For divergent and parallel flap configurations (i.e., MAD of 1.2 and 1) the ejector surface pressures range between 0.4 to 0.8 times of ambient pressure (i.e., 6 to 12 psi). The isentropic Mach number variation corresponding to this pressure range for nozzle pressure ratio of 4 is 2.1 to 1.7. However, with convergent flap configuration (i.e., MAD=0.8) the ejector surface pressures were much higher, varying between 15 to 24 psi (corresponding isentropic Mach number variation being 1.5 to 1.23).

Assuming the static pressure on the HSCT ejector surface would vary between 15 and 25 psi the corresponding flow Mach number variation would be between 1.5 and 1.2 (for heated flow with specific heat ratio of 1.3).

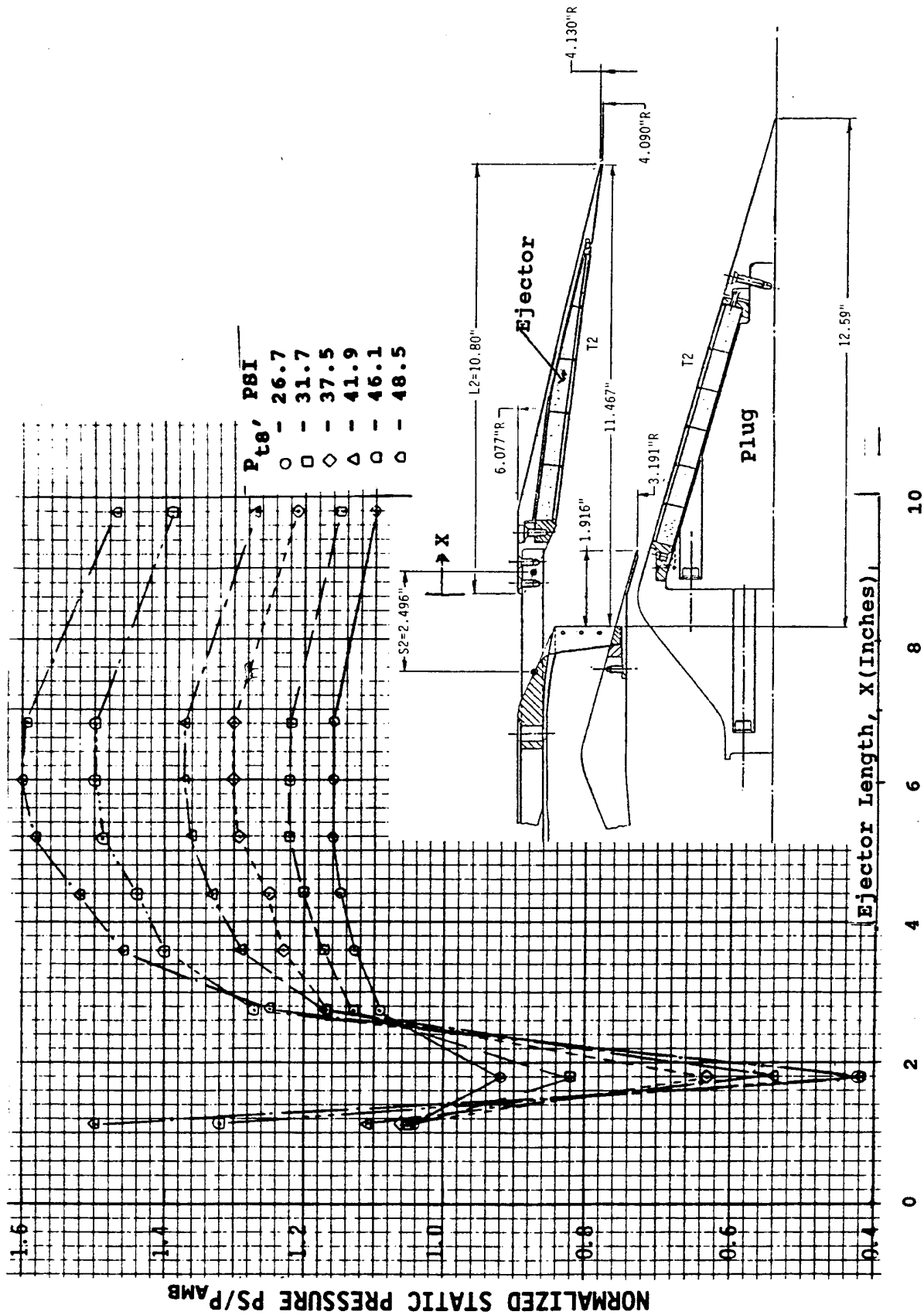


Figure 9. Typical static pressure distribution along the ejector inner flow surface for coannular inverted-velocity-profile plug nozzle with 20-shallow chute outer stream suppressor and with treated plug and treated ejector (Ref. 2).

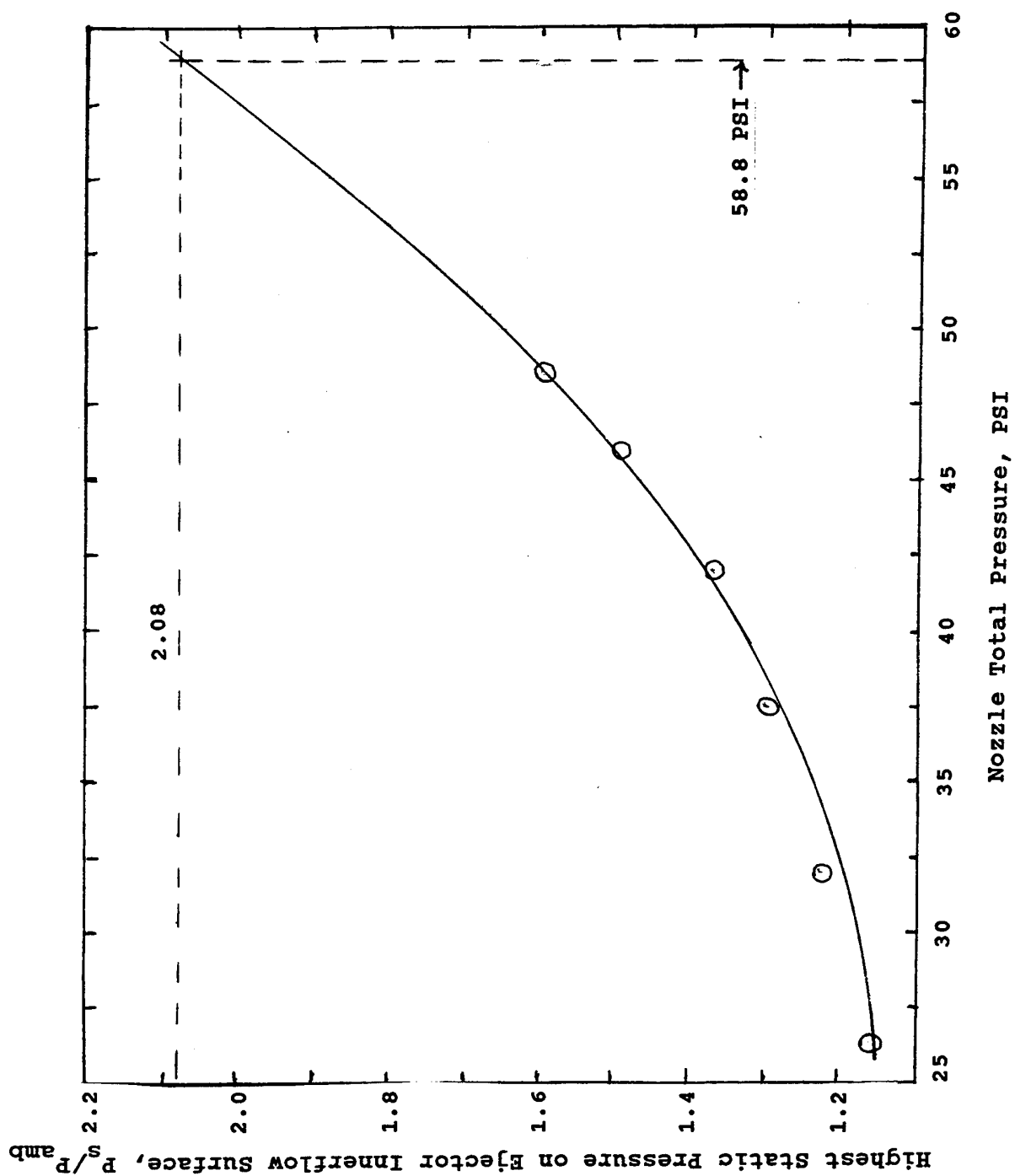


Figure 10. Expected ejector surface static pressure for takeoff condition evaluated from axisymmetric coannular 20-chute suppressor/ejector nozzle data.

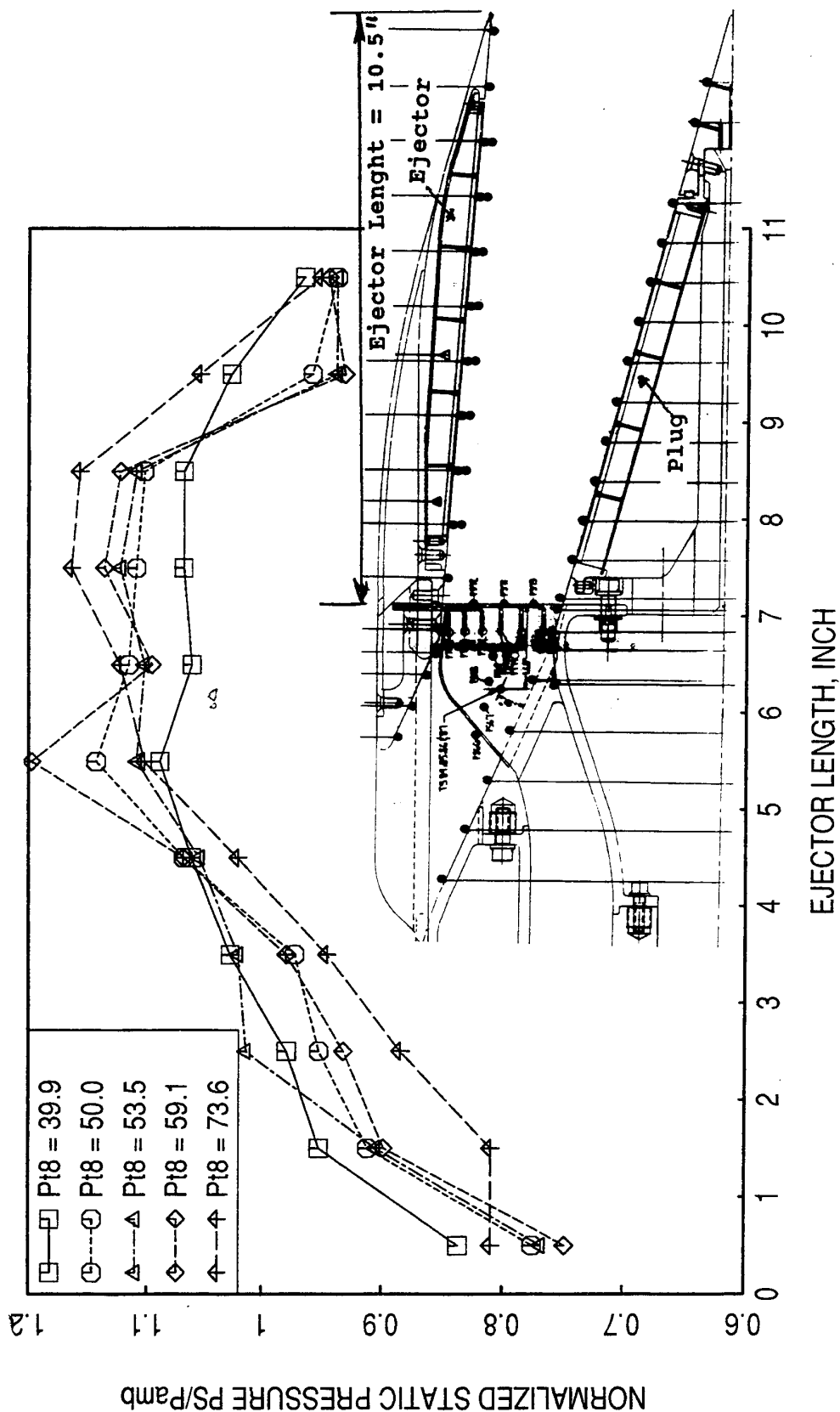


Figure 11. Typical static pressure distribution along the ejector inner flow surface for a 13.2 in² model scale plug nozzle with 24-chute suppressor and ejector.

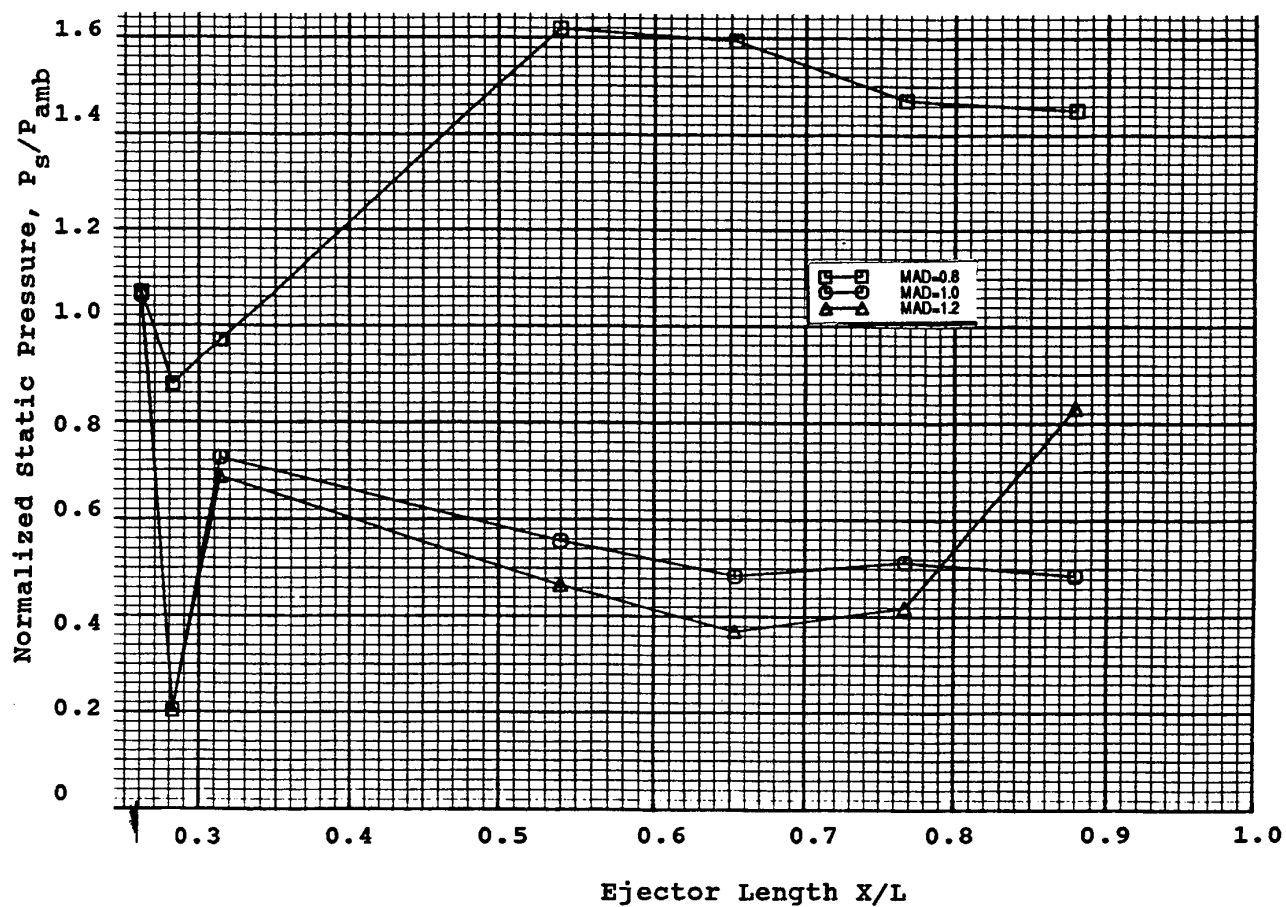
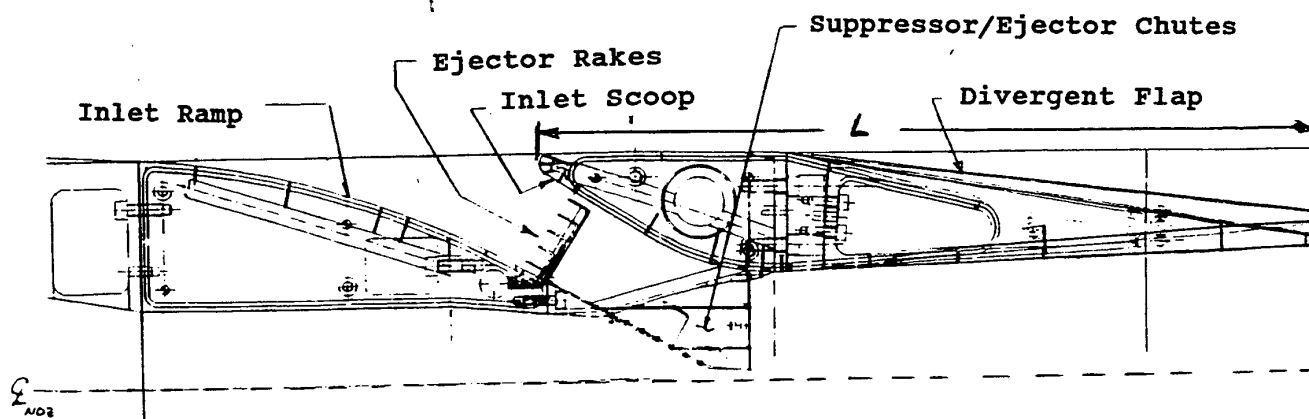


Figure 12. Typical static pressure distribution along the ejector inner flow surface for a 2D model scale nozzle with CD-chute suppressor (chute expansion ratio = 1.22) and ejector of variable mixing area divergence (MAD).

5. Normal Impedance Goals: Based on previous test data and modal analysis results of acoustic suppression for varying normal impedance values a range for normal impedance is established for maximum suppression. The range for normalized resistance and reactance is 1.5 to 2.0 and -0.5 to 0.0, respectively. These values are based on the experimental results of mock-up exhaust duct tests, conducted at GEAE under internal programs (Ref. 3). In addition, the experimental results of reference 1 were used to develop an optimum impedance prediction correlation for ejector treatment. The predicted impedance values for the treatment used in that study lie within the range of above mentioned impedance goals.

In summary, the liner design criteria for HSCT application are as follows:

- **FREQUENCY RANGE**

1 to 5 kHz, Peak Around 2 kHz - Full Scale
7 to 35 kHz, Peak Around 14 kHz - 1/7-th Scale
10 to 50 kHz, Peak Around 20 kHz - 1/10-th Scale

- **NOISE LEVELS**

Induct 1/3-Octave Band Sound Pressure Level (SPL) \approx 150 to 155 dB
Induct Overall Sound Pressure Level (OASPL) \approx 160 TO 170 dB

- **TREATMENT PANEL OPERATIONAL FLOW CONDITIONS**

Static Temperature \approx 1670°R to 1780°R
Static Pressure \approx 15 to 25 PSI
Mach Number \approx 1.2 to 1.5

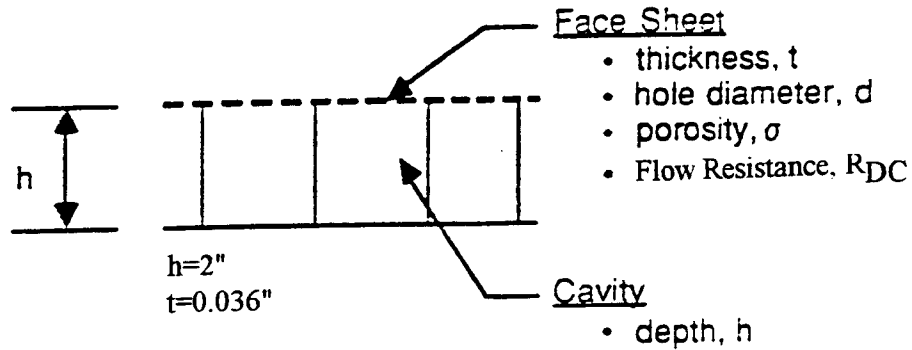
- **NORMAL IMPEDANCE GOALS**

Normalized Resistance, $R/\rho c \approx$ 1.5 to 2.0
Normalized Reactance, $X/\rho c \approx$ -0.5 to 0.0

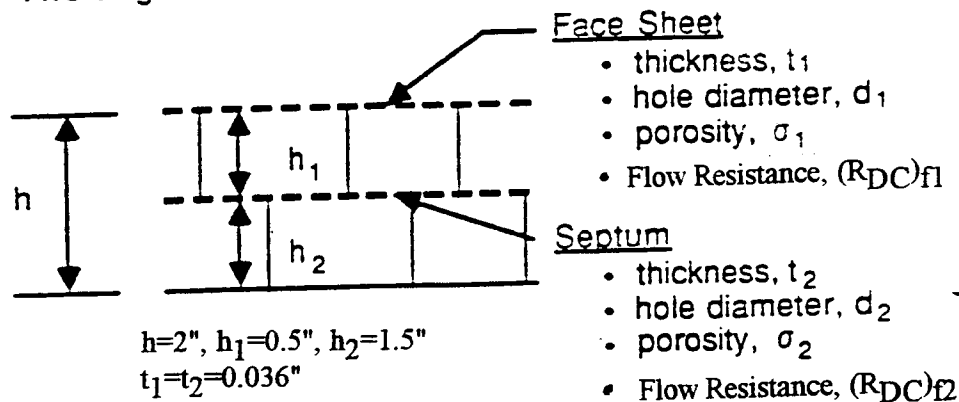
Where, density and speed of sound of the medium are represented by ρ and c , respectively.

2.3 Preliminary Design of Liners: Preliminary designs for three basic concepts of acoustic treatment for the HSCT ejector liner were developed. The design concepts considered are (a) Single-Degree-of-Freedom (SDOF), (b) Two-Degree-of-Freedom (2DOF), and (c) Extended-Reacting-Type Bulk Absorber (see Figure 13). Two types of SDOF treatment are considered, one with a Millipore (perforated) type face plate and the other with a wiremesh (woven) type facesheet. In total, four liner designs are considered. The panels are designed for full-scale

A. Single-Degree-of-Freedom



B. Two-Degree-of-Freedom



C. Bulk Absorber

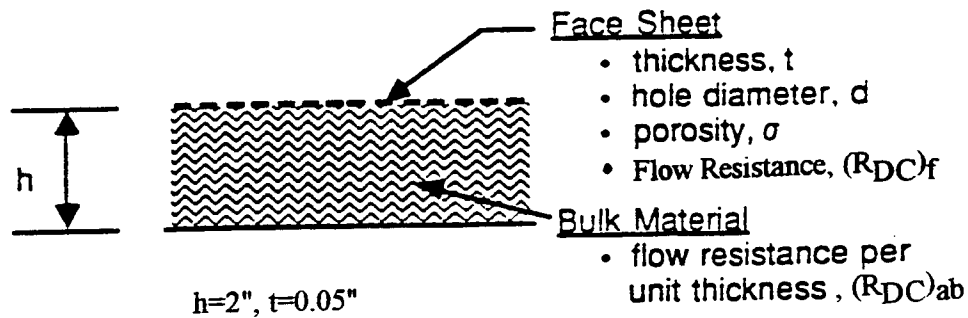


Figure 13. Treatment panel design parameters for three basic concepts.

application at realistic flow conditions. Impedance, absorption coefficient, and acoustic suppression spectra for the nominal design panels are predicted. In addition, sensitivity of these results are studied by altering the parameters associated with each of the concepts.

Full-scale liners were designed for the following acoustic and flow conditions based on the established criteria;

Full Scale Frequency Range = 1 to 5 kHz

OASPL at Liner Surface = 167.5 dB

Average Flow Mach Number = 1.2 to 1.5

Static Temperature at Liner Surface = 1750°R

Static Pressure at Liner Surface = 22 ps

The corresponding air density, speed of sound, and the characteristic impedance (i.e., product of density and speed of sound) are as follows:

Air Density in Liner, $\rho = 5.45 \times 10^{-4} \text{ gm/cm}^3$

Speed of Sound, $c = 2050 \text{ ft/sec (624.8 m/sec)}$

Characteristic Impedance, $\rho c = 34.05 \text{ cgs Rayls}$

2.3.1 Assumptions for Impedance Prediction: For the preliminary design following assumptions are made for impedance prediction:

1. Flow effects on liner facesheet resistance are neglected.
2. Mass reactance effects are not included.
3. Facesheet and septum properties are described entirely in terms of DC flow resistance at a through flow velocity of 100 cm/sec (R_{100}) and a nonlinear factor $NLF_{150/20}$, which is the ratio of DC flow resistances at 150 cm/sec and 20 cm/sec. The DC flow resistance is defined as $R = A + BU$ (Ref. 3), where A and B are the constants and U is the through flow velocity. Thus,

$$R_{100} = A + B \times 100 \text{ and}$$

$$NLF_{150/20} = (A + B \times 150)/(A + B \times 20).$$

The constants A and B can be expressed as :

$$A = (1.5 - 0.2 \times NLF_{150/20}) R_{100}/(1.5 - 0.2 \times NLF_{150/20})$$

$$B = (NLF_{150/20} - 1) R_{100}/[100 (0.5 + 0.8 \times NLF_{150/20})]$$

4. Conversions between properties at room temperature and pressure and operating conditions are accounted for by the changes in temperature of the medium ($T^{\circ}R$), pressure (P), and viscosity (coefficient of viscosity μ).

$$A \propto \mu, \text{ and } \mu \propto 216 (T)^{1.5}/(T+216)$$

$$B \propto \rho \propto P/T$$

The relationship between μ and T are based on Sutherland's equation (Ref. 4)

5. All liner panels are assumed to be locally reacting. For nonlinear panels, like SDOF and 2DOF type liners, an overall SPL of 167.5 dB is used to account for broadband excitation effects on nonlinear resistance.
6. Based on the treatment panel maximum depth constraint of less than 3 inches a nominal depth (h) of 2 inches is used for all the liner designs.

The impedance prediction method for SDOF and 2DOF type liners are based on the analytical models of Reference 5 and the bulk absorber formulas are adapted from Reference 6. Application of these models for impedance prediction are summarized in Reference 3. Specific values of porosity and hole diameter for the face sheet and septum are not required at this stage, since the mass reactance and grazing flow effects are excluded in the present design process. Therefore, the only design parameters required to predict impedance spectra are R_{100} and $NLF_{150/20}$ for facesheet and septum for SDOF and 2DOF type liners and the linear part of the DC flow resistance (i.e., A) for the facesheet ($(R_{DC})_f$) and bulk material ($(R_{DC})_{ab}$) for bulk absorber. Design parameters for each of the concepts are optimized, such that the liner impedance spectra would lie within the impedance goals.

2.3.2 Acoustic Suppression Prediction: Acoustic suppressions are also computed for a full scale rectangular duct, with two of the 67.5" sides being lined (see Figure 14), at various flow Mach numbers, M . In actual full scale design, side walls are treated also. The predictions are made by two methods, one is an empirical method, based on the correlation of measured insertion loss data and the second by a modal analysis technique.

Empirical Method: The correlation of the experimental results of mock-up exhaust duct tests (Ref. 3), conducted at GEAE under internal programs, was utilized for the acoustic suppression prediction of the lined ejectors up to a flow Mach number of 0.8. Since the suppression measurements were limited to lower flow Mach Numbers up to 0.4, the correlation utilized for prediction is more applicable up to about $M=0.4$. Hence, the validity of

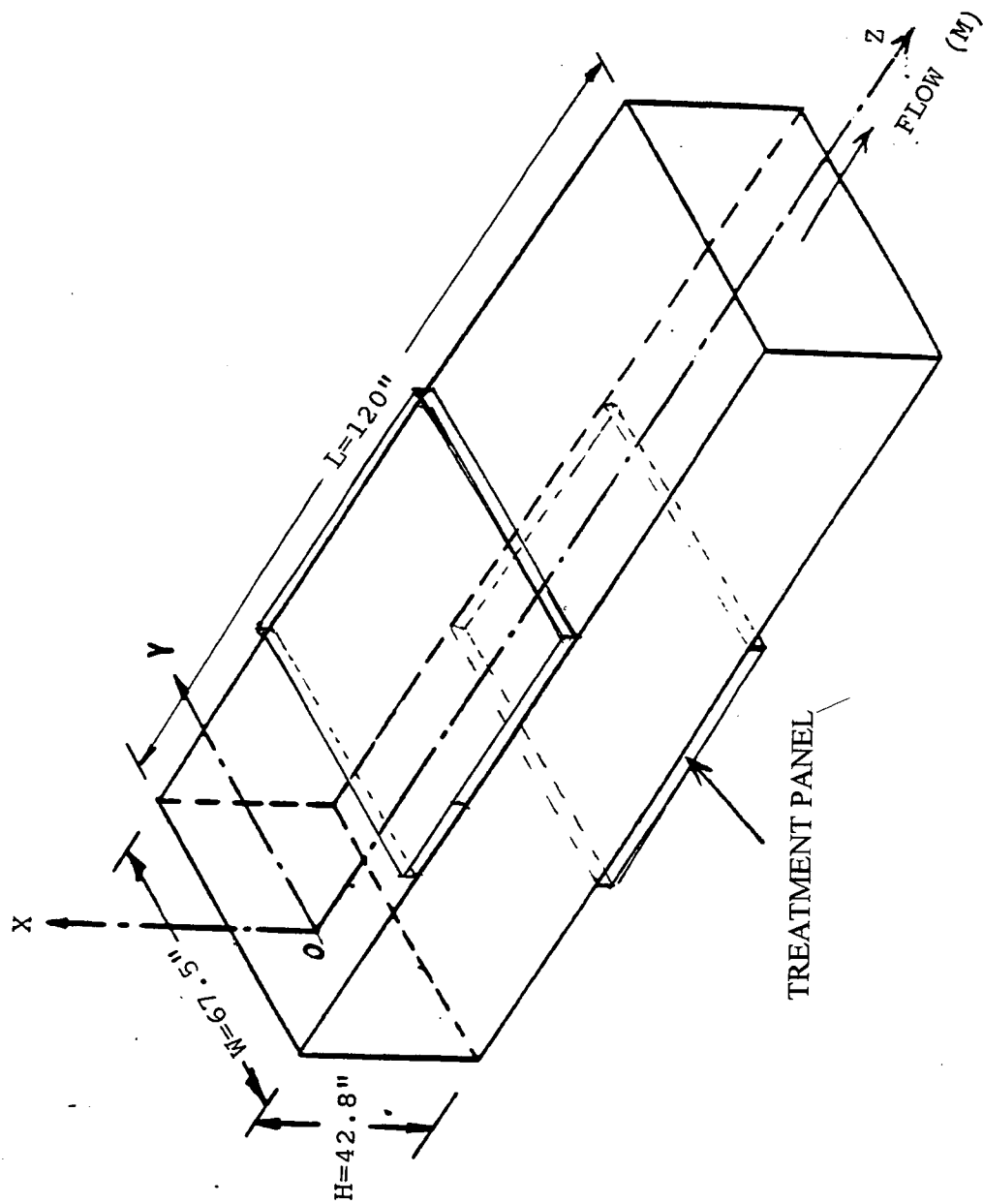


Figure 14. Schematic of the treated rectangular duct

results for Mach numbers greater than $M=0.4$ is not known at this time. During the lab test phase of this program, the range of validity of these correlation will be extended up to about $M=0.8$ by obtaining data at high subsonic Mach numbers. At this time, the method is exercised up to $M=0.8$ and not any higher due to concern over extending these correlation to supersonic Mach numbers. Acoustic suppressions are computed for liners of 1 foot long. However, the suppressions for any desired liner lengths can be obtained by multiplication of the length with the suppression per unit length.

Modal Analysis Technique: A rectangular duct modal analysis computer program has been adapted to evaluate the acoustic suppression performance of treated rectangular ejectors. It has been developed to assess different treatment concepts prior to fabrication. The intent here is only to assess the sound absorbing capability of acoustically lined surfaces inside ejectors operating at high speed and high temperature. No effort is made to account for source distributions. The analytical method has therefore been simplified to duct modal analysis with the assumption of equal modal energy distribution. The following input specifications are required to predict acoustic suppression utilizing the modal analysis computer program :

- 1) Frequency Range (actual frequencies and number of steps)
- 2) Impedance spectra at corresponding frequencies of one or more of the four surfaces of a rectangular duct.
- 3) Geometry of the rectangular ejector (height, width and length of treatment).
- 4) Mean axial Mach number and boundary layer thicknesses as a percentage of the appropriate transverse dimension.
- 5) Mean temperature and appropriate thermal boundary layer thickness.
- 6) Number of transverse modes to be included in the transmission loss evaluation.

Acoustic energy is being carried by all cut on modes starting at the source or at the beginning of the ejector treatment. Each mode loses energy to the duct wall by different amounts depending on the duct wall impedance spectra, the flow Mach number and temperature. The decay of energy from each mode is evaluated by solving a reduced form of the convected wave-equation and subjecting the solution to wall boundary conditions at the liner surfaces. The spectral energy flow in the ejector may be written as:

$$E(\omega, z) = E_{mn}(\omega, 0)e^{-2\alpha_{mn}z} \quad (1)$$

where $E(\omega, z)$ is spectral energy flux at an angular frequency ω and axial location z (see Figure 14). $E_{mn}(\omega, 0)$ is the spectral energy flux at the source location or at the entrance of the lined segment of the ejector for mn mode. α_{mn} is the modal decay rate of the treated ejector and is evaluated by solving the convected wave equation using all the input described above. It depends on the duct geometry, the wall impedance spectra and the Mach number. Derivation of Equation (1) and the method to evaluate modal decay rate are briefly described in the Appendix A. In the present method, at each frequency, $E_{mn}(\omega, 0)$ is assumed to be unity for all the cut on modes. This assumption may or may not be right, but does allow evaluation of an effective overall transmission loss and is suitable for making comparisons. If a more suitable modal energy distribution becomes available, it may be used as input in this program. It will not change the modal suppression but can impact on the overall suppression. The transmission loss T.L is evaluated from

$$T.L = 10 \log_{10}[E(\omega, z)/E(\omega, 0)] \quad \text{in dB} \quad (2)$$

The overall acoustic suppression of the treated ejector expressed by equation 2 is a measure of the wall absorbing property. Other factors such as jet noise reduction due to reduced velocity as a result of entrainment of ambient air and corresponding source modification are not included. The influence of turbulence inside the ejector is not taken into account. For the preliminary design study the acoustic suppression due to 10 transverse modes along the lined sides of the ejector is predicted.

Impedance spectra used for acoustic suppression prediction are assumed to be the same at all flow Mach numbers. Acoustic suppression spectra at different flow Mach numbers for the nominal design panels are predicted. In addition, sensitivity of these results are studied by altering the parameters associated with each of the liner concepts at a fixed Mach number of $M=0.8$.

2.3.3 Optimum Liner Designs: The geometric parameters (i.e., liner depths, facesheet and septum thicknesses) of the liners are assumed before optimizing the design parameters (i.e., DC flow resistance and nonlinear factor). Each liner panel is designed with same depth (h) of 2 inches. A 0.036 inches thick (t) face sheet is assumed for the SDOF liner. For 2DOF liner the cavity is divided by the septum, such that the depths of upper and lower layers (i.e., h_1 and h_2) become 0.5 and 1.5 inches, respectively. The facesheet and septum thicknesses are kept the same and are 0.036 inches. For the bulk absorber a face sheet of 0.05 inches thick and the bulk material of 1.95 inches thick are assumed. The optimum design parameters for each of the liners are listed below:

	Parameters	At 1750°R	At Room Temperature
1.	Millipore Facesheet for SDOF:		
	R_{100} , cgs Rayls	50	102.7
	$NLF_{150/20}$	5	6.8
	A, cgs Rayls	5.55	2.44
	B, cgs Rayls/(cm/s)	0.444	1.003
2.	Wiremesh Facesheet for SDOF:		
	R_{100} , cgs Rayls	55	71.8
	$NLF_{150/20}$	2	4.1
	A, cgs Rayls	28.8	12.65
	B, cgs Rayls/(cm/s)	0.262	0.59
3a	Millipore Facesheet for 2DOF:		
	R_{100} , cgs Rayls	25	51.4
	$NLF_{150/20}$	5	6.8
	A, cgs Rayls	2.78	1.22
	B, cgs Rayls/(cm/s)	0.222	0.5
3b	Millipore Septum for 2DOF:		
	R_{100} , cgs Rayls	40	82.2
	$NLF_{150/20}$	5	6.8
	A, cgs Rayls	4.44	1.95
	B, cgs Rayls/(cm/s)	0.356	0.8
4a	Linear Facesheet Resistivity for Bulk Absorber:, $(R_{DC})_f$, cgs Rayls	19.35	8.5
4b	Bulk Material Resistivity for Bulk Absorber, $(R_{DC})_{ab}$, cgs Rayls	56.9	25

It should be noted that the impedance prediction method utilized for bulk absorber does not account for any nonlinear effects. In addition, the computer program utilizes the input resistance value at room temperature and converts it for the operating temperature. Therefore, the optimization is carried out for room temperature input.

2.3.4 Predicted Normal Impedance Spectra: Impedance spectra for the optimum liner designs are compared in Figure 15. The SDOF designs achieve the resistance goal for almost entire frequency range. Whereas, the reactance values are out side the limits for lower and higher ends of the frequency range. The 2DOF design achieves resistance and reactance goals for higher frequencies. The bulk absorber seems to achieve the impedance goal more closely compared to other designs. The impedance behavior is reflected in the absorption coefficient spectrum for normal incidence (see Figure 16). The SDOF design exhibit very poor level of absorption coefficients at both ends of frequency range, whereas, 2DOF design suffers this

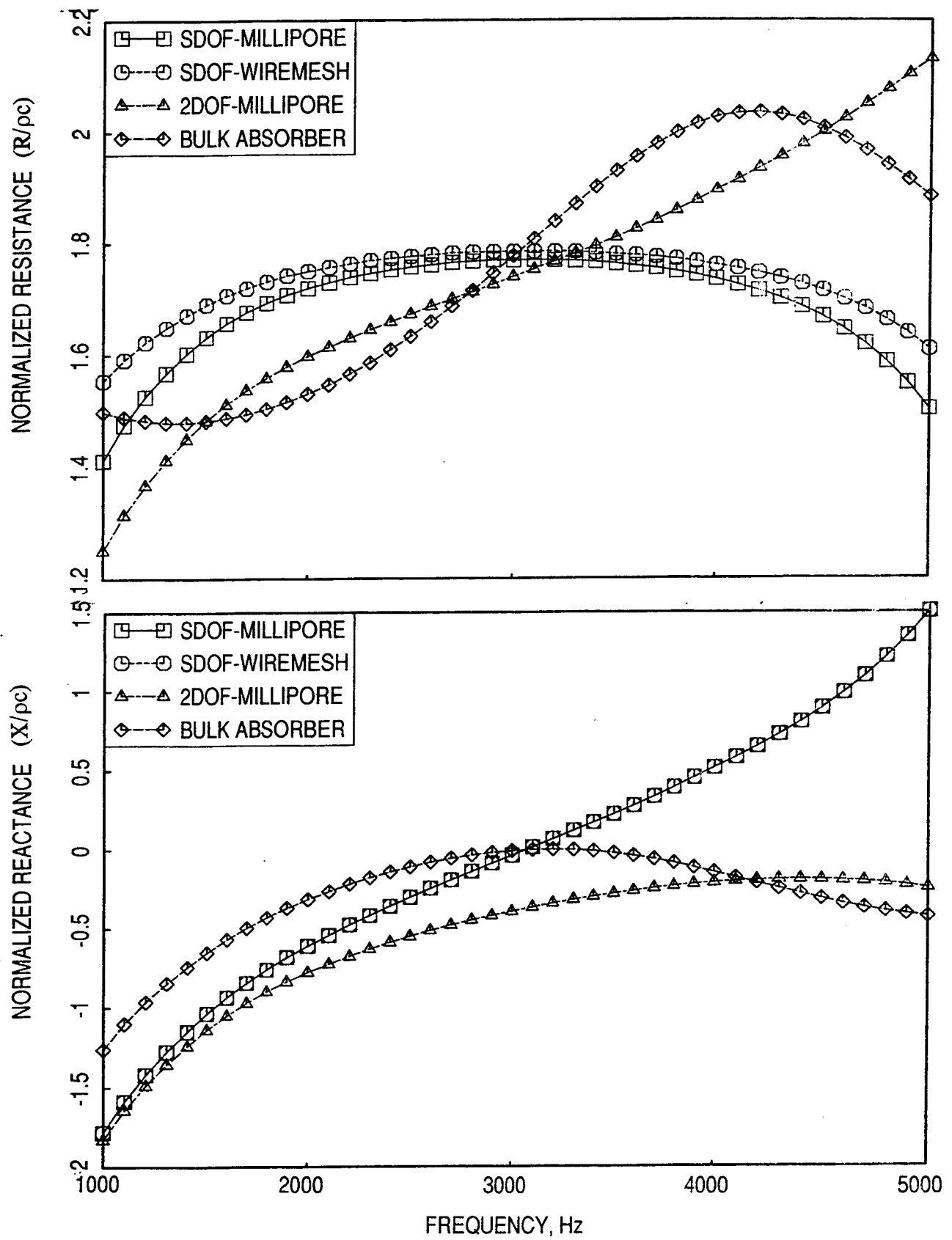


Figure 15. Predicted normal impedance spectra for four optimum liner designs.

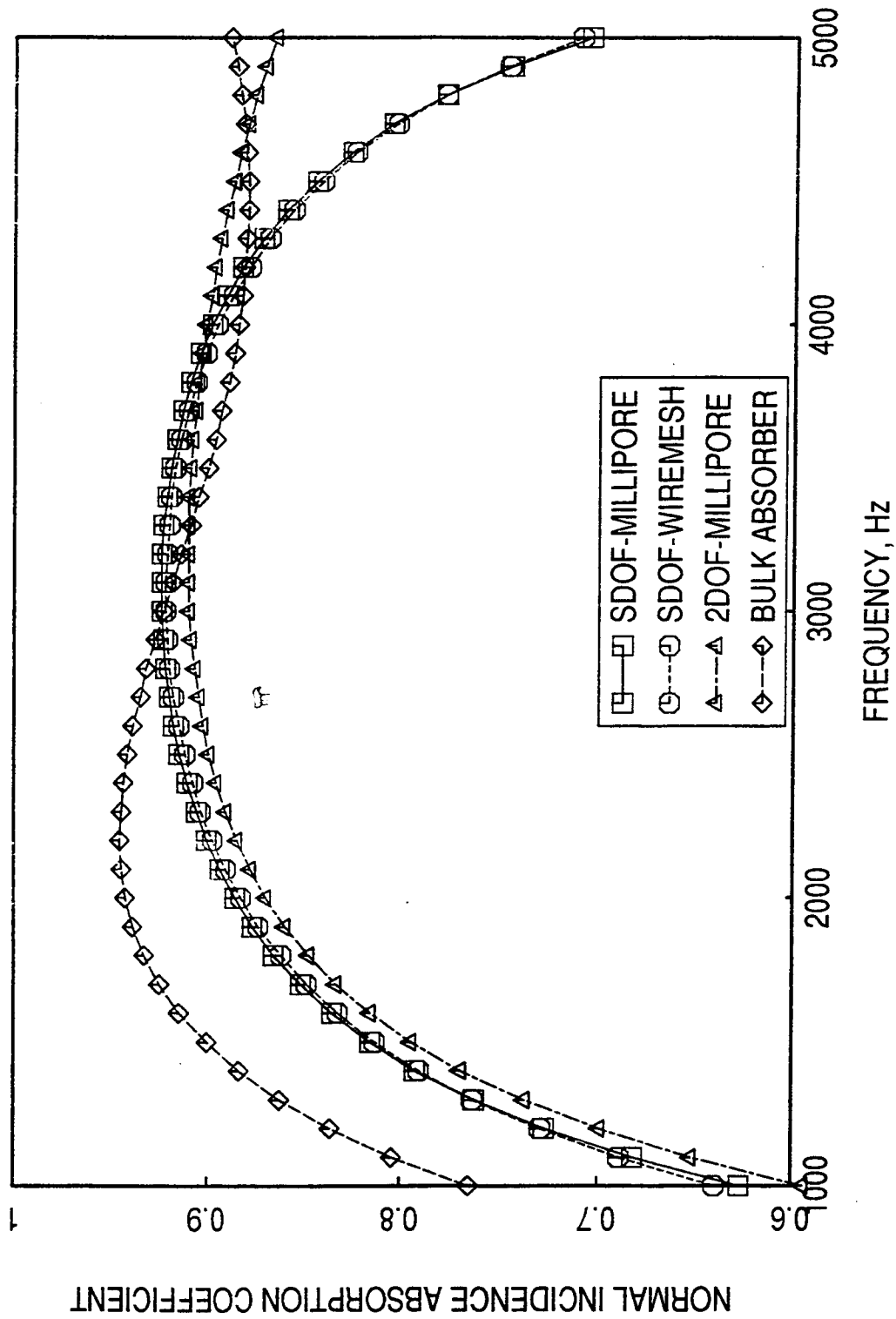


Figure 16. Predicted normal incidence absorption coefficient spectra for four optimum liner designs.

problem only at lower frequency end. The bulk absorber shows reasonably higher absorption coefficients for entire frequency range.

The impedance models used to predict the design impedance spectra are based on current treatment materials, which are applicable to subsonic inlet treatment designs and are not validated/calibrated for high temperature and high Mach flow regions of ejector nozzles. The normal incidence absorption coefficient spectra are deemed useful for relative assessment, since the source distribution is not well defined and also acoustic waves may not be normally incident to the liner surfaces.

2.3.5 Empirically Predicted Acoustic Suppression: Acoustic suppression spectra for all the four optimum liners are computed at a number of flow Mach numbers utilizing the impedance spectra of Figure 15. These results are shown in Figures 17 through 20. For each liners the amount of acoustic suppression decreases with increasing Mach number. The peak suppression occurs at about 2 kHz for SDOF and 2DOF type liners, whereas, for bulk absorber the peak suppression frequency is slightly lower than 2 kHz. These results are cross plotted in Figure 21 along with the impedance spectra of Figure 15 to compare the suppression capability of the liners at a given Mach number. At each Mach number the suppression characteristics between the liners are similar. The bulk absorber suppresses more acoustic energy compared to others, especially at lower frequencies. Suppressions due to 2DOF type liner matches with those due to SDOF type liners at lower frequencies and with those due to bulk absorber at higher frequencies. These characteristics are similar to those observed in predicted normal incidence absorption coefficient spectra of Figure 16.

At grazing flow of Mach number 0.8, suppressions as high as 0.75 dB per foot of treatment length (i.e., 7.5 dB for total treatment of 10 feet long flaps of the full scale nozzle) is obtained for SDOF and 2DOF type liners at about 2 kHz (i.e., peak frequency). The bulk absorber yields even higher suppressions, that the peak suppression level is about 0.9 dB per foot of treatment length (i.e., 9 dB for full-length treatment) at about 1600 Hz. These suppression levels are the insertion losses in terms of PWL within the lined duct and are not the farfield PWL or EPNL suppression

2.3.6 Predicted Acoustic Suppression by Modal Analysis: Acoustic suppressions due to the optimized Single-Degree-of-Freedom (SDOF) type liner with a Millipore (perforated) type facesheet, are predicted for a full scale 10' long rectangular duct, with two of the 67.5" sides being lined (see Figure 14), at several flow Mach numbers (between 0 and 2). Effect of number of modes, flow Mach number and number of treated sides on acoustic suppression are

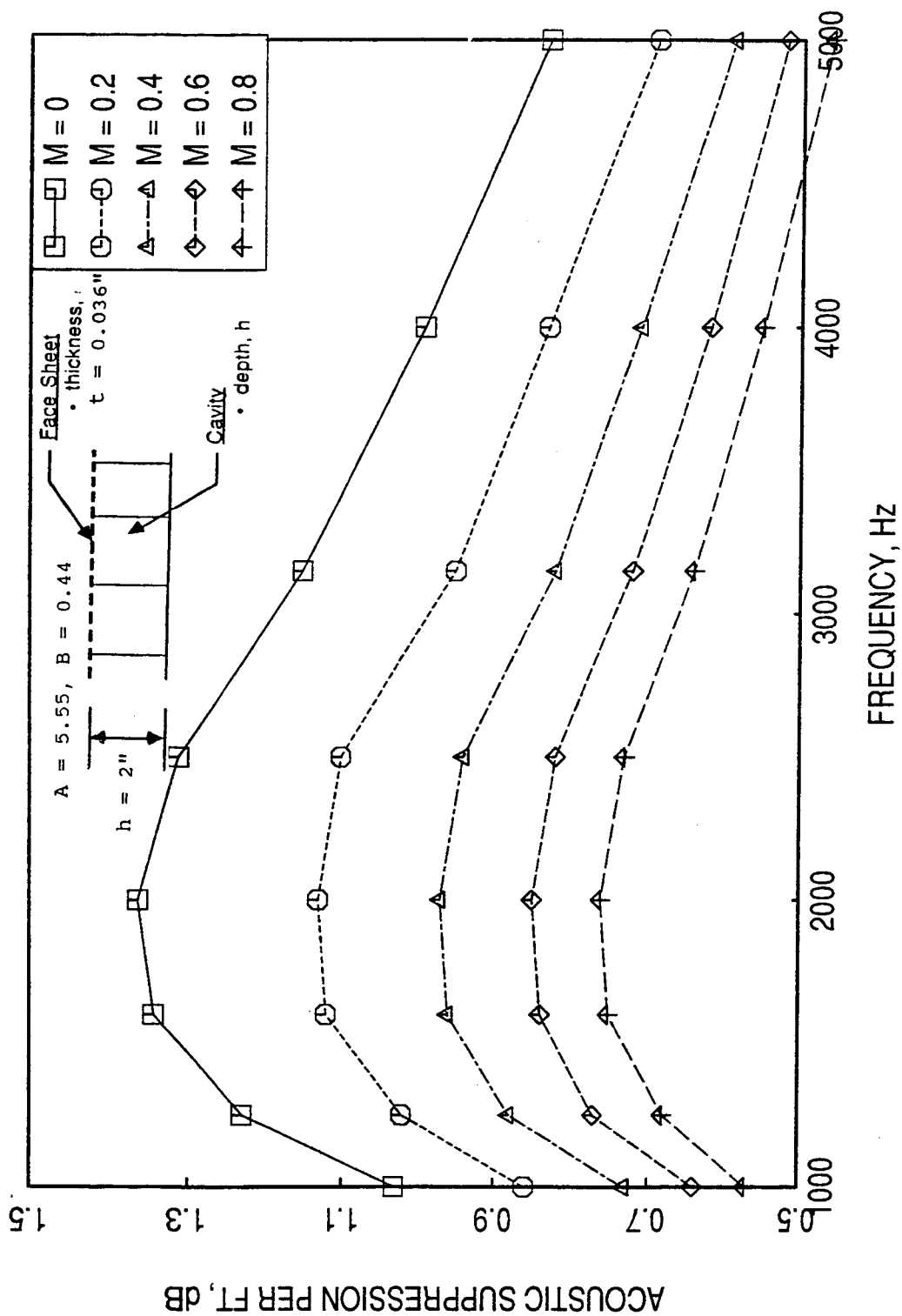


Figure 17. Effect of grazing flow (Mach number M) on empirically predicted acoustic suppression for an SDOF type liner with Millipore facesheet.

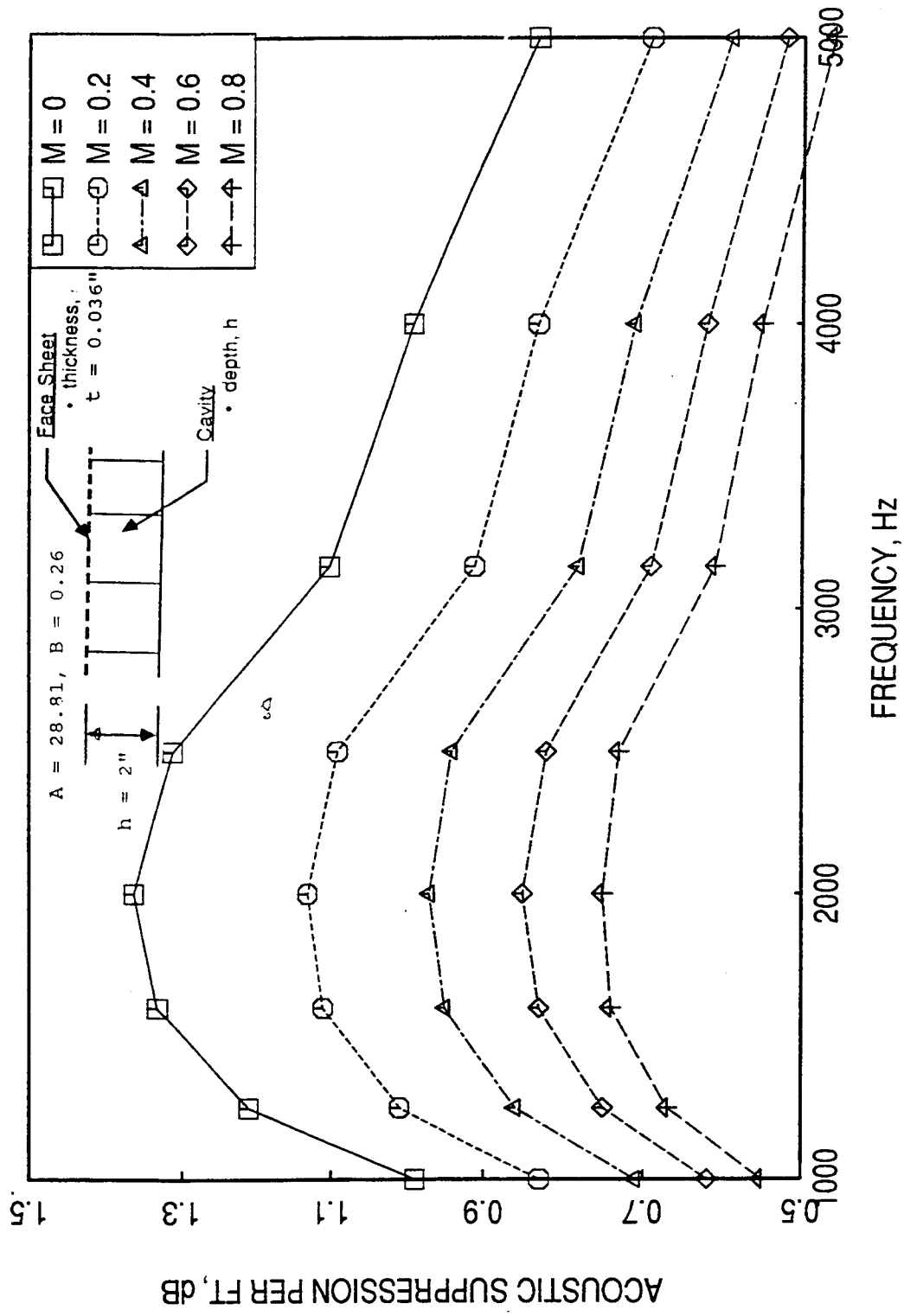


Figure 18. Effect of grazing flow (Mach number M) on empirically predicted acoustic suppression for an SDOF type liner with wiremesh facesheet.

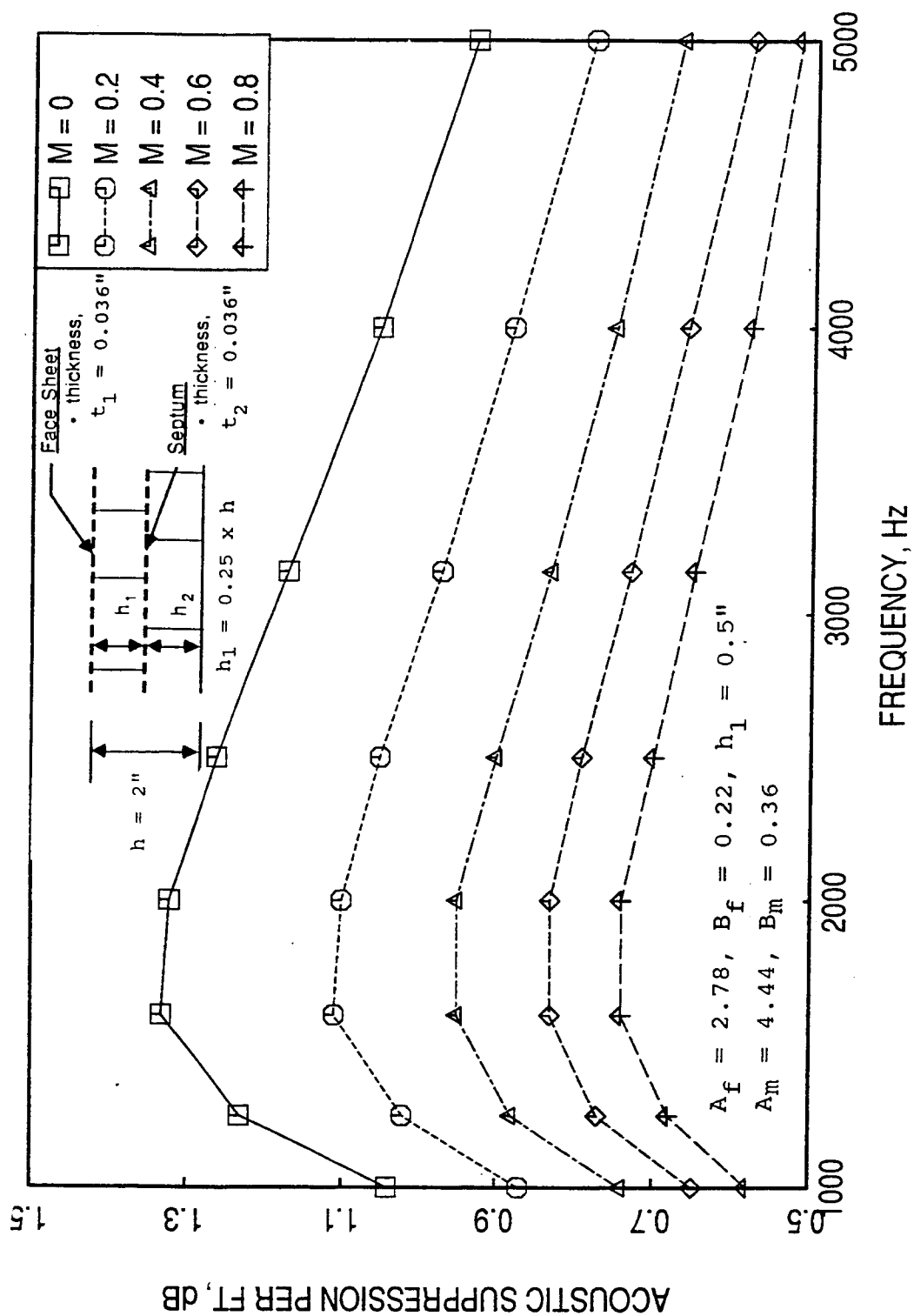


Figure 19. Effect of grazing flow (Mach number M) on empirically predicted acoustic suppression for a 2DOF type liner with Millipore facesheet and septum.

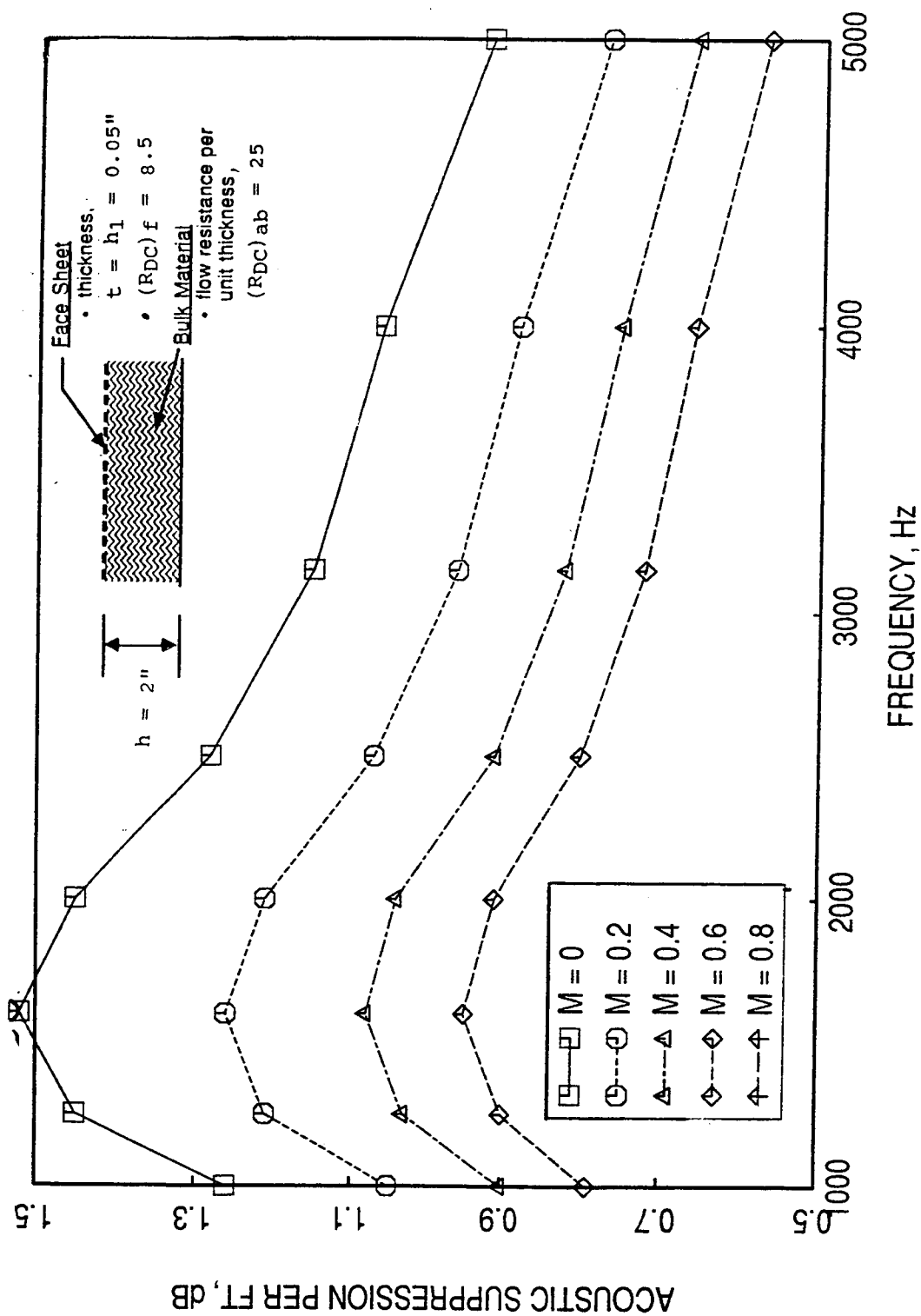


Figure 20. Effect of grazing flow (Mach number M) on empirically predicted acoustic suppression for a bulk absorber liner with a thin resistive facesheet.

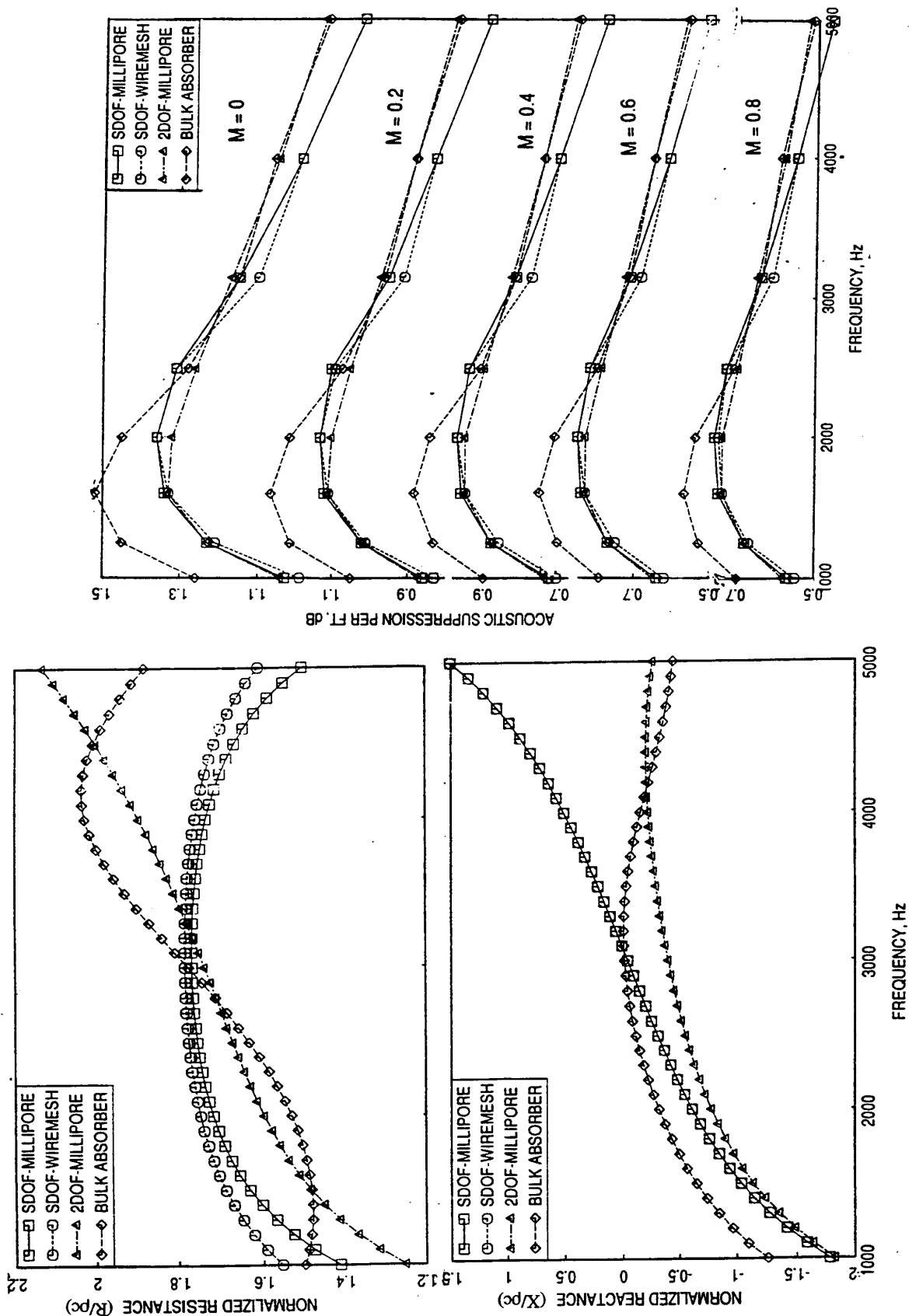


Figure 21. Predicted normal impedance spectra and acoustic suppression (empirical) spectra at a number of grazing flow Mach numbers (M) for four optimum liner designs.

evaluated. Impedance spectra used for acoustic suppression prediction were assumed to be the same at all flow Mach numbers.

Figure 22 shows the acoustic suppression due to the two sided lined duct for a number of transverse modes along x-direction at $M = 0.0$ and 0.4 . The computation is performed for the first 10 modes. At lower frequencies less than 10 modes are cut-on, since there is no contribution due to higher order modes. First 8 modes seem to contribute up to 2200 Hz and the 9th mode cuts on. The 10th mode cuts on at about 2500 Hz. Beyond this frequency all 10 modes are contributing to the acoustic suppression. To account for the complete suppression more number of modes need to be considered at frequencies above 2500 Hz. However, the contribution due to a mode diminishes with increasing mode order. Therefore, the first 10 modes may be adequate for the present analysis. Similar results for flow Mach numbers of 0.8, 1.2, 1.6, and 2.0 are presented in Figures 23 and 24. More number of modes propagate in the duct with increasing Mach number. All 10 modes are cut on from 1000 Hz at and above $M = 1.2$. The suppression peaks up at about 2000 Hz at and above $M = 0.8$, the optimization being aimed at $M = 0.8$ with tuning frequency of 2000 Hz.

Figure 25 shows the acoustic performance due to the two sided lined duct for the first 10 transverse modes along x-direction for different axial Mach number. The main observation is that axial Mach number seems to reduce the maximum achievable suppression. The peak suppression for $M > 0.8$ occurs in the range of 1.5 to 2.5 kHz. Figure 26 is a cross plot of Figure 25 to show the effect of axial Mach number on the suppression at different frequencies. Maximum suppression is obtained at 1500 to 2000 Hz at all Mach numbers. At higher frequencies, the flow effects are relatively small. Figure 27 shows the effect of treating only one side of the ejector compared to both sides at different Mach numbers. Two sided lined ejector gives more suppression compared to single sided treatment at all frequencies and at all flow conditions. However, the amount of suppression is not simply doubled due to twice the amount of treatment. Except for $M = 0.0$ and 0.2 , where, more than 6 dB increase in suppression is observed at lower frequencies, the amount of increase is less than 6 dB (i.e., doubling of suppression in dB) for all frequencies and Mach numbers.

Acoustic suppression predictions obtained by empirical correlation (reported in the last two monthly narratives) are compared with the present prediction method in Figure 28. While, the trends with respect to frequency are similar, the actual suppressions derived by these methods are quite different. At $M = 0.0$ the empirical correlation yields more suppression compared to the amount evaluated by modal analysis. The trend is reversed with increasing flow Mach number.

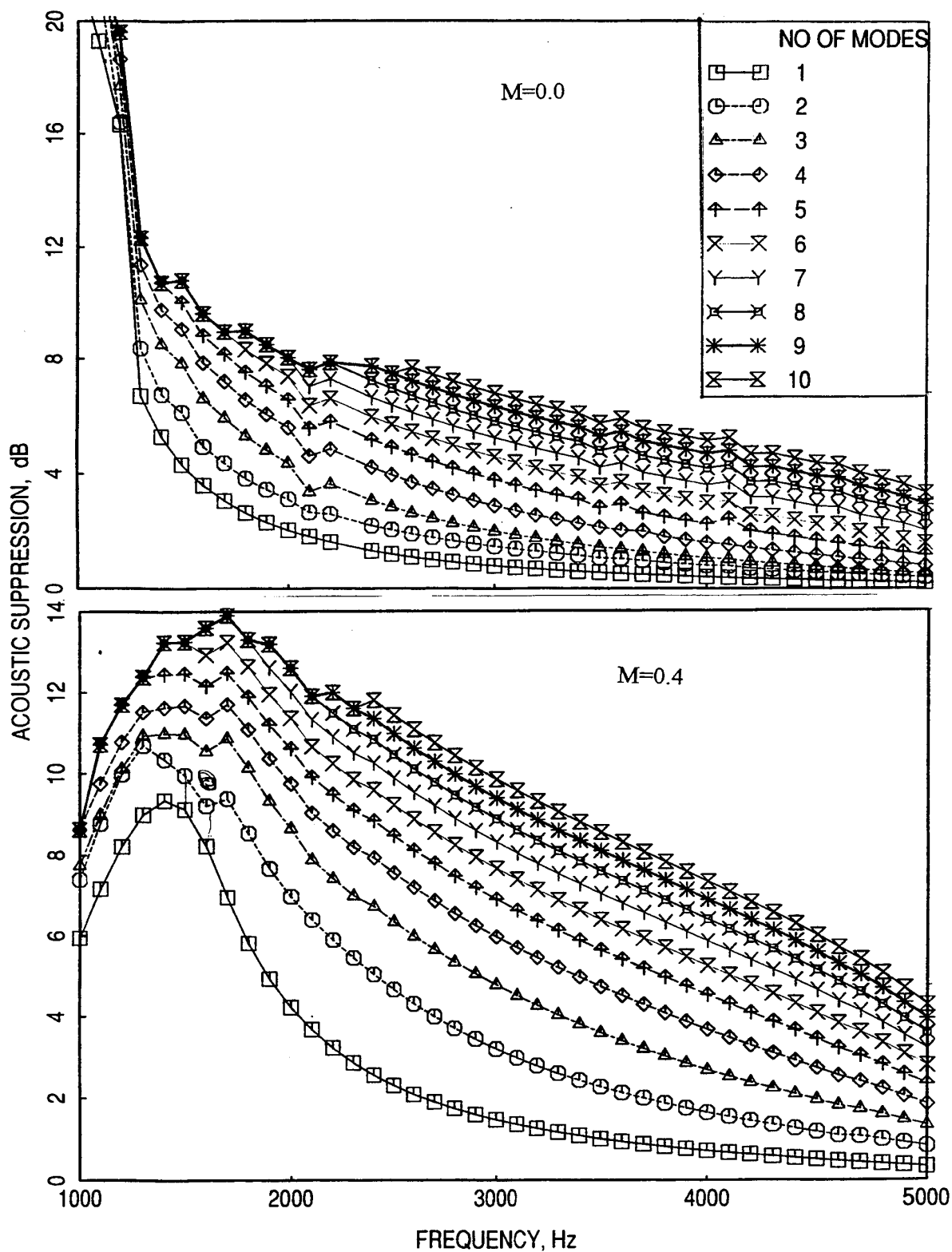


Figure 22. Acoustic suppression spectra, predicted by modal analysis, for a two sided lined duct due to several transverse modes (in X direction) evaluated at $M=0$ and 0.4 .

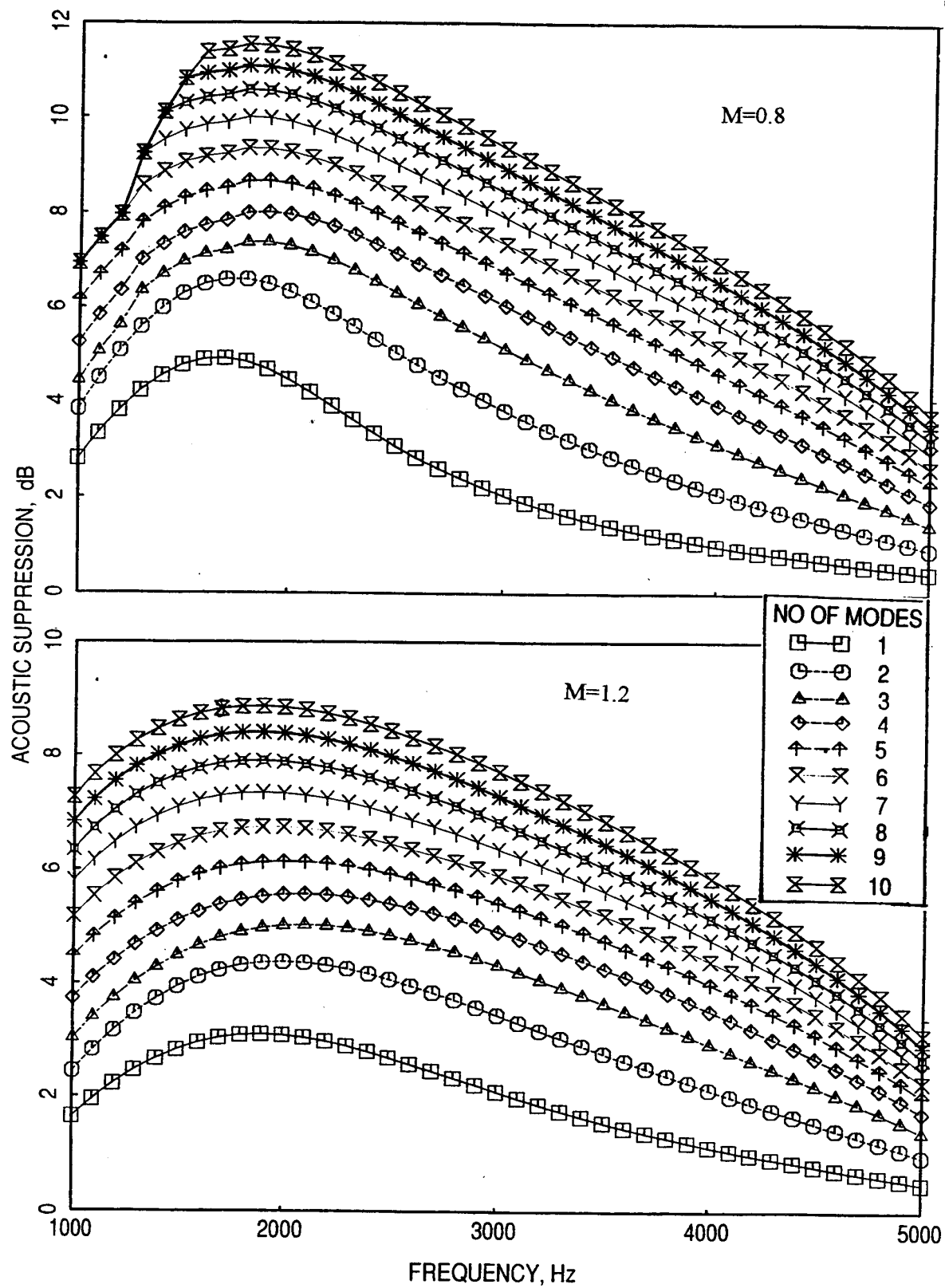


Figure 23. Acoustic suppression spectra, predicted by modal analysis, for a two sided lined duct due to several transverse modes (in X direction) evaluated at $M=0.8$ and 1.2 .

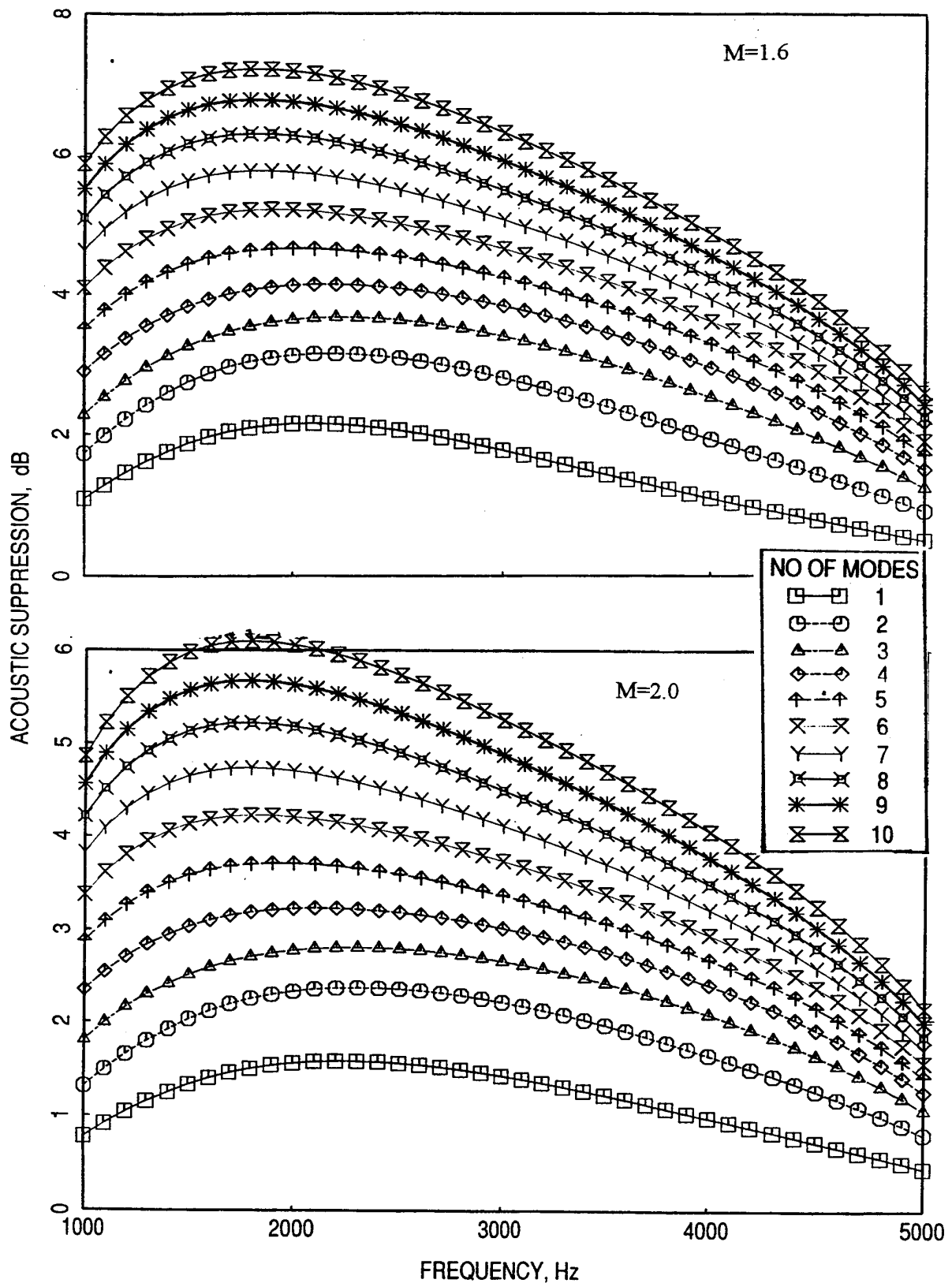


Figure 24. Acoustic suppression spectra, predicted by modal analysis, for a two sided lined duct due to several transverse modes (in X direction) evaluated at $M=1.6$ and 2.0 .

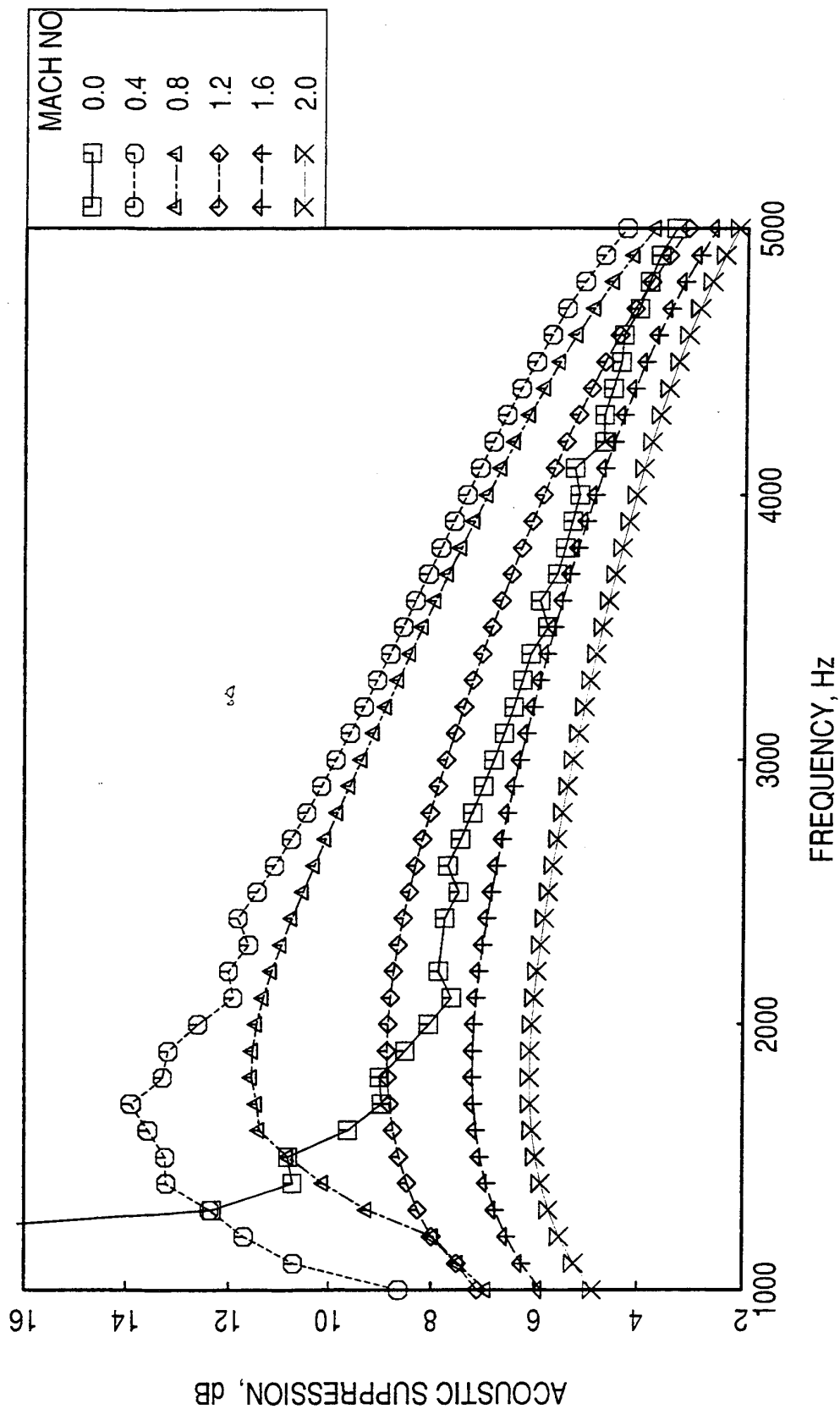


Figure 25. Effect of flow Mach number on acoustic suppression spectra, predicted by modal analysis, for a two sided lined duct due to 10 transverse modes (in X direction).

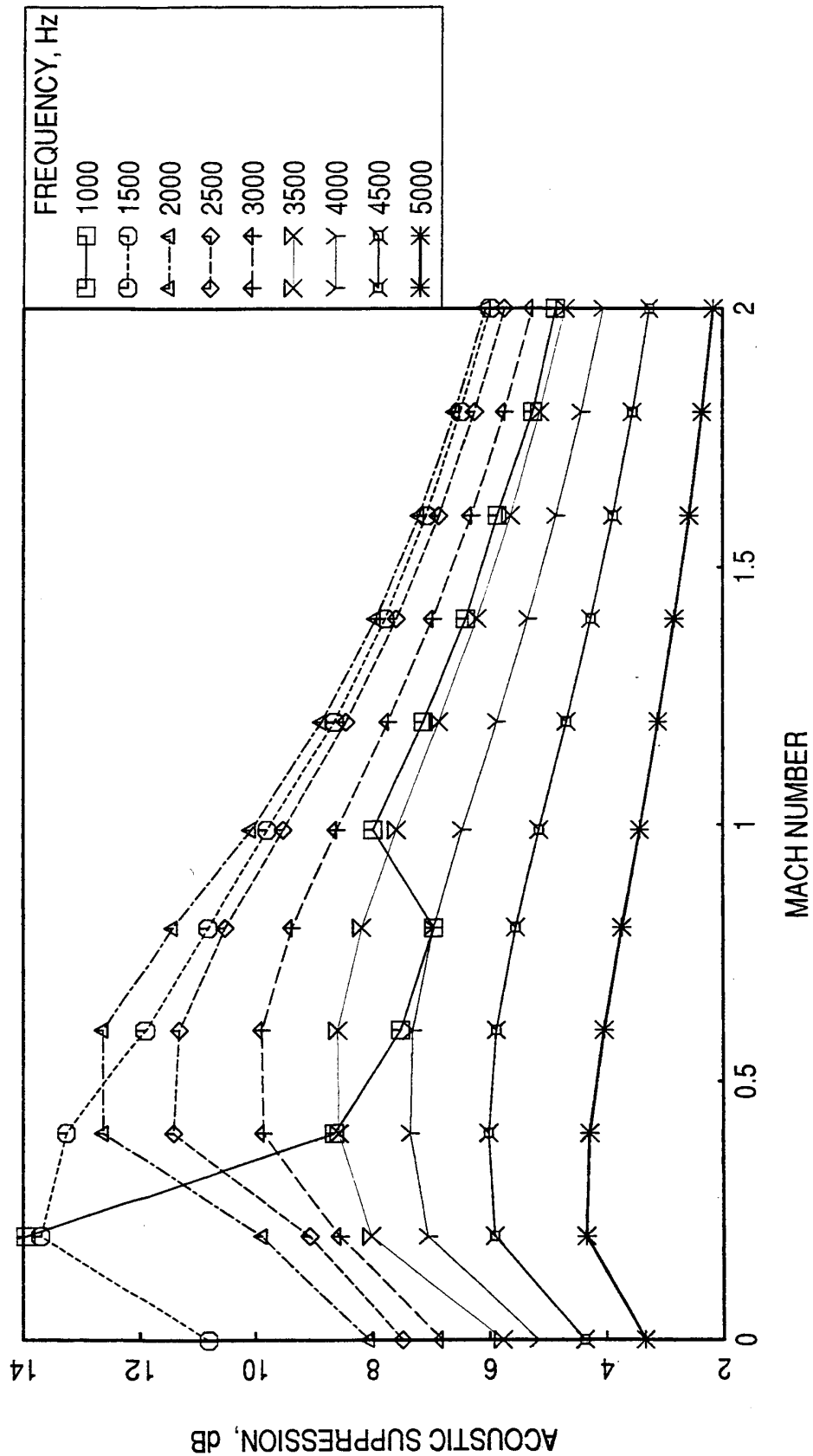


Figure 26. Effect of flow Mach number on acoustic suppression, predicted by modal analysis, at a number of frequencies for a two sided lined duct due to 10 transverse modes (in X direction).

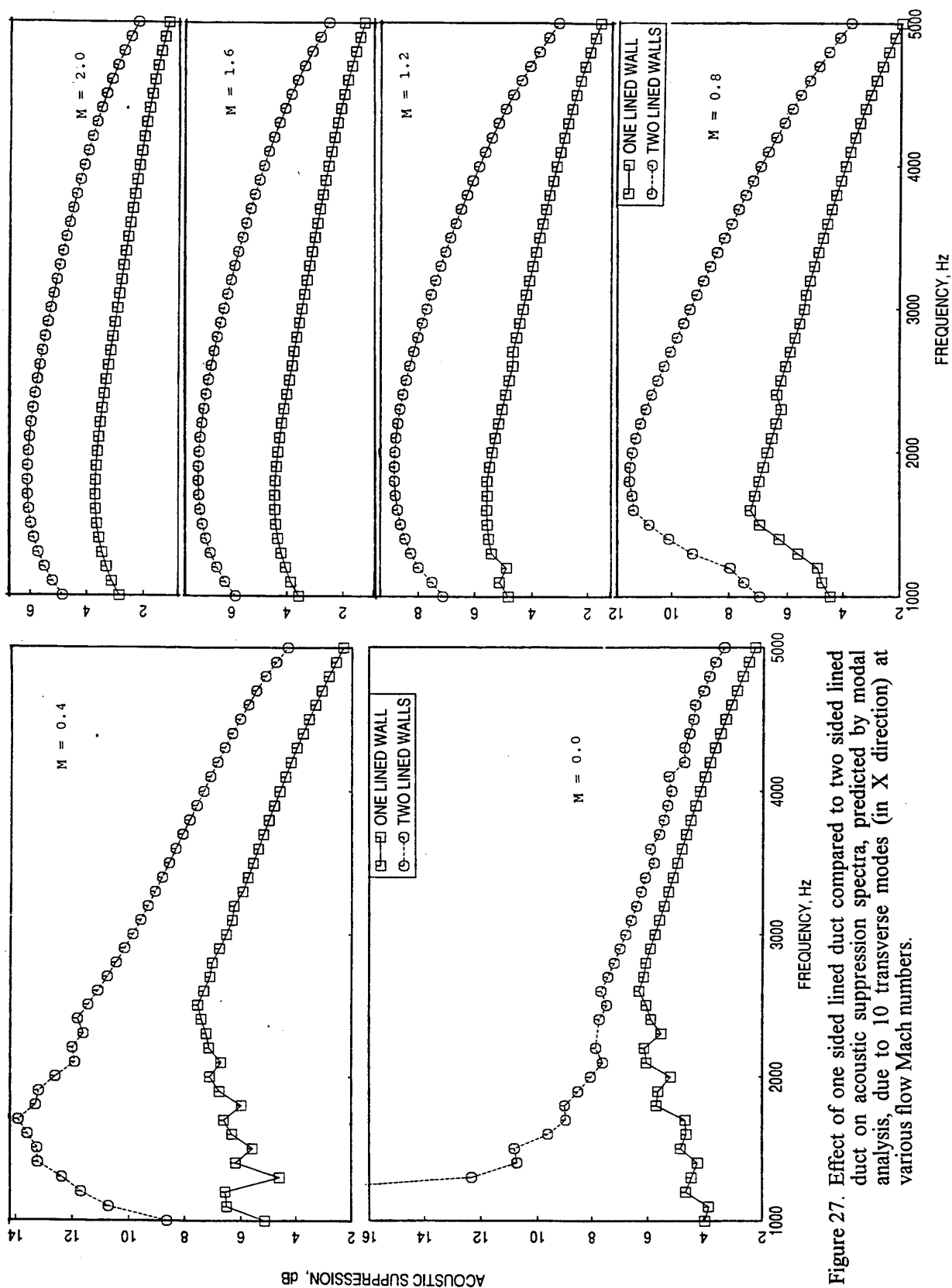


Figure 27. Effect of one sided lined duct compared to two sided lined duct on acoustic suppression spectra, predicted by modal analysis, due to 10 transverse modes (in X direction) at various flow Mach numbers.

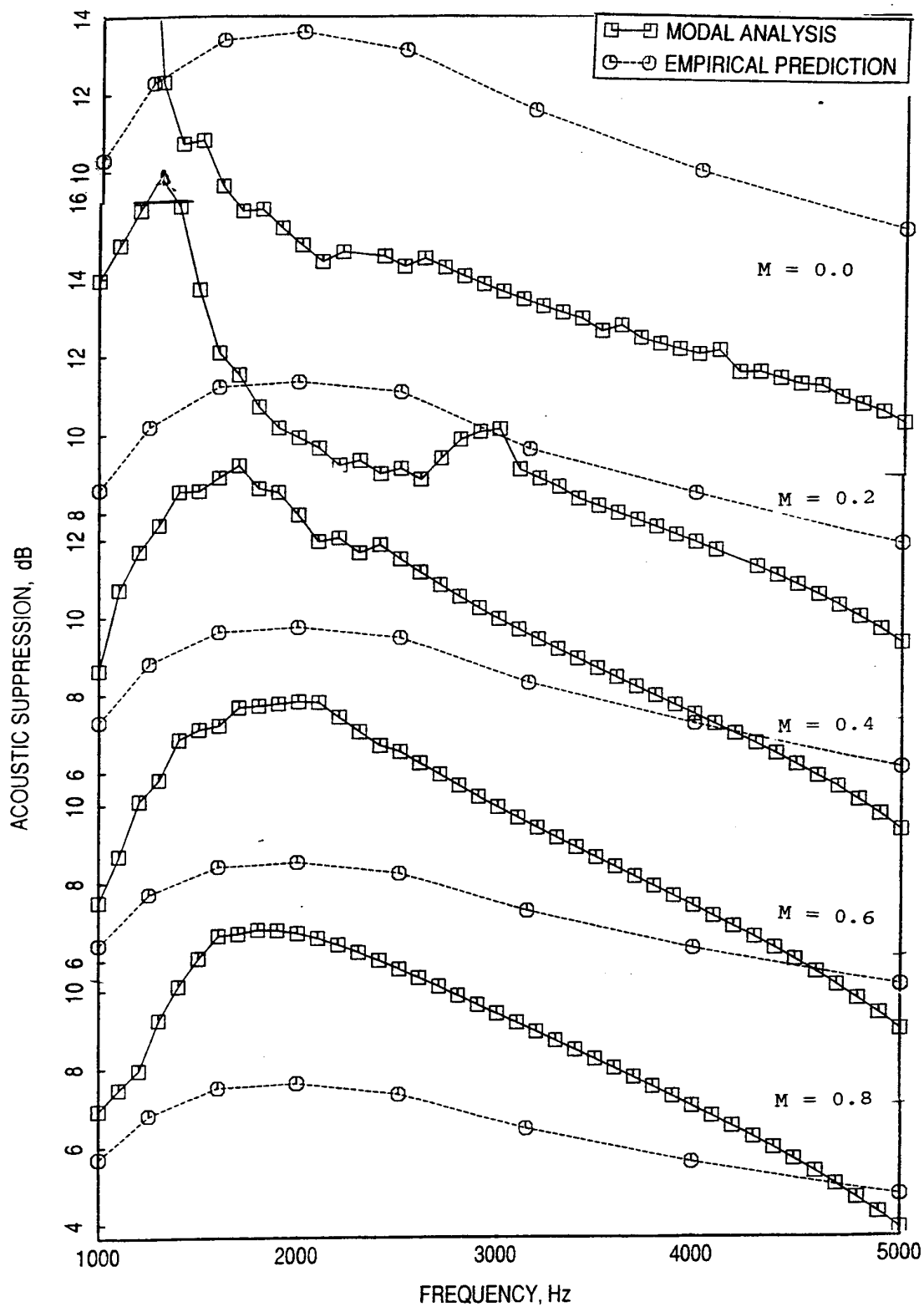


Figure 28. Comparison of acoustic suppression spectra predicted by modal analysis method (for 10 transverse modes along x direction) with those predicted by empirical correlation for a two sided lined duct.

2.3.7 Influence of Design Parameters: Geometric and design parameters for each of the four liners are varied and the corresponding normal impedance, absorption coefficient, and acoustic suppression spectra are evaluated to study the effect of these parameters on liner characteristics. Objective of these studies is to identify the sensitivity of liner characteristics due to various parametric variation, so that final design can incorporate parameters that yield large levels of acoustic suppression over most of the desired frequency range.

1. SDOF with Millipore Face Sheet: The input resistance, R_{100} , is increased and decreased by 50% of the design value of 50 cgs Rayls, keeping all other parameters the same as those of the optimum design case. The corresponding A and B values for R_{100} of 75, 50, and 25 are used as the parameters in the comparison of resistance, absorption coefficient, acoustic suppression spectra, shown in Figure 29. The reactance values do not change since the cavity dimensions are not altered and the mass reactance portion is ignored in the present analysis. As expected the resistance level increases proportionately with increasing A and B. The absorption coefficient levels at mid frequencies increase with decreasing resistance, but fall rapidly at both ends of the frequency range. The acoustic suppression levels predicted by both methods, increase with decreasing resistance at lower frequencies, but the trend is reversed at higher frequencies.

Next, the cavity depth is altered and the corresponding impedance and acoustic suppression spectra are plotted in Figure 30. With a lower cavity depth, compared to design height of 2", the acoustic suppression improves slightly at higher end of the frequency range, whereas, the values are lower at most frequencies. For a deeper cavity the performance is improved at lower frequencies, but a "null" is noted at about 4 kHz.

2. SDOF with Wiremesh Face Sheet: Parametric results for this liner are generated similar to those for the SDOF with Millipore face sheet and are shown in Figures 31 and 32. The trends are very similar to the results for the SDOF with Millipore face sheet.

3. 2DOF with Millipore Facesheet and Septum: For this configuration the parameters varied include the facesheet resistance (A_f & B_f), septum or mid-plate resistance (A_m & B_m), relative position of mid-plate (h_1), and total cavity depth (h). Effect of facesheet and septum resistance on impedance, absorption coefficient, and acoustic suppression spectra are shown in Figures 33 and 34. Increasing resistivity of facesheet or septum basically increases the resistance of the liner, whereas, the reactance increases with facesheet resistivity but decreases with septum resistivity. Absorption coefficient increases with decreasing face sheet resistivity except for very low end of the frequency range, where, the trend is reversed. Septum

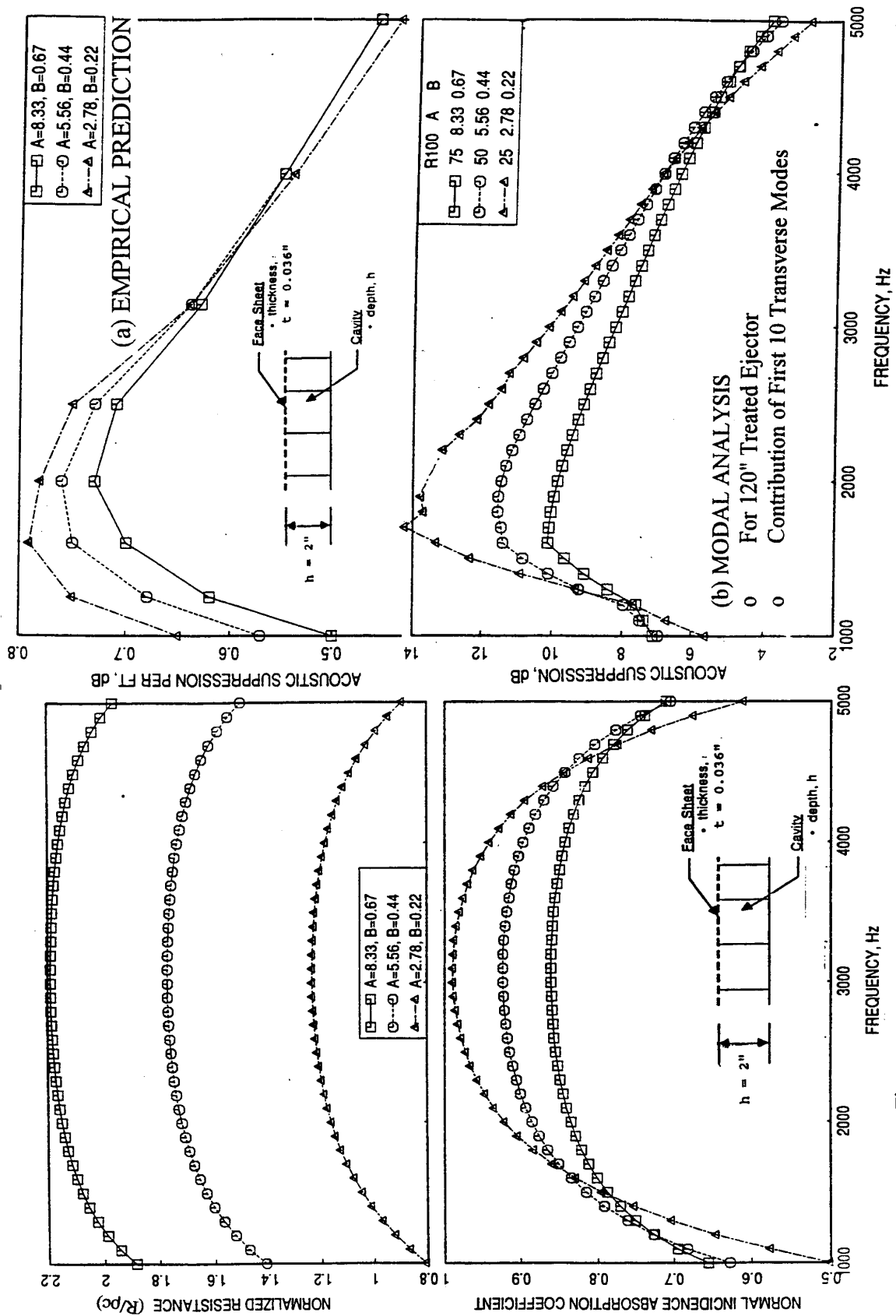


Figure 29. Influence of DC flow resistance (A & B) on predicted acoustic resistance, absorption coefficient, and acoustic suppression (at $M=0.8$) spectra for an SDOF type liner with Millipore facesheet.

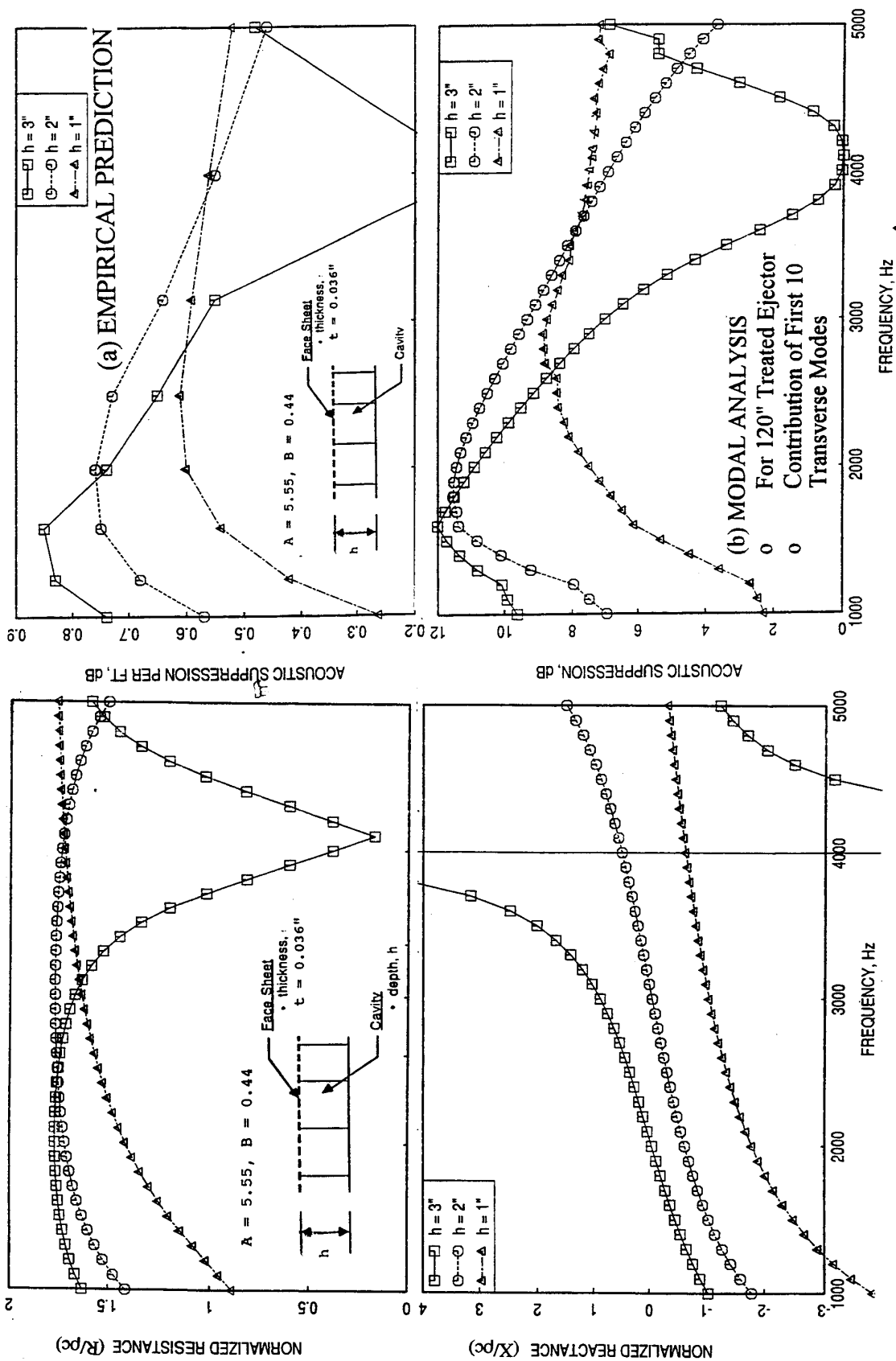


Figure 30. Effect of cavity depth (h) on predicted impedance and acoustic suppression (at $M=0.8$) spectra for an SDOF type liner with Millipore facesheet.

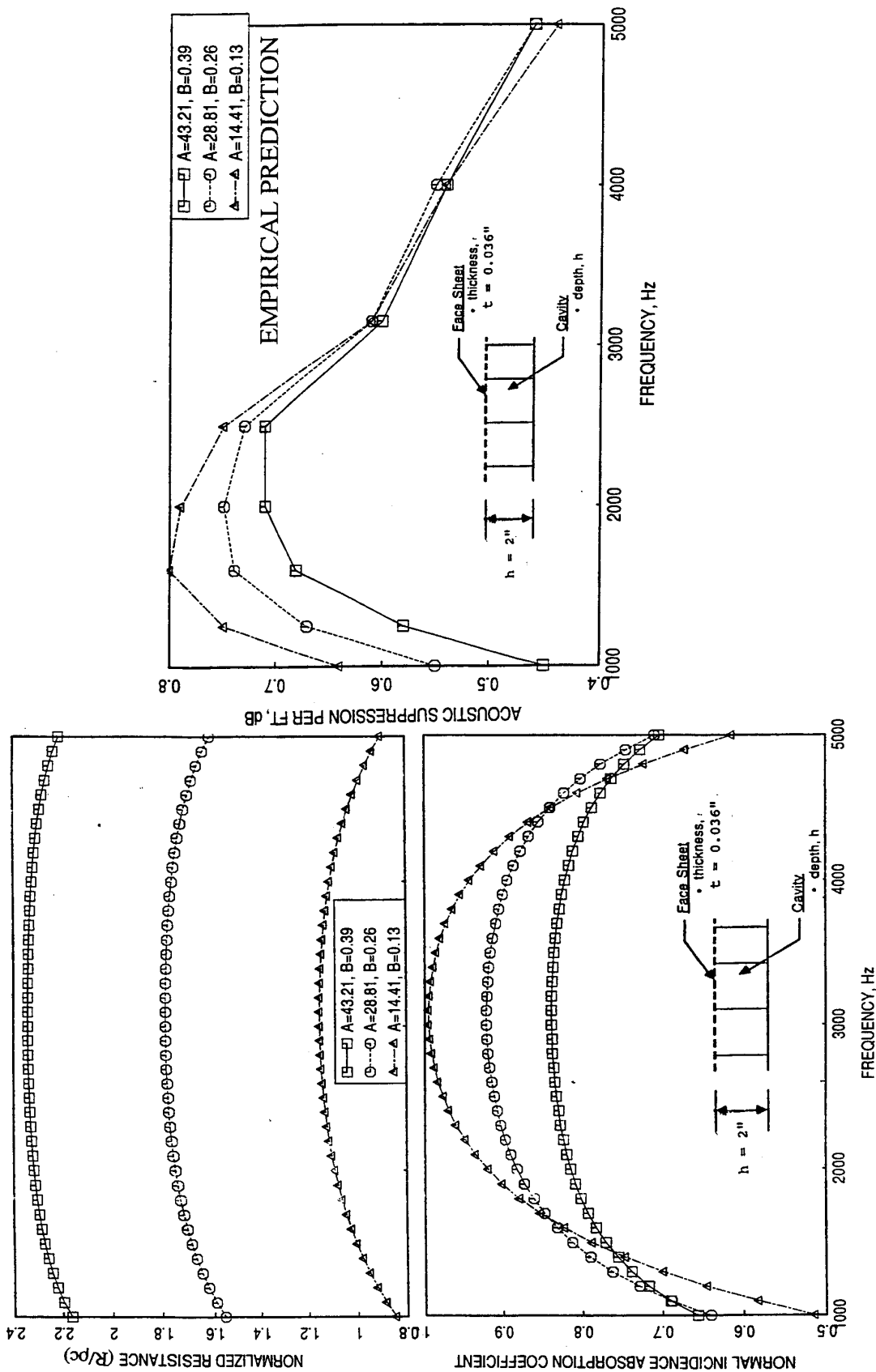


Figure 31. Influence of DC flow resistance (A & B) on predicted acoustic resistance, absorption coefficient, and acoustic suppression (at $M=0.8$) spectra for an SDOF type liner with wiremesh facesheet.

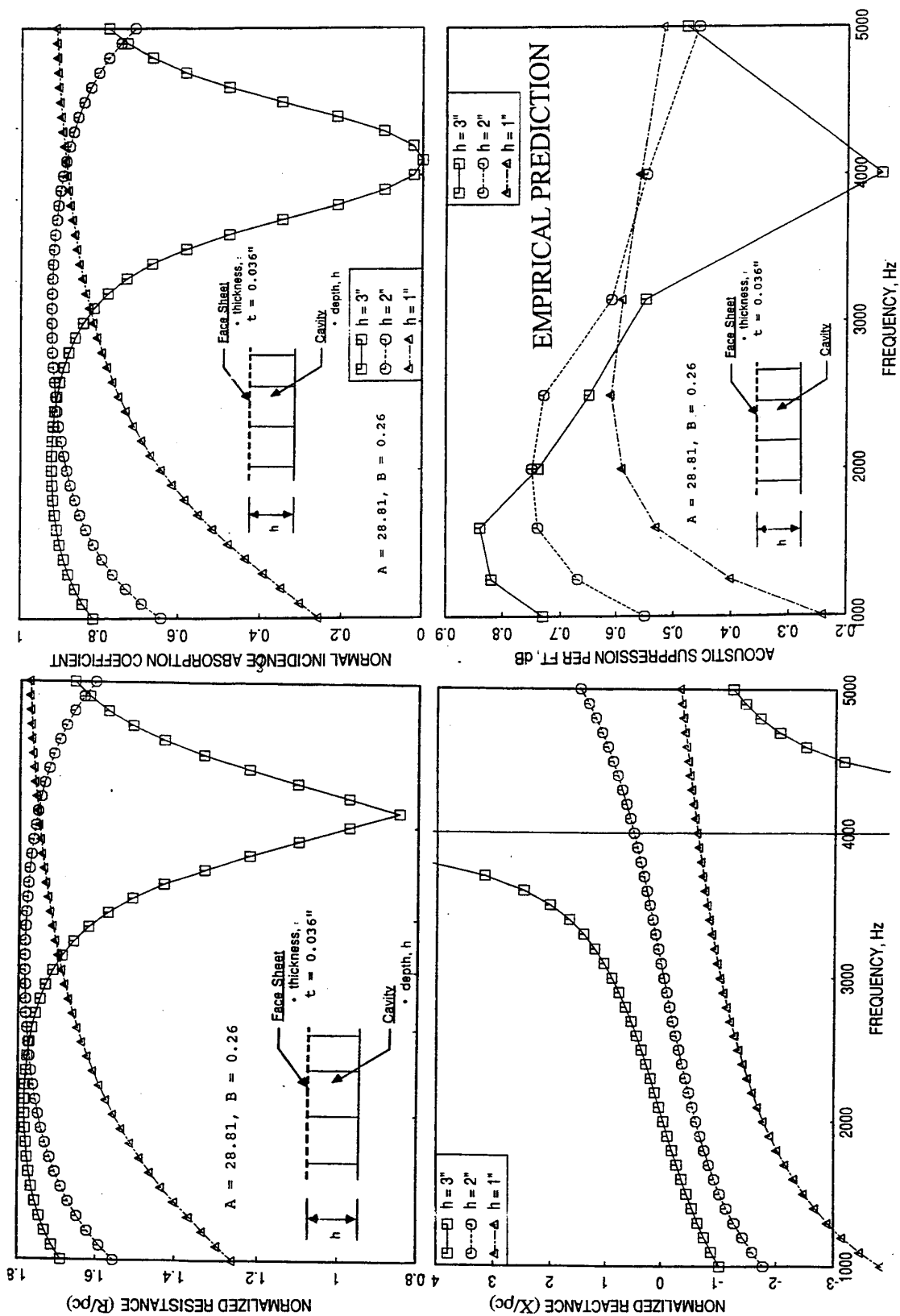


Figure 32. Effect of cavity depth (h) on predicted impedance, absorption coefficient, and acoustic suppression (at $M=0.8$) spectra for an SDOF type liner with wiremesh facesheet.

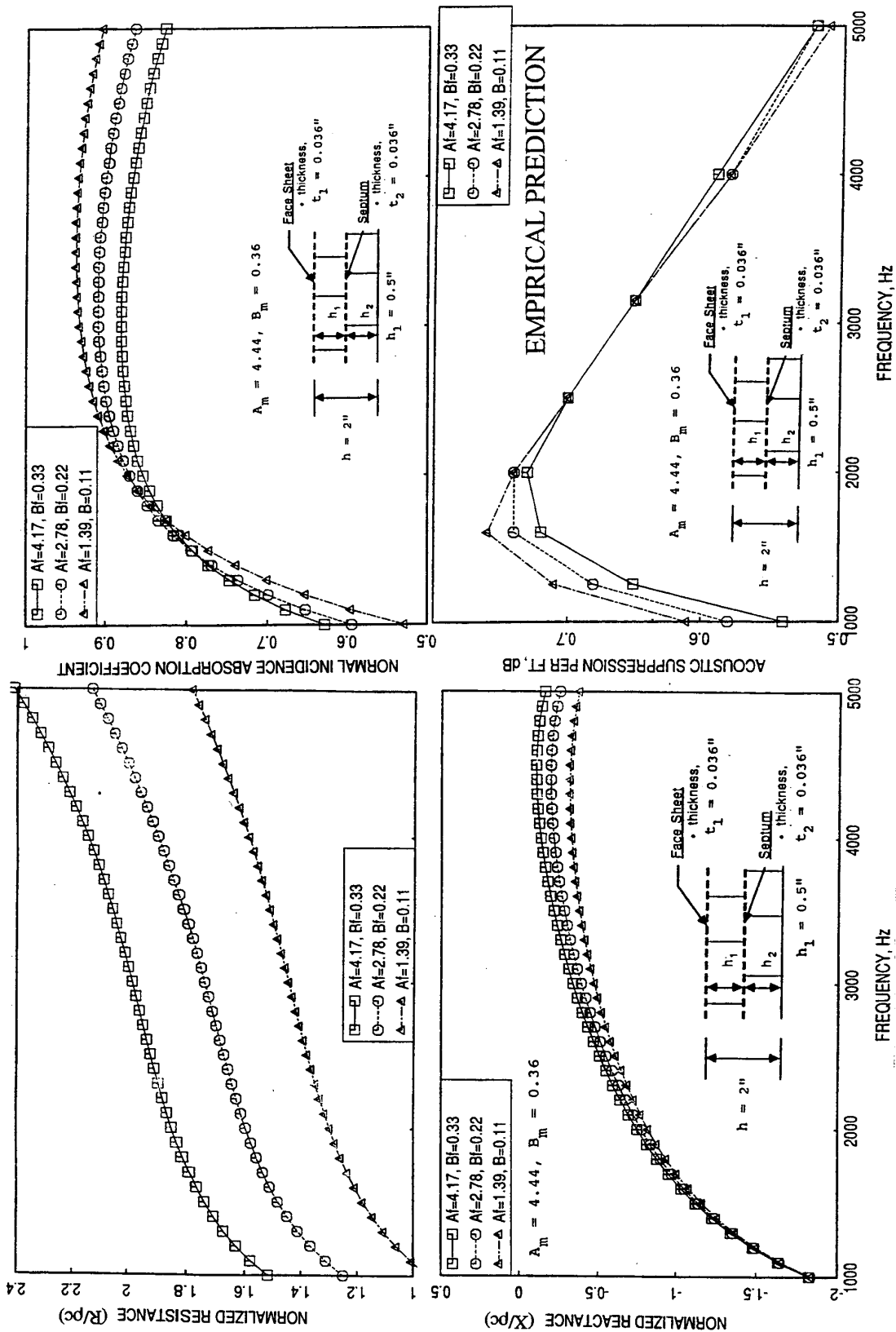


Figure 33. Influence of facesheet DC flow resistance (A & B) on predicted impedance, absorption coefficient, and acoustic suppression (at $M=0.8$) spectra for a 2DOF type liner with Millipore facesheet and septum.

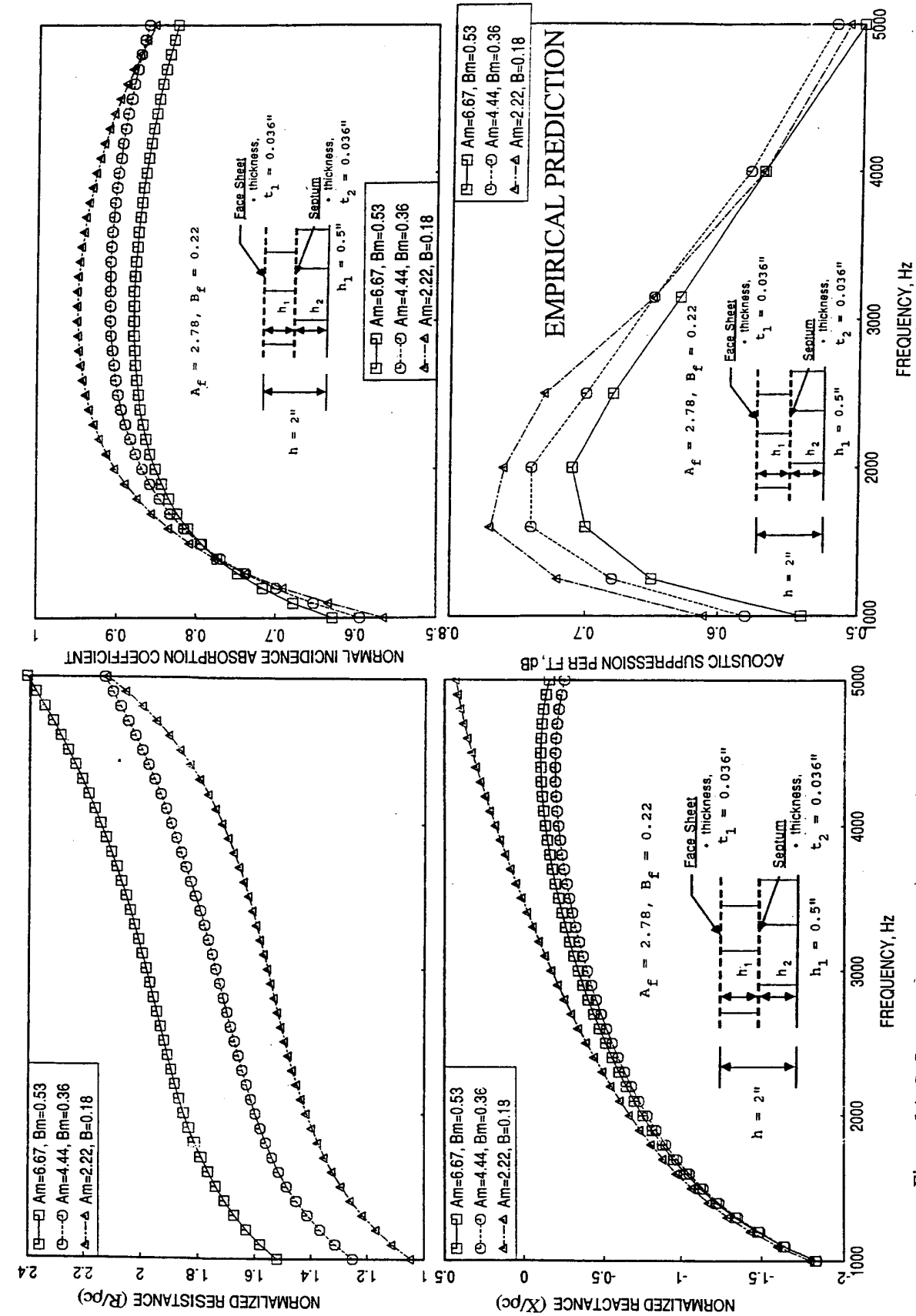


Figure 34. Influence of septum (mid-plate) DC flow resistance (A & B) on predicted impedance, absorption coefficient, and acoustic suppression (at $M=0.8$) spectra for a 2DOF type liner with Millipore facesheet and septum.

resistivity increases the absorption coefficient at mid-frequency range. Decreasing resistivity of facesheet or septum basically increases the amounts of acoustic suppression at lower frequencies, whereas, the effect is small at higher frequencies.

Figure 35 shows the effect of upper cavity depth (h_1) on impedance, absorption coefficient, and acoustic suppression spectra. Resistance level decreases with increasing h_1 , whereas, the reactance decreases and then increases with increasing h_1 . Absorption coefficient increases with increasing h_1 for almost entire frequency range, except for very lower end of the frequency range. Suppression level increases with increasing h_1 for entire frequency range, however, the increase is small at higher frequencies. Effect of cavity depth (h) on impedance, absorption coefficient, and acoustic suppression spectra are shown in Figure 36. The trends observed in these figures are similar to those of the SDOF type liners.

4. Bulk Absorber: Effect of facesheet resistivity on impedance, absorption coefficient, and acoustic suppression spectra are shown in Figure 37. Both resistance and reactance increase with increasing facesheet resistivity, whereas, the trend is opposite for absorption coefficient. Effect of face sheet resistivity on acoustic suppression spectra indicates increase in suppression level with decreasing face sheet resistivity at lower frequencies and the effect is insignificant at higher frequencies.

Effect of bulk material resistivity on impedance, absorption coefficient, and acoustic suppression is shown in Figure 38. Effect of bulk material resistivity on acoustic suppression is to increase the suppression levels with decreasing resistivity at lower frequencies, whereas, the optimum resistivity gives the highest levels of suppression at higher frequencies. Effect of cavity depth (h) is illustrated in Figure 39. Higher cavity depth compared to the design value of 2" does not significantly alter the liner characteristics, whereas, a drastic effect is observed by decreasing the depth to 1". Acoustic suppression increases with liner depth at lower frequencies; however, the optimum liner gives maximum suppression at most frequency range.

2.3.8 Influence of Grazing Flow: Impedance spectra for the four liner designs, described above, are optimized by using facesheet and septum properties, which are described entirely in terms of DC flow resistance at a through flow velocity of 100 cm/sec (R_{100}) and a nonlinear factor $NLF_{150/20}$. In these designs flow effects on liner facesheet resistance are neglected. In addition, mass reactance effects are not included. The physical parameters assumed are the liner depth and facesheet and/or septum thicknesses. Specific values of porosity and hole diameter for the facesheet and septum are not evaluated, since the mass reactance and grazing flow effects are excluded in the design process. However, grazing flow effects on acoustic

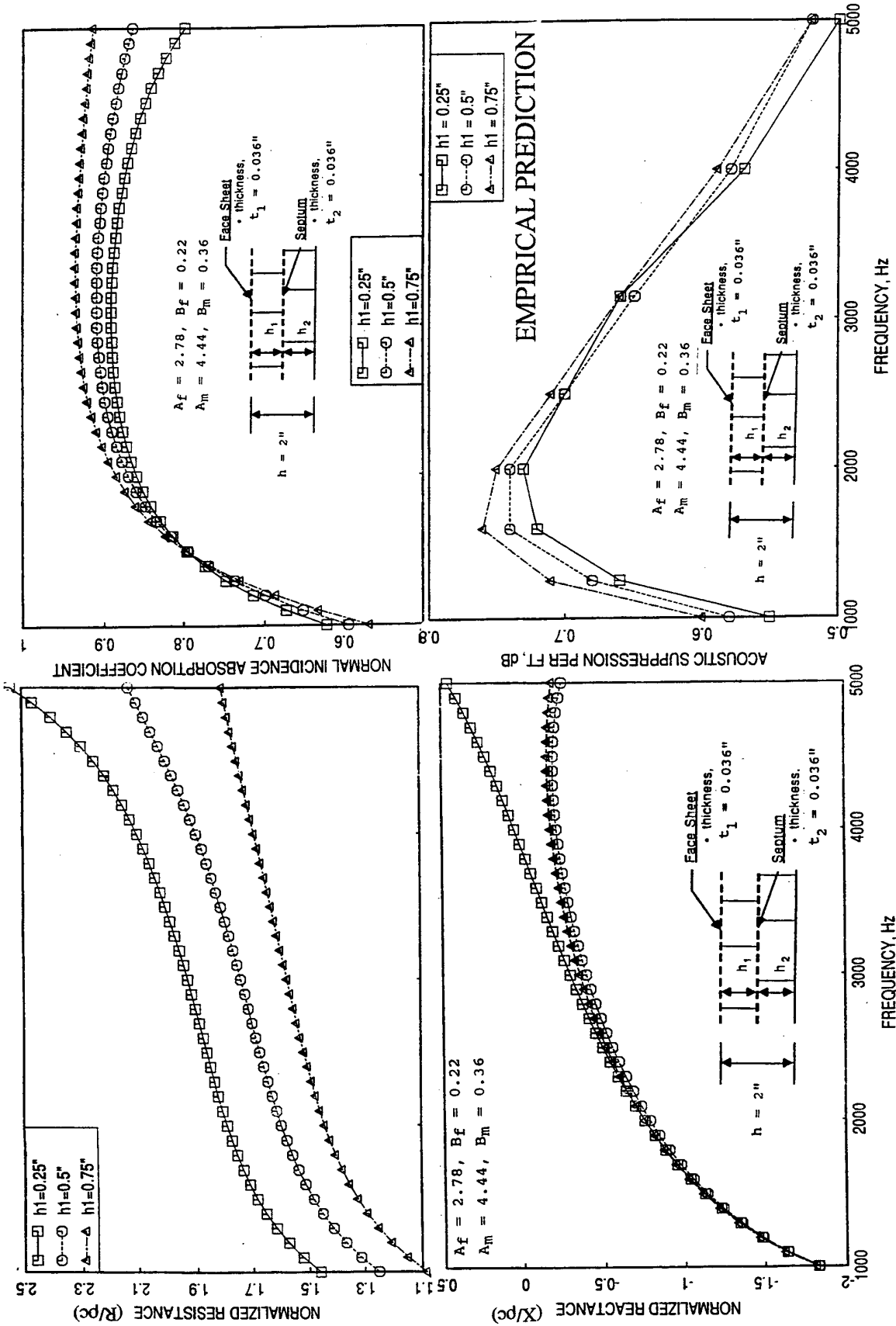


Figure 35. Effect of septum (mid-plate) position (h_1) on predicted impedance, absorption coefficient, and acoustic suppression (at $M=0.8$) spectra for a 2DOF type liner with fixed cavity depth (h) and with Millipore facesheet and septum.

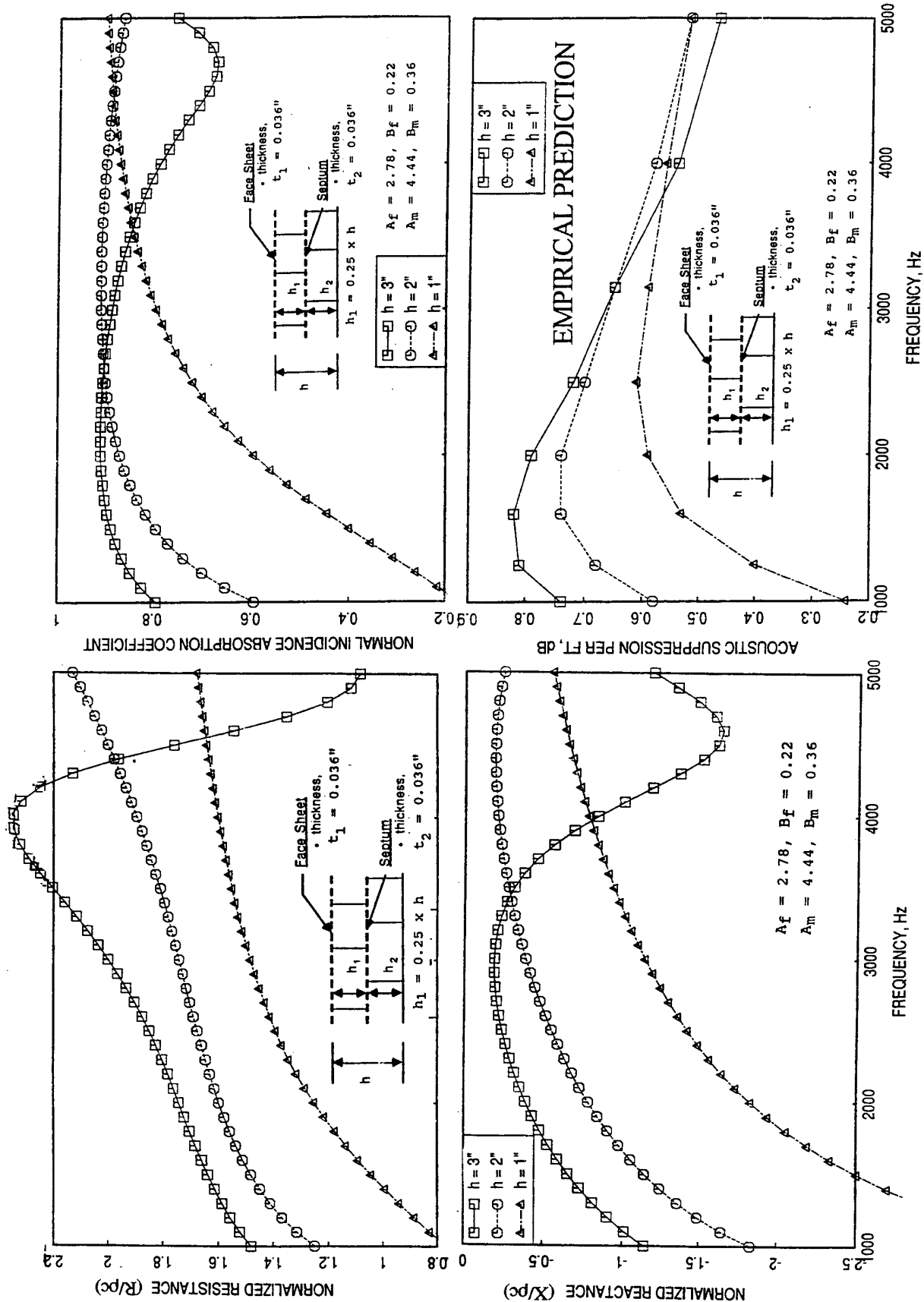


Figure 36. Effect of cavity depth (h) on predicted impedance, absorption coefficient, and acoustic suppression (at $M=0.8$) spectra for a 2DOF type liner with Millipore facesheet and septum.

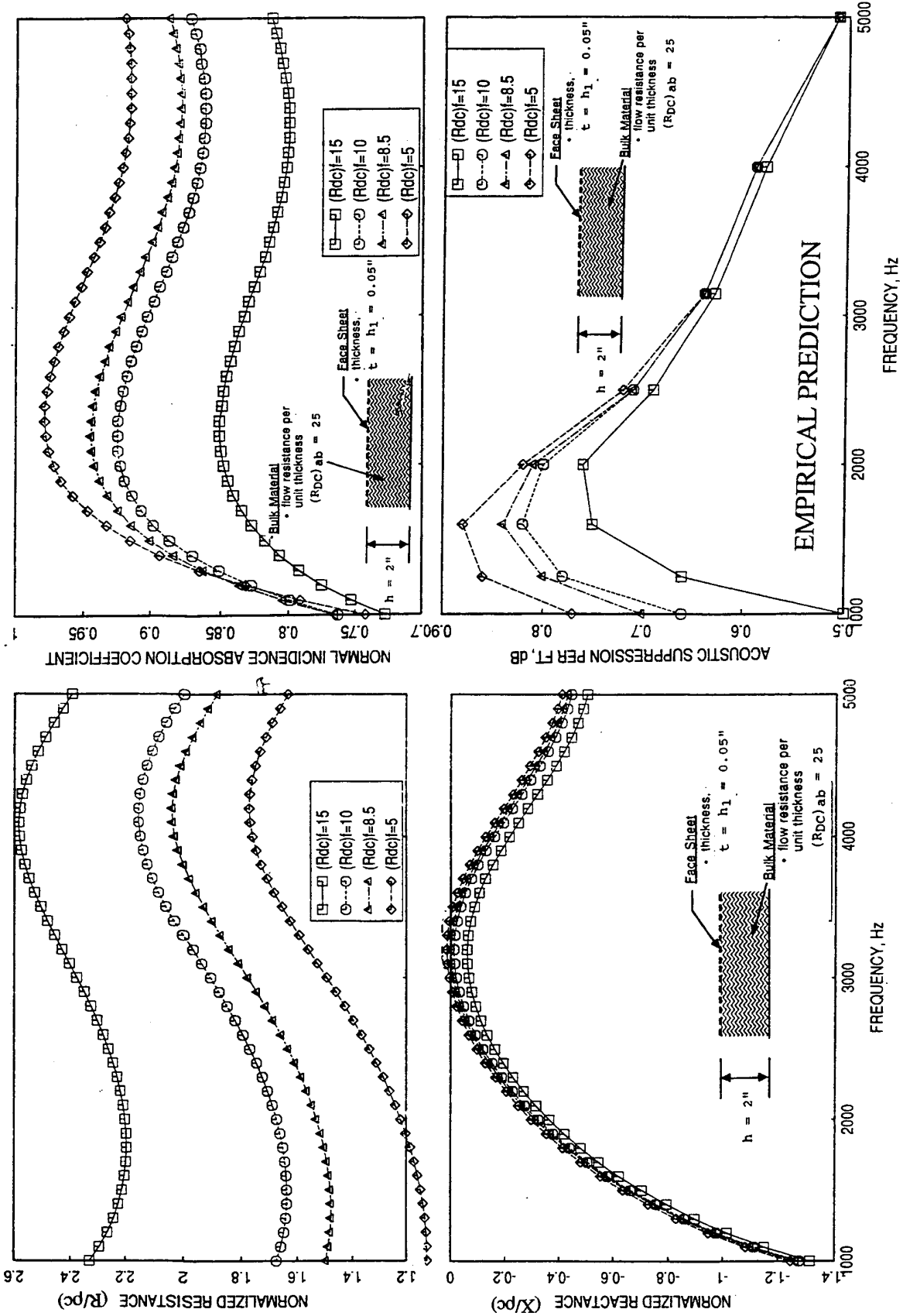


Figure 37. Influence of facesheet DC flow resistance (linear component only) on predicted impedance, absorption coefficient, and acoustic suppression (at $M=0.8$) spectra for a bulk absorber liner with a thin resistive facesheet.

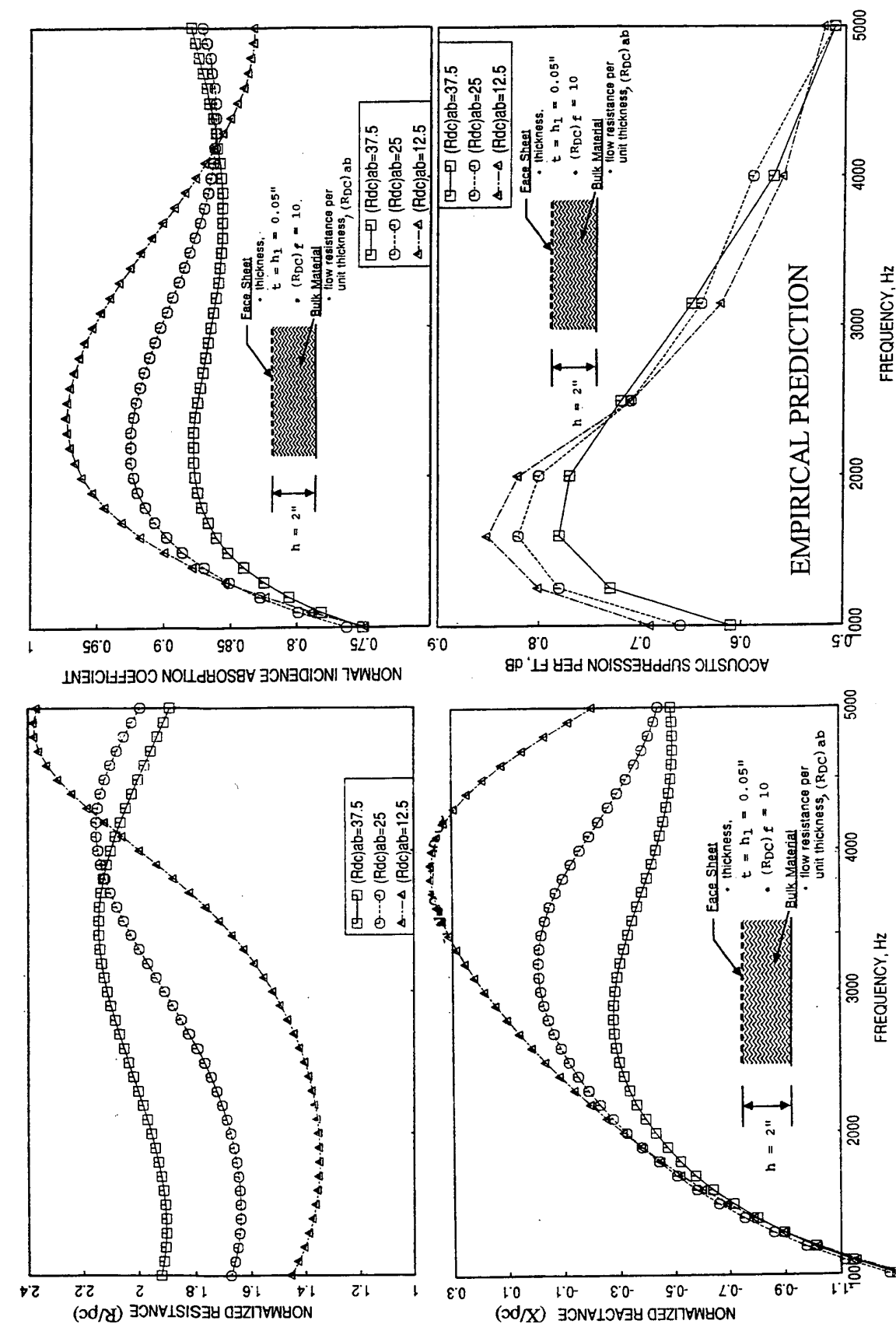


Figure 38. Influence of bulk material DC flow resistance (linear component only) on predicted impedance, absorption coefficient, and acoustic suppression (at $M=0.8$) spectra for a bulk absorber liner with a thin resistive facesheet.

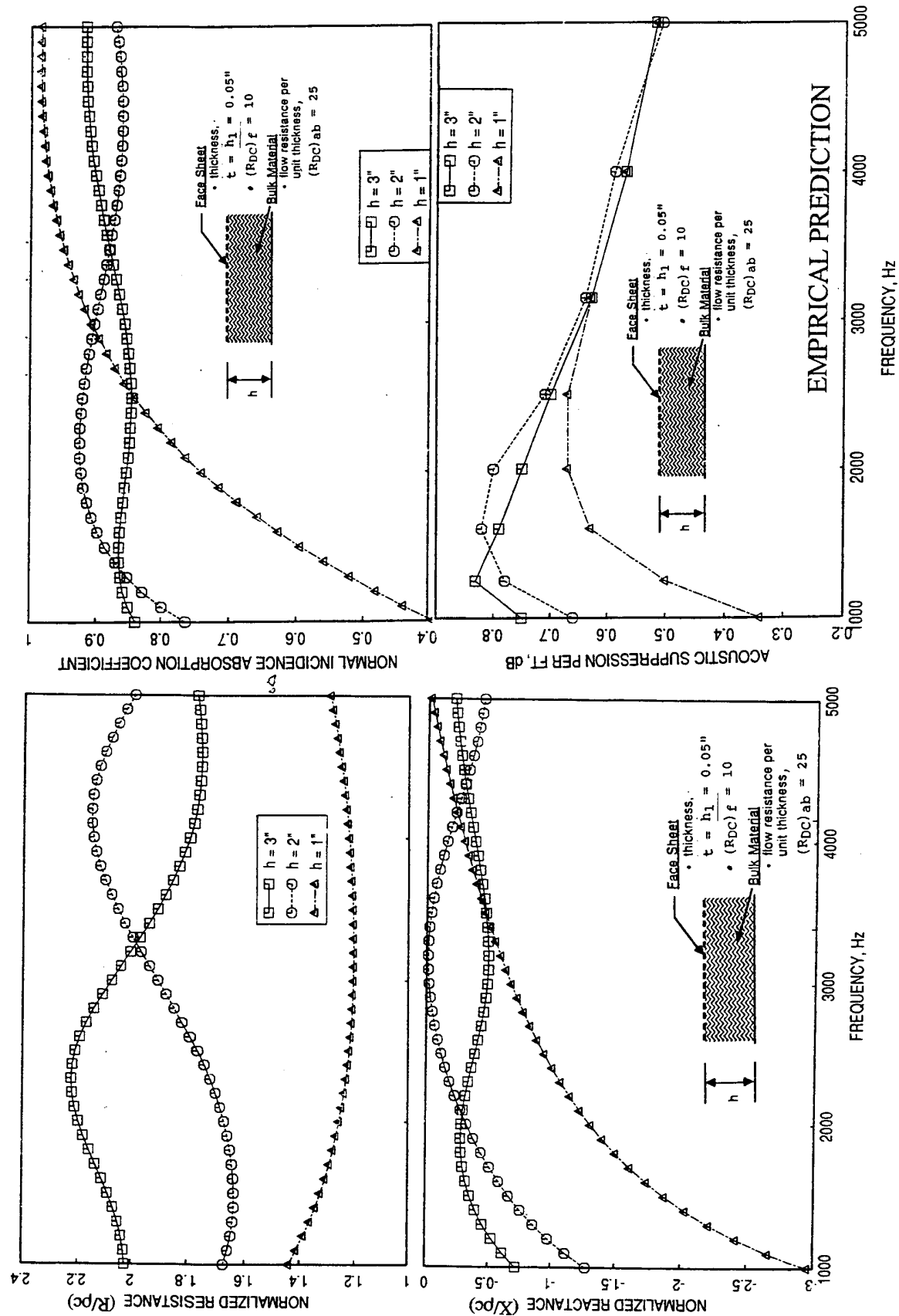


Figure 39. Effect of cavity depth (h) on predicted impedance, absorption coefficient, and acoustic suppression (at $M=0.8$) spectra for a bulk absorber liner with a thin resistive facesheet.

suppression are included in the above study. These levels are evaluated by assuming the same impedance spectra at all flow conditions.

Therefore, to study the effect of grazing flow, not only on the acoustic suppression, but also, on the impedance characteristics, an SDOF type liner with Millipore face sheet is designed by setting all the physical parameters, including the face sheet porosity and hole diameter. Grazing flow effects on the face sheet resistance and the mass reaction effects are included in the impedance evaluation. The impedance spectra for this design is optimized for 167.5 OASPL dB sound field and for a flow Mach number of $M=0.8$. The design parameters thus established are listed below:

Cavity Depth = 2"
Face Sheet Porosity = 16 %
Face Sheet Thickness = 0.032"
Hole Diameter = 0.05"

The impedance and absorption coefficient spectra for this liner are predicted at different flow Mach numbers by accounting for the flow resistance and mass reactance of the face plate. These values are used in the computation of acoustic suppression. Acoustic characteristics, thus evaluated for this liner, are presented in Figure 40. Resistance levels increase substantially with increasing Mach number. However, a reverse trend, though very small, is observed with reactance values. Normal incidence absorption coefficient levels decrease with decreasing Mach number. Even though, the optimum impedance spectra are achieved at $M=0.8$, the acoustic suppression is still much smaller at this Mach number compared to other Mach numbers due to grazing flow effects. At $M=0$, since the resistance levels are very small, except at mid frequencies, the acoustic suppressions reduce drastically at both ends of the frequency range with very high levels at the middle. In presence of grazing flow, the suppression levels reduce at the middle and increase at both ends of the frequency range compared to $M=0$.

Influence of detailed geometric design, modeling of grazing flow, and inclusion of mass reactance on impedance and absorption coefficient are shown in Figure 41. Even though, the predicted resistance spectrum with grazing flow effect is significantly different compared to the one optimized without grazing flow effect, the difference is small on reactance and absorption coefficient spectra. Similar comparisons of acoustic suppression spectra at different flow Mach numbers (M), shown in Figure 42, differ significantly at no flow condition, but are in reasonable agreement at higher flow Mach numbers, especially, at the design Mach number of 0.8. In other words, acoustic suppressions at higher flow conditions are not very sensitive to the design parameters of Millipore type facesheets.

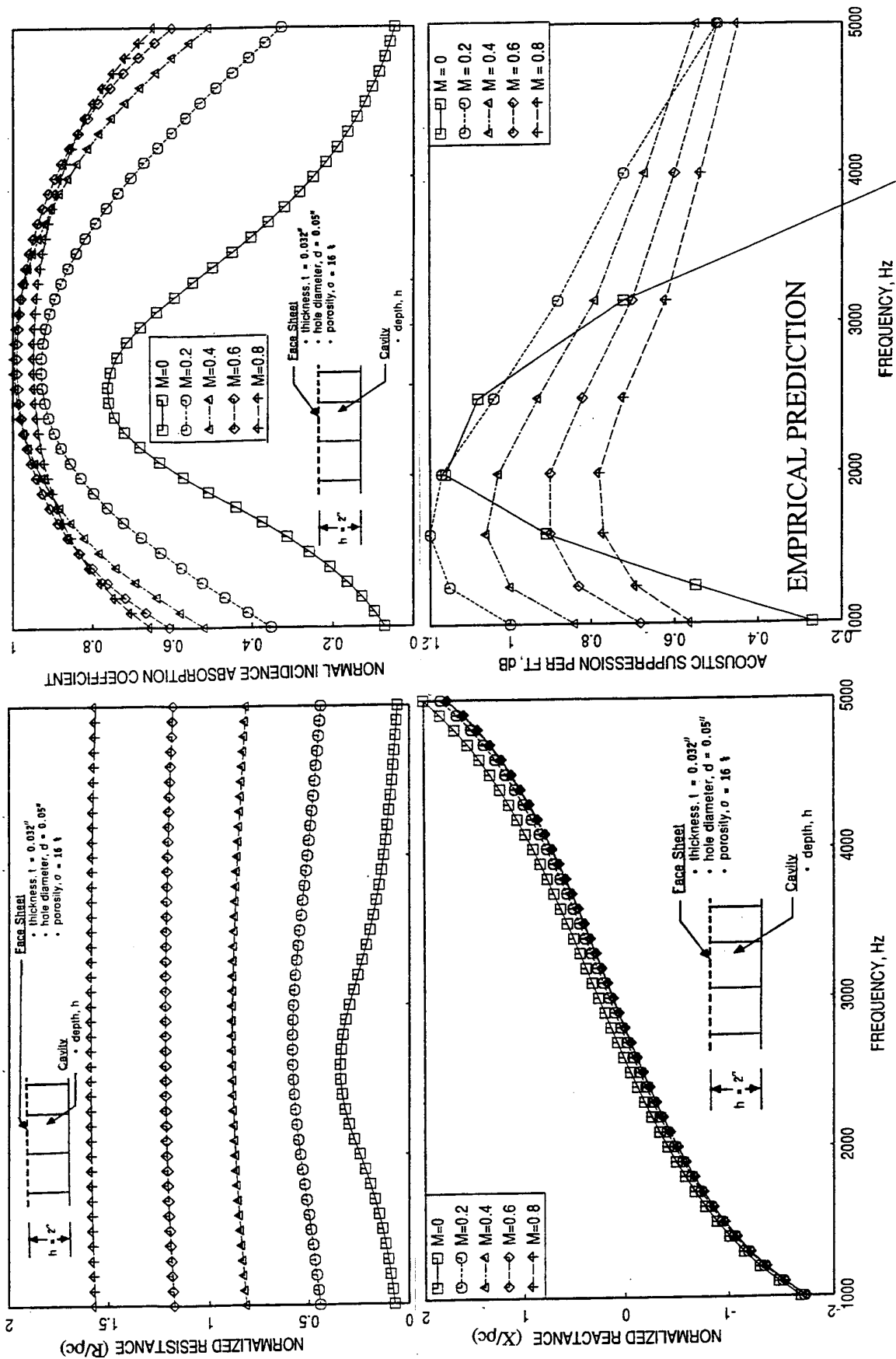


Figure 40. Effect of grazing flow (Mach number M) on predicted impedance, absorption coefficient, and acoustic suppression spectra for an SDOF type liner with Millipore facesheet.

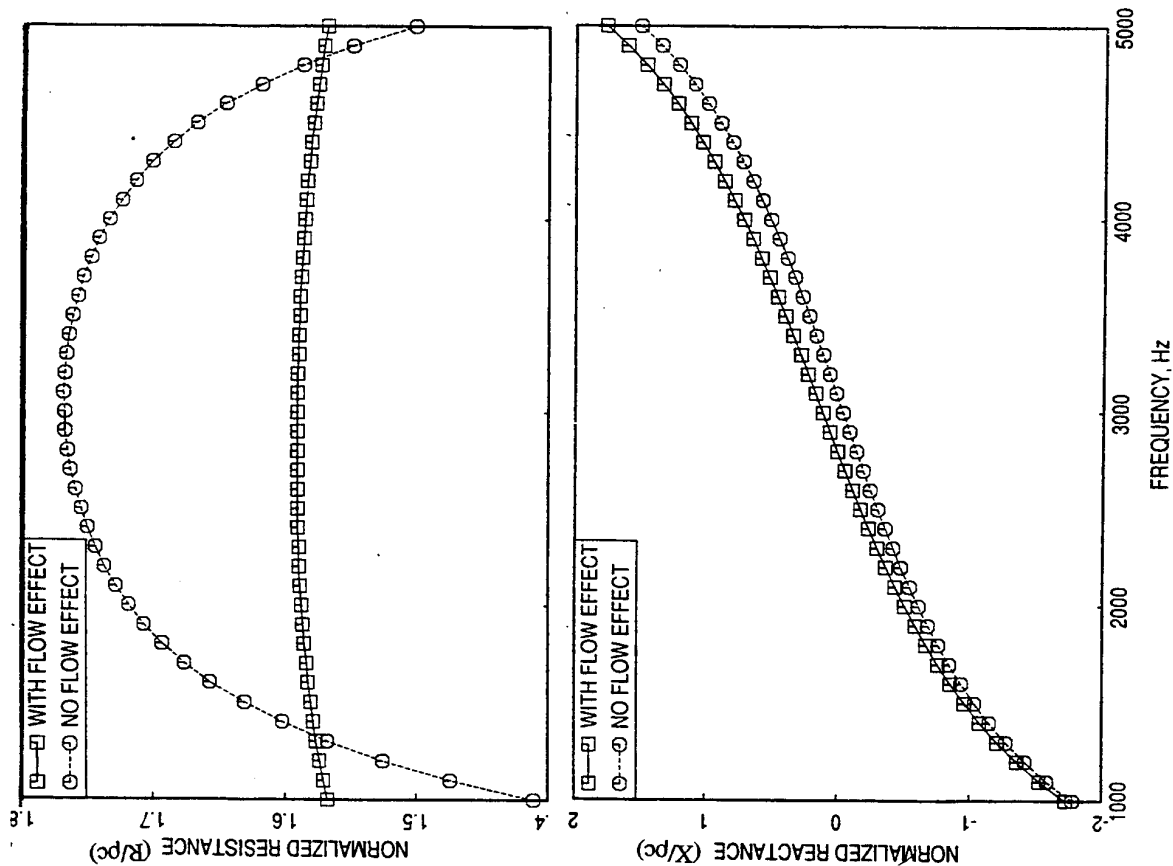


Figure 41. Predicted impedance and absorption coefficient spectra for an SDOF type liner optimized by using DC flow resistance and nonlinear factor only and by neglecting grazing flow effects compared with those of an SDOF type liner optimized for $M=0.8$ with grazing flow effects and by using all the facesheet physical parameters.

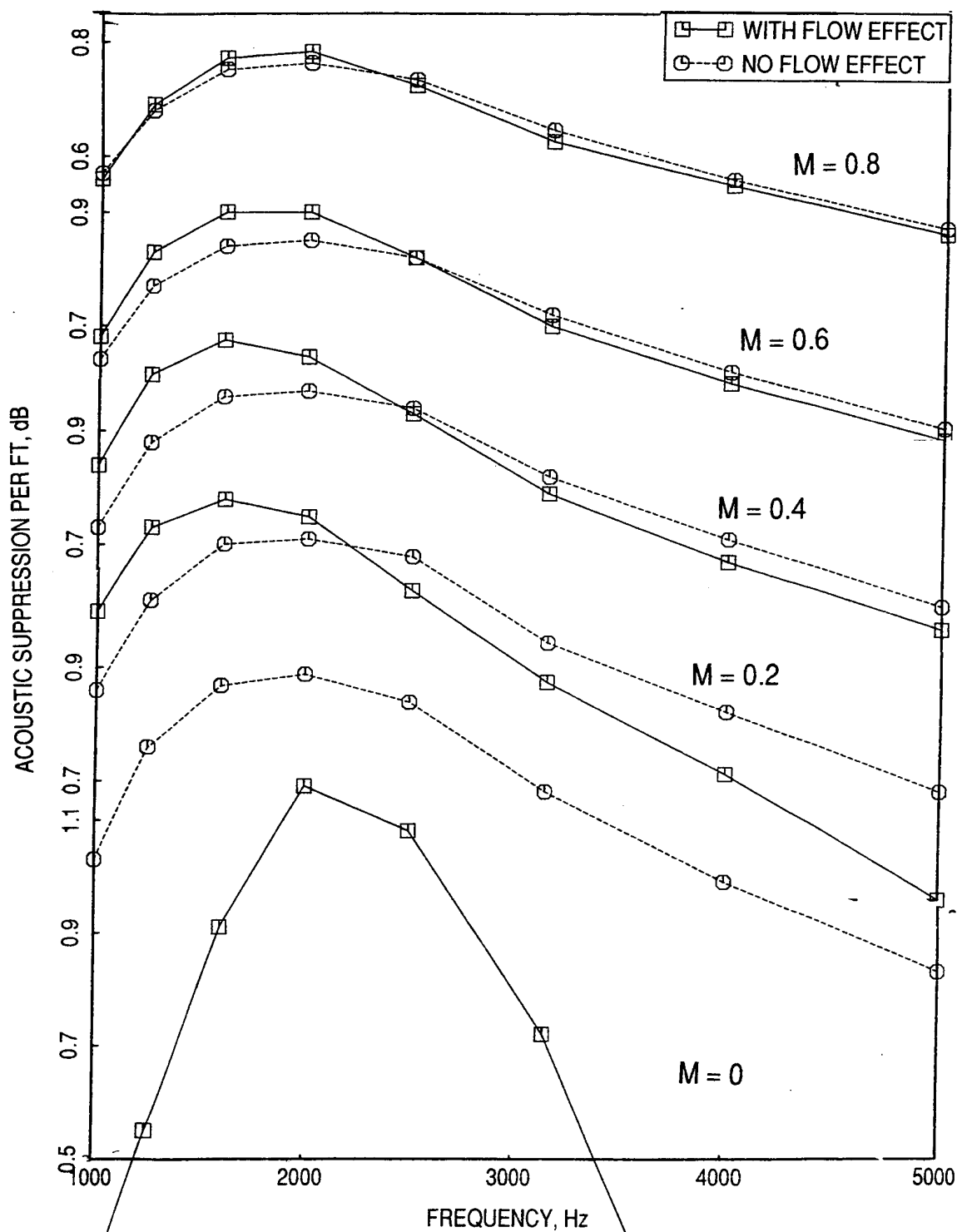


Figure 42. Predicted acoustic suppressions (empirical correlation) at a number of flow Mach numbers (M) for an SDOF type liner optimized by using DC flow resistance and nonlinear factor only and by neglecting grazing flow effects compared with those of an SDOF type liner optimized for $M=0.8$ with grazing flow effects and by using all the facesheet physical parameters.

3.0 TEST FACILITY AND TEST APPROACH

Acoustic laboratory testing consists of (1) normal impedance measurement, (2) DC flow resistance measurement, and (3) measurement of acoustic suppression, in-situ impedance, and boundary layer profile for liner panels, using a flow duct in the presence of grazing flow. Acoustic suppression for various liner panels is also measured at Rohr Inc.

3.1 Normal Incidence Impedance Measurements

3.1.1 Low Frequency Normal Impedance Measurements: A low frequency impedance tube with 1.25 inch diameter (see Figure 43(a)) is used to measure the normal impedance spectra up to about 6000 Hz at room temperature and pressure conditions. These measurements are conducted at different broadband or discrete frequency noise excitation sound pressure levels to identify the nonlinear behavior of the test samples. The impedance is evaluated by measuring the sound field of the tube at two axial locations. The sound field consists of plane waves reflected from the 'test sample' surface combining with the incident sound waves. One-dimensional propagation of plane wave sound is assumed in an inviscid, irrotational, adiabatic, and perfect gas medium.

The one-dimensional wave equation for inviscid, irrotational, adiabatic, and perfect gas in the absence of flow can be expressed as follows (see Figure 43(a)):

$$d^2p/dx^2 + k^2p = 0 \quad (3)$$

Where, p is the acoustic pressure at location x and k is the wave number (i.e., $k = 2\pi f/c$, f and c being the frequency and the speed of sound). For plane wave mode the solution of equation (3) is as follows:

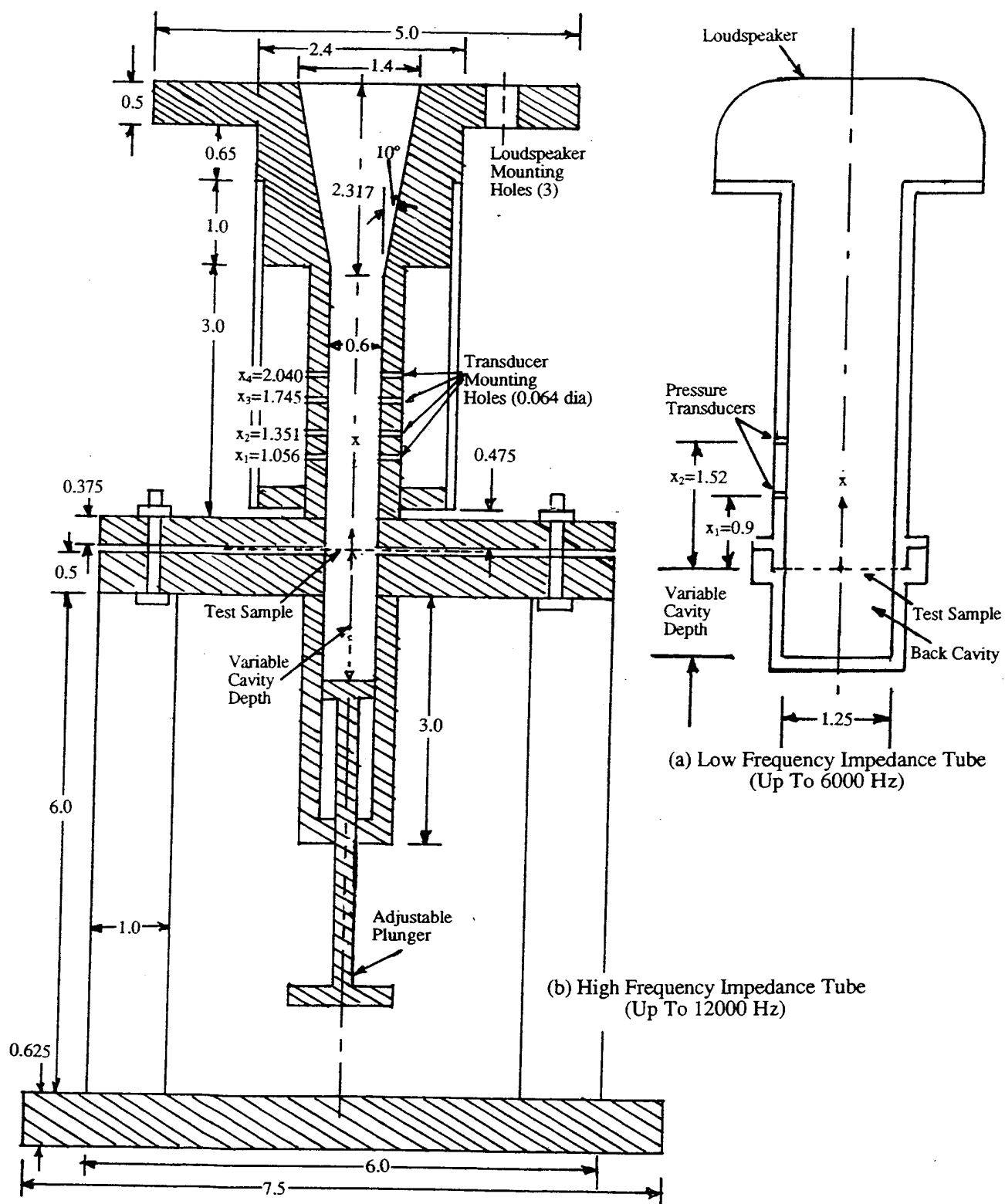
$$p = A_+ \exp(-ikx) + A_- \exp(ikx) \quad (4)$$

Where, A_+ and A_- are the complex incident and reflected pressures at $x = 0$. The linearized momentum equation for this situation can be written as:

$$\rho cu = -(dp/dx)/(ik) = A_+ \exp(-ikx) - A_- \exp(ikx) \quad (5)$$

Where, u is the acoustic velocity and ρ is the density of the medium. The specific impedance, Z at any x location is defined as :

$$Z = p/(\rho cu) = R + iX \quad (6)$$



Where, R and X are the specific resistance and reactance at x. The absorption coefficient α_{abs} can be expressed as:

$$\alpha_{\text{abs}} = 4R/[(1 + R)^2 + X^2] \quad (7)$$

At $x = 0$, conventionally where the test sample is located, the specific impedance for plane wave mode can be expressed as:

$$Z_{x=0} = (A_+ + A_-)/(A_+ - A_-) \quad (8)$$

The complex A_+ and A_- for plane wave mode are evaluated from the measured pressure data by the two transducers.

3.1.2 High Frequency Normal Impedance Measurements: The 1.25-inch diameter impedance tube is inaccurate above about 6 kHz. due to the presence of higher order cut-on modes in the tube. The first circumferential mode appears at $kR_D=1.74$, where, k is the wave number and R_D is the radius of the tube. Based on the diameter of 1.25" the cut on frequency for the first circumferential mode is about 6000 Hz at room temperature conditions. The cut-on frequency, f_1 , of the first higher order mode in a circular impedance tube can also be expressed as [Ref. 7]:

$$f_1 = 1.841c/(\pi D) \quad (9)$$

Where, D is the diameter of the impedance tube and c is the speed of sound. Even though below the frequency f_1 only plane waves should propagate, slight non uniformity of the test sample characteristics or the tube cross section may produce the higher order modes at frequencies slightly below f_1 . However, this phenomenon affects measurement accuracy at frequencies just below f_1 where the axial damping per unit length of the first higher order mode is relatively small. Thus the practical upper frequency limit for accurate impedance measurement is slightly less than f_1 . Based on the experience gained in GEAE's acoustic duct lab work, this upper frequency limit is approximately $0.85f_1$. Hence, to extend the plane wave frequency range to higher values, it is necessary to use a smaller diameter tube. Use of very small diameter impedance tube in normal impedance evaluation has other problems. Hence, an optimum tube diameter should be determined for accurate impedance measurement.

Based on the above criteria a tube diameter of 0.55" is required to extend the plane wave frequency range to 12000 Hz. However, this diameter is in the conservative side. Hence, a high frequency impedance tube (see Figure 43b) is built with a slightly higher tube diameter of

0.6" to evaluate the impedance spectra up to about 12 kHz. Either broad band or discrete frequency excitation is used in this apparatus for impedance evaluation. The results presented in this report are evaluated by utilizing broadband excitations at room temperature and pressure conditions.

The impedance tube is instrumented with four pairs of 0.064" diameter dynamic transducers, each pair being mounted at a different axial location. The two transducers of each pair are placed opposite to each other (i.e., angularly spaced by 180°). An adjustable cavity with hardwall termination follows the test sample (see Figure 43b). The purpose of two transducers at one location is to minimize any nonuniformity of the soundfield by averaging the output of these transducers. However, for the present study the soundfield seems to be uniform up to 12 kHz and hence the tests are conducted utilizing four transducers at one side of the tube.

In the current tests a broadband sound is utilized, so that the impedance spectra for the sample is derived by a single test. An overall sound pressure level (OASPL) at $x=0$ is determined by summing the pressure amplitudes over the frequency range and is expressed in dB. An average acoustic velocity U_e at $x=0$ is also computed (see Ref. 5) and is expressed as follows:

$$U_e = \left\{ \sum_{i=1}^{i=N} |u_i|^2 \right\}^{1/2} \quad (10)$$

Where, N is the number of frequencies in the entire range. The OASPL is maintained constant for all the test samples. While, the OASPL values for different samples are almost the same, the particle velocity varies considerably due to the impedance variation from sample to sample.

Even though, the impedance is evaluated up to 12 kHz using this apparatus, the need for even higher frequency impedance measurement is important for scale model HSCT nozzle configurations and $\sim 1/2$ scale nozzles such as LSM or demo nozzle. In a simpler way this can be achieved by reducing the duct diameter even more. However, by doing so the test sample sizes become smaller and the uniformity of the representative sample for complex liner concepts are likely to be lost. To avoid this problem, the impedance evaluation process is modified, such that the impedance spectra can be evaluated up to about 22 kHz using the same apparatus with 0.6" diameter samples. In this process the signal measured by the oppositely mounted transducers are added and an average complex value from each pair of transducers is used in the impedance evaluation. Thus, the contribution of the first circumferential mode, which is measured with opposing direction, but with equal magnitude, by the $\phi=180^\circ$ spaced transducers of a pair, is eliminated. Thus, the plane wave impedance

spectra is obtained up to 22 kHz at room temperature conditions, which corresponds to the cut on frequency of second circumferential mode (i.e., $kR_D=3.14$). It should be noted that the plane wave impedance above 12 kHz might be influenced by the presence of the first circumferential mode signal, even though its contribution is eliminated.

The complex acoustic pressure measured on the impedance tube wall surface at x_j ($j=1, 2, 3$, & 4, corresponding to four axial locations for transducers), with in the frequency range up to $kR_D=3.14$, can be expressed as (for plane wave and first circumferential mode);

$$(p)_{\varphi=0} = (p)_{00} + (p)_{10} \quad (11)$$

$$(p)_{\varphi=180} = (p)_{00} - (p)_{10} \quad (12)$$

where; $(p)_{00}$ is the plane wave acoustic pressure as expressed in equation (4) and $(p)_{10}$ is the acoustic pressure of first circumferential mode. An average of these two measurements gives the plane wave mode contribution, similar to equation (4) as follows;

$$p_j = A_+ \exp(-ikx_j) + A_- \exp(ikx_j) \quad (13)$$

In the impedance tube technique, using any two sets of data out of four in the present study, the normal impedance of the test sample can be determined. However, inaccuracies in the measurements result in errors in the computed impedance values. These errors can be minimized by increasing the number of axial measurements and utilizing a least-squares technique in the data reduction. For the present study this is achieved by using all four measured data (when measured up to 12 kHz) or four pairs of measured data (when measured up to 20 kHz) in the impedance computation. This process is illustrated by expressing the Equation (11) or (4) in the following matrix form;

$$[G]_{4 \times 2} \{P\}_{2 \times 1} = \{p\}_{4 \times 1} \quad (14)$$

Where, $[G]$ is a coefficient matrix of order 4×2 of elements a_{ji} , $\{P\}$ is a column matrix of order 2×1 of elements A_+ and A_- , $\{p\}$ is a column matrix of order 4×1 of elements (p_j) . The elements (p_j) are the complex pressures derived from measurements as shown in equation (13), and the elements a_{ji} are given below.

$$a_{j1} = \exp(-ikx_j) \quad (15)$$

$$a_{j2} = \exp(ikx_j)$$

Where, j varies from 1 to 4, 4 being the number of measurement locations. It should be noted that equation (14) is an overdetermined system of linear equations; the matrix $[G]$ has more rows than columns, since the number of measurement locations, 4, is greater than the number of unknowns, 2. Overdetermined systems arise in experimental or computational work, whenever more results are generated than would be required, to minimize experimental or computational errors. A least square solution is used to solve such an overdetermined system. In this study, the least square solution is applied to equation (14) to determine A_+ and A_- by minimizing any measurement error in constructing the standing wave in the impedance tube. By utilizing the least square procedure the solutions of equation (14) are given by

$$\{P\} = [G \cdot G^*]_{2 \times 2} \{G \cdot p\}_{2 \times 1} \quad (16)$$

where, $[G^*]$ is the transpose of the conjugate of $[G]$. The modal coefficients A_+ and A_- are derived from equation (16). Thus, the normal impedance is derived using Equation (8).

3.2 DC Flow Resistance Measurements

DC flow resistance measurements provide critical information about the nonlinearity of resistive materials that form elements of the treatment panels. The resistive elements may be either thin porous sheets such as perforated or woven materials or bulk absorbers of larger thickness, such as, fibrous mats or reticulated foams. For thin sheets, the overall resistance is obtained as a lumped parameter as a function of through-flow velocity. For bulk materials, the overall resistance is measured in terms of a resistance per unit thickness, which is a resistivity parameter.

3.2.1 Room Temperature DC Flow Measurements: The apparatus shown in Figure 44 measures DC flow resistance at room temperature at velocities up to 400 cm/sec. Samples of thin isolated facesheets or thick samples of bulk absorber or any other type without the back plate are used in this apparatus. Thin facesheet samples are of about 2 or 3 inch in diameter. Bulk absorber samples of 1.25 inch diameter are mounted in a holder (see Figure 45), which is inserted into the DC flow measurement apparatus. Samples of different thicknesses can be tested in this apparatus. The test result is used to evaluate the linear and nonlinear parts of the resistance (i.e., A and BU , U being the DC flow velocity) and the nonlinearity factor (i.e., NLF) of the test samples. The DC flow resistance R_{DC} is expressed as follows:

$$R_{DC} = A + BU \quad (17)$$

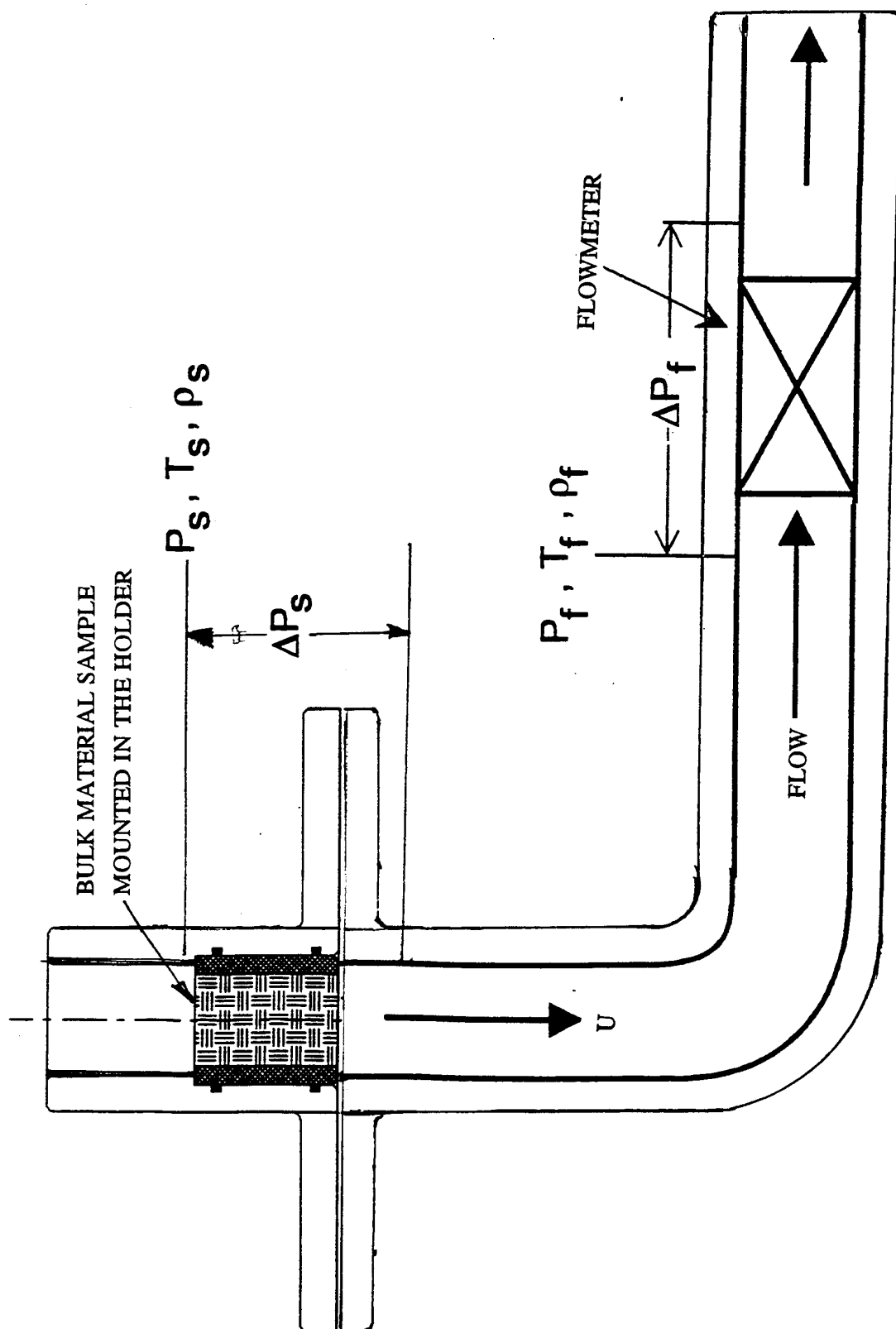


Figure 44. DC flow apparatus for bulk materials.

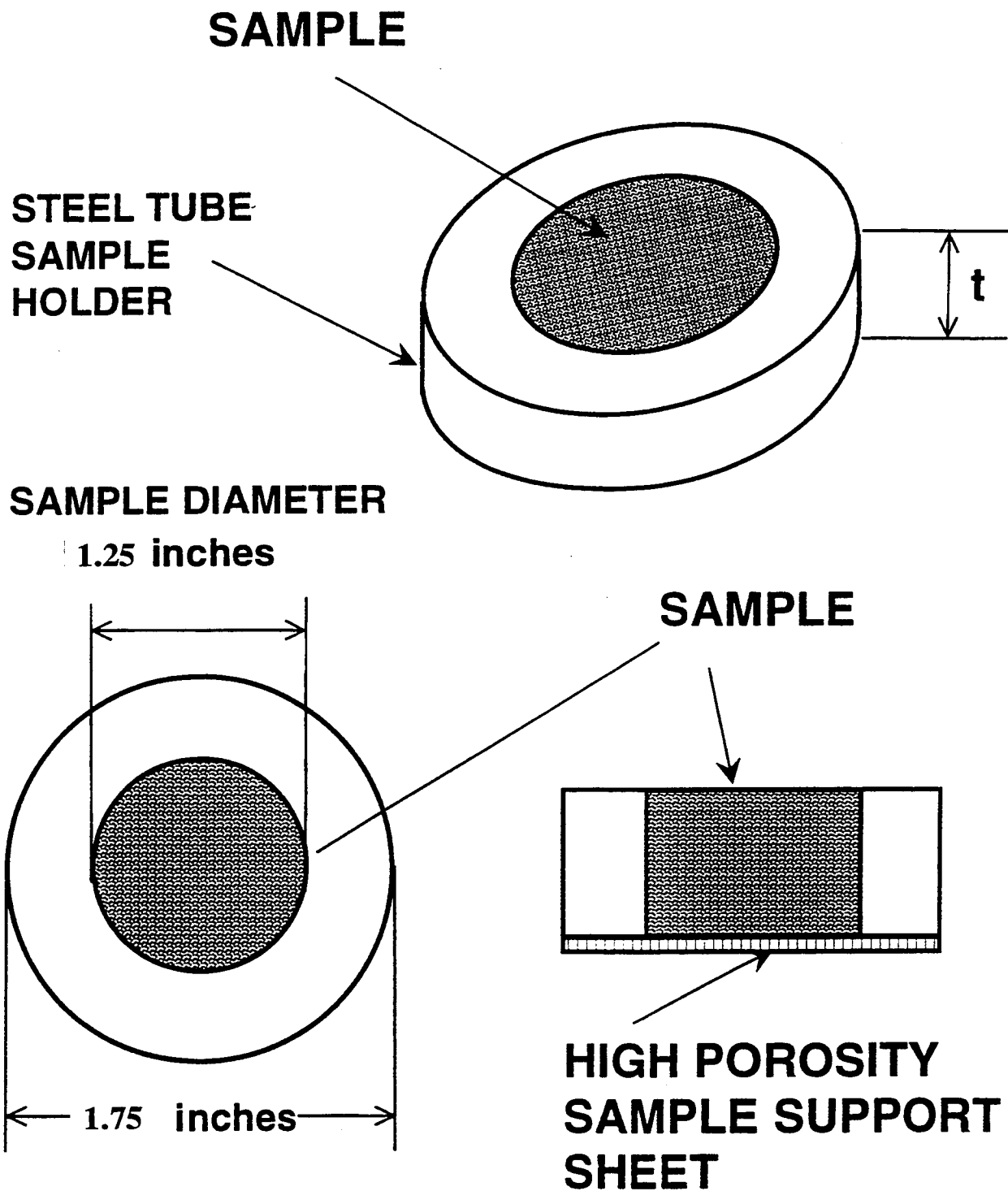


Figure 45. DC flow measurement bulk absorber sample holder.

3.2.2 High Temperature DC Flow Measurements: The DC flow resistance of perforates as well as bulk materials is temperature dependent. The DC flow resistance variation of such components with respect to temperature is crucial in designing liners for high temperature application. A different apparatus is used for high temperature DC flow resistance measurements (see Figure 46). This is similar to the one for room temperature application, except that the high temperature apparatus contains a heating element that can heat the air up to a temperature of 1000°F. Test samples for this apparatus are similar to those for room temperature application, except the samples and sample holders are constructed using high temperature materials.

The measured DC flow resistance data is usually corrected by utilizing the following expressions to compensate for any small temperature and pressure differences between the tests and to express the data, especially for heated conditions, at standard temperature (70° F) and pressure(14.7 psia or 29.92 inches of Hg.) conditions;

$$\{ (R_{DC}) \}_{T_O, P_O} = \{ (R_{DC}) \}_{T, P} \cdot (\mu_O / \mu) \quad (18)$$

$$\{ u \}_{T_O, P_O} = \{ u \}_{T, P} \cdot (\rho / \rho_O) \cdot (\mu_O / \mu) \quad (19)$$

Where;

(R_{DC}) is the DC flow resistance in Rayls

T is the temperature under test conditions just upstream of test sample

T_O is a reference temperature (70° F)

P is the pressure under test conditions just upstream of test sample

P_O is a reference pressure (14.7 psia or 29.92 inches of Hg.)

ρ is the density of the fluid under test conditions just upstream of test sample

ρ_O is the density of the fluid at reference temperature and pressure

μ is the absolute coefficient of viscosity of the fluid at temperature T

μ_O is the absolute coefficient of viscosity of the fluid at temperature T_O

3.3 Flow Duct Facility at GEAE

The flow duct facility, schematically illustrated in Figure 47, is used to evaluate acoustic suppression in terms of insertion loss in the presence of grazing flow for treatment panels. The duct cross section is 4 inches x 5 inches, and treatment panels of sizes up to 5 inches x 18 inches can be used either on one side or on two opposing sides of the duct. The flow Mach number can be varied from 0 to about 0.8. The acoustic excitation can be provided either by a

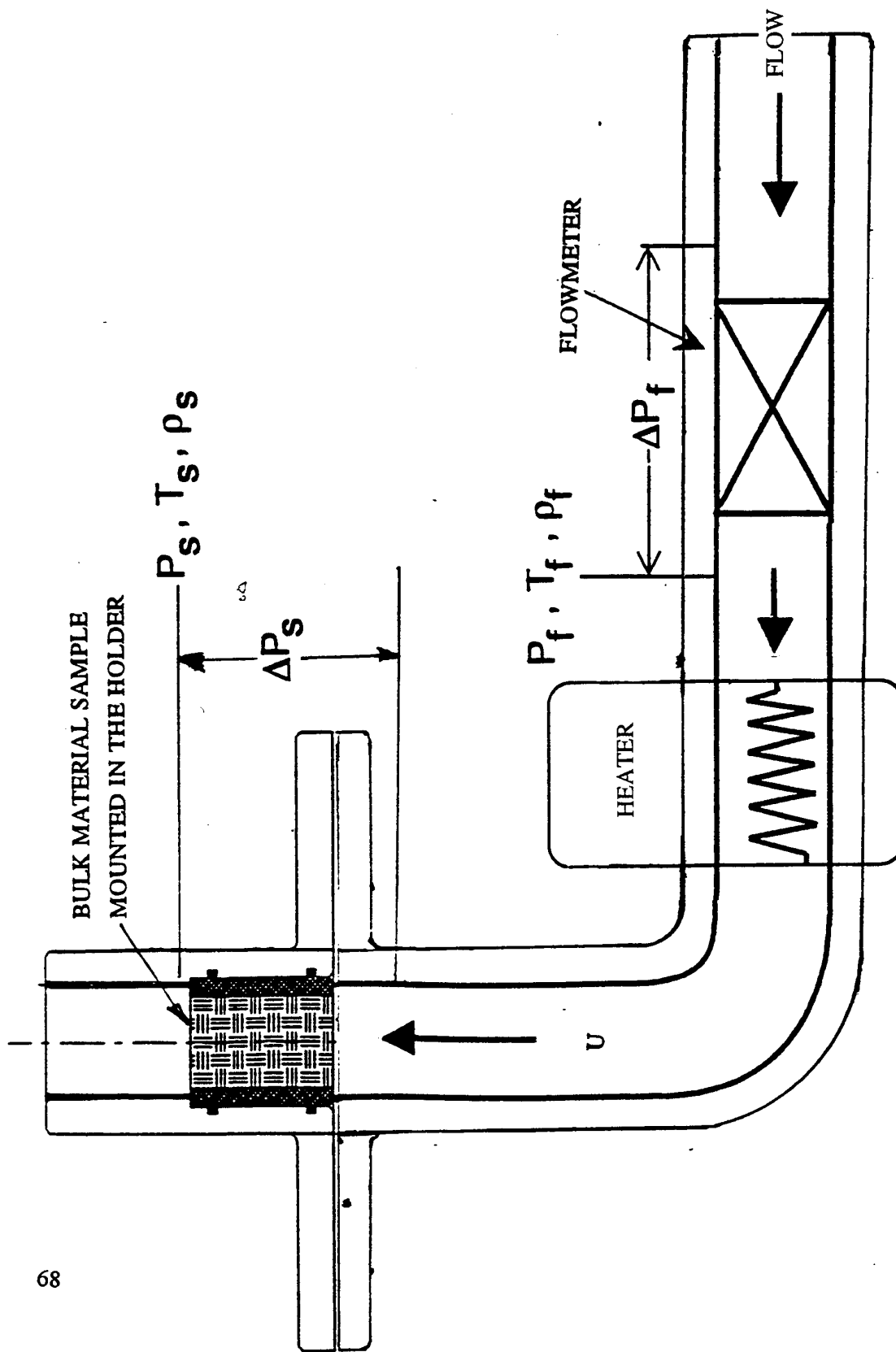


Figure 46. Schematic of DC flow apparatus for high temperature operation.

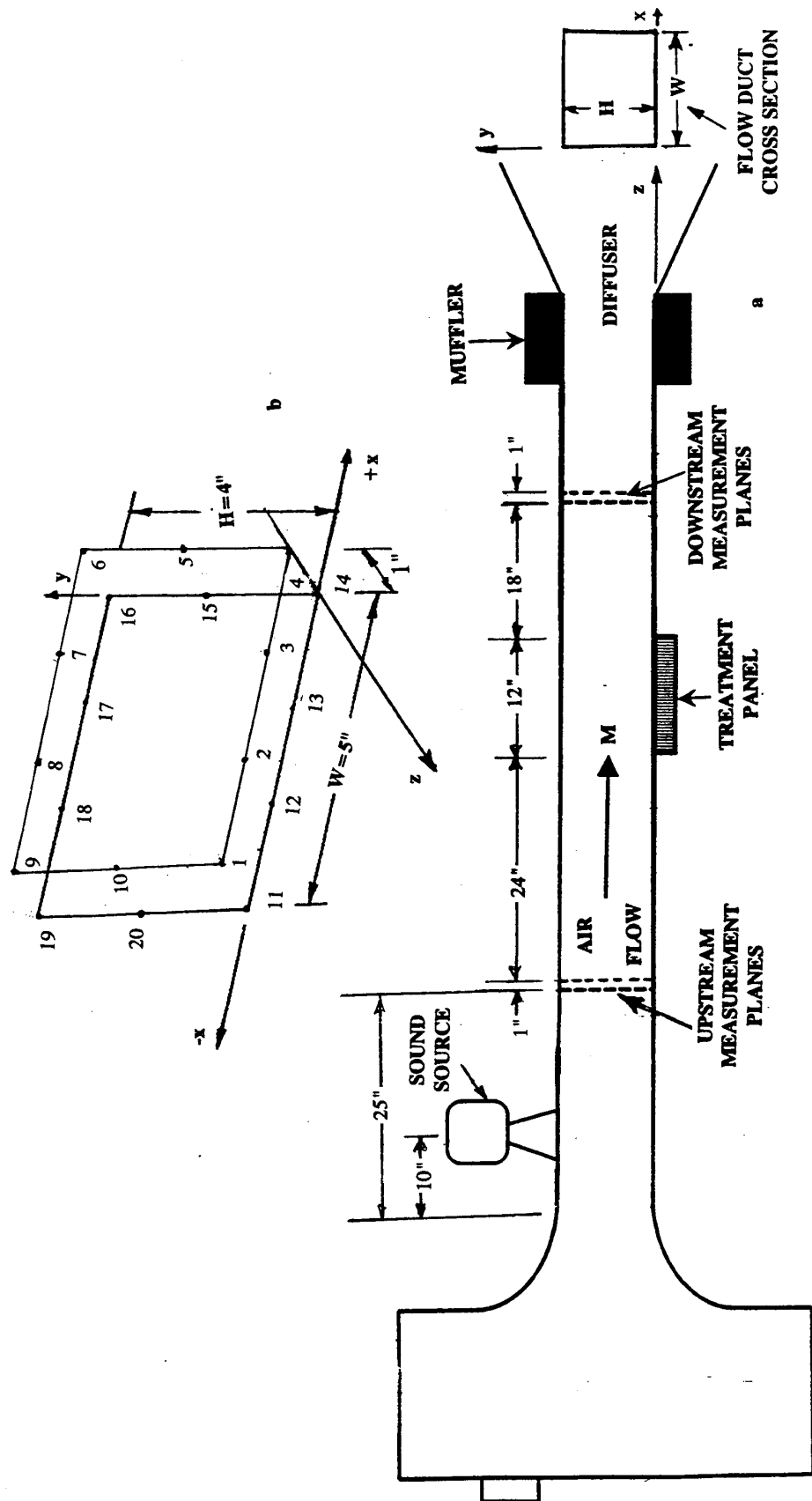


Figure 47. (a) Schematic of the flow duct apparatus with sound source and (b) transducer locations on measurement planes.

single or by four 100-watt Altec driver(s). The acoustic energy flux measurements are made by flush-mounted transducer arrays upstream and downstream of the treatment panel.

3.3.1 Suppression Measurements: The objective of the suppression measurements is to determine the suppression of forward traveling acoustic energy, in terms of Δ PWL (i.e., change in sound power level), for each panel. The most accurate method to do this is to perform modal decomposition of the pressure patterns at two planes upstream and two planes downstream of the treatment section (see Figure 47). The two-plane measurement allows the forward traveling and backward traveling energy to be analytically separated. The number of sensors required for the modal measurement at a plane is, at a minimum one more than the number of cut-on modes at a given frequency.

Suppression Measurement using p^2 Method: The number of sensors is limited to 10 per plane (see Figure 47(b)) in the current set-up. This will permit the measurement up to the frequency at which the 9th mode becomes cut on. Above this frequency, it will be necessary to use a less accurate p^2 estimate of the energy flux. For the p^2 method, the insertion loss is expressed as the difference between the sum of the squared pressure amplitudes averaged over the sensor measurements at the upstream and downstream transducer planes. Insertion loss in terms of Δ dB is expressed below.

$$\Delta \text{dB} = 10 \log_{10} \left[\frac{1}{N} \sum_{i=1}^{i=N} p_{ui}^2 \right] - 10 \log_{10} \left[\frac{1}{N} \sum_{i=1}^{i=N} p_{di}^2 \right] \quad (20)$$

where, p_{ui} is the pressure measured at the i^{th} upstream microphone, p_{di} is the pressure measured at the i^{th} downstream microphone, and N is the number of microphones per plane. The results presented in this report are obtained using the p^2 method for entire frequency range without separating the forward traveling wave from the combined forward and backward traveling waves and the effect of higher order modes is also ignored. Data measured by 8 upstream and 8 downstream probes are utilized in insertion loss evaluation. The probes mounted in the corners of all four planes are arbitrarily selected for this exercise. The Δ dB derived from the above expression is normalized with the similar parameter for hardwall configuration to minimize the errors due to the simplifications made in the evaluation of insertion loss. Thus, the insertion loss is defined as follows:

$$\left\{ 10 \log_{10} \left[\frac{1}{8} \sum_{i=1}^{i=8} p_{ui}^2 \right] - 10 \log_{10} \left[\frac{1}{8} \sum_{i=1}^{i=8} p_{di}^2 \right] \right\}_{\text{RELATIVE TO HARDWALL}} \quad (21)$$

Suppression Measurement using Modal Analysis: Consider a long rectangular duct bounded at $x=0$, $x=W$, $y=0$, and $y=H$ by duct walls (see Figure 47(b)). The acoustic pressure p , derived from the linearized equation of motion in the presence of a steady mean flow Mach number M along the axial direction z , for inviscid, irrotational, adiabatic and perfect gas, considering both forward and backward moving waves in the flow duct, can be expressed as follows (Ref. 8):

$$p = \cos(k_x x) \cos(k_y y) \{A_{mn}^+ \exp(-ik_z^+ z) + A_{mn}^- \exp(-ik_z^- z)\} \quad (22)$$

A_{mn}^+ and A_{mn}^- are the complex pressure coefficients for the (m,n) mode in forward and backward moving waves, respectively. The wave numbers along the x , y , and z directions, represented by k_x , k_y , and k_z , are defined as:

$$\begin{aligned} k_x &= m\pi/W & k_y &= n\pi/H \\ k_z^+ &= [-Mk + \sqrt{k^2 - (1-M^2)\mu^2}]/(1-M^2) \\ k_z^- &= [-Mk - \sqrt{k^2 - (1-M^2)\mu^2}]/(1-M^2) \end{aligned} \quad (23)$$

where, $\mu^2 = \{k_x^2 + k_y^2\}$ and $k = 2\pi f/c$, c and f being the speed of sound and frequency in Hertz, respectively. Measuring acoustic pressures at two different axial locations (i.e., z) the coefficients A_{mn}^+ and A_{mn}^- can be separately evaluated. Based on the multiple measurements at given axial plane modal coefficients for individual modes can also be separately evaluated. The forward traveling acoustic energy at upstream and downstream planes of the treatment panel are utilized to determine the insertion loss in the following manner:

The modal acoustic energy intensity at a location (x, y, z) is given by [Ref. 9]:

$$N_z = \left\{ \frac{1+M^2}{2} \right\} [pu^* + p^*u] + M \left[\frac{pp^*}{\rho c} + \rho c u u^* \right] \quad (24)$$

where, u is the acoustic particle velocity in the z direction. Superscript $*$ represents the complex conjugate of the variable. Acoustic particle velocity is expressed as:

$$u = \frac{i \frac{\partial p}{\partial z}}{\rho c k \left(1 - \frac{k_z}{k} M \right)} \quad (25)$$

Simplifying Equation (24) the acoustic intensity at (x,y,z) can be expressed as [Ref. 9] :

$$N_z = \left\{ (1 + M^2) Q + M \left(\frac{1}{\rho c} + \rho c Q^2 \right) \right\} (pp^*) \quad (26)$$

$$\text{where, } Q = \left\{ \frac{\left(\frac{k_z^+}{k} \right)}{\rho c \left[1 - \left(\frac{k_z^+}{k} \right) M \right]} \right\} \text{ and } pp^* = |A_{mn}^+|^2 \cos^2 \left(\frac{m\pi x}{W} \right) \cos^2 \left(\frac{n\pi y}{H} \right) \quad (27)$$

Energy flux for mn mode is:

$$\begin{aligned} E_{mn} &= \int_0^W \int_0^H N_z dx dy \\ &= \left\{ (1 + M^2) Q + M \left(\frac{1}{\rho c} + \rho c Q^2 \right) \right\} |A_{mn}^+|^2 \Phi_{mn} \end{aligned} \quad (28)$$

where, $\Phi_{mn} = 1$, when $m = n = 0$

$$\Phi_{mn} = \frac{1}{4}, \text{ when } m \neq 0, n \neq 0$$

$$\Phi_{mn} = \frac{1}{2}, \text{ when } m = 0, n \neq 0 \text{ or } m \neq 0, n = 0$$

The difference of energy flux for the forward traveling wave between the upstream and downstream of the treatment panel is the acoustic insertion loss.

3.3.2 Boundary-Layer Profile Measurements: The boundary layer profiles for the panels are measured in the flow duct facility with a dedicated traverse system at a single location using a total pressure probe traversed by a computer controlled traversing system. The closest vertical location with respect to the panel surface is 0.015" at which the measurement is made, since the probe diameter is about 0.03". Total pressure data measured by the traversing probe are utilized to evaluate the boundary layer velocity profile over the panel surface.

The boundary layer data are also used to evaluate the local skin friction coefficient, displacement thickness, momentum thickness, and pressure recovery factor. The Reynolds numbers based on the hydraulic diameter of 4.44" for the rectangular pipe of 4"x5" lies between 0.78×10^6 to 2.08×10^6 for grazing flow Mach numbers of 0.3 to 0.8, which fall in the turbulent flow region. Based on the Reynolds number values the duct flow for the present

study is assumed to be turbulent and fully developed, since the measurement location is way downstream from the contraction portion of the duct connecting the constant area flow duct and the plenum chamber. For turbulent boundary layer the shear stress at the surface (or wall) τ_w is given by [Ref. 10] :

$$\tau_w = (\mu + A_\tau) \frac{dU}{dy} \quad (29)$$

where, $\mu \frac{dU}{dy}$ is a laminar contribution and $A_\tau \frac{dU}{dy}$ is a turbulent contribution due to turbulent mixing to the shear stress and μ , A_τ , U , and y are the coefficient of viscosity, the mixing coefficient, velocity in the boundary layer, and vertical distance from the wall surface, respectively. The local skin friction coefficient C_f can thus be derived as;

$$C_f = \frac{\tau_w}{\frac{1}{2} \rho U_\infty^2} \quad (30)$$

where, U_∞ is the freestream velocity.

A more suitable procedure to derive skin friction coefficient is developed by Bobba and Lahti [Ref. 11] using Coles' method [Ref. 12]. This method utilizes the three boundary layer regions, namely, a laminar sublayer region where the flow is fully laminar, a turbulent region where the flow is fully turbulent, and an overlap region in between the two. The overlap region is often referred to as the wall region where the logarithmic law of the wall prevails, and the fully turbulent region is referred to as the wake region where the profiles are described by Coles' law of the wake [Ref. 12]. It was suggested by Coles that the boundary layer profiles may be represented by a linear combination of two universal functions, the law of the wall and the law of the wake. These functions were established on an empirical basis by Coles and the correlated velocity profile is given by :

$$\frac{U}{U_\infty} = \left(\sqrt{\frac{C_f}{2}} \right) \left[B + \frac{1}{\kappa} \ln \left(\sqrt{\frac{C_f}{2}} \right) \frac{U_\infty y}{\nu} + \frac{\Pi}{\kappa} 2 \sin^2 \left(\frac{\pi y}{2 \delta} \right) \right] \quad (31)$$

where; $\kappa = 0.41$, Karaman constant

Π = Coles' equilibrium parameter in the wake region

δ = boundary layer thickness

$B = 5.0$

In the above equation the first two terms correspond to the law of the wall and the third term represents the law of the wake. An iterative procedure for a least square fit of the above equation with the measured boundary layer profile is developed by Bobba and Lahti [Ref. 11] to determine the skin friction coefficient C_f and the boundary layer thickness δ . Thus the computer program developed in Ref. 11 is utilized for the present study.

3.3.3 In-situ Method of Normal Impedance Measurements: In addition to acoustic suppression and boundary-layer profile measurements, DC flow resistance and in-situ impedance for liners in the presence of grazing flow are measured simultaneously in this facility for single degree of freedom type treatment panels with additional instrumentation (see Figure 48). The in-situ method is used to study the effect of grazing flow on the acoustic impedance of locally reacting single degree of freedom type treatment panels [Ref. 13]. The panel, for this type of measurement, consists of a thin porous facesheet, a honeycomb cavity, and a hard back plate. The walls of the honeycomb cavity are regarded as perfectly rigid, so that there is no transmission of sound between the adjacent cavities. In addition, the cavities should be sufficiently narrow, so that the assumption of only plane wave propagation in the cavity between the facesheet and back wall can be made. Two transducers are mounted in the cavity, one is flush on the facesheet and the other is flush on the back wall, to measure complex acoustic pressures at A (i.e., p_A) and B (i.e., p_B). The incident and reflected pressures in the cavity can be expressed as follows:

$$\text{Incident Pressure: } p_+ = p_o e^{i(\alpha x - ky)} \quad (32)$$

$$\text{Reflected Pressure: } p_- = p_o e^{i(\alpha x + ky)} \quad (33)$$

$$\text{Acoustic Pressure of Standing Wave: } p = 2p_o e^{i\alpha x} \cos ky \quad (34)$$

$$\text{Normal Acoustic Particle Velocity: } u = -i \frac{2p_o}{\rho c} e^{i\alpha x} \sin ky \quad (35)$$

Considering facesheet to be acoustically thin, the particle velocity at A is given by :

$$u_A = -\frac{2p_o}{\rho c} i e^{i\alpha x} \sin ky_A = -\frac{p_B}{\rho c} i e^{i\alpha x} \sin ky_A \quad (36)$$

Specific impedance at the liner surface is thus expressed as :

$$Z = -\frac{p_A}{\rho c u_A} = -i H_{AB} e^{i(\Delta f)} \text{cosec } ky_A \quad (37)$$

where, $H_{AB} = \left| \frac{p_A}{p_B} \right|$, $\omega = 2\pi f$, Δf and H_{AB} are the phase and magnitude of the transfer

function $\frac{p_A}{p_B}$, respectively.

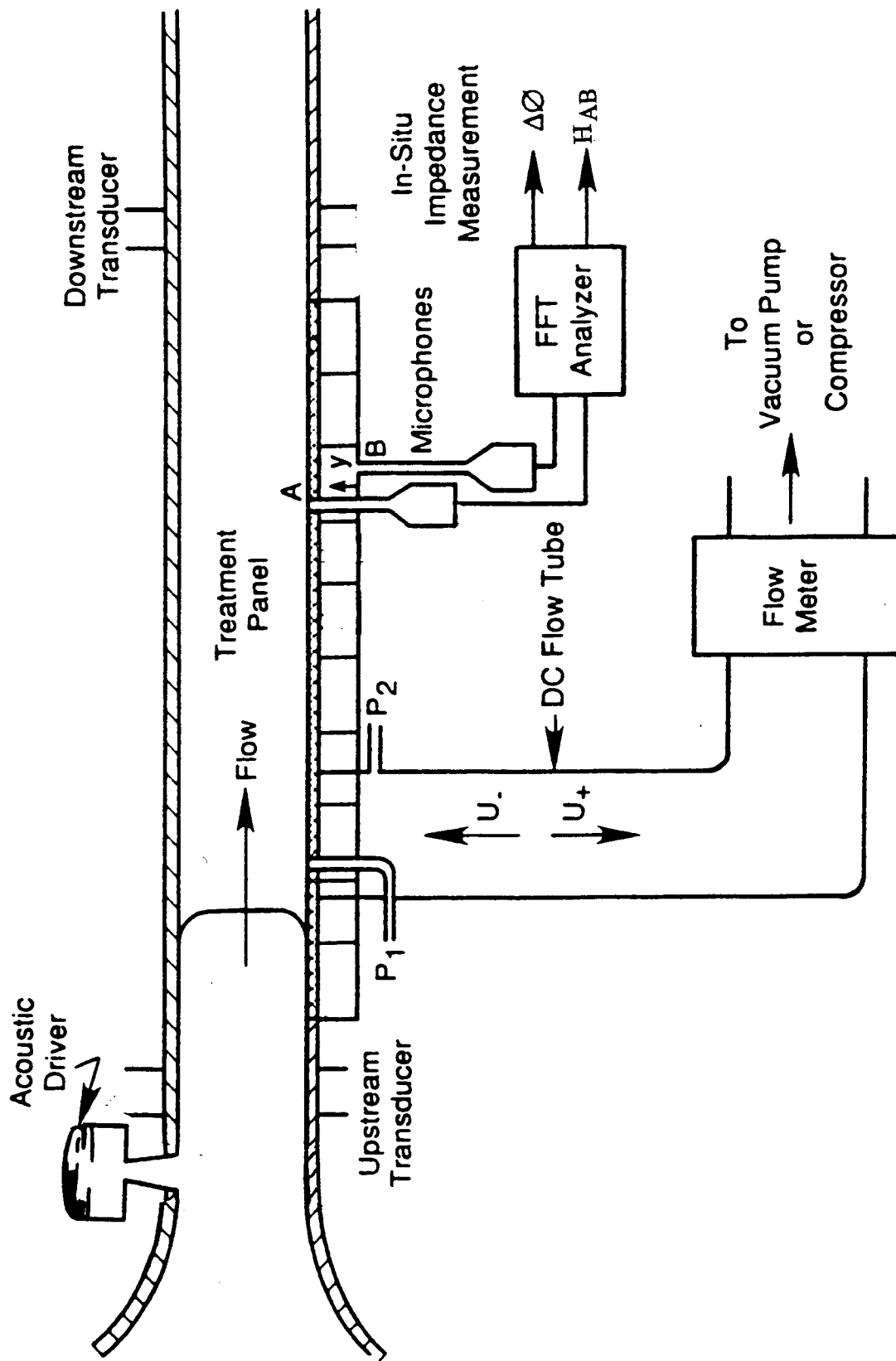


Figure 48. Simultaneous measurement of acoustic suppression (i.e., insertion loss), In-situ impedance, and DC flow resistance in a flow duct.

These panels designed for in-situ impedance measurement have deeper honeycomb cells to provide lower reactance values at the frequencies of measurement that are appropriate to the method (higher numerical values of reactance introduce inaccuracies into the method).

Flow duct tests are planned to evaluate in-situ impedance, DC flow resistance, and skin friction loss for various liner panels in the presence of grazing flow, up to a Mach number of 0.8, at ambient conditions. A computer controlled traverse system with a total head pressure probe, installed on the upper wall of the test section, is used for boundary layer profile measurement. Thus, the boundary layer profile is measured for each liner panel at a fixed location. This data is used to evaluate the skin friction loss of the panel. Figure 49 shows the flow duct facility with air supply system. The high-pressure air is connected to the plenum chamber for the flow duct through a moisture separator and a filter system. Figure 50 is a close-up view of the flow duct with an instrumented panel. The DC flow and boundary layer profile measurement instrumentations are shown in this figure.

Impulse technique for Flow Duct Tests: Both discrete frequency and broadband type acoustic excitations are employed in these types of tests. Testing using discrete frequency excitation to cover a large range of frequencies is time-consuming since the data has to be acquired at each discrete frequency. Broadband excitation (such as a random broadband noise or impulsive noise) gives the result for the entire frequency range simultaneously. A random broadband signal can be used in the normal impedance tube since there is no flow noise contamination concern. However, in the flow duct tests, random noise broadband sound may not be practical due to signal-to-noise-ratio problems caused by the flow noise. This can be overcome by the use of the impulse technique [Refs. 14 and 15].

Extensive acoustic impulse related research is found in the literature [Refs. 16 - 26]. An important feature of the impulse technique is that the signal contains spectral information over a wide frequency band. An impulse is defined explicitly by its time history, which, can be Fourier-transformed to give its spectral content. If the impulse were a true Dirac delta function, the Fourier transform would provide an infinitely broadband noise spectrum of constant amplitude. This ideal pulse shape is not physically realizable, but a pulse of sufficiently short duration can be generated and can be used to produce the frequency response of a system using impulse technique. One of the means to generate a pulse, used in the present study, is to excite acoustic driver system (or a single driver) by electronic pulse.

For successful application of this technique, generation of pulses separated from their reflections in time domain is essential. Hence, based on the facility configuration, the hardware

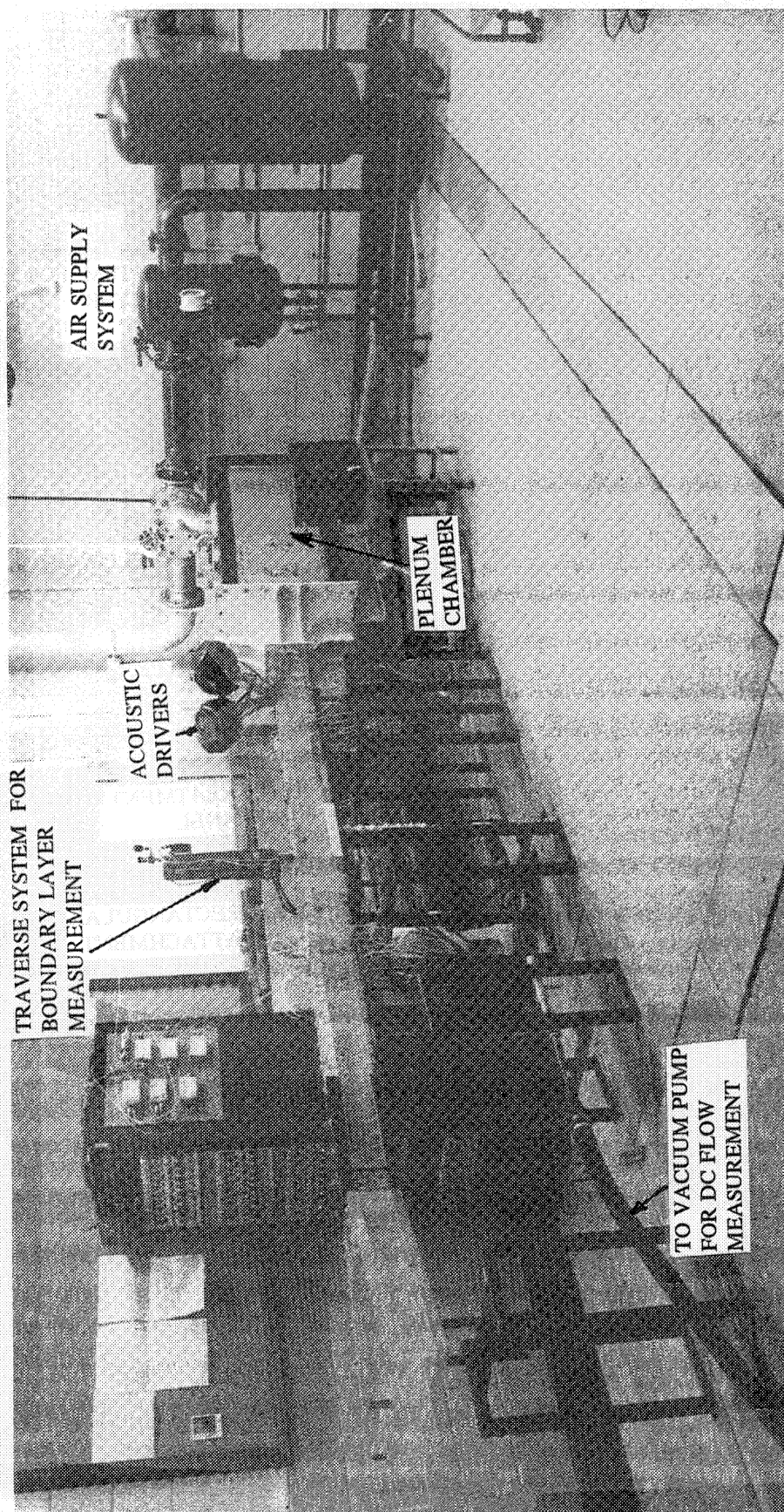


Figure 49. Flow duct facility with air supply system and DC flow instrumentation.

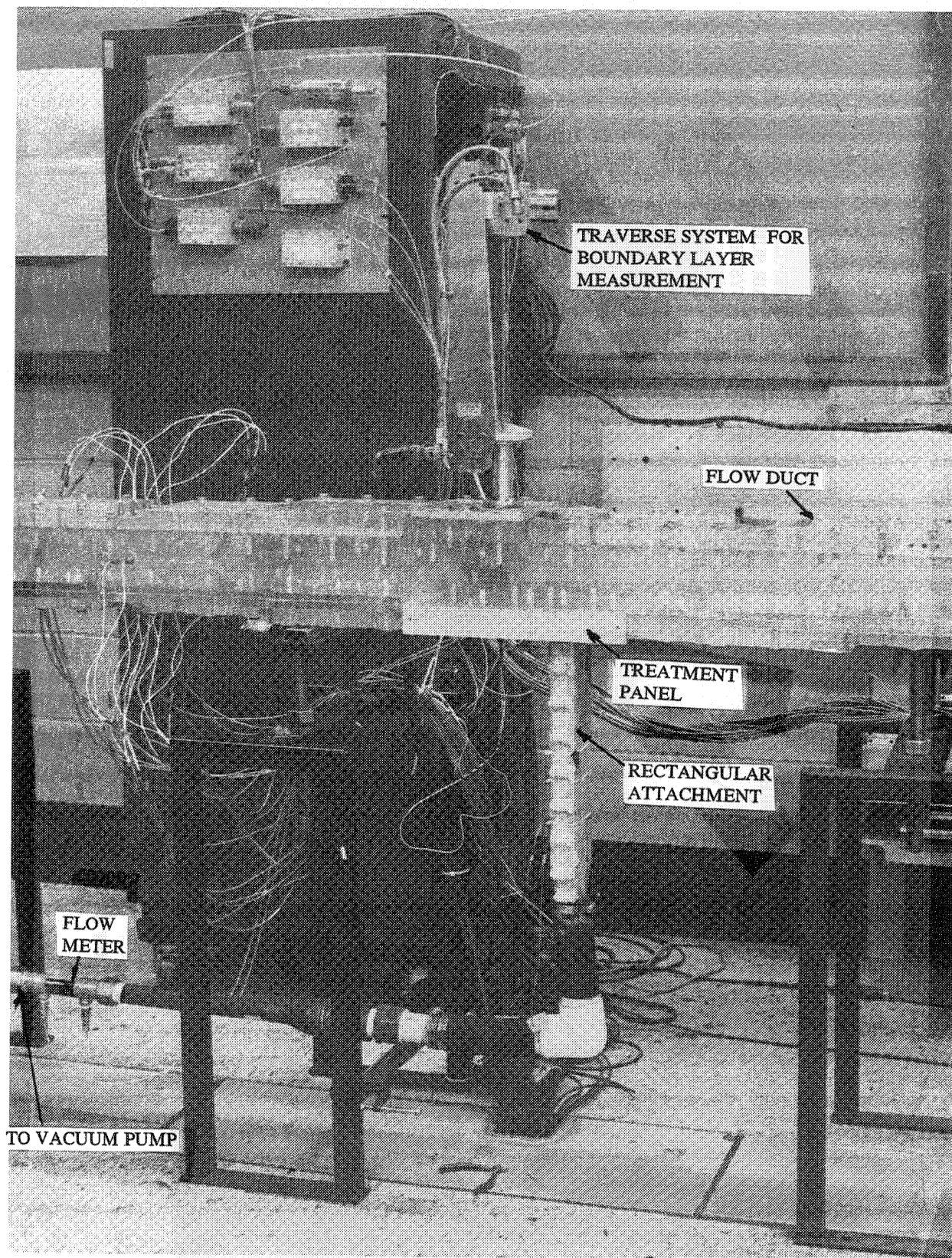


Figure 50. A close-up view of the flow duct facility with an instrumented panel, instrumented for DC flow resistance, In-situ impedance, and boundary layer profile measurement.

associated with pulse generation must be appropriately designed to prevent the reflection contamination. Certain amount of insulation may be necessary to absorb the reflections, which may not coalesce during the propagation of the pulse. In addition, sufficient propagation length must be allowed for the reflections to coalesce with the direct pulse before it arrives at the measurement location. If the facility limitation does not allow achieving these requirements, then it may not be possible to use this technique. If the application of impulse technique is successful, more tests can be conducted within the allocated time and budget. In addition, the measurements are necessary only at two planes, one upstream and the other downstream of the treatment panel for flow duct application, since forward moving waves are separated from backward moving waves in the time domain. For the flow duct application, appropriate hardware is designed and fabricated for proper pulse generation (see Figure 51).

Enhancement of Signal-to-Noise Ratio: In the presence of high velocity flow, it becomes difficult to isolate the signal (i.e., pulse or discrete frequency) from dominant broadband flow noise. In this situation a time domain signal averaging technique can be used to recover the periodic signal (i.e., pulse or discrete frequency) from the flow noise. For an impulsive sound source, if a sufficient number of individual pulse records, separated by adequate time interval, are averaged, the contribution from the flow-associated random fluctuations are averaged to zero, thus enabling recovery of the pulse time history. A synchronizing signal is used to find the start of each record. The simple summation process increases the signal-to-noise ratio because the noise that is not coherent with the synchronizing signal averages toward zero with an increasing number of samples. The signal averaging, illustrated in Figure 52, involves the generation of a train of pulses from the acoustic driver system using a pulse generator. The acoustic pulse train contaminated with flow noise is measured by the microphones and is fed to a signal analyzer in real time. The analyzer is simultaneously triggered by the same electronic signal used to excite the acoustic driver system. Thus the pulse is recovered applying a large number of averages.

Similar process is also utilized to enhance signal-to-noise ratio for periodic discrete frequency signal (see Figure 53). The continuous train of waveform, generated by acoustic device for excitation, is utilized to trigger and extract the signal.

3.4 Flow Duct Facility for Insertion Loss Evaluation (Rohr):

Insertion loss results obtained from the flow duct tests did not exhibit expected trends with respect to grazing flow Mach number, facesheet geometric parameters, and bulk resistivity. These results were obtained using acoustic pressure measurements on flow duct surface at 8

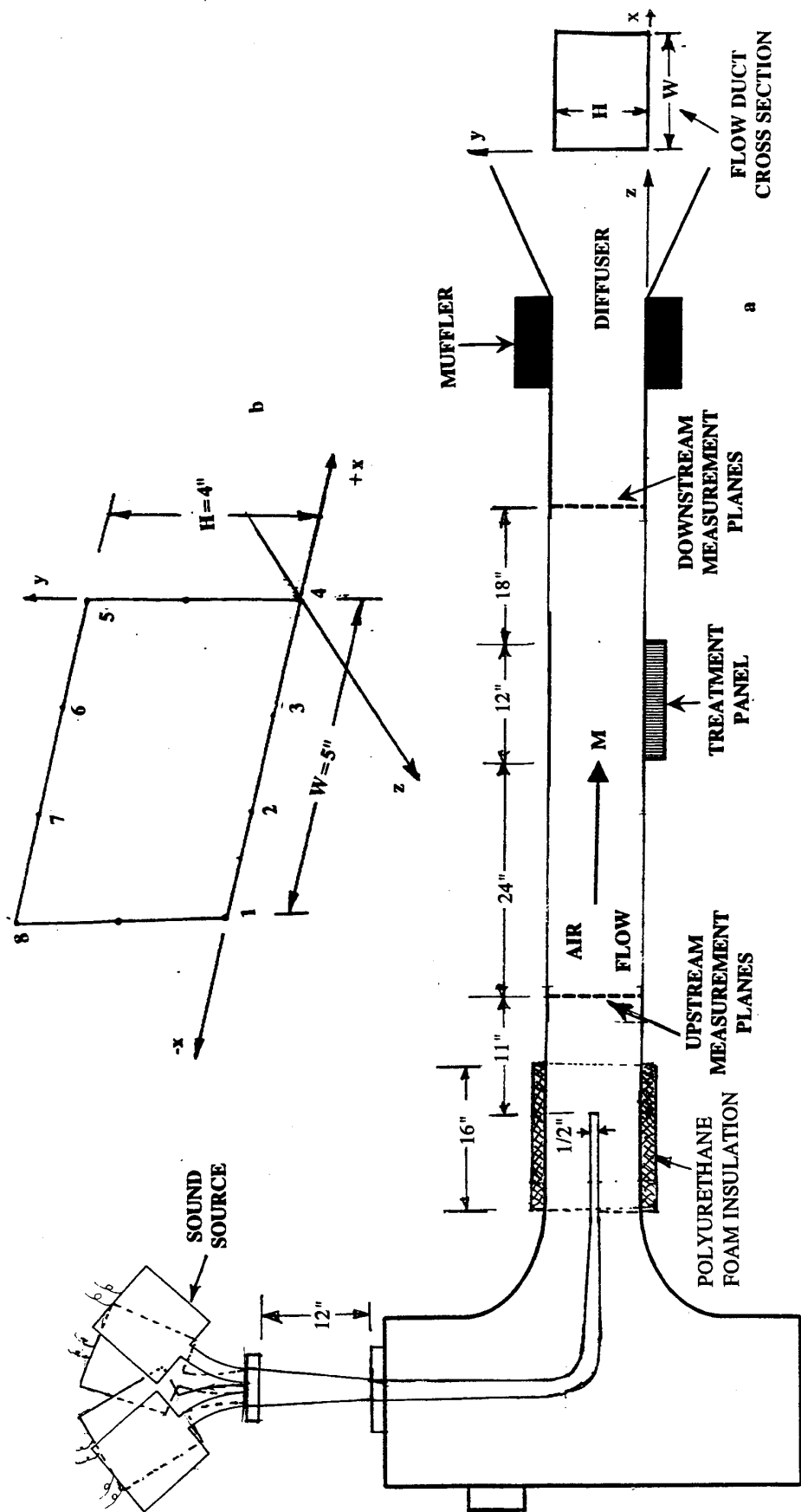


Figure 51. (a) Schematic of the flow duct apparatus with impulsive sound source and (b) transducer locations on a measurement plane.

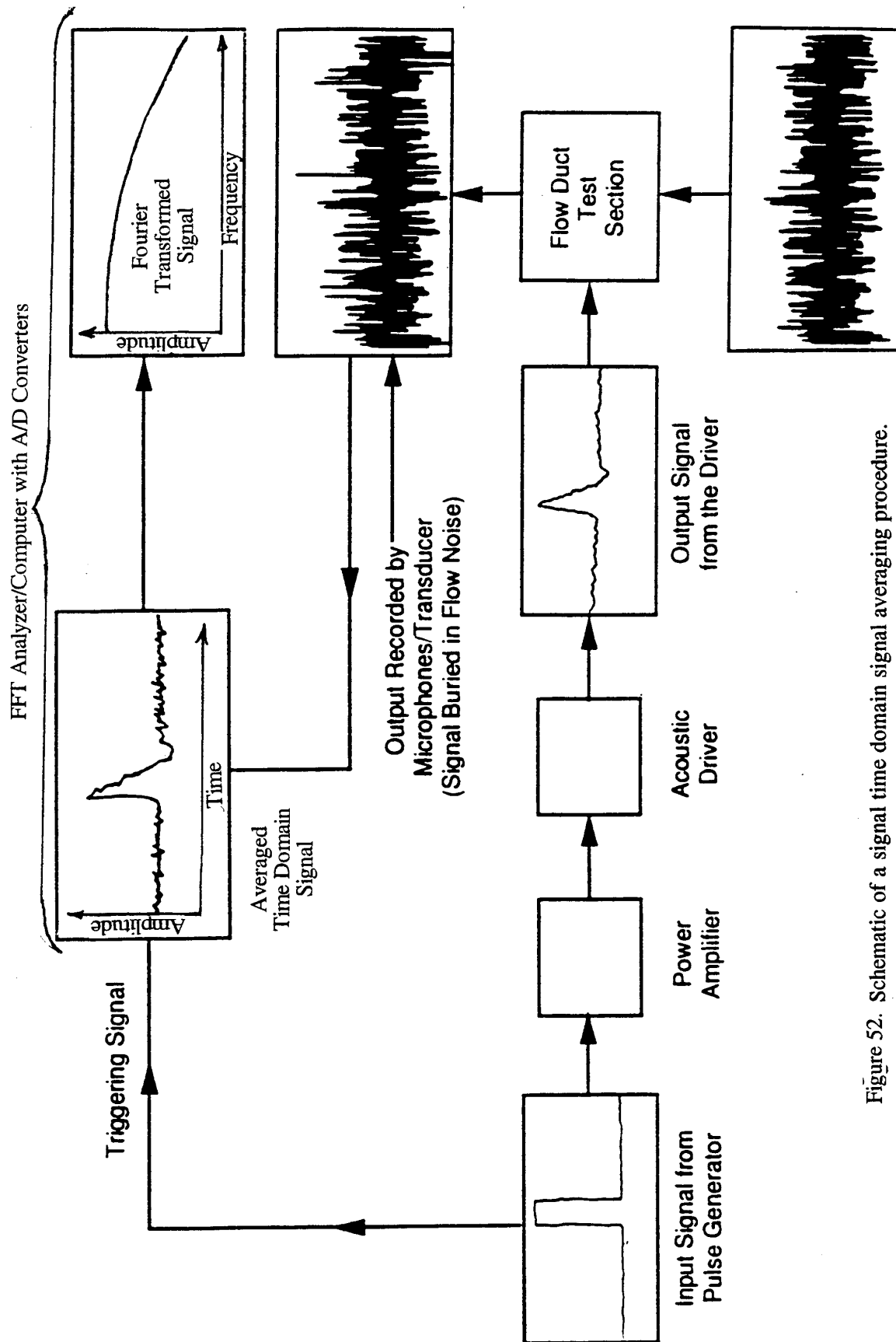


Figure 52. Schematic of a signal time domain signal averaging procedure.

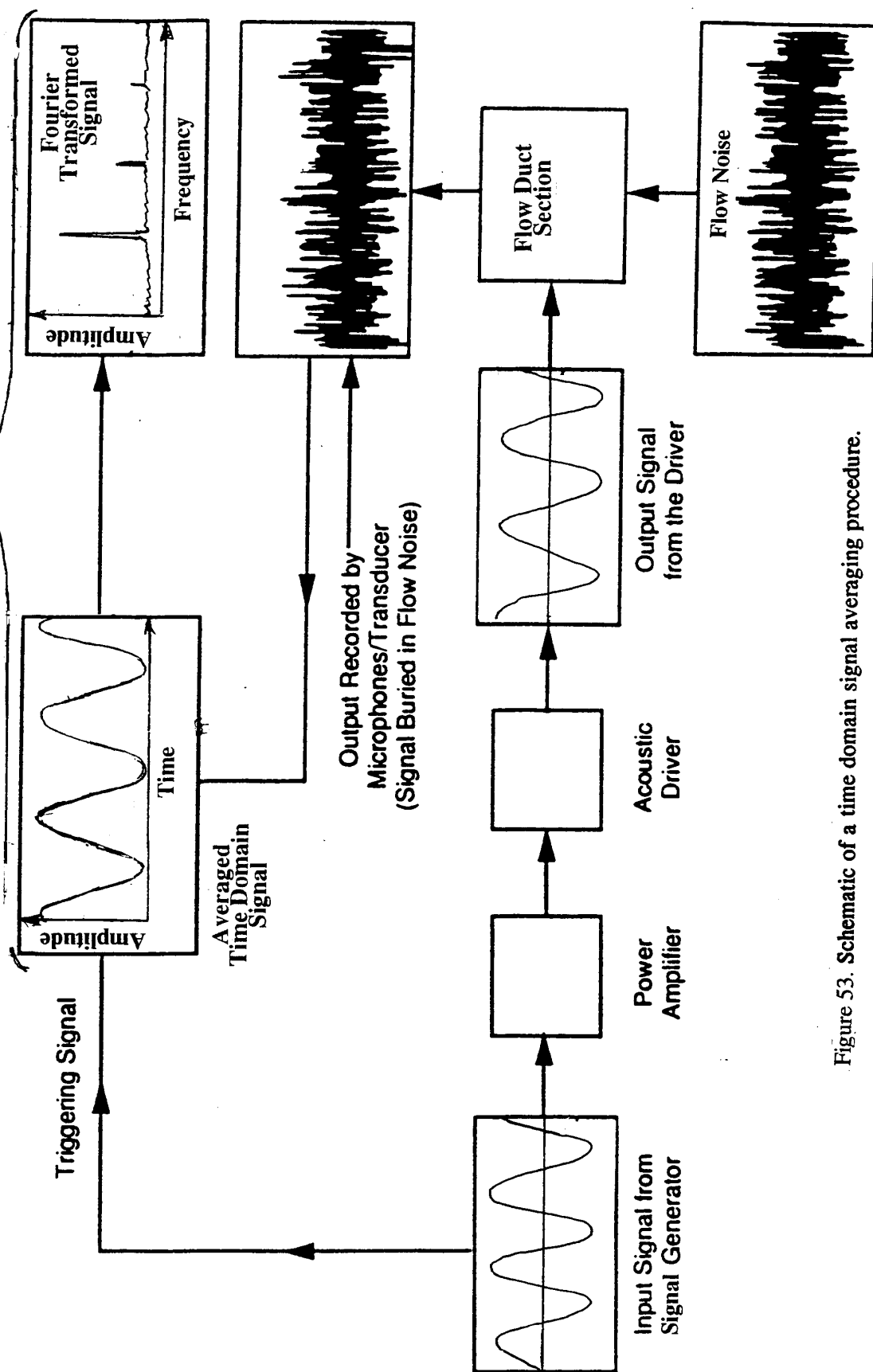


Figure 53. Schematic of a time domain signal averaging procedure.

upstream and 8 downstream locations of the panel, utilizing p^2 method. The insertion loss was evaluated from the difference of the summation of square of the acoustic pressures measured upstream and downstream of the panel. This is a crude method to estimate insertion loss, especially at higher frequencies, at which a large number of modes would be propagating. A modal decomposition method would probably give more accurate results. However, to evaluate insertion loss by modal decomposition method for higher frequency range a very large number of upstream and downstream dynamic pressure measurements would be required. To facilitate the flow duct with so many transducers was not practical. The insertion loss results obtained from the GEAE's flow duct tests and the understanding of these results, that the results are inaccurate, are described in Appendix B.

An alternate way to evaluate the insertion loss is to utilize a diffused acoustic field in the flow duct, generated by a reverberant chamber. In this situation, the identities of individual modes are highly diminished and a more uniform sound field propagates through the flow duct. Such a facility exists at Rohr Inc. (see Figure 54) to measure insertion loss up to a flow Mach number of 0.8. Rohr's in-house test results indicate a definite trend of insertion loss with respect to grazing flow Mach number and frequency for SDOF type panels. Thus, the liner panels, acquired under HSR program, were tested in the flow duct facility of Rohr Inc., which is equipped with reverberant terminations, to determine if the measured insertion loss would exhibit expected trends with respect to flow and facesheet parameters. In this facility, the acoustic energy flux at the upstream and downstream of the panel are measured at ambient temperature conditions. The insertion loss is the difference between these two measurements. Measured insertion loss is further corrected relative to a hardwall configuration.

The insertion loss spectra are generated with respect to narrowband frequency up to 15 kHz with a 50 Hz bandwidth. One-third octave data up to 12 kHz is generated using the narrowband data. Both narrowband and 1/3-octave band data are used in the current study. The narrowband data as measured exhibits significant oscillations. For practical use such large oscillations are eliminated applying a smoothing process. Figure 55 illustrates an example of such smoothing. The smoothed spectra agree well with the 1/3-octave data.

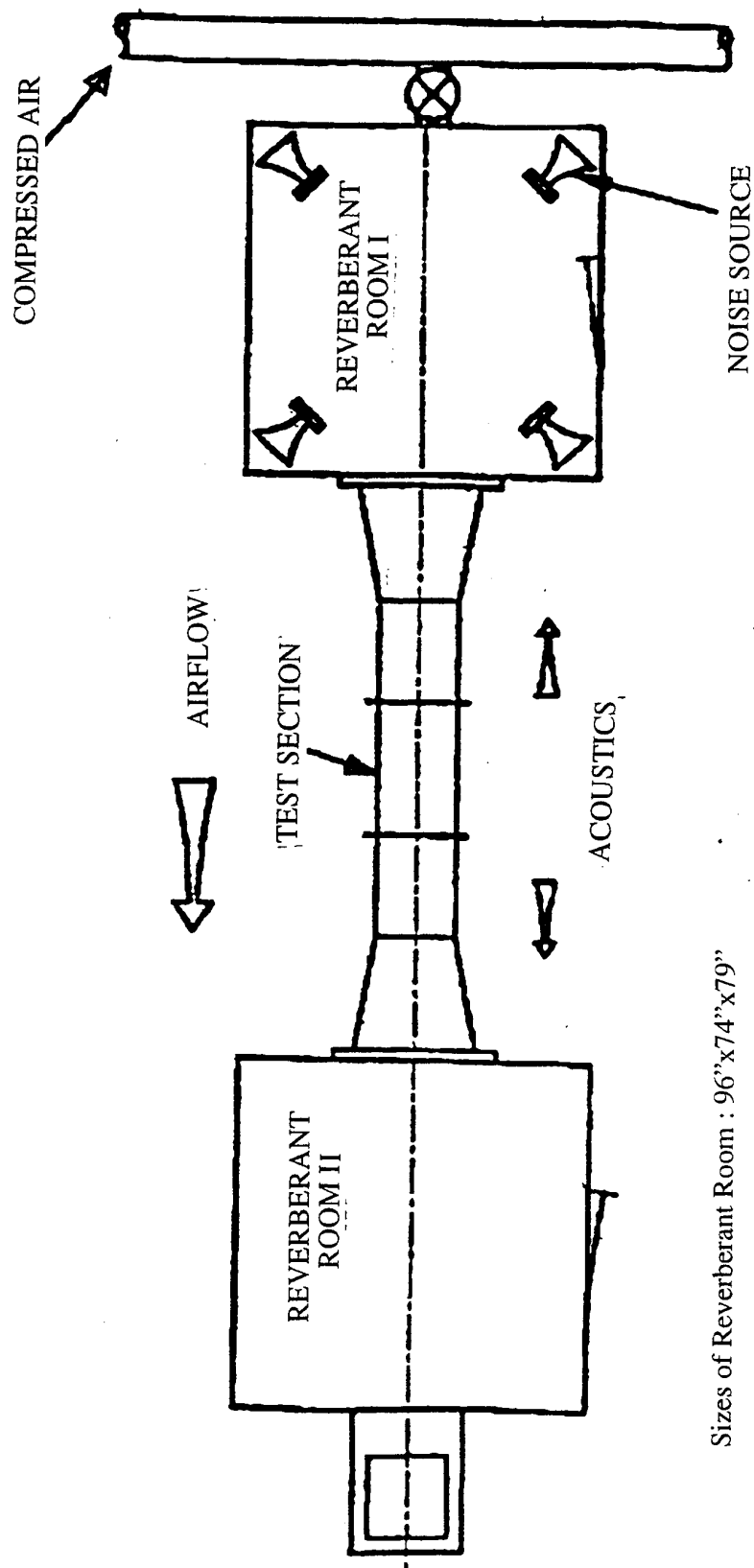


Figure 54. Schematic of Rohr's flow duct facility with reverberant terminations.

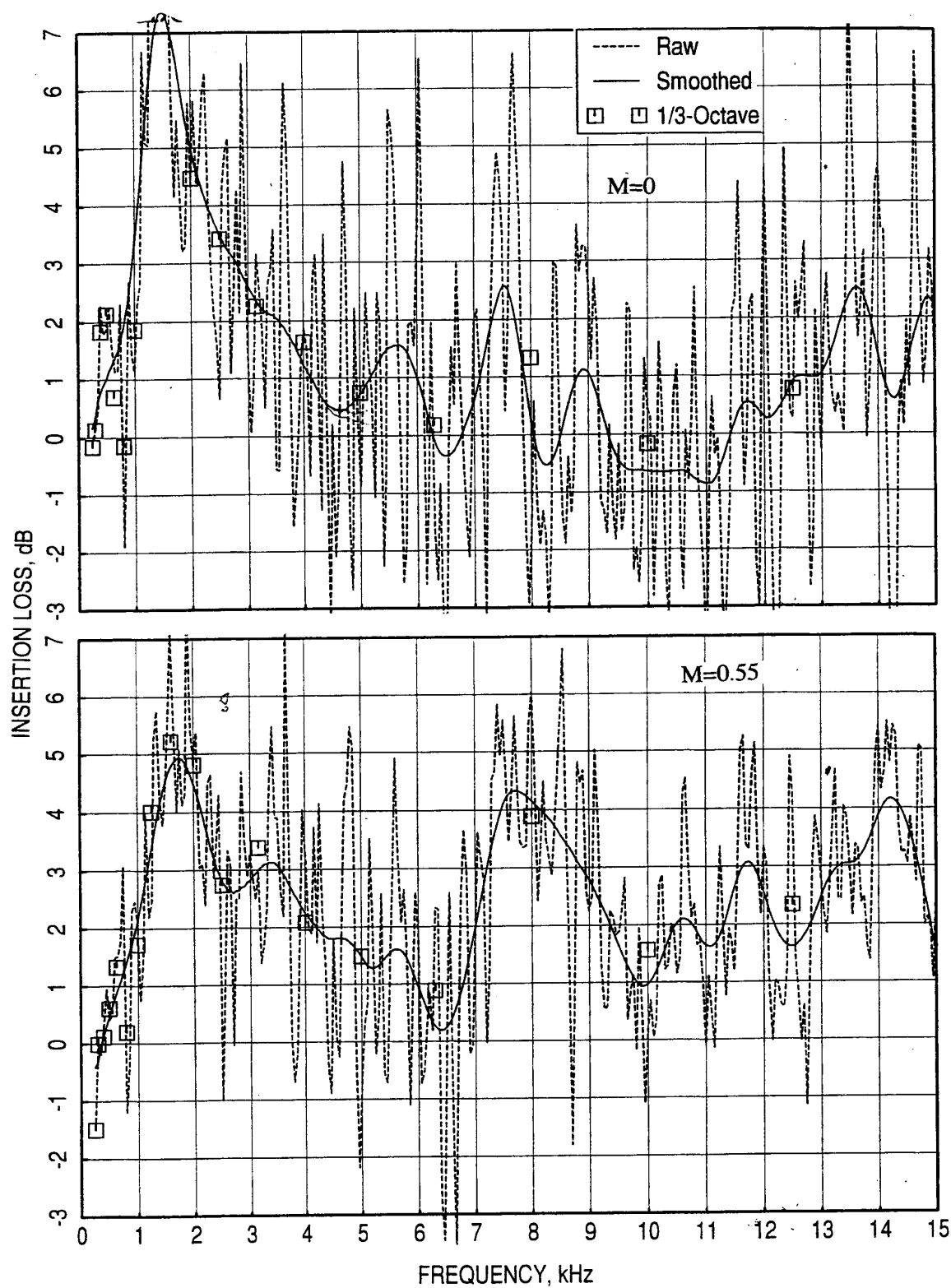


Figure 55. Effect of smoothing on the narrowband insertion loss data for a 1"-deep SDOF panel; $\sigma=7.5\%$, $d=0.039"$, $t=0.025"$.

4.0 DESIGN AND PROCUREMENT OF TEST SAMPLES

4.1 Design of Panels for Flow Duct Test:

Several treatment panels, based on a number of concepts, are designed. The design concepts considered are Single-Degree-of-Freedom (SDOF), Two-Degree-of-Freedom (2DOF), and Bulk Absorber. Two types of SDOF treatment are considered, one with a perforated type face plate and the other with a wiremesh (woven) type faceplate. In addition, special configurations of these concepts are also included in the design. Several treatment panels are designed for parametric study. In these panels the facesheets of different porosity σ , hole diameter d , and sheet thickness t are utilized. Several deep panels (i.e., 1 inch deep) are designed to be instrumented to measure DC flow resistance and in-situ impedance in the presence of grazing flow. All the panels are designed for a grazing flow Mach number of 0.75 at room temperature and pressure conditions. An OASPL of 143.8 dB is assumed for these designs. A boundary-layer displacement thickness of 0.1" is used for SDOF type liners with perforated facesheets. Impedance prediction methods described earlier are utilized in designing the treatment panels. The liner panels are designed for the following studies:

- Scaling Study (SDOF Type with perforated facesheet)
- Parametric study (SDOF Type, Perforated as well as linear facesheets including bulk-filled designs)
- Instrumented panels (1"-Deep SDOF Type with perforated facesheet)
- 2DOF Type Panels

Scaling Study: One of the objectives of the liner panel design is to develop appropriate scaling between the full-scale ejector at heated environment and the flow duct apparatus for laboratory tests. The full-scale ejector height H is 42.8" and the temperature at takeoff being 1290°F, the speed of sound c becomes 2050 ft/sec. A parameter L/H_e for symmetric duct of any geometry of treated length L is defined as:

$$L/H_e = \text{Treated Area} / (2 \times \text{Flow Area})$$

For a rectangular duct of height h and width w , lined on one side the parameter L/H_e becomes;

$L/H_e = L \times w / (2 \times h \times w) = L/2h$, where, $2h$ is the effective duct height H_e . The effective height H_e remains the same as h for a rectangular duct treated on both sides.

The flow duct for laboratory tests is a rectangular duct of height $h=4''$ and width $w=5''$ and the operating temperature being ambient (70°F) the speed of sound c_1 is 1128 ft/sec. Thus the effective height H_e becomes 8'' or 4'' based on one side or two-side treatment of the duct.

The acoustic suppression is based on the following nondimensional parameter;

$\eta = f H_e / c$, where f is the frequency in Hz. Equating η for full-scale ejector and one-sided treated flow duct the following frequency relationship is obtained;

$$\text{Flow Duct frequency } f_1 = f \times (H/2h) \times (c_1/c) = 2.95 f \cong 3 f.$$

Based on the design criteria that the peak noise for full-scale engine will be at 2 kHz. the η becomes 3.4. For scaling study when the flow duct is lined on one side (i.e., $H_e = 8''$) the frequency f_1 becomes 5750 Hz for $\eta = 3.4$, which represents 1/3-scale compared to the full-scale ejector frequency of 2000 Hz. By lining the duct on both sides the frequency becomes 11500 Hz (i.e., $H_e = 4''$) for $\eta = 3.4$, which represents 1/6-scale compared to the full-scale ejector frequency of 2000 Hz. For 1/6-scale liner to have optimum impedance at 11500 Hz the liner needs to be extremely thin (about 0.1''), which is difficult to fabricate. Thus for scaling study η is lowered to 1.75 which allowed the liner depths to be 0.7'' and 0.3'' for 1/3-scale and 1/6-scale panels, respectively. A full-scale panel for ambient condition is also designed, which would require a 12'' high one-sided lined duct and the panel depth would be 2.2'' for optimum impedance requirement.

A porosity of 9 %, a thickness of 0.02'', and a hole diameter of 0.04'' are selected for the facesheets for all three panels. Facesheet thickness is kept small (i.e., 0.02'') to minimize mass reactance effects. Hence, the only remaining parameter for the panels is the panel depth, which is adjusted to achieve the same impedance spectra with respect to nondimensional frequency for panels of different scale factors. The design parameters are tabulated below;

Config. Number	Design Description	Facesheet Parameters			Cavity
		Porosity σ , %	Hole Dia. d, in	Thickness t, in	
	SDOF Panel with Perforated Facesheet, $\eta=1.75$				
1	1/3-Scale , One-Sided Treatment ($H=4''$)	9	0.04	0.02	0.7
2	1/6-Scale , Two-Sided Treatment ($H=4''$)	9	0.04	0.02	0.3
3	1/1-Scale , One-Sided Treatment ($H=12''$)	9	0.04	0.02	2.2

Normalized impedance and absorption coefficient spectra with respect to frequency for these three panels are compared in Figures 56 and 57. The corresponding results plotted with

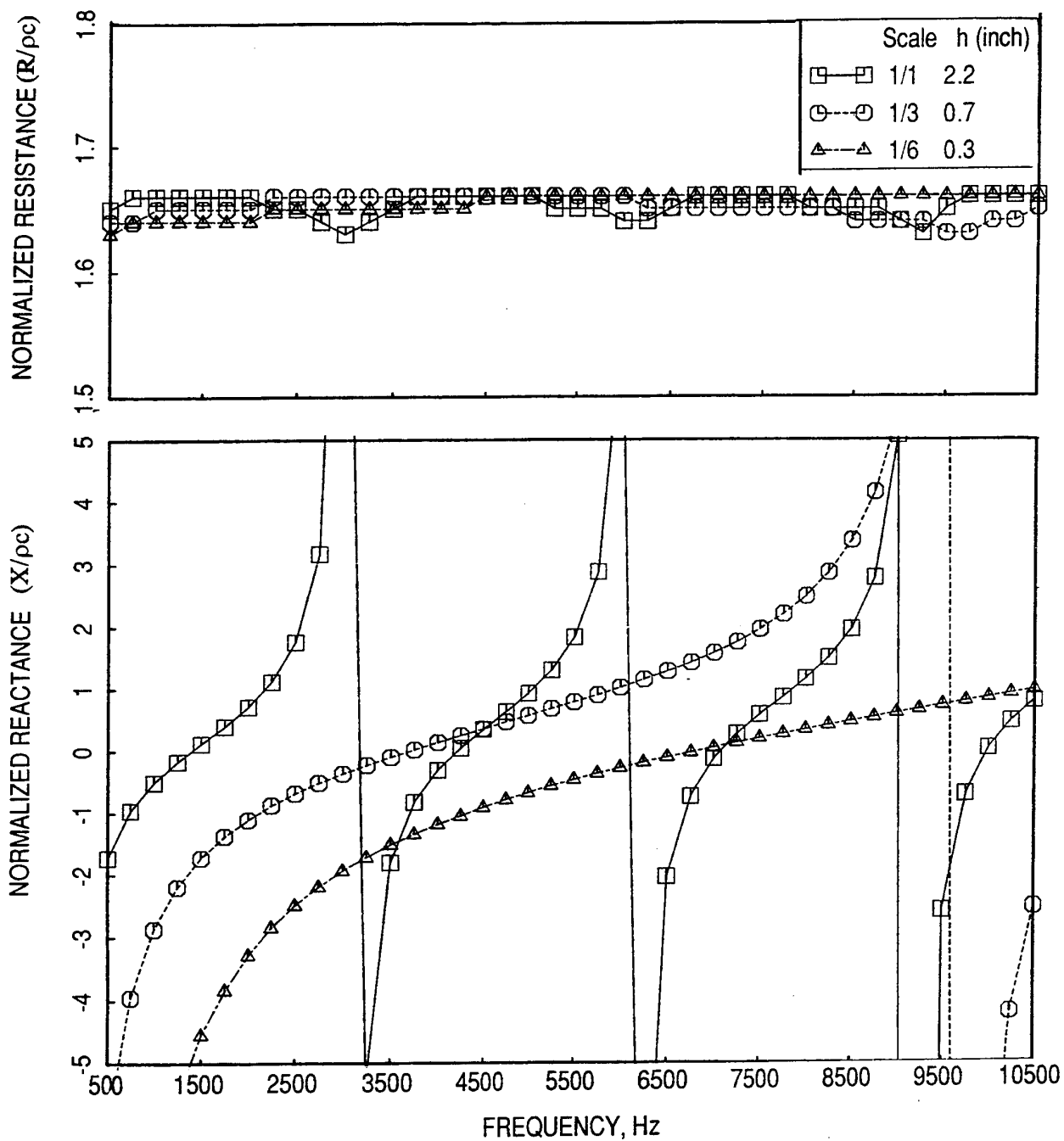


Figure 56. Effect of frequency scaling on normalized impedance spectra for SDOF type liners designed for $\eta = 1.75$; facesheet: $\sigma = 9\%$, $t = 0.02''$, $d = 0.04''$.

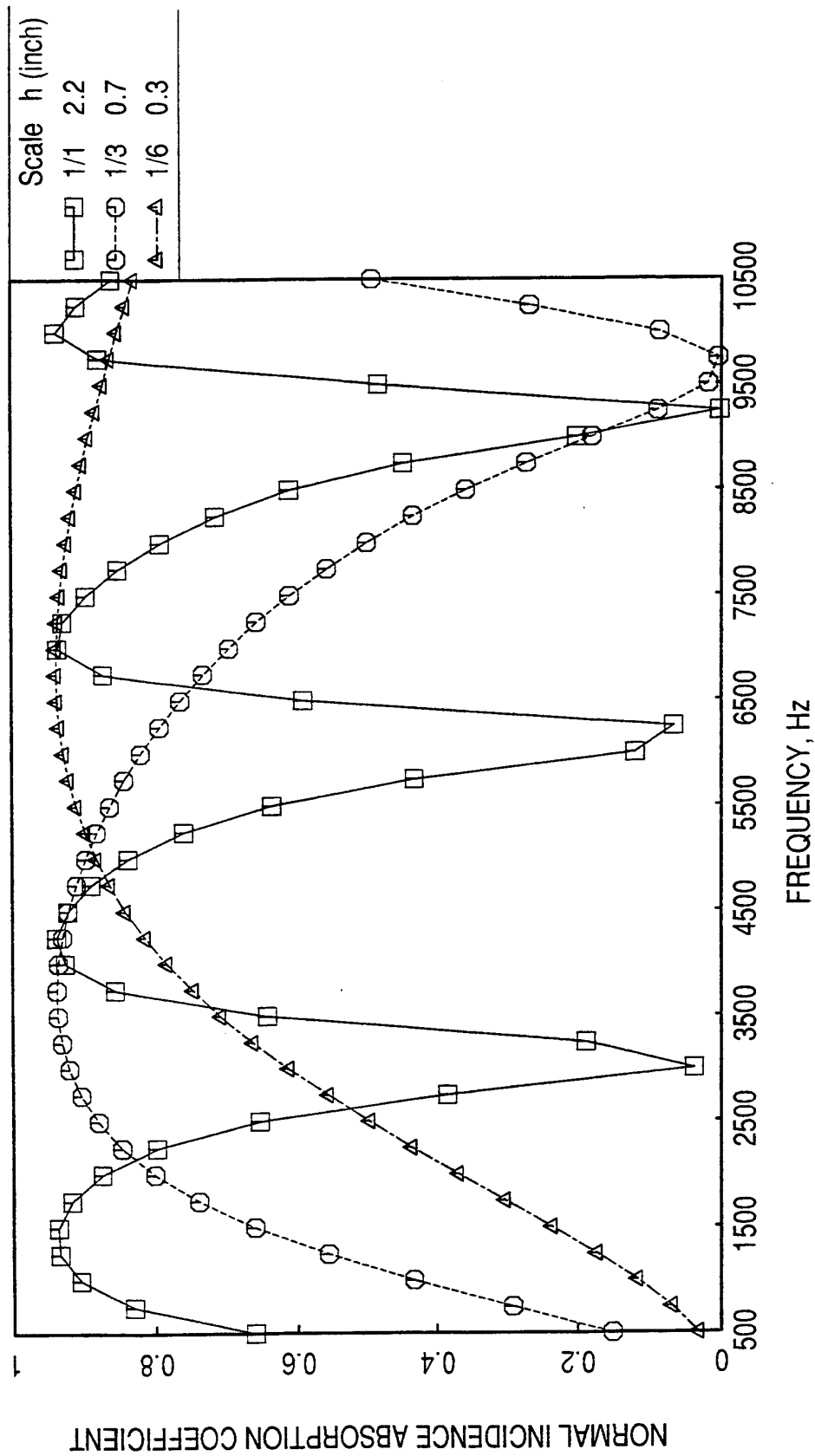


Figure 57. Effect of frequency scaling on absorption coefficient spectra for SDOF type liners designed for $\eta = 1.75$; facesheet: $\sigma = 9\%$, $t = 0.02$ ", $d = 0.04$ ".

respect to nondimensional frequency η are shown in Figures 58 and 59. While the impedance and absorption coefficient vary widely between the panels in Figures 56 and 57, they collapse very well in Figures 58 and 59 as expected.

Parametric study: For this study 1/3-scale panels with $\eta=3.4$ are designed. The liner depths vary between 0.25" and 0.5". These panels are categorized under 4 different groups.

Baseline Perforated Plate SDOF and Impedance Variations: The baseline design is a 1/3-scale SDOF panel based on the full scale nondimensional frequency of 3.4. The cavity depth for this panel is 0.25" and the facesheet porosity, thickness, and hole diameter are 9 %, 0.028", and 0.04", respectively. A set of 1/3-scale SDOF with perforated facesheet are designed with fixed facesheet thickness of 0.028" and hole diameter of 0.04" to study the impact of impedance variation on acoustic suppression due to cavity depth h and facesheet porosity variation. The design parameters are listed below;

Config. Number	Design Description	Facesheet Parameters			Cavity
	1/3-Scale SDOF Panels with Perforated Facesheet, $\eta=3.4$ One-Sided Treatment ($H=4"$)	Porosity σ , %	Hole Dia. d, in	Thickness t, in	Depth h, in
1	Baseline	9	0.04	0.028	0.25
2	High Resistive Facesheet (Increased by 1.5 times relative to Baseline)	6	0.04	0.028	0.19
3	Low Resistive Facesheet (Decreased by 0.5 times relative to Baseline)	18	0.04	0.028	0.32
4	Deep Panel, Shifts Tuning Frequency Down by 1 1/3-Octave	9	0.04	0.028	0.42
5	Thin Panel, Shifts Tuning Frequency Up by 1 1/3-Octave	9	0.04	0.028	0.16

For configurations 2 and 3, the panel depths are adjusted to maintain reactance values. Effect of cavity depth on impedance and absorption coefficient spectra for fixed facesheet porosity of 9 % are shown in Figures 60 and 61. The panel resistance does not change in these designs. However, the reactance and hence the absorption coefficient do change due to cavity depth. Effect of porosity on normalized impedance and absorption coefficient spectra for this group of panels are shown in Figures 62 and 63. Along with the porosity variation the cavity depth is also altered to attain the desired impedance limits. The resistance level is varied with decreasing porosity. The variation of reactance is basically due to the change in cavity depth.

Effect of Thick Facesheets on Suppression of Perforated Plate SDOF Panels : Three 1/3-scale panels are designed with facesheet thickness of 0.08" (equivalent to 0.24" thick at full scale), which is substantially higher compared to the baseline design. In these designs the

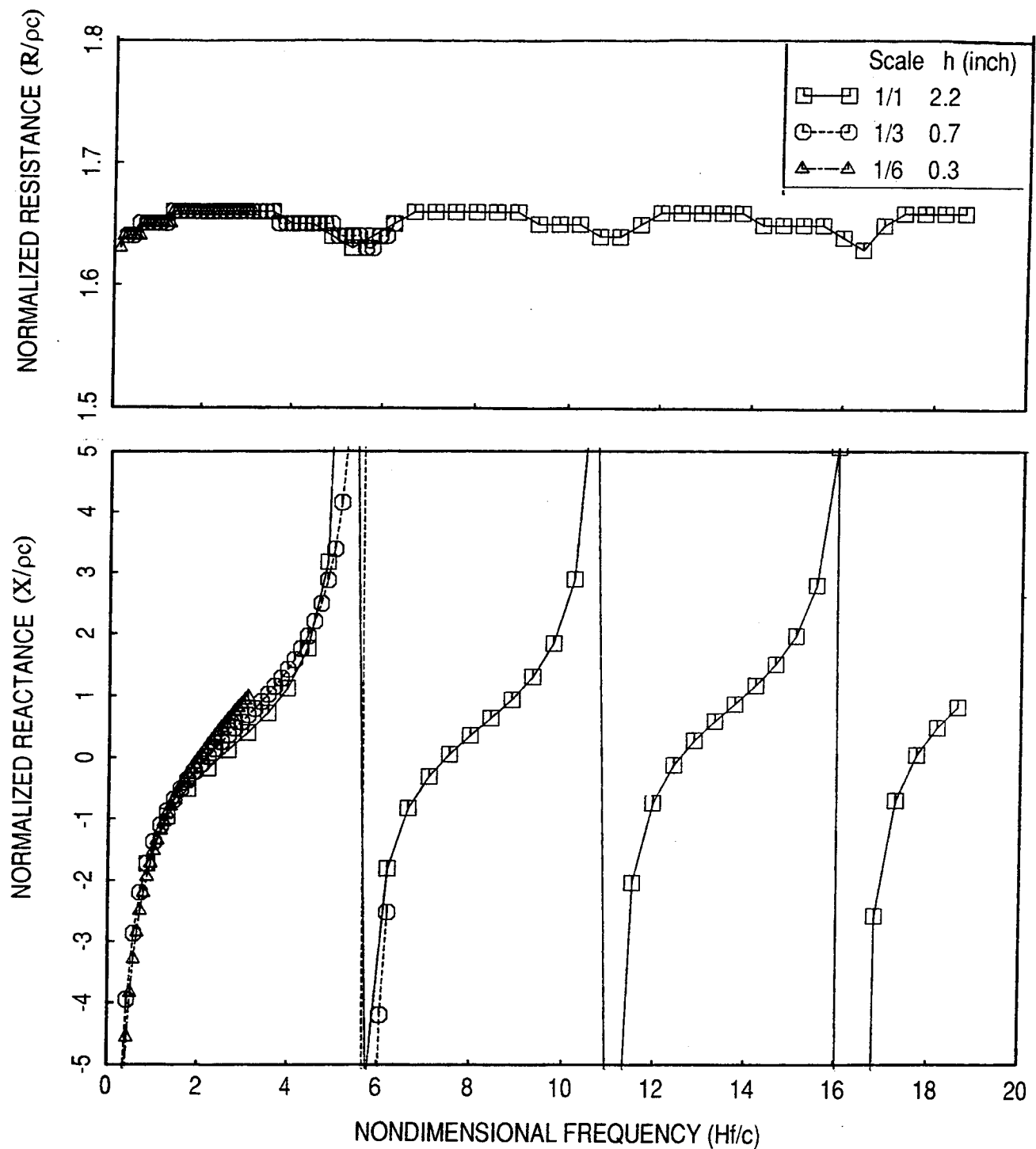


Figure 58. Effect of frequency scaling on normalized impedance spectra for SDOF type liners designed for $\eta = 1.75$; facesheet: $\sigma = 9\%$, $t = 0.02$ ", $d = 0.04$ ".

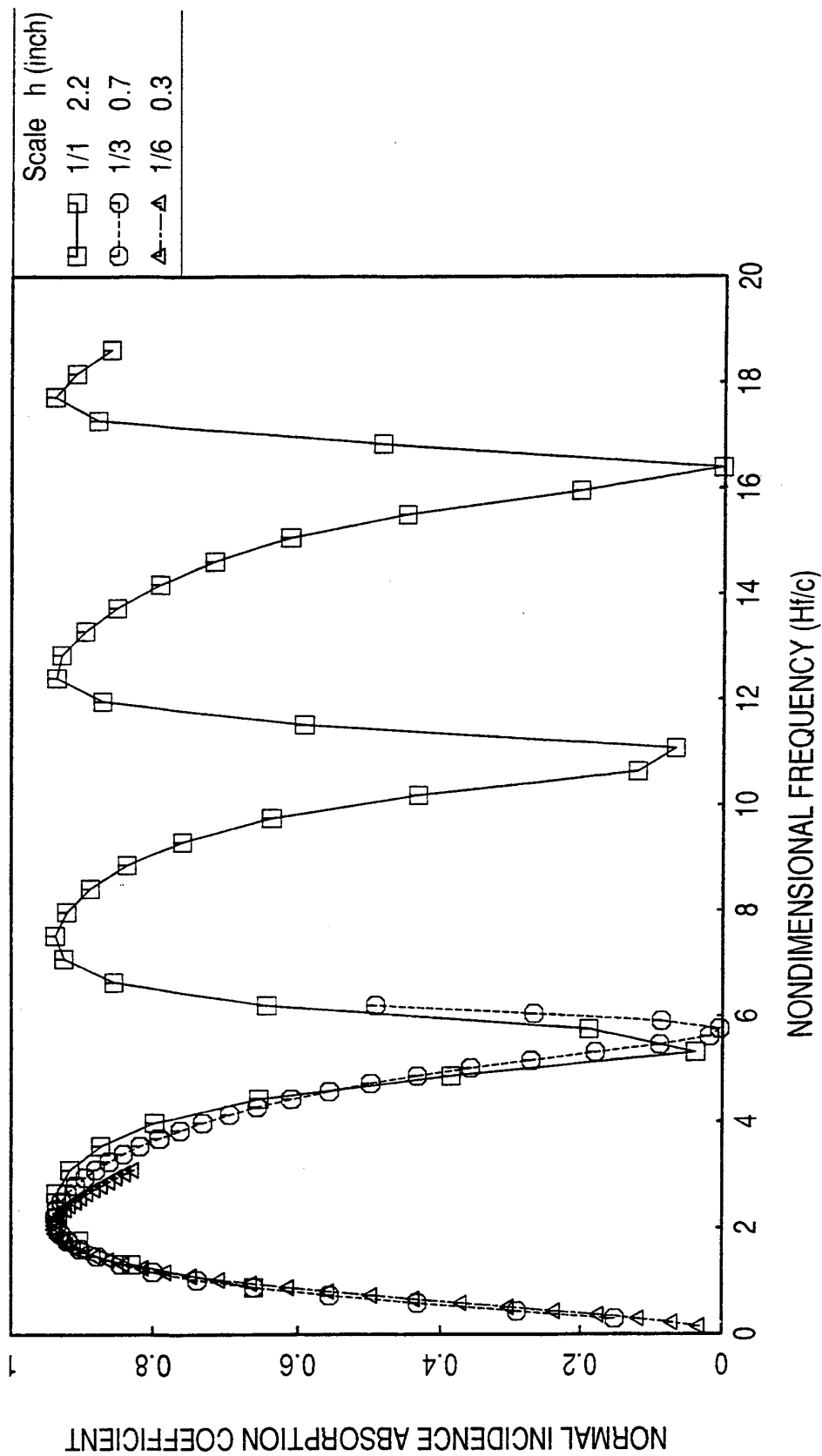


Figure 59. Effect of frequency scaling on absorption coefficient spectra for SDOF type liners designed for $\eta = 1.75$; facesheet: $\sigma = 9\%$, $t = 0.02$ ", $d = 0.04$ ".

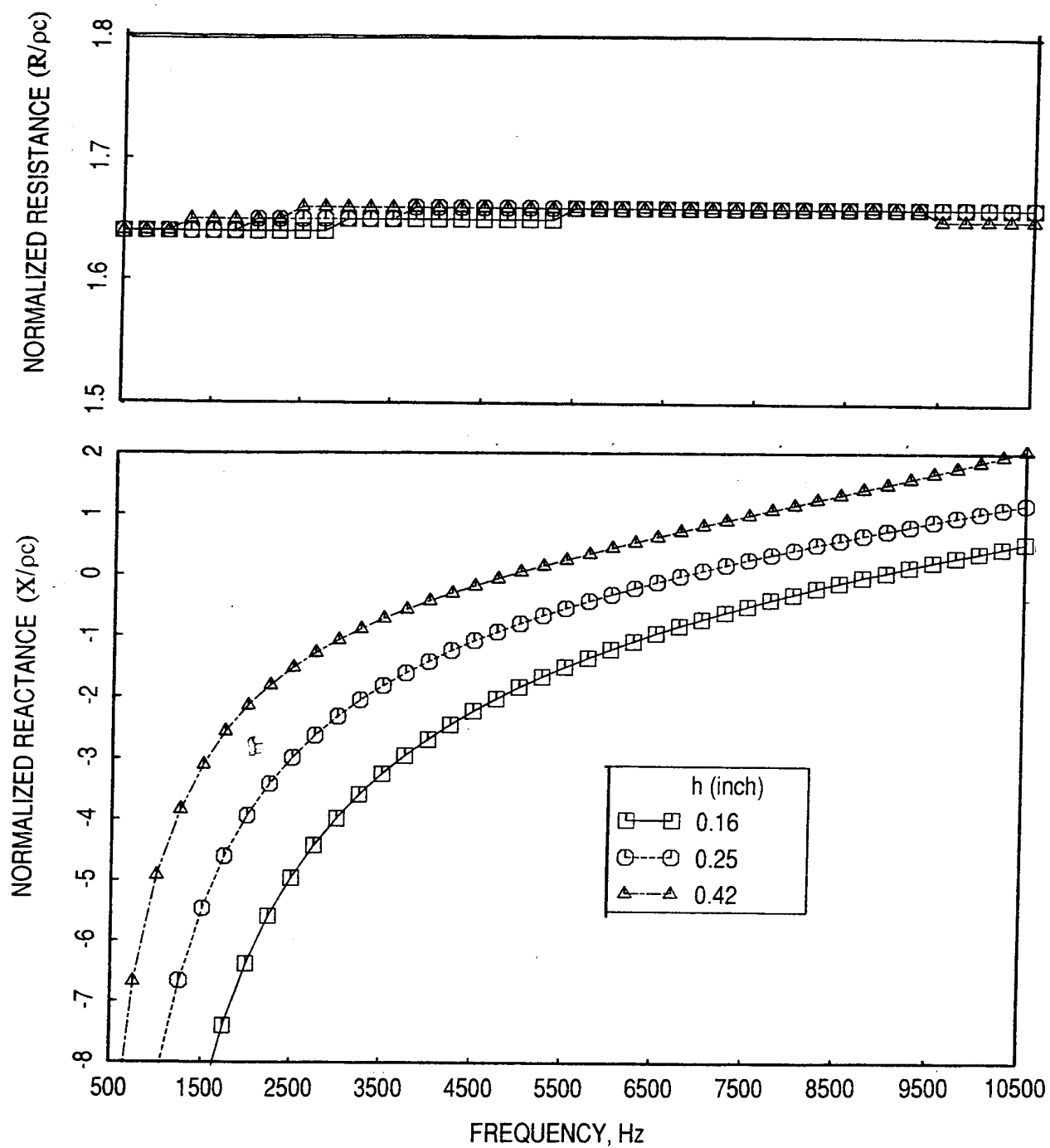


Figure 60. Effect of cavity depth, h on normalized impedance spectra for 1/3-scale SDOF type liners designed for $\eta = 3.4$; facesheet: $\sigma = 9\%$, $t = 0.028''$, $d = 0.04''$.

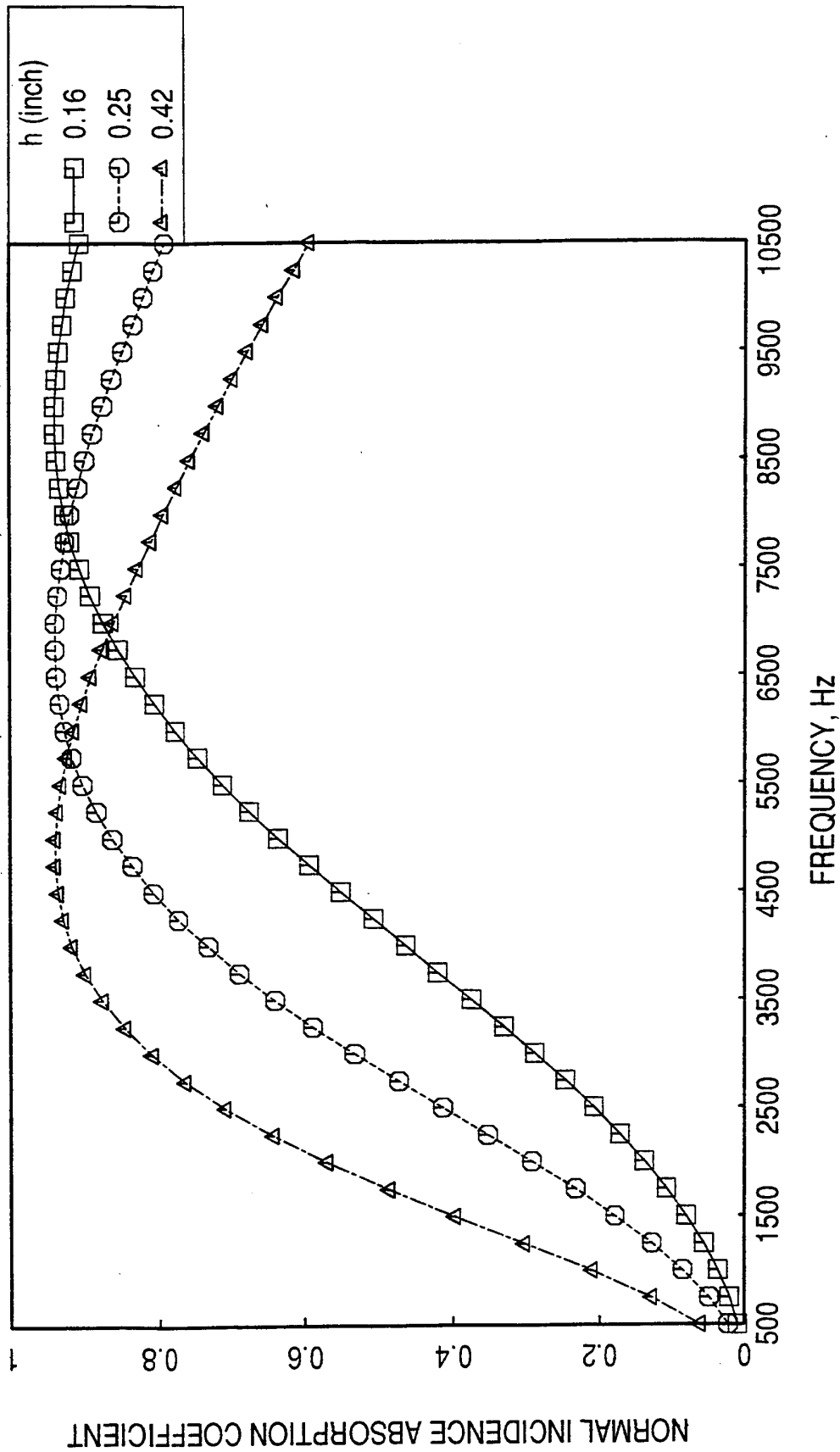


Figure 61. Effect of cavity depth, h on absorption coefficient spectra for 1/3-scale SDOF type liners designed for $\eta=3.4$; facesheet: $\sigma=9\%$, $t=0.028"$, $d=0.04"$.

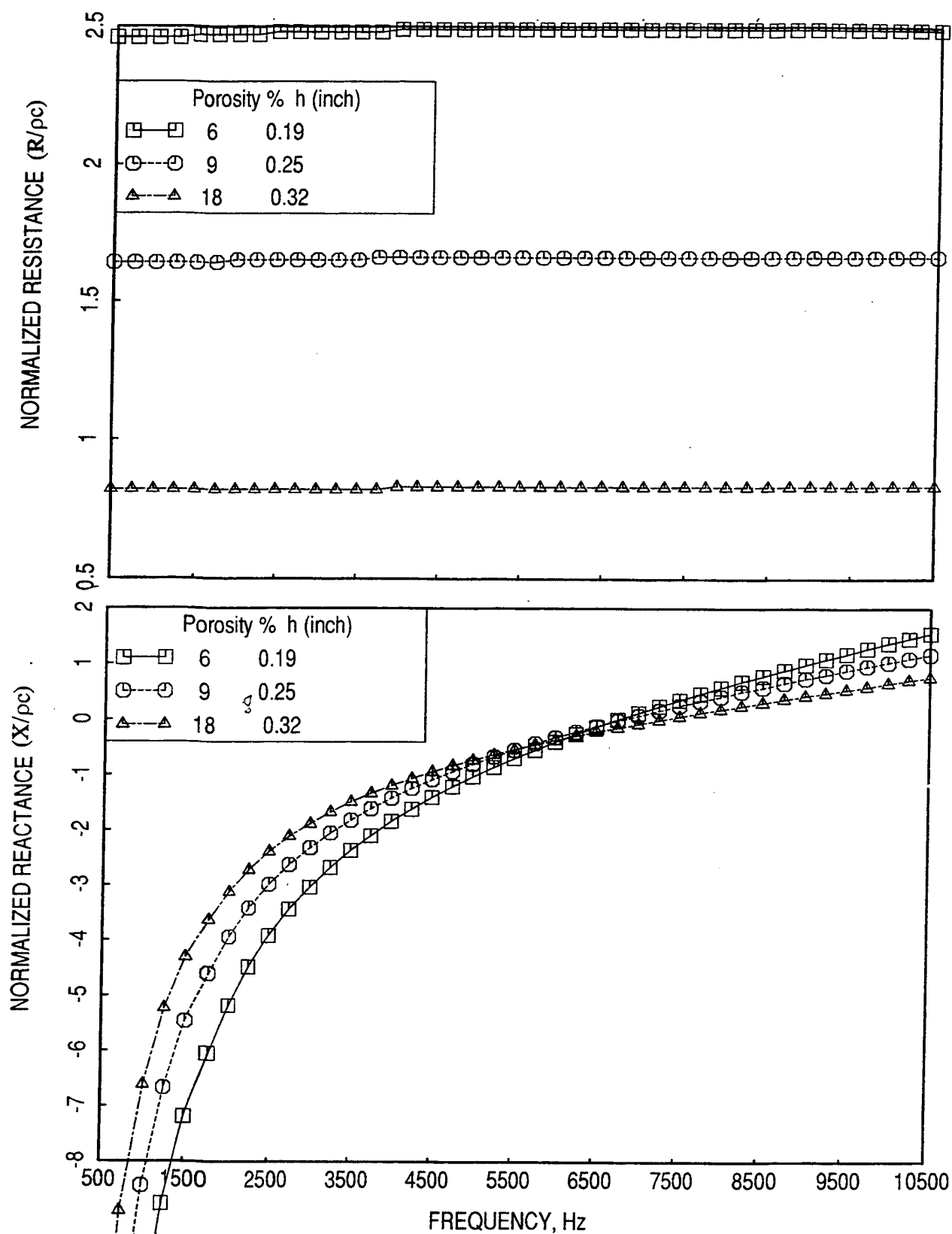


Figure 62. Effect of cavity depth, h and facesheet porosity, σ on normalized impedance spectra for 1/3-scale SDOF type liners designed for $\eta = 3.4$; facesheet: $t = 0.028$ ", $d = 0.04$ ".

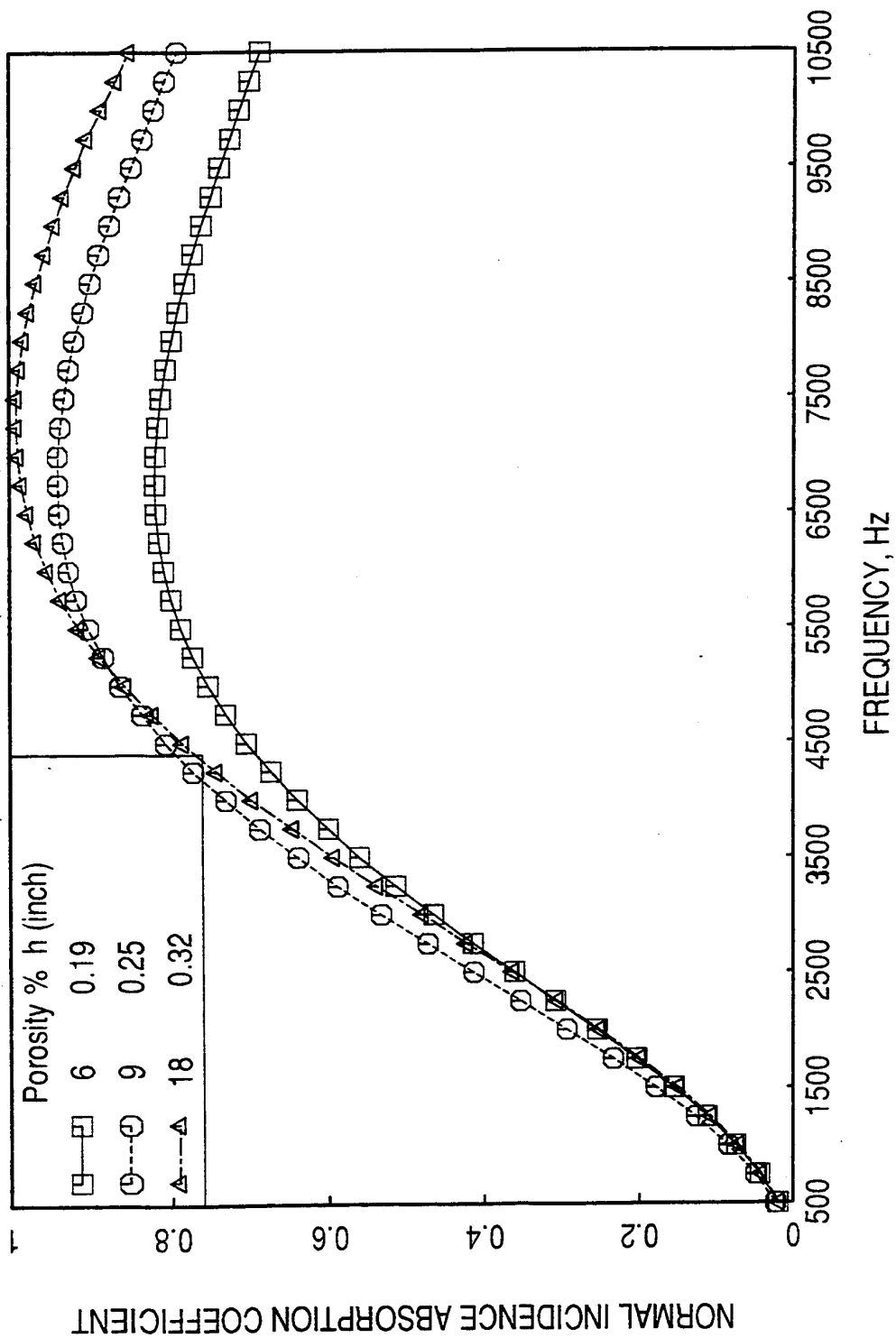


Figure 63. Effect of cavity depth, h and facesheet porosity, σ on absorption coefficient spectra for 1/3-scale SDOF type liners designed for $\eta = 3.4$; facesheet : $t = 0.028$ ", $d = 0.04$ ".

facesheet porosity as well as the hole diameter are varied in steps. The cavity depth h is then adjusted to obtain the same impedance spectra for all three panels.

Config. Number	Design Description	Facesheet Parameters			Cavity
	1/3-Scale SDOF Panels with Thick Perforated Facesheet, $\eta=1.75$, One-Sided Treatment ($H=4''$)	Porosity σ , %	Hole Dia. d , in	Thickness t , in	Depth h , in
1	Small Holes, $d/t=0.625$	9	0.04	0.08	0.38
2	Medium Holes, $d/t=1$	13	0.08	0.08	0.45
3	Large Holes, $d/t=1.5$	15	0.12	0.08	0.48

The predicted normal impedance and absorption coefficient spectra for these panels are shown in Figures 64 and 65, and they show similar trends with frequency.

Linear (Wiremesh or Equivalent) Facesheet SDOF Panels: Three 1/3-scale panels are designed (see Table 1) with linear facesheet with a nonlinear factor $NLF_{150/20} = 1.325$. The impedance of these types of liners is least effected by sound intensity and grazing flow. The resistance and reactance are the functions of DC flow resistance (R_{100}) and the cavity depth, respectively. These panels are designed with a fixed cavity depth of 0.38" and with varying R_{100} .

Table 1. Specifications for Linear facesheet SDOF panels for flow duct tests.

Config. Number	Design Description	Facesheet Parameters		Cavity
	1/3-Scale SDOF Panels with Linear Facesheet, $\eta=3.4$ One-Sided Treatment ($H=4''$)	Resistance R_{100} , Rayls	$NLF_{150/20}$	Depth h , in
1	Matched to Baseline	85	1.325	0.38
2	Low Resistive Facesheet	50	1.325	0.38
3	High Resistive Facesheet	130	1.325	0.38

The predicted normal impedance and absorption coefficient spectra for these panels are shown in Figures 66 and 67. As expected, the resistance levels are widely different, since R_{100} values are different for each case, and the reactance spectra remain the same for all three panels, since the cavity depth is unchanged for these panels.

Bulk Absorber Treatment Designs: Four 1/3-scale bulk absorber liner panels with fixed depth of 0.4" are designed. For three panels the bulk material with different resistivity is filled in the SDOF type liner cavity with a linear facesheet of very low resistivity $R_{100}=5$. The fourth panel is an extended reaction type bulk absorber without any partition, but with a linear facesheet. The design parameters for these panels are listed in Table 2. Comparison of normalized

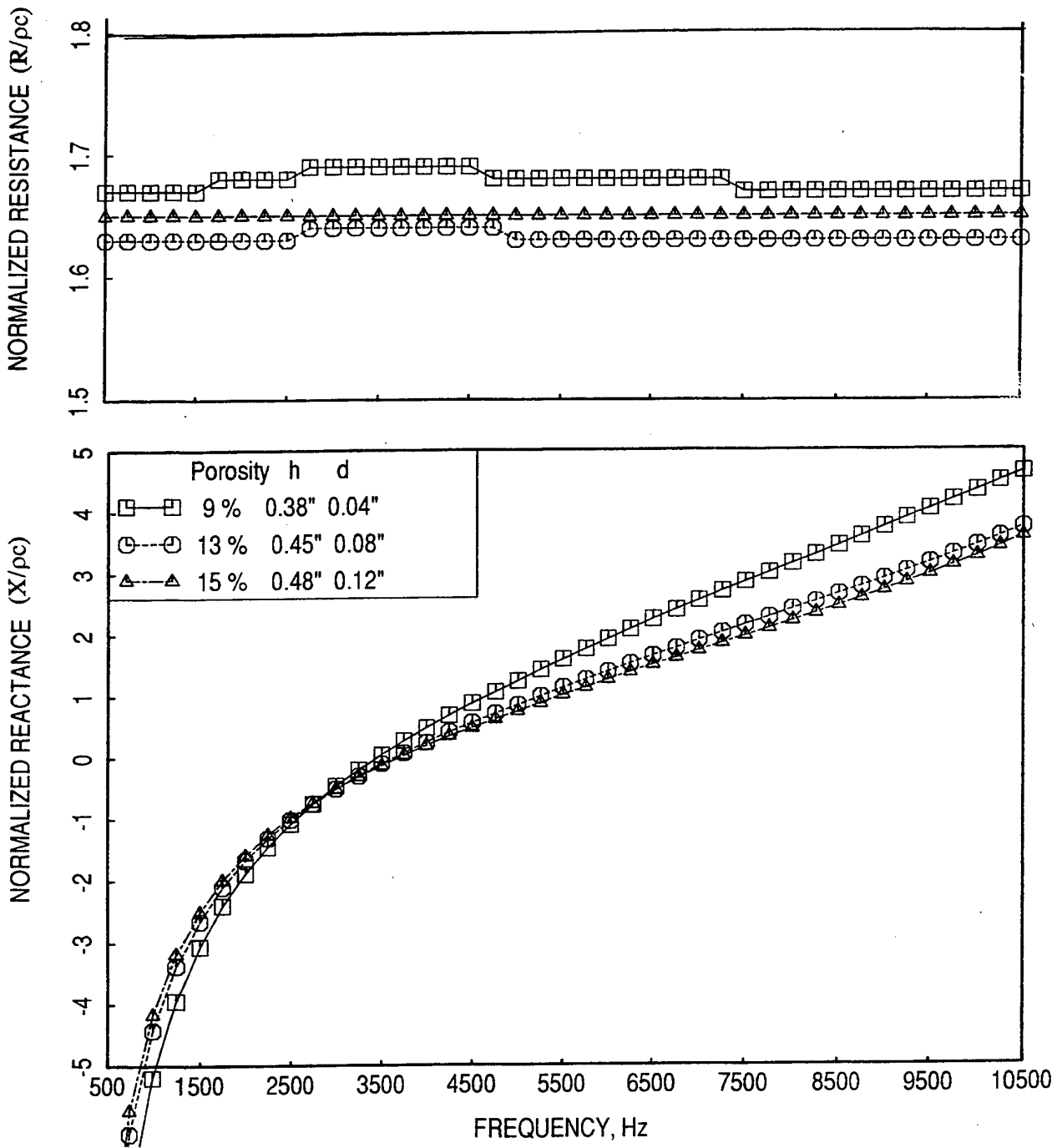


Figure 64. Normalized impedance spectra for 1/3-scale SDOF type liners with 0.08"-thick facesheets designed for $\eta = 3.4$.

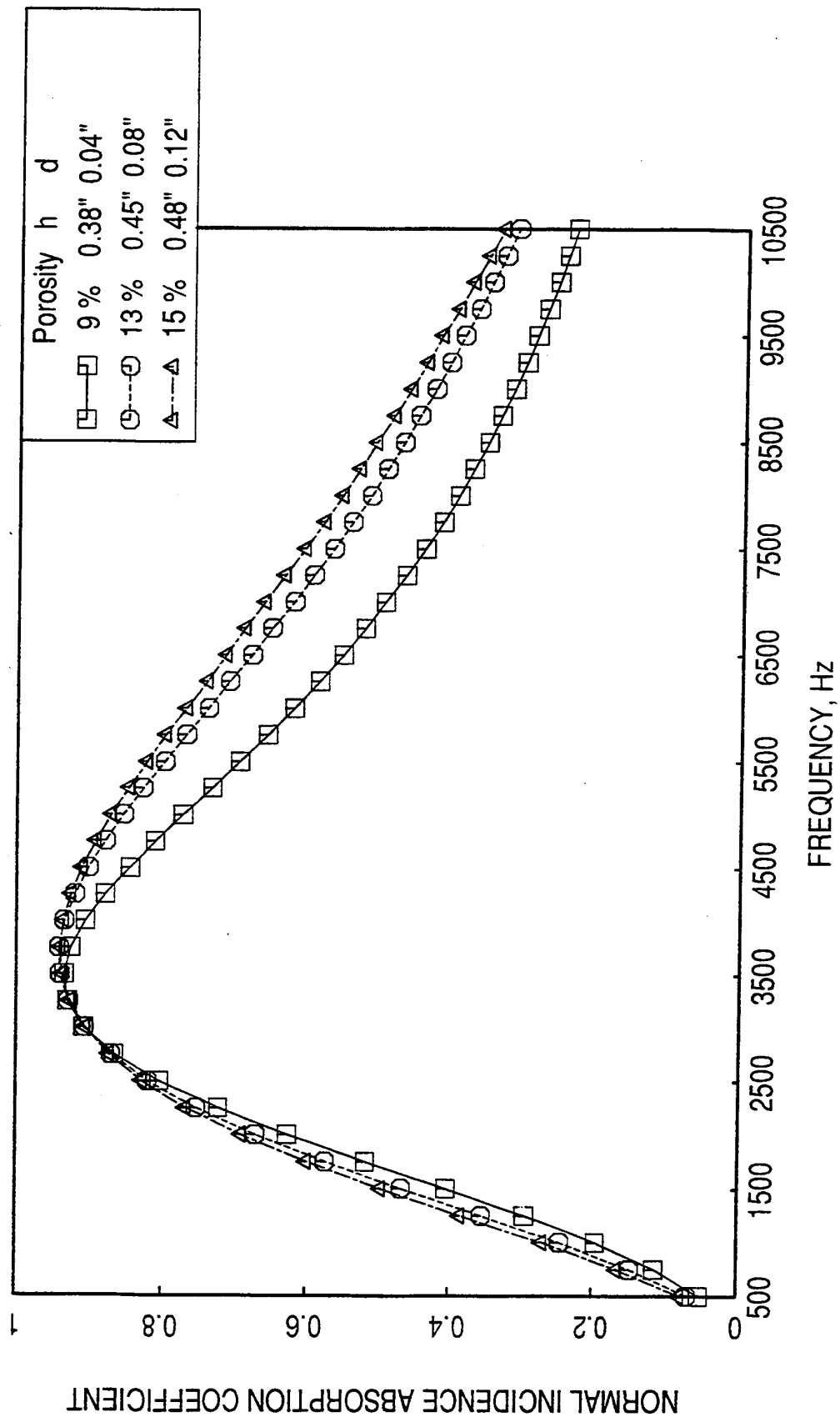


Figure 65. Absorption coefficient spectra for 1/3-scale SDOF type liners with 0.08"-thick facesheets designed for $\eta = 3.4$.

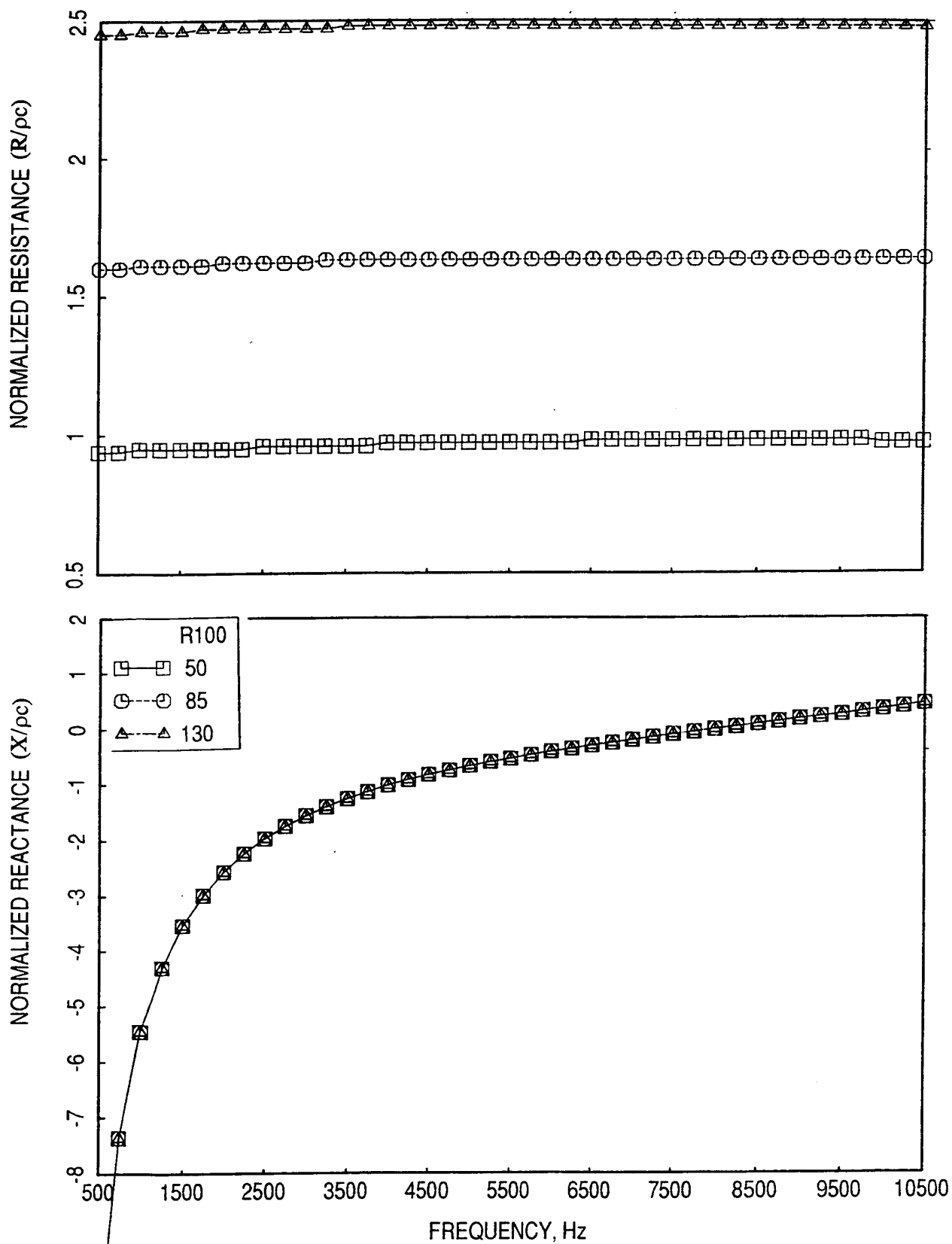


Figure 66. Effect of DC-flow resistance of linear facesheet on normalized impedance spectra for 1/3-scale SDOF type liners designed for $\eta = 3.4$; $h = 0.38$ ".

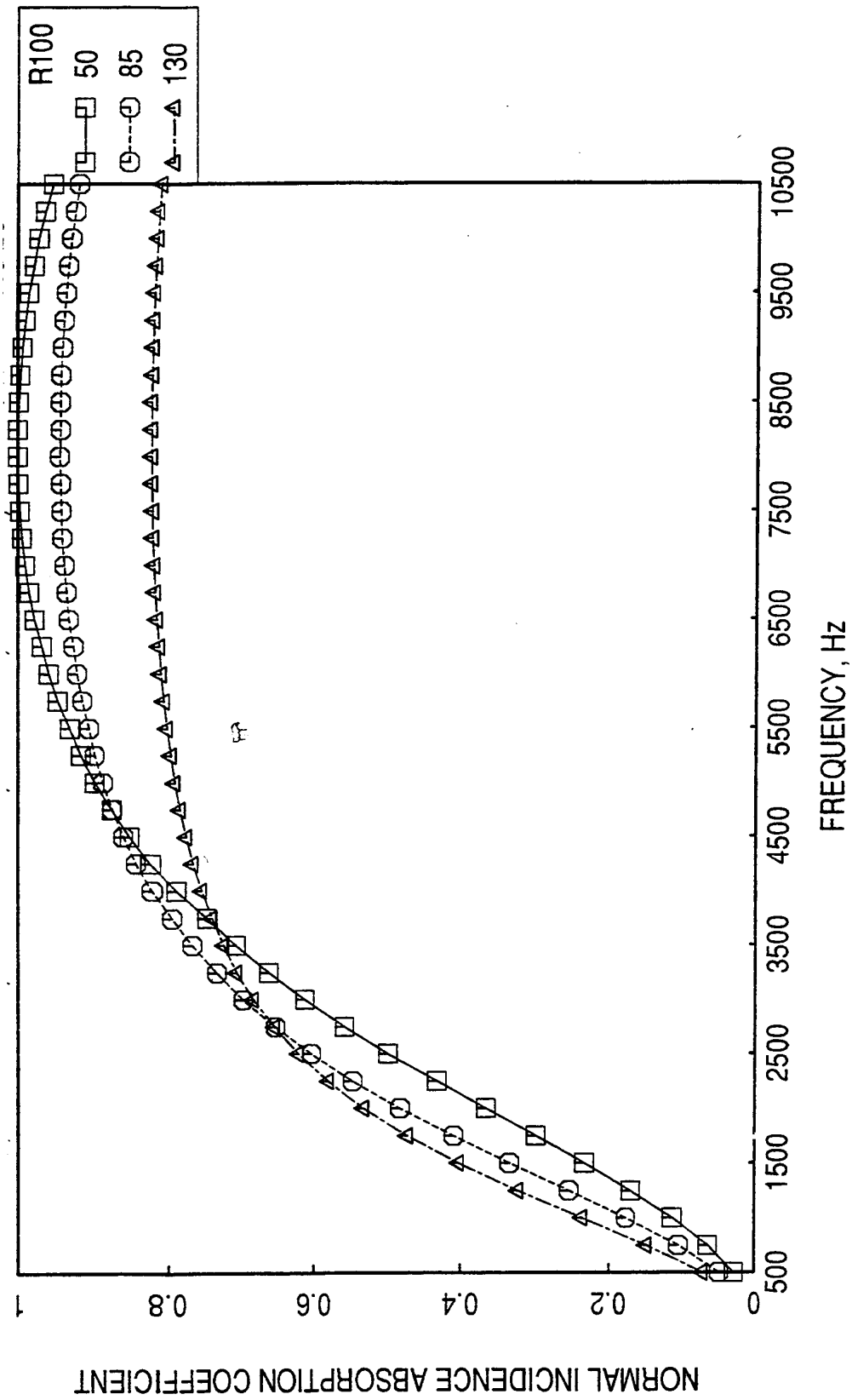


Figure 67. Effect of DC-flow resistance of linear facesheet on absorption coefficient spectra for 1/3-scale SDOF type liners designed for $\eta = 3.4$, $h = 0.38$.

impedance and absorption coefficient spectra for the three locally reacting bulk absorbers are illustrated in Figures 68 and 69.

Table 2. Specifications for bulk filled SDOF panels with linear facesheets for flow duct tests

Config. Number	Design Description	Resistivity, R_{100} , Rayls		Cavity
		Bulk	Facesheet	Depth h, in
	1/3-Scale Bulk Filled Panels with Linear Facesheet, $\eta=3.4$, One-Sided Treatment ($H=4''$)			
1	Matched to Baseline	150	5	0.4
2	Low Resistive Bulk Filled SDOF Facesheet	40	5	0.4
3	Low Resistive Bulk Filled SDOF Facesheet	300	5	0.4
4	Bulk Filled Non-Locally Reacting Panel	150	15	0.4

Instrumented panels for Grazing Flow In-Situ Impedance and DC-Flow Resistance Measurements: Eight 1.0" deep SDOF panels with perforated facesheet are designed by varying the facesheet properties (i.e., porosity, hole diameter, and thickness). These are not designed for optimum impedance. The objective here is to study the effect of grazing flow on the impedance and DC-flow resistance. The instrumentation for impedance measurement (i.e., In-Situ method) required higher cavity depth, and therefore, these panels are 1.0" deep. The design parameters for these panels are listed in Table 3.

Table 3. Specifications for 1"-deep instrumented perforated facesheet SDOF panels for flow duct tests.

Config. Number	Design Description	Facesheet Parameters			Cavity
		Porosity σ , %	Hole Dia. d, in	Thickness t, in	Depth h, in
	Deep SDOF Panels with Perforated Facesheet to be Instrumented, One-Sided Treatment ($H=4''$)				
1	Low Porosity	7.5	0.04	0.028	1.0
2	Medium Porosity	9	0.04	0.028	1.0
3	Medium-High Porosity	12.5	0.04	0.028	1.0
4	High Porosity	15	0.04	0.028	1.0
5	Small Holes	9	0.018	0.028	1.0
6	Large Holes	9	0.08	0.028	1.0
7	Thick Facesheet with Small Holes	9	0.04	0.08	1.0
8	Thick Facesheet with Large Holes	15	0.12	0.08	1.0

2DOF Type Panels: A single 1/3-scale 2DOF type panel with linear facesheet and septum is designed. The design parameters for this panel are listed in Table 4. In addition, several variable depth 2DOF panels are also designed.

The normalized impedance and absorption coefficient spectra for 1/3-scale panels of different designs (i.e., SDOF with thick facesheet, SDOF with linear facesheet, 2DOF with linear

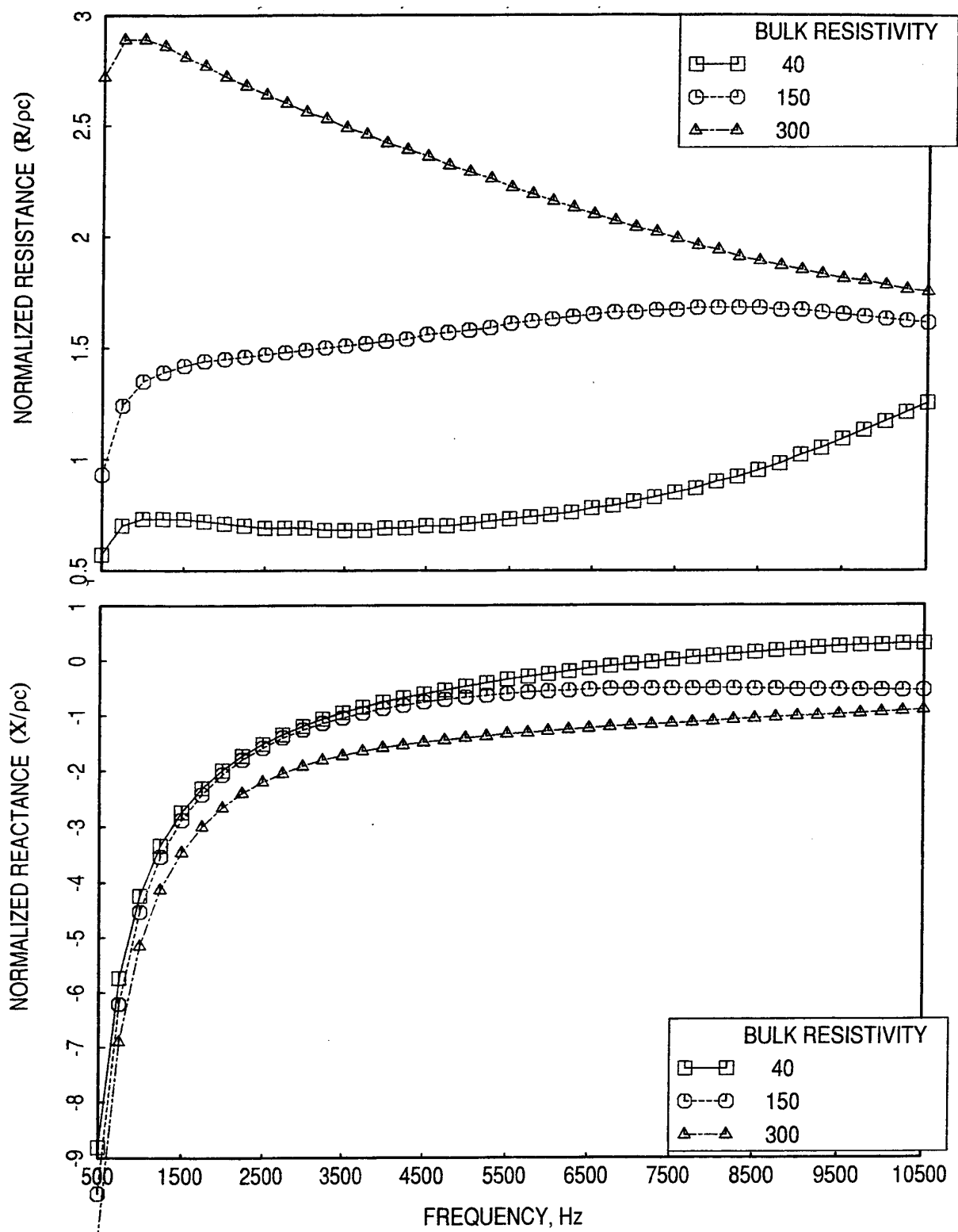


Figure 68. Effect of bulk absorber resistivity on normalized impedance spectra for 1/3-scale bulk-filled SDOF type liners designed for $\eta = 3.4$; $h = 0.4$ ", facesheet DC-flow resistance = 5 cgs Rayls.

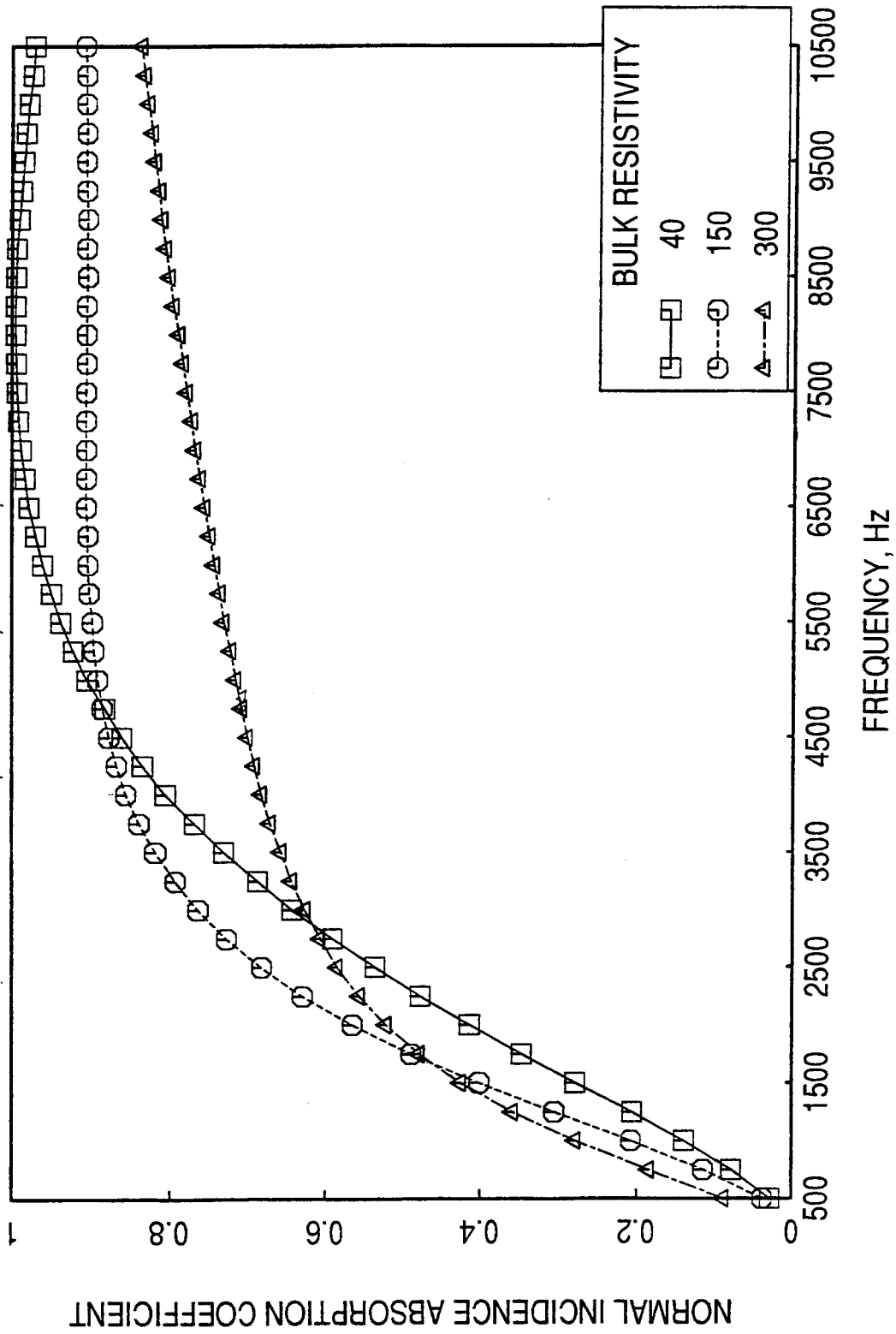


Figure 69. Effect of bulk absorber resistivity on absorption coefficient spectra for 1/3-scale bulk-filled SDOF type liners designed for $\eta = 3.4$; $h = 0.4$ ", facesheet DC-flow resistance = 5 cgs rays.

Table 4. Specifications for 2DOF panel with linear facesheet and septum for flow duct tests

Config. Number	Design Description	Facesheet Parameters			Cavity
	1/3-Scale 2DOF Panels with Linear Facesheet and Septum, $\eta=3.4$, One-Sided Treatment ($H=4''$)	Layer	Resistance R_{100} , Rayls	NLF _{150/20}	Depth h , in
1	Matched to Baseline	Upper	40	1.325	0.3
		Lower	90	1.325	0.55

facesheet and septum, and bulk absorber) are compared with the baseline 1/3-scale SDOF design in Figures 70 and 71. While resistance spectra for all the SDOF designs are flat and close to each other, those for 2DOF and bulk absorber show some variation with frequency and are somewhat different from SDOF values. The reactance spectra for all the designs, except for the thick facesheet SDOF panel, are similar and flatter for most frequency range. The thick facesheet has significant mass reactance, which makes the total reactance to increase with frequency. Due to the same reason the absorption coefficient spectra are relatively similar for all the designs, except for the thick facesheet SDOF panel, for which, the level peaks at about 3000 Hz and then falls rapidly with frequency.

4.2 Detail Design of Test Samples

A total of 29 treatment panels for flow duct test, based on a number of different concepts, are designed and fabricated for laboratory tests. While the 29 panel samples are used in flow duct tests, a large number of additional samples, based on various parametric variations of the panel components (i.e., faceplate, bulk material, etc.) are fabricated for impedance tube and DC flow resistance tests.

Flow duct tests are conducted in 5 inch by 4-inch cross section ducts by installing the panels of 12-inch treatment length on one or two 5-inch wide surfaces. Hence, the treated panel size for these tests is 5 inch by 12 inch. The treatment panels are mounted in 7.5 inch by 14-inch size trays as shown in Figure 72. The trays are bolted to the flow duct, such that the treatment surface remains flush with the duct wall.

The treatment panel is inserted into the tray such that the outer surface of the perforate sheet (or in general, the surface of the panel) aligns flush with the surface of the side and end rails, particularly at the ends that cross the flow duct. A small amount of filling and smoothing is applied, as required, between the tray side rail and the facesheet at these adjoining edges. Assuming the thickness of the tray side rail is equal to the sum of the facesheet thickness and the honeycomb core thickness, the treatment panel backplate overlaps the rails of the tray for

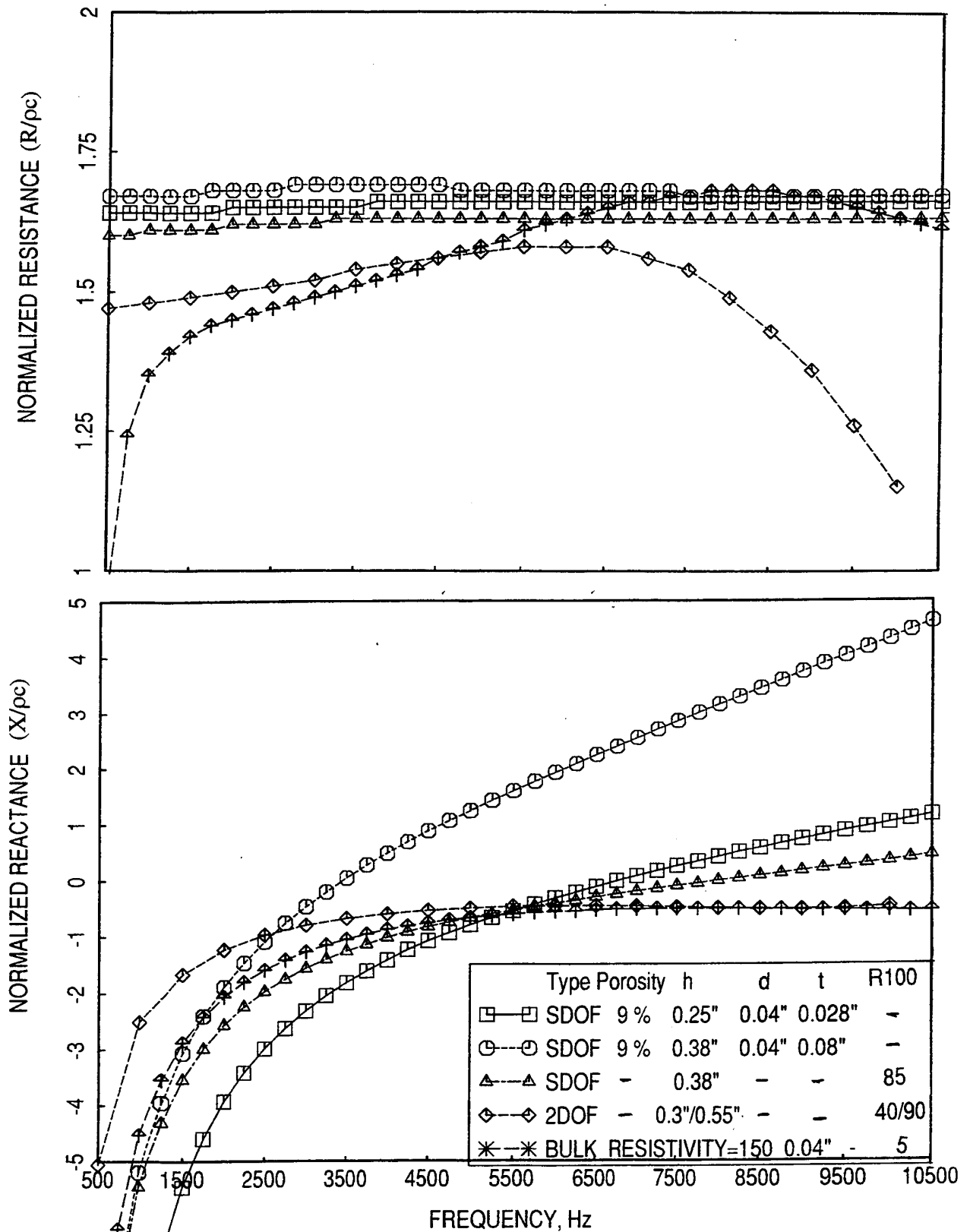


Figure 70. Normalized impedance spectra for 1/3-scale liners of different types designed for $\eta = 3.4$.

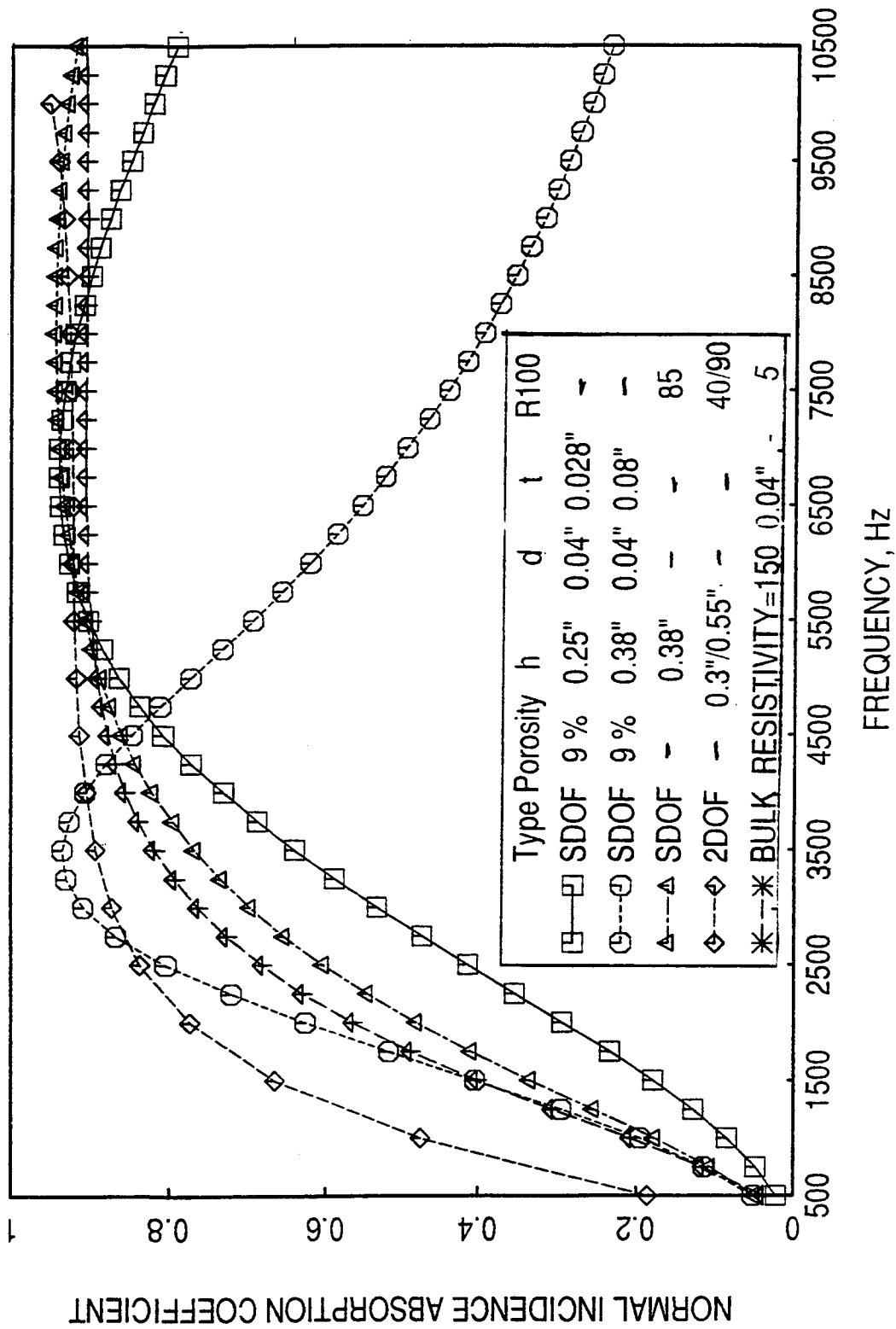


Figure 71. Absorption coefficient spectra for 1/3-scale liners of different types designed for $\eta=3.4$.



added support, forming the bottom of the tray as well as the treatment backplate. Aluminum backplates of 0.05"-thick are used for all the panel trays, except for 1:-deep instrumented panels.

The tray rails are constructed from solid but easily worked materials such as high quality wood or aluminum. The total thickness of the tray depends on the thickness of the treatment panels. Holes are drilled through the side rails of the tray so that it can be bolted to the flow duct. The length of the sample tray is a critical dimension in order to fit into the slot in the flow duct with minimal gap. The dimension and tolerance for this length is 14.000 +0.000/-0.020 inches.

The design concepts, covering the various test objectives, are Single-Degree-of-Freedom (SDOF), Two-Degree-of-Freedom (2DOF), and Bulk Absorber. Two types of SDOF treatment are fabricated, one with a perforated type face plate and the other with a wiremesh (woven) type faceplate. In addition, special configurations of these concepts are also included in the design. Several treatment panels are designed for parametric study. In these panels the facesheets of different porosity σ , hole diameter d , and sheet thickness t are utilized. Several deep panels (i.e., 1 inch deep) are instrumented to measure DC flow resistance and in-situ impedance in the presence of grazing flow. The test samples are broadly divided into the following six sets on the basis of their general design and fabrication criteria:

Set #1 - Perforated Plate SDOF Panels: The basic sandwich construction of this type of panels is shown in Figure 72. The perforated sheet is bonded to one side of the Aluminum honeycomb layer of specified thickness, and a rigid non-porous back plate is bonded to the other side of the honeycomb. The tolerances for facesheet parameters over their nominal values are within $\pm 1\%$ for porosity, ± 0.005 inch for hole diameter, and ± 0.003 inch for thickness. Tolerances for honeycomb parameters over their nominal values are within ± 0.005 inch for depth and $\pm 1/16$ inch for cell size of $3/8$ inch. The honeycomb wall thickness is 0.003". Reticulating adhesives that result in minimal blockage for bonding the facesheet to honeycomb are used. Aluminum (AL-2024) perforated facesheets are used for room temperature tests. Titanium alloy (Ti64) is used for the facesheets for high temperature tests. Aluminum is also used for honeycomb as well as for backplate construction.

Flow Duct Samples: Table 5 contains the design specifications for 10 perforated plate SDOF treatment panel configurations of 5 inch by 12 inch size for flow duct test. The treatment panels are mounted in 7.5 inch by 14-inch size trays as shown in Figure 72 in the manner described earlier.

Table 5. Specifications for perforated facesheet SDOF panels for flow duct tests (set #1)

Config. Number		Design Description	Facesheet Parameters			Cavity
	WBS		Porosity σ , %	Hole Dia. d, in	Thickness t, in	Depth h, in
1	1.1	1/3-Scale , One-Sided Treatment, $\eta=1.75$	9	0.039	0.02	0.7
2	1.2&1.3	1/6-Scale , Two-Sided Treatment, $\eta=1.75$	9	0.039	0.02	0.3
3	1.4	Baseline, 1/3-Scale , One-Sided Treatment, $\eta=3.4$	9	0.039	0.025	0.25
4	1.5	High Resistive Facesheet (Increased by 1.5 times relative to Baseline), 1/3-Scale, $\eta=3.4$	6	0.039	0.025	0.19
5	1.6	Low Resistive Facesheet (Decreased by 0.5 times relative to Baseline), 1/3-Scale, $\eta=3.4$	18	0.039	0.025	0.32
6	1.7	Deep Panel, Shifts Tuning Frequency Down by one 1/3-Octave, 1/3-Scale, $\eta=3.4$	9	0.039	0.025	0.42
7	1.8	Thin Panel, Shifts Tuning Frequency Up by one 1/3-Octave, 1/3-Scale, $\eta=3.4$	9	0.039	0.025	0.16
8	1.9	Small Holes, $d/t=0.625$, 1/3-Scale, $\eta=3.4$	9	0.039	0.08	0.38
9	1.10	Medium Holes, $d/t=1$, 1/3-Scale, $\eta=3.4$	13	0.078	0.08	0.45
10	1.11	Large Holes, $d/t=1.5$, 1/3-Scale, $\eta=3.4$	15	0.125	0.08	0.48

Samples for DC Flow Resistance Tests: Ten samples of the same designs as listed in Table 5 are fabricated for DC flow resistance test, for which there is no backplate and are of 5 inch by 8 inch size (WBS 1.12 through WBS 1.21). Test samples of appropriate size to fit the DC flow apparatus are cut from the 5-inch by 8-inch size panels.

An additional set of 15 panel structures (WBS 1.22 through WBS 1.36) with facesheet (without backplate) is fabricated. These panels are of 0.5 inch deep and of 5 inch by 8-inch square inch size. The facesheet specifications are listed in Table 6. Fifteen (15) samples of facesheet alone are also fabricated for high temperature (as high as 1000°F) DC flow resistance tests. These samples are of 5 inch by 8 inch in size with the specifications of Table 6 (WBS 1.37 through WBS 1.51). Again, the test samples of appropriate size to fit the DC flow apparatus are cut from above panels and facesheets. The purpose of testing these two sets one with honeycomb and the other facesheet alone, is to determine the blockage created by the honeycomb installation.

Samples for Normal Incident Impedance Tube Tests: Normal impedance for the 15 facesheet samples as per Table 6 are evaluated by impedance tube test using the appropriate size samples, cut from the same rectangular pieces, to fit the apparatus.

Table 6. Specifications for perforated plate SDOF panel designs, one set with 0.5"-deep honeycomb and the other facesheets alone, for DC flow resistance and normal impedance tests (set #1).

Sample Number	Facesheet Parameters		
	Porosity, %	Hole Diameter, inch	Thickness, inch
1	5.0	0.039	0.025
2	7.5	0.039	0.025
3	7.5	0.02	0.025
4	7.5	0.01	0.025
5	7.5	0.005	0.025
6	11.0	0.04	0.025
7	11.0	0.015	0.025
8	11.0	0.005	0.025
9	15.0	0.04	0.025
10	15.0	0.015	0.025
11	15.0	0.005	0.025
12	11.0	0.04	0.05
13	11.0	0.04	0.08
14	11.0	0.04	0.12
15	11.0	0.06	0.025

Set #2 - Linear Faceplate SDOF Panels: As shown in Figure 73, these designs are similar to those of Set #1, except the facesheets are linear in nature. All the facesheets for this set of samples are aluminum wire mesh. The linear facesheet is characterized by DC flow resistance R_{100} and nonlinear factor $NLF_{150/20}$, where R_{100} is the DC flow resistance in cgs Rayls for a through flow of 100 cm/sec and $NLF_{150/20}$ is the ratio of DC flow resistance between through flows of 150 cm/sec and 20 cm/sec.

Wiremesh facesheets with flow resistances of 50 and 85 Rayls are bonded directly to the honeycomb core, which have very thin cell walls. The facesheet for 130 Rayls is bonded to a high porosity perforated sheet before bonding to the honeycomb. The thickness of the perforated sheet is 0.020 inch and its porosity is 34% before installation. The tolerance for facesheet resistance is within $\pm 5\%$ of nominal value as installed after bonding (i.e., effective value). Tolerances for honeycomb parameters over their nominal values and the bonding requirements of facesheet to the honeycomb are the same as those for set #1 samples. Aluminum is used for honeycomb and backplate construction.

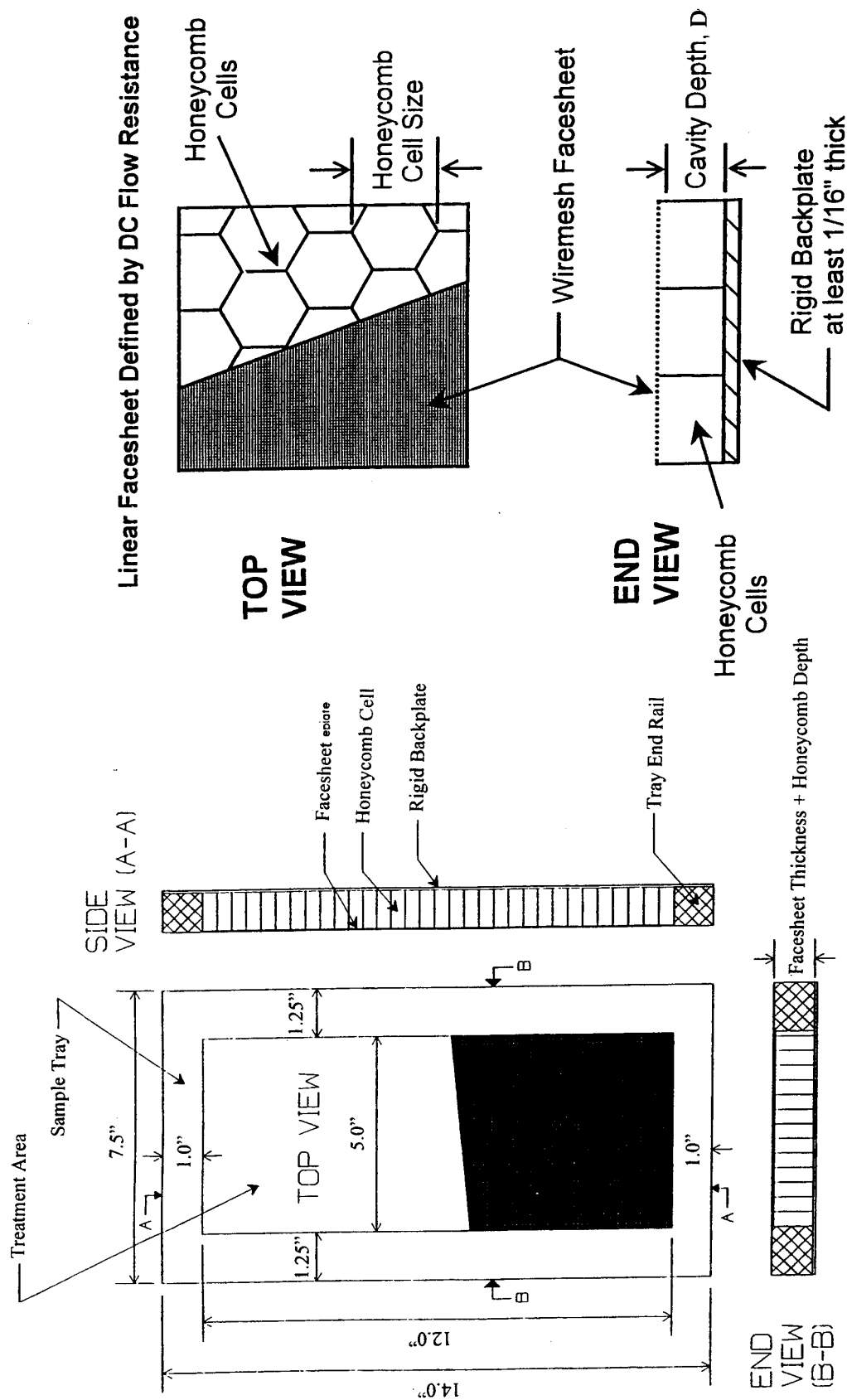


Figure 73. SDOF type treatment panel tray with linear facesheet for flow duct test and its basic acoustic design parameters.

Flow Duct Samples: Table 7 contains the design specifications for 3 linear facesheet SDOF treatment panel configurations of 5 inch by 12 inch size for flow duct test. The treatment panels are mounted in trays as illustrated in Figure 73 in the way described earlier.

Table 7. Specifications for Linear facesheet SDOF panels for flow duct tests (set #2).

Config. Number		Design Description	Bonding Method	Facesheet Parameters					Cavity
	WBS	1/3-Scale SDOF Panels with Linear Facesheet, $\eta=3.4$ One-Sided Treatment		Resistance R_{100} , Rayls	Wiremesh	Initial Perf. Porosity, %	Perf. Hole Diameter, in	Perf. Thickness, in	Depth h, in
1	2.1	Matched to Baseline	Core Reticulate	85	12	-	-	-	0.38
2	2.2	Low Resistive Facesheet	Core Reticulate	50	6	-	-	-	0.38
3	2.3	High Resistive Facesheet	Perf. Reticulate	130	7	34	0.05	0.02	0.38

Samples for DC Flow Resistance Tests: Samples of the same designs as listed in Table 7 are also fabricated for DC flow test (WBS 2.4 through WBS 2.6). For these panels there is no backplate and the size is 5 inch by 8 inch. Test samples of appropriate size to fit the DC flow apparatus are cut from the 5 inch by 8 inch panels.

Samples for Normal Incident Impedance Tube Tests: Fully-assembled but unmounted panels consisting of faceplate, honeycomb, and backplate are fabricated for each treatment configuration of Table 7 in a 5 inch by 6 inch rectangular shape for impedance tube test (WBS 2.7 through WBS 2.9). Samples to fit the 1.25 inch and 0.6 inch diameter impedance tubes are cut from the rectangular panels.

Set #3 - Bulk Material Panels: The basic sandwich construction of a bulk absorber panel, as illustrated in Figure 74, consists of a low resistance linear facesheet bonded to one side and a rigid non-porous backplate bonded to the other side of a bulk-filled honeycomb layer of specified thickness. The bulk material is an advanced material, such as, carbon foam for room temperature tests and silicon carbide foam for high temperature tests. The appropriate bulk material to meet the impedance criteria is evaluated, first, by conducting a preliminary study of a number of available bulk materials. In this study the normal impedance using a plunker device are measured (details of this study is presented in appendix C). Silicon carbide/carbon reticulated foam types of materials are chosen for the current program on the basis of plunker results.

Several carbon reticulated foam samples are obtained to measure the DC flow resistance to correlate the resistivity with the physical properties of these materials, namely, pores/inch and

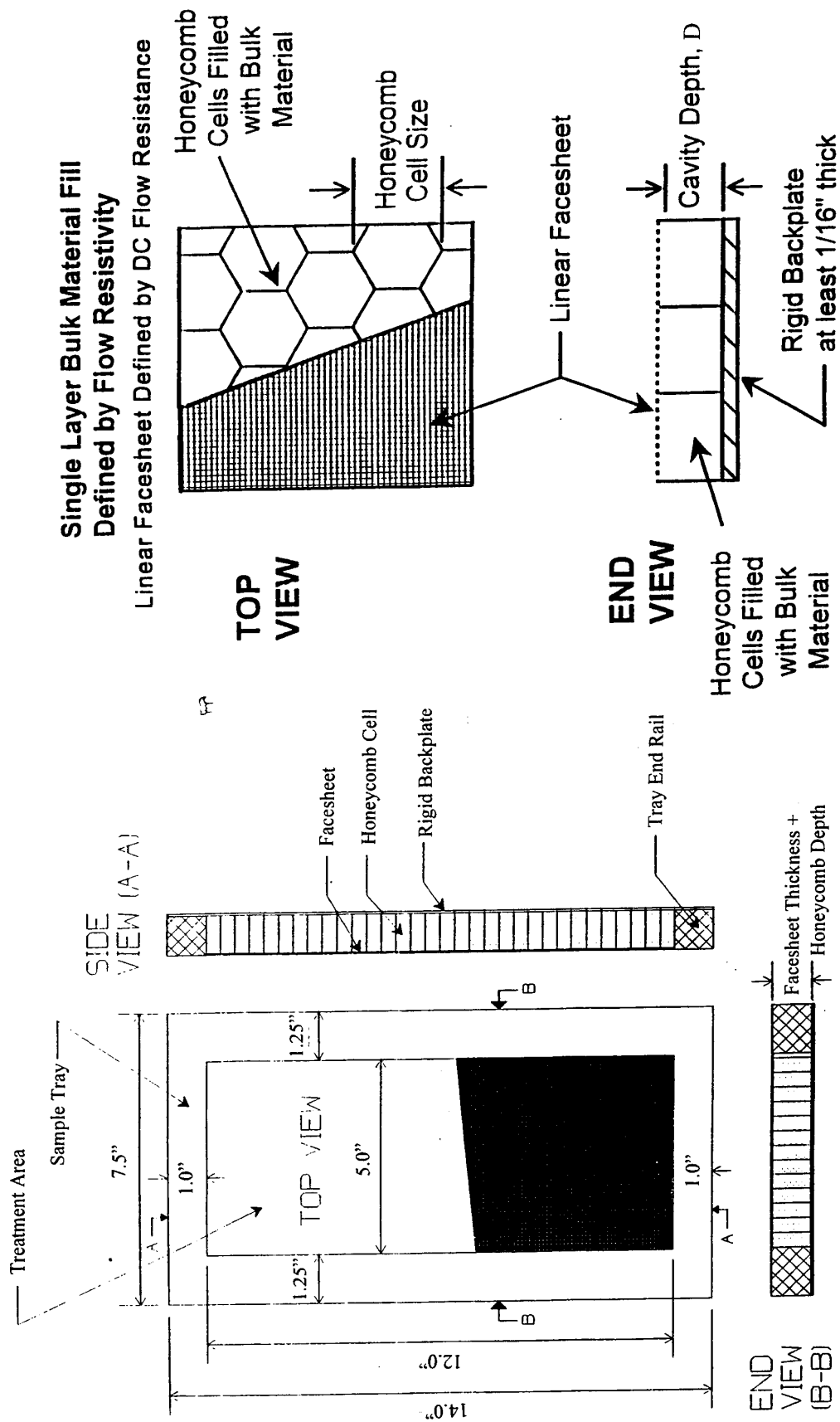


Figure 74. Bulk-filled SDOF type treatment panel tray with linear facesheet for flow duct test and its basic acoustic design parameters.

density. Normal impedance for these samples is also measured. Six different pore size (i.e., 20, 45, 80, 100, 200, and 400 ppi) samples of carbon reticulated foam are obtained from Ultramet. Seven samples of reticulated carbide foam with different pore size (i.e., 10, 30, 60, and 80 ppi) and with two different densities for the same ppi are obtained from Amercom Corporation. Test samples are fabricated by mounting the material samples in the aluminum sleeves (see Figure 45) using a special size hole saw on a drill press and RTV as a sealant. It is more difficult to make a test sample out of low pore samples (i.e., 10 to 30 ppi) than higher ppi materials.

All these samples are tested in a DC flow apparatus (see Figure 44) at ambient temperature to evaluate the resistivity R . The physical properties (i.e., ppi, depth, and density) and the measured DC flow properties, like A , B , R_{100} , and $NFL_{150/20}$, for all the samples are listed in Table 8. Among these properties R_{100} is the resistivity when $U=100$ cm/sec and $NFL_{150/20}$ is the nonlinear factor defined as the ratio of R_{150} and R_{20} .

The samples can be divided into three groups, namely, the Ultramet carbon samples, the low-density Amercom, and high-density Amercom samples. The resistivity of all these three sample groups are plotted with respect to pores per inch in Figure 75. For Ultramet samples both the R_{100}/cm and the A/cm are plotted in this figure. The resistivity appears to follow roughly an exponential behavior as a function of ppi, as the log-log plot is linear above about 40 ppi. There are distinct bias shifts between these sample groups, which could be the effect of density, that a sample of higher density with same ppi may have higher resistivity. In addition, the matrix frames vary in effective fiber diameter, which would indicate that the bulk porosity (air volume/solid volume) would influence the resistivity. Fiber drag coefficient may also influence the resistivity.

Some of the samples are tested in a normal impedance tube to measure their impedance spectra. In addition, measured DC flow resistivities are used in the Delaney and Bazely bulk absorber model to predict the normal impedance of the foam materials and are compared with the measurements. Figures 76, 77, and 78 compare the predicted impedance results with the measured data for the 80, 200, and 400 ppi Ultramet carbon foam materials with 140 dB excitation. The agreement between prediction and measurement is reasonably good for mass reaction spectra for all three samples. Some amount of deviation is observed for samples of 80 ppi and 200 ppi beyond 4000 Hz. However, the agreement between prediction and measurement for acoustic resistance is good for the sample with 80 ppi and not so for the other two higher ppi samples. Measured resistance levels are higher compared to the

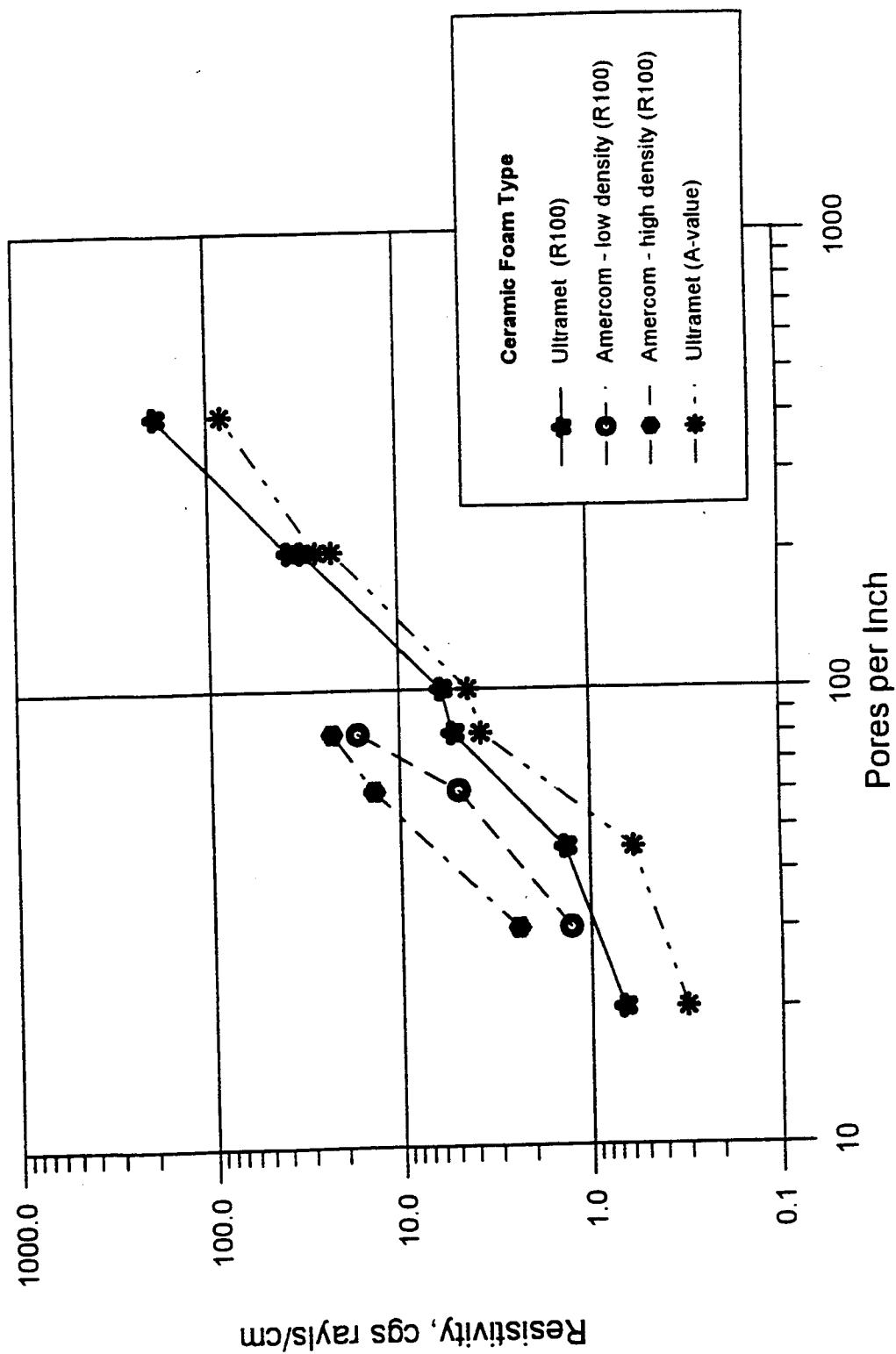


Figure 75. Resistivity vs. pores per inch for the three group of foam materials.

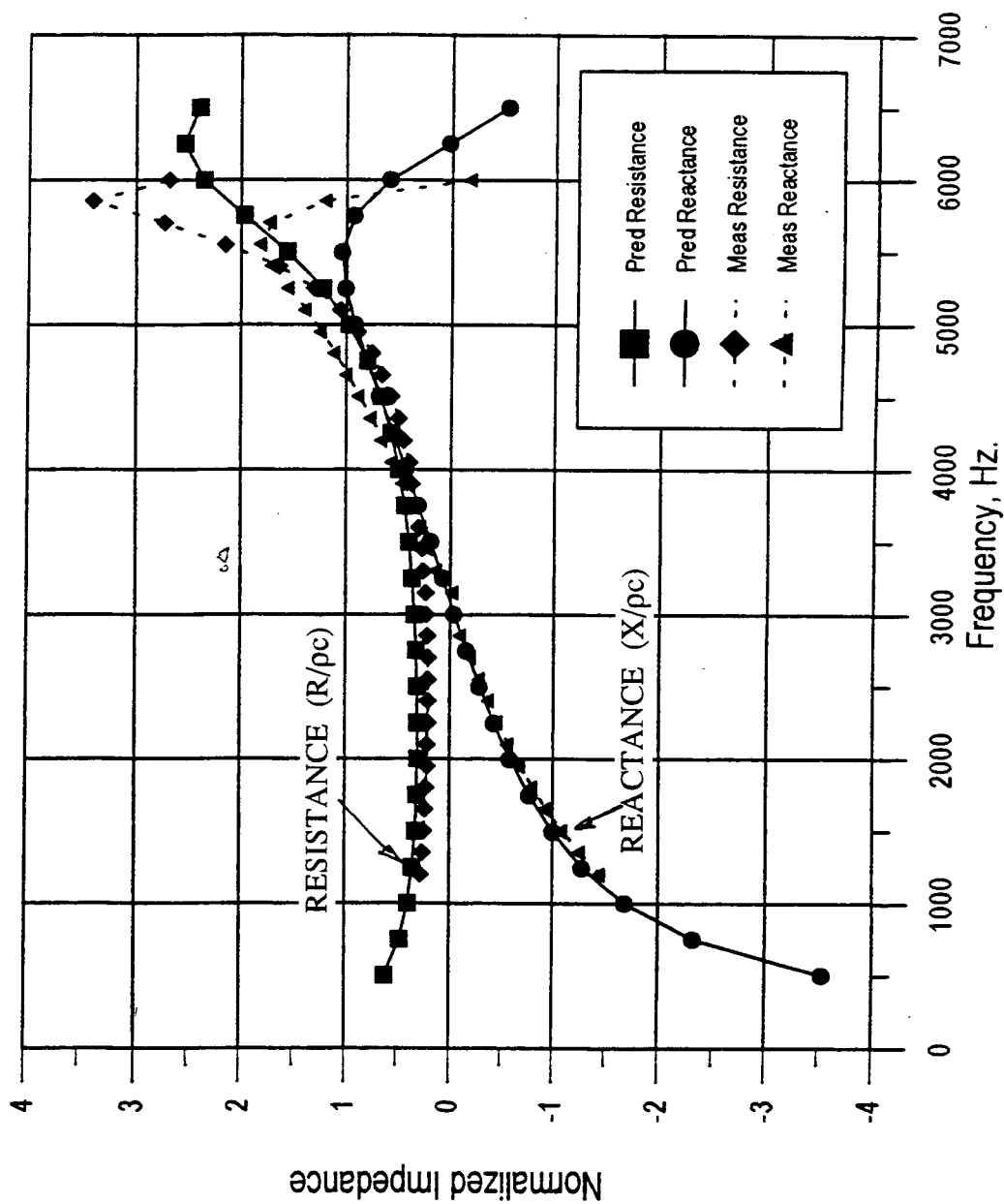


Figure 76. Comparison between predicted and measured impedance spectra for Ultramet 80 ppi 1"-thick sample; $R_{100}=5.2$ cgs rays/cm for Delaney & Bazely prediction, 140 dB SPL excitation for impedance tube test.

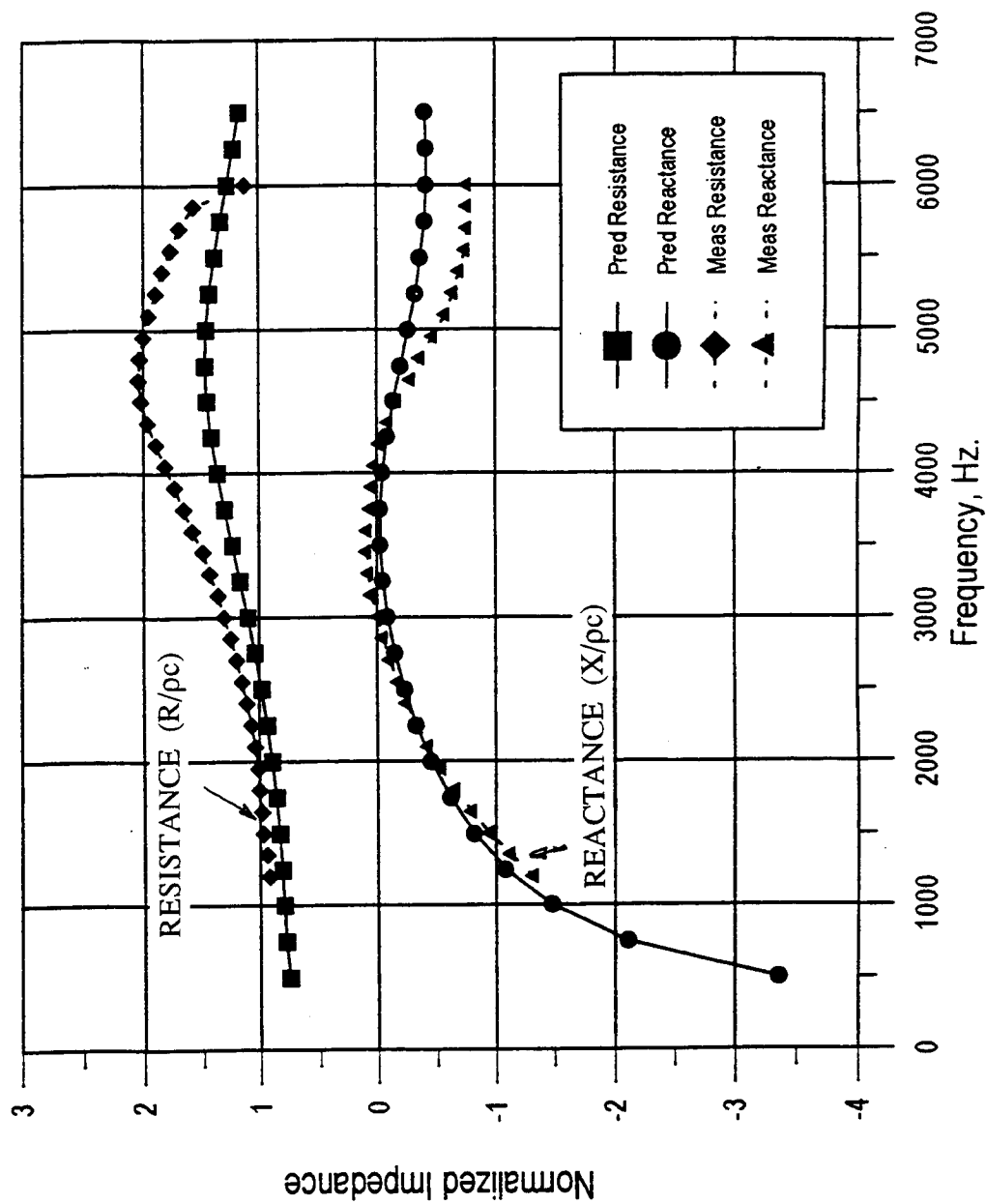


Figure 77. Comparison between predicted and measured impedance spectra for Ultramet 200 ppi 1"-thick sample; $R_{100}=32.2$ cgs rays/cm for Delaney & Bazely prediction, 140 dB SPL excitation for impedance tube test.

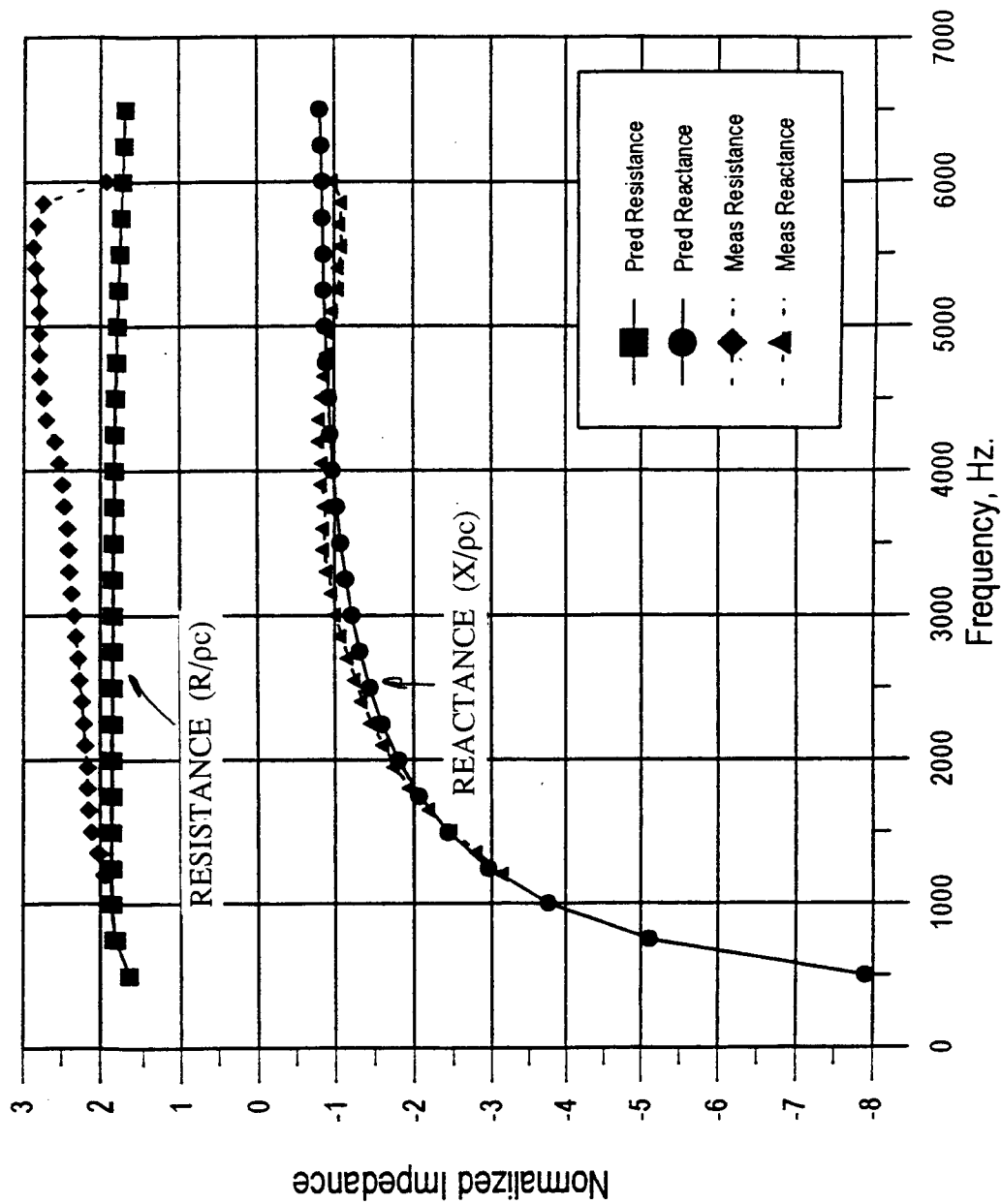


Figure 78. Comparison between predicted and measured impedance spectra for Ultramet 400 ppi 1" -thick sample; $R_{100}=186.0$ cgs rays/cm for Delaney & Bazely prediction, 140 dB SPL excitation for impedance tube test.

prediction, especially at higher frequencies for these two higher ppi samples. Deviations between the prediction and

Table 8. Physical and measured DC flow properties of various foam materials.

Manufacturer	ppi	Depth, inch	Density, lbs/ft ³	A, rayls	B, rayls/cm/sec	R100, rayls	NFL _{150/20}	R100 rayls/cm	A, rayls/cm
Ultramet	20	1.0	N/A	0.79	0.009	1.7	2.21	0.67	0.31
Ultramet	45	1.0	N/A	1.50	0.019	3.4	2.33	1.35	0.59
Ultramet	80	1.0	N/A	9.39	0.038	13.2	1.49	5.19	3.7
Ultramet	100	1.0	N/A	10.9	0.041	15.1	1.46	5.93	4.3
Ultramet	200	1.0	N/A	56.5	0.257	81.8	1.53	32.2	22.2
Ultramet	200	0.5	N/A	34.4	0.137	48.1	1.48	37.9	27.0
Ultramet	400	0.5	N/A	107	1.29	236.3	2.26	186.0	84.6
Amercom	30	1.0	3.12	1.77	0.015	3.2	1.92	1.27	0.7
Amercom	30	1.0	10.6	3.01	0.031	6.1	2.10	2.39	1.2
Amercom	60	1.0	9.36	8.1	0.042	12.4	1.62	4.86	3.2
Amercom	60	1.0	33.7	23.1	0.118	34.8	1.60	13.7	9.1
Amercom	80	1.0	12.5	29.6	0.125	42.1	1.51	16.6	11.6
Amercom	80	1.0	28.7	36.2	0.219	58.0	1.70	22.8	14.2

measurement could have been caused by the nonlinearity of the bulk material, which is likely to be so for material with higher resistivity.

Based on the DC flow results an approximate correlation is established between the resistivity and the pores per inch and hence the ppi for the bulk materials needed for set #3 panels are established. Ultramet is selected to provide the material to fabricate the samples of set #3 designs. As listed in Table 9, for three panels the bulk material is inserted into standard hexagonal honeycomb cells. One panel configuration is just a slab of bulk material without any partition.

Table 9. Specifications of bulk filled panels with linear facesheets for flow duct tests (set #3).

Config. Number	Design Description	Bulk Parameters		Facesheet Parameters		Cavity
	WBS 1/3-Scale Bulk Filled Panels with Linear Facesheet, $\eta=3.4$, One-Sided Treatment (H=4")	Pores/in (ppi)	R ₁₀₀ , Rayls	Wiremesh	R ₁₀₀ , Rayls	Depth h, in
1	3.1 Matched to Baseline	400	150	3	5	0.4
2	3.2 Low Resistive Bulk Filled SDOF Facesheet	200	40	3	5	0.4
3	3.3 Low Resistive Bulk Filled SDOF Facesheet	500	300	3	5	0.4
4	3.4 Bulk Filled Non-Locally Reacting Panel	400	150	11	15	0.4

The facesheet characteristics are specified by its nonlinear factor $NLF_{150/20}$, DC flow resistance R_{100} , thickness, and porosity, which is the same as those for set #2 panels. Bulk material DC flow resistivity is the DC flow resistance of a bulk material for a given thickness, divided by the thickness. The R_{100} and $NLF_{150/20}$ are defined in the same manner as those for the linear facesheet. The $NLF_{150/20}$ is assumed to be negligible for most bulk materials. Hence, the bulk material is characterized by its resistivity R_{100} only. Honeycomb properties are the same as those for sets #1 and #2. Tolerances and materials for facesheet, backplate, and honeycomb are the same as those for set #2 panels. Tolerance for bulk material resistivity is within $\pm 5\%$ of the nominal values, listed in Table 9.

Flow Duct Samples: Table 9 contains the design specifications for 4 linear facesheet bulk material treatment panel configurations of 5 inch by 12 inch size for flow duct test. The treatment panels are mounted in trays as illustrated in Figure 74 in the way as described earlier.

Samples for DC Flow Resistance Tests: Three samples of the same designs as listed in Table 9 (i.e., WBS 3.1 through WBS 3.3) are also be fabricated for DC flow resistance testing (WBS 3.5 through 3.7). These samples do not have any backplate and are of 5 inch by 8 inch size. Samples to fit the DC flow apparatus are cut from these panels.

A separate set of test samples of the three bulk materials, listed in Table 9, are prepared for DC flow resistance testing, by mounting in aluminum sleeves of 1.75 inch OD and 1.25 inch ID, with 0.4 inch in depth, as shown in Figure 45. The samples fit tightly into the holder to avoid leakage between the bulk material and the sleeve wall.

Twelve additional samples of different silicon carbide foam bulk materials, listed in Table 10, are also fabricated for DC flow resistance tests to cover a wide range of bulk material properties at high temperature conditions (as high as 1000°F). Depths for these samples are listed in Table 10. Stainless steel sample holders are used for these samples to withstand the desired temperature.

Samples for Normal Incident Impedance Tube Tests: Test samples for DC flow resistance tests are also used for impedance tube tests to evaluate normal incidence impedance.

Set #4 - Linear Faceplate and Septum 2DOF Panel: One panel of two-degree-of-freedom (2DOF) type sandwich construction, consisting of two layers of linear sheet material over

Table 10. Specifications for bulk samples for DC flow resistance and normal impedance tests (set #3).

Configuration Number		Bulk Parameters	
	WBS	Pores/inch	Depth, inch
1	3.11	10	2.0
2	3.12	20	2.0
3	3.13	45	2.0
4	3.14	65	2.0
5	3.15	80	2.0
6	3.16	100	1.0
7	3.17	200	1.0
8	3.18	400	0.5
9	3.19	500	0.5
10	3.20	600	0.5
11	3.21	800	0.5
12	3.22	1000	0.5

honeycomb backing and with a rigid non-porous backplate is designed (see Figure 79). The faceplate and septum designs are similar to those for the faceplate of set #2 with wiremesh 7. The honeycomb layers and backplate designs are also similar to those for Sets #1 and #2.

Flow Duct Samples: Table 4 contains the design specifications for the 2DOF treatment panel configuration (WBS 4.1) of 5 inch by 12 inch size for flow duct test. The treatment panel is mounted in a tray as illustrated in Figure 79 in the way it is described earlier.

Samples for DC Flow Resistance Tests: Two different DC flow resistance measurement samples (WBS 4.2 and WBS 4.3) are fabricated for the 2DOF panel tests. One sample consists of a 5 inch by 8-inch rectangular facesheet bonded to the upper layer of honeycomb cell, without the septum, lower honeycomb, and backplate. The second sample of the same 5-inch by 8-inch size consists of the septum bonded to the upper and lower layers of honeycomb, without faceplate and backplate. Test samples to fit DC flow apparatus are cut from these rectangular panels.

Samples for Normal Incident Impedance Tube Tests: A fully-assembled but unmounted panel (WBS 4.4) consisting of faceplate, upper honeycomb layer, septum, lower honeycomb layer, and backplate is fabricated for the treatment configuration of Table 4 in a 5 inch by 6 inch rectangular shape and test samples to fit the impedance tubes is cut from this panel.

Set #5 - Instrumented Perforated Plate SDOF Panels: These panels, as listed in Table 11, are similar to the SDOF panels of Set #1 (see Figure 72), but of greater depth (i.e., 1 inch

deep) to accommodate special instrumentation. The panels are fabricated only for flow duct tests and they are specially instrumented for two-microphone impedance measurement (i.e., in-situ impedance measurement) and DC flow resistance measurement in the presence of grazing flow during flow ducts testing. The treatment panel designs, the tolerances for various components, and the materials for their fabrication are the same as those for panels of Set #1, except the backplate in these panels are of 0.5 inch thick Plexiglass and the aluminum honeycomb is 0.005" thick construction for steadiness of the structure. The panels are mounted in the tray in the same way as those of Set#1 (see Figure 72).

Table 11. Specifications for 1"-deep instrumented perforated facesheet SDOF panels for flow duct tests.

Config. Number	Design Description	Facesheet Parameters			Cavity
		Porosity σ , %	Hole Dia. d, in	Thickness t, in	
	Deep SDOF Panels with Perforated Facesheet to be Instrumented, One-Sided Treatment (H=4")				
1	Low Porosity	7.5	0.039	0.025	1.0
2	Medium Porosity	9	0.039	0.025	1.0
3	Medium-High Porosity	12.5	0.039	0.025	1.0
4	High Porosity	15	0.039	0.025	1.0
5	Small Holes (Facesheet : TI6242)	9	0.018	0.025	1.0
6	Large Holes	9	0.078	0.025	1.0
7	Thick Facesheet with Small Holes	9	0.039	0.08	1.0
8	Thick Facesheet with Large Holes	15	0.125	0.08	1.0

Special Instrumentation: Each treatment tray is instrumented in two locations, as shown in Figure 80, one for in-situ impedance measurement and the other for DC flow resistance measurement.

For the **in-situ impedance measurement**, two Kulite transducers (Type XCS-062) are to be mounted in a single honeycomb cell. Mounting both the transducers in the same cell is a critical part of the design, and the purpose of the 1/2 inch thick plexiglass backplate is to facilitate locating the particular cell that will house the transducers and drilling the mounting holes. The exact location of this instrumentation is not critical, but is chosen to be at least 2 inches from all the panel edges.

Transducers are to be mounted in a manner so that one would be flush with the liner surface and the other would be flush with the inner side of the backplate. To mount the first transducer, a long sleeve is put into the honeycomb cell as shown in Figure 80. No leakage would be allowed through the transducer mounting passages.

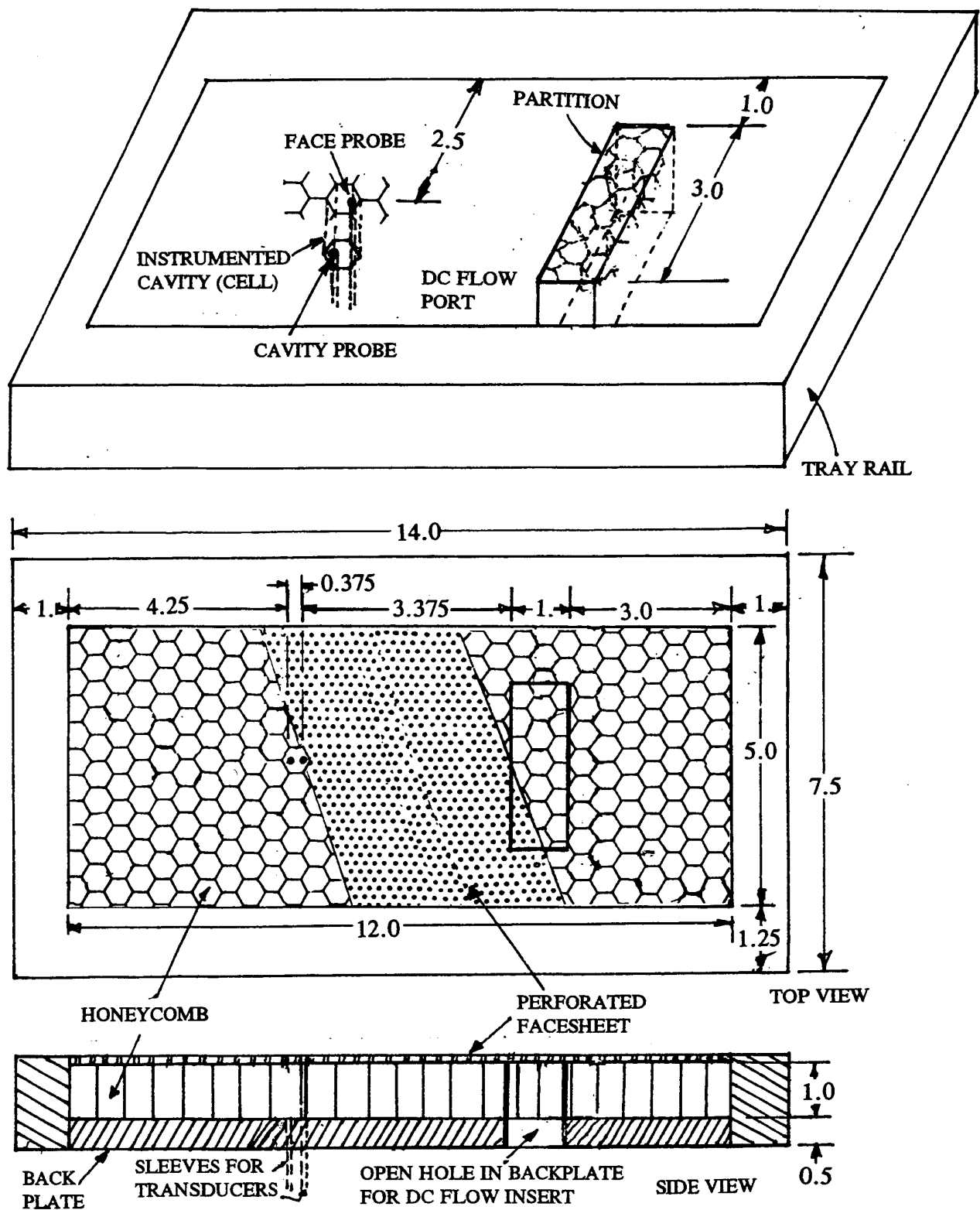


Figure 80. Instrumented perforated plate 1" deep (D) SDOF type panes for flow duct tests (all dimensions are in inches).

For the **DC flow resistance measurement**, a rectangular partition is inserted into the panel (see Figure 80). The walls of the partition are 1/16 inch thick and are welded to form a rectangular box. The top edge of the partition forms a leak-free fit against the back side of the faceplate, and the bottom of the partition forms a tight seal against the edge of a 3 inch by 1 inch cutout in the baseplate beneath the partition. A thin bead of adhesive might be used to guarantee a leak-free seal. The inside of the partition is filled with the same 1 inch deep honeycomb used in the remainder of the panel and is bonded to the faceplate. There is no backplate inside the DC flow measurement cross-section.

Set #6 - Linear Variable Depth Septum Panels: This set includes two special panel designs of variable-depth septum sandwich construction, illustrated in Figure 81, consisting of a linear material facesheet, linear material septum, and a double honeycomb backing cut at an angle. The characteristics of the faceplate and the septum are similar to those for the 2DOF panel of Set #4. Materials and construction tolerances for different components of these panels are also the same as those for Set #4. The septum is installed at an angle to the faceplate. It should be noted that the angled 2-inch segments run in the lengthwise direction of the panel.

Flow Duct Samples: Figure 81 contains the design specifications for the variable-depth treatment panel configurations of 5 inch by 12 inch size for the flow duct test (WBS 6.1 and WBS 6.2). The panels are mounted in trays as illustrated in Figure 81 in the same way as other sets.

Samples for DC Flow Resistance Tests: Two different DC flow resistance measurement test samples are fabricated for these panels. One of the samples consists of 5 inch by 8 inch rectangular facesheet ($R_{100}=10$ Rayls) bonded to the upper layer of honeycomb cell of constant depth of 0.5 inch, without the septum, lower honeycomb, and backplate. The second set of samples are of the same 5 inch by 8 inch size consisting of the septums of each type (i.e., R_{100} of 280 Rayls for design I and 180 Rayls for design II) bonded to the variable depth upper and lower layers of honeycomb, without faceplate and backplate. Test samples to fit the DC flow apparatus are cut from these panels.

Samples for Normal Incident Impedance Tube Tests: A fully-assembled but unmounted panel consisting of faceplate, upper honeycomb layer, septum, lower honeycomb layer, and backplate are fabricated for each configuration in a 5 inch by 6 inch rectangular shape. Samples to fit the impedance tubes are cut from these panels.

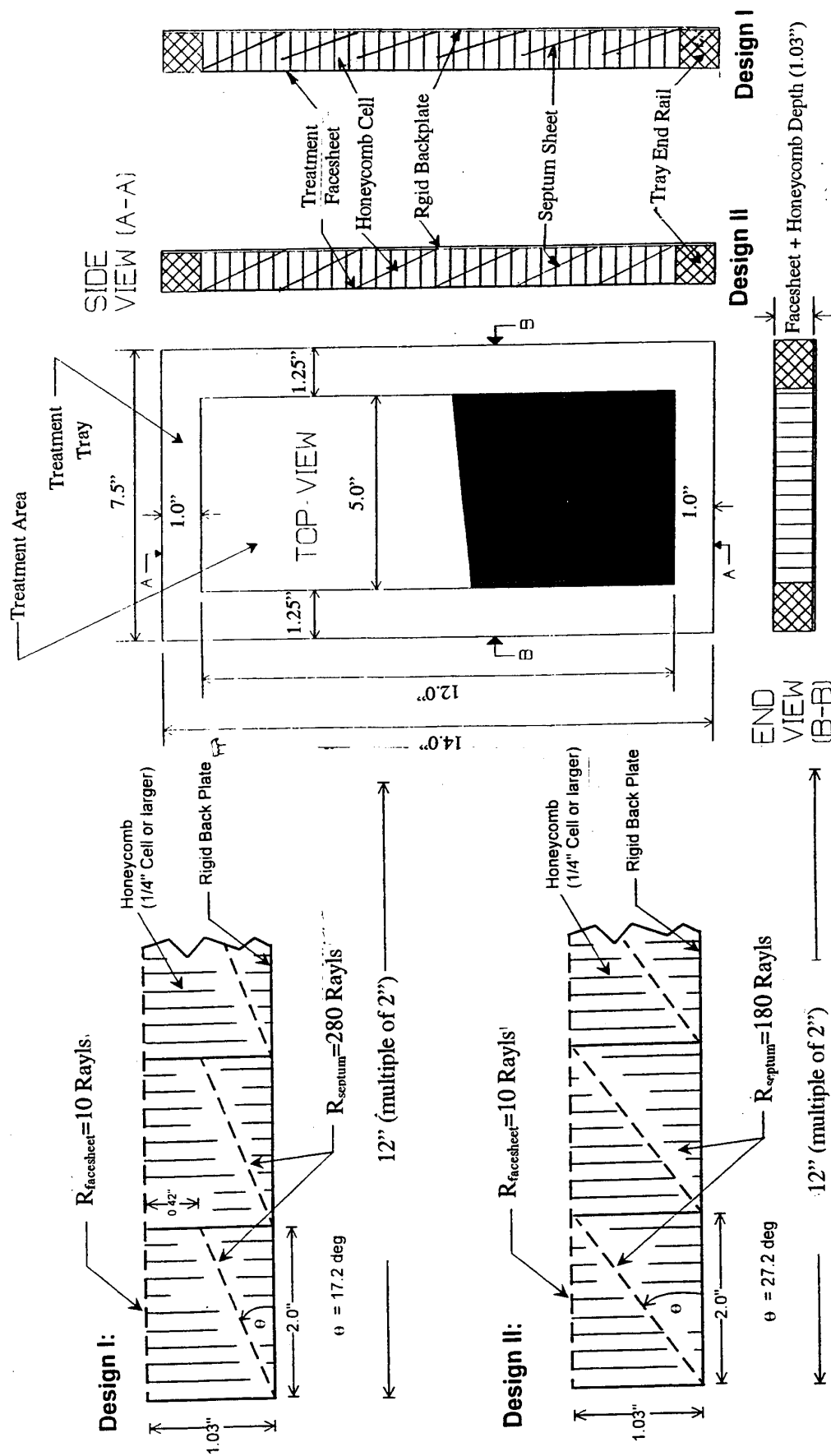


Figure 81. Variable depth 2DOF type treatment panel trays with linear facesheet and septum for flow duct test and its basic acoustic design parameters.

5.0 LABORATORY TESTS AND RESULTS

There are two primary objectives to the HSCT ejector liner laboratory duct tests. The primary objective is to screen treatment panel designs to determine the limited number of panels that would be tested in a scale model mixer-ejector system in the Cell 41 Anechoic Chamber. In these tests, the ejector flap and sidewalls will be treated with the selected panels. The secondary objective is to investigate the implications of designing treatment panels using sub-scale tests.

Contributions are to be made to both objectives within the limited number of tests planned and the limited range of temperature and flow variables afforded by the laboratory rectangular duct. It is important to note that both primary and secondary objectives must be achieved to be able to translate the results of the screening tests to scale model mixer-ejector designs that are appropriate for the high temperature and flow conditions at which the tests are run in the anechoic chamber. This design translation would be accomplished through the knowledge gained from the laboratory tests that correlate liner impedance and suppression for the scale model liners under varying grazing flow and sound intensity conditions.

The first objective, treatment panel design screening, are achieved under the assumption that, although the laboratory duct does not replicate the temperature, flow field, and sound field characteristics that are obtained in either the anechoic chamber scale model rig or the full-scale engine, the tests of suppression performance in the laboratory duct would determine, at least in a relative sense, which treatment panel designs are better than others. That is, it is assumed that if one treatment panel design gives better suppression performance in the rectangular duct tests than another design, under equivalent test conditions, then it would give better performance in the anechoic chamber tests. It is not anticipated that the absolute levels of suppression measured in the rectangular duct would accurately predict the levels that are obtained in the anechoic chamber rig.

The second objective, increasing the understanding of treatment scaling effects, would allow greater confidence in interpreting the results of the laboratory duct tests and applying the designs to the scale model or full-scale HSCT ejector. Knowledge of the effects of scaling on treatment impedance is critical to be able to translate the results of the scale model testing to full-scale design. Compensation must be made for those effects on impedance that do not scale with length (or frequency), such as the resistance and mass reactance of a perforate. Grazing flow effects and temperature effects must be accounted for. These effects are investigated using the parametric studies of normal incidence impedance at low and high

frequency, grazing flow impedance measurements, and DC flow resistance measurements, with and without grazing flow.

5.1 Acoustic Characteristics of Perforated Facesheets:

Table 12 contains the DC flow resistance parameters and the list of data files containing normal impedance for a number of perforated sheets, described in Table 6, with varying porosity, thickness, and hole diameters.

5.1.1 DC Flow Resistance:

Before testing the high temperature perforated sheet samples the high temperature DC flow apparatus (see Figures 46 and 82) is checked out at room temperature conditions. In this process, the DC flow resistance for a standard perforated sheet is measured several times by the room temperature (see Figure 44) and high temperature DC flow apparatus at room temperature conditions and the data is plotted in Figure 83. These data are corrected by utilizing Equations 18 and 19 to compensate for any small temperature and pressure differences between the tests.

Very good agreement is observed between the results obtained by the two different apparatus. In addition, good repeatability of the data is observed. Based on this validation process, it is assumed that the high temperature DC flow apparatus is performing correctly, at least, at the room temperature conditions.

Eight out of 15 perforated sheet samples are tested in the high temperature apparatus at a number of different temperatures, up to about 1000°F, including the room temperature conditions. The measured DC flow resistance data is normalized using Equations 18 and 19. to determine if the normalization process on the basis of similarity principle holds good for the perforated sheet materials:

All the results are shown in Figures 84 through 91. In each figure, the "as measured" and "normalized" DC flow resistances at different temperatures are presented. For all the samples, the DC flow resistance decreases with increasing temperature. However, the normalized results for all the samples show very good collapse, indicating the applicability of the similarity principles for perforated sheets.

The DC flow resistance characteristics of perforated sheets with increasing porosity (i.e., σ) can be observed from Figures 84 through 87, respectively, for which the hole diameter and

Table 12. Geometrical Properties, DC Flow Resistance Parameters, and File Names for Normal Impedance Data for Perforated Facesheets

Sample #	Thickness, t in inches	Hole Dia, d in inches	Porosity, σ in %	A Rayls	B Rayls/cm	R100 Rayls	NLF (R150/R20)	Normal Impedance File @ 130 dB OASPL	Normal Impedance File @ 150 dB OASPL
1.37	0.025	0.039	5	2.062	0.33	35.066	5.953	m137-0375130.smt	m137-0375150.smt
1.38	0.025	0.039	7.5	-0.702	0.172	16.5	9.166	m138-0375130.smt	m138-0375150.smt
1.39	0.025	0.02	7.5	2.02	0.0895	10.97	4.05	m139-0375130.smt	m139-0375150.smt
1.40	0.025	0.01	7.5	4.56	0.0469	9.25	2.11	m140-0375130.smt	m140-0375150.smt
1.41	0.025	0.005	7.5	14.39	0.0693	21.32	1.57	m141-0375130.smt	m141-0375150.smt
1.42	0.025	0.039	11	0.398	0.0407	4.467	5.365	m142-0375130.smt	m142-0375150.smt
1.43	0.025	0.015	11	2.50	0.0451	7.01	2.73	m143-0375130.smt	m143-0375150.smt
1.44	0.025	0.005	11	14.87	0.0446	19.33	1.37	m144-0375130.smt	m144-0375150.smt
1.45	0.025	0.04	15	0.285	0.029	3.191	5.029	m145-0375130.smt	m145-0375150.smt
1.46	0.025	0.015	15	2.68	0.0209	4.77	1.88		m146-0375150.smt
1.47	0.025	0.005	15	12.17	0.0265	14.82	1.27		m147-0375150.smt
1.48	0.05	0.04	11	0.537	0.03278	3.814	4.573	m148-0375130.smt	m148-0375150.smt
1.49	0.08	0.04	11	0.636	0.0357	4.203	4.438	m149-0375130.smt	m149-0375150.smt
1.50	0.12	0.04	11	0.723	0.0312	3.839	4.011	m150-0375130.smt	m150-0375150.smt
1.51	0.025	0.06	11	-0.382	0.089	8.515	9.276	m151-0375130.smt	m151-0375150.smt



Figure 82. Photographic view of the DC flow apparatus for high temperature operation.

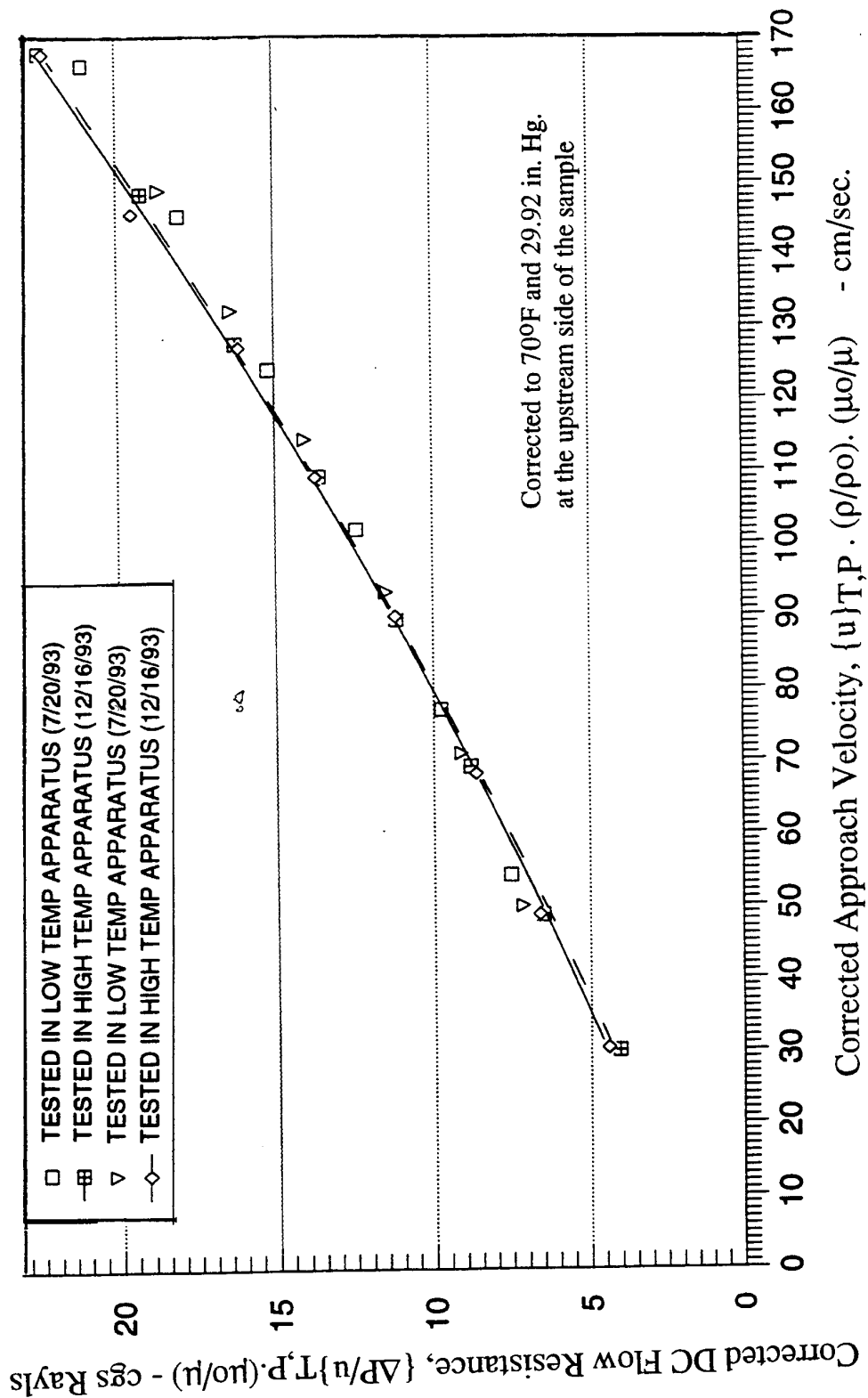


Figure 83. Comparison of DC flow resistance data for the "standard" perforated sheet measured by the low temperature apparatus in the acoustic duct lab and the new high temperature apparatus in the heat transfer lab at room temperature and pressure conditions.

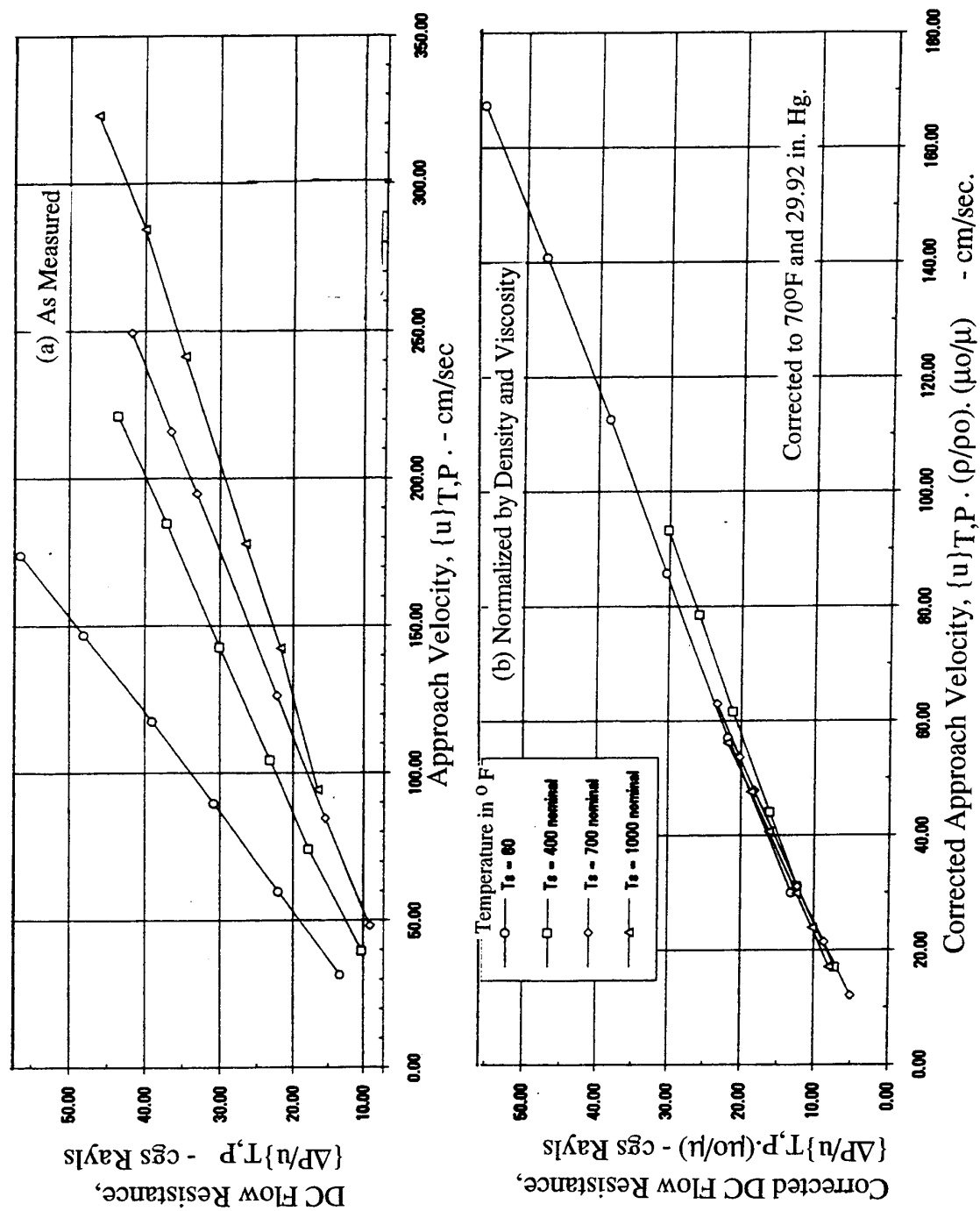


Figure 84. High temperature DC flow resistance data for a titanium alloy perforated plate; nominal porosity $\sigma = 4.5\%$, hole diameter $d = 0.039$ ", thickness $t = 0.025$ ".

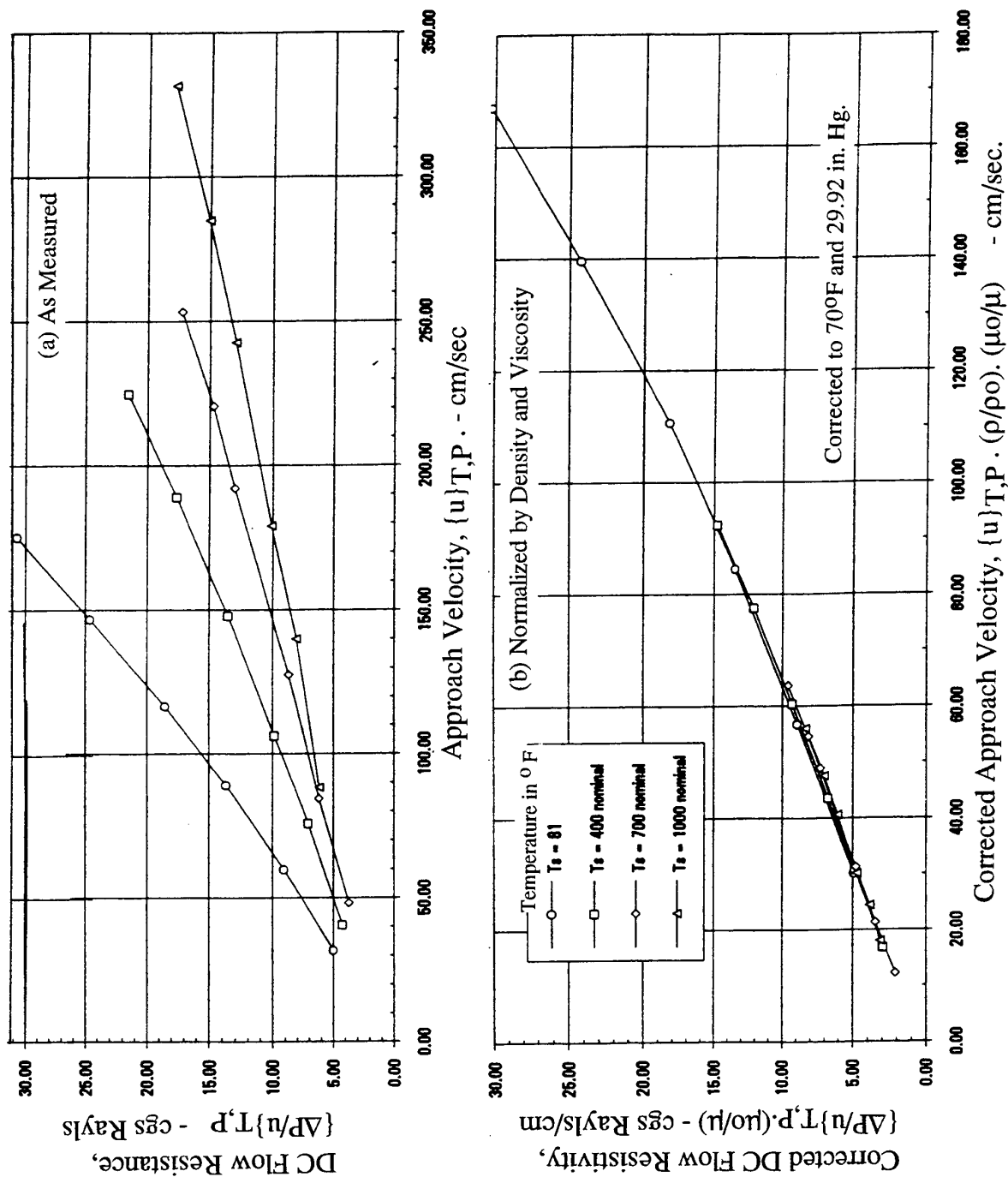


Figure 85. High temperature DC flow resistance data for a titanium alloy perforated plate; nominal porosity $\sigma = 8\%$, hole diameter $d = 0.039$ ", thickness $t = 0.025$ ".

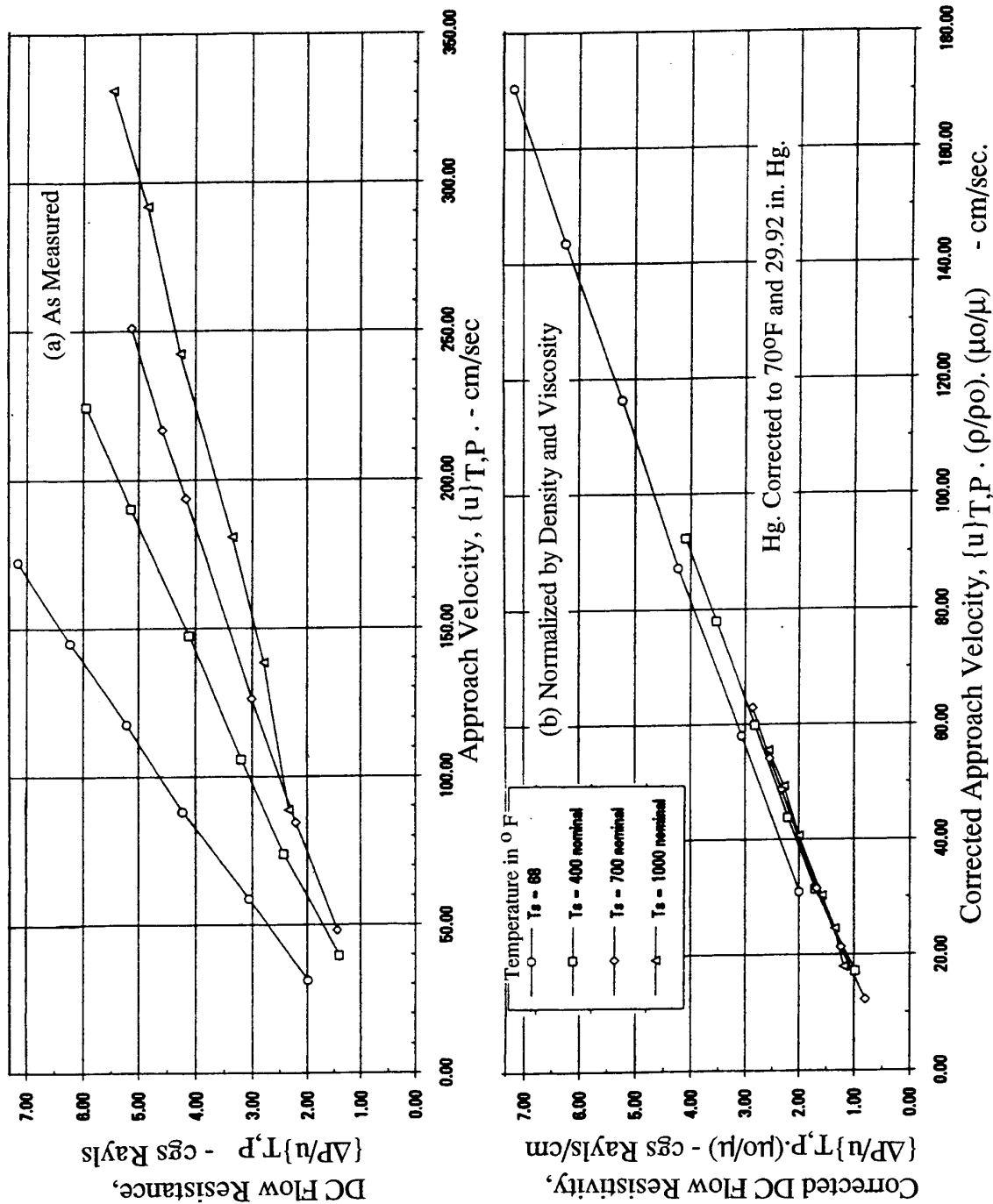


Figure 86. High temperature DC flow resistance data for a titanium alloy perforated plate; nominal porosity $\sigma = 14\%$, hole diameter $d = 0.039$ ", thickness $t = 0.025$ ".

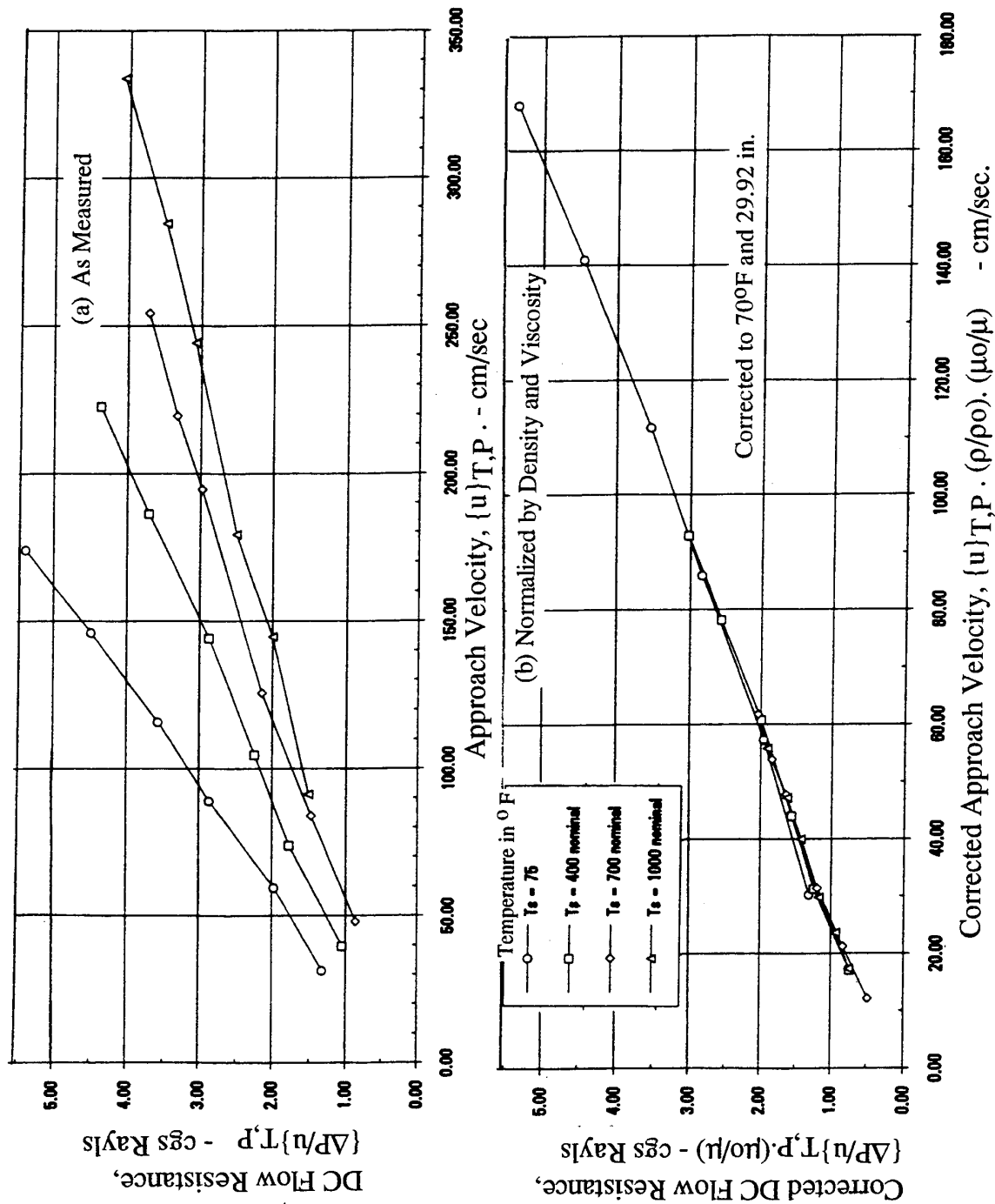


Figure 87. High temperature DC flow resistance data for a titanium alloy perforated plate; nominal porosity $\sigma = 17\%$, hole diameter $d = 0.039$ in, thickness $t = 0.025$ in.

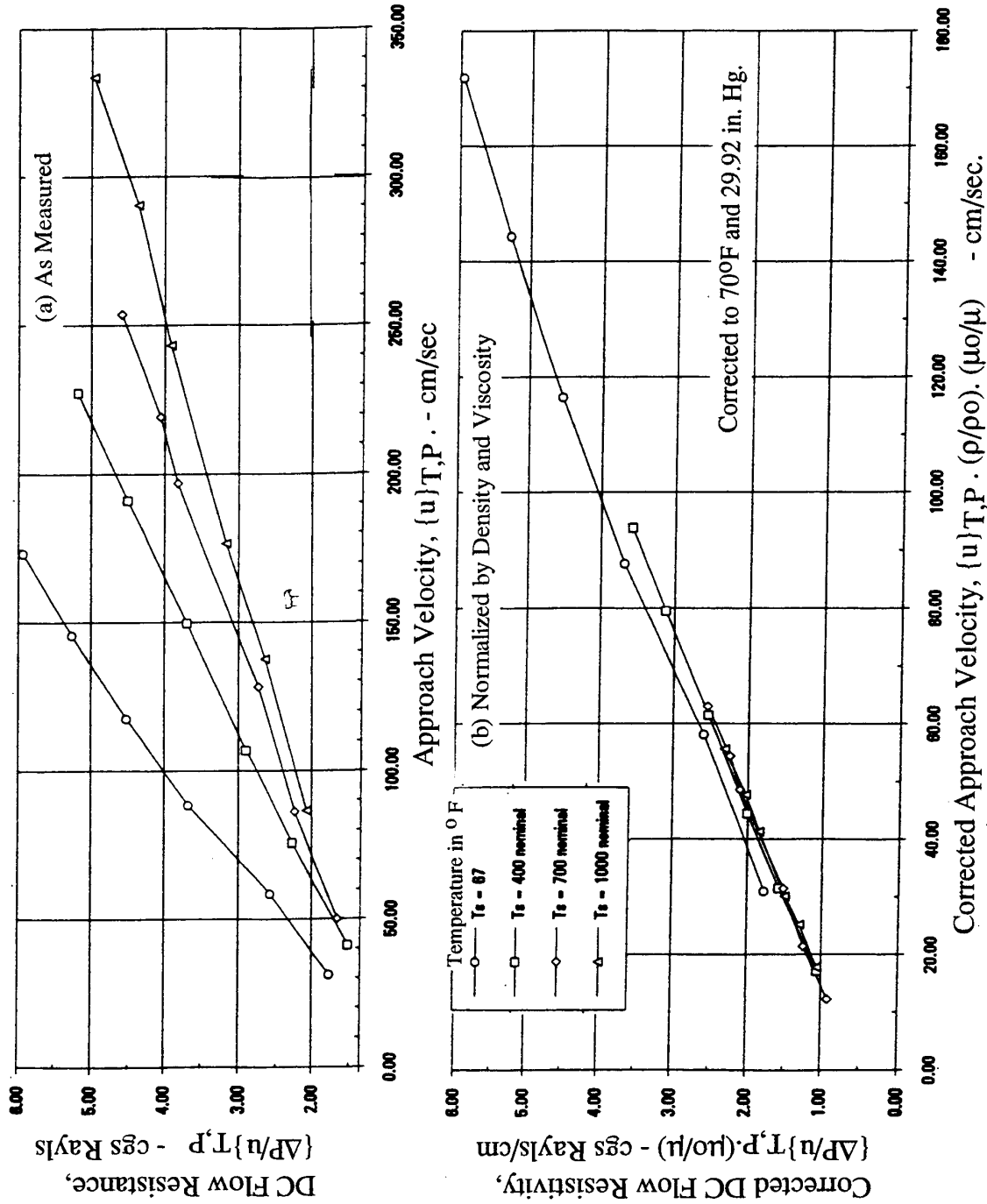


Figure 88. High temperature DC flow resistance data for a titanium alloy perforated plate; nominal porosity $\sigma = 14\%$, hole diameter $d = 0.039$ ", thickness $t = 0.05$ ".

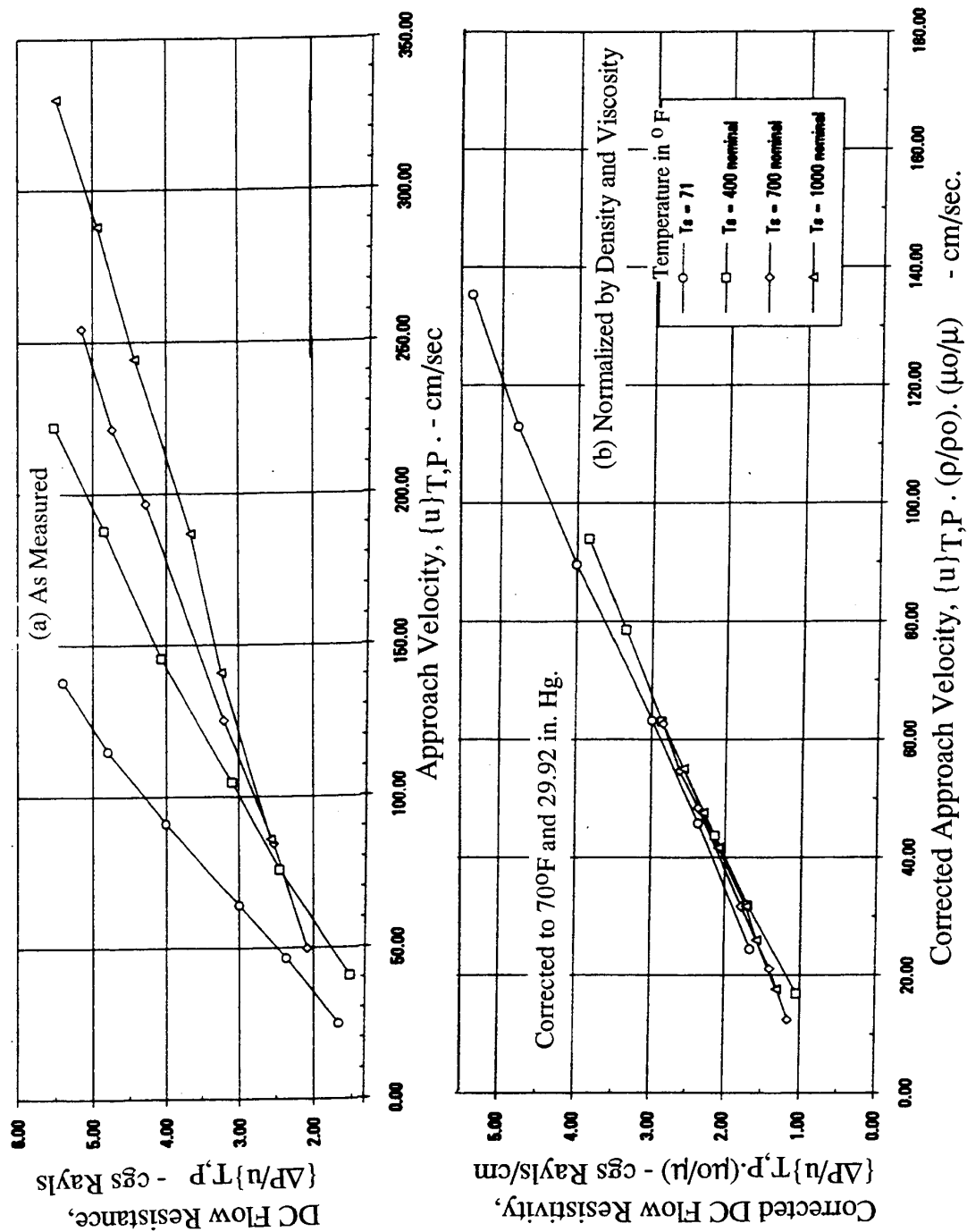


Figure 89. High temperature DC flow resistance data for a titanium alloy perforated plate; nominal porosity $\sigma = 12\%$, hole diameter $d = 0.039$ ", thickness $t = 0.08$ ".

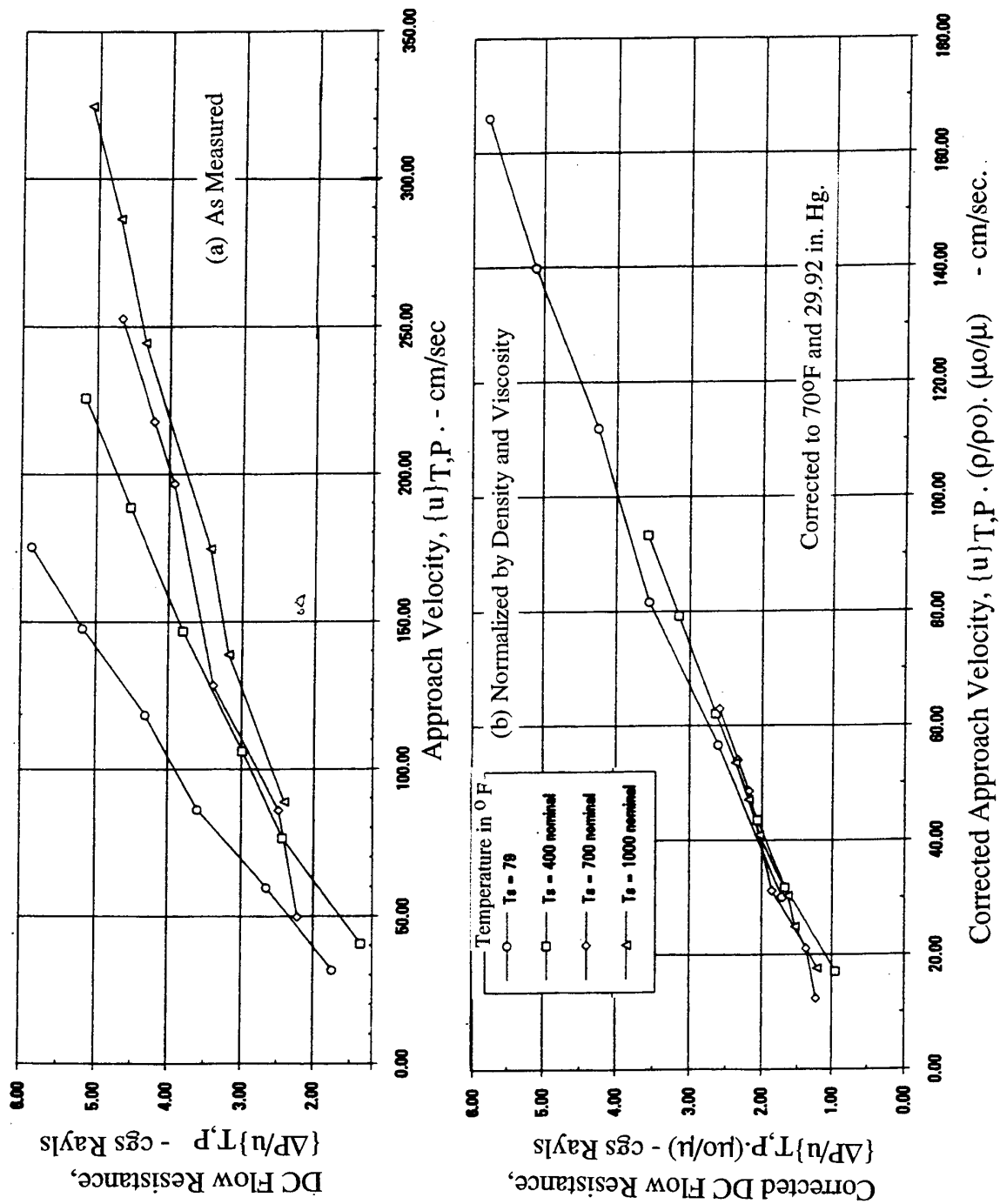


Figure 90. High temperature DC flow resistance data for a titanium alloy perforated plate; nominal porosity $\sigma = 11\%$, hole diameter $d = 0.039''$, thickness $t = 0.12''$.

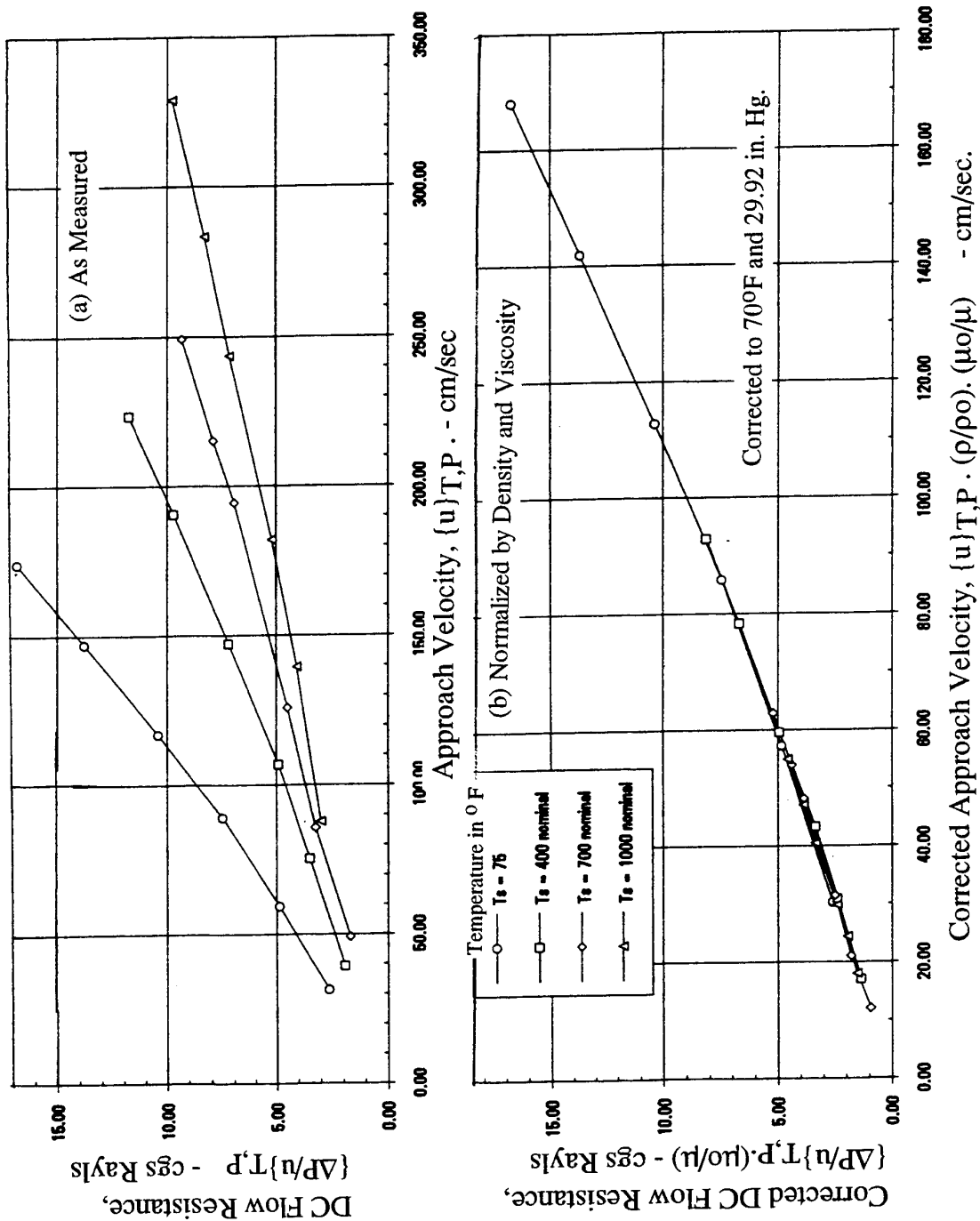


Figure 91. High temperature DC flow resistance data for a titanium alloy perforated plate; nominal porosity $\sigma = 11\%$, hole diameter $d = 0.06$ ", thickness $t = 0.025$ ".

sheet thickness are kept the same for each case (i.e., $d=0.039''$ and $t=0.025''$). A general trend observed from these figures, is the decreasing DC flow resistance with increasing porosity. Similarly, the effect of increasing sheet thickness (i.e., t) can be observed from Figures 86 and 88, as well as from Figures 89 and 90, for which the porosity and the hole diameters are kept the same. Since the effect of thickness is relatively small, it is difficult to identify directly from these individual figures. However, the influence of various physical parameters can be accurately demonstrated by superimposing the normalized DC flow resistance data for a varying physical parameter.

The normalized data for each sample is curve fitted utilizing a least square fit method to the expression of Equation 15 (i.e., $A + B u$). The data for most of the samples are well fitted by the straight line equation of $A + B u$. However, for two samples, with $\sigma = 8\%$, $d=0.039''$, $t=0.025''$ and $\sigma = 11\%$, $d=0.06''$, $t=0.025''$, as shown in Figures 85 and 91, the data did not fit well with the straight line expression. Instead, a second order polynomial of u (i.e., $A + B u + C u^2$) fitted well with these data (see Figure 92).

The influence of porosity (σ), hole diameter (d), and the sheet thickness (t) on the DC flow resistance for the perforated sheets described in Table 12 is shown in Figures 93 through 97, by utilizing the data and the polynomial fitted curves. Figure 93 clearly indicates the increasing DC flow resistance with decreasing porosity. In addition, the constant "A" and the slope "B" decrease with increasing porosity (see Figure 94). The nonlinear factor, NLF (i.e., R_{150}/R_{20}) remains more or less the same for the samples, except for one with $\sigma = 7.5\%$, for which the value of NLF is relatively higher. The DC flow resistance for lower porosity (see Figures 95 and 96) decreases with hole diameter and then increases with further decrease of diameter. However, for higher porosity the resistance increases with hole diameter. The DC flow resistance is not very sensitive to the sheet thickness, as indicated in Figure 97. Small increase in DC flow resistance is observed with decreasing sheet thickness.

5.1.2 Normal Impedance:

High Frequency Normal Impedance Measurements :

To evaluate the normal impedance of a perforated sample (i.e., not rigidly blocked at the outer surface) the test sample in the impedance tube is followed by a cavity (see Figure 43b). Adjusting the plunger location can vary the cavity depth. In the present study two different cavity depths, namely, $0.75''$ and $0.375''$, are utilized. Two different nominal values for OASPL, namely, 130 dB and 150 dB, are used for all the current tests. The acoustic pressures

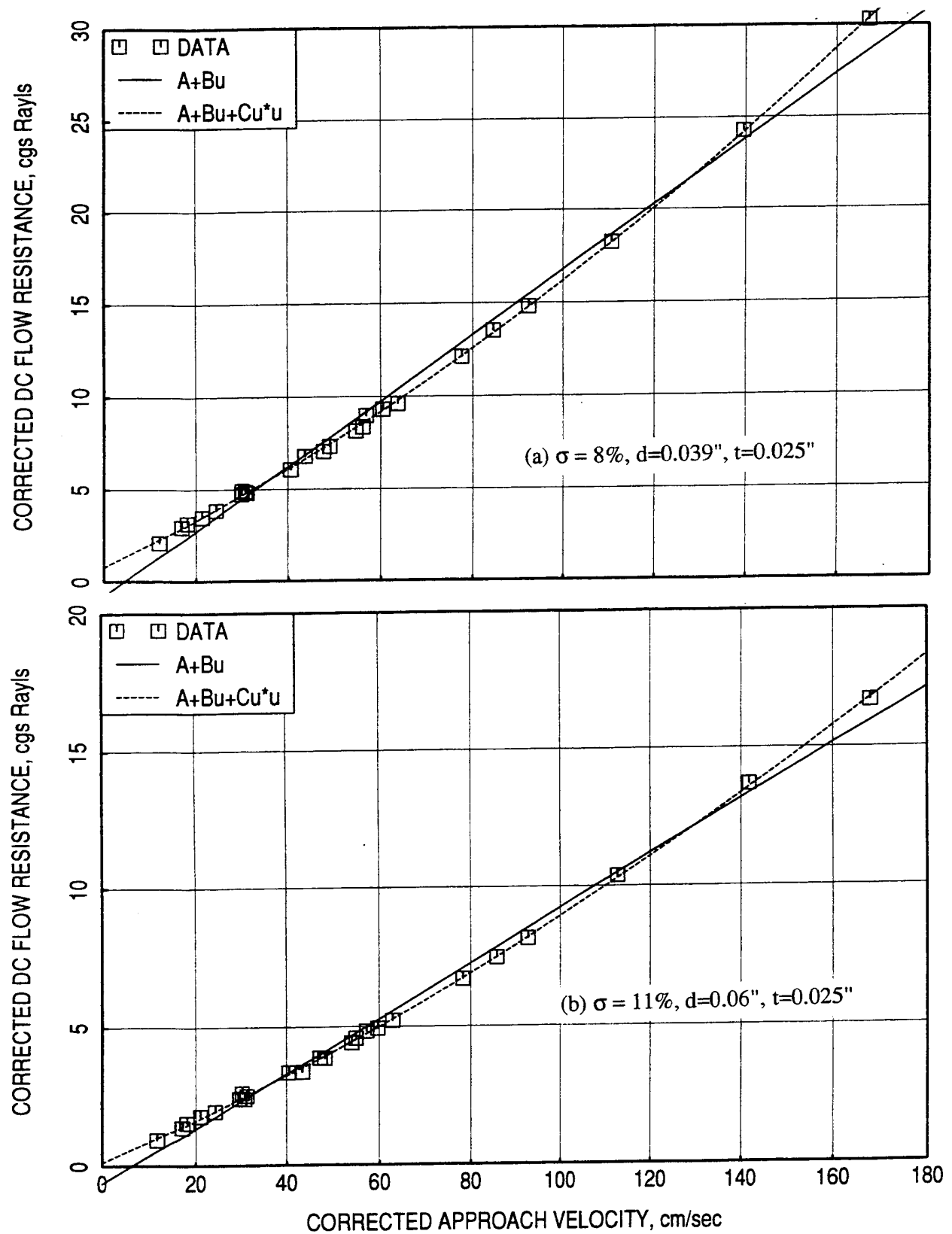


Figure 92. Polynomial curve fitting for DC flow resistance for perforated sheets.

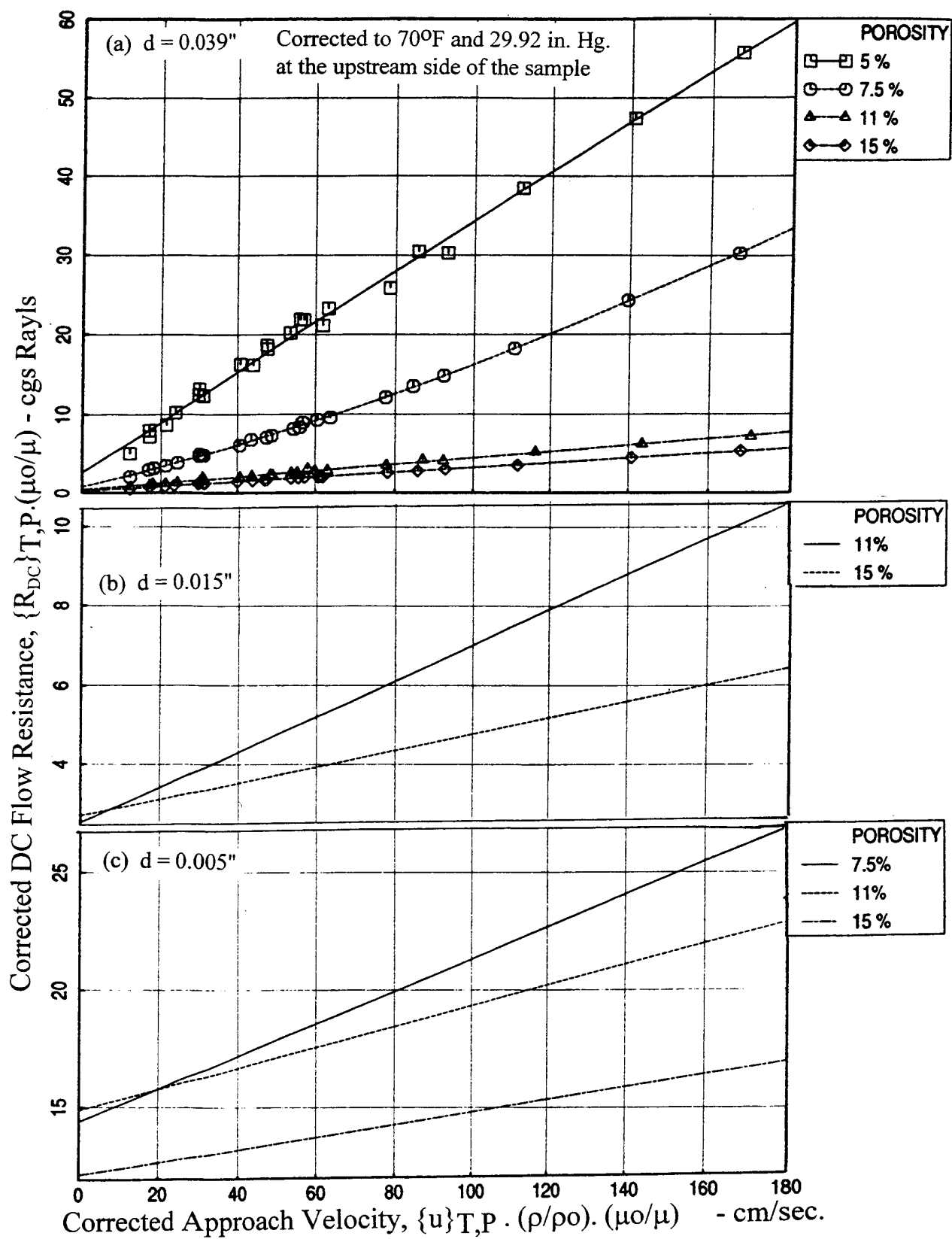


Figure 93. Effect of porosity (σ) on DC flow resistance for perforated sheets with fixed nominal thickness $t = 0.025''$ for different nominal hole diameters, d .

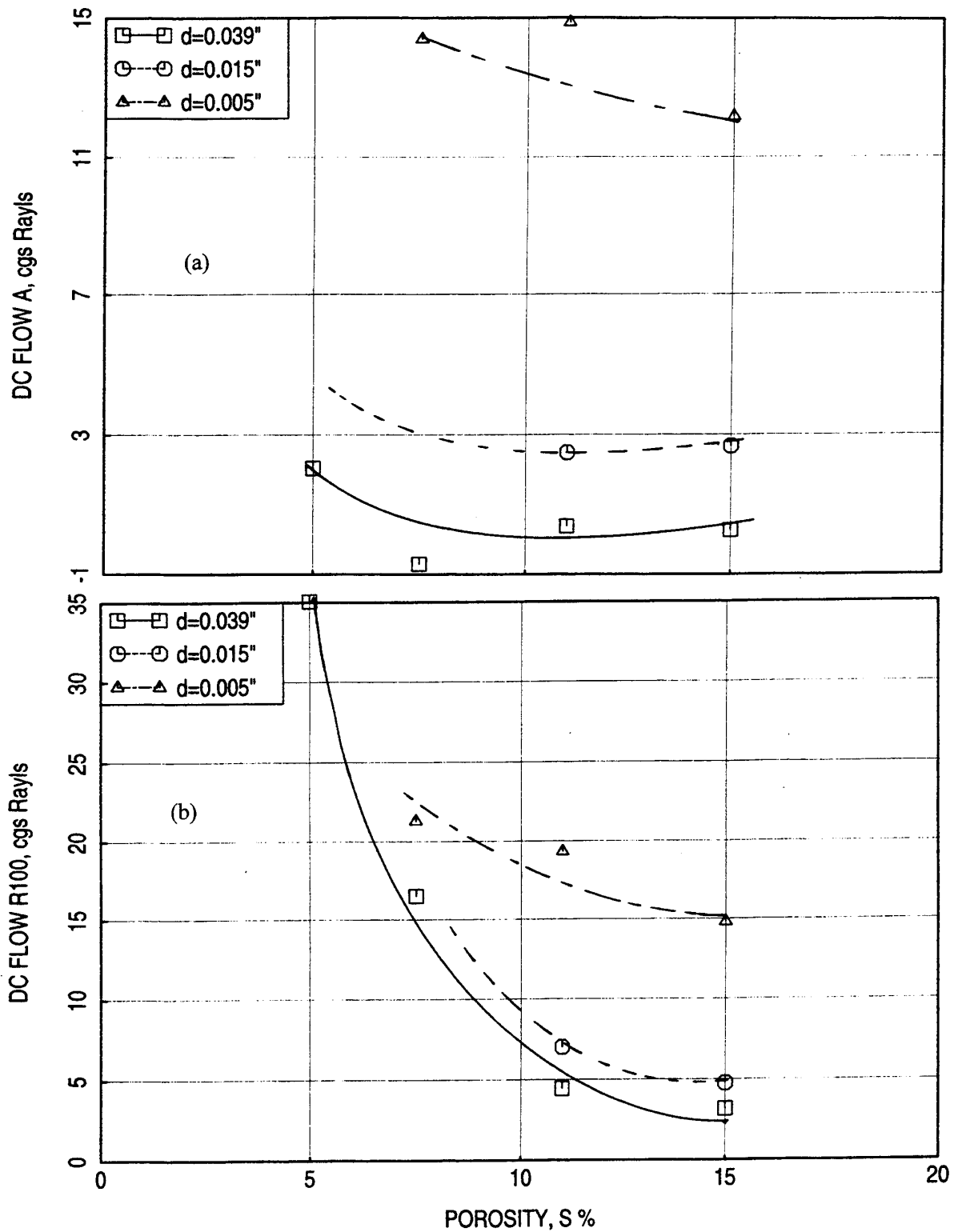


Figure 94. Variation of DC flow resistance, (a) A and (b) R100, with respect to porosity (σ) for perforated sheets with fixed nominal thickness $t = 0.025$ for different nominal hole diameters, d .

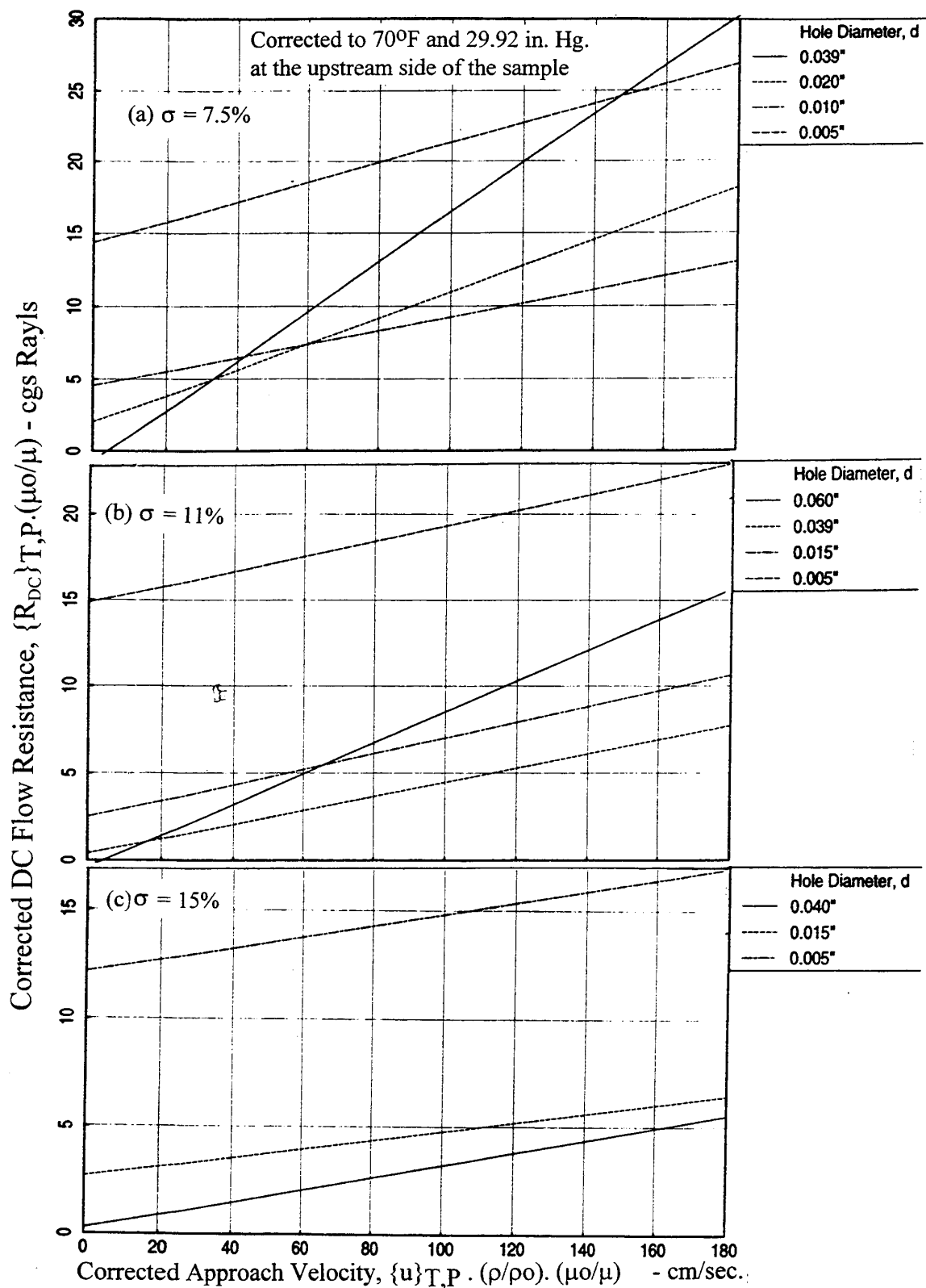


Figure 95. Effect of hole diameter (d) on DC flow resistance for perforated sheets with fixed nominal thickness $t = 0.025$ " for different nominal porosity, σ .

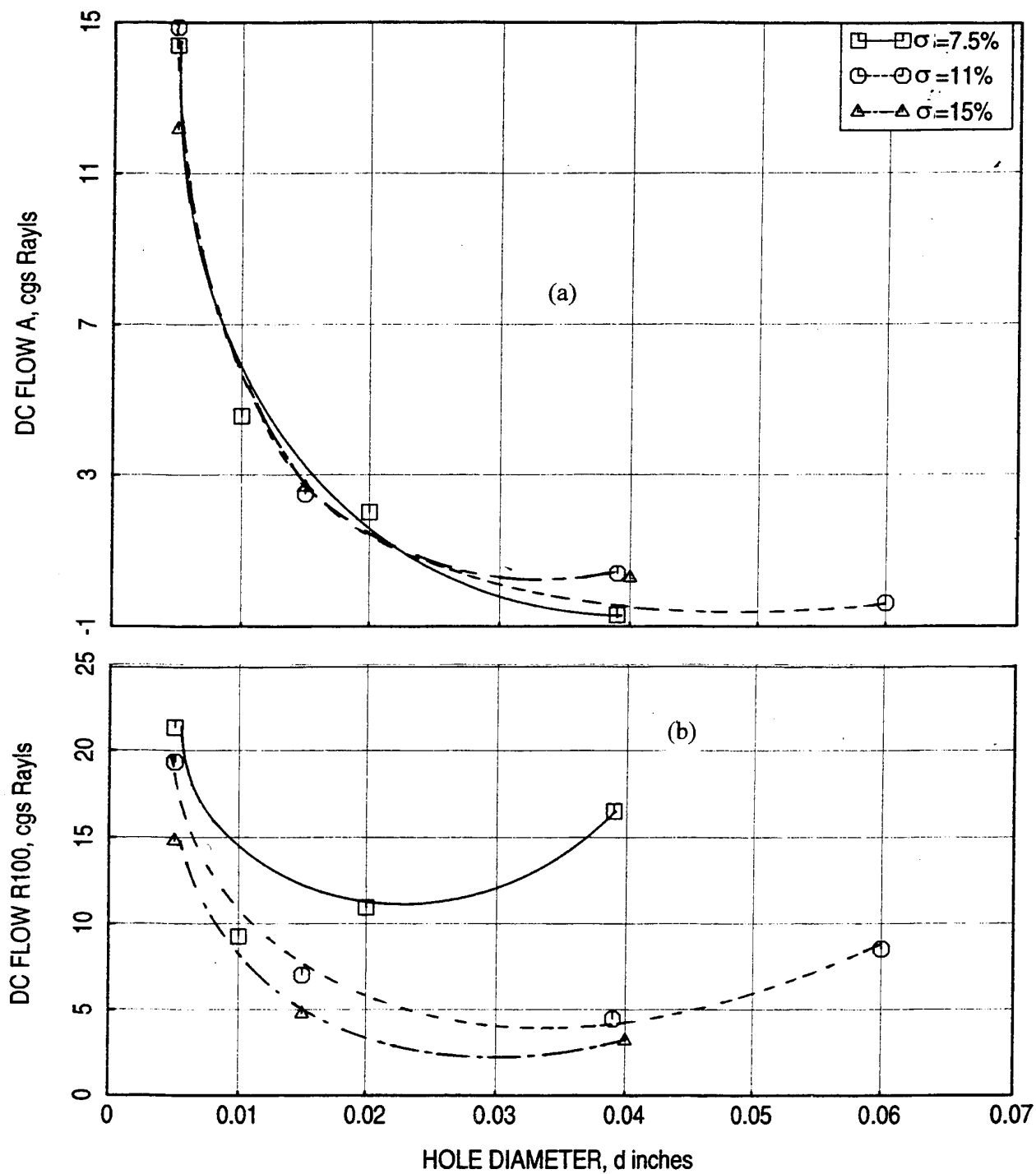


Figure 96. Variation of DC flow resistance, (a) A and (b) R100, with respect to hole diameter (d) for perforated sheets with fixed nominal thickness $t = 0.025$ inches for different nominal porosities, σ .

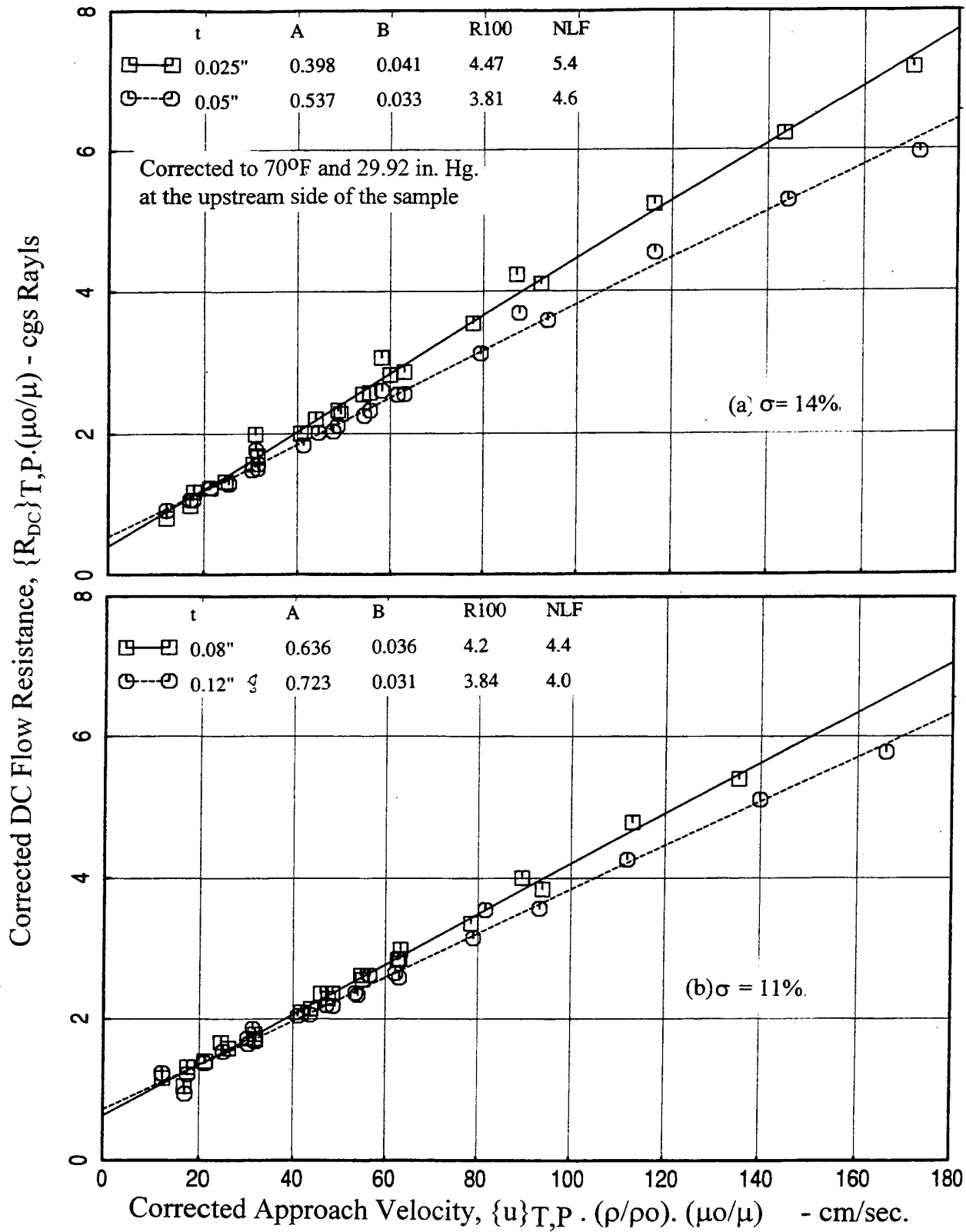


Figure 97. Effect of thickness (t) on DC flow resistance for perforated sheets with fixed nominal hole diameter $d = 0.039''$ and porosity (a) $\sigma = 14\%$ (b) $\sigma = 11\%$.

measured in the impedance tube in the presence of a test sample are used to evaluate the combined impedance of the sample and of the extended cavity, whereas, the acoustic pressures measured in the impedance tube in the absence of any test sample are used to evaluate the impedance of the cavity only. Thus, by subtracting the cavity impedance from the combined value the impedance of the test sample alone is extracted.

Cavity Only: The excitation broadband sound pressure level spectra for nominal OASPLs of 130 dB and 150 dB for a 0.75" deep cavity (without any test sample) are shown in Figure 98a. Substantial variation of SPL with respect to frequency is observed due to the standing wave pattern at $x=0$ for a nominal OASPL condition. A strong SPL drop is observed at about 4.5 kHz, which is the resonance frequency of 0.75" deep cavity (i.e., $\cot(2\pi fh/c)=\infty$, or $2\pi fh/c=\pi/2$ or $f=c/4h$, f being the frequency and h being the depth of the cavity). The specific resistance and reactance spectra for the cavity, showing the effect of excitation level, are plotted in Figure 98b. The high value of resistance occurring at frequency of about 9 kHz where the reactance changes its sign from high positive to negative, indicates the anti-resonating frequency of the cavity behind $x=0$ location of the impedance tube (i.e., At anti-resonant frequency: $\cot(2\pi fh/c)=0$, or $2\pi fh/c=0$ or π or $f=0$ or $c/2h$). Influence of excitation level on cavity impedance is insignificant. Reaptability of cavity impedance is demonstrated in Figure 99 for both the nominal OASPLs.

The impedance results of a test sample close to anti-resonance frequency of the cavity will be erroneous. To increase the anti-resonance frequency, so that it falls beyond the desired frequency range of 12 kHz, tests are performed for a 0.375" deep cavity. Figure 100a shows the spectral variation of excitation SPL of 150 dB nominal OASPL for 0.75" and 0.375" deep cavities. The resonance frequency for 0.375" cavity has occurred at about 9 kHz compared to 4.5 kHz for 0.75" deep cavity. The impedance spectra, shown in Figure 100b, indicate that the antiresonance frequency for the 0.375" deep cavity has pushed out of the 12 kHz frequency range. It appears that the 0.375" deep cavity can be used for impedance measurement up to 12 kHz range. However, accurate results at lower frequencies can not be obtained by this method. Hence for the present study, results below 1 kHz are ignored.

Perforated Face Sheets: Perforated face sheet samples of different porosity (σ), hole diameter (d), and thickness (t) for SDOF type liners, listed in Table 12, are tested to evaluate the effect of porosity, hole diameter, sheet thickness, and excitation sound level on their normal impedance characteristics. The combined normal impedance values for the sample and the cavity together are first evaluated from the measured acoustic data. Assuming that the net

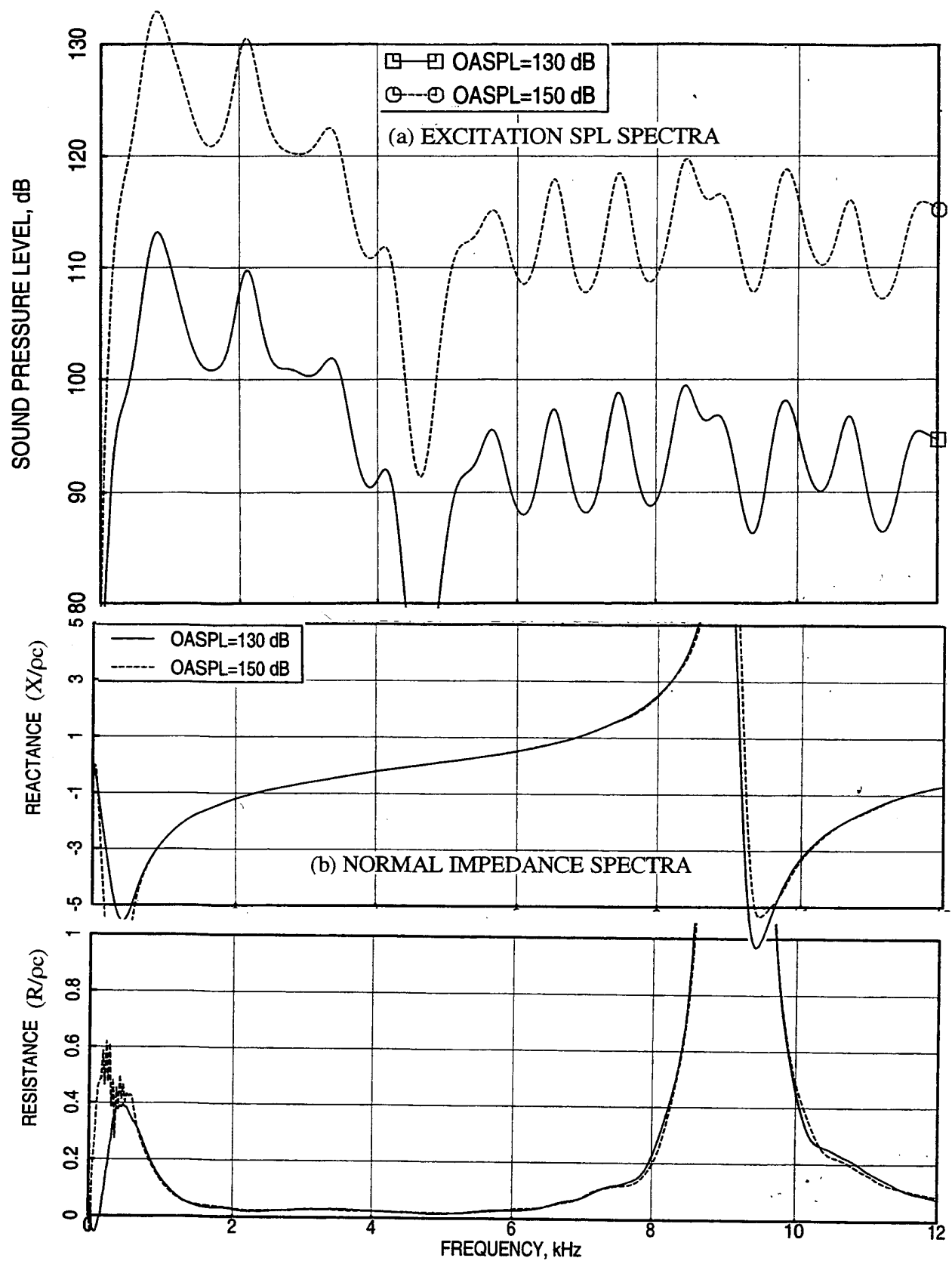


Figure 98. Sound pressure level and corresponding normal impedance spectra at two OASPLs for a 0.75"-deep cavity.

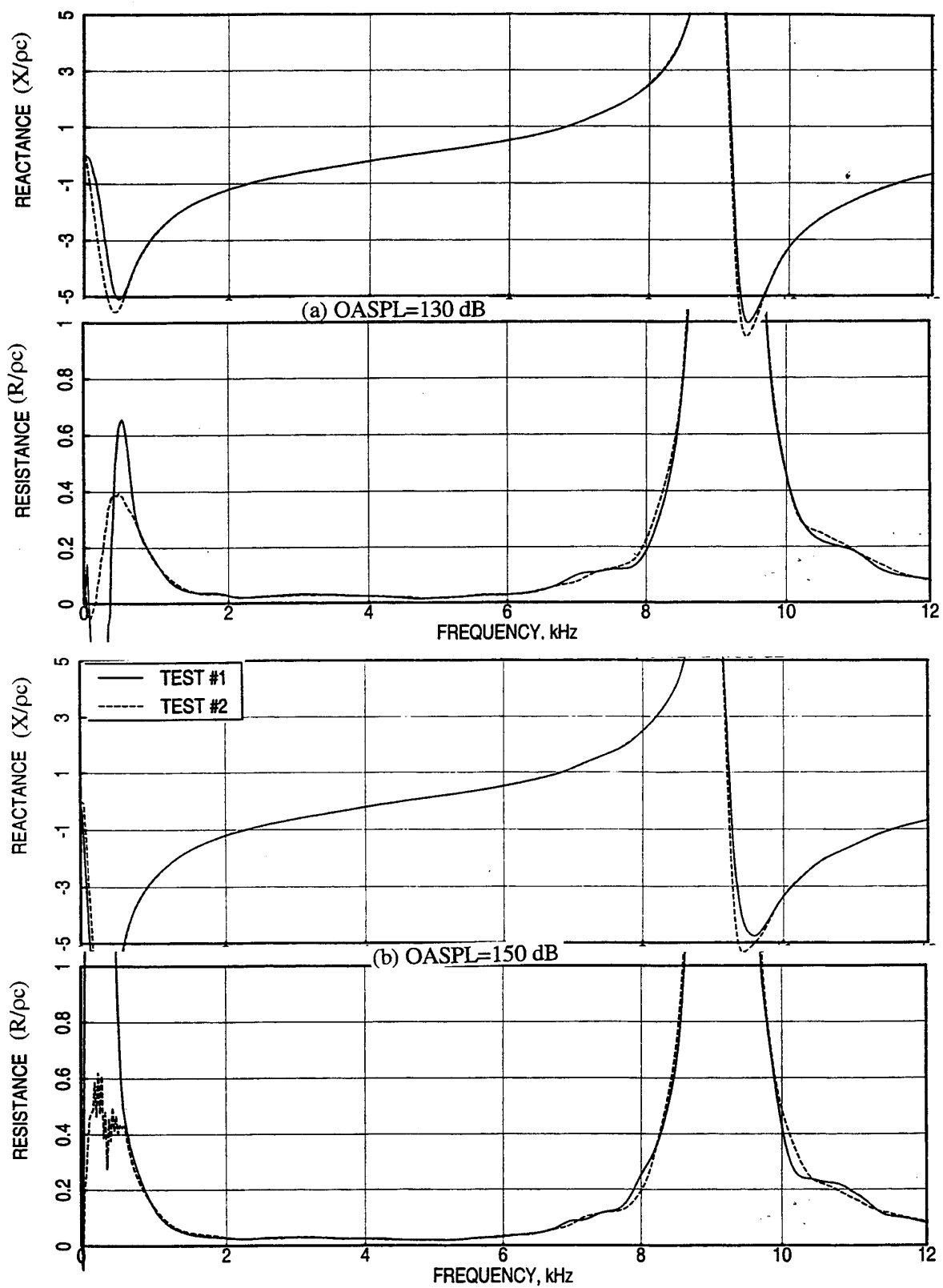


Figure 99. Repeatability of normal impedance spectra for a 0.75''-deep cavity at two nominal OASPLs.

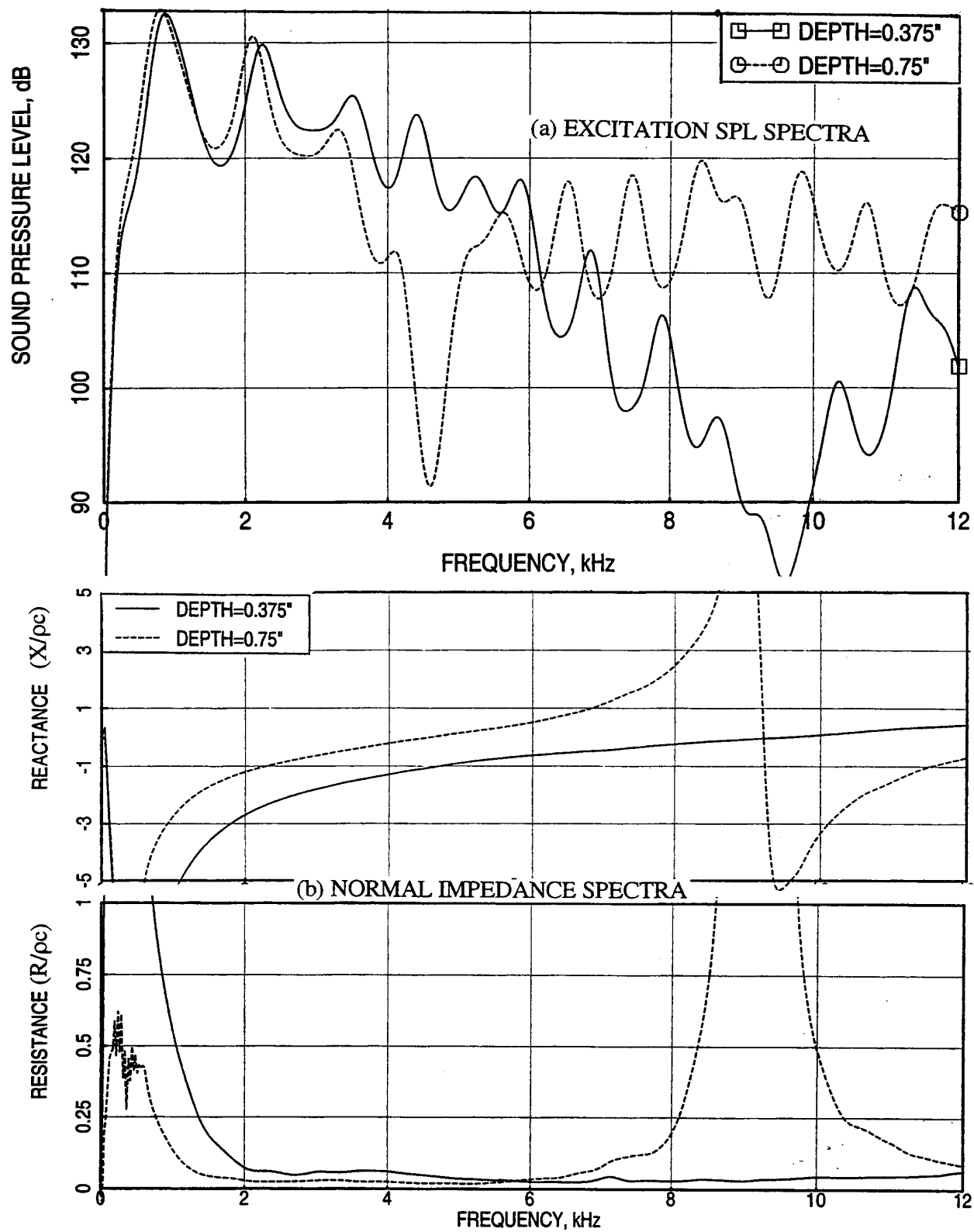


Figure 100. Sound pressure level and corresponding normal impedance spectra for cavities of two different depths for a nominal OASPL of 150 dB.

impedance of the sample and the cavity together is a linear sum of the individual impedances, the sample impedances are derived from the sample with cavity and the cavity alone results.

Figure 101 shows the specific reactance and resistance spectra evaluated for three perforated samples with different porosities using two cavity depths. As expected, the results for 0.75" deep cavity are significantly off from those derived using 0.375" deep cavity. Reactance results show very good agreement between two cavity depths below the antiresonance frequency for 0.75" deep cavity. However, some amount of difference is observed for resistance results between the two configurations, especially, for samples with lower porosity. This is most probably due to the effect of excitation sound level, which is cavity dependent, even with the same nominal OASPL (see Figure 100a). The excitation levels are higher for 0.75" cavity compared to 0.375" one. Hence, it is expected that the resistance levels will be higher with higher level of excitation for less porous samples due to nonlinear effects. The 0.375" cavity configuration seems to be a reasonable choice to study the effect of various parameters on the normal impedance Up to to about 12 kHz range. Hence, all the subsequent results are for the samples with 0.375" deep back cavity.

Effect of Porosity (σ): The excitation SPL levels for perforated samples with different porosity for fixed nominal OASPLs are shown in Figure 102. The cavity effect on excitation SPL is significant at higher frequencies and for more porous samples. Spectral variation of normal impedance with porosity is shown in Figures 103 and 104. The resistance behavior with decreasing porosity is somewhat similar to that produced by increasing OASPL, that the resistance increases with decreasing porosity. This is expected, since with a fixed excitation level the acoustic intensity increases across the perforation with decreasing porosity. However, unlike the effect of excitation intensity, the reactance increases with decreasing porosity.

Effect of Hole Diameter (d): For nominal porosities of 7.5%, 11%, and 15% the effect of hole diameter on normal impedance spectra is shown in Figures 105 and 106. The reactance increases considerably with increasing hole diameter. Whereas, the resistance decreases with decreasing hole diameter first and then increases back for very small hole diameter (i.e., 0.005" for current study) for less porous samples (i.e., for 7.5% and 11%). For $\sigma=15\%$, the resistance increases consistently with decreasing hole diameter.

Effect of Sample Thickness (t): Normal impedance spectra for samples of different thicknesses with a nominal porosity of 11% and hole diameter of 0.04" are shown in Figure

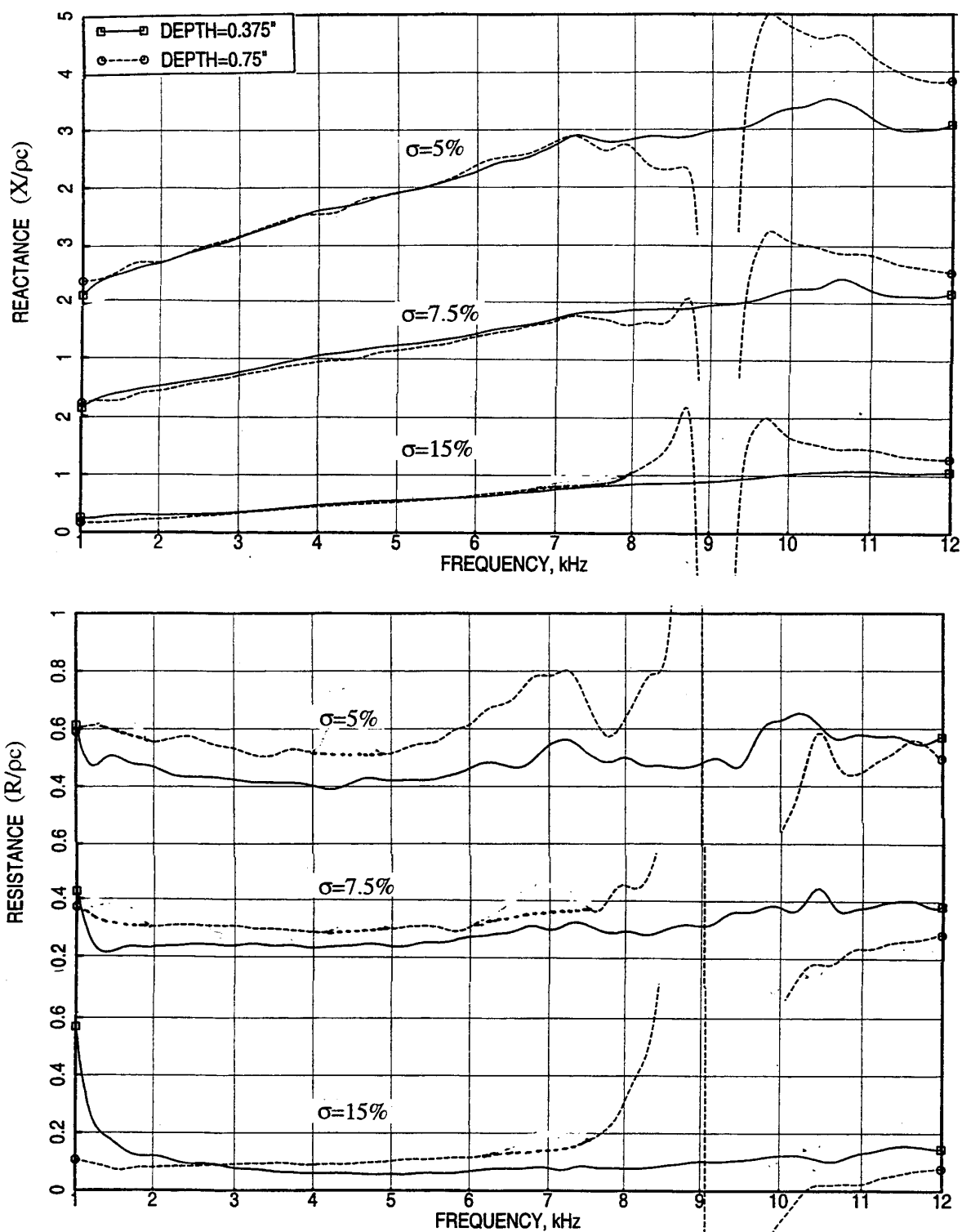


Figure 101. Effect of cavity depth on normal impedance spectra (cavity contribution removed) for perforated sheets of different porosities (σ); $d=0.039''$, $t=0.025''$, nominal OASPL=150 dB.

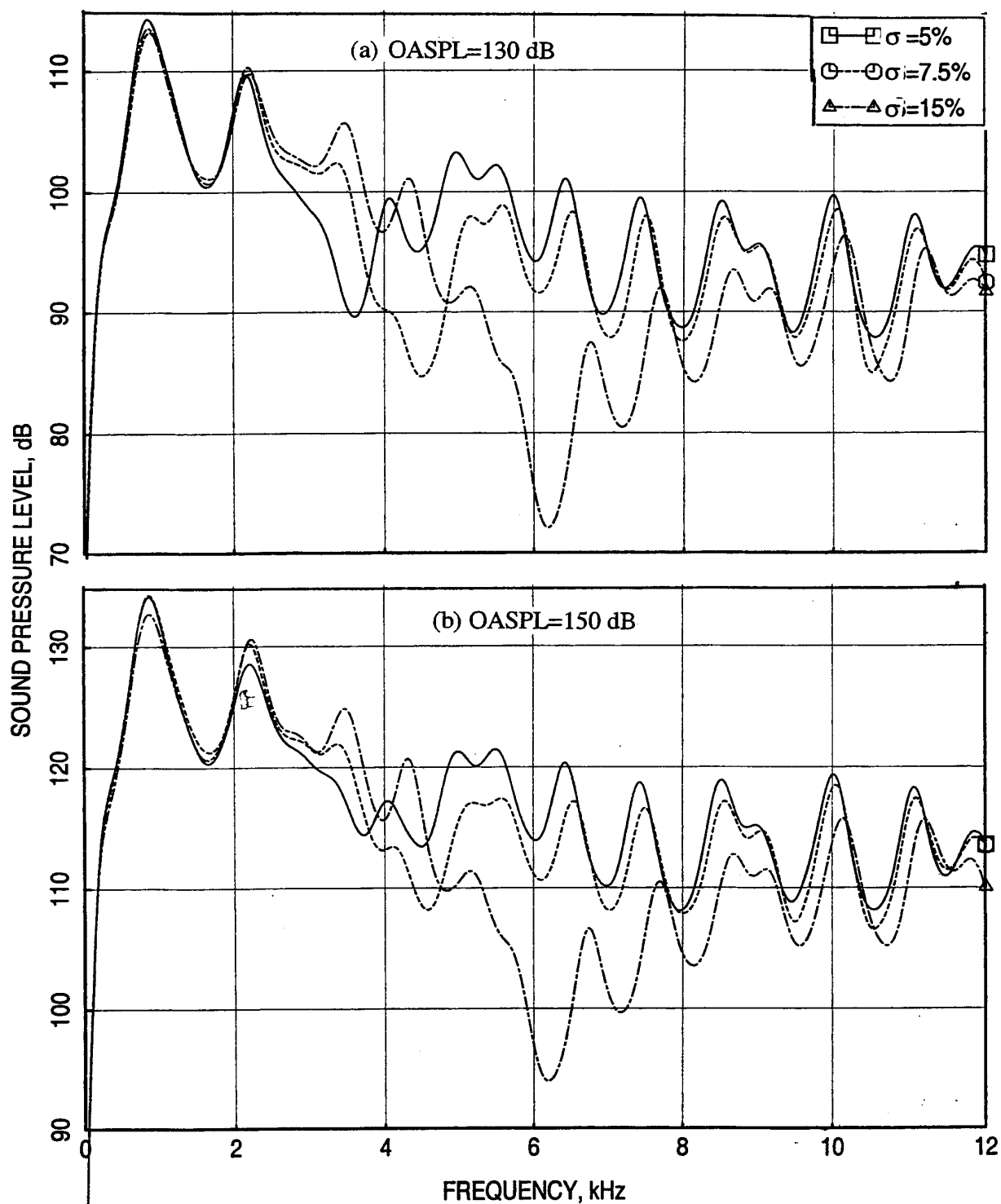


Figure 102. Influence of perforated sheet porosity (σ) on sound pressure level spectra at two nominal OASPL with a back cavity of 0.375" deep; $d=0.039$ ", $t=0.025$ ".

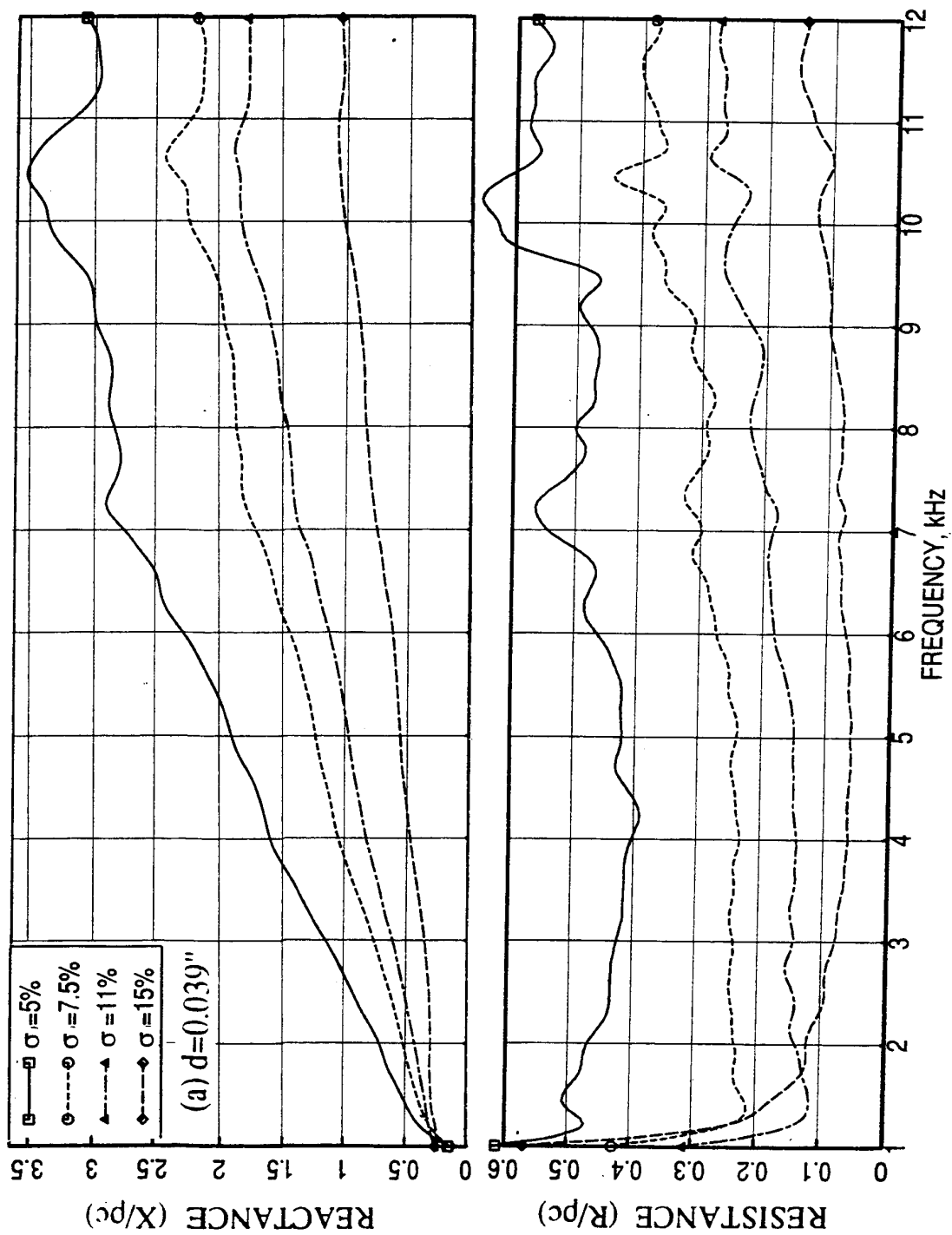


Figure 103. Effect of perforated sheet porosity (σ) on normal impedance spectra (cavity contribution removed) with a 0.375" deep back cavity; $d=0.039$ ", $t=0.025$ ", nominal OASPL=150 dB.

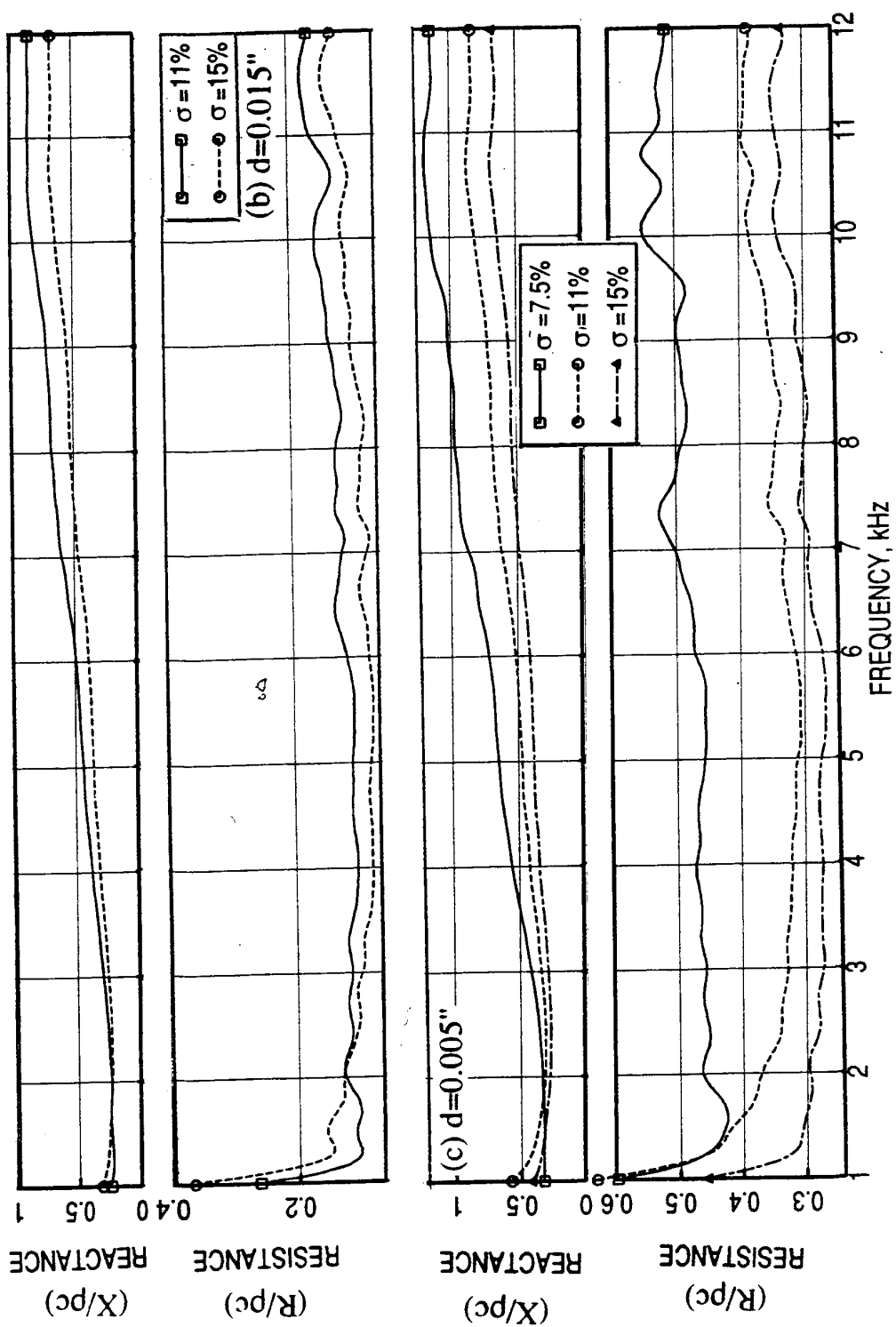


Figure 104. Effect of perforated sheet porosity (σ) on normal impedance spectra (cavity contribution removed) with a 0.375" deep back cavity; $t=0.025$ ", nominal OASPL=150 dB.

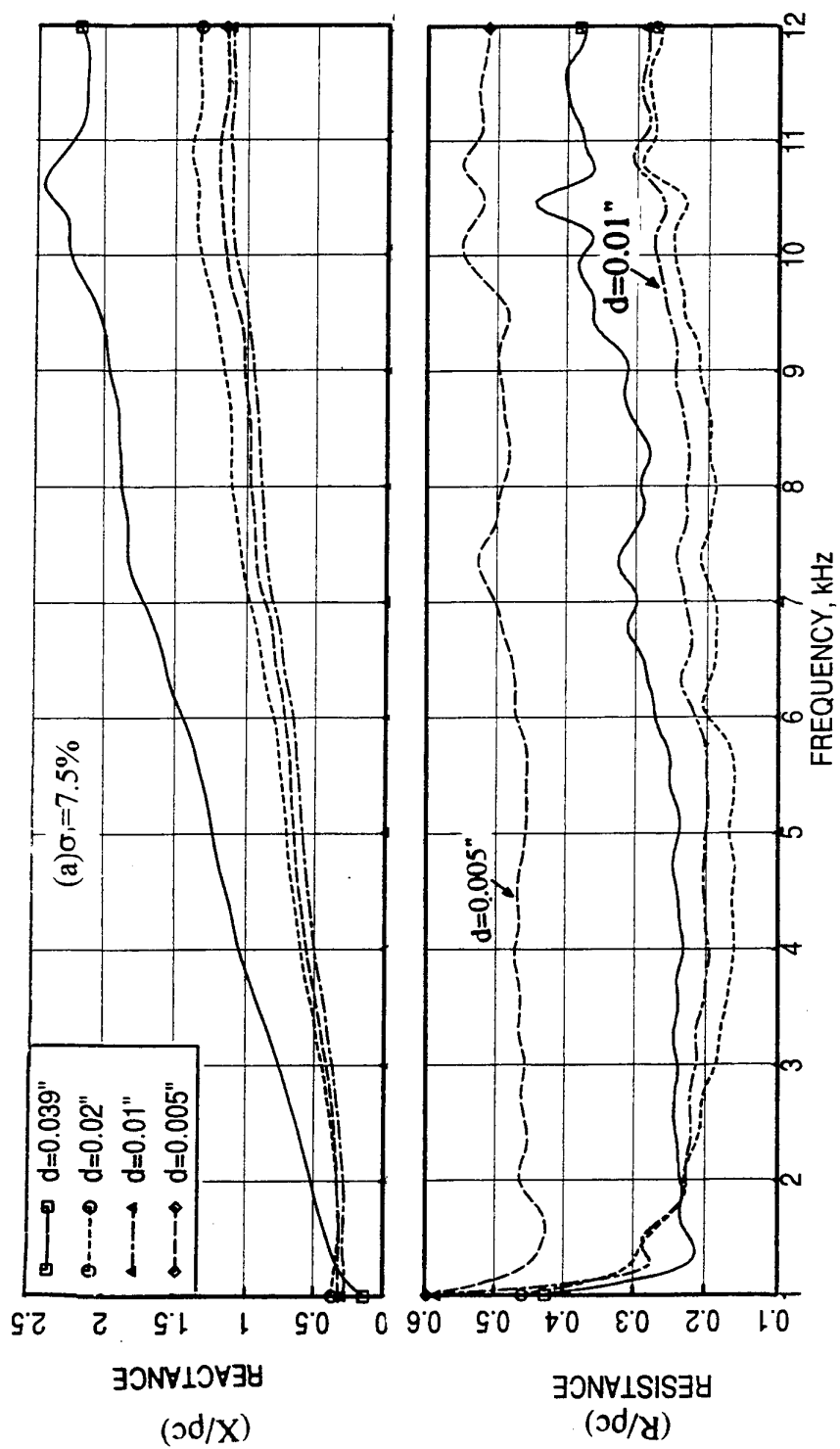


Figure 105. Effect of perforated sheet hole diameter (d) on normal impedance spectra (cavity contribution removed) with a 0.375" deep back cavity; $t=0.025''$, $\sigma=7.5\%$, nominal OASPL=150 dB.

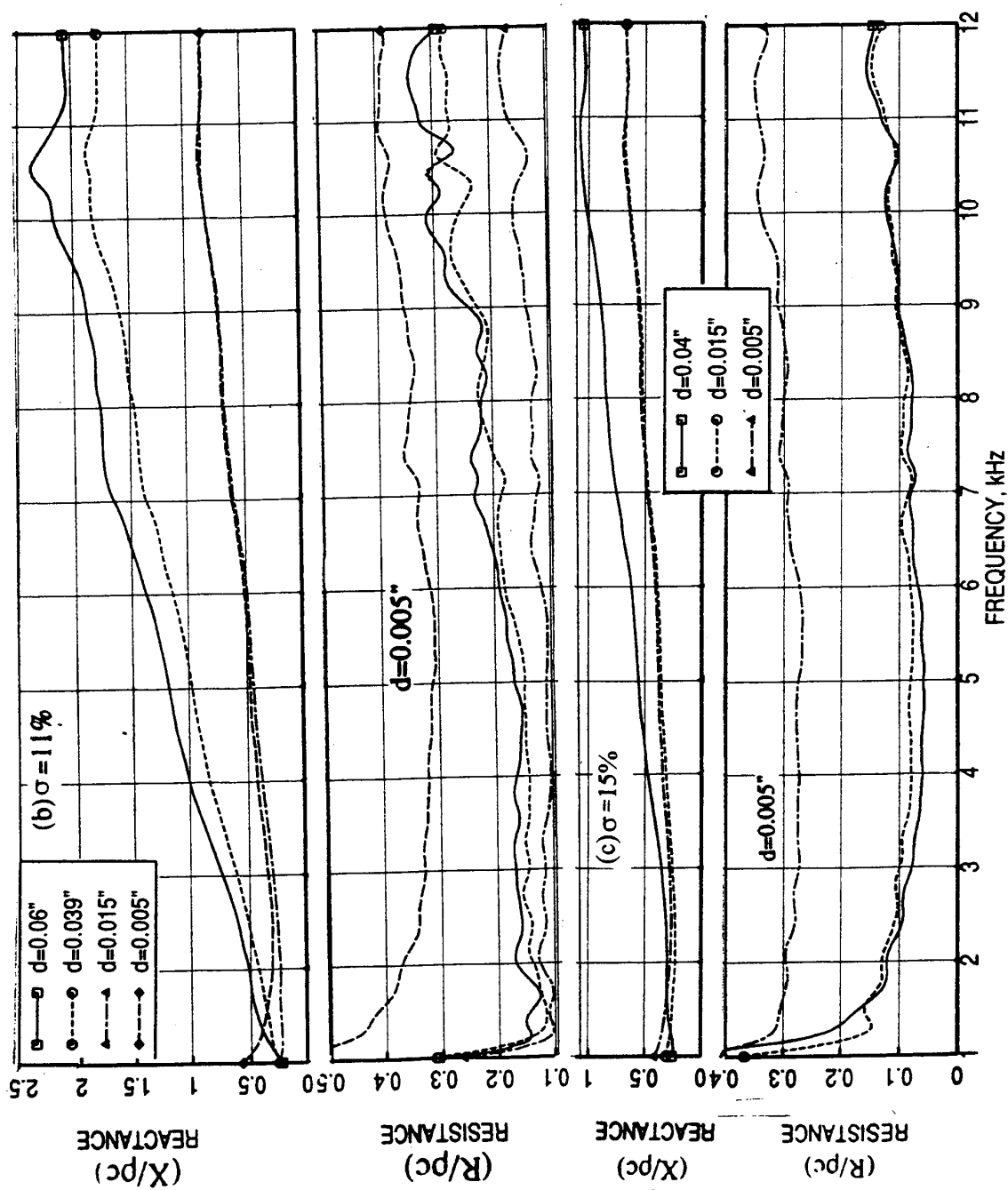


Figure 106. Effect of perforated sheet hole diameter (d) on normal impedance spectra (cavity contribution removed) with a 0.375" deep back cavity; $t=0.025$ ", nominal OASPL=150 dB.

107. The reactance increases with increasing t and the resistance behaves in the same way for higher frequencies. At lower frequencies a much higher resistance is observed for $t=0.05$ "

Effect of Excitation Level: Figure 108 shows the excitation SPL levels for two nominal OASPLs with two perforated samples of different porosity. The excitation levels seem to be effected due to the sample porosity, especially at higher frequencies. Figures 109 and 110 show the effect of excitation level on the normal impedance for four perforated samples of different porosity. The general trend is the reduction of reactance and increase of resistance with increasing excitation level. The effect is more significant at lower frequencies. The effect of excitation level is small for reactance and is significant for resistance. These are the nonlinear effects of high intensity sound field. Portion of the sound energy is dissipated into vortical form at the sample and streams out through the perforation. The sensitivity of the acoustic characteristics to high intensity reduces considerably with increasing porosity. Effect of excitation level on normal impedance for different facesheet hole diameter at fixed porosity and thickness is shown in Figures 111 and 112. While, the reactance is unaffected by acoustic intensity the resistance increases with intensity, and the influence is higher at higher hole diameter. Similar results for different facesheet thickness with fixed porosity and hole diameter is shown in Figures 113 and 114. The excitation level influences very little on impedance for thinner facesheets. However, the resistance decreases and reactance increases with higher excitation level for thick facesheets.

5.2 Acoustic Characteristics of Perforated Facesheets Mounted on 0.5"-Deep Honeycomb Structure (No Backplate):

The perforated sheets described in Table 12 are also mounted on 0.5"-deep honeycomb structure. These samples are tested for DC flow resistance to estimate the blockage introduced by honeycomb structures and by the adhesive used in the mounting process. The DC flow parameters for these samples are listed in Table 13. In general, the DC flow resistance is higher for these mounted samples compared to the bare perforated facesheets.

5.3 Acoustic Characteristics of SDOF Type Panels with Perforated Facesheets:

Perforated Plate SDOF Panels: The basic sandwich construction of this type of panels is shown in Figure 72 and described in section 4. Table 5 contains the design specifications for 10 perforated plate SDOF treatment panel configurations of 5"X12" size for flow duct test. These panels are tested in flow duct facilities to evaluate skin friction and insertion loss spectra at different grazing flow conditions. Samples of the same designs as listed in Table 5

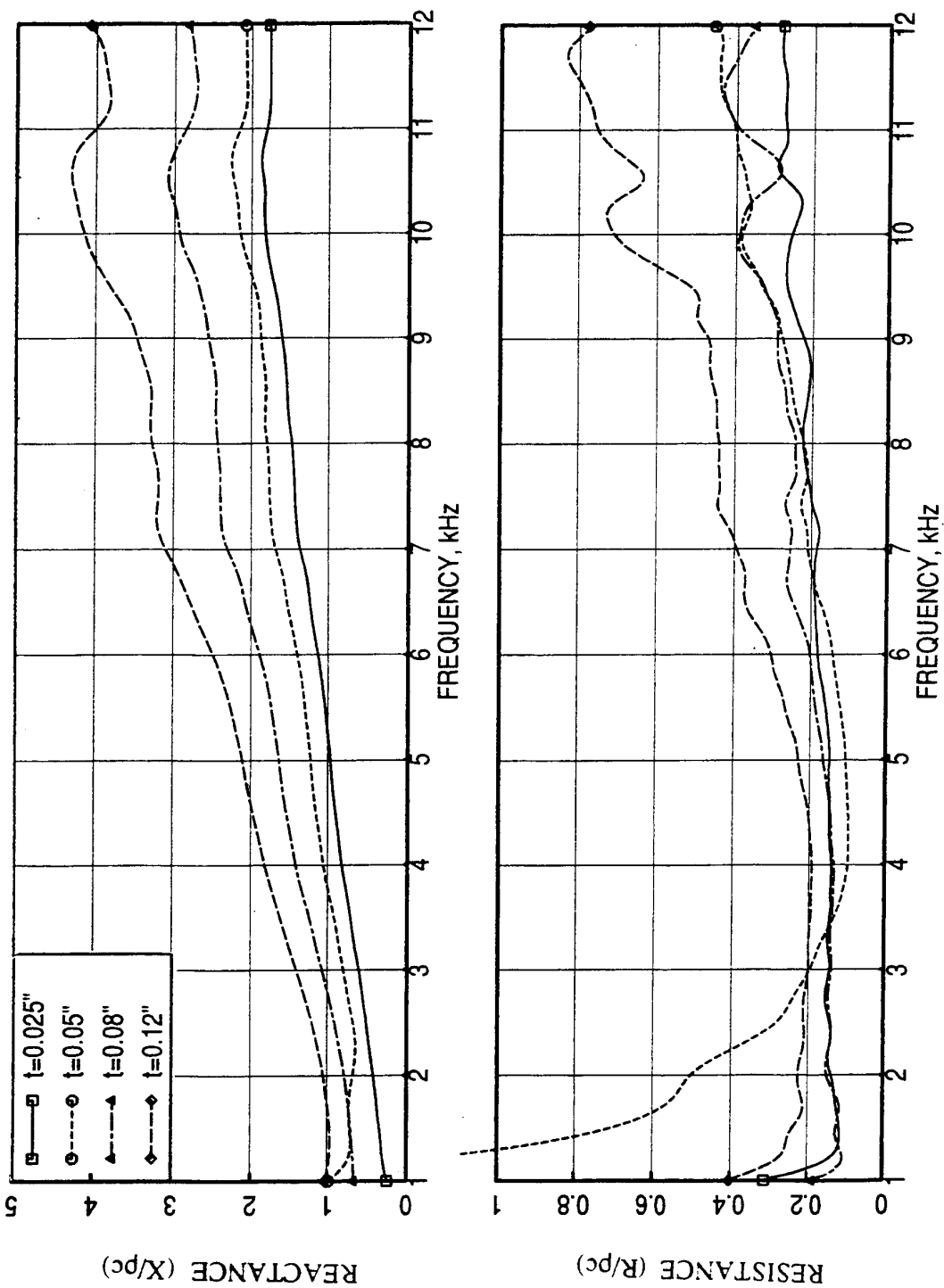


Figure 107. Effect of perforated sheet thickness (t) on normal impedance spectra (cavity contribution removed) with a 0.375" deep back cavity; $d=0.039''$, $\sigma=11\%$, nominal OASPL=150 dB.

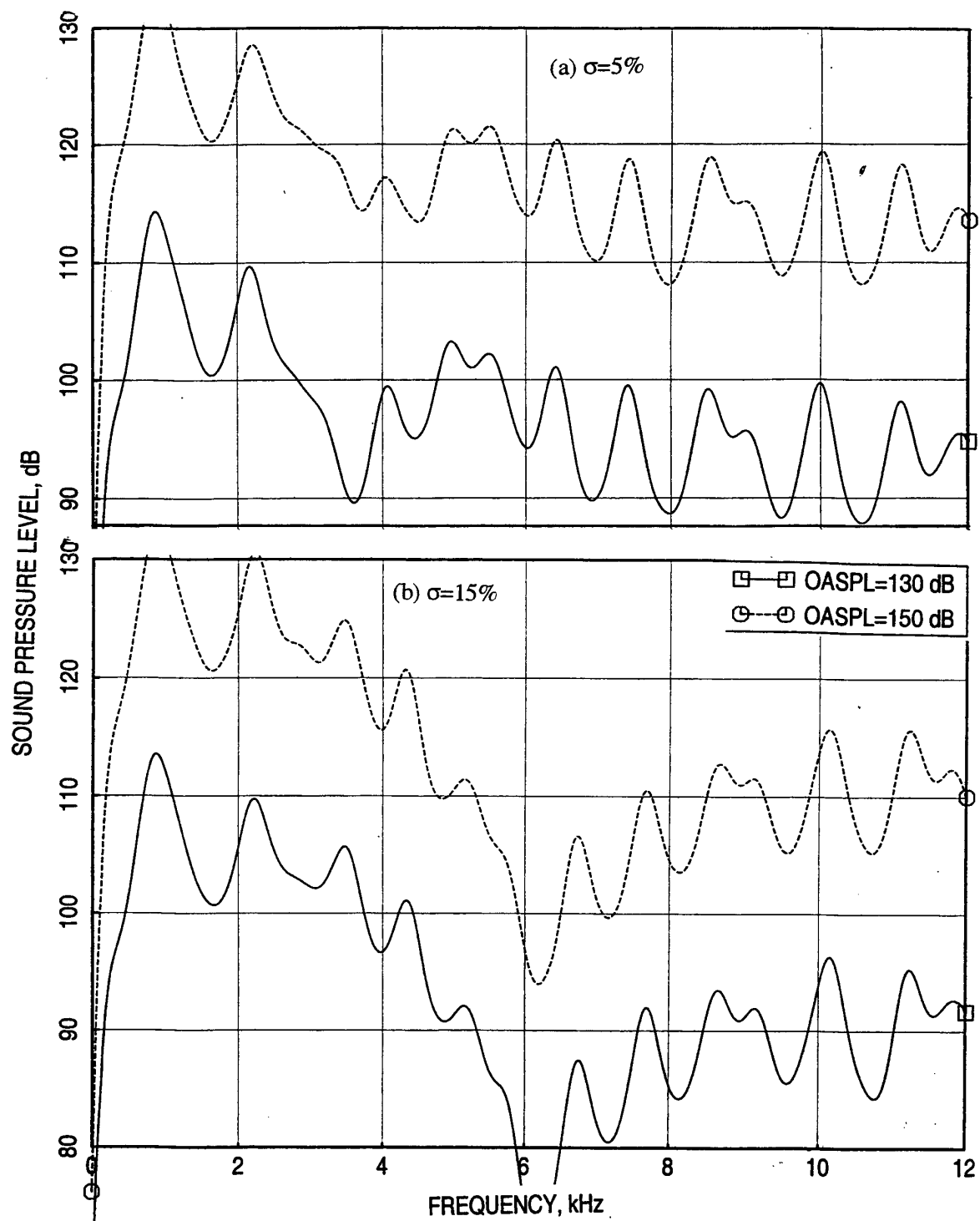


Figure 108. Sound pressure level spectra at two nominal OASPL for perforated sheets of different porosities (σ) with a back cavity of 0.375" deep; $d=0.039$ ", $t=0.025$ ".

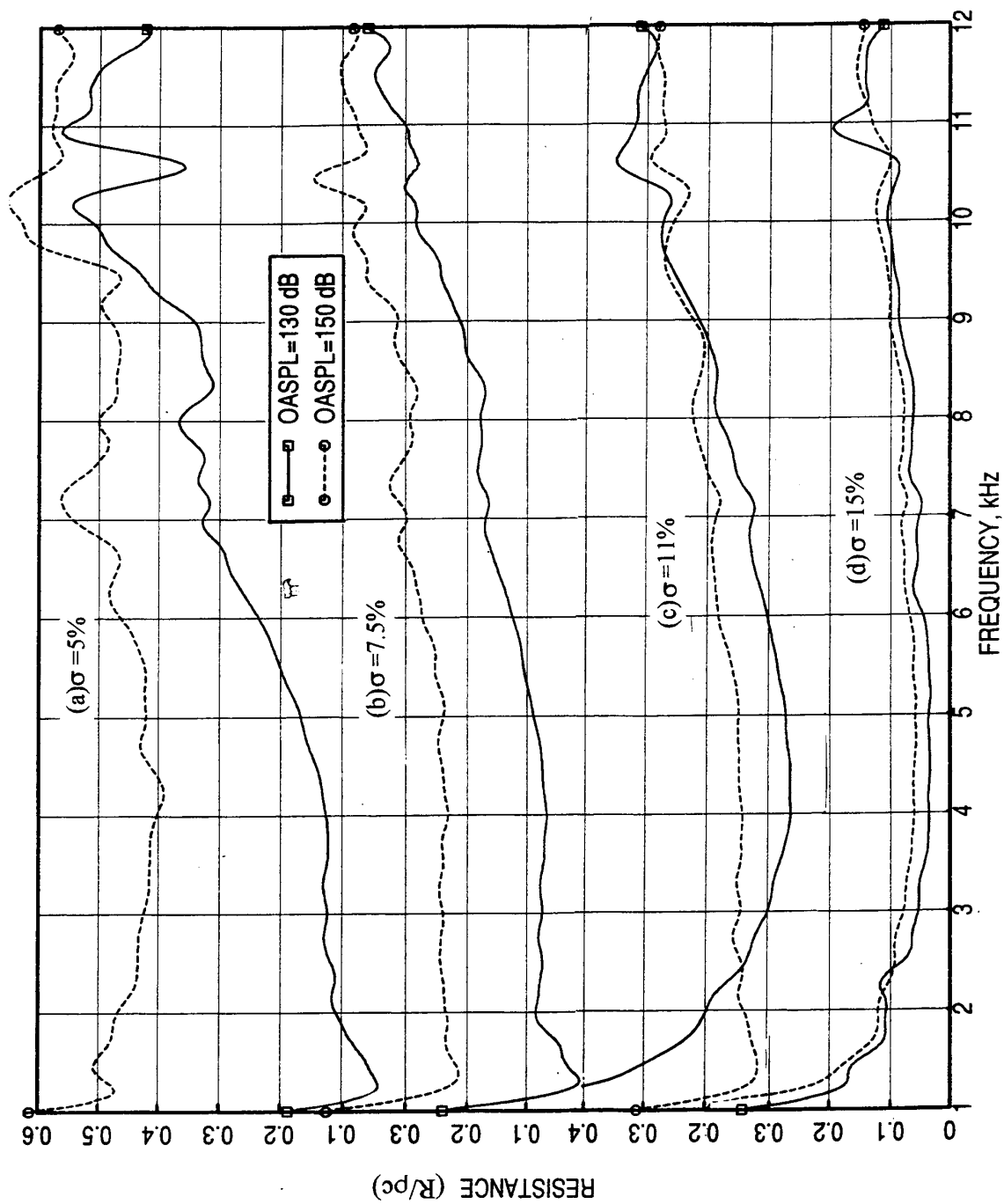


Figure 109. Effect of excitation level on normal acoustic resistance spectrum (cavity contribution removed) with a 0.375" deep back cavity for different perforated sheet porosities (σ); $t=0.025$ ", $d=0.039$ ".

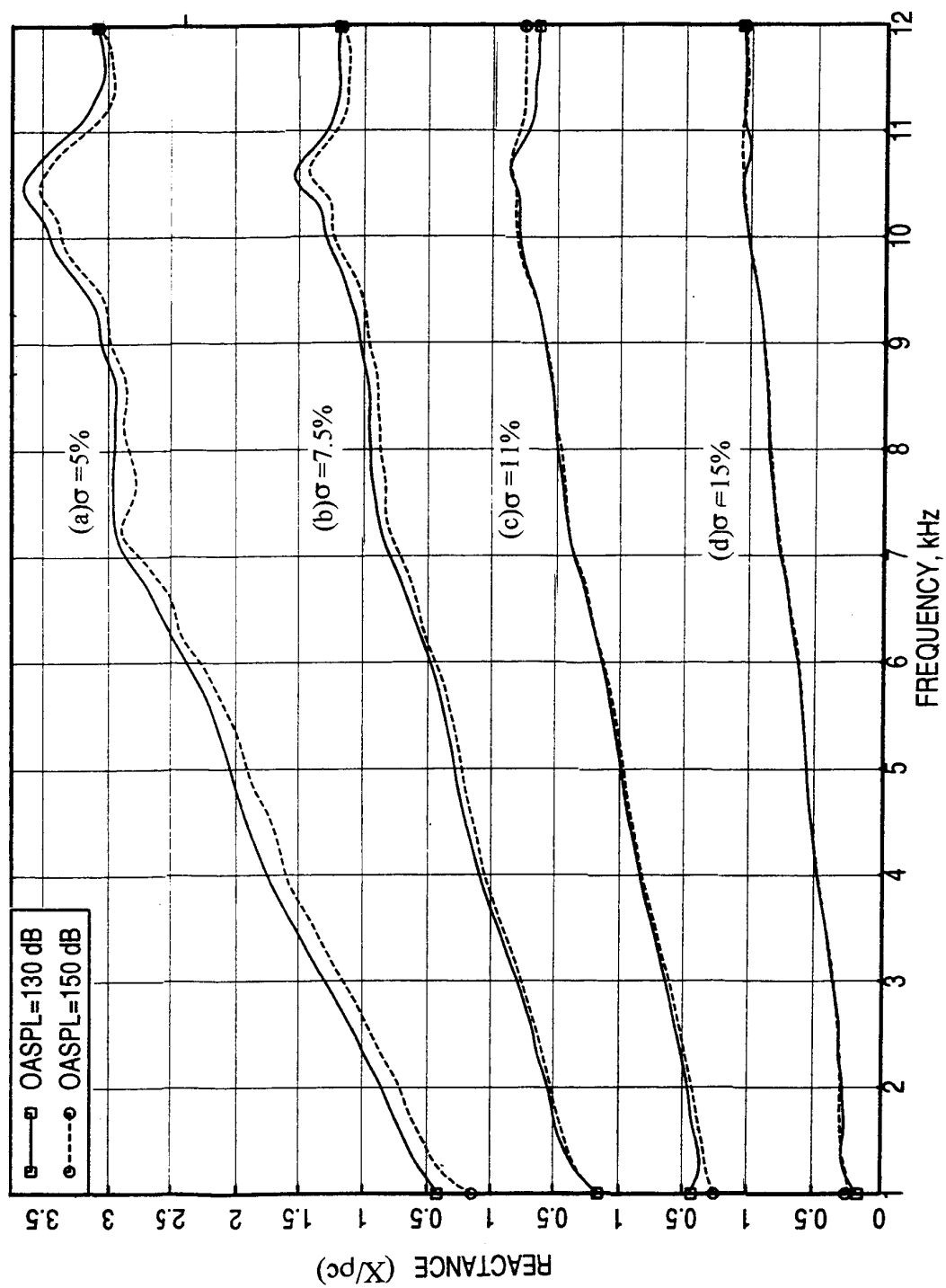


Figure 110. Effect of excitation level on normal acoustic reactance spectrum (cavity contribution removed) with a 0.375" deep back cavity for different perforated sheet porosities (σ); $t=0.025"$, $d=0.039"$.

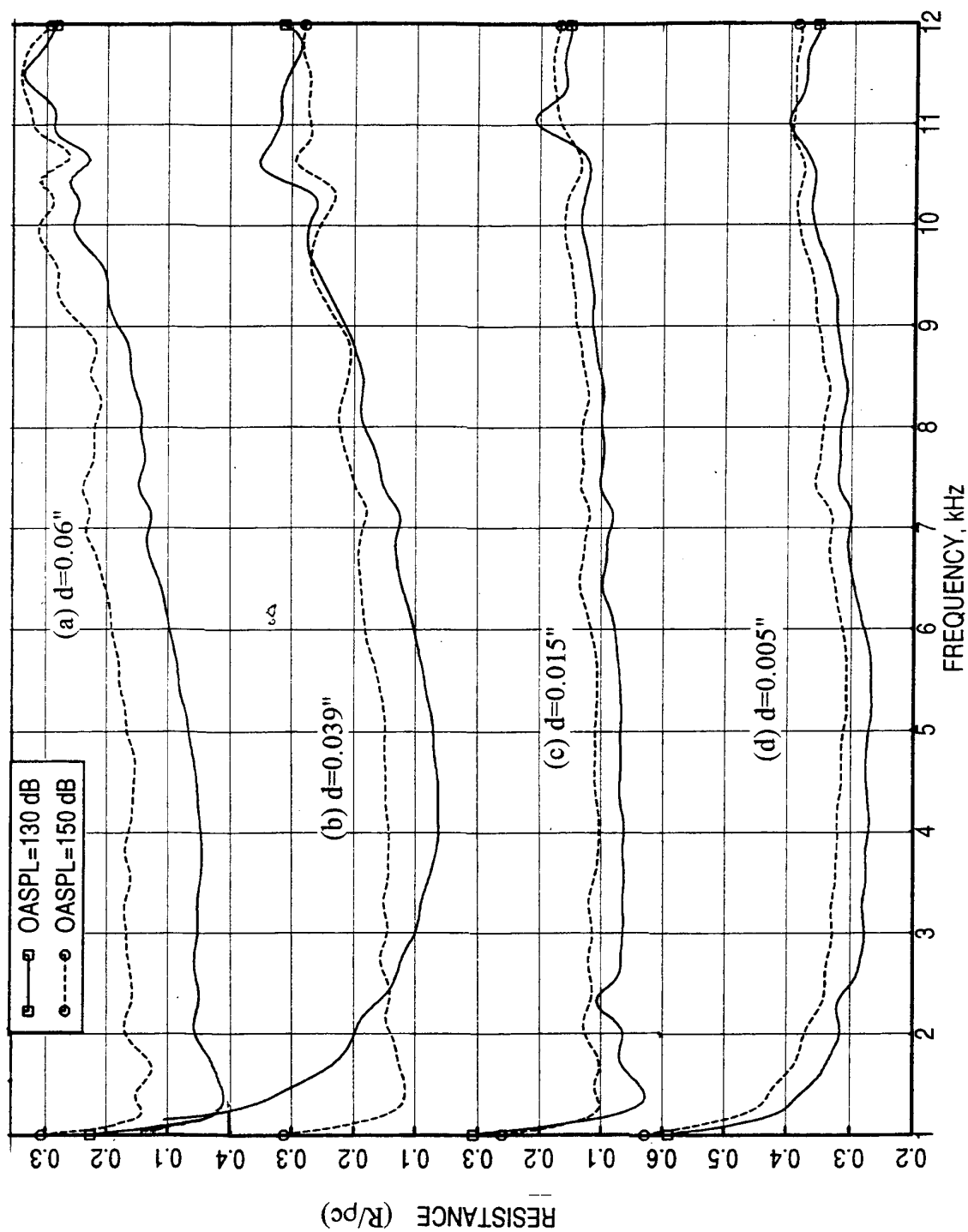


Figure 111. Effect of excitation level on normal acoustic resistance spectrum (cavity contribution removed) with a 0.375" deep back cavity for different perforated sheet hole diameter (d); $t=0.025''$, $\sigma=11\%$.

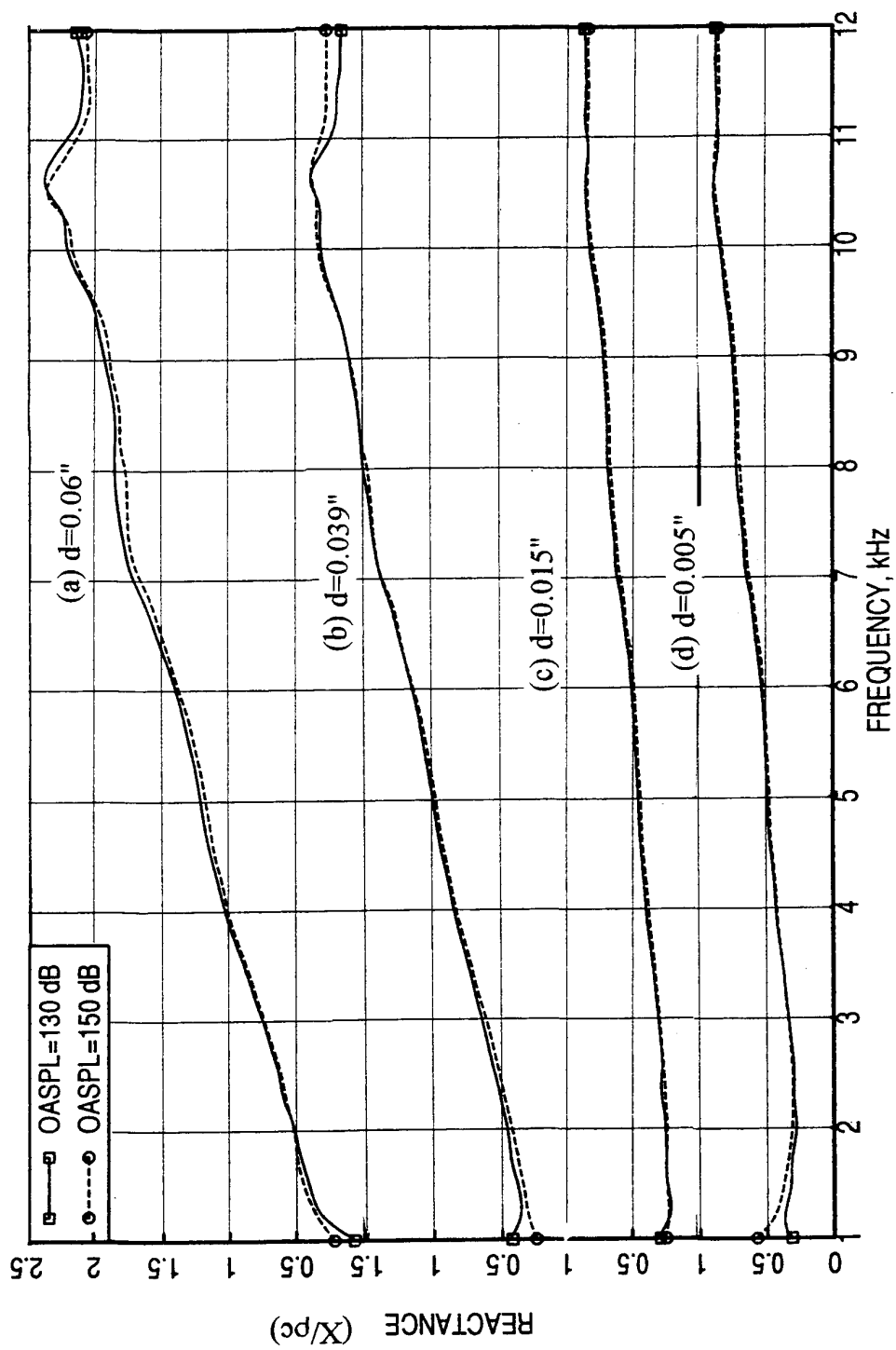


Figure 112. Effect of excitation level on normal acoustic reactance spectrum (cavity contribution removed) with a 0.375" deep back cavity for different perforated sheet hole diameter (d); $t=0.025''$, $\sigma=11\%$.

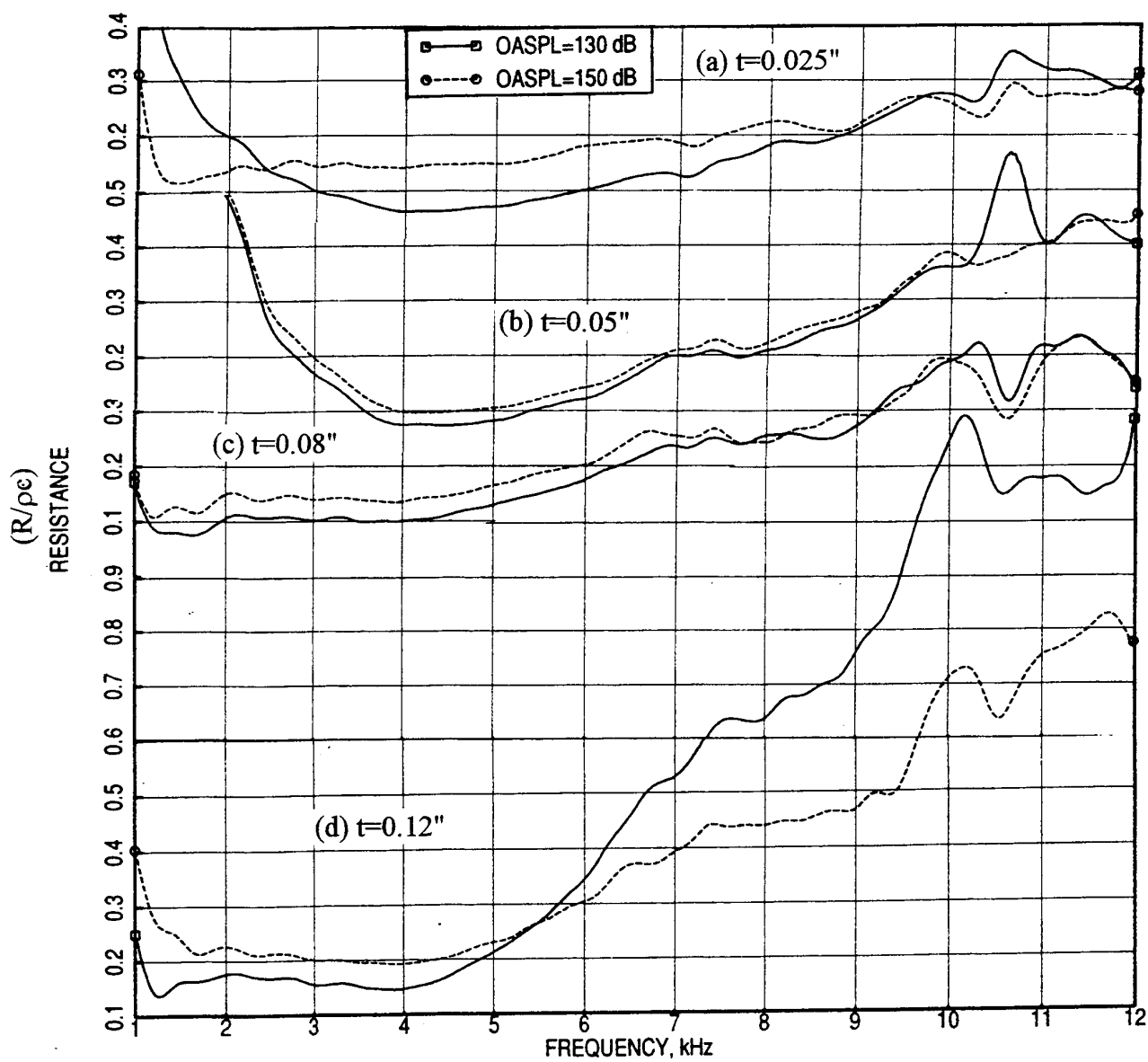


Figure 113. Effect of excitation level on normal acoustic resistance spectrum (cavity contribution removed) with a 0.375" deep back cavity for different perforated sheet thickness (t); $d=0.039''$, $\sigma=11\%$.

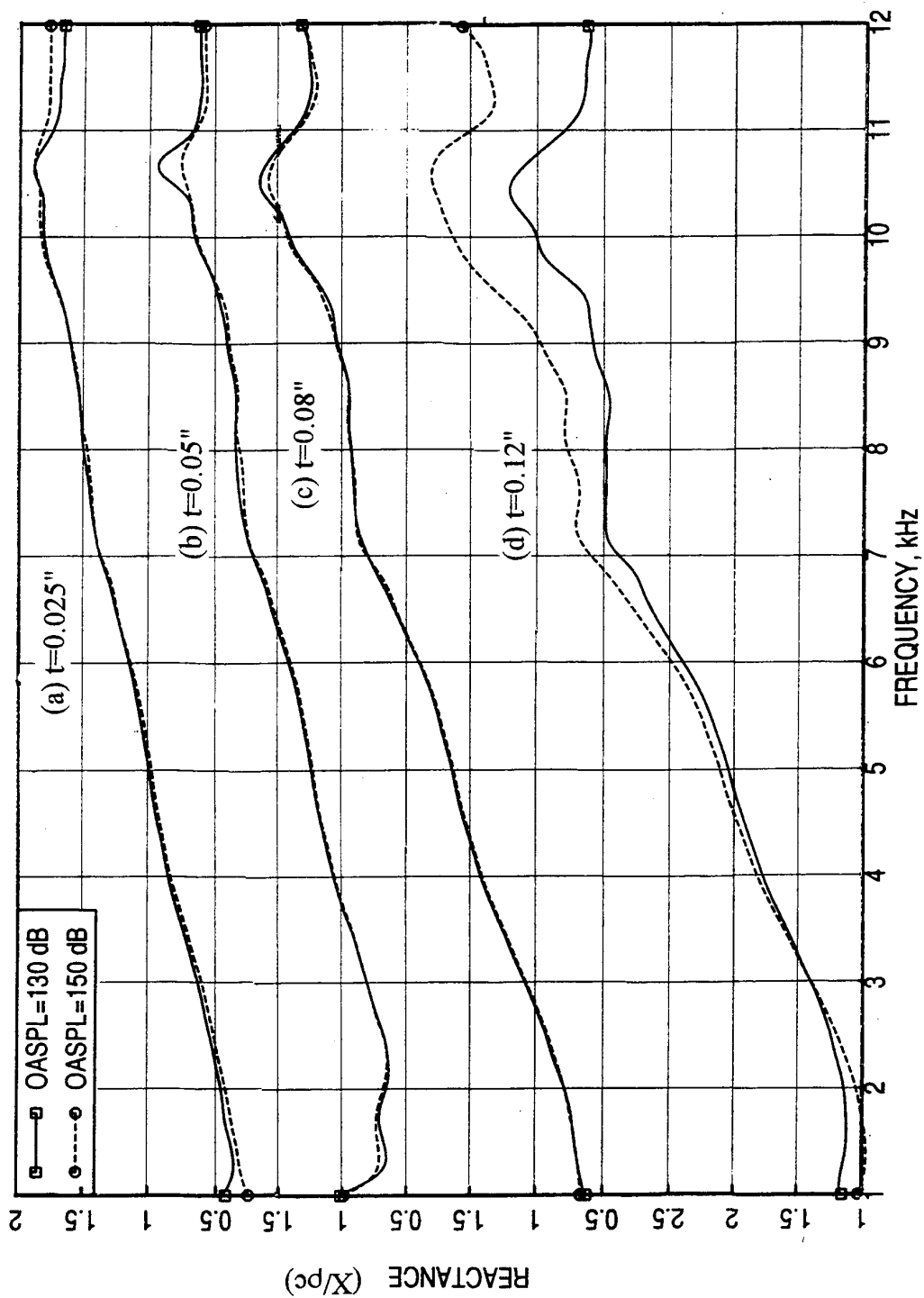


Figure 114. Effect of excitation level on normal acoustic reactance spectrum (cavity contribution removed) with a 0.375" deep back cavity for different perforated sheet thickness (t); $d=0.039"$, $\sigma=11\%$.

are also fabricated for DC flow resistance (without any backplate) and normal impedance tests. These samples are also listed in Table 14 along with their DC flow characteristics.

Table 13. Geometrical Properties and DC Flow Resistance Parameters for Perforated Facesheets Mounted on 0.5" deep 3/8" size Honeycomb Structure of 0.003" thick Wall

Sample #	Thickness, t in inches	Hole Dia, d in inches	Porosity, σ in %	A Rayls	B Rayls/cm	R100 Rayls	NLF (R150/R20)
1.22	0.025	0.039	5	0.5695	0.3978	40.35	7.07
1.23	0.025	0.039	7.5	1.25	0.15	16.55	5.62
1.24	0.025	0.02	7.5	1.93	0.21	22.82	5.44
1.25	0.025	0.01	7.5	4.966	0.1261	17.57	3.19
1.26	0.025	0.005	7.5	14.499	0.0935	23.85	1.74
1.27	0.025	0.039	11	0.9285	0.0512	6.05	4.41
1.28	0.025	0.015	11	2.025	0.0701	9.04	3.66
1.29	0.025	0.005	11	10.833	0.0433	15.16	1.48
1.30	0.025	0.04	15	-0.01	0.04	4.12	7.56
1.31	0.025	0.015	15	1.88	0.03	5.23	2.71
1.32	0.025	0.005	15				
1.33	0.05	0.04	11	1.62	0.0424	5.86	3.23
1.34	0.08	0.04	11	1.9095	0.0454	6.45	3.09
1.35	0.12	0.04	11	3.815	0.0482	8.63	2.31
1.36	0.025	0.06	11	-0.017	0.1126	11.24	7.55

5.3.1 Boundary Layer Results :

The boundary layer profiles for the panels are measured at a single axial location using a total pressure probe traversed by a computer controlled traversing system. Boundary layer parameters (i.e., local friction coefficient, displacement thickness, etc.) are evaluated utilizing the method described in section 4. Figure 115 shows the boundary layer profiles for three different panels at different grazing flow Mach numbers. The velocity profiles seem to be fully developed at this location and the boundary layer thicknesses are relatively higher.

The effect of facesheet thickness for slightly varying panel depth on boundary layer profiles and skin friction coefficients are shown in Figure 116. The velocity profiles indicate that the boundary layer becomes more turbulent with increasing facesheet thickness (t). The skin friction increases with increasing thickness. The effect of panel depth (D) on boundary layer profiles and skin friction coefficients are shown in Figure 117. The boundary layer becomes more turbulent with increasing panel depth. The skin friction is slightly higher for the thicker panel. Boundary layer parameters evaluated using boundary layer profiles are listed in Table 15.

Table 14. Geometrical Properties, DC Flow Resistance Parameters, and File Names for Normal Impedance and Insertion Loss Data for SDOF Type Panels with Perforated Facesheets

Panel Config #	Sample #	Thickness, t in inches	Hole Dia, d in inch	Porosity, σ in %	Panel Depth, D in inch	A Rayls	B Rayls/cm	R100 Rayls	NLF (R150/R20)	Normal Impedance File @ 150 dB OASPL	Normal Impedance File @ 157 dB OASPL	Insertion Loss 1/3-Octave Band Data Files	Insertion Loss Narrowband Data Files
1.1	1.12	0.02	0.039	9	0.7	0.80	0.11	11.45	5.73	wbsl12.smt	wbsl12h.smt	twbsl-1.dat	rwbsl-1.smt
1.2	1.13	0.02	0.039	9	0.3	0.89	0.11	11.55	5.58	wbsl13.smt	wbsl13h.smt	twbsl-2.dat	rwbsl-2.smt
1.2-3	1.13	0.02	0.039	9	0.3	0.89	0.11	11.55	5.58	wbsl13.smt	wbsl13h.smt	twbsl-23.dat	rwbsl-23.smt
1.4	1.14	0.025	0.039	9	0.25	1.05	0.10	11.09	5.27	wbsl14.smt	wbsl14h.smt	twbsl-4.dat	rwbsl-4.smt
1.5	1.15	0.025	0.039	6	0.19	1.60	0.21	22.25	5.69	wbsl15.smt	wbsl15h.smt	twbsl-5.dat	rwbsl-5.smt
1.6	1.16	0.025	0.039	18	0.32	0.17	0.02	2.65	5.82	wbsl16.smt	wbsl16h.smt	twbsl-6.dat	rwbsl-6.smt
1.7	1.17	0.025	0.039	9	0.42	1.09	0.10	10.80	5.17	wbsl17.smt	wbsl17h.smt	twbsl-7.dat	rwbsl-7.smt
1.8	1.18	0.025	0.039	9	0.16	0.96	0.10	10.75	5.37	wbsl18.smt	wbsl18h.smt	twbsl-8.dat	rwbsl-8.smt
1.9	1.19	0.08	0.039	9	0.38	2.715	0.0494	7.66	2.73	wbsl19.smt	wbsl19h.smt	twbsl-9.dat	rwbsl-9.smt
1.10	1.20	0.08	0.078	13	0.45	2.07	0.05	7.20	3.15	wbsl20.smt	wbsl20h.smt	twbsl-10.dat	rwbsl-10.smt
1.11	1.21	0.08	0.125	15	0.48	0.436	0.0311	3.54	4.82	wbsl21.smt	wbsl21h.smt	twbsl-11.dat	rwbsl-11.smt

- Note: 1. Panel Config #: Panels of 12"x5" Treated area tested for Insertion Loss Measurement in a Flow Duct of 4" height with one side treated (i.e., the duct height becomes 8"), except for config 1-2-3 for which two identical panels (1.2 & 1.3) were mounted on both sides of flow duct (i.e., flow duct height 4")
2. Sample # - Samples for DC Flow Resistance & Normal Impedance Tests, identical to the corresponding panel geometry (for DC flow resistance backplates not used)
3. The files containing acoustic excitation SPL spectra for flow duct tests, measured in the upstream chamber, are listed below:

Grazing Flow Mach Number	1/3-Octave Band SPL Data Files	Narrowband SPL Data Files	OASPL, dB
0.0	trd_00.spl	r_00.spl	147.0
0.30	trd_30.spl	r_30.spl	147.2
0.55	trd_55.spl	r_55.spl	147.6
0.60	trd_60.spl	r_60.spl	147.8
0.70	trd_70.spl	r_70.spl	148.1

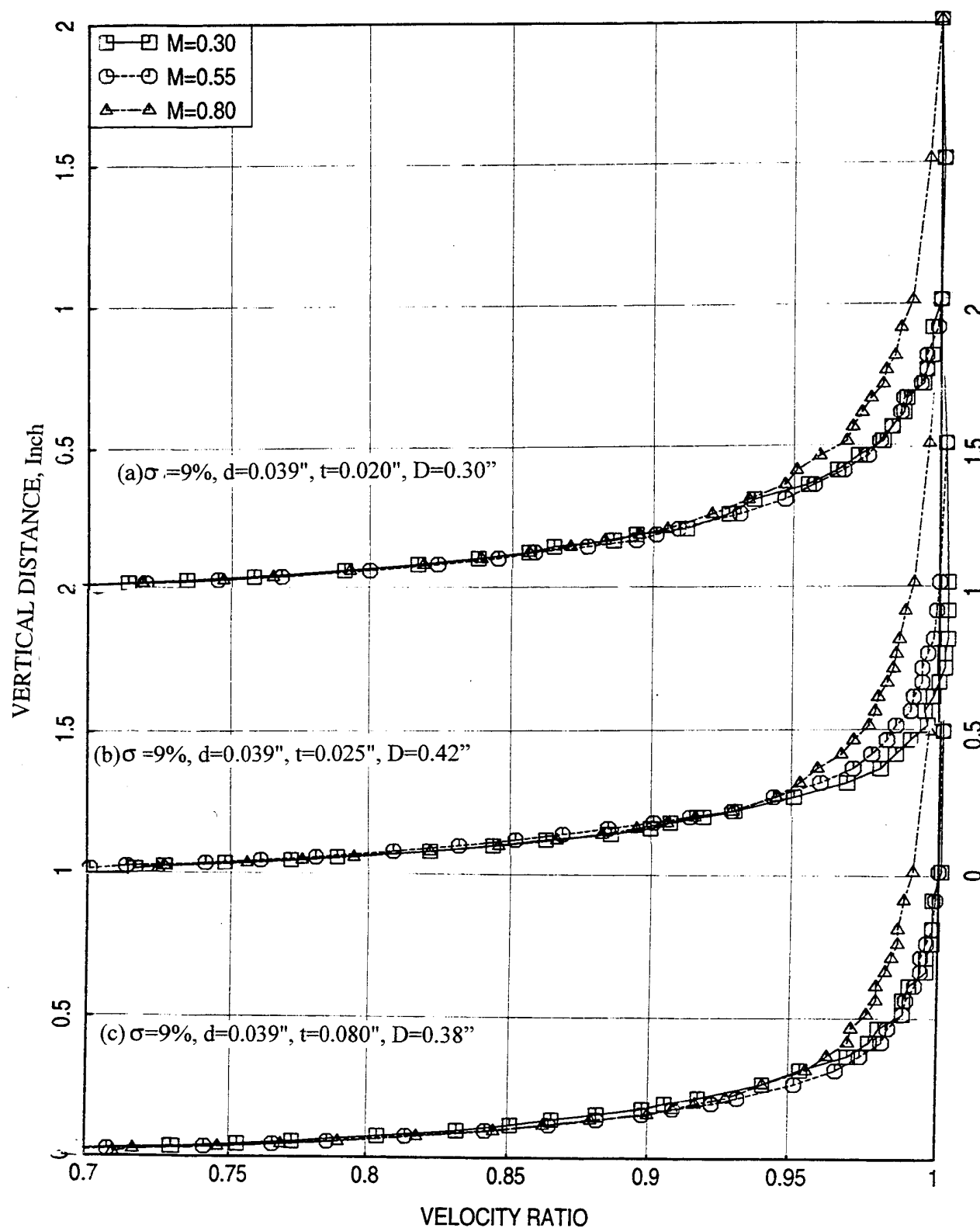


Figure 115. Effect of grazing flow Mach number (M) on velocity profile in the flow duct for SDOF type panels with perforated facesheets.

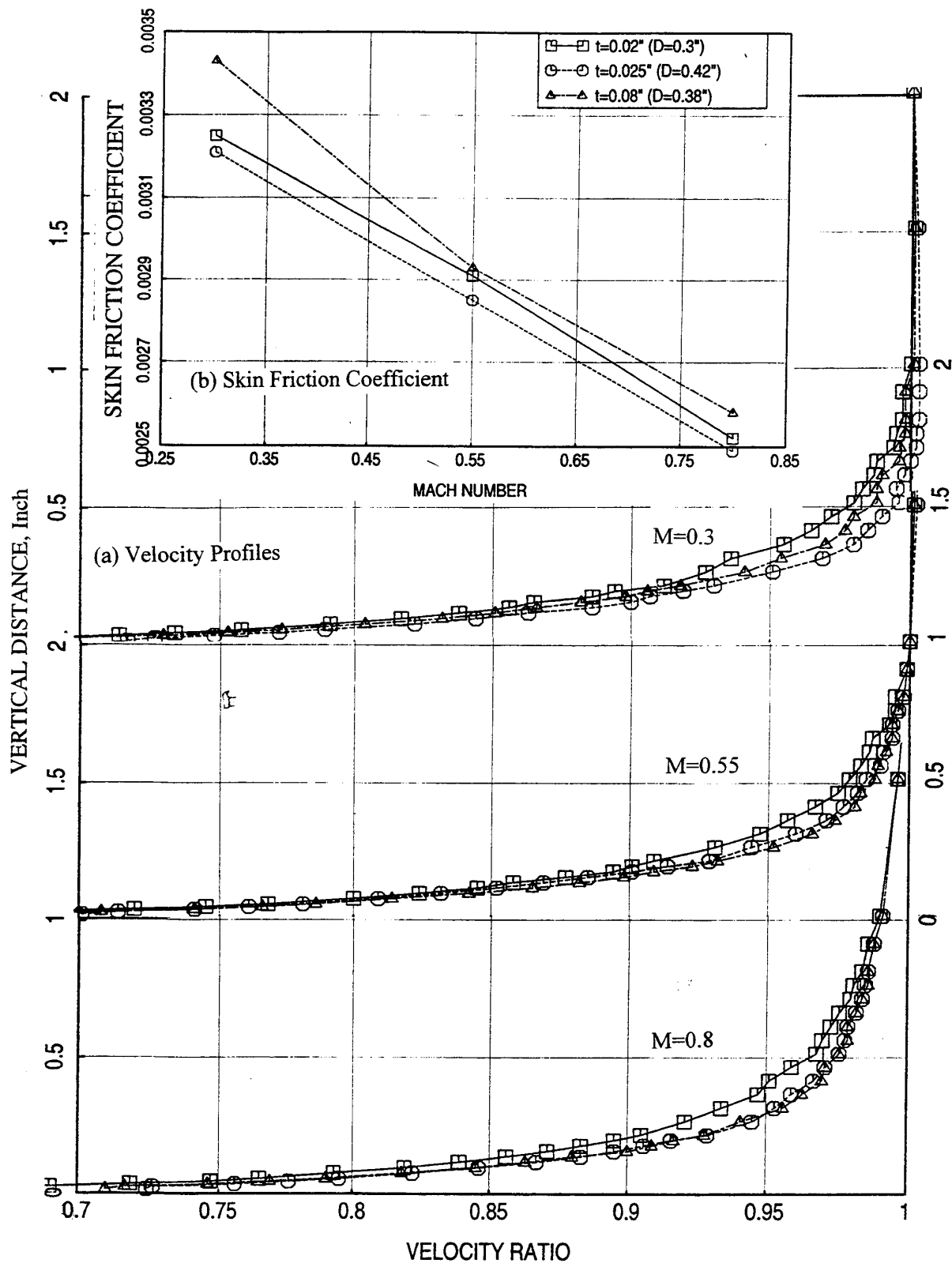


Figure 116. Effect of facesheet thickness t on (a) velocity profile in the flow duct and (b) local skin friction coefficient for SDOF type panels with perforated facesheets; $\sigma=9\%$, $d=0.039''$.

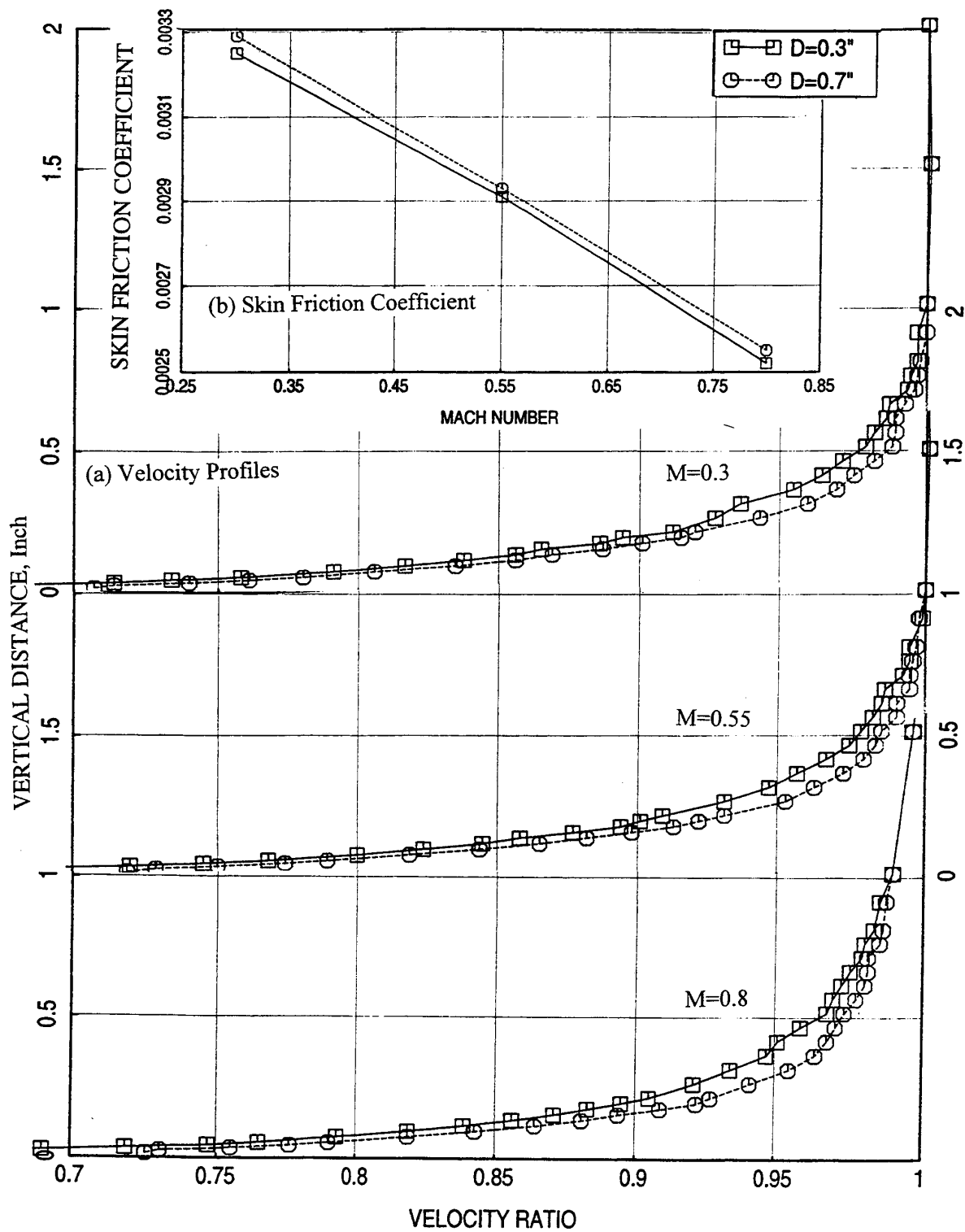


Figure 117. Effect of panel depth D on (a) velocity profile in the flow duct and (b) local skin friction coefficient for SDOF type panels with perforated facesheets; $\sigma=9\%$, $d=0.039$ ", $t=0.020$ ".

Table 15. Boundary Layer Parameters and Local Friction Coefficient for Various SDOF type Panels (Continued).

Panel Config #	Description	Measured Mach Number	Friction Coefficient C_f	Mach Number M	Boundary Layer Thickness δ , in	Displacement Thickness δ^* , in	Momentum Thickness θ , in	Pressure Recovery Factor P_T/P_{TE}
Hard Wall		0.30	0.00325	0.305	0.9	0.06064	0.04344	0.99264
		0.55	0.00291	0.55453	1.25	0.06111	0.03874	0.98411
		0.80	0.00252	0.7603	1.9	0.07621	0.04205	0.97827
1.1	see Table 14	0.30	0.00329	0.29902	0.9	0.05862	0.04187	0.99317
		0.55	0.00293	0.54904	1.25	0.05932	0.03738	0.98489
		0.80	0.00255	0.7603	1.9	0.07335	0.03988	0.97921
1.2	see Table 14	0.30	0.00325	0.30429	0.9	0.06474	0.04666	0.99216
		0.55	0.00291	0.558	1.25	0.06742	0.04362	0.98212
		0.80	0.00252	0.7603	1.94141	0.09505	0.05565	0.97282
1.6	see Table 14	0.30	0.00321	0.304	0.9	0.06715	0.04855	0.99188
		0.55	0.00285	0.558	1.25	0.07401	0.04874	0.98023
		0.80	0.00249	0.7603	2.0	0.09855	0.05782	0.97262
1.7	see Table 14	0.30	0.00343	0.29914	1.0	0.05411	0.03748	0.99439
		0.55	0.00291	0.558	1.25	0.06701	0.04331	0.98223
		0.80	0.00258	0.7603	1.9	0.07359	0.04003	0.97914
1.9	see Table 14	0.30	0.00333	0.306	0.9	0.06038	0.04318	0.99263
		0.55	0.00299	0.55678	1.25	0.05914	0.03709	0.98457
		0.80	0.00261	0.7603	1.9	0.07299	0.03955	0.97935
5.2	see Table 16	0.30	0.00319	0.306	0.99798	0.07134	0.05141	0.99213
		0.55	0.00272	0.558	1.2	0.08778	0.5937	0.97533
		0.80	0.00246	0.7603	1.9	0.09543	0.05628	0.97203

Table 15. Boundary Layer Parameters and Local Friction Coefficient for Various SDOF type Panels (Continued).

Panel Config #	Description	Measured Mach Number	Friction Coefficient C_f	Mach Number M	Boundary Layer Thickness δ , in	Displacement Thickness δ^* , in	Momentum Thickness θ , in	Pressure Recovery Factor P_T/P_{TE}
5.3	see Table 16	0.30	0.00313	0.306	0.96869	0.07065	0.05103	0.99196
		0.55	0.00281	0.55576	1.25	0.07297	0.04802	0.98065
		0.80	0.00252	0.7603	1.9	0.07621	0.04205	0.97827
5.8	see Table 16	0.30	0.00309	0.30586	0.9	0.07519	0.05469	0.99077
		0.55	0.00279	0.558	1.25	0.0052	0.5372	0.97838
		0.80	0.00252	0.7603	1.9	0.09105	0.05303	0.97345
2.1	see Table 17	0.30	0.00327	0.306	0.9	0.06487	0.04673	0.99206
		0.55	0.00293	0.558	1.25	0.066664	0.043	0.98234
		0.80	0.00255	0.78333	1.9	0.07753	0.04253	0.97678
2.2	see Table 17	0.30	0.00323	0.306	0.9	0.06425	0.04627	0.99214
		0.55	0.00291	0.558	1.25	0.06561	0.04222	0.98263
		0.80	0.00255	0.76515	1.9	0.0805	0.04511	0.97664
3.1	see Table 19	0.30	0.00303	0.306	0.9	0.07898	0.05752	0.9903
		0.55	0.00272	0.558	1.2	0.08661	0.05852	0.97566
		0.80	0.00246	0.79	2.0	0.09524	0.05466	0.97198
3.2	see Table 19	0.30	0.00309	0.306	0.9	0.0741	0.005388	0.9909
		0.55	0.00277	0.558	1.25	0.08217	0.05497	0.97791
		0.80	0.00249	0.79	1.98889	0.088	0.04945	0.9742
3.3	see Table 19	0.30	0.00309	0.306	0.9	0.0759	0.05521	0.99068
		0.55	0.00274	0.558	1.2	0.08548	0.05767	0.97599
		0.80	0.00249	0.79	2.0	0.09546	0.05478	0.97192
3.4	see Table 19	0.30	0.00303	0.306	0.9	0.07897	0.05751	0.9903
		0.55	0.00268	0.558	1.2	0.091	0.06174	0.97439
		0.80						

Table 15. Boundary Layer Parameters and Local Friction Coefficient for Various SDOF type Panels (Concluded).

Panel Config #	Description	Measured Mach Number	Friction Coefficient C_f	Mach Number M	Boundary Layer Thickness δ , in	Displacement Thickness δ^* , in	Momentum Thickness θ , in	Pressure Recovery Factor P_T/P_{TE}
4.1	see Table 21	0.30	0.00331	0.305	0.90	0.06016	0.04302	0.99271
		0.55	0.00295	0.5578	1.25	0.06185	0.03925	0.98373
		0.80	0.00258	0.7603	1.90	0.077	0.04258	0.097803
6.1	see Table 21	0.30	0.00313	0.30	0.90	0.07447	0.05419	0.9912
		0.55	0.00281	0.551	1.25	0.08115	0.05431	0.97869
		0.80	0.00249	0.787	2.0	0.09921	0.05757	0.97088
6.2	see Table 21	0.30	0.00311	0.306	0.90	0.07504	0.05456	0.99079
		0.55	0.00281	0.558	1.25	0.08001	0.05331	0.97853
		0.80	0.00249	0.79	2.0	0.09636	0.05544	0.97163

5.3.2 Insertion Loss Results :

Effect of Grazing Flow:

The insertion loss measurements were made in a flow duct with two reverberant chambers, one upstream and the other downstream of the duct. The acoustic excitation is generated in the upstream chamber. The SPL spectra as measured in the upstream chamber for different flow conditions are shown in Figure 118. The excitation level in the upstream chamber is not effected significantly with flow. While, the excitation level in this chamber is known, the actual level in the test section interacting with the treatment panel is not known.

Figure 119 shows the insertion loss spectra at different grazing flow Mach numbers for a typical SDOF panel. Insertion loss increases with flow. However, with further increase of grazing flow, the insertion loss decreases. The data show two insertion loss peaks. For panels with lower depth the second peak may not be observed, since its occurrence moves to a higher frequency above the current measurement range. While, the insertion loss data is available both in 1/3-octave band and in narrowband forms, the subsequent presentations are made only for narrowband data. Figure 120 shows the effect of grazing flow Mach number on insertion loss levels for one-sided and two-sided treated configurations.

Effect of Porosity (σ) & Panel Depth (D): Panels of different depths are designed for the optimum impedance limits by varying the facesheet porosity. Figure 121 shows the normal impedance spectra for these configurations. Figure 122 shows the influence of excitation level on normal impedance. The corresponding insertion loss spectra at various grazing flow conditions are shown in Figures 123 and 124. While the insertion loss levels for the panels with porosity 6% and 9% are very close to each other, the insertion loss levels for 18% porous panel is relatively lower, especially, in the presence of flow.

Effect of Porosity (σ), Hole Diameter (d), & Panel Depth (D): Again, panels of different depths are designed for the optimum impedance limits by varying the facesheet porosity and hole diameter for a thicker facesheet (i.e., $t=0.08''$). Figure 125 shows the normal impedance spectra for these configurations. Figure 126 shows the influence of excitation level on normal impedance. The corresponding insertion loss spectra at various grazing flow conditions are shown Figures 127 and 128. Insertion loss levels for these panels are reasonably close to each other. For $M=0.3$ the panel with 15% porosity shows a large insertion loss drop in the mid frequency range (3 to 8 kHz). It is suspected that the mid-frequency range excitation might be inoperative during this test.

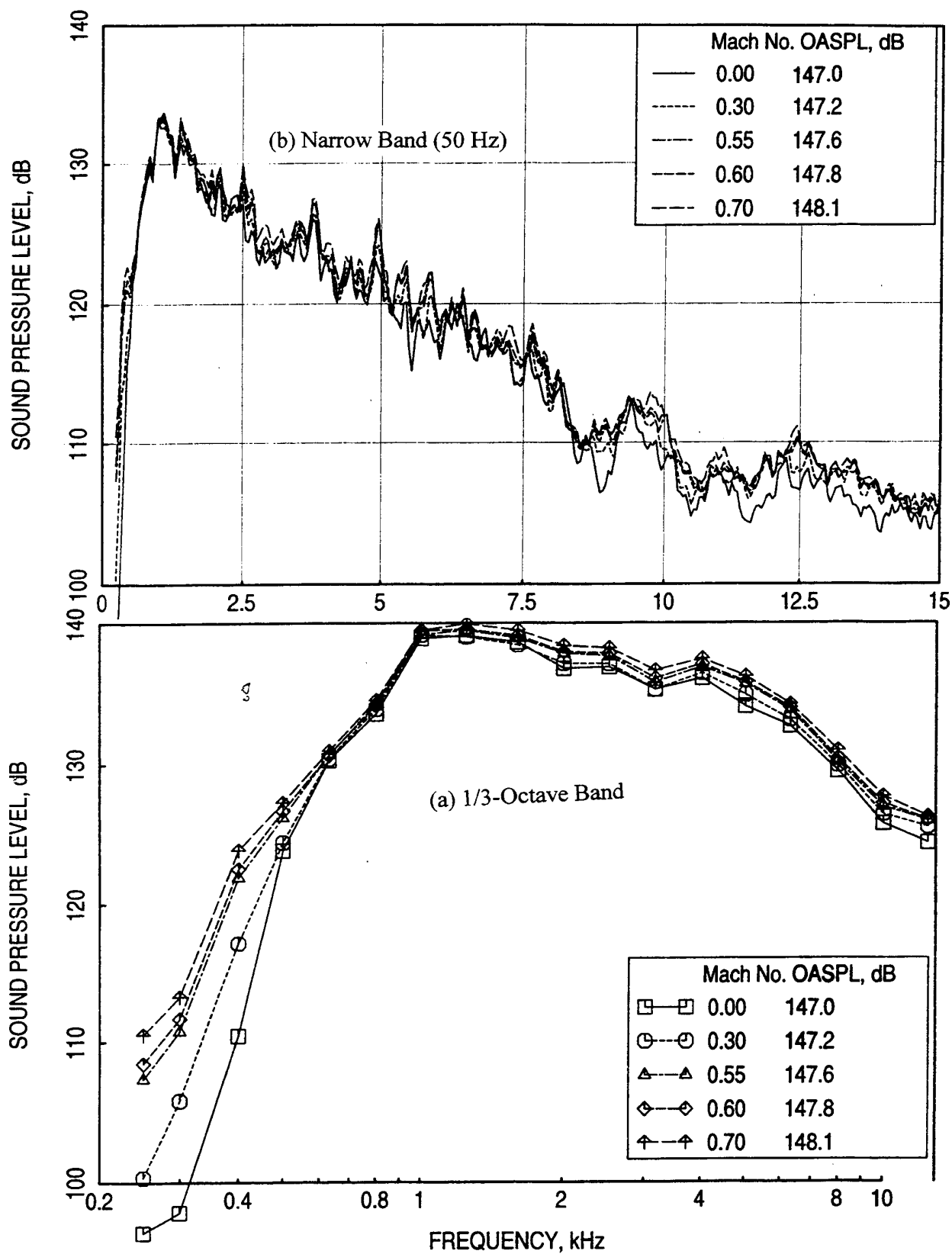


Figure 118. Acoustic excitation levels at different flow conditions in the flow duct measured in the upstream chamber.

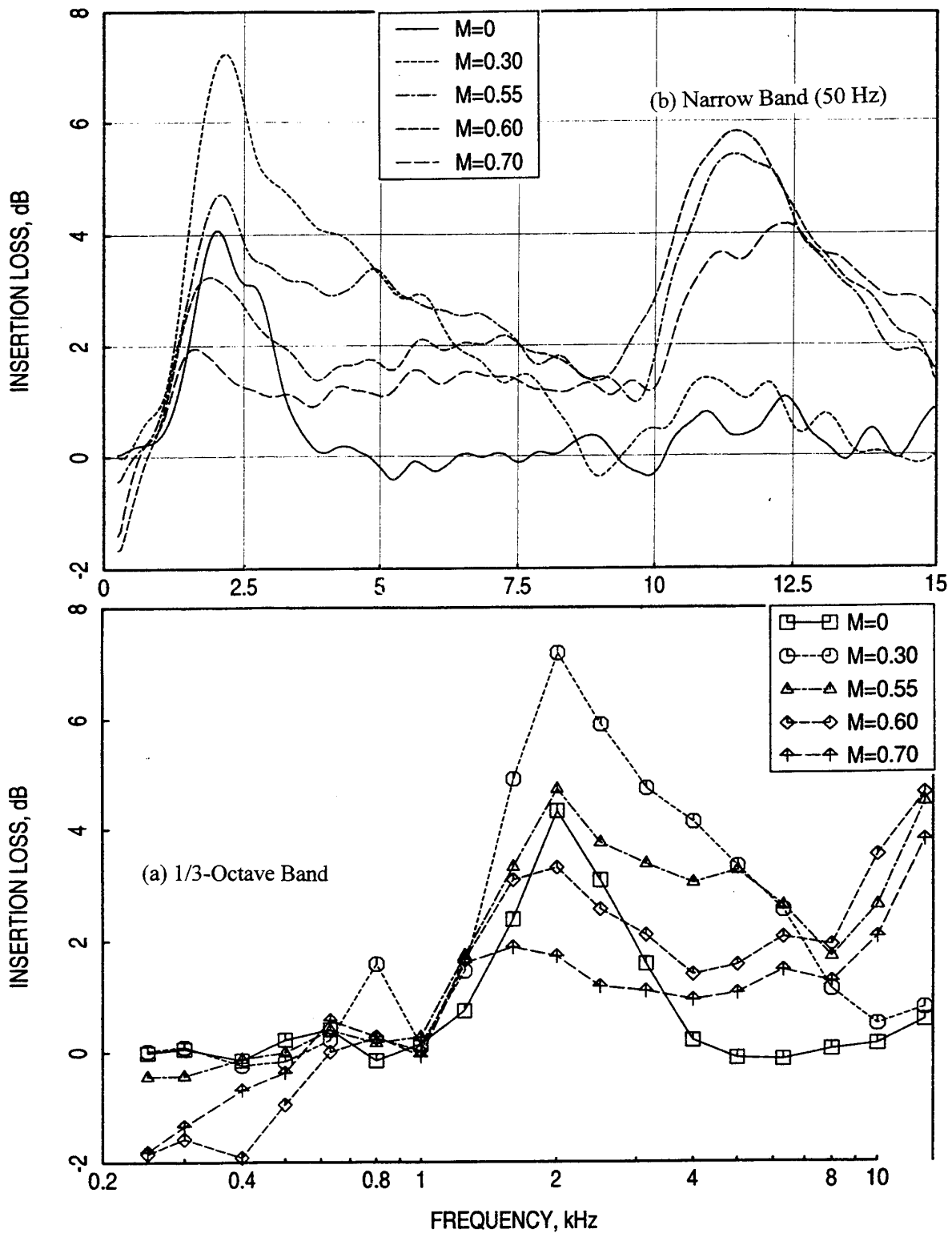


Figure 119. Influence of grazing flow Mach number on insertion loss spectra measured in a 4"- high (H) flow duct for a typical SDOF type panel mounted on one side, $t=0.02''$, $d=0.039''$, $\sigma=9\%$, $D=0.7''$.

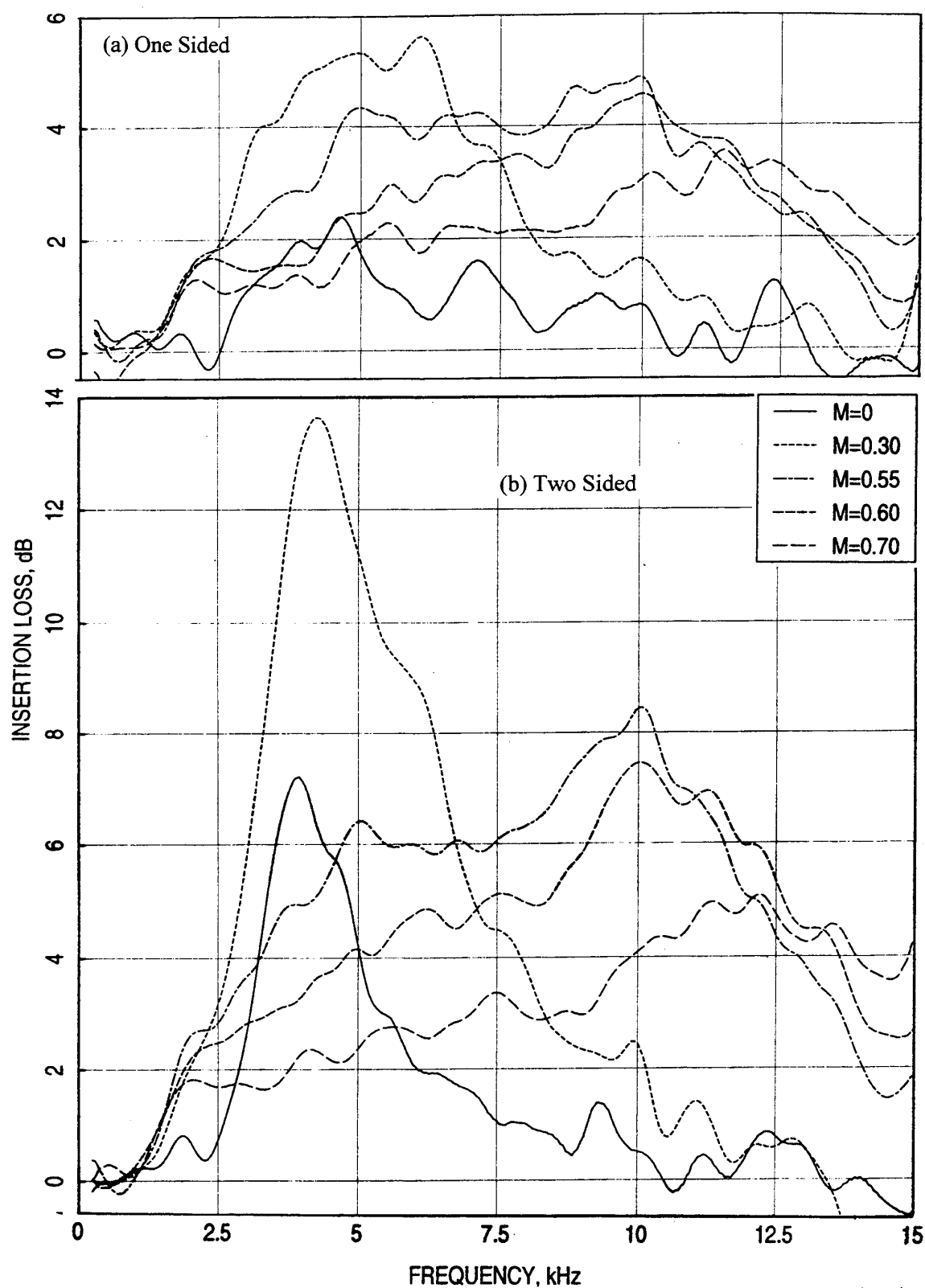


Figure 120. Influence of grazing flow Mach number on insertion loss spectra for one side versus two side mounted 4"-high (H) flow duct for SDOF type panel, $t=0.02''$, $d=0.039''$, $\sigma=9\%$, $D=0.3''$.

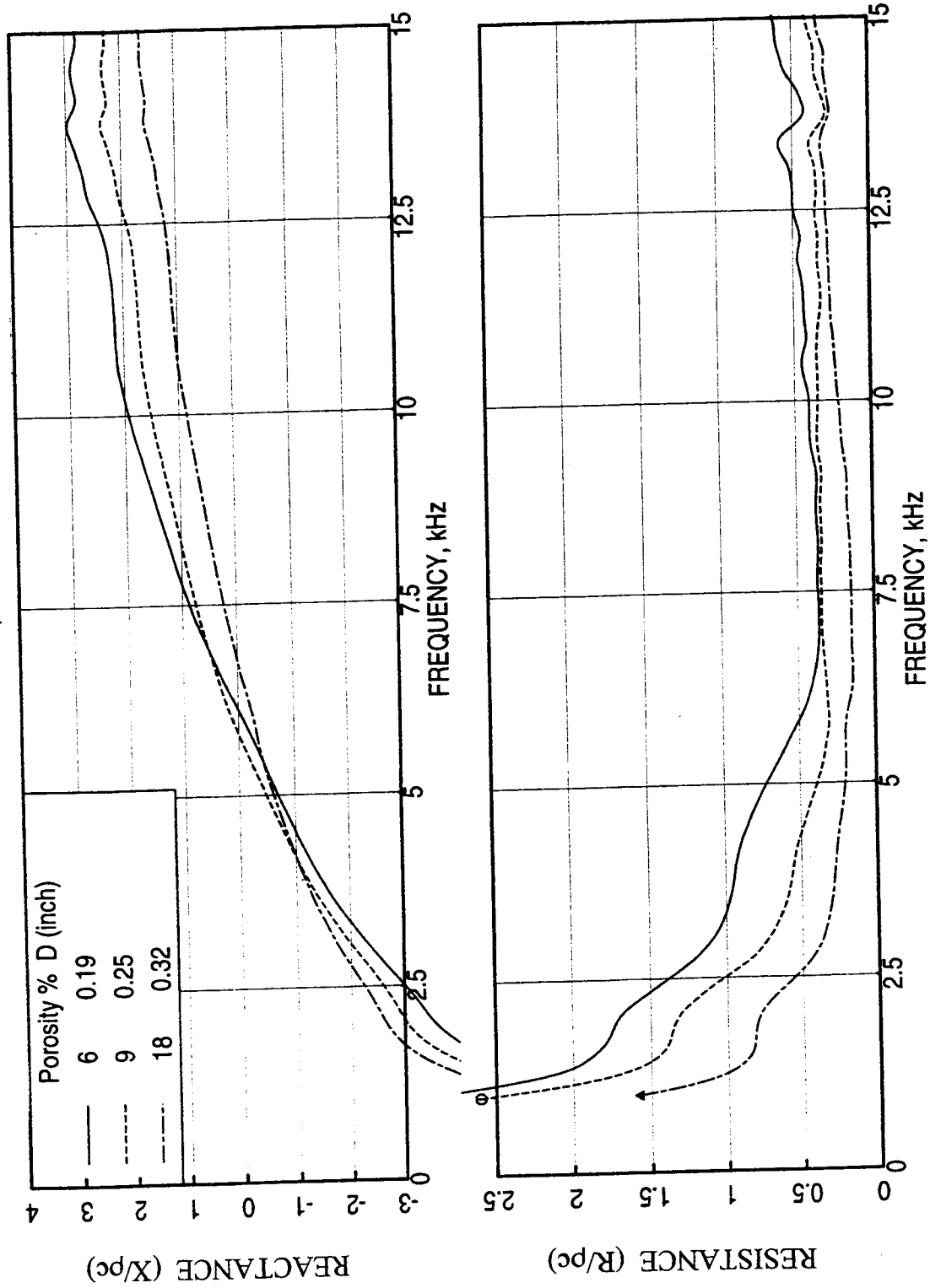


Figure 121. Effect of perforated sheet porosity (S) and panel depth (D) on normal impedance spectra for SDOF type panels; $t=0.025"$, $d=0.039"$, nominal OASPL=150 dB.

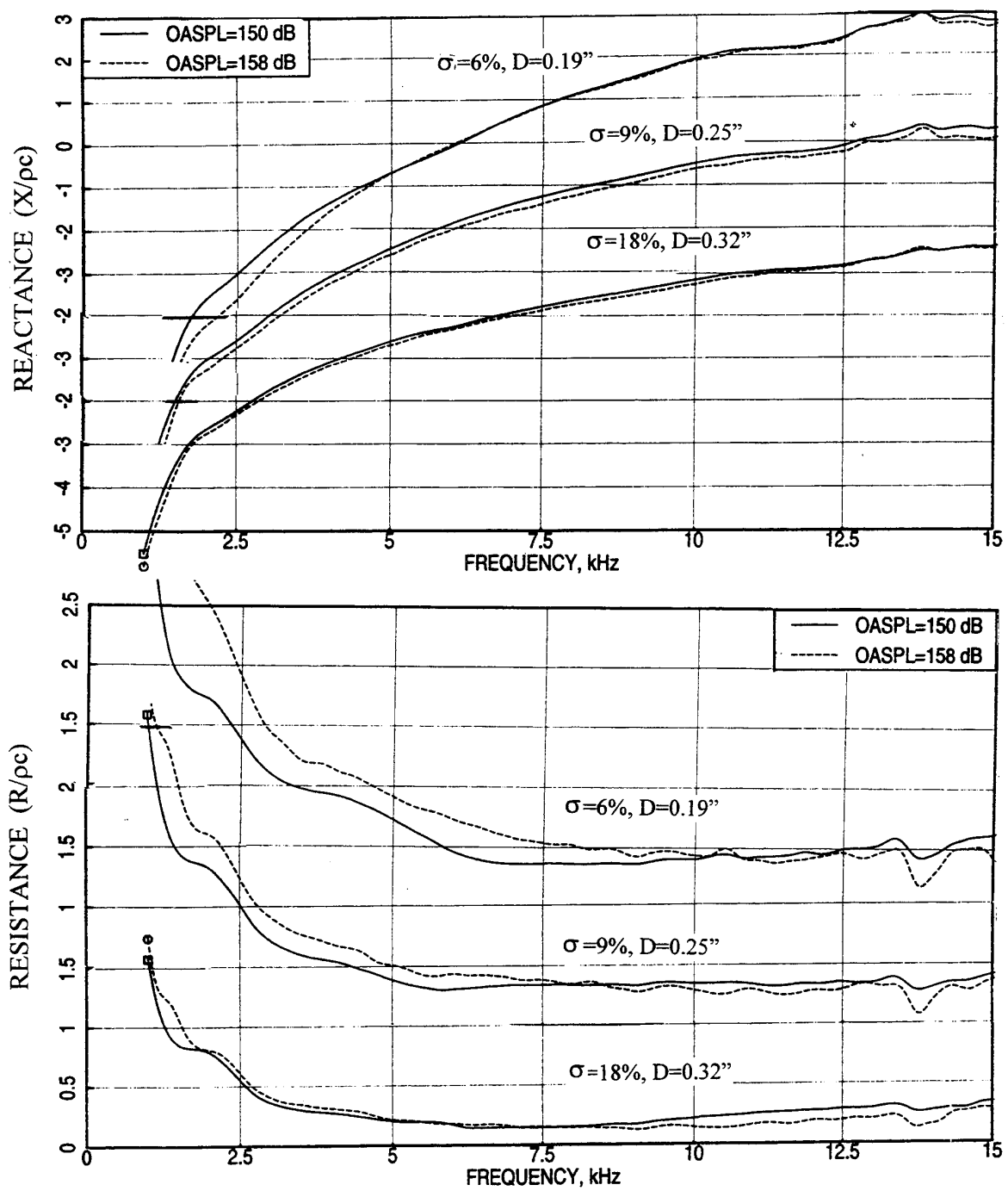


Figure 122. Effect of excitation level on normal impedance spectra for SDOF type panels; with respect to perforated sheet porosity (σ) and panel depth (D), $t=0.025''$, $d=0.039''$.

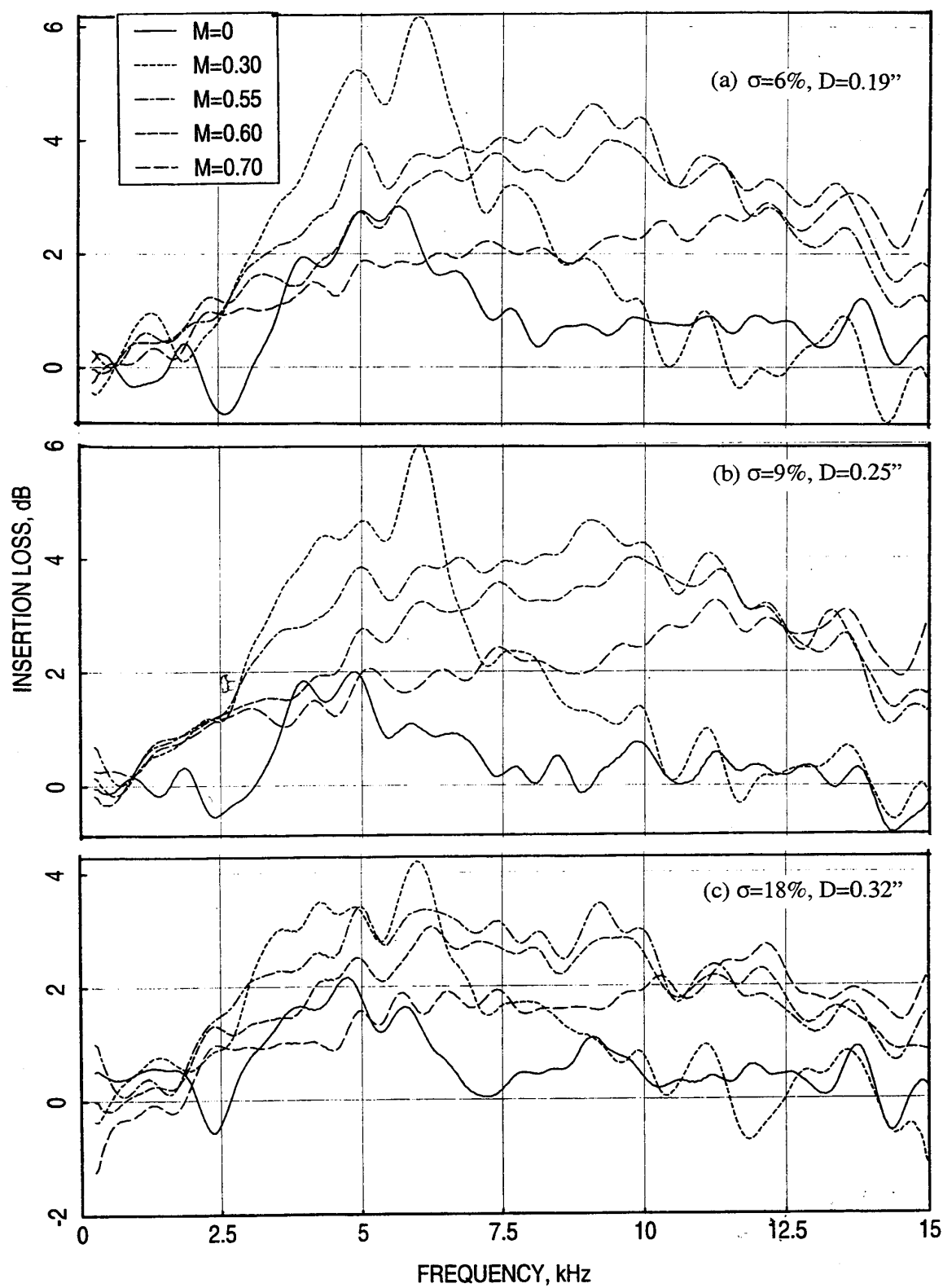


Figure 123. Influence of grazing flow Mach number (M) on insertion loss spectra for a number of SDOF 1/3-scale panels ($\eta=3.4$) with perforated facesheets, measured in a 4"- high (H) flow duct, mounted on one side, $d=0.039''$, $t=0.025''$.

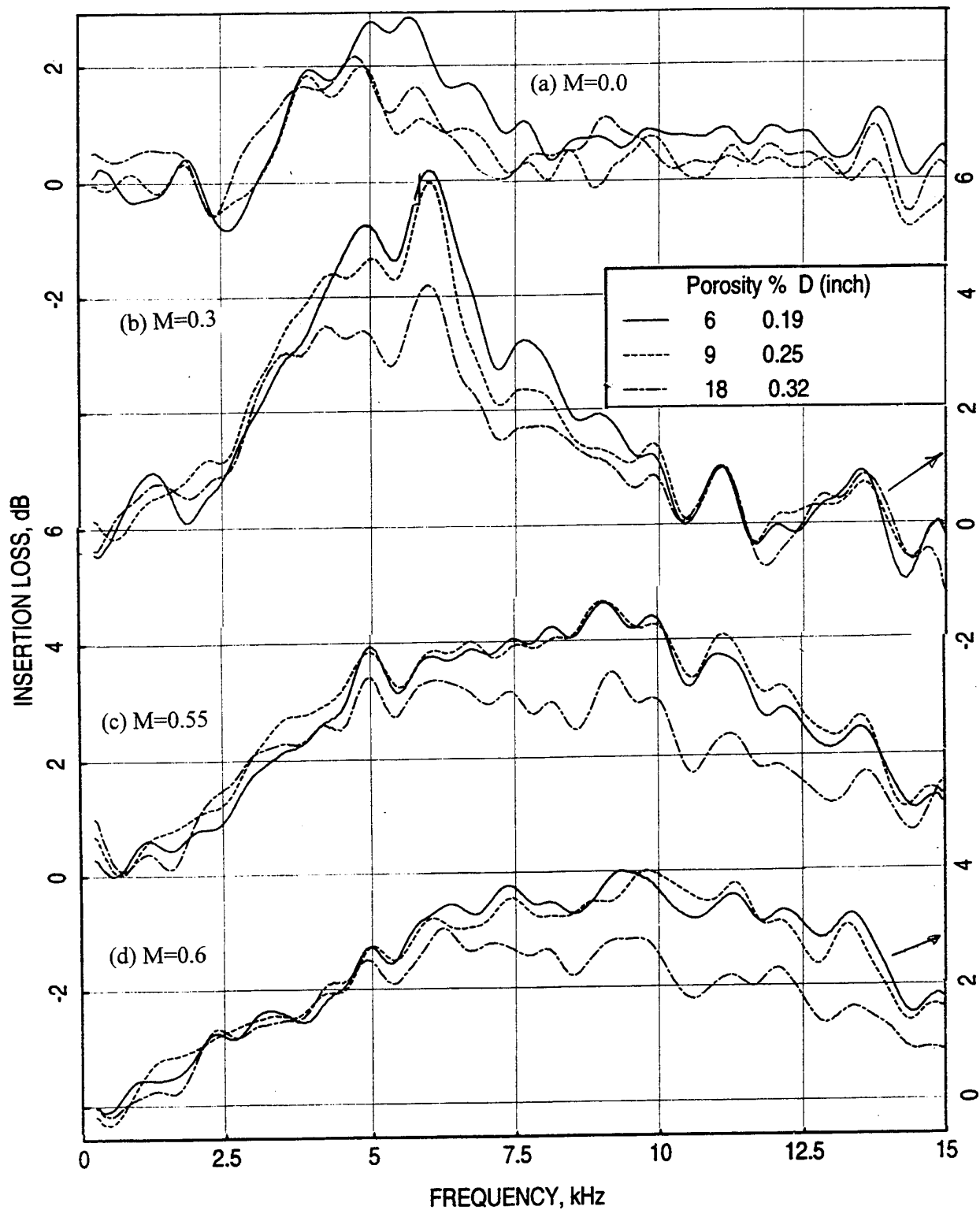


Figure 124. Effect of perforated sheet porosity ($\bar{\sigma}$) and panel depth (D) on insertion loss spectra for SDOF type panels at different grazing flow Mach numbers (M), mounted on one side of the 4"-high flow duct; $t=0.025"$, $d=0.039"$.

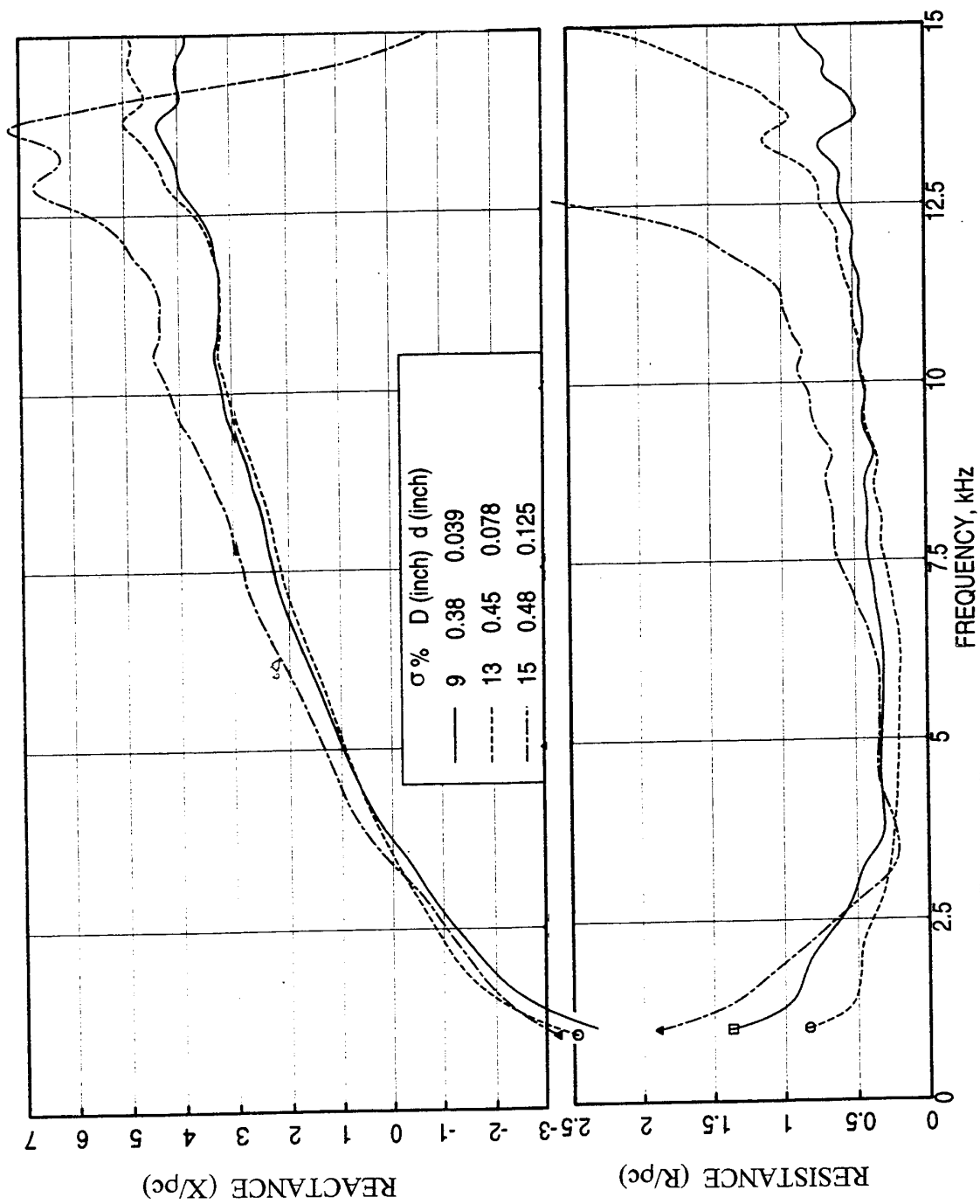


Figure 125. Effect of perforated sheet porosity (σ), hole diameter (d), and panel depth (D) on normal impedance spectra for SDOF type panels; $t=0.08"$, nominal OASPL=150 dB.

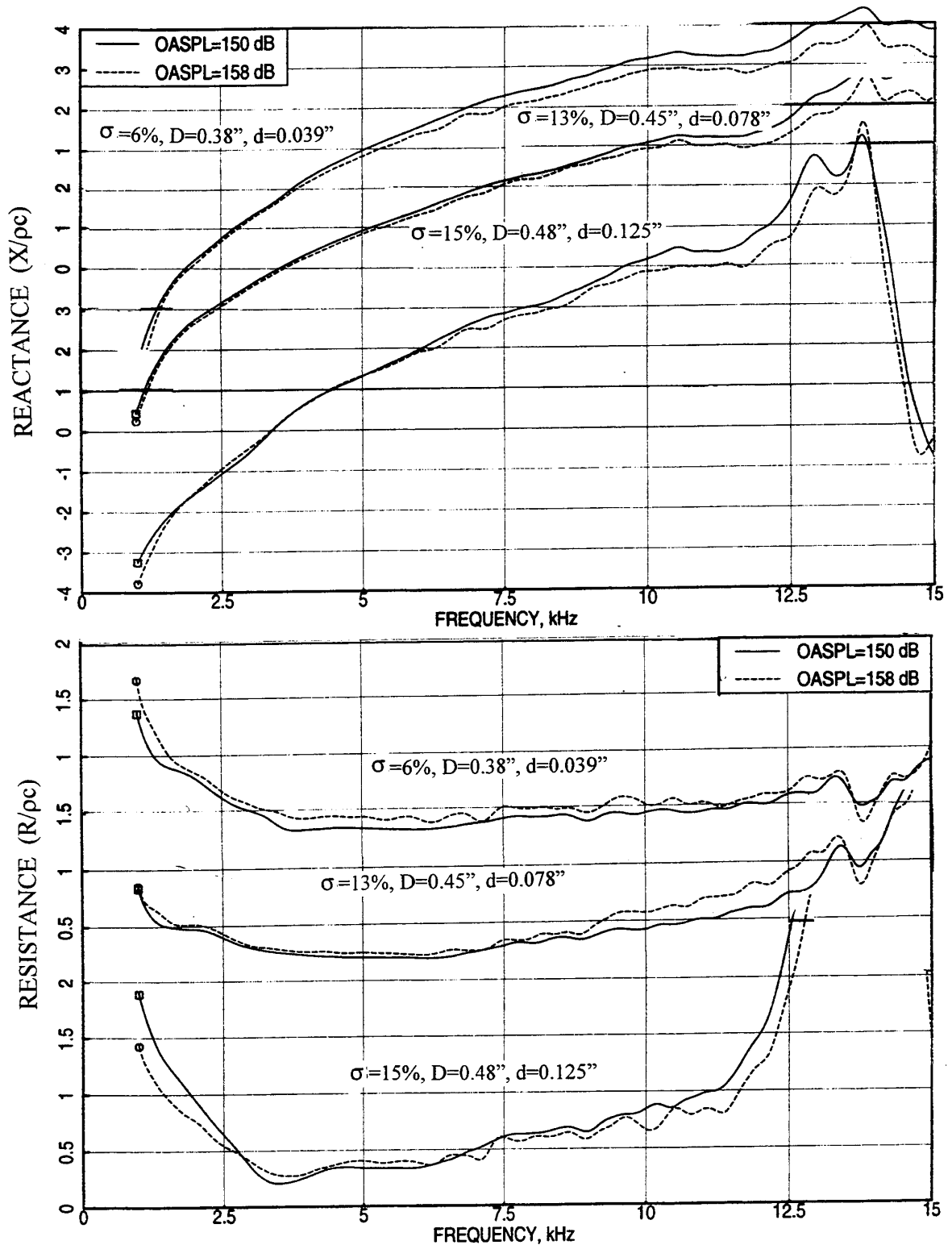


Figure 126. Effect of excitation level on normal impedance spectra for SDOF type panels; with respect to perforated sheet porosity (σ), hole diameter (d), and panel depth (D), $t=0.08''$.

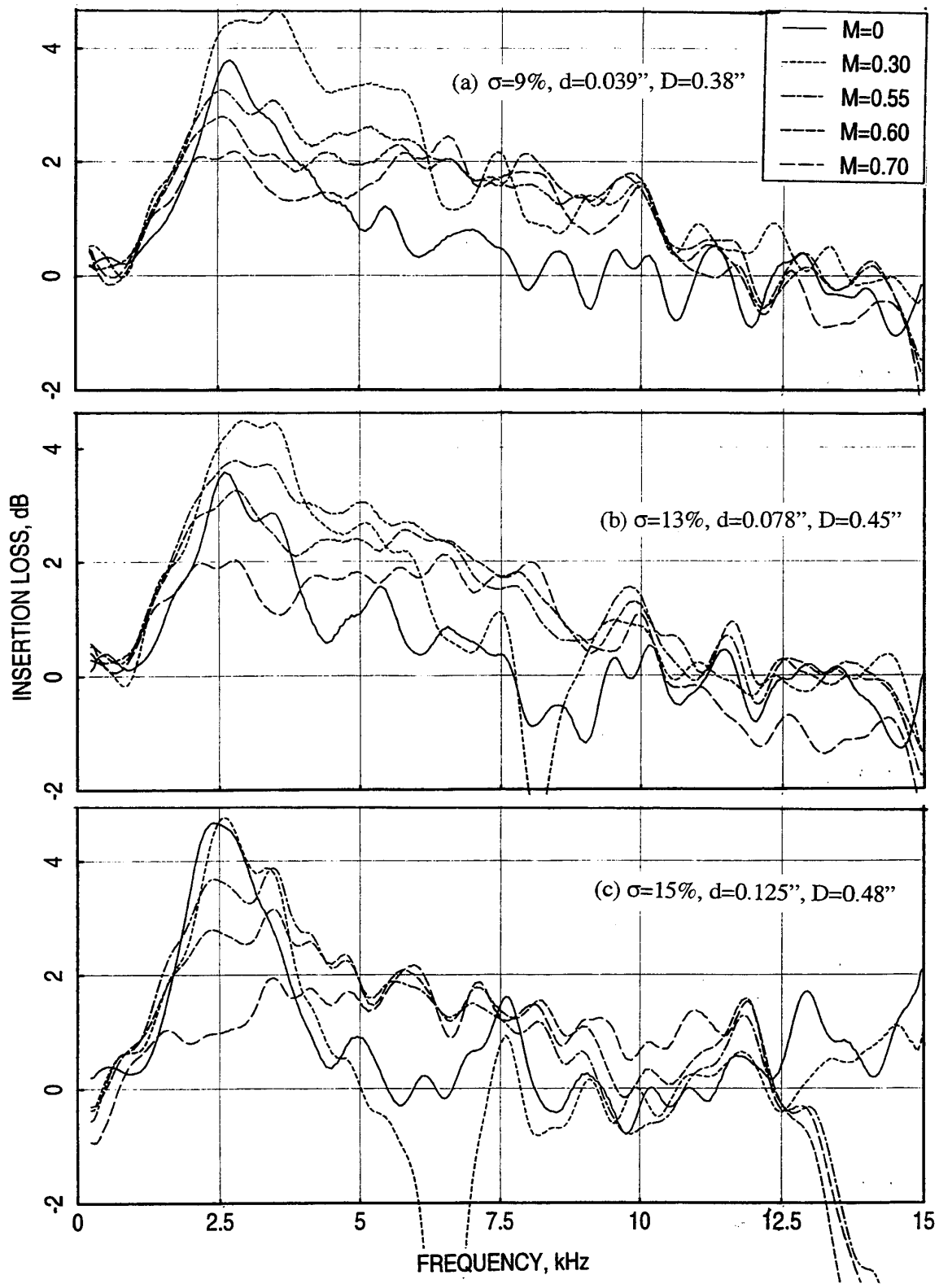


Figure 127. Influence of grazing flow Mach number (M) on insertion loss spectra for a number of SDOF 1/3-scale panels ($\eta=3.4$) with perforated facesheets, measured in a 4"- high (H) flow duct, mounted on one side, $t=0.08''$.

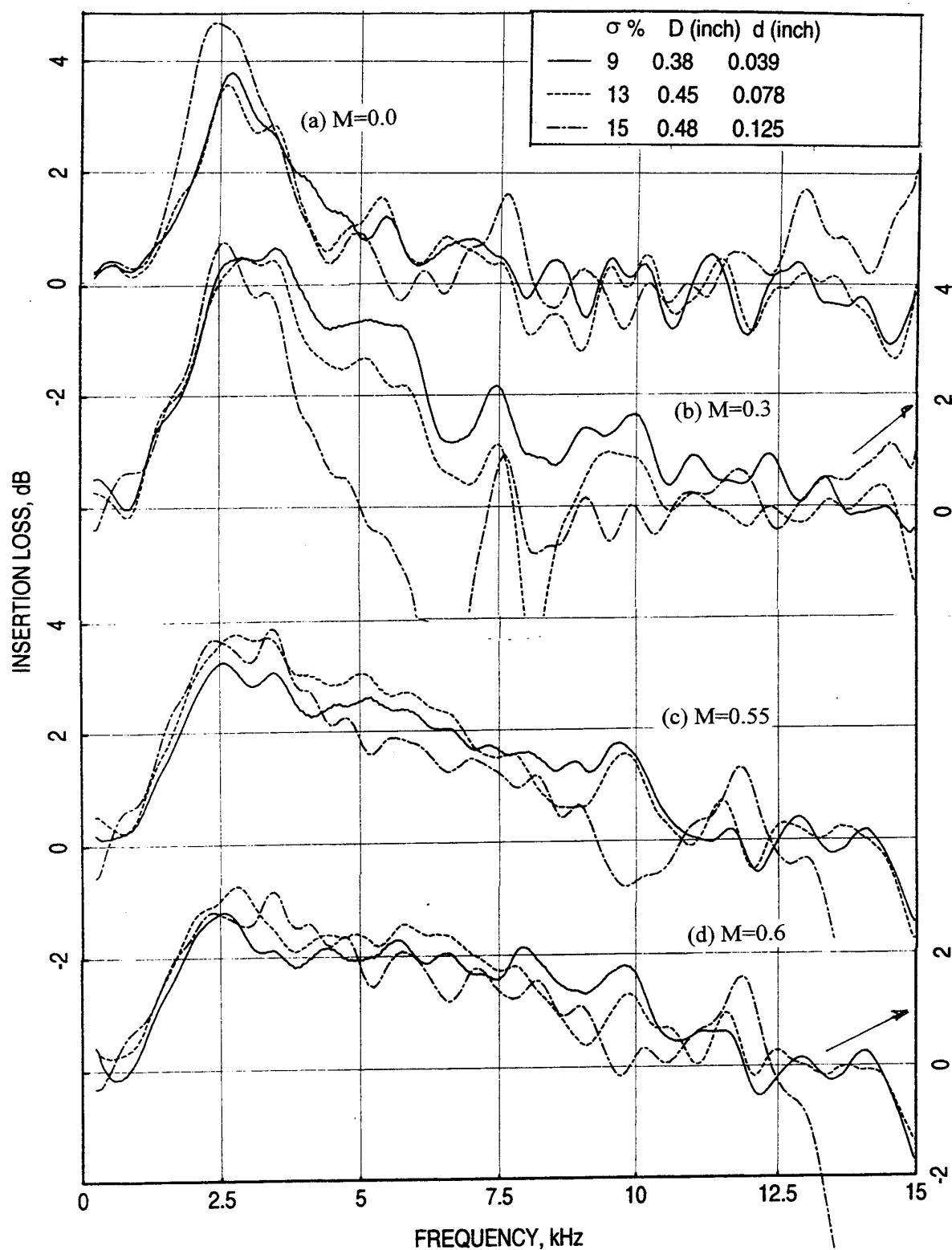


Figure 128. Effect of perforated sheet porosity (σ), hole diameter (d), and panel depth (D) on insertion loss spectra for SDOF type panels at different grazing flow Mach numbers (M), mounted on one side of the 4"-high flow duct; $t=0.08$ ".

Effect of Panel Depth (D): Panels of different depths are designed for the optimum impedance limits for one-sided and two-sided treatment configurations (for scaling study) with the same facesheet characteristics. Figure 129 shows the normal impedance spectra for these configurations. Figure 130 shows the influence of excitation level on normal impedance. While, the 0.3"-deep panel is designed for two-sided treatment, it was also tested with one-sided treatment and compared with the results of 0.7"-deep panel (one-sided). The insertion loss spectra at various grazing flow conditions are shown Figure 131. As expected, the insertion loss spectral levels as well as shapes do not agree with each other. Figure 132 shows the effect of one-side versus two-side treatment on insertion loss spectra for the 0.3"-deep panel. While, the spectral shapes are similar, the insertion loss magnitudes are higher for two-sided treated configuration compared to one sided configuration. Figure 133 shows the effect of scaling by comparing the insertion loss spectra for one-sided treated 0.7"-deep panel with the insertion loss spectra of two-sided treated 0.3" panel with respect to the nondimensional frequency, based on the flow duct height (H). The insertion loss peaks for both configurations appear at the same nondimensional frequency, confirming the scaling principle.

5.4 Acoustic Characteristics of Instrumented 1"-Deep SDOF Type Panels with Perforated Facesheets:

These panels, as listed in Table 16 and shown in Figure 80, are similar to the SDOF panels (see Figure 72), but of much higher depth (i.e., 1" deep) to accommodate special instrumentation.

5.4.1 DC Flow Results :

Figure 134 shows the DC flow resistance with respect to through flow velocity for two panels at different grazing flow Mach numbers. The effect of grazing flow is significant on DC flow resistance that it increases with increasing grazing flow. Figure 135 shows comparisons of R100 (i.e., DC flow resistance at a throughflow velocity of 100 cm/sec) and NLF_{150/20} (i.e., the nonlinear factor, which is the ratio of DC flow resistances at throughflow velocities of 150 and 20 cm/sec) between the three panels with respect to grazing flow Mach number (M). For each panel the R100 increases and NLF_{150/20} decreases with increasing grazing flow Mach number. For a fixed d/t of 1.56 for these three panels the variation of R100 and NLF_{150/20} with respect to porosity do not exhibit any definite trend. However, for the two panels with same facesheet thickness and hole diameter, R100 decreases and NLF_{150/20} increases with increasing porosity.

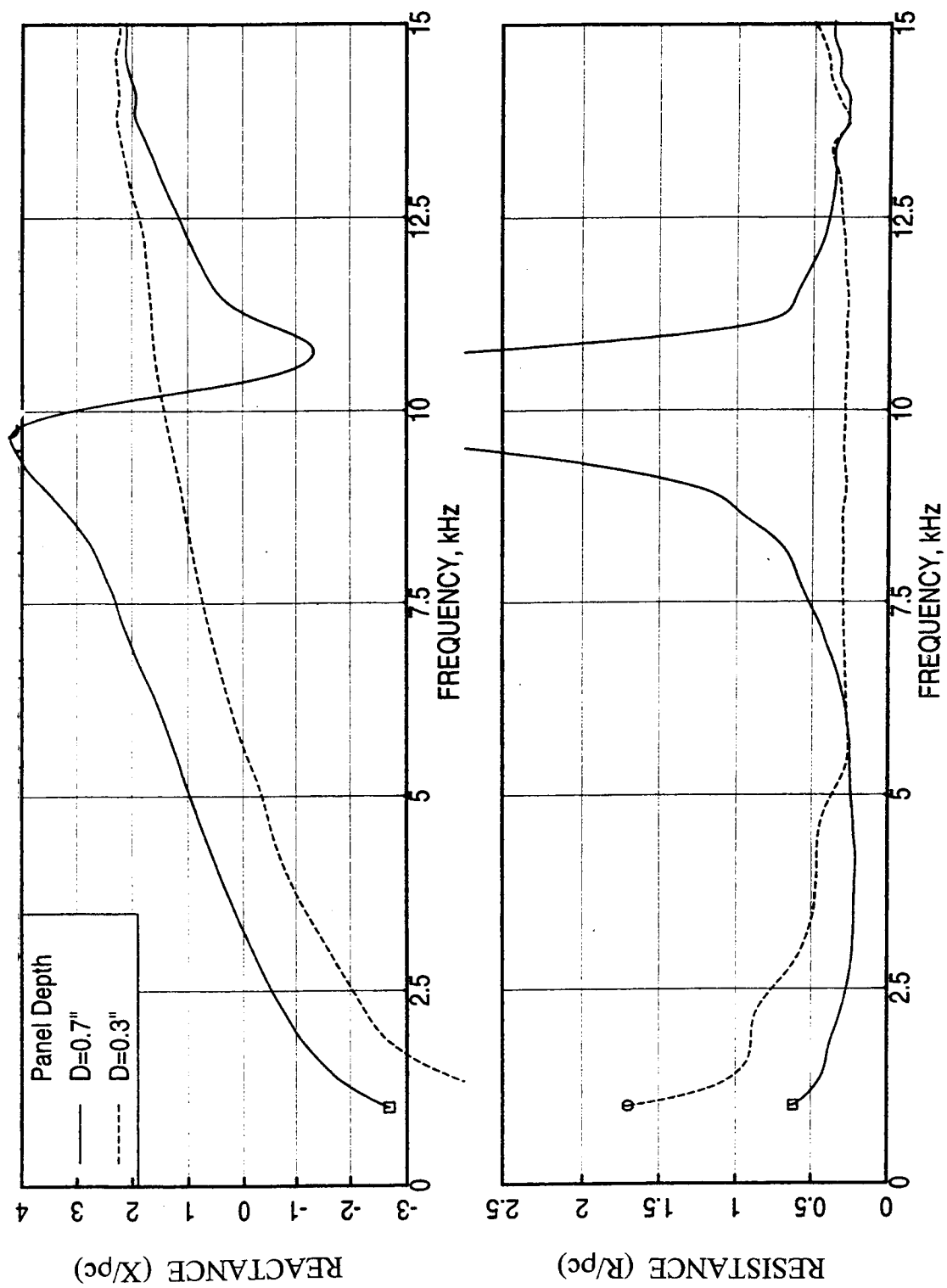


Figure 129. Effect of panel depth (D) on normal impedance spectra for SDOF type panels; $t=0.02''$, $d=0.039''$, $\sigma=9\%$, nominal OASPL=150 dB.

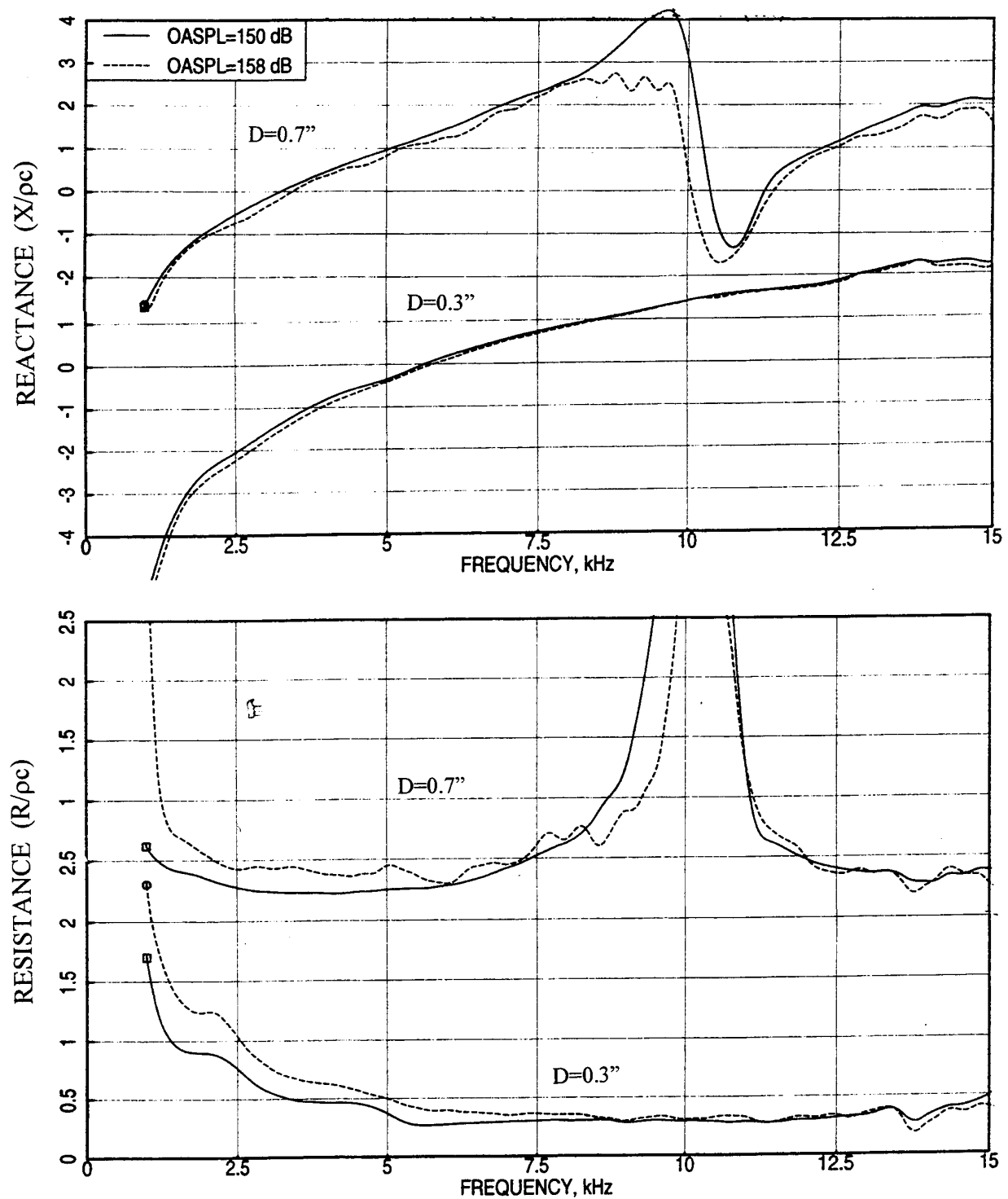


Figure 130. Effect of excitation level on normal impedance spectra for SDOF type panels; with respect to panel depth (D), $t=0.02''$, $d=0.039''$, $\sigma=9\%$.

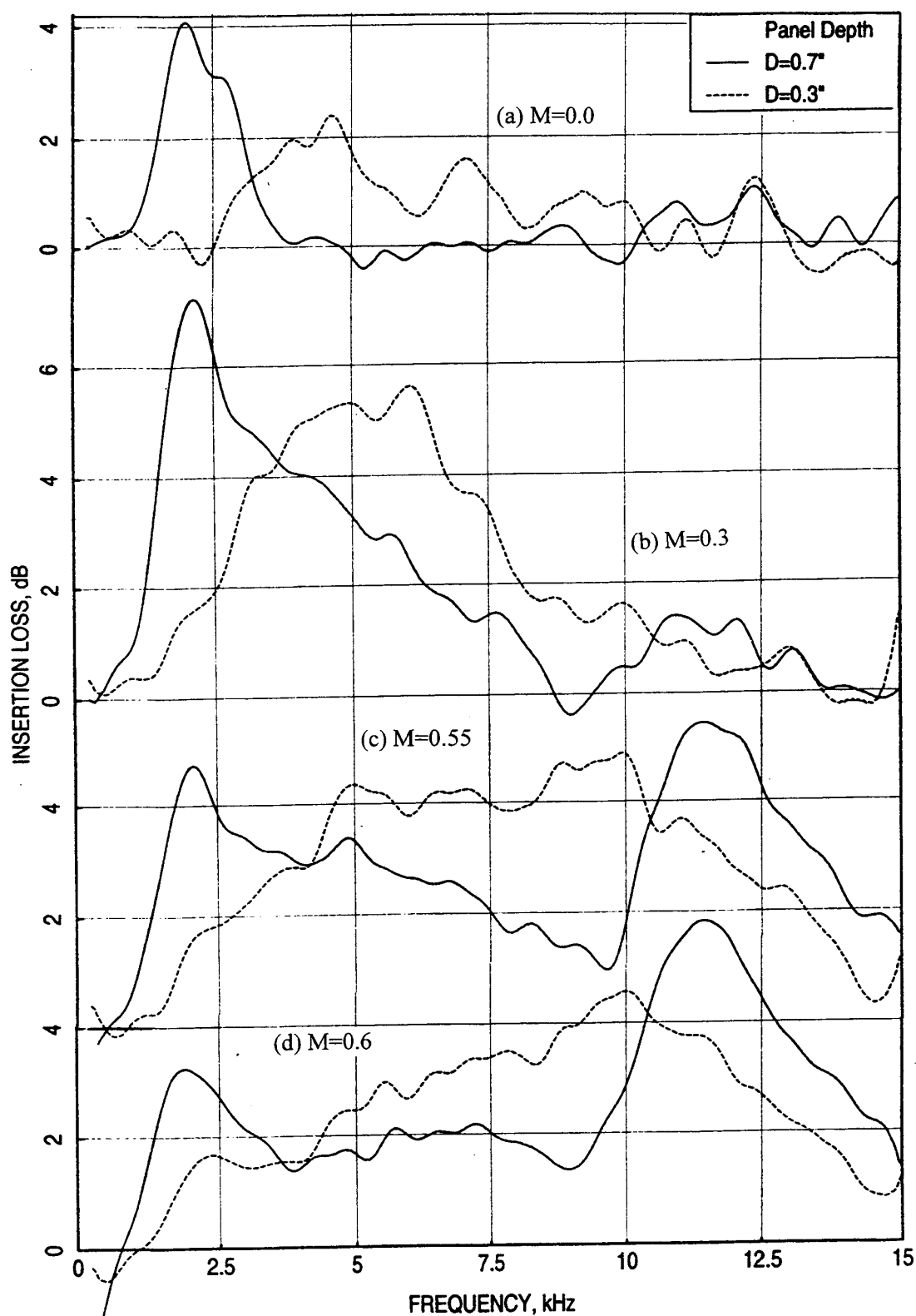


Figure 131. Effect of panel depth (D) on insertion loss spectra for SDOF type panels at different grazing flow Mach numbers (M), mounted on one side of the 4"-high flow duct; $t=0.02"$, $d=0.039"$, $\sigma=9\%$.

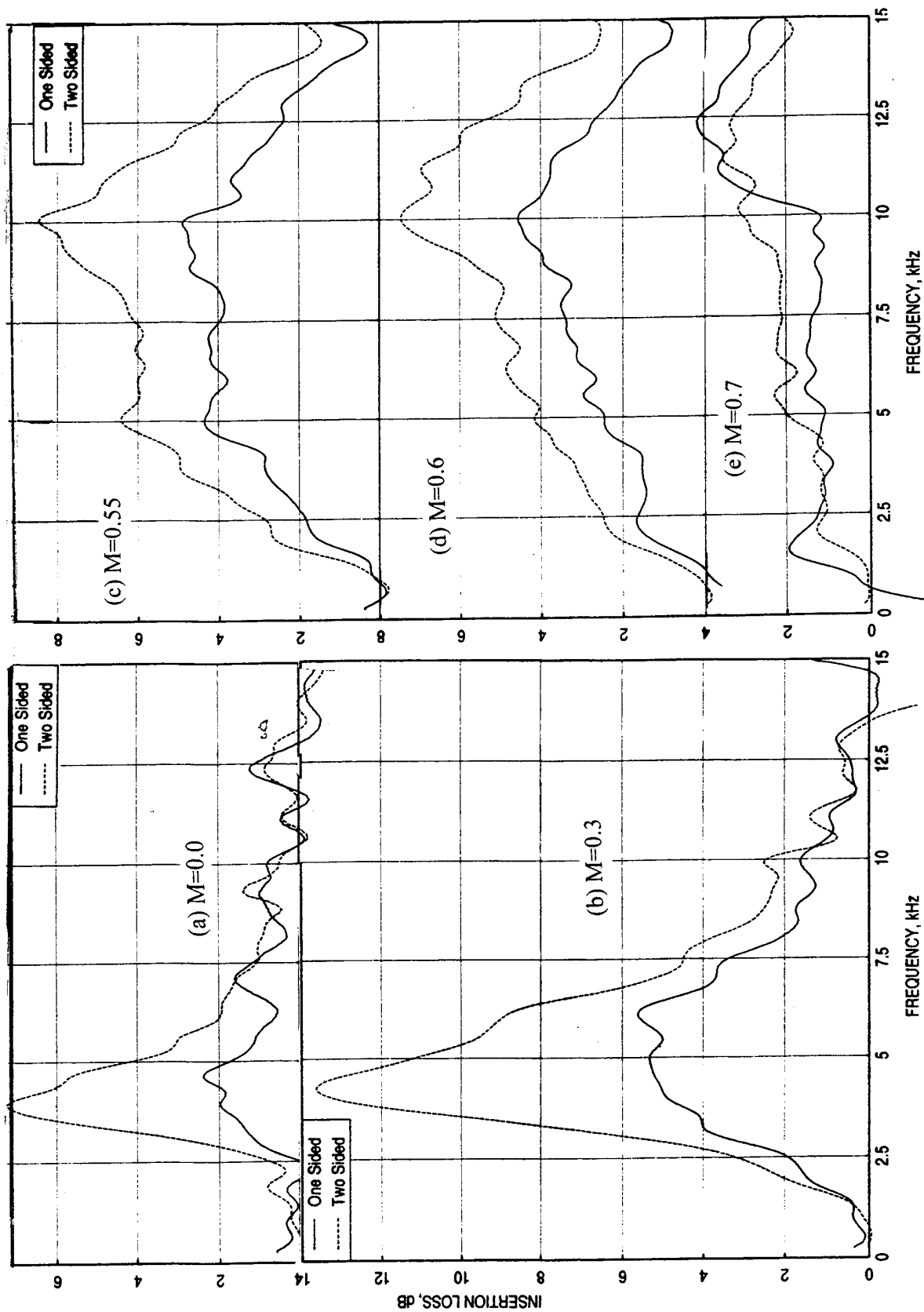


Figure 132. Effect of one-side versus two-side mounted 4"-high flow duct on insertion loss spectra for SDOF type panels at different grazing flow Mach numbers (M); $t=0.02$ ", $d=0.039$ ", $\sigma=9\%$, $D=0.3$ ".

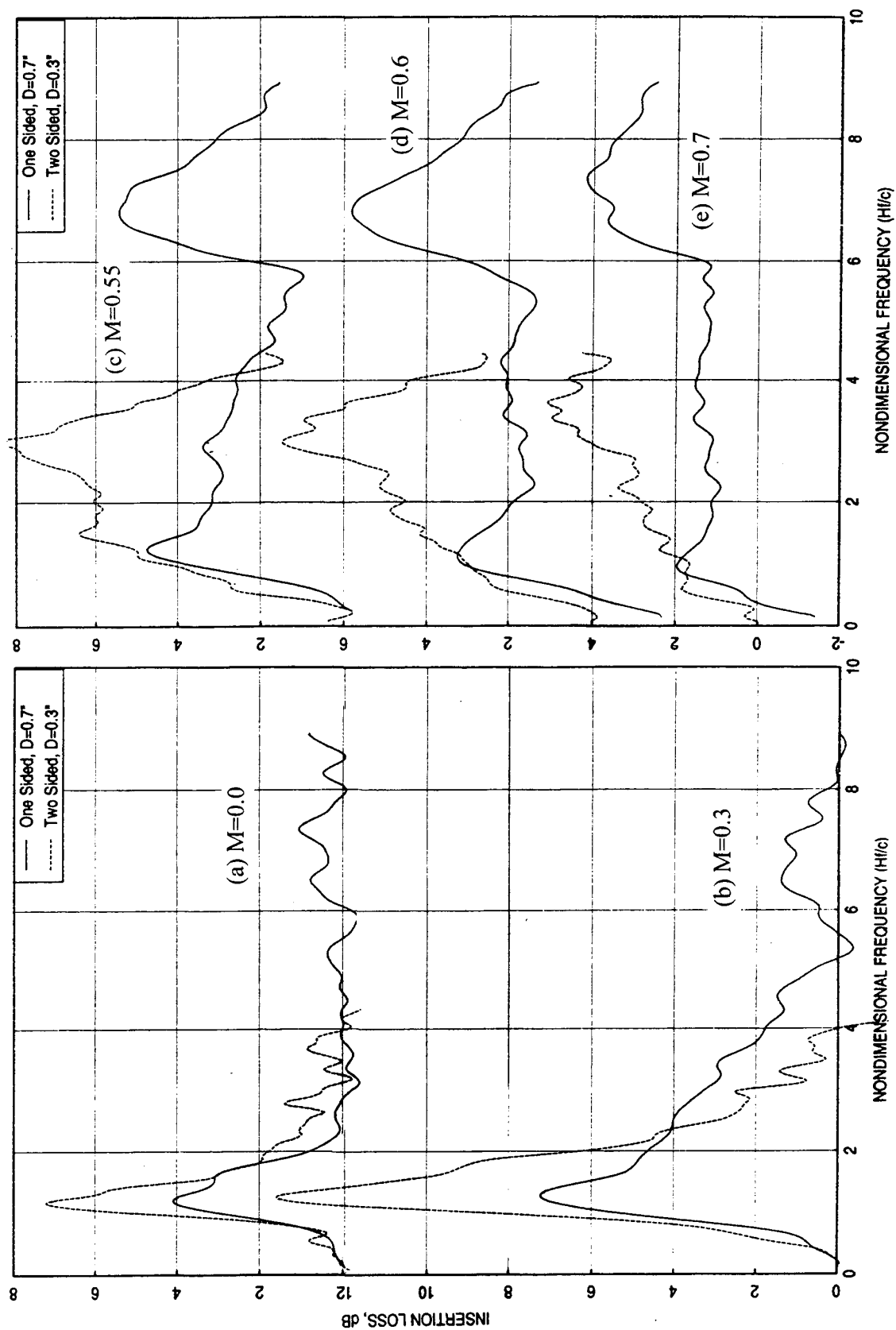


Figure 133. Effect of scaling (1/3-rd scale for one-sided treatment of $D=0.7$ " panel and 1/6-th scale for two-sided treatment of $D=0.3$ " panels) on insertion loss spectra for SDOF type panels at different grazing flow Mach numbers (M); $t=0.02$ ", $d=0.039$ ", $\sigma=9\%$.

Table 16. Geometrical Properties and File Names for Insertion Loss Data for 1"-Deep SDOF Type Panels with Perforated Facesheets, 3/8" size Honeycomb of 0.005" thick Wall

Panel Config. #	Thickness, t in inches	Hole Dia, d in inch	Porosity, σ in %	Broadband Frequency Insitu Impedance Data Files, M=0	Discrete Frequency Insitu Impedance Data Files, M=0.3	Discrete Frequency Insitu Impedance Data Files, M=0.55	Discrete Frequency Insitu Impedance Data Files, M=0.8	Insertion Loss 1/3-Octave Band Data Files	Insertion Loss Narrowband Data Files
5.1	0.025	0.039	7.5	insitu51-0-dat wnp.smt	insitu51-3-dat	insitu51-5-dat	insitu51-8-dat	ttwbs5-1.dat	rrwbs5-1h.smt
5.2	0.025	0.039	9	insitu52-0-dat wnp.smt	insitu52-3-dat	insitu52-5-dat	insitu52-8-dat	ttwbs5-2.dat	rrwbs5-2h.smt
5.3	0.025	0.039	12.5	insitu53-0-dat wnp.smt	insitu53-3-dat	insitu53-5-dat	insitu53-8-dat	ttwbs5-3.dat	rrwbs5-3h.smt
5.4	0.025	0.039	15	insitu54-0-dat inp.smt	insitu54-3-dat	insitu54-5-dat	insitu54-8-dat	ttwbs5-4.dat	rrwbs5-4h.smt
5.5	0.025	0.018	9	insitu55-0-dat wnp.smt	insitu55-3-dat	insitu55-5-dat	insitu55-8-dat	ttwbs5-5.dat	rrwbs5-5h.smt
5.6	0.025	0.078	9	insitu56-0-dat wnp.smt	insitu56-3-dat	insitu56-5-dat	insitu56-8-dat	ttwbs5-6.dat	rrwbs5-6h.smt
5.7	0.08	0.039	9	insitu57-0-dat wnp.smt	insitu57-3-dat	insitu57-5-dat	insitu57-8-dat	ttwbs5-7.dat	rrwbs5-7h.smt
5.8	0.08	0.125	15	insitu58-0-dat wnp.smt	insitu58-3-dat	insitu58-5-dat	insitu58-8-dat	ttwbs5-8.dat	rrwbs5-8h.smt

Note: Panel Config #: Panels of 12"x5" Treated area tested for Insertion Loss Measurement in a Flow Duct of 4" height with one side treated (i.e., the duct height becomes 8").

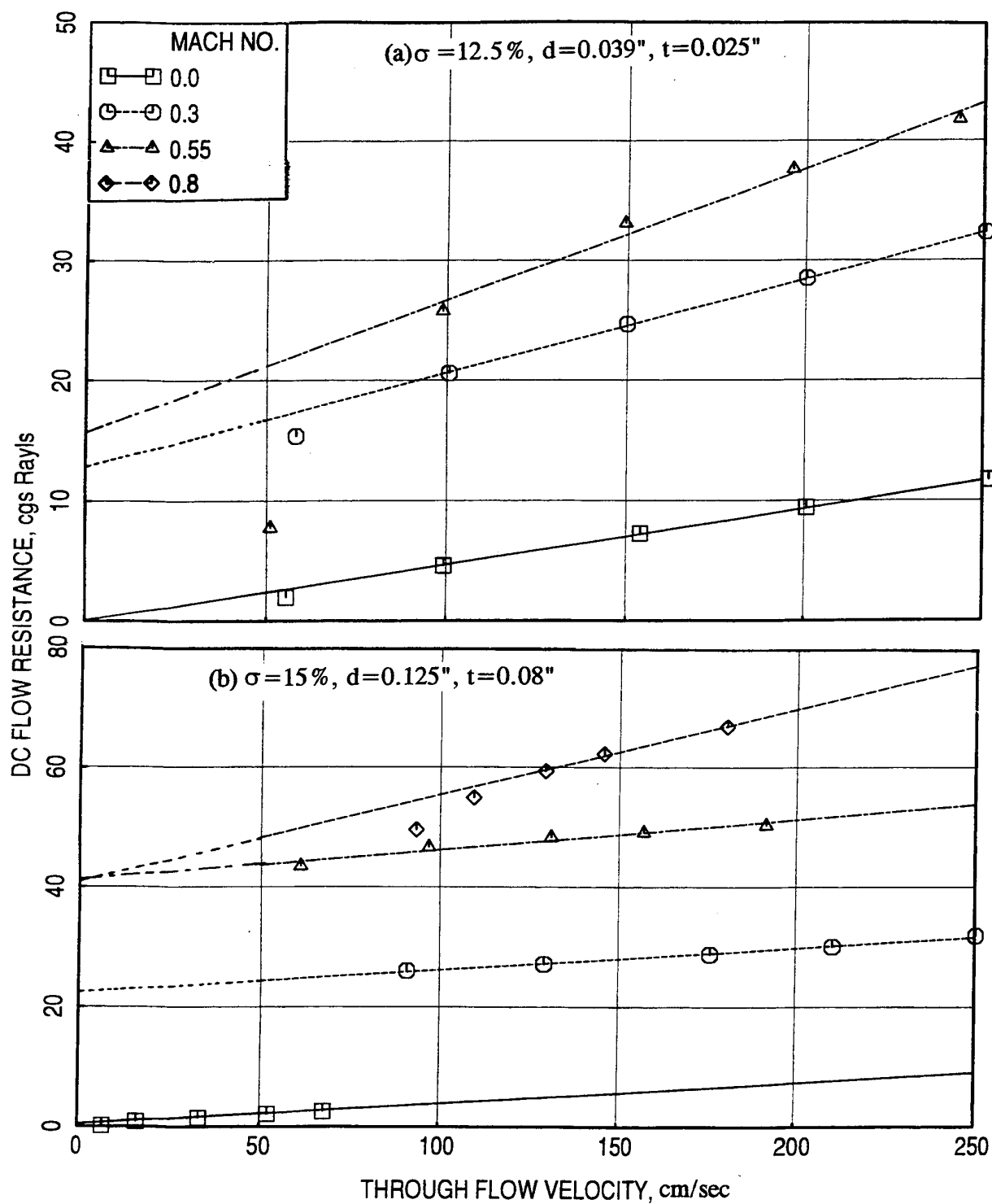


Figure 134. Effect of grazing flow Mach number (M) on DC flow resistance for 1"-deep SDOF type panels with perforated facesheets.

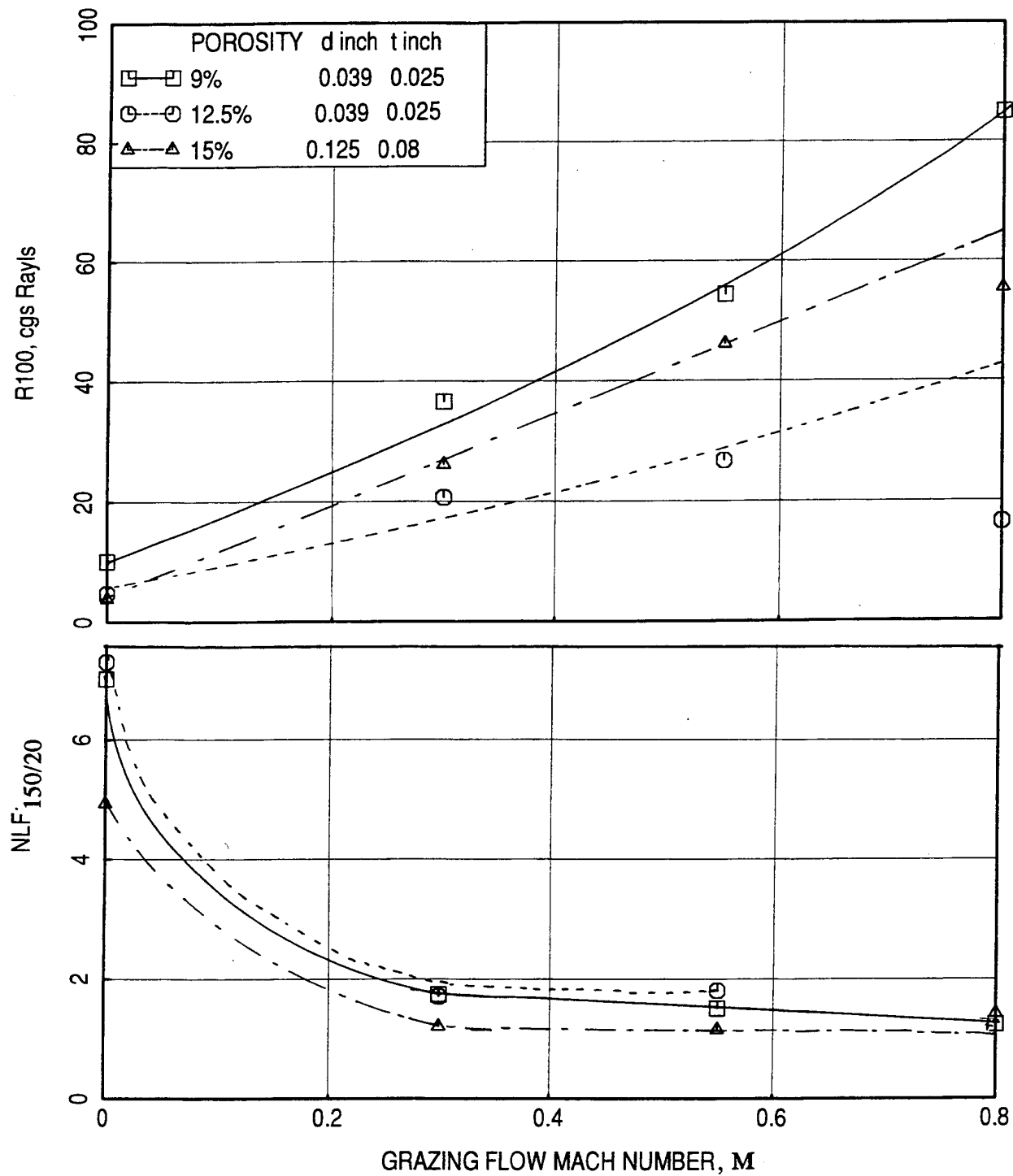


Figure 135. Effect of facesheet porosity on DC flow resistance at 100 cm/sec (R100) and nonlinear factor (NLF_{150/20}) with respect to grazing flow Mach number for 1"-deep SDOF type panels with perforated facesheets; d/t=1.56.

5.4.2 In-situ Impedance Results:

In-situ impedance is evaluated with and without grazing flow [Ref. 13]. In the absence of grazing flow the impedance is evaluated using broadband (BB) as well as discrete frequency excitation. The broadband results are useful to determine the basic trends of the impedance spectral behavior, since the discrete frequency results are obtained at a limited number of frequencies.

Figure 136 shows the spectral distribution of sound pressure level amplitudes measured by the probe flush with the facesheet (i.e., face probe) and the probe flush with the backplate inside the cavity (i.e., cavity probe) due to broadband excitation in the absence of grazing flow for the panel with 12.5% porosity ($d=0.039''$ and $t=0.025''$). The corresponding impedance spectra in terms of specific resistance and reactance are shown in Figure 137. The high values of resistances occurring at frequencies where the reactance changes its sign from high positive to negative, indicate the anti-resonating frequencies of the cavity behind the facesheet of the panel. The data scatter observed in Figures 136 and 137 are due to the limited spectral averaging (i.e., 40 times). To minimize the sharp oscillations of spectral data a numerical smoothing is applied and the smoothed data are also plotted in these figures.

The repeatability of in-situ measurement with broadband excitation is checked out by conducting the tests several times. The results are shown in Figures 138 and 139 for the panel with 12.5% porosity ($d=0.039''$ and $t=0.025''$). The SPL amplitudes measured by the face and cavity probes do vary by certain amount. However, the influence of these variations is small on the in-situ impedance, especially at low frequencies (see Figure 139).

The effect of grazing flow on in-situ impedance for three panels are examined by plotting the impedance spectra at different grazing flow Mach number and impedance with respect to grazing flow Mach number at different frequencies in Figures 140 through 145. The high values of resistances occurring at frequencies where the reactance changes its sign from high positive to negative (see Figures 140, 142, and 144), indicate the anti-resonating frequencies of the cavity behind the facesheet of the panel. In-situ impedance results for some panels are more reliable than the others. For some panels the instrumented honeycomb cell was not rigid enough and for some panels the facesheet was not properly sealed to the honeycomb cell. Thus, the results for some of the panels should be utilized with caution.

Figures 140 and 141 show in-situ impedance results for the panel with 9% porosity ($d=0.039''$ and $t=0.025''$). The resistance increases significantly with grazing flow Mach number. The

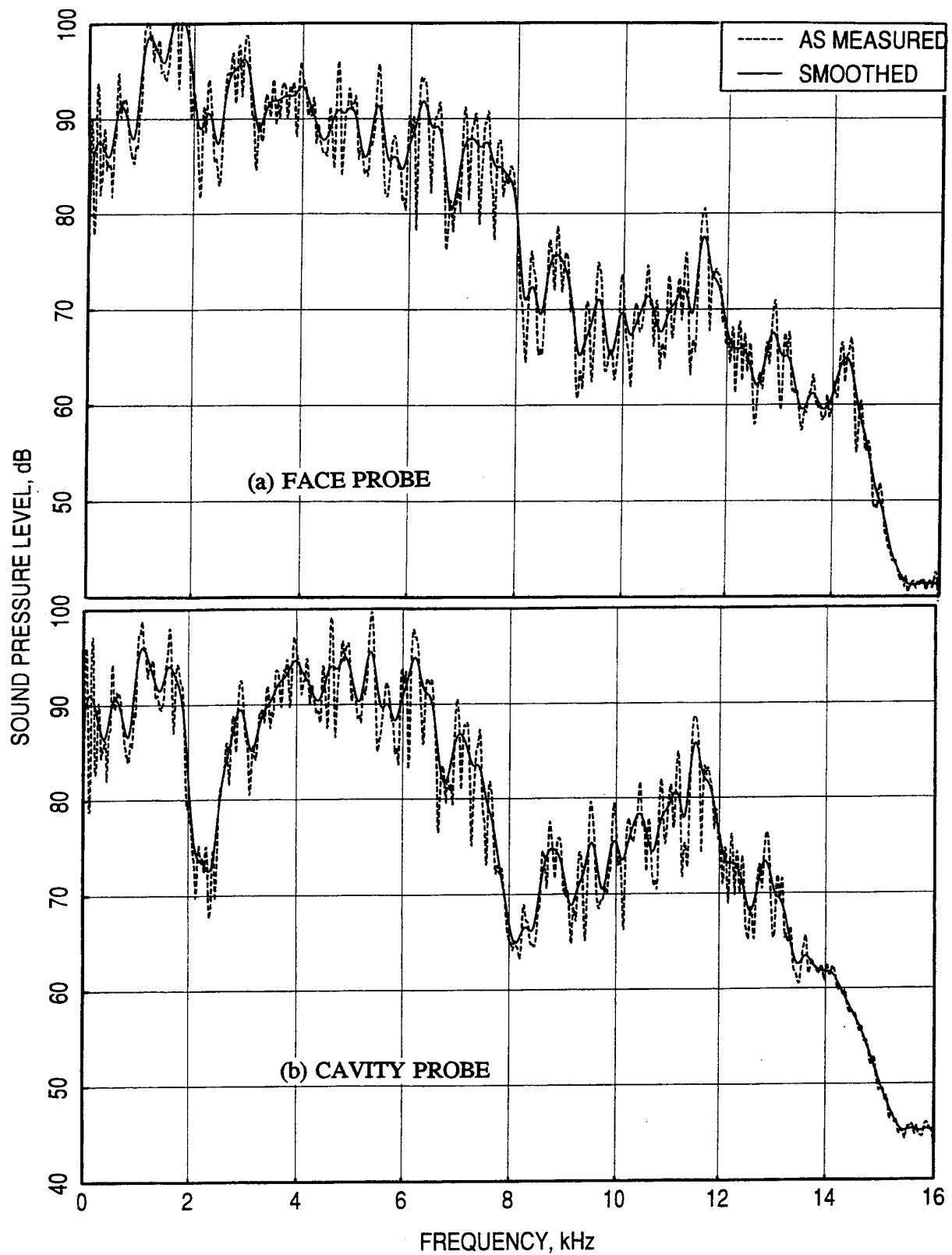


Figure 136. Broadband sound pressure levels measured by the face and cavity mounted transducers for in-situ impedance evaluation without grazing flow for an 1"-deep SDOF type panel with perforated facesheet; $\sigma=12.5\%$, $d=0.039"$, $t=0.025"$.

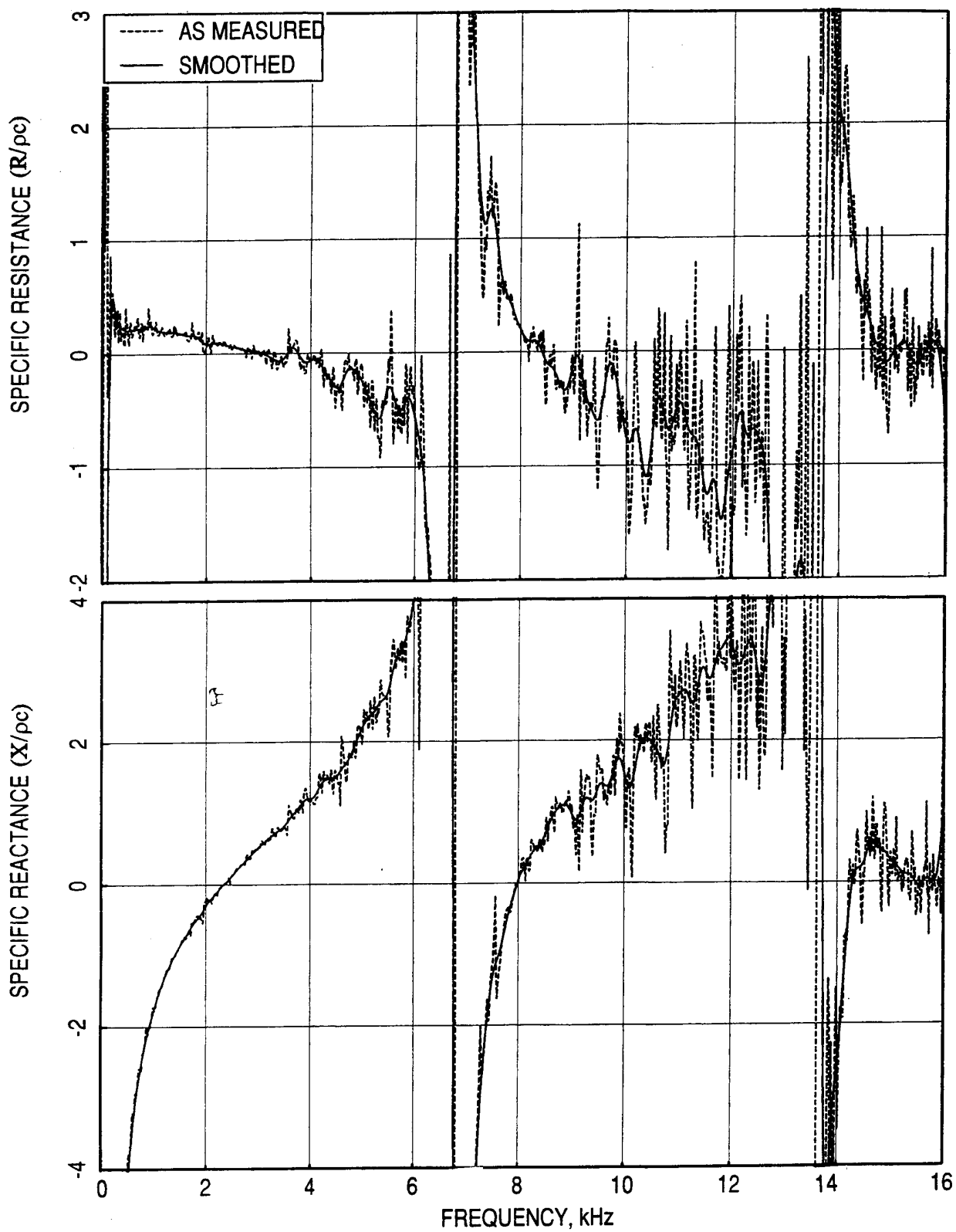


Figure 137. In-situ impedance spectra due to broadband excitation, without grazing flow, for an 1"-deep SDOF type panel with perforated facesheet; $\sigma=12.5\%$, $d=0.039"$, $t=0.025"$.

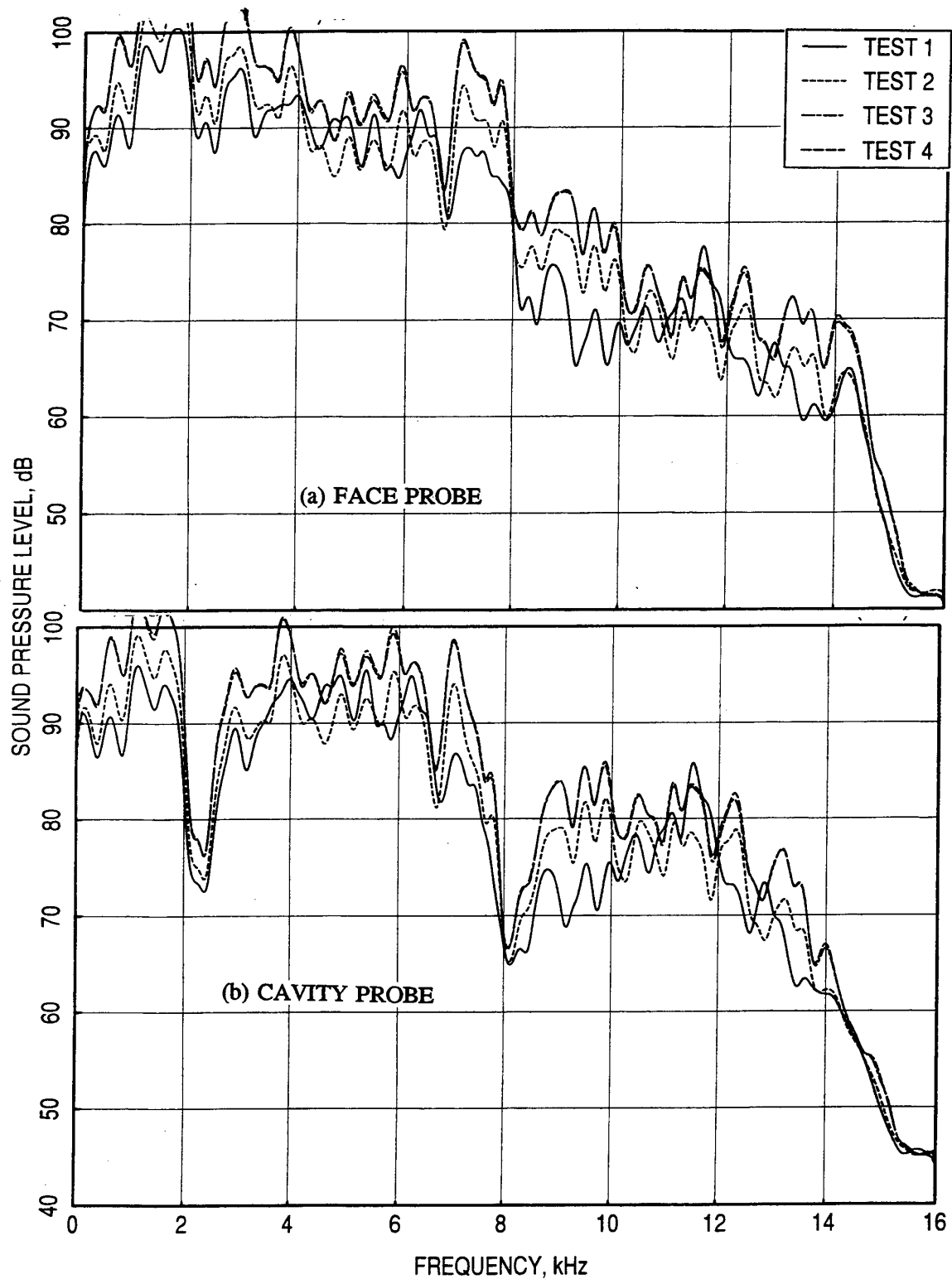


Figure 138. Repeatability of broadband sound pressure levels measured by the face and cavity mounted transducers for in-situ impedance evaluation without grazing flow for an 1"-deep SDOF type panel with perforated facesheet; $\sigma=12.5\%$, $d=0.039"$, $t=0.025"$.

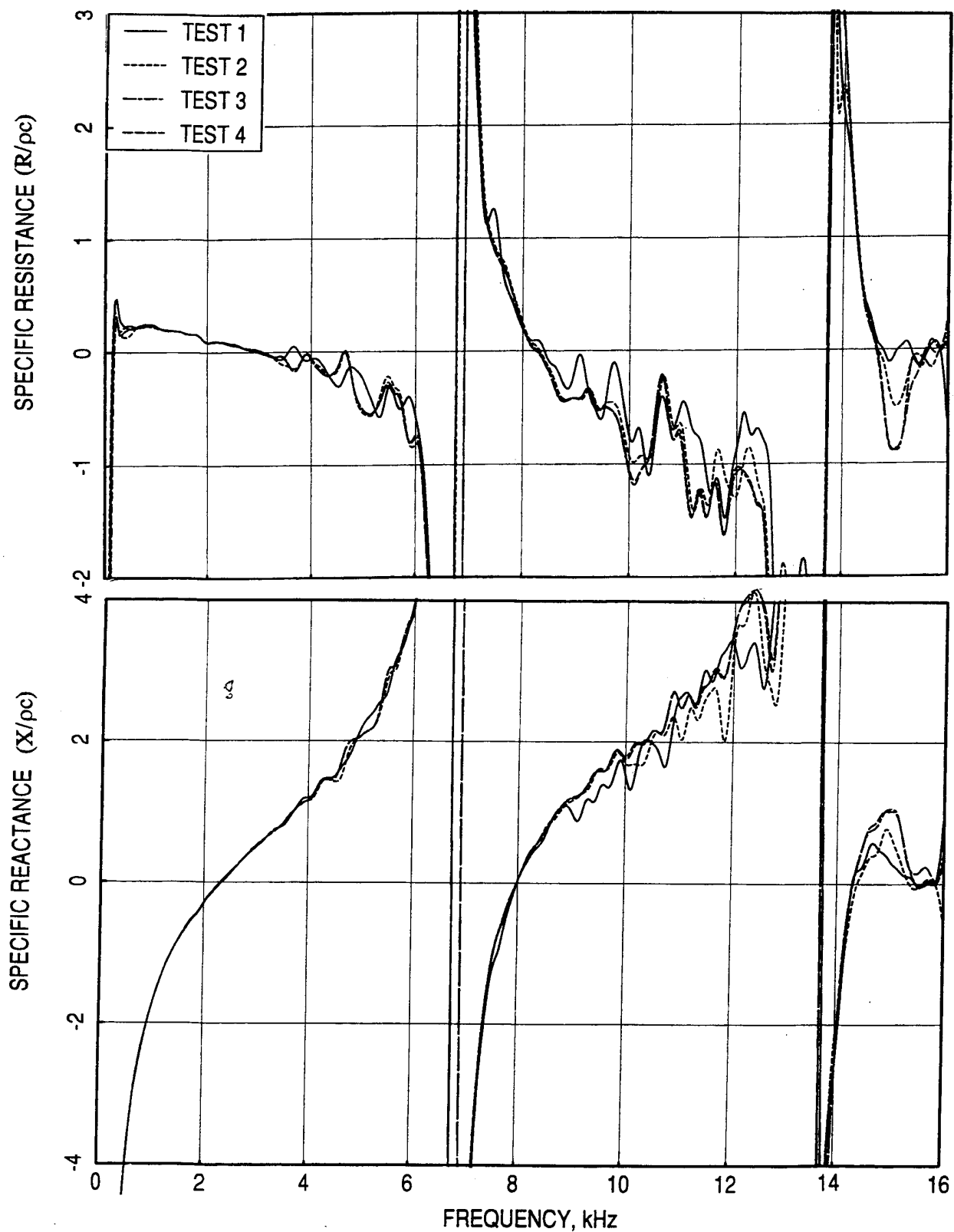


Figure 139. Repeatability of in-situ impedance spectra due to broadband excitation, without grazing flow, for an 1"-deep SDOF type panel with perforated facesheet; $\sigma = 12.5\%$, $d = 0.039$ ", $t = 0.025$ ".

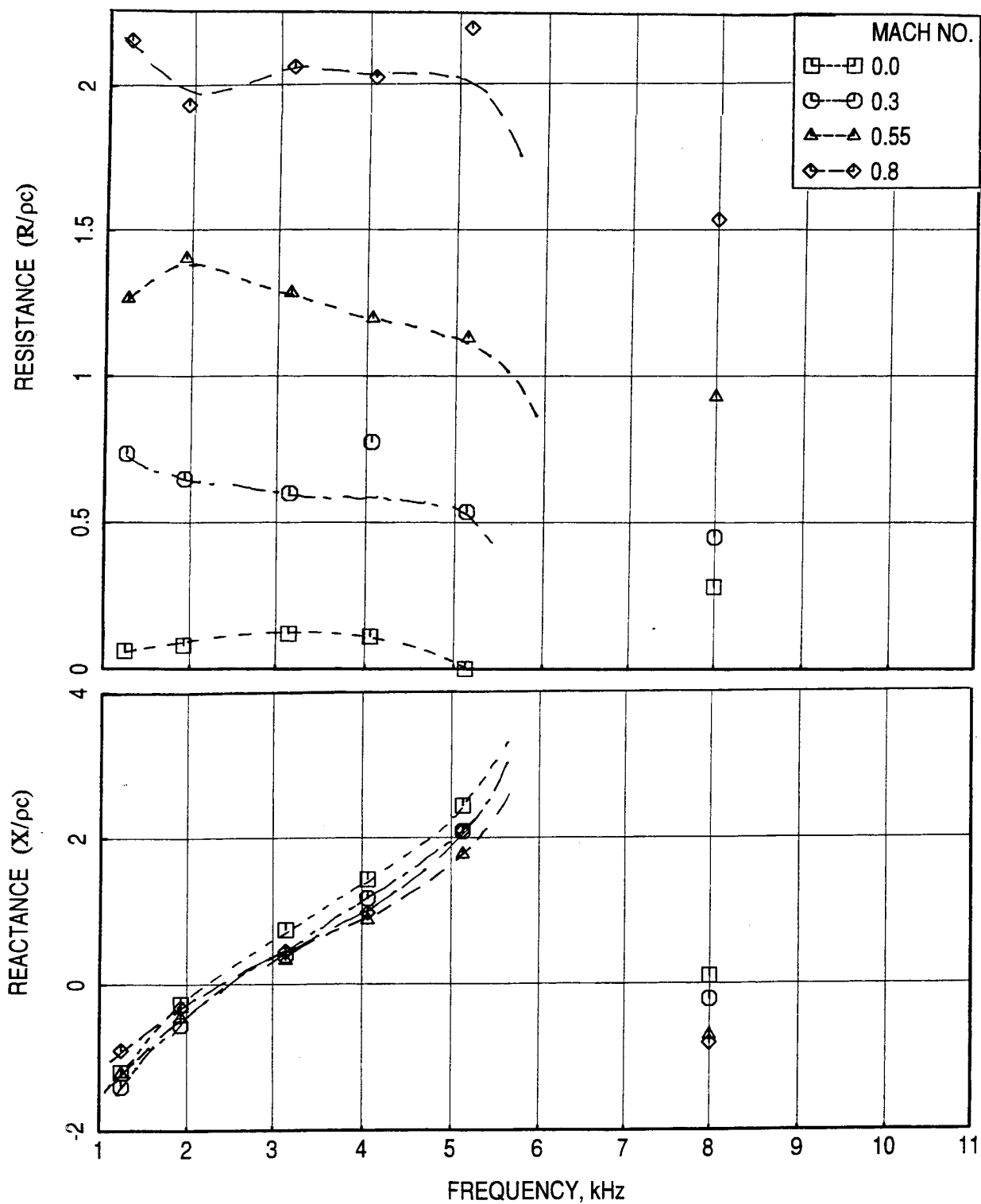


Figure 140. Effect of grazing flow Mach number (M) on in-situ impedance spectra for an 1"-deep SDOF type panel with perforated facesheet; $\sigma = 9\%$, $d = 0.039"$, $t = 0.025"$.

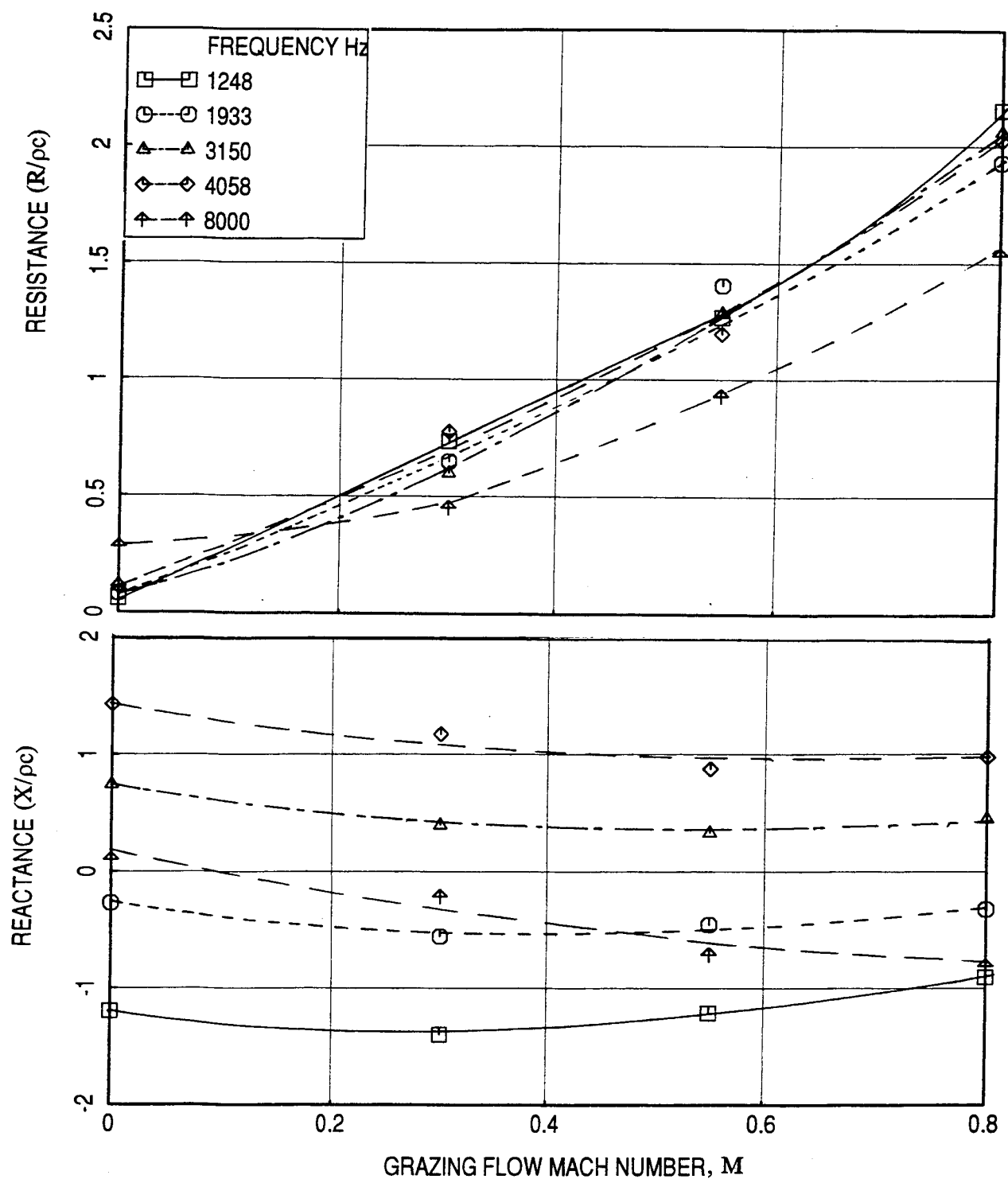


Figure 141. Effect of grazing flow Mach number (M) on in-situ impedance at different excitation frequencies for an 1"-deep SDOF type panel with perforated facesheet; $\sigma = 9\%$, $d = 0.039"$, $t = 0.025"$.

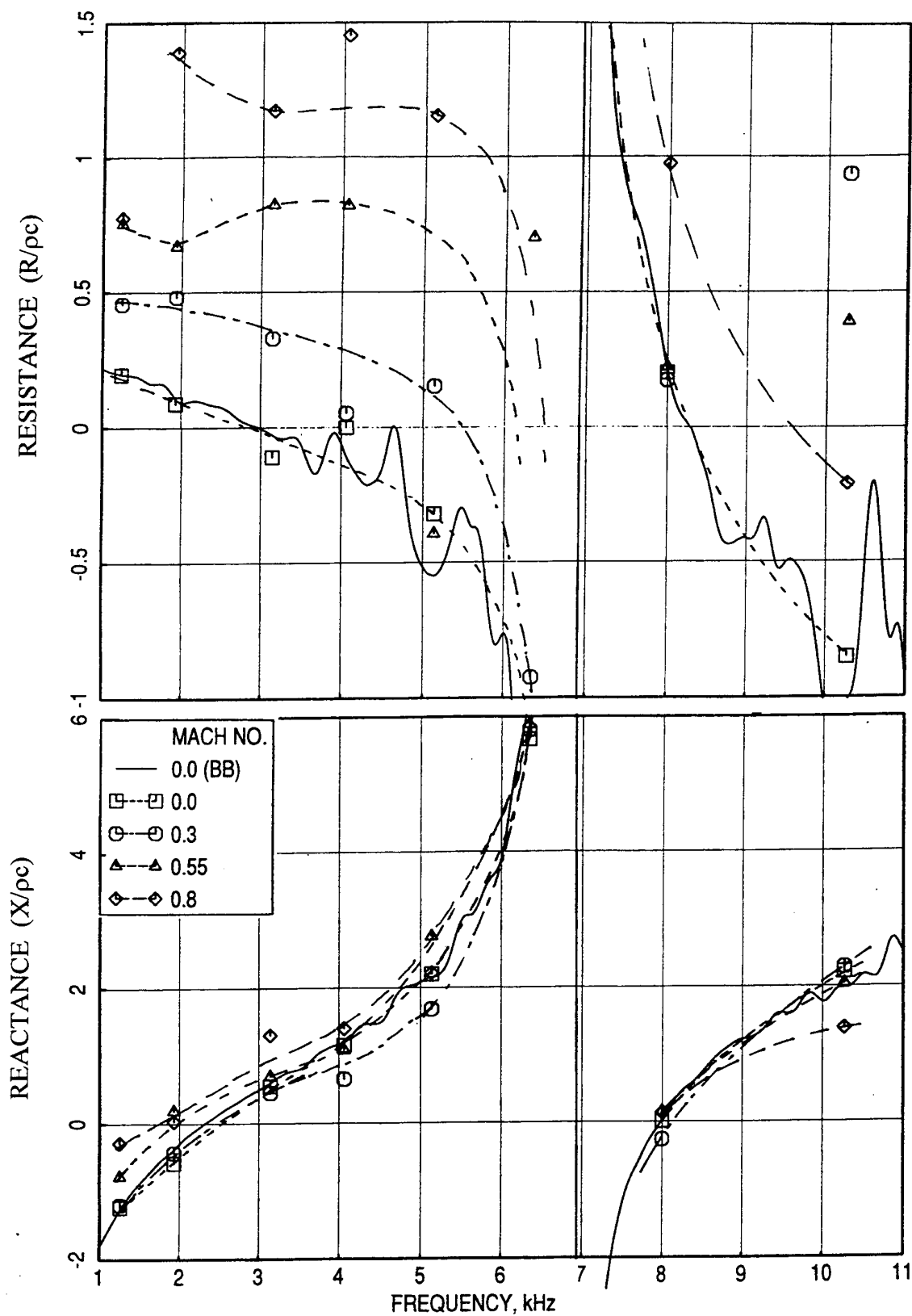


Figure 142. Effect of grazing flow Mach number (M) on in-situ impedance spectra for an 1"-deep SDOF type panel with perforated facesheet; $\sigma = 12.5\%$, $d = 0.039"$, $t = 0.025"$.

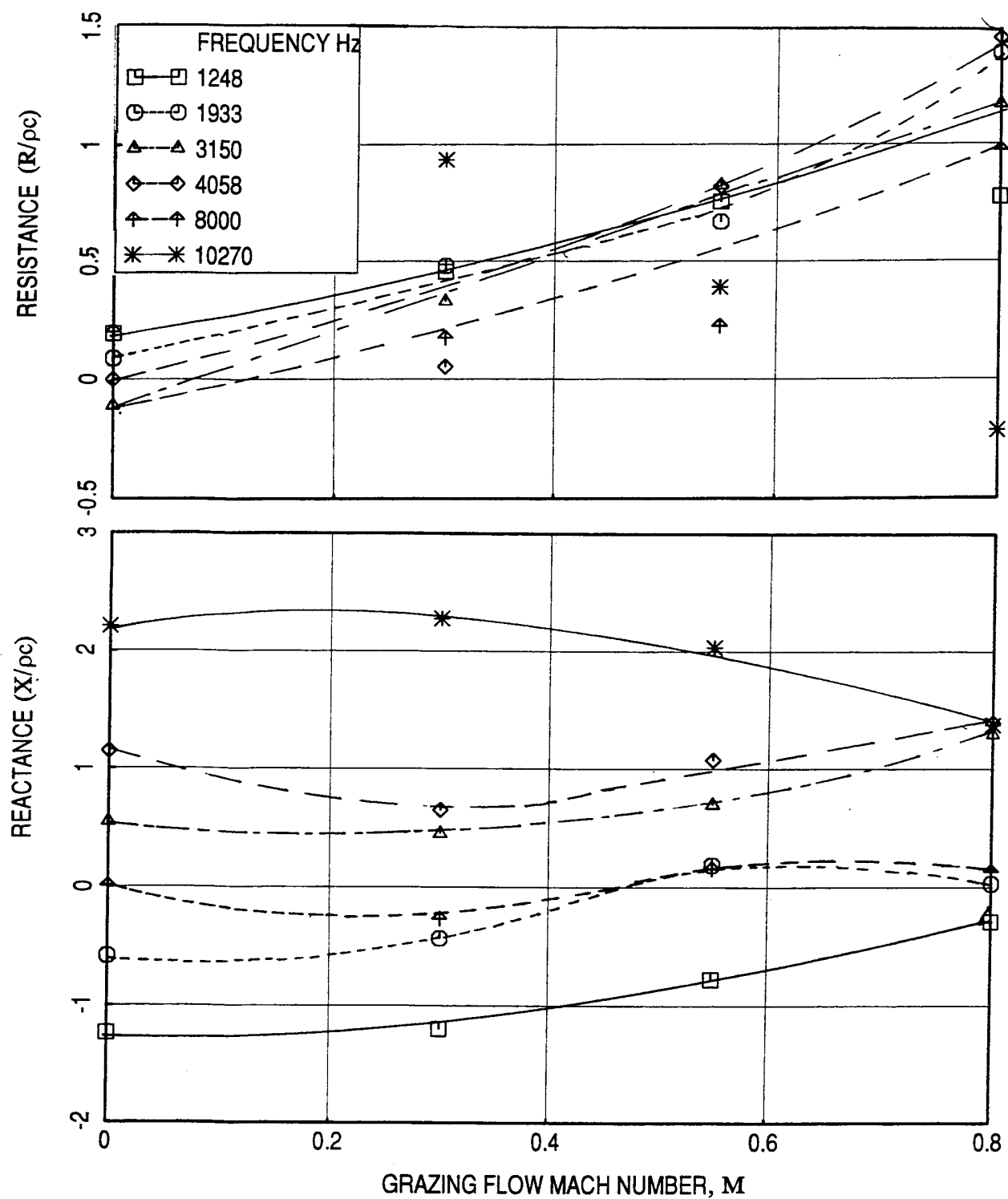


Figure 143. Effect of grazing flow Mach number (M) on in-situ impedance at different excitation frequencies for an 1"-deep SDOF type panel with perforated facesheet; $\sigma = 12.5\%$, $d = 0.039"$, $t = 0.025"$.

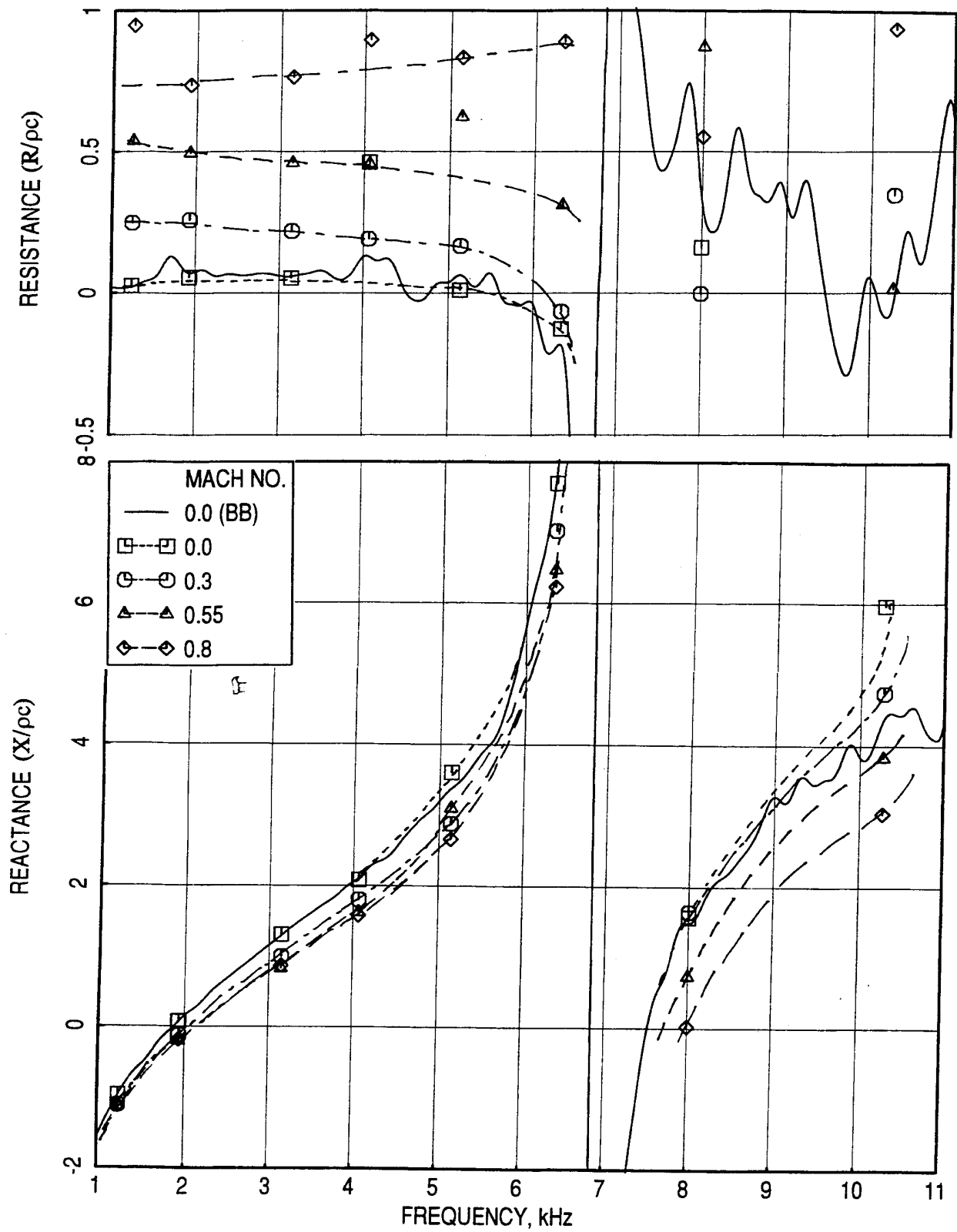


Figure 144. Effect of grazing flow Mach number (M) on in-situ impedance spectra for an 1"-deep SDOF type panel with perforated facesheet; $\sigma = 15\%$, $d = 0.125"$, $t = 0.08"$.

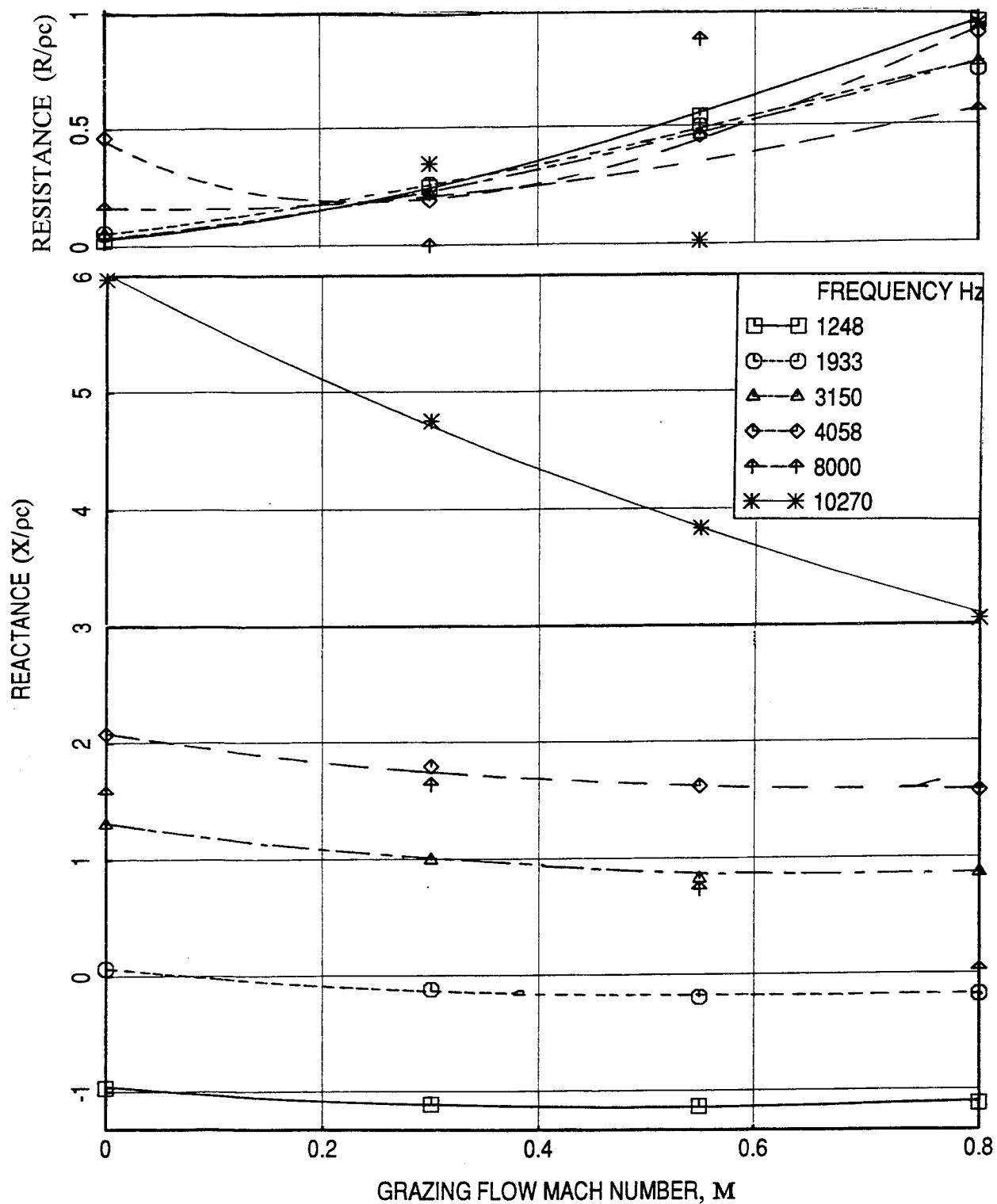


Figure 145. Effect of grazing flow Mach number (M) on in-situ impedance at different excitation frequencies for an 1"-deep SDOF type panel with perforated facesheet; $\sigma=15\%$, $d=0.125"$, $t=0.08"$.

reactance seems to decrease slightly with grazing flow, especially at higher frequencies. Similar results for the panels with porosities 12.5% ($d=0.035''$ and $t=0.025''$) and 15% ($d=0.125''$ and $t=0.08''$) are plotted in Figures 142 and 143 and Figures 144 and 145, respectively. The general behavior is the significant resistance increase with increasing grazing flow. Similar behavior is also observed for the perforated sheets with through flow, that the resistance increases significantly with increasing through flow [Ref. 27]. Due to the presence of flow, a portion of the acoustic energy is most probably converted into vortical energy, which is responsible for increasing the resistance.

For the fixed hole diameter ($d=0.039''$) and facesheet thickness ($t=0.025''$) the effect of porosity on in-situ impedance spectra is examined at different grazing flow Mach numbers and are shown in Figures 146 through 149. The resistance decreases with increasing porosity. The effect is more dominant at higher grazing flow Mach numbers. The reactance decreases with increasing porosity at lower grazing flow conditions. However, the trend reverses at higher grazing flow Mach numbers.

5.4.3 Boundary Layer Results :

Figure 150 shows the boundary layer profiles for three different panels at different grazing flow Mach numbers. The velocity profiles seem to be fully developed at this location and the boundary layer thicknesses are relatively higher. The effect of facesheet porosity on boundary layer profiles and skin friction coefficients are shown in Figure 151. The velocity profiles indicate that the boundary layer becomes more turbulent with increasing porosity. The skin friction increases with increasing porosity. The effect of panel depth (D) on boundary layer profiles and skin friction coefficients are shown in Figure 152. The boundary layer becomes more turbulent for the panel with lower depth (i.e., $D=0.42''$), which is opposite to the behavior observed in Figure 117. The skin friction is significantly higher for the thinner panel.

Since the boundary layer profiles are measured way downstream from the initiation of boundary layer the boundary layer is relatively thick compared to duct height. To examine the effect of a thinner boundary layer, a situation where the treatment panels be closer to the boundary layer initiation location, some amount of suction is applied for the 12.5% porous panel at two grazing flow Mach numbers. The suction is applied through the DC flow vacuum pump. The velocity profiles and the skin friction coefficients with and without suction are compared in Figure 153. Again, with suction, the boundary layer thickness is reduced and hence the skin friction coefficients increase due to increased slope (i.e., dU/dy).

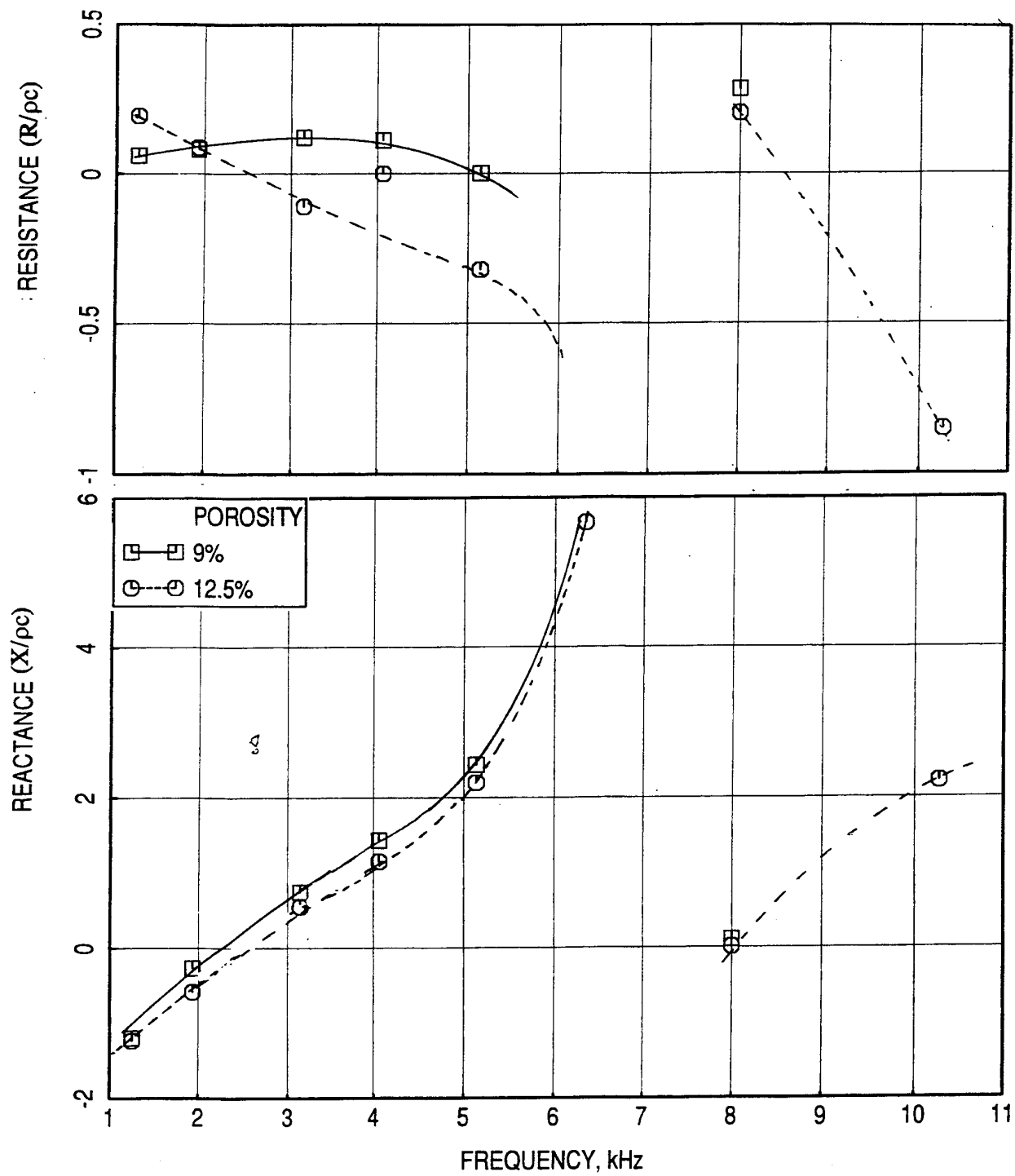


Figure 146. Effect of facesheet porosity on in-situ impedance spectra for 1"-deep SDOF type panels with perforated facesheets; $d=0.039$ ", $t=0.025$ ", $M=0$.

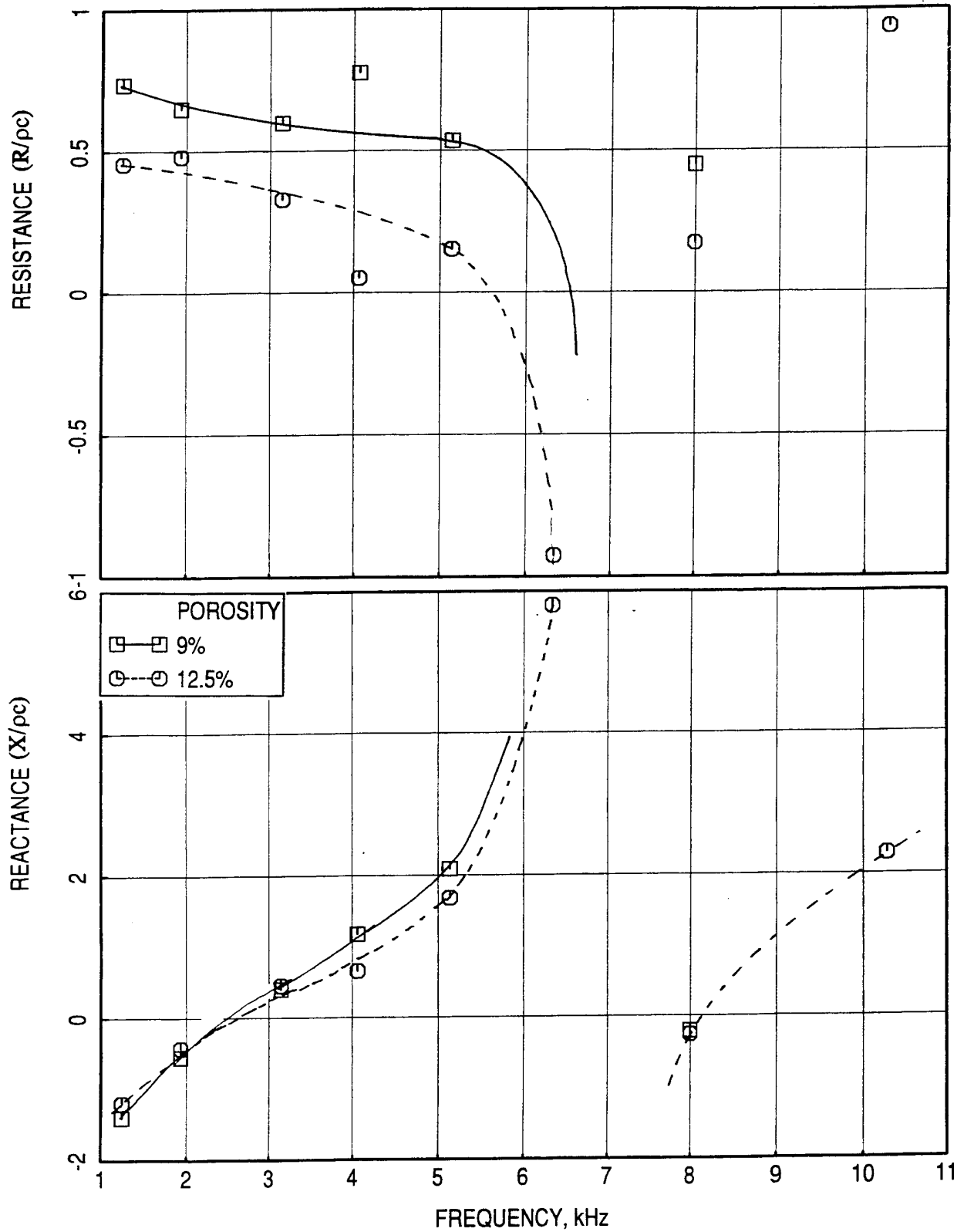


Figure 147. Effect of facesheet porosity on in-situ impedance spectra for 1"-deep SDOF type panels with perforated facesheets; $d=0.039"$, $t=0.025"$, $M=0.3$.

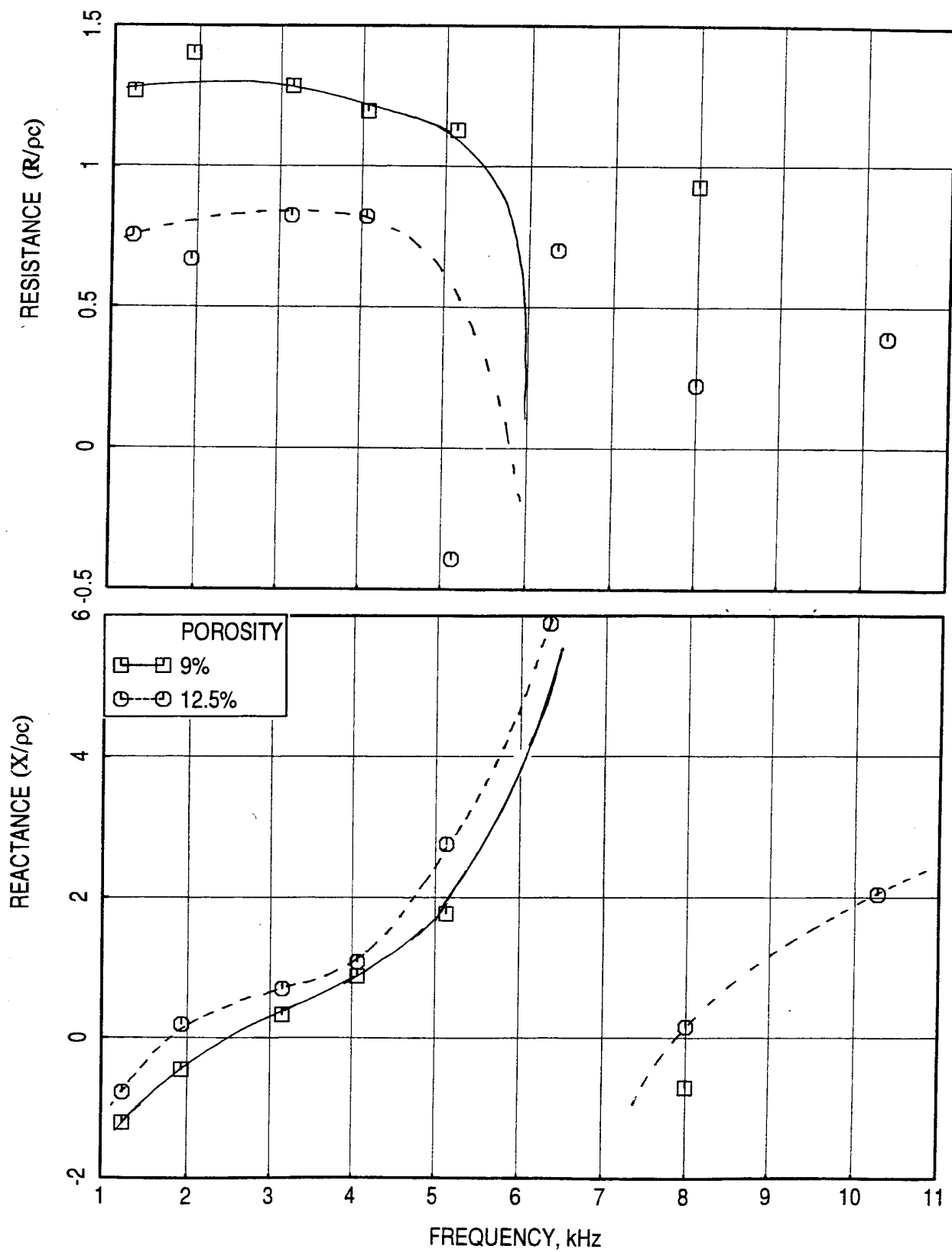


Figure 148. Effect of facesheet porosity on in-situ impedance spectra for 1"-deep SDOF type panels with perforated facesheets; $d=0.039"$, $t=0.025"$, $M=0.55$.

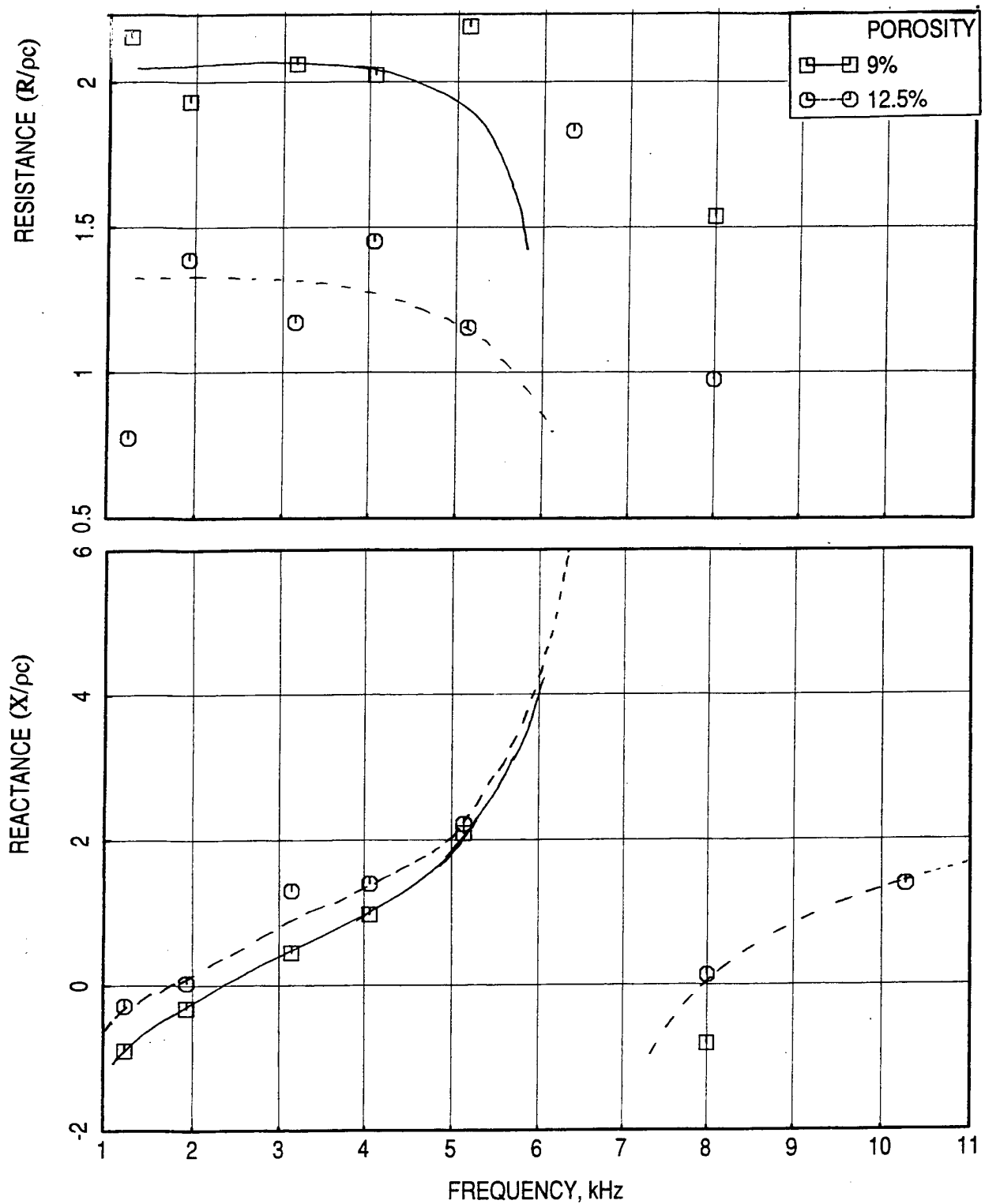


Figure 149. Effect of facesheet porosity on in-situ impedance spectra for 1"-deep SDOF type panels with perforated facesheets; $d=0.039"$, $t=0.025"$, $M=0.8$.

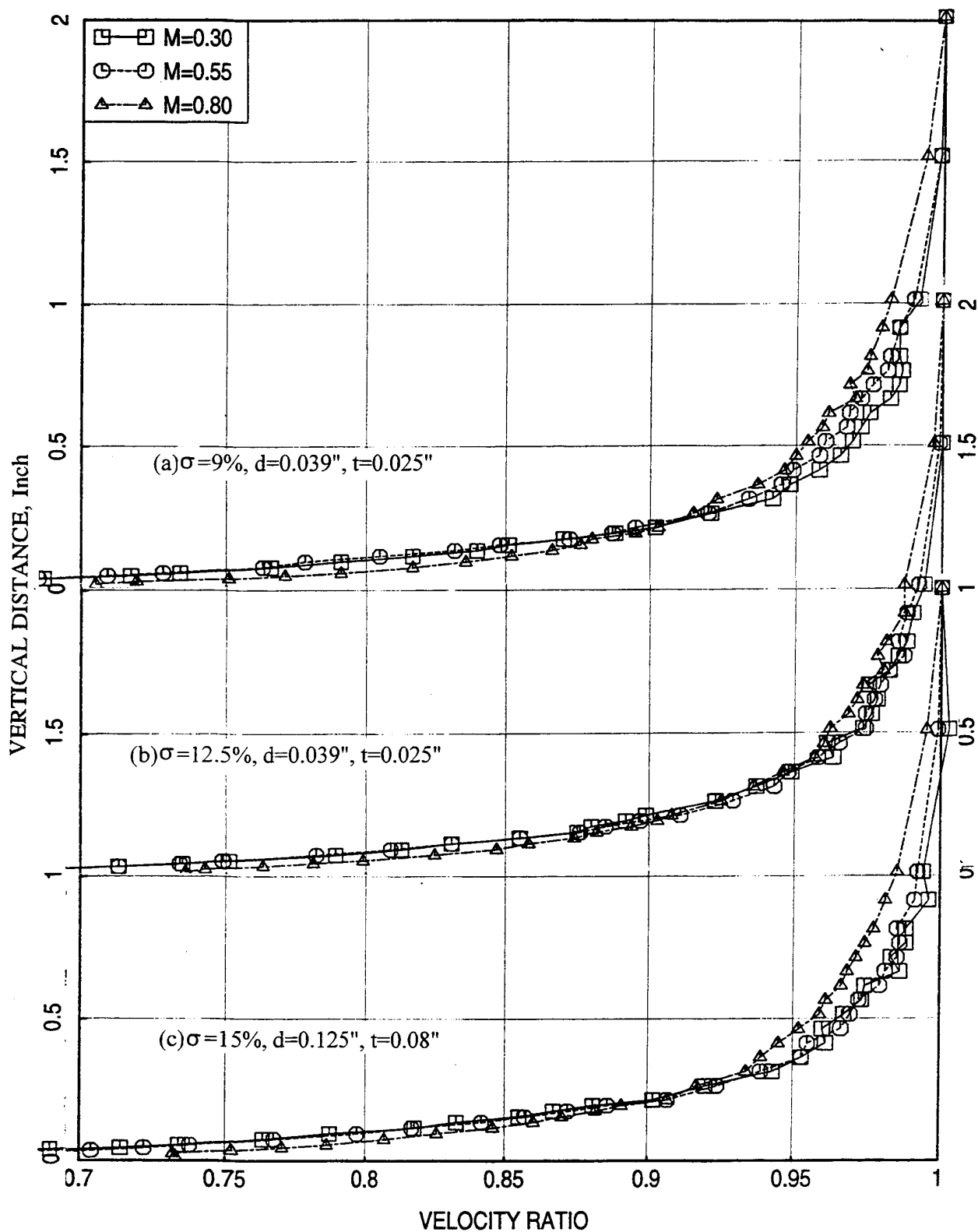


Figure 150. Effect of grazing flow Mach number (M) on velocity profile in the flow duct for 1"-deep SDOF type panels with perforated facesheets.

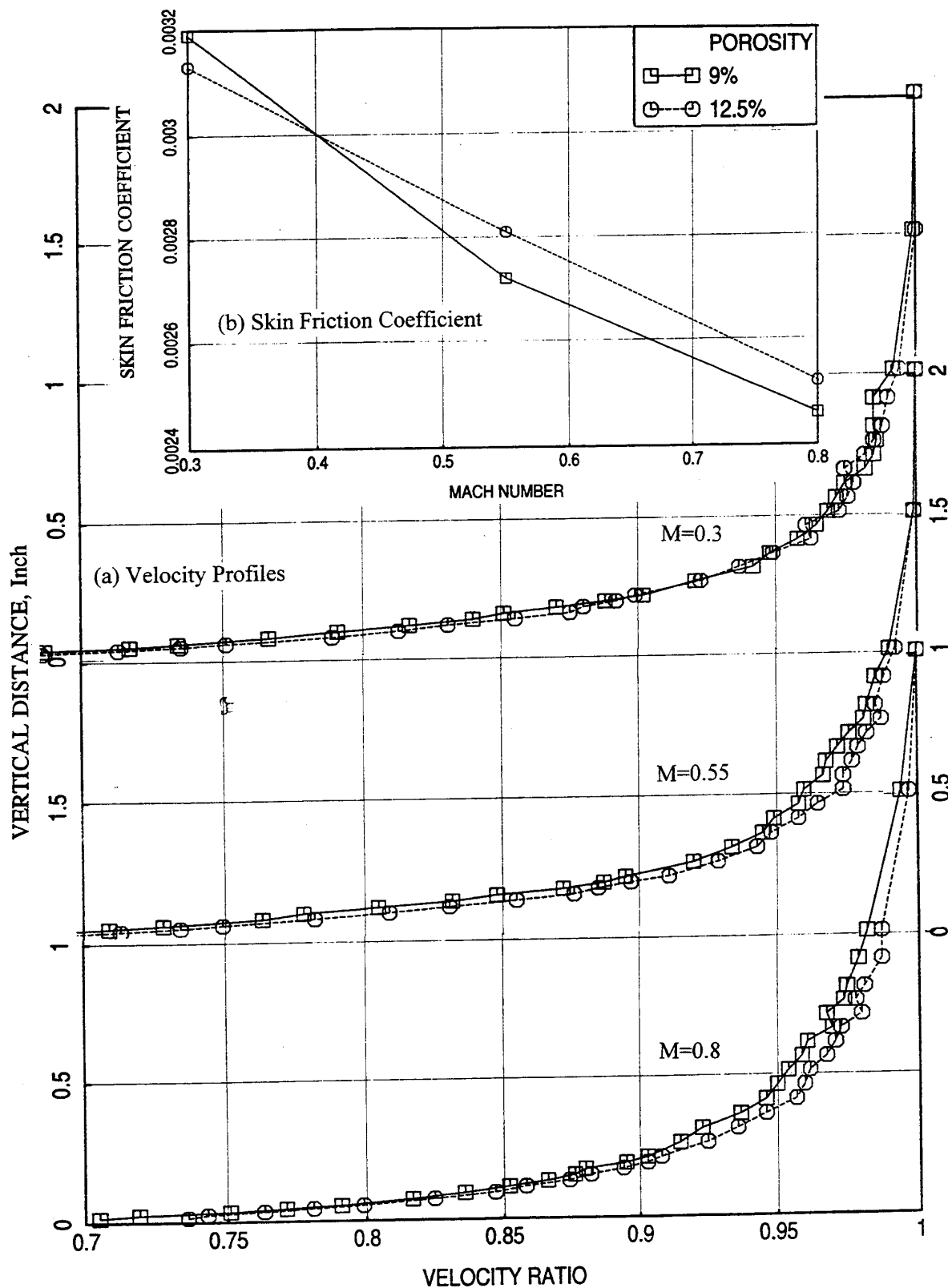


Figure 151. Effect of facesheet porosity on (a) velocity profile in the flow duct and (b) local skin friction coefficient for 1"-deep SDOF type panels with perforated facesheets; $d=0.039"$, $t=0.025"$.

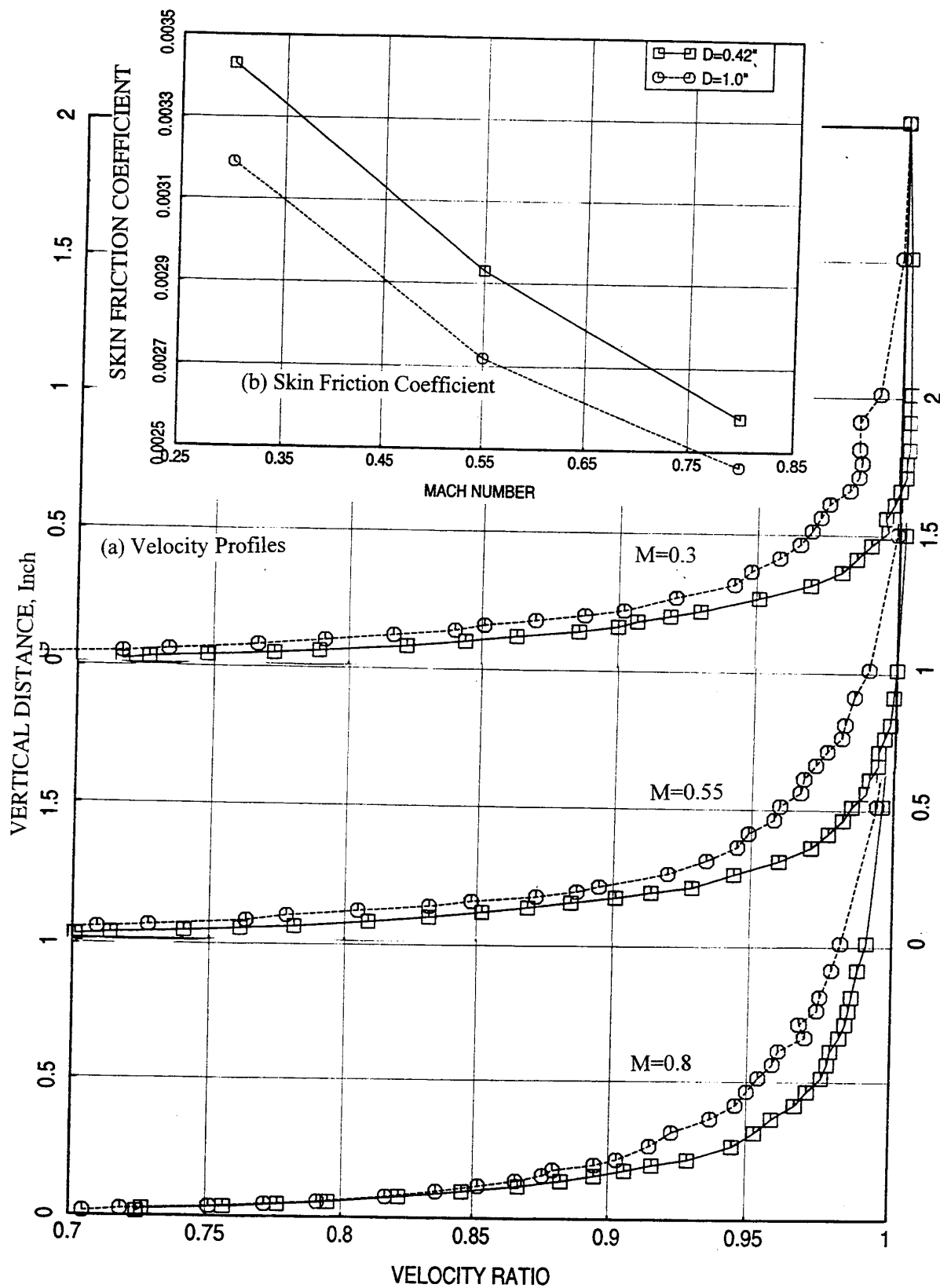


Figure 152. Effect of panel depth D on (a) velocity profile in the flow duct and (b) local skin friction coefficient for SDOF type panels with perforated facesheets; $\sigma = 9\%$, $d = 0.039$ ", $t = 0.025$ ".

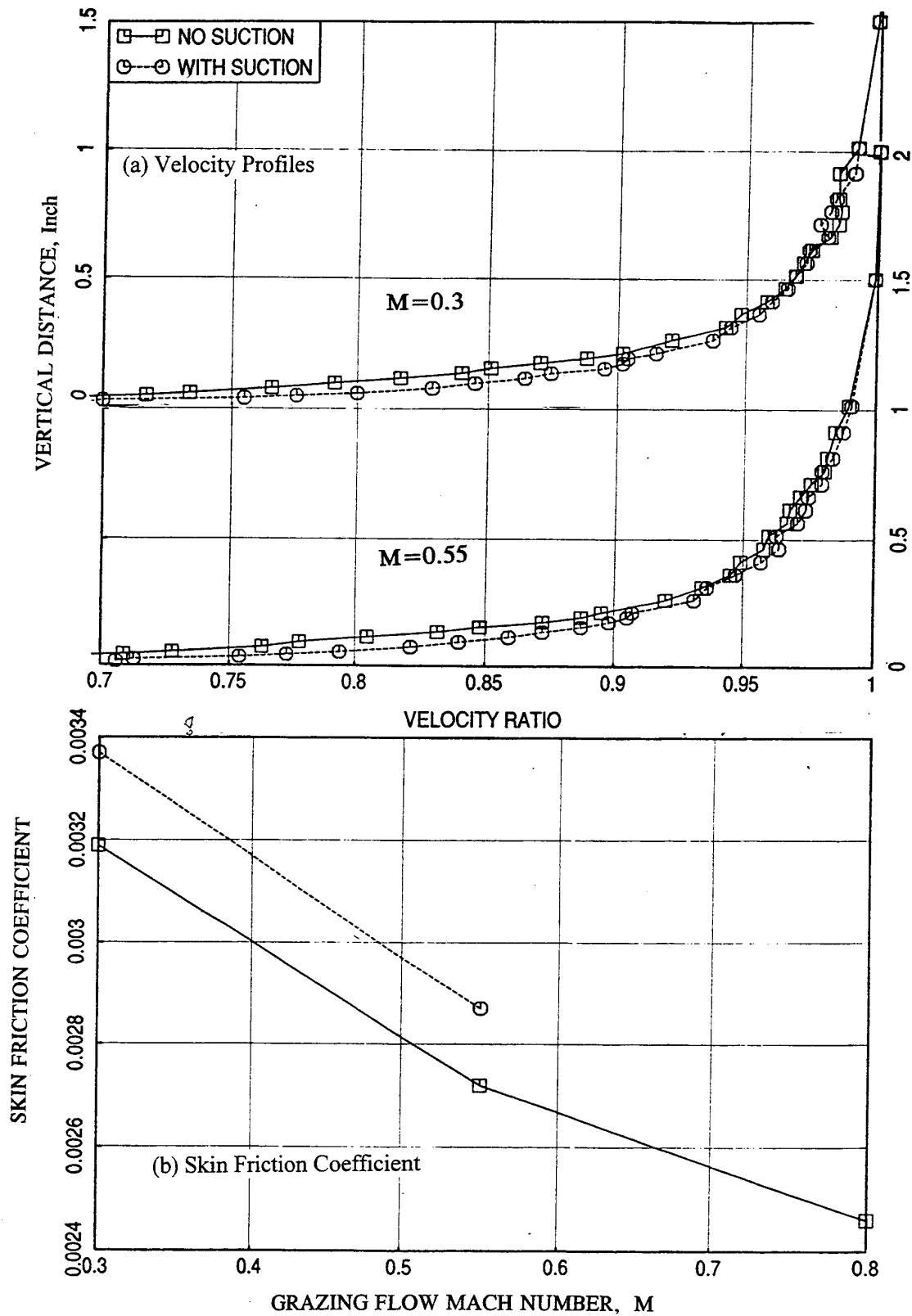


Figure 153. Effect of suction on (a) velocity profile in the flow duct and (b) local skin friction coefficient for an 1"-deep SDOF type panel with perforated facesheet; $S=12.5\%$, $d=0.039"$, $t=0.025"$.

5.4.4 Insertion Loss Results:

Effect of Grazing Flow:

Acoustic insertion loss for all the 1"-thick SDOF type panels are evaluated at different grazing flow Mach numbers. Typical results are shown in Figure 154. Since, these panels are 1"-deep, the tuning frequencies at which the most acoustic suppression is expected are relatively low. Based on the data of Figure 154, it appears, that the most acoustic suppression for these panels is occurring at frequencies up to about 4 kHz.

Effect of Porosity (σ): The effect of porosity on insertion loss spectra at various grazing flow conditions are shown in Figure 155. While the insertion loss levels for the panel with porosity 7.5% are higher at no flow condition, the levels become very close to each other in the presence of flow.

Effect of Hole Diameter (d): The effect of facesheet hole diameter on insertion loss spectra at various grazing flow conditions are shown in Figure 156. Facesheet with higher hole diameter seems to suppress more at no flow condition. However, the trend gradually reversed with increasing flow Mach number.

Effect of Thickness (t): The effect of facesheet thickness on insertion loss spectra at various grazing flow conditions are shown in Figure 157. Acoustic suppression seems to be higher for the panel with thicker facesheet.

Effect of Panel Depth (D): Panels with the same facesheet properties ($\sigma=95$, $d=0.039''$, and $t=0.025''$) but with different depths (i.e., 0.16'', 0.25'', and 0.42'') from set#1 panels are tested. One among the instrumented panels of 1"-deep has the same facesheet characteristics. Thus, the results of set #1 and set #5 are combined together to study the effect of the panel depth only. Figure 158 shows the effect of depth on normal impedance for set #1 panels (normal impedance is not measured for set #5 panels). Reactance levels are higher for deeper samples due to cavity effect. The resistance levels are expected to be the same for all three panels. Cavity depth plays an important role in normal resistance measurement. The low frequency data is more accurate if the cavity behind the facesheet is deeper. Thus, the low frequency range at which the inaccuracy in resistance occurs increases with decreasing cavity depth. Figure 158 indicates this phenomena. For 0.16"-deep panel the resistance is expected to agree with those of other two panels at least above 7 kHz. However, for 0.16"-deep panel the resistance levels are higher even above 7 kHz. This could be the result of increased blockage in the process of facesheet-honeycomb installation, which might have contributed to

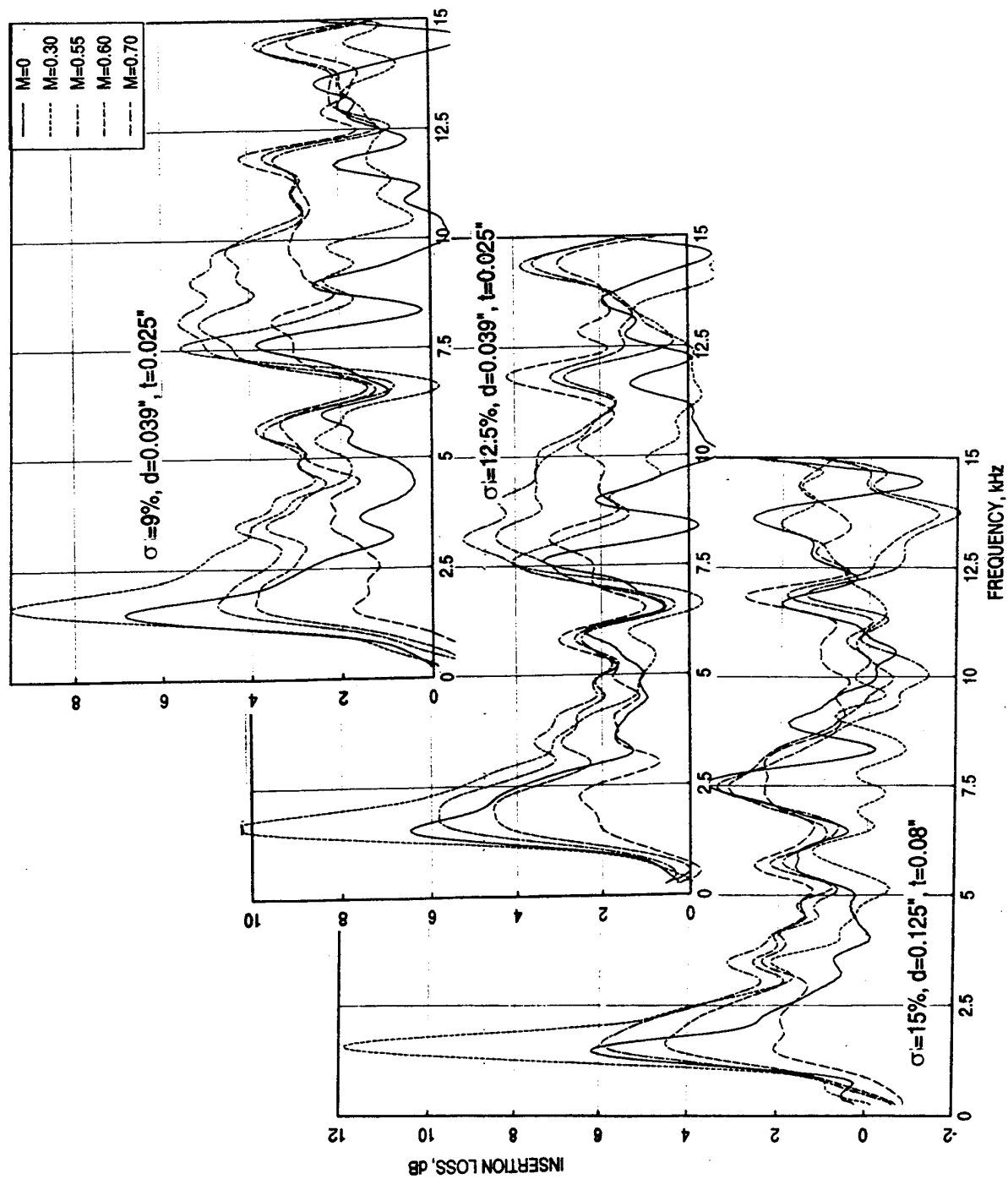


Figure 154. Influence of grazing flow Mach number (M) on insertion loss spectra for 1"-deep SDOF type panels with perforated facesheets.

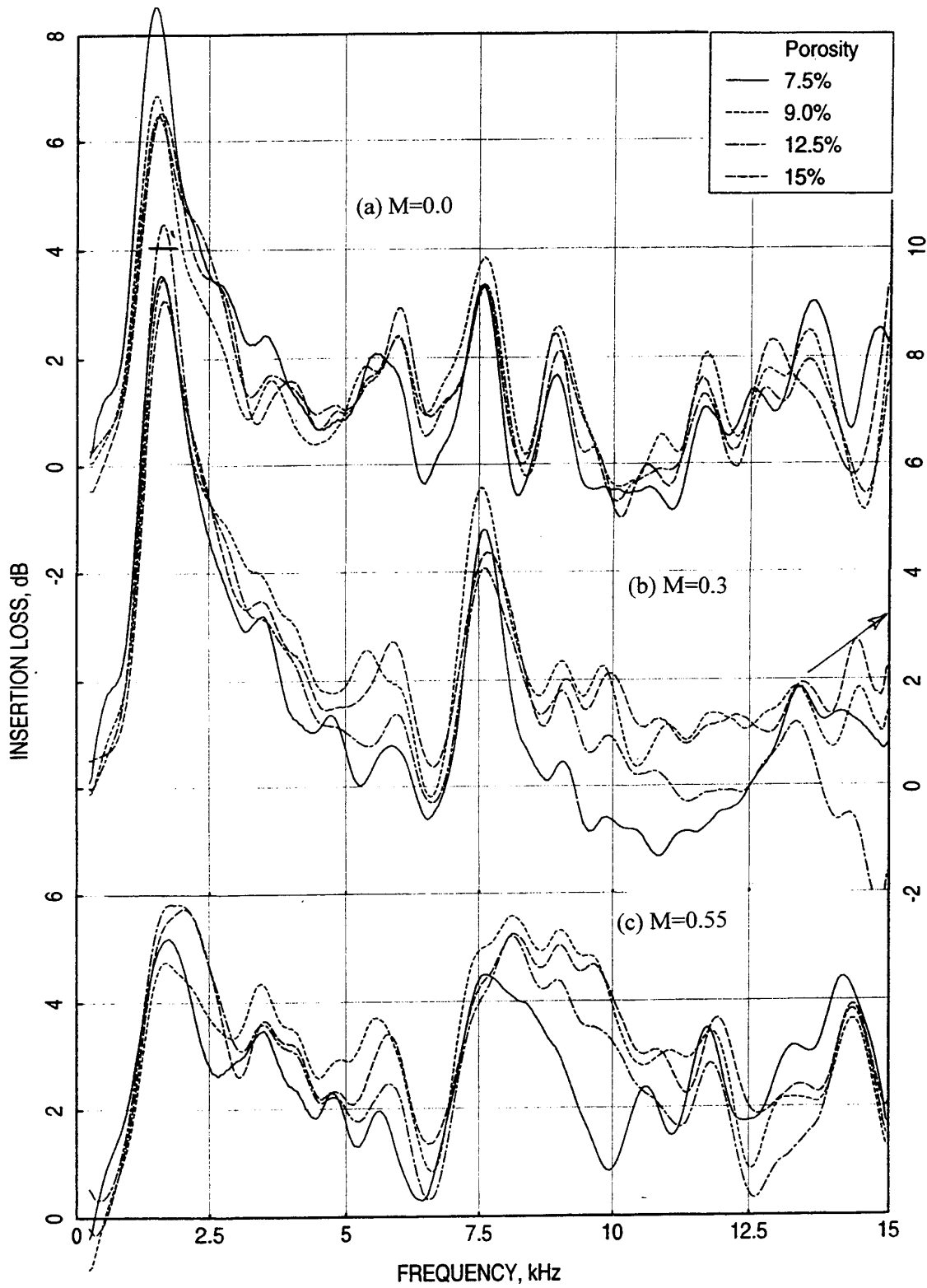


Figure 155. Effect of facesheet porosity (S) on insertion loss spectra at various grazing flow Mach numbers (M) for 1"-deep SDOF type panels with perforated facesheets; $d=0.039"$, $t=0.025"$.

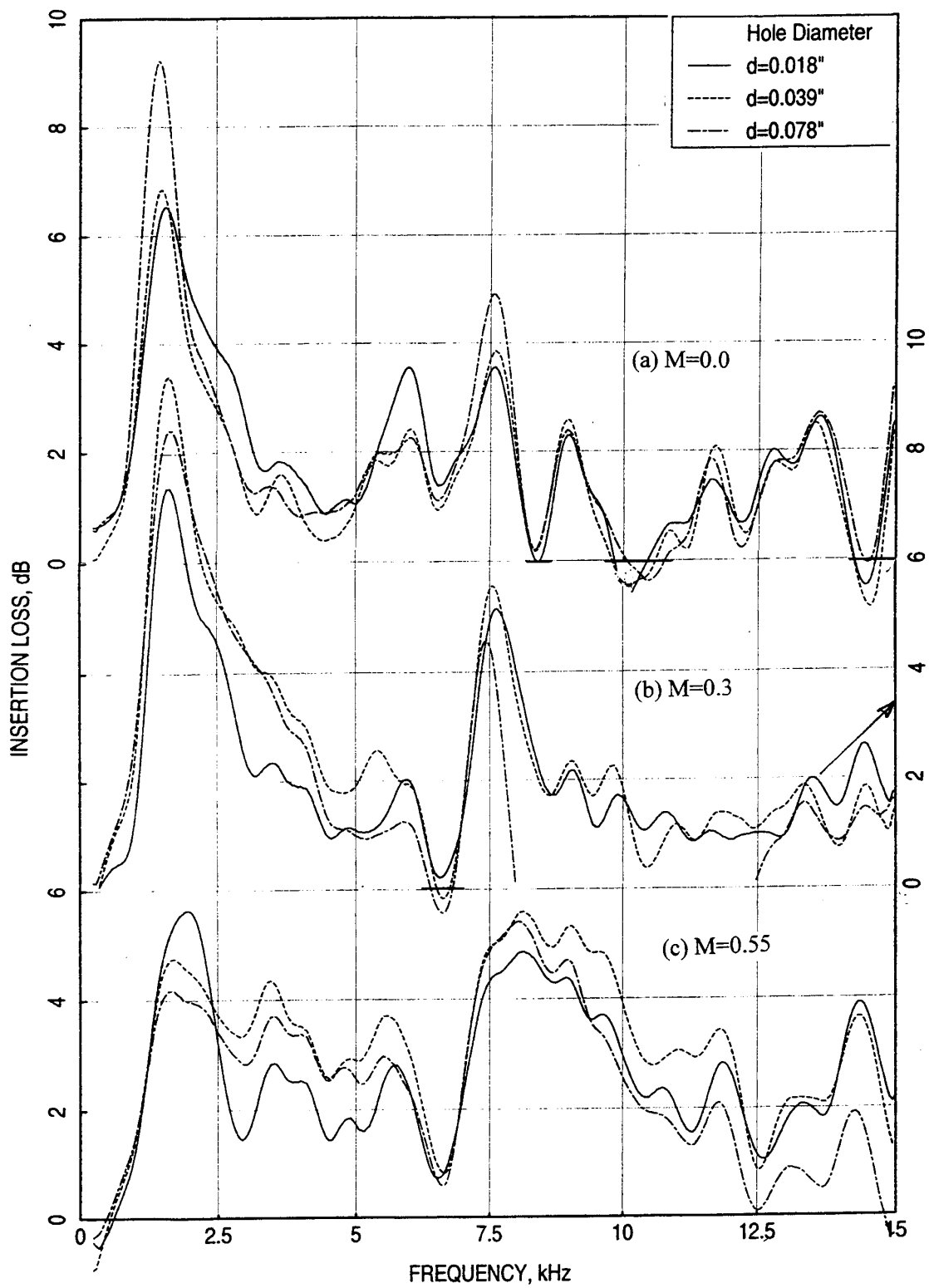


Figure 156. Effect of facesheet hole diameter (d) on insertion loss spectra at various grazing flow Mach numbers (M) for 1"-deep SDOF type panels with perforated facesheets: $\sigma=9\%$, $t=0.025''$.

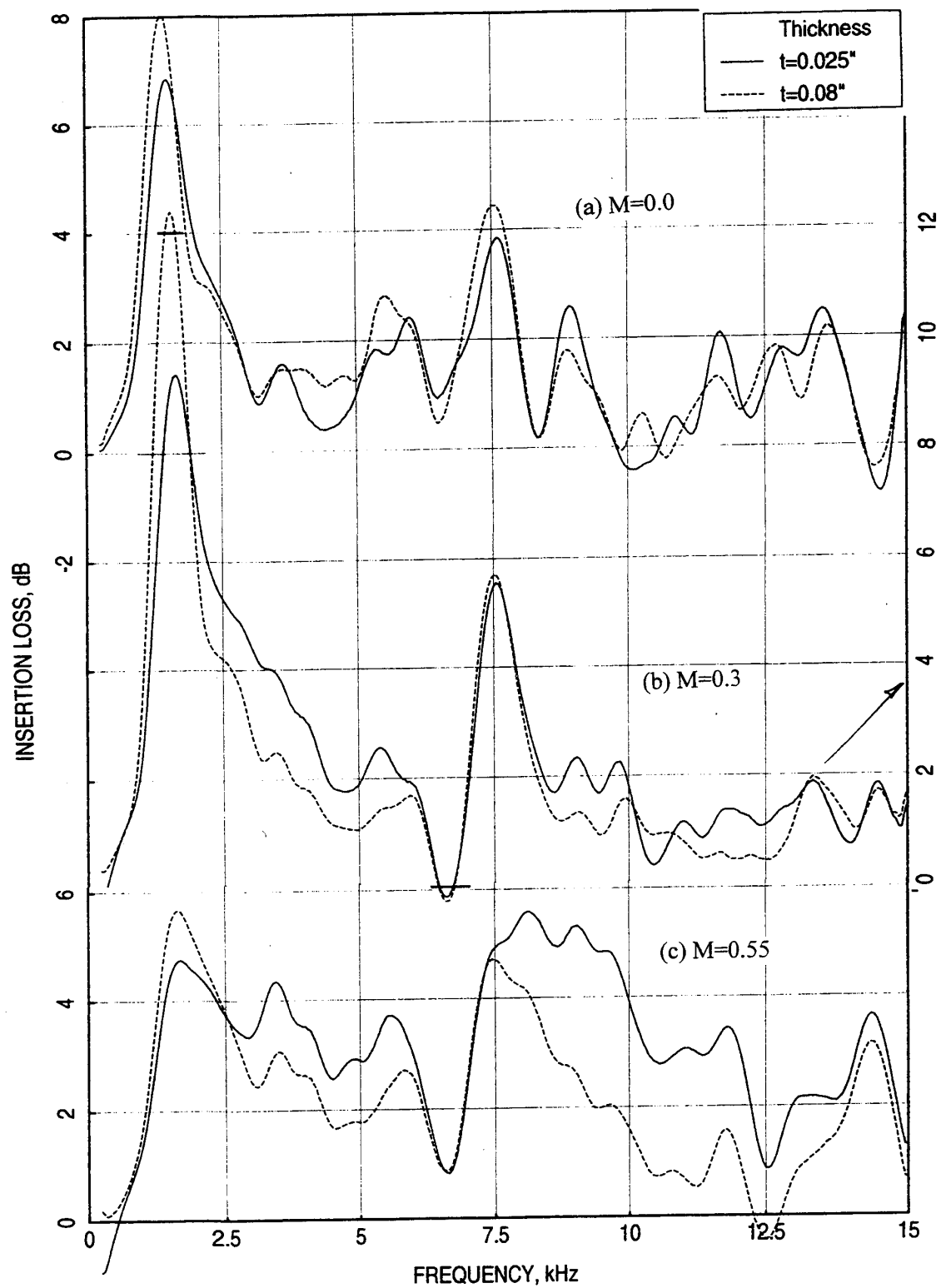


Figure 157. Effect of facesheet thickness (t) on insertion loss spectra at various grazing flow Mach numbers (M) for 1"-deep SDOF type panels with perforated facesheets; $\sigma=9\%$, $d=0.039"$.

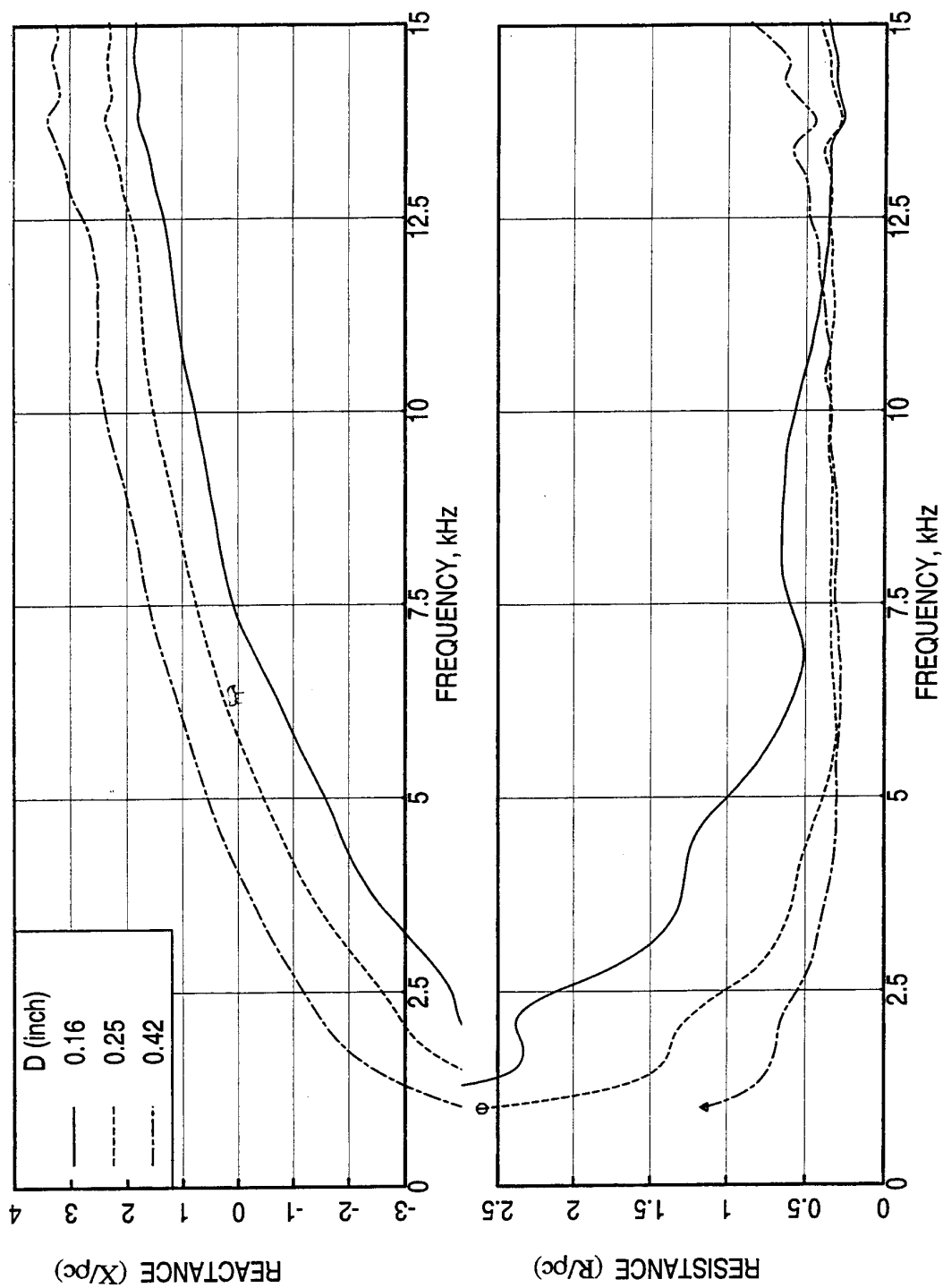


Figure 158 Effect of panel depth D on normal impedance spectrum for SDOF type panels with perforated facesheet, $\sigma=9\%$, $d=0.039''$, $t=0.025''$.

the resistance level increase. The insertion loss data presented in Figures 159 and 160 indicate shift of peak levels towards higher frequency with decreasing panel depth.

5.5. Acoustic Characteristics of SDOF Type Panels with Linear Facesheets:

Linear Facesheet SDOF Panels : As shown in Figure 73, this design is similar to those of SDOF type liners with perforated facesheets, except the facesheet, which is linear in nature. Three 5"X12" SDOF type panels with linear facesheets of different resistivity, namely, 50, 85, and 130 Rayls, and with a nominal nonlinear factor of 1.325 (NLF) are manufactured for flow duct tests (see Table 17).

DC Flow and Normal Impedance Results : DC flow resistance parameters, as evaluated experimentally, are listed in Table 17. Figure 161 shows the effect of excitation level on normal impedance spectra for the three linear facesheet panels of different resistivity. The effect is insignificant on the reactance for all three panels. However, for resistance the effect of excitation level is very little for the panels with wiremesh facesheets of 50 and 85 Rayls resistivity, whereas, the panel with the facesheet of 130 Rayls resistivity shows some amount of nonlinearity, that the resistance increases with excitation level. It should be noted that the facesheet for this panel is a wiremesh bonded to a perforated sheet. The effect of facesheet resistivity on normal impedance is shown in Figure 162. The reactance and the resistance of the panel increase with increasing resistivity.

Boundary Layer Results : The effect of facesheet resistivity on boundary layer profiles and skin friction coefficients are shown in Figure 163. The effect seems to be insignificant on boundary layer profiles as well as on skin friction.

Insertion Loss Results : Figures 164 through 166 show the insertion loss spectra at different grazing flow Mach number for the three SDOF panels with different linear facesheet resistivity. The results are presented both in terms of 1/3-octave band and narrowband basis. In general, the insertion loss decreases with flow for all three cases. The effect of facesheet resistivity on insertion loss spectra at different grazing flow conditions is shown in Figure 167. Facesheet resistivity has insignificant effect on insertion loss, especially at $M=0$ and 0.3. At higher flow conditions, the insertion loss is lower for the panel with the facesheet of $R_{100}=130$ Rayls.

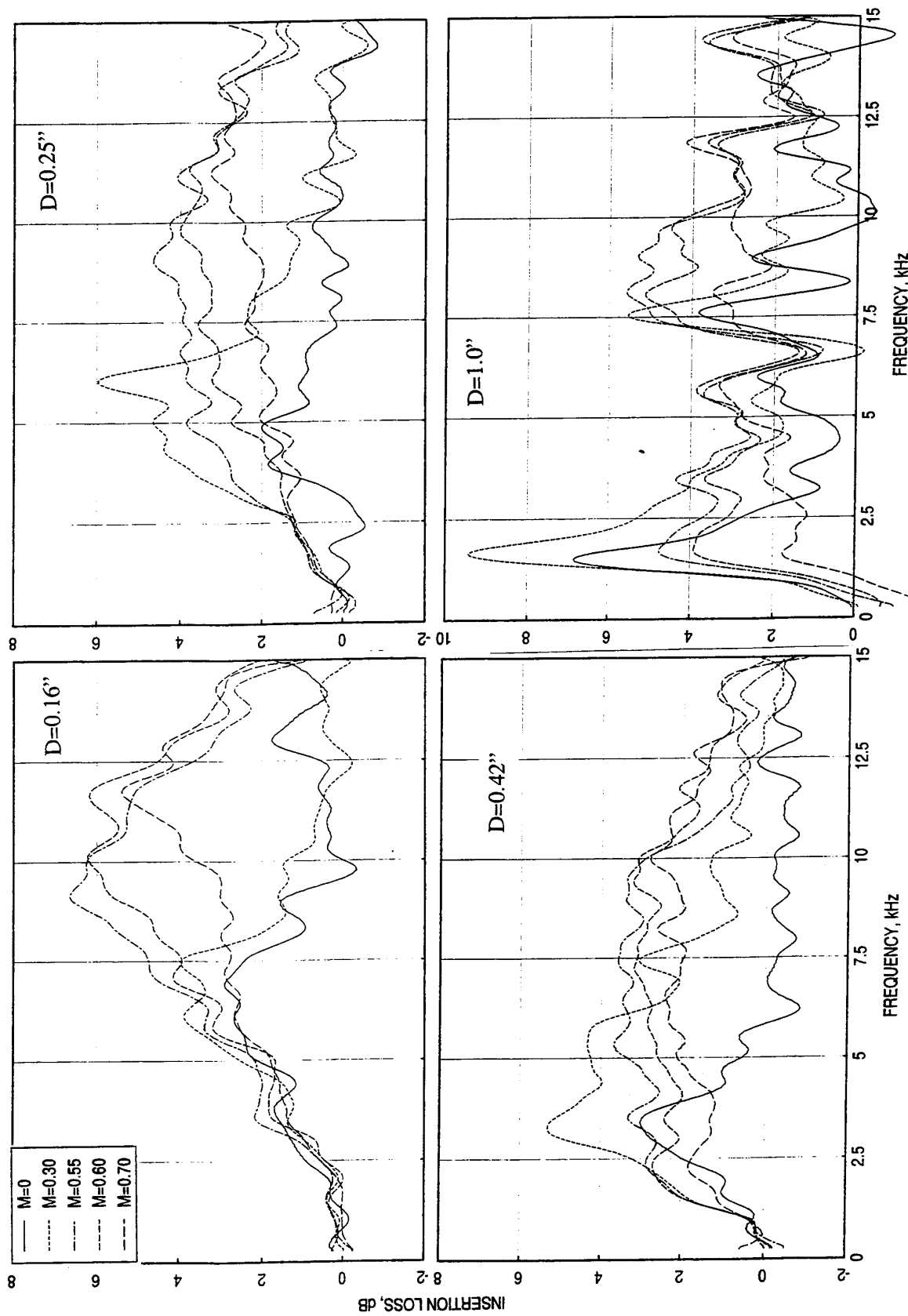


Figure 159. Influence of grazing flow Mach number (M) on insertion loss spectra for four SDOF panels of different depth with perforated facesheet, measured in a 4"-high (H) flow duct, mounted on one side; $\sigma=9\%$, $d=0.039$ ", $t=0.025$ ".

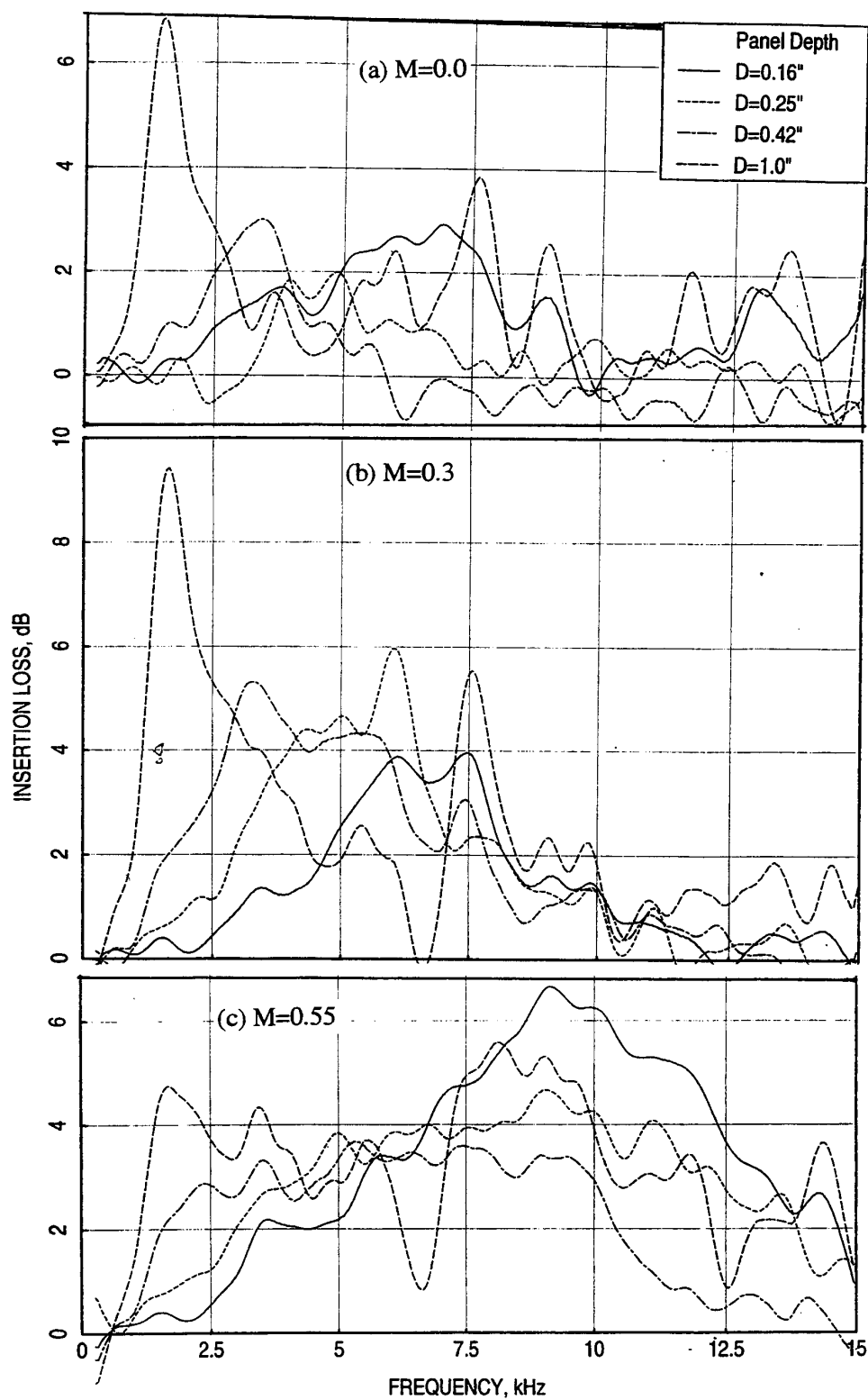


Figure 160. Effect of panel depth D on insertion loss spectrum for SDOF type panels with perforated facesheet, measured in a 4"- high (H) flow duct, mounted on one side, $\sigma=9\%$, $d=0.039''$, $t=0.025''$.

Table 17. Geometrical Properties, DC Flow Resistance Parameters, and File Names for Normal Impedance and Insertion Loss Data for SDOF Type Panels with Linear Facesheets, 0.38" deep, 3/8" size Honeycomb Structure of 0.003" thick wall.

Panel Config. #	Sample # for DC Flow Tests	Sample # for Normal Impedance Tests	Nominal Resistivity, R_{90} in Rayls	Nominal NLF (R_{150}/R_{30})	A Rayls	B Rayls/cm	R100 Rayls	NLF (R_{150}/R_{20})	Normal Impedance File @ 130 dB OASPL	Normal Impedance File @ 150 dB OASPL	Normal Impedance File @ 158 dB OASPL	Insertion Loss 1/3-Octave Band Data Files	Insertion Loss Narrowband Data Files
2.2	2.5	2.8	50	1.325	46.21	0.03	49.47	1.09	m280-0375130.dat	wbs28.smt	wbs28h.smt	ffwbs2-2.dat	rwbs2-2.smt
2.1	2.4	2.7	85	1.325	78.58	0.05	83.44	1.08	m270-0375130.dat	wbs27.smt	wbs27h.smt	ffwbs2-1.dat	rwbs2-1.smt
2.3	2.6	2.9	130	1.325	114.58	0.32	146.36	1.34	m290-0375130.dat	wbs29.smt	wbs29h.smt	ffwbs2-3.dat	rwbs2-3.smt

Note: 1. Panel Config #: Panels of 12"x5" Treated area tested for Insertion Loss Measurement in a Flow Duct of 4" height with one side treated (i.e., the duct height becomes 8").
2. Sample # - Samples for DC Flow Resistance & Normal Impedance Tests, identical to the corresponding panel geometry (for DC flow resistance backplates not used).

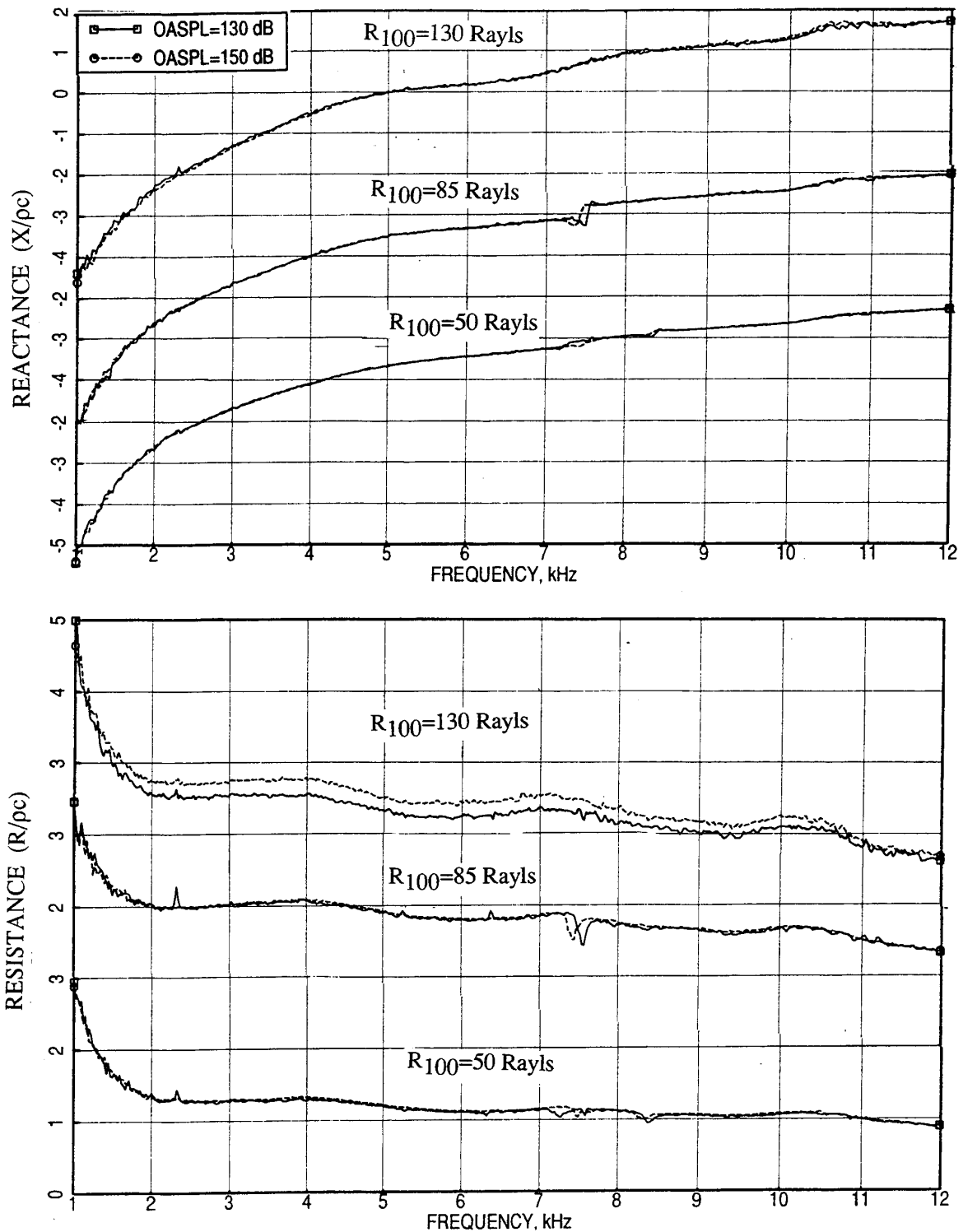


Figure 161. Effect of excitation level on normal impedance spectra for linear face sheets of different resistivities (R_{100}) bonded to 0.38" deep and 0.375" wide (cell size) honeycomb structures with a rigid backplate.

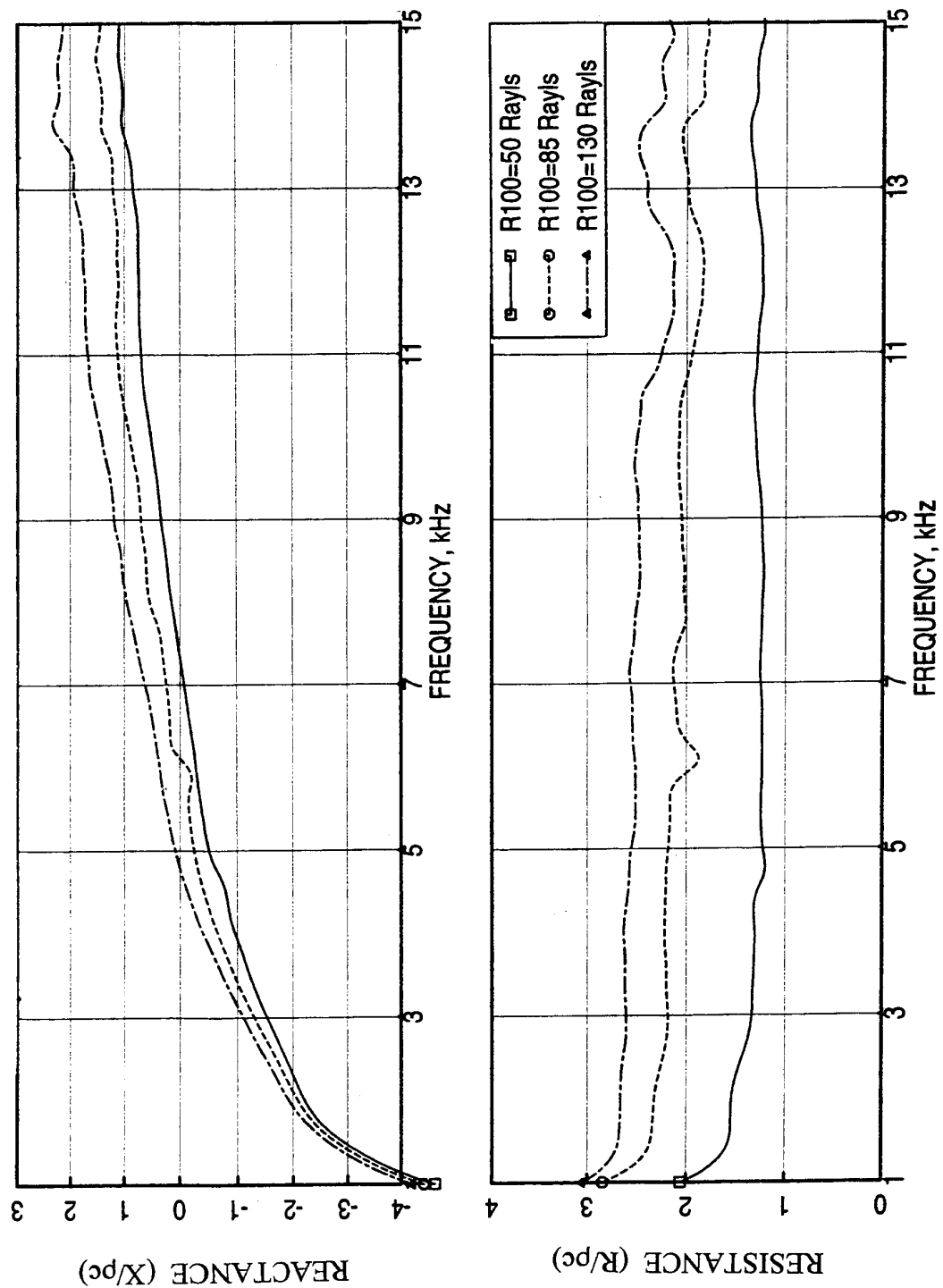


Figure 162. Effect of linear face sheet resistivity (R_{100}) on the normal impedance spectra for the facesheets bonded to 0.38" deep and 0.375" wide (cell size) honeycomb structures with a rigid backplate, OASPL=150dB.

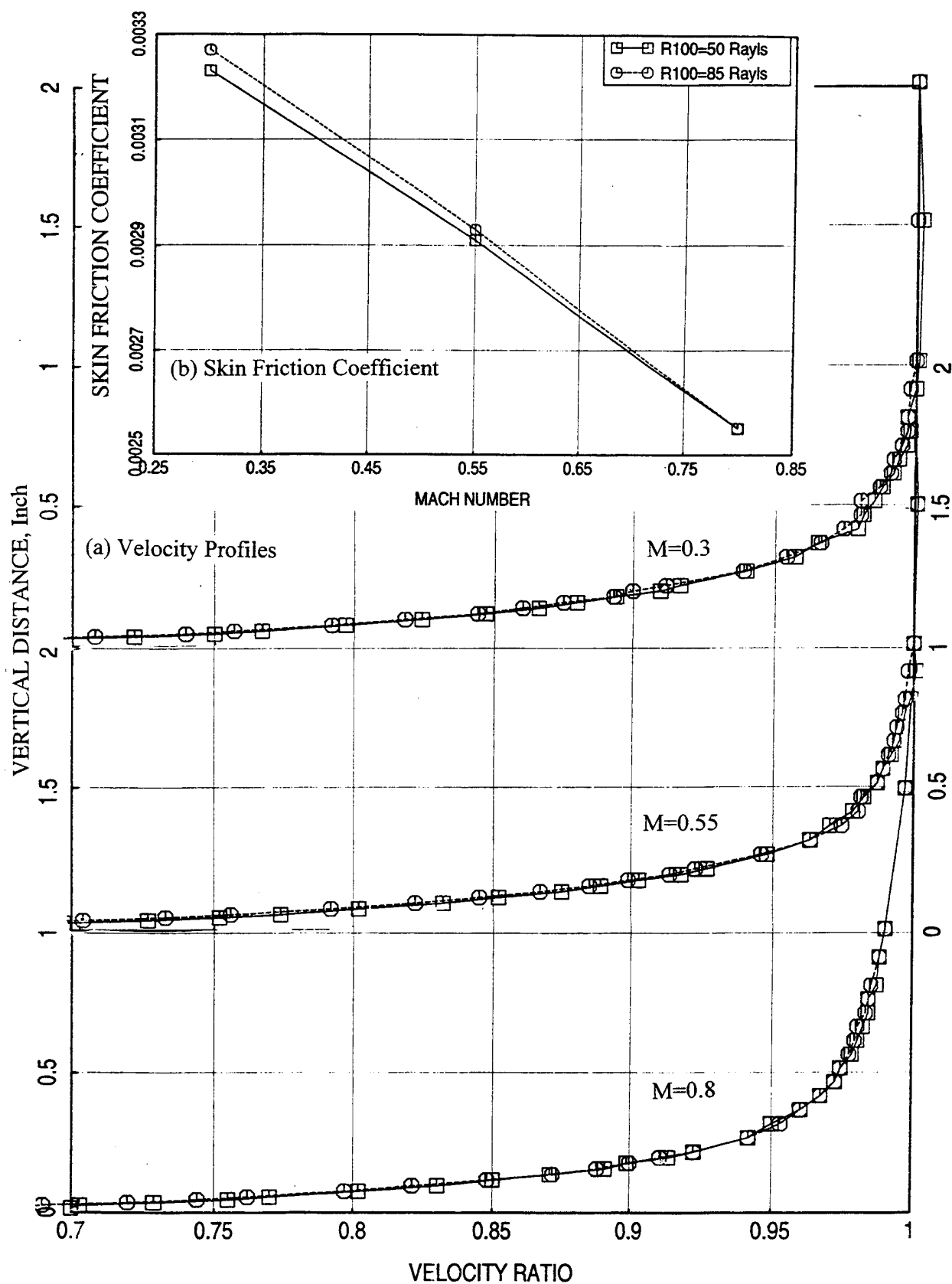


Figure 163. Effect of facesheet resistivity on (a) velocity profile in the flow duct and (b) local skin friction coefficient for 0.38"-deep SDOF type panels with linear facesheets.

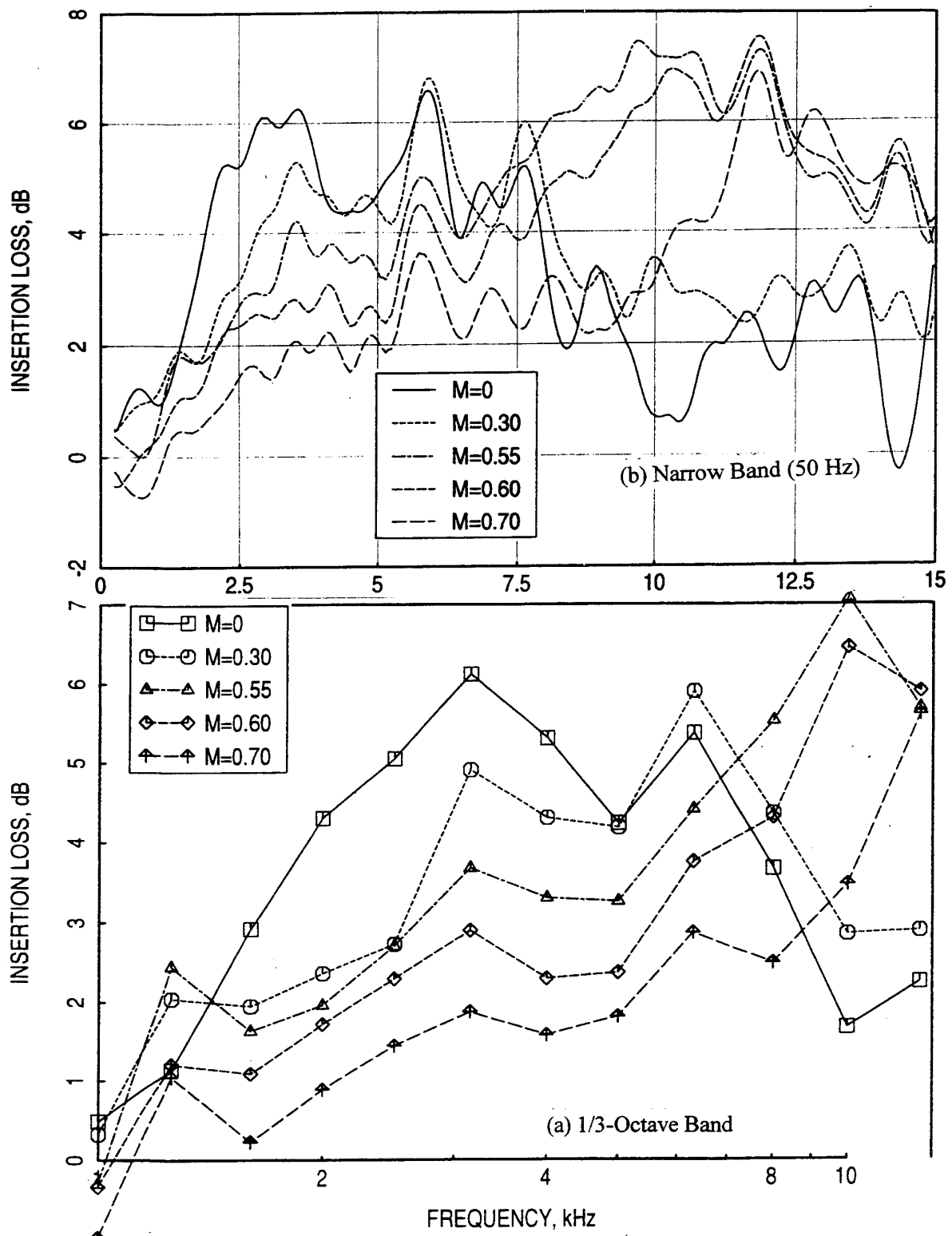


Figure 164. Influence of grazing flow Mach number on insertion loss spectra for an SDOF type panel with linear facesheet, mounted on one side of the 4"-high flow duct; $R100=50$ Rayls, $D=0.38$ ".

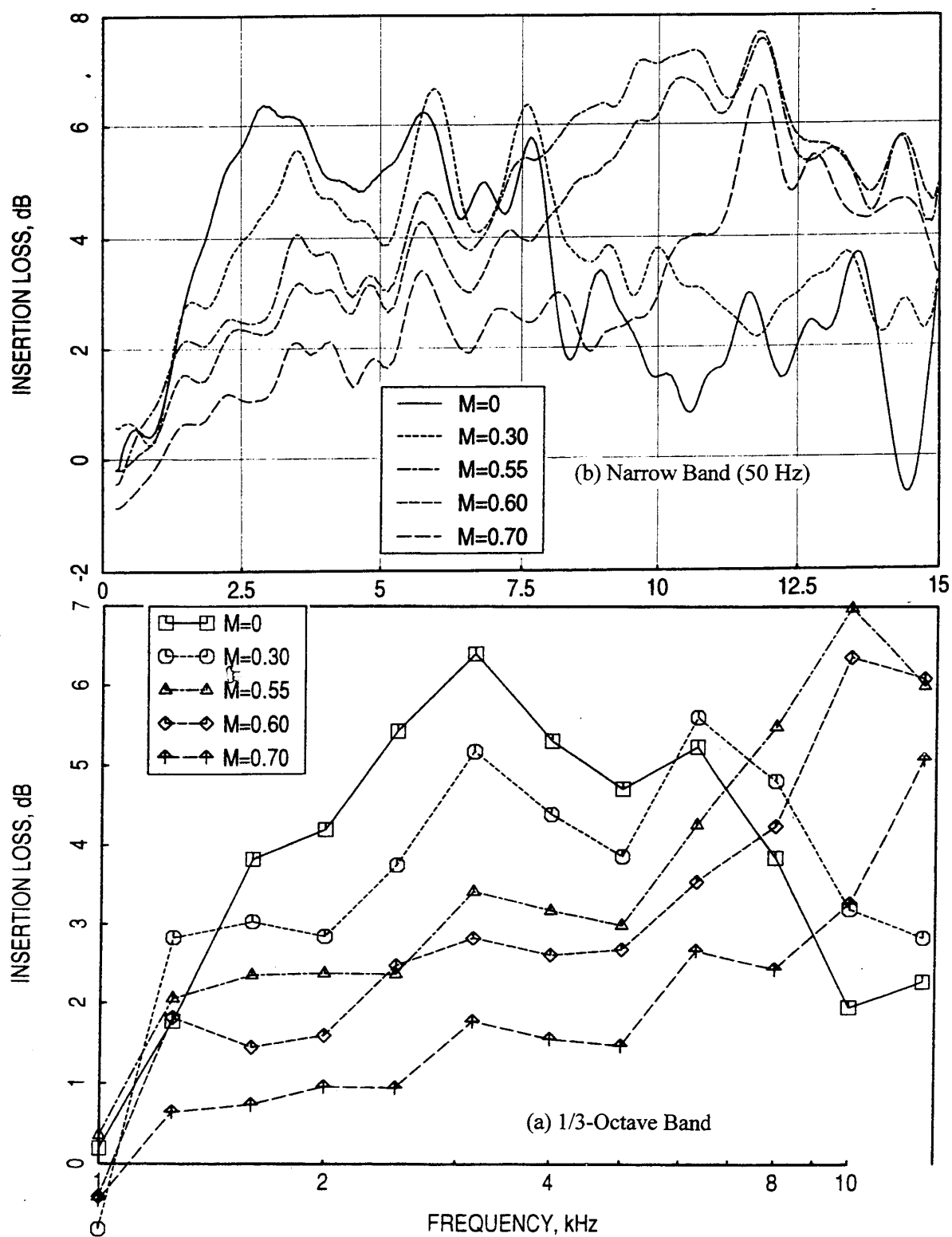


Figure 165. Influence of grazing flow Mach number on insertion loss spectra for an SDOF type panel with linear facesheet, mounted on one side of the 4"-high flow duct; R100=85 Rayls, D=0.38".

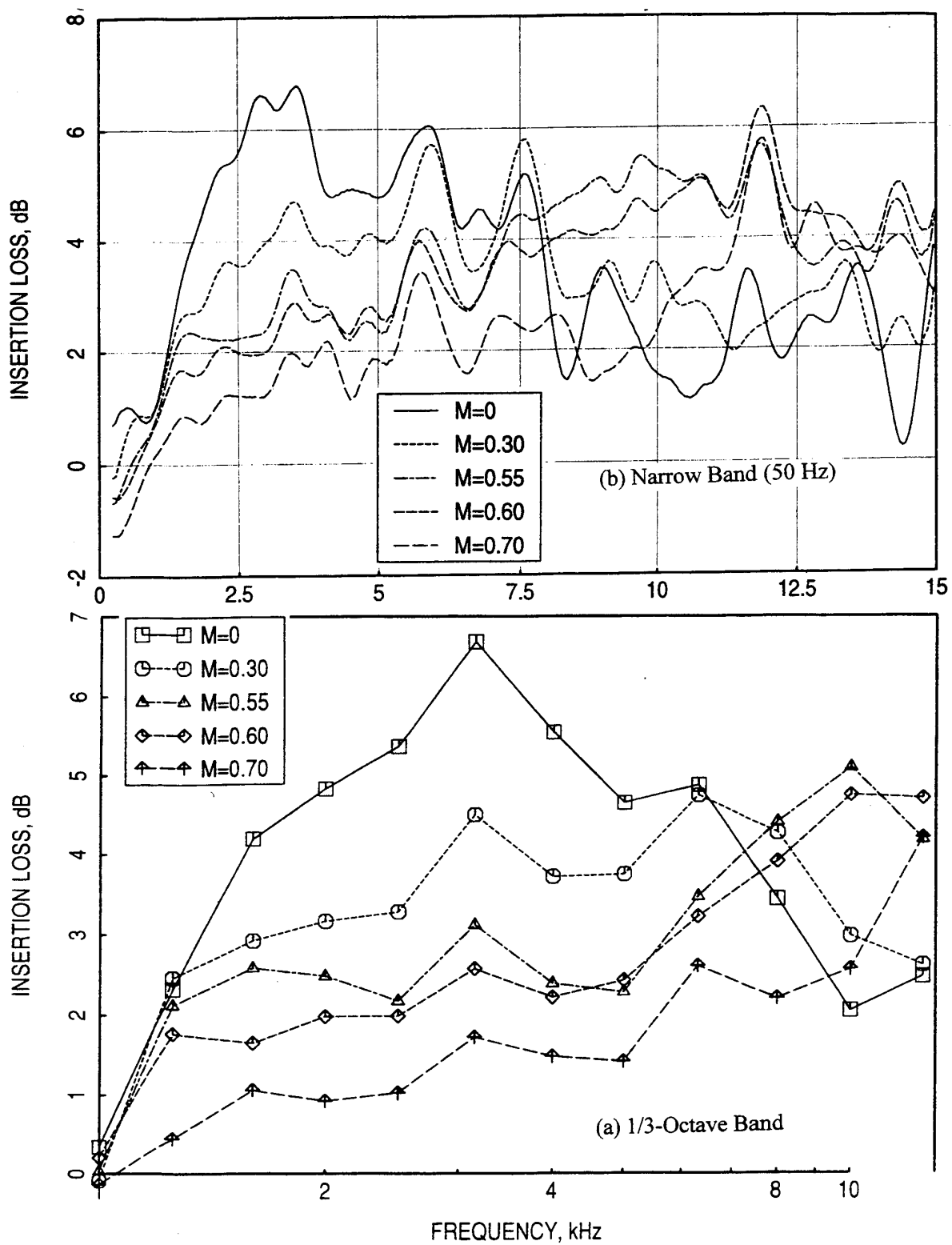


Figure 166. Influence of grazing flow Mach number on insertion loss spectra for an SDOF type panel with linear facesheet, mounted on one side of the 4"-high flow duct, R100=130 Rayls, D=0.38".

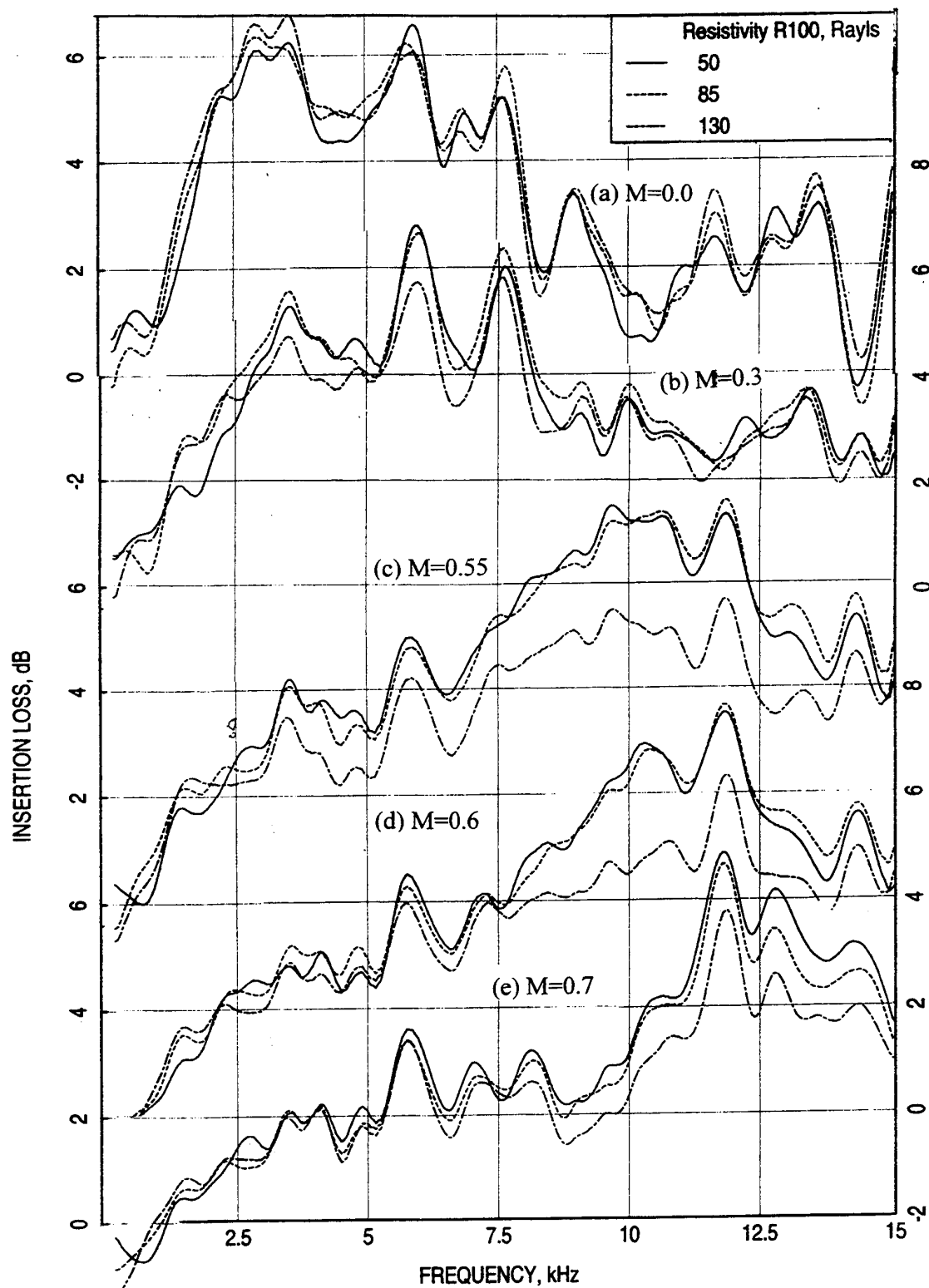


Figure 167. Effect of linear facesheet resistivity (R_{100}) on insertion loss spectra for SDOF type panels at different grazing flow Mach numbers (M), mounted on one side of the 4"-high flow duct; $D=0.38$ ".

5.6. Acoustic Characteristics of Bulk-filled SDOF Type and Bulk Only Panels with Linear Facesheets:

5.6.1 Bulk Samples without Facesheet for DC Flow & Normal Impedance Tests

A set of silicon carbide foam samples of different pores per inch (ppi), listed in Table 18, are prepared for high temperature DC flow resistance and normal impedance tests. These samples are mounted in an aluminum sleeve of 1.75" OD and 1.25" ID, with different depths (see Figure 168). The samples are tightly fitted into the holder to avoid leakage between the bulk material and the sleeve wall.

DC Flow Resistance: Several bulk material samples are tested at different high temperature conditions utilizing the apparatus described in section 4 (see Figures 46, 169, and 170). Thermocouples are attached to the test sample during testing to obtain a realistic temperature measurement. All the bulk absorber samples are tested at room temperature conditions. The measured DC flow resistances corrected to standard temperature and pressure conditions of 70°F and 29.92 in. of Hg, respectively, from room temperature and high temperature tests, are plotted in Figures 171 through 173 for different sets of samples. It is evident from these results that the DC flow resistance increases with pores per inch (ppi) for most cases. The DC flow resistance at 100 cm/sec (R100) and the "A" value of DC flow resistance are plotted with respect to pores per inch in Figure 174. In general the R100 and "A" value increase with pores per inch. However, some discrepancy is observed in the variation of the DC flow resistance parameters with ppi. Results for the samples of same depth are showing more systematic variation with ppi. Since, the samples are sealed to the holder using high temperature RTV, which has covered some portion of the sample, especially for high porosity materials, it is likely that the flow area utilized in the DC flow resistance evaluation is inaccurate. In addition, the manufacturing process for the bulk material does not maintain the same density for each batch of the bulk materials, especially, for higher ppi of 400 and above and the DC flow resistance depends on porosity and density. These reasons might have contributed to the scatter observed in Figure 174.

Several bulk material samples are tested at different high temperature conditions. The measured DC flow resistance data is normalized using Equations 18 and 19 to determine if the normalization process on the basis of similarity principle holds good for bulk absorbers. Typical results for five bulk material samples with 45, 100, 200, 400, and 500 PPI are shown in Figures 175 through 179, respectively. In each figure, the "as measured" and normalized DC flow resistances at different temperatures are presented. For 45 PPI sample (see Figure

Table 18. Geometrical Properties, DC Flow Resistance Parameters, and File Names for Normal Impedance Data for Silicon Carbide Foam Samples

Sample #	Pores per inch (ppi)	Sample Depth, in	Sample Diameter, in	A Rayls/cm	R100 Rayls/cm	NLF (R150/R20)	Normal Impedance File @ 130 dB OASPL	Normal Impedance File @ 150 dB OASPL
3.11	10	2.0	1.25	0.17	0.69	2.31	3-11-130.dat	3-11-150.dat
3.12	20	2.0	1.25	0.32	0.88	1.9	3-12-130.dat	3-12-150.dat
3.13	45	2.0	1.25	0.46	1.45	2.05	3-13-130.dat	3-13-150.dat
3.14	65	2.0	1.25	4.95	9.13	1.52	3-14-130.dat	3-14-150.dat
3.15	80	2.0	1.25	7.21	10.87	1.34	3-15-130.dat	3-15-150.dat
3.16	100	1.0	1.25	4.45	7.85	1.48	3-16-130.dat	3-16-150.dat
3.17	200	1.0	1.25	21.84	36.6	1.43	3-17-130.dat	3-17-150.dat
3.18	400	0.5	1.25	48.75	73.48	1.34	3-18-130.dat	3-18-150.dat
3.19	500	0.5	1.25	78.43	115.93	1.32	3-19-130.dat	3-19-150.dat
3.20	600	0.5	1.25	324.32	487.42	1.34	3-20-130.dat	3-20-150.dat
3.21	800	0.5	1.25	375.12	561.6	1.33	3-21-130.dat	3-21-150.dat
3.22	1000	0.5	1.25	471.3	701.77	1.32	3-22-130.dat	3-22-150.dat

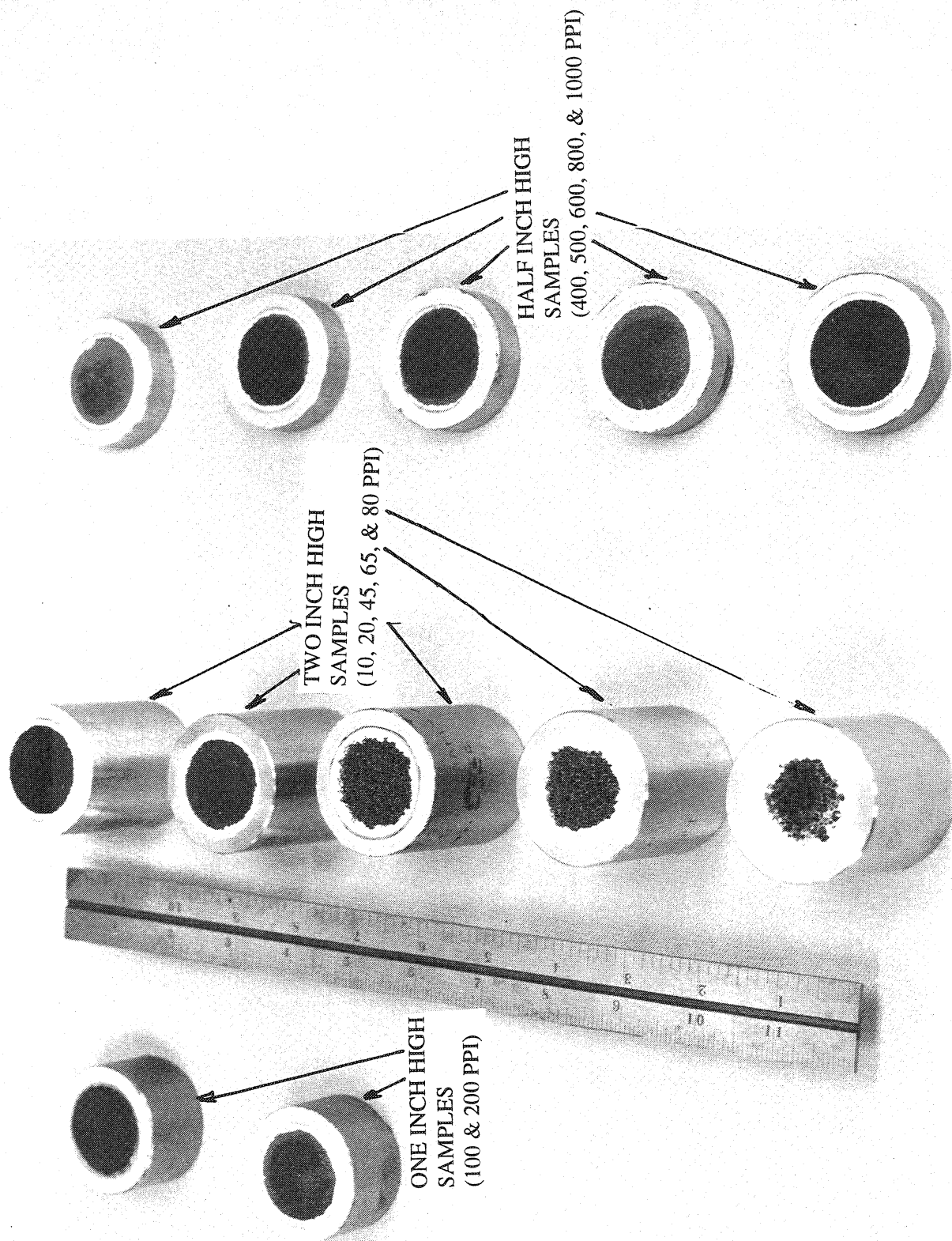


Figure 168. High temperature silicon carbide bulk material samples mounted in the sample holders.

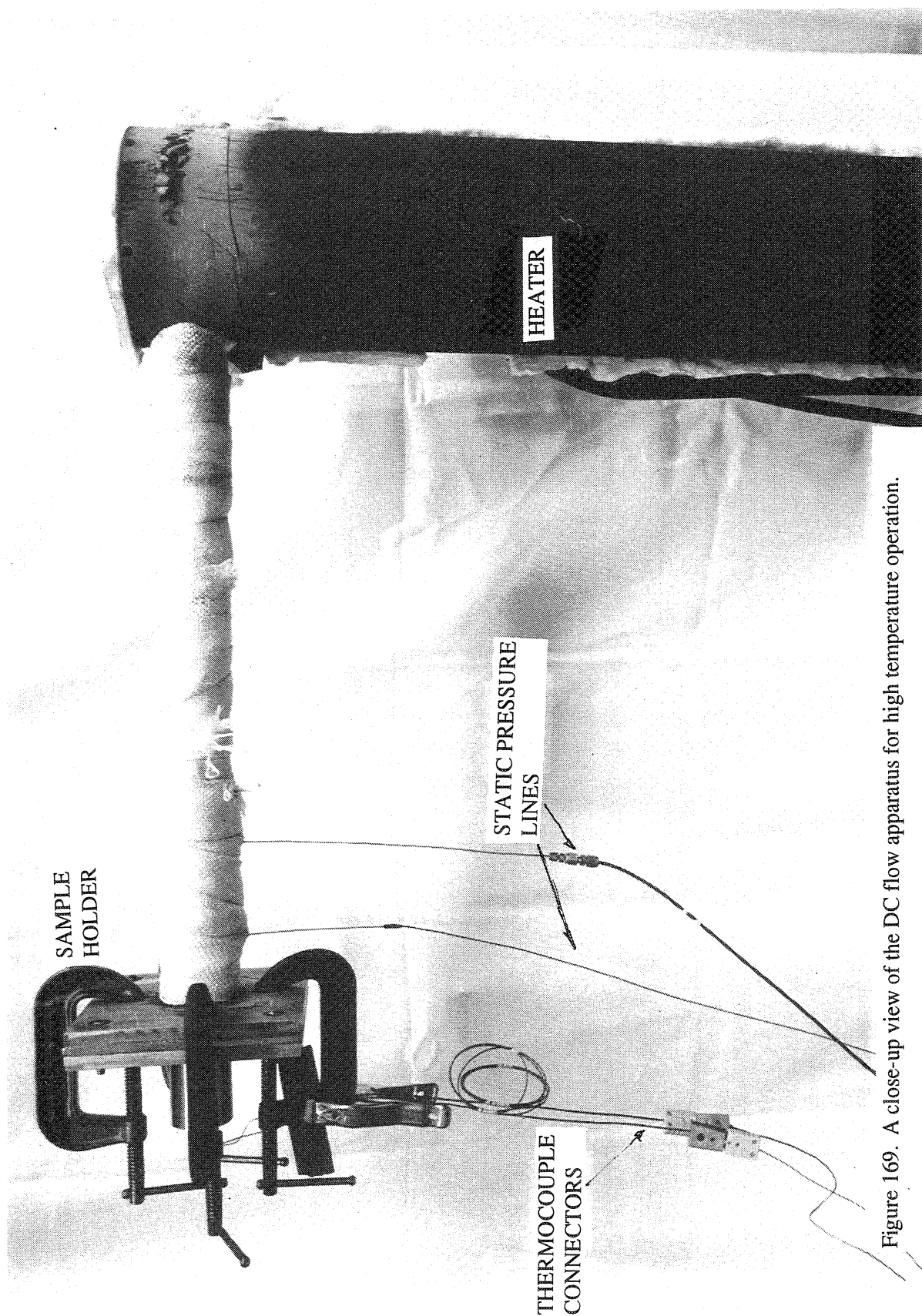


Figure 169. A close-up view of the DC flow apparatus for high temperature operation.

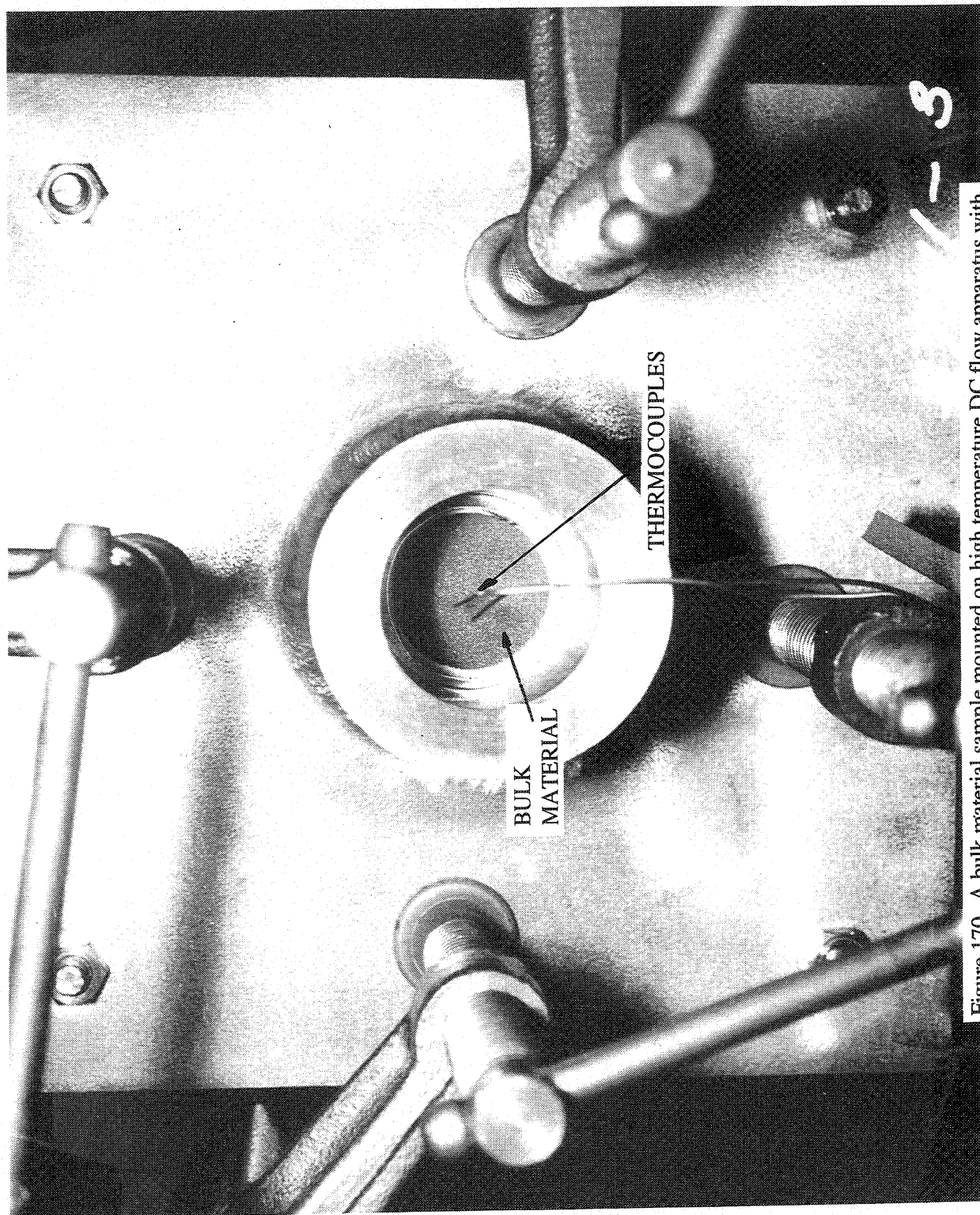


Figure 170. A bulk material sample mounted on high temperature DC flow apparatus with thermocouples.

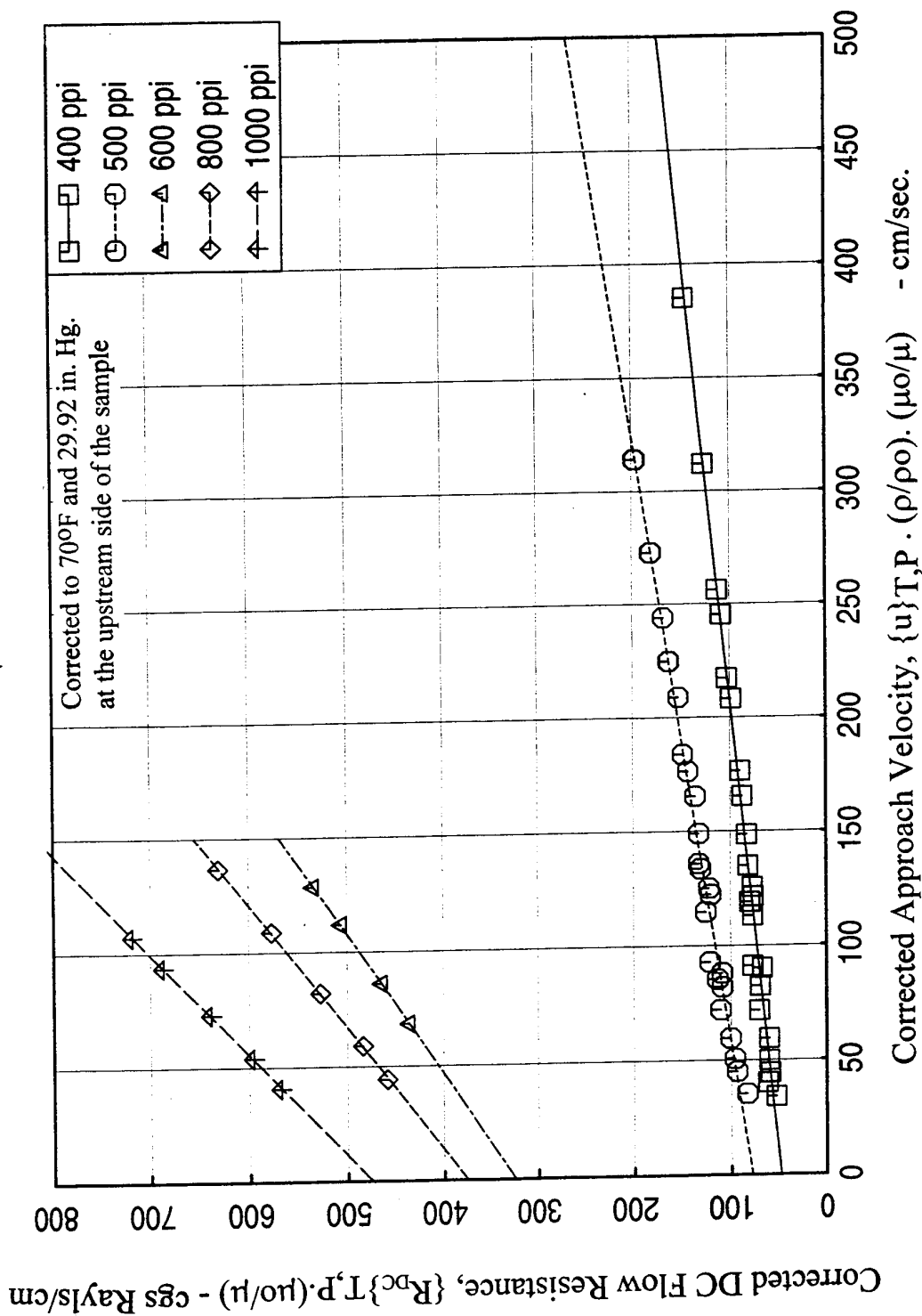


Figure 171. DC flow resistance data for low porosity (i.e., 400 to 1000 ppi samples) silicon carbide bulk material samples of 0.5" deep and 1.25" diameter measured at room temperature and pressure conditions.

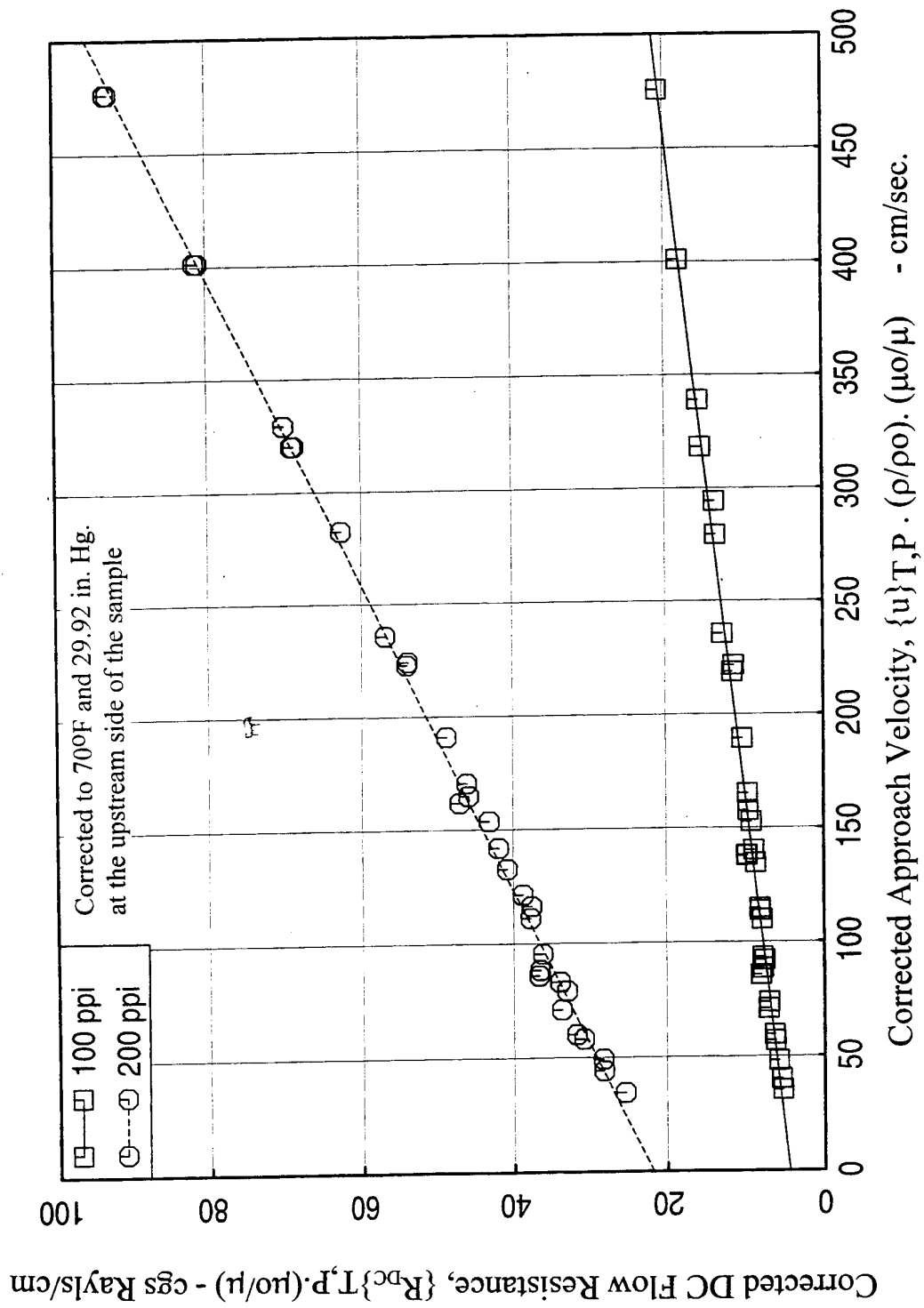


Figure 172. DC flow resistance data for medium porosity (i.e., 100 and 200 ppi samples) silicon carbide bulk material samples of 1.0" deep and 1.25" diameter measured at room temperature and pressure conditions.

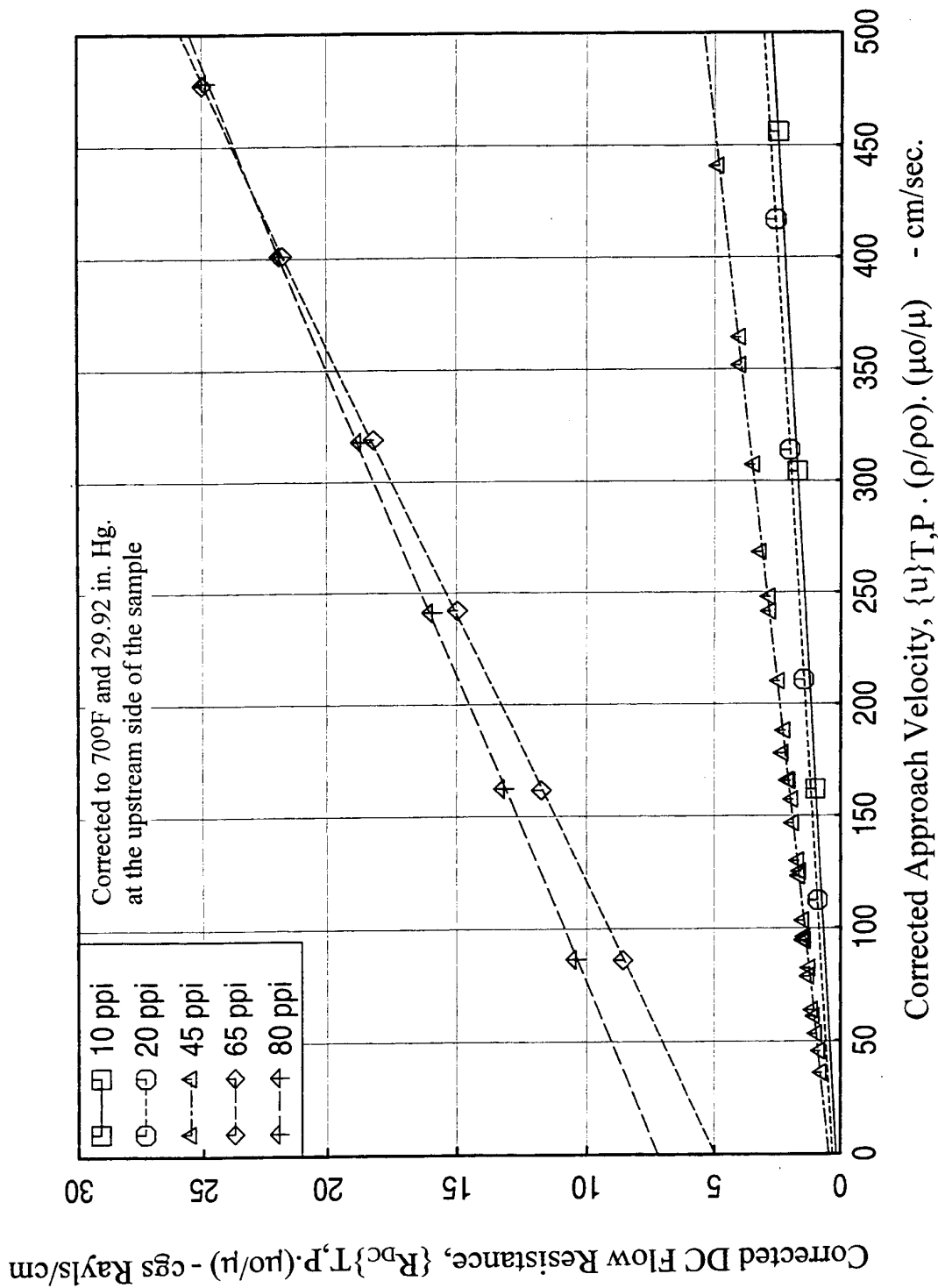


Figure 173. DC flow resistance data for high porosity (i.e., 10 to 80 ppi samples) silicon carbide bulk material samples of 2.0" deep and 1.25" diameter measured at room temperature and pressure conditions.

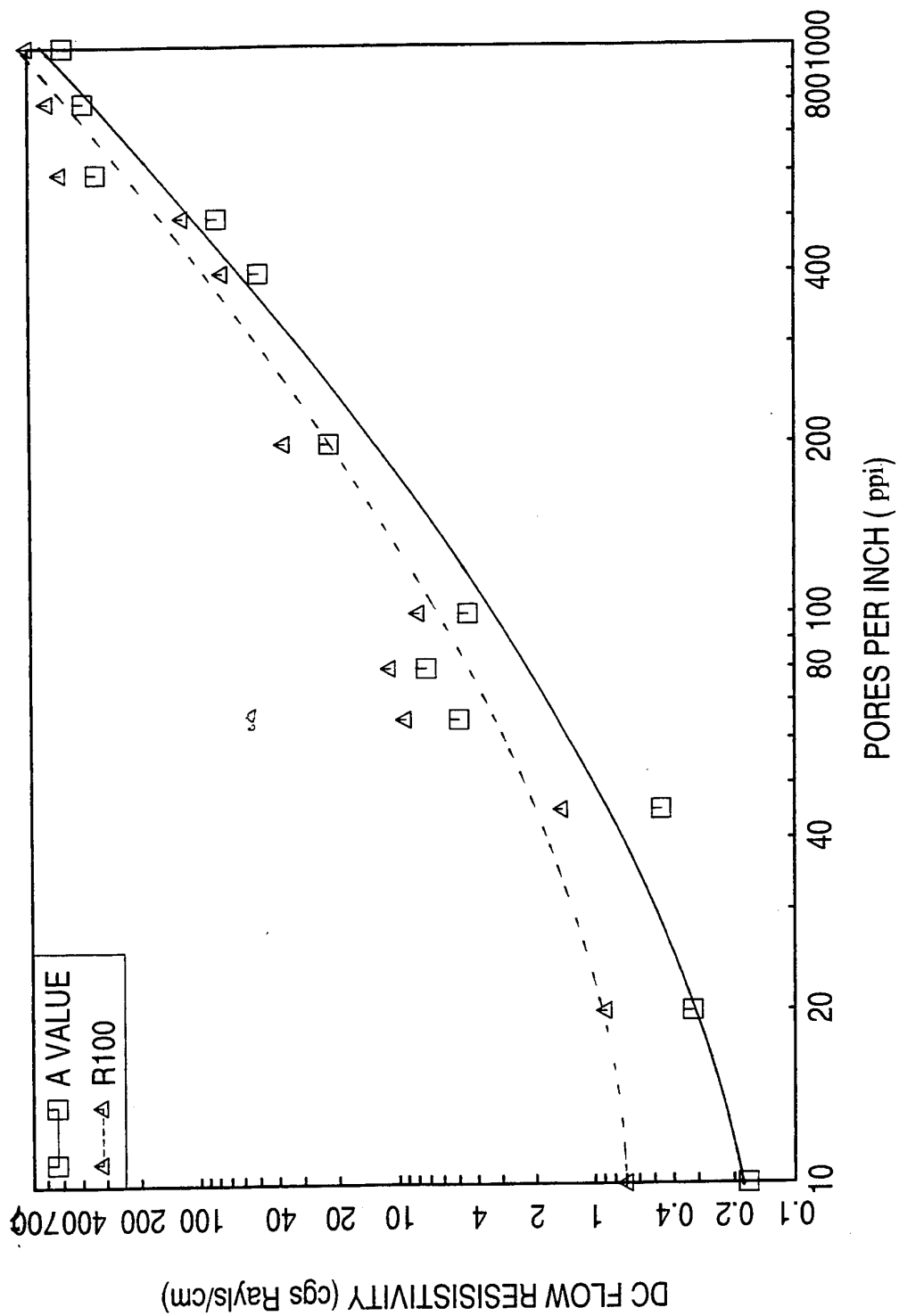


Figure 174. Resistivity versus pores per inch for the silicon carbide foam materials at room temperature and pressure conditions.

175), the DC flow resistance variation with temperature is similar to those for the perforated sheet, that the resistance decreases with increasing temperature. For samples with higher ppi (see Figures 176 through 179), the resistance decreases first and then increases with increasing temperature. However, the normalized results for all the samples show very good collapse, indicating the applicability of the similarity principles for bulk absorbers.

Normal Impedance: Tests were conducted for the silicon carbide bulk absorber samples used for high temperature DC flow tests. During the impedance tube tests the samples were mounted with a rigid back plate at the termination. The test samples are categorized by their depths, namely, 2", 1", and 0.5" deep silicon carbide samples. Effect of excitation level on normal impedance is examined for each individual sample by comparing the specific resistance and reactance spectra for two different excitation levels (i.e., 130 and 150 dB OASPL). In addition, the impedance spectra for the samples of each category are compared for fixed nominal excitation levels to examine their relative behavior on the basis of porosity (i.e., ppi).

Two Inch Deep High Porosity Silicon Carbide Samples: Five high porosity samples with different pores per inch (ppi) of 10, 20, 45, 65, and 80 were tested. The impedance spectra (i.e., the specific resistance and reactance) measured at two different OASPL levels (nominal levels being 130 dB and 150 dB) for each samples are shown in Figures 180 through 184. The corresponding sound pressure level spectra at $x=0$ are also included in these figures. Very little difference in impedance values is observed due to change in excitation level. The effect of excitation intensity (i.e., variation in OASPL) gradually increases with increasing ppi (i.e., decreasing porosity). In these results the high values of resistance occurring at frequencies at which the reactance changes its sign from high positive to negative, indicate the anti-resonating frequencies of the sample holder as a cavity. For high porosity samples most of the sound is transmitted through the bulk material and is reflected back from the rigid back plate and hence the holder contributes strongly to the resistance and reactance as a cavity behind the sample surface. This effect gradually diminishes as the porosity decreases with increasing ppi.

The specific resistance and reactance spectra for different ppi samples are compared in Figures 185 and 186 for the nominal OASPL of 130 and 150 dB, respectively. As indicated earlier, the particle velocities are significantly different with respect to ppi. For a rigid surface, while the sound pressure level becomes a maximum at $x=0$ the particle velocity goes to zero. Hence, one would expect a higher particle velocity for a sample with higher porosity. For these samples, due to the strong influence of the backplate, such a consistent behavior of particle

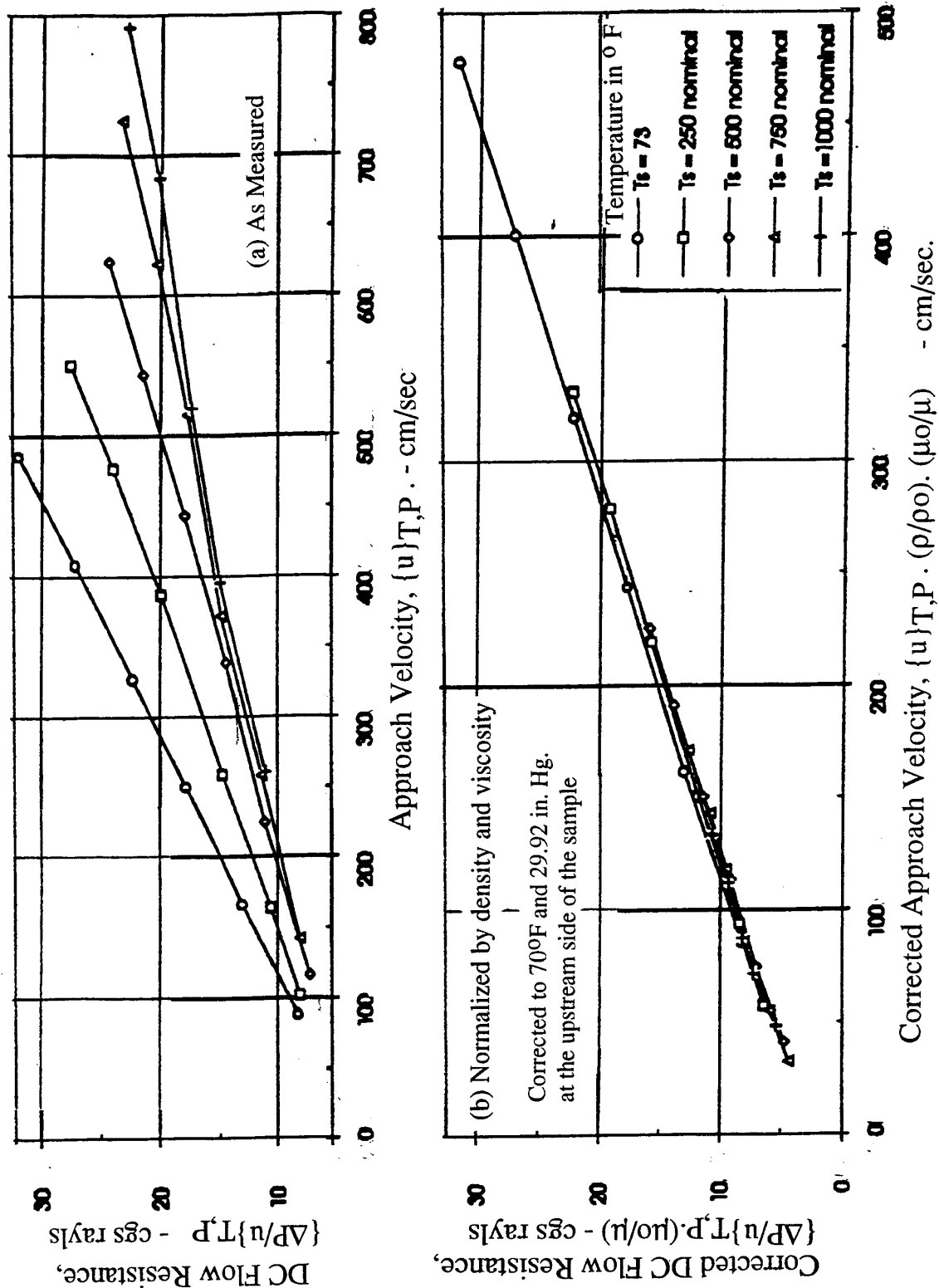


Figure 175. High temperature DC flow resistance data for a 2.0"-deep 45ppi silicon carbide bulk absorber sample.

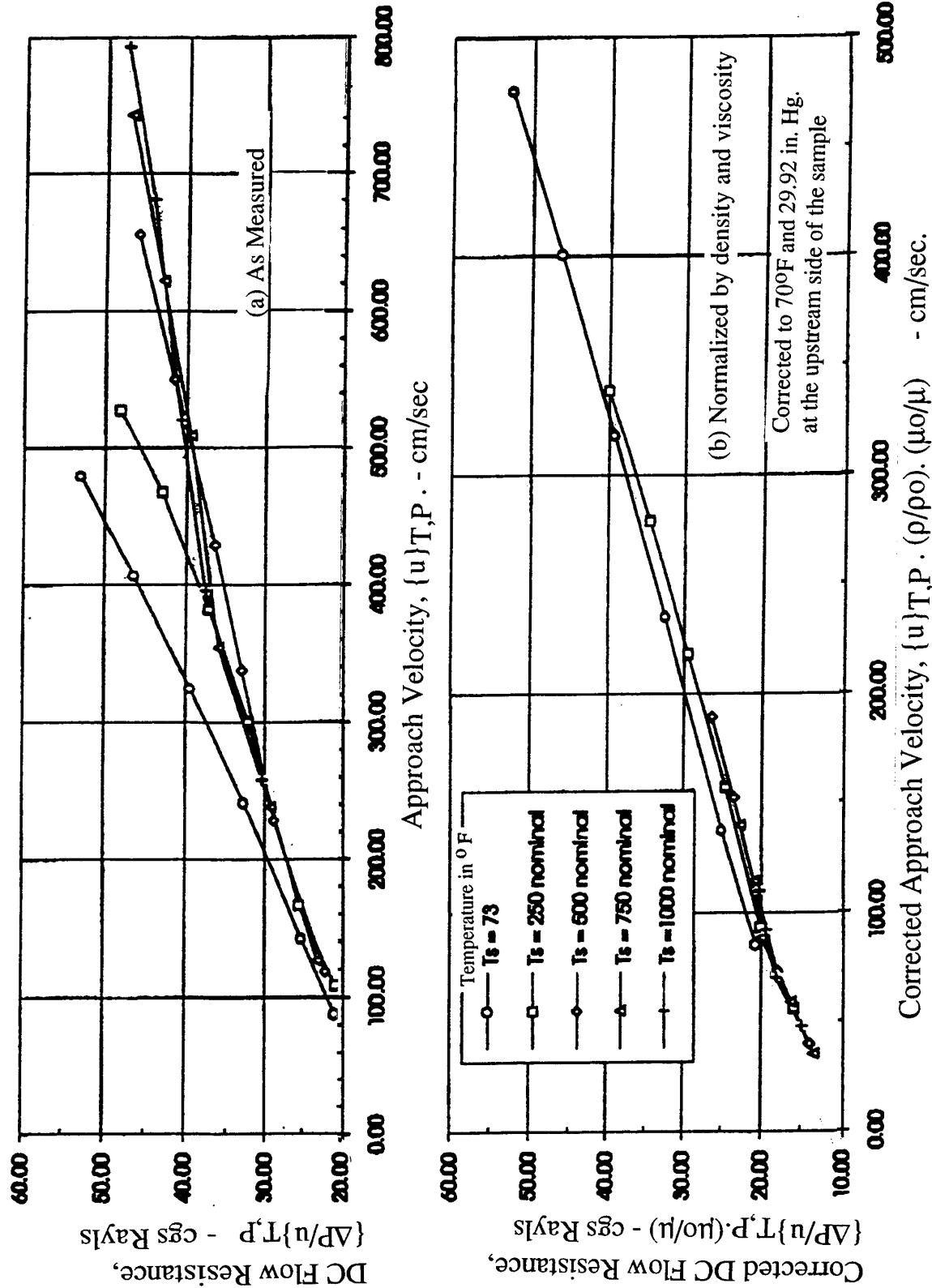


Figure 176. High temperature DC flow resistance data for a 1.0"-deep 100ppi silicon carbide bulk absorber sample.

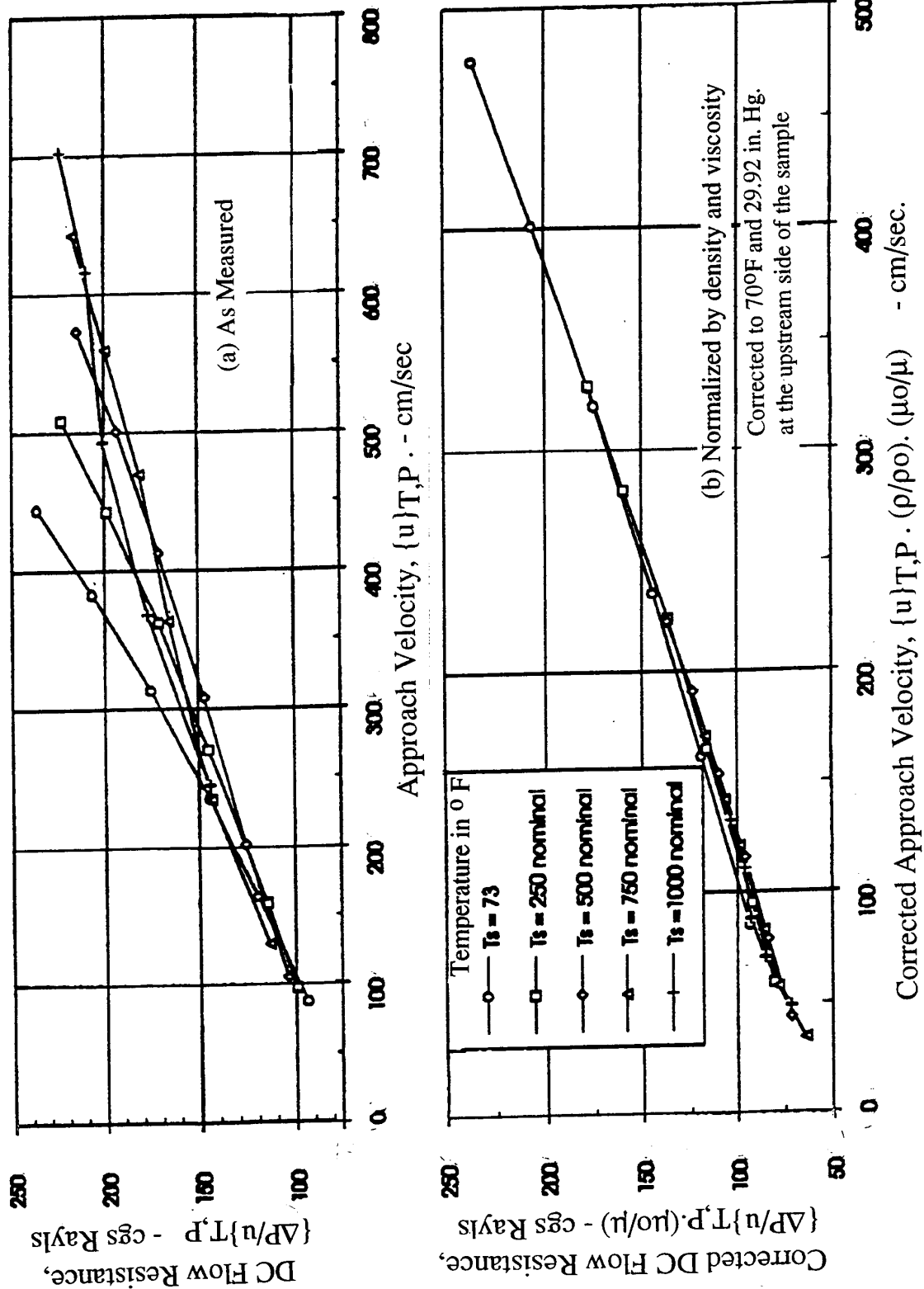


Figure 177. High temperature DC flow resistance data for a 1.0"-deep 200ppi silicon carbide bulk absorber sample.

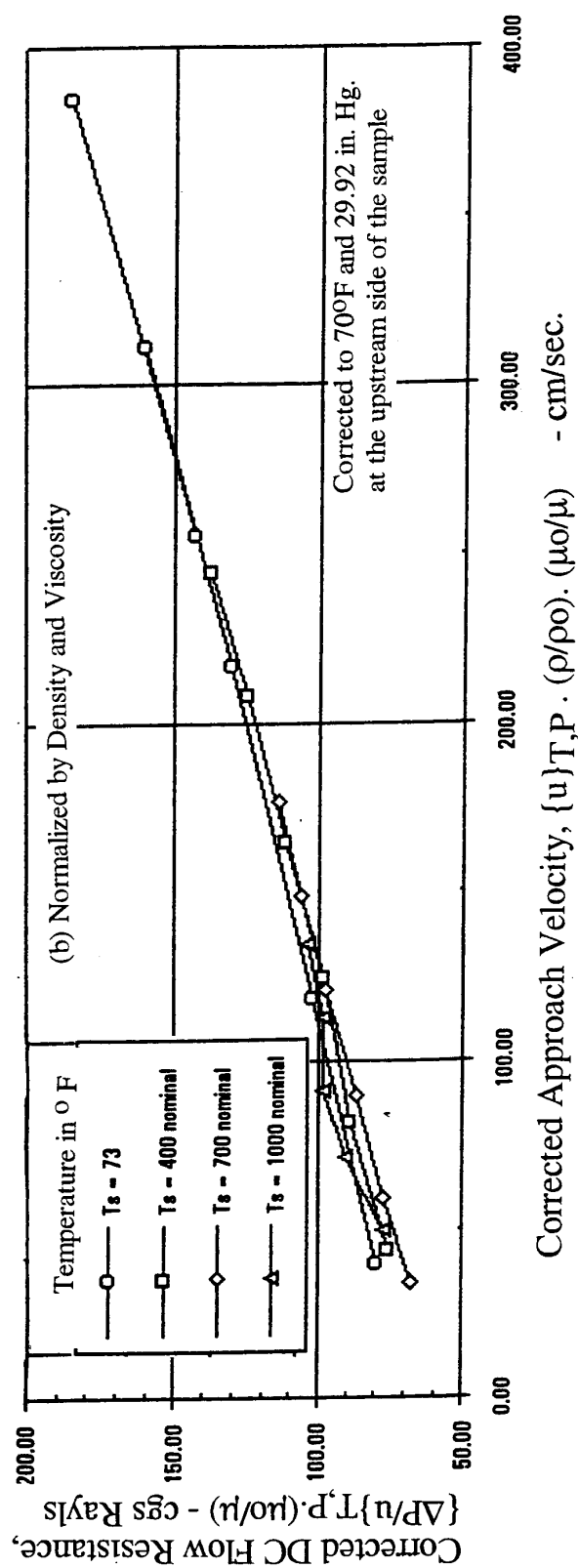
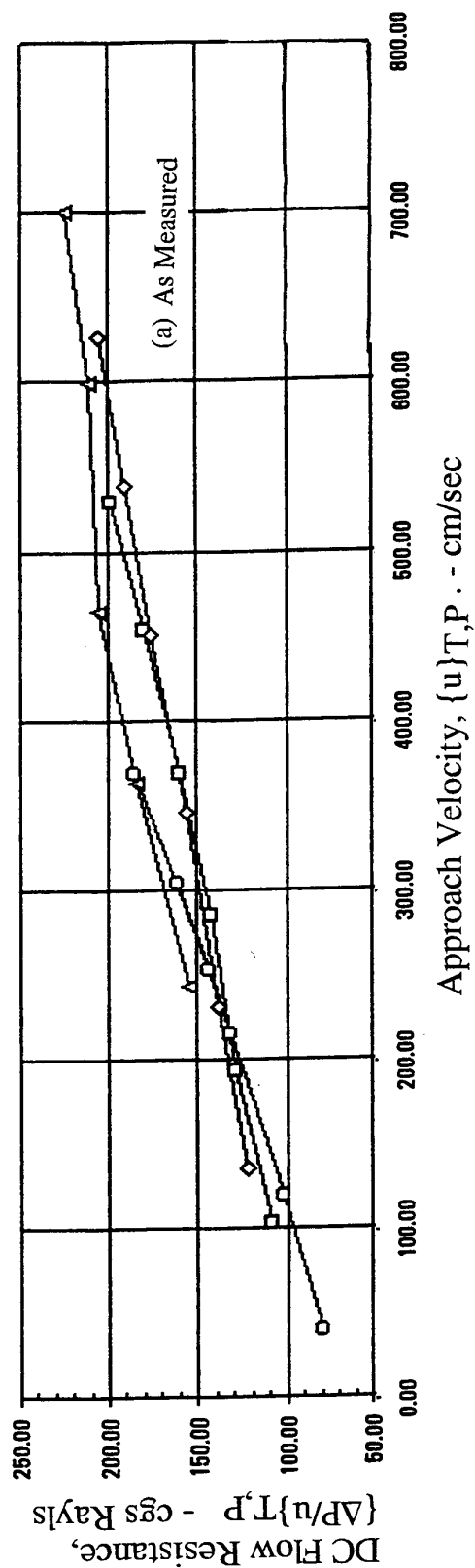


Figure 178. High temperature DC flow resistance data for a 0.5"-deep 400ppi silicon carbide bulk absorber sample.

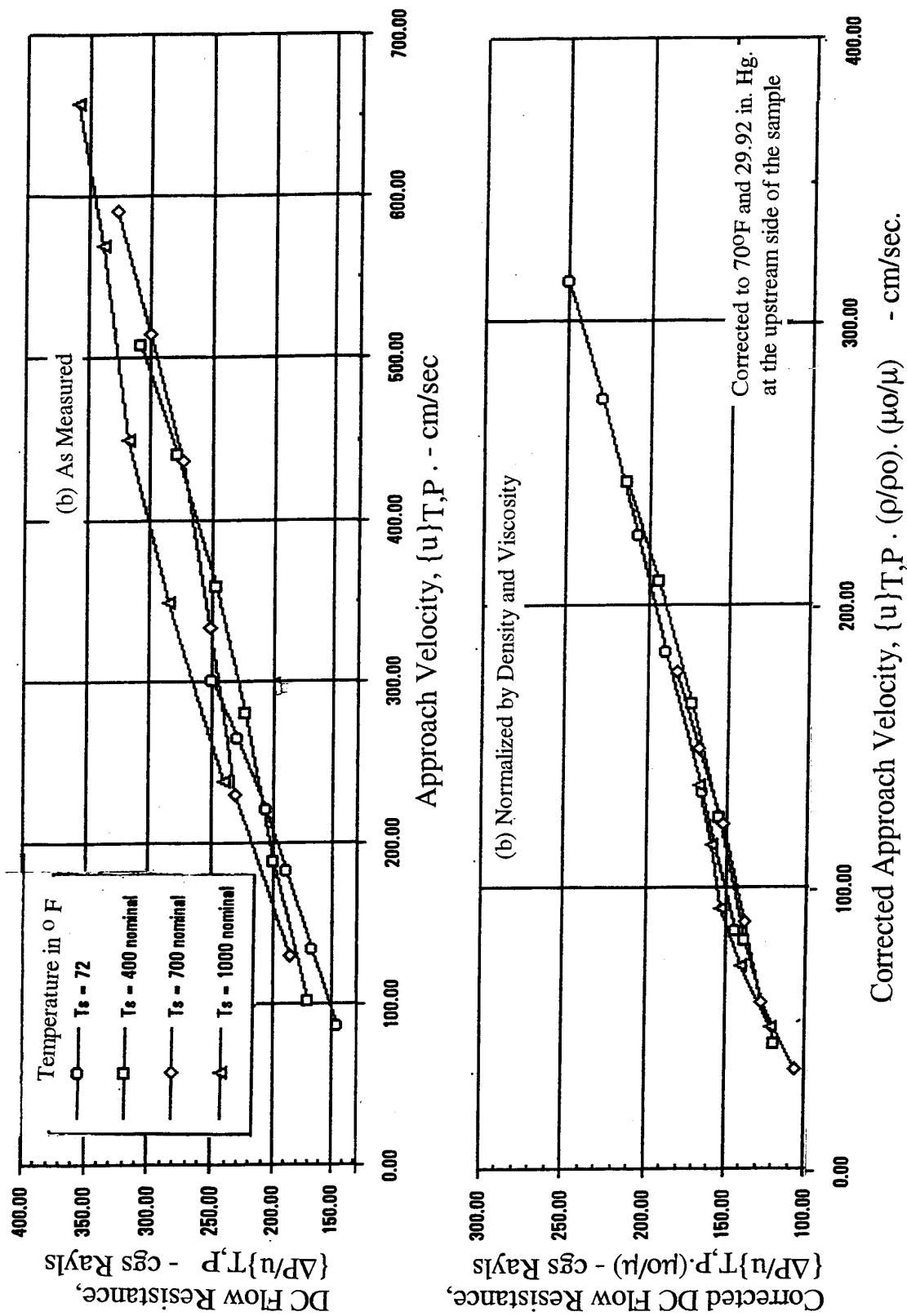


Figure 179. High temperature DC flow resistance data for a 0.5"-deep 500ppi silicon carbide bulk absorber sample.

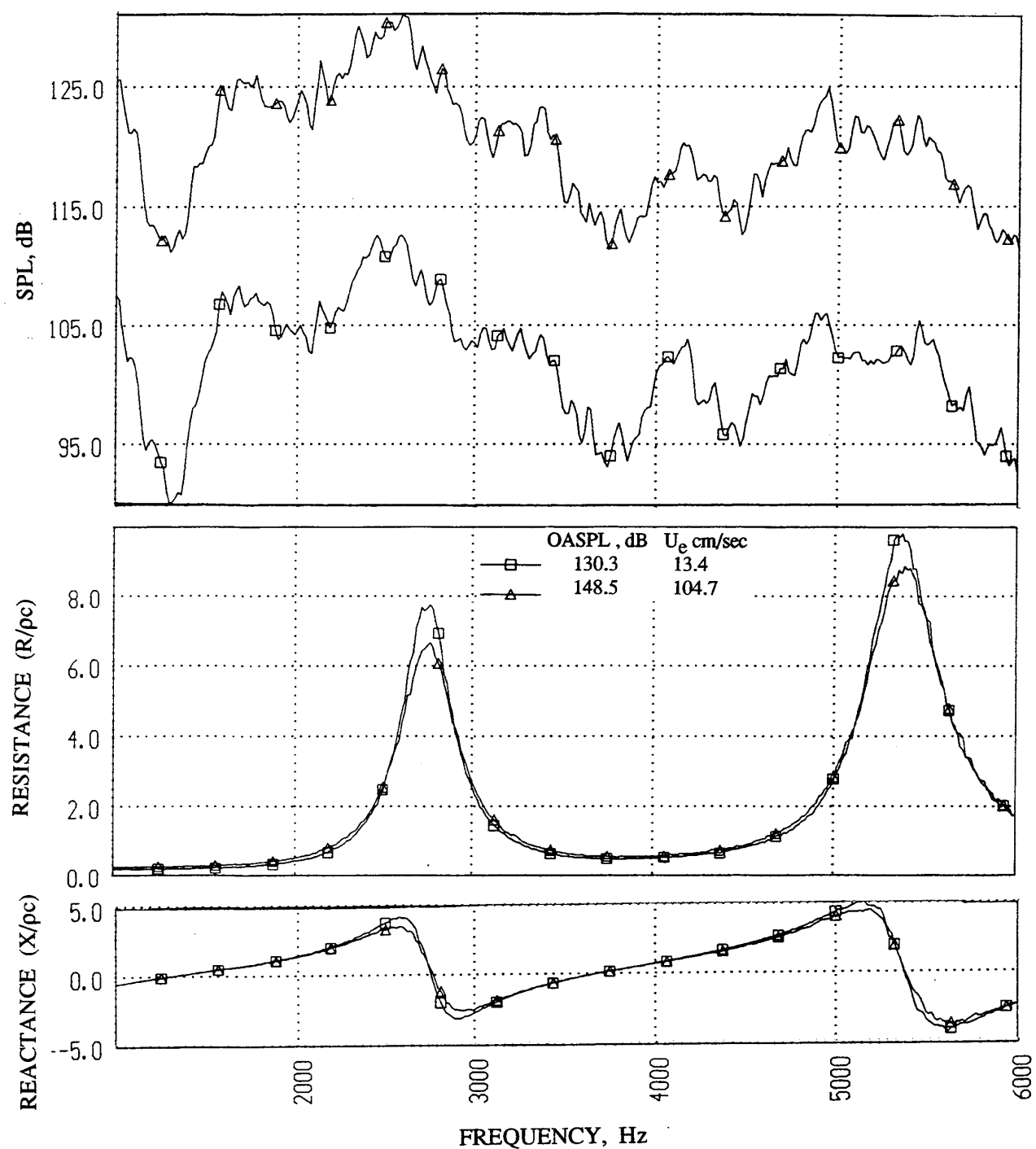


Figure 180. Sound Pressure level and corresponding normal impedance spectra at two OASPL levels for 1.25" diameter and 2"-deep silicon carbide sample of 10 ppi.

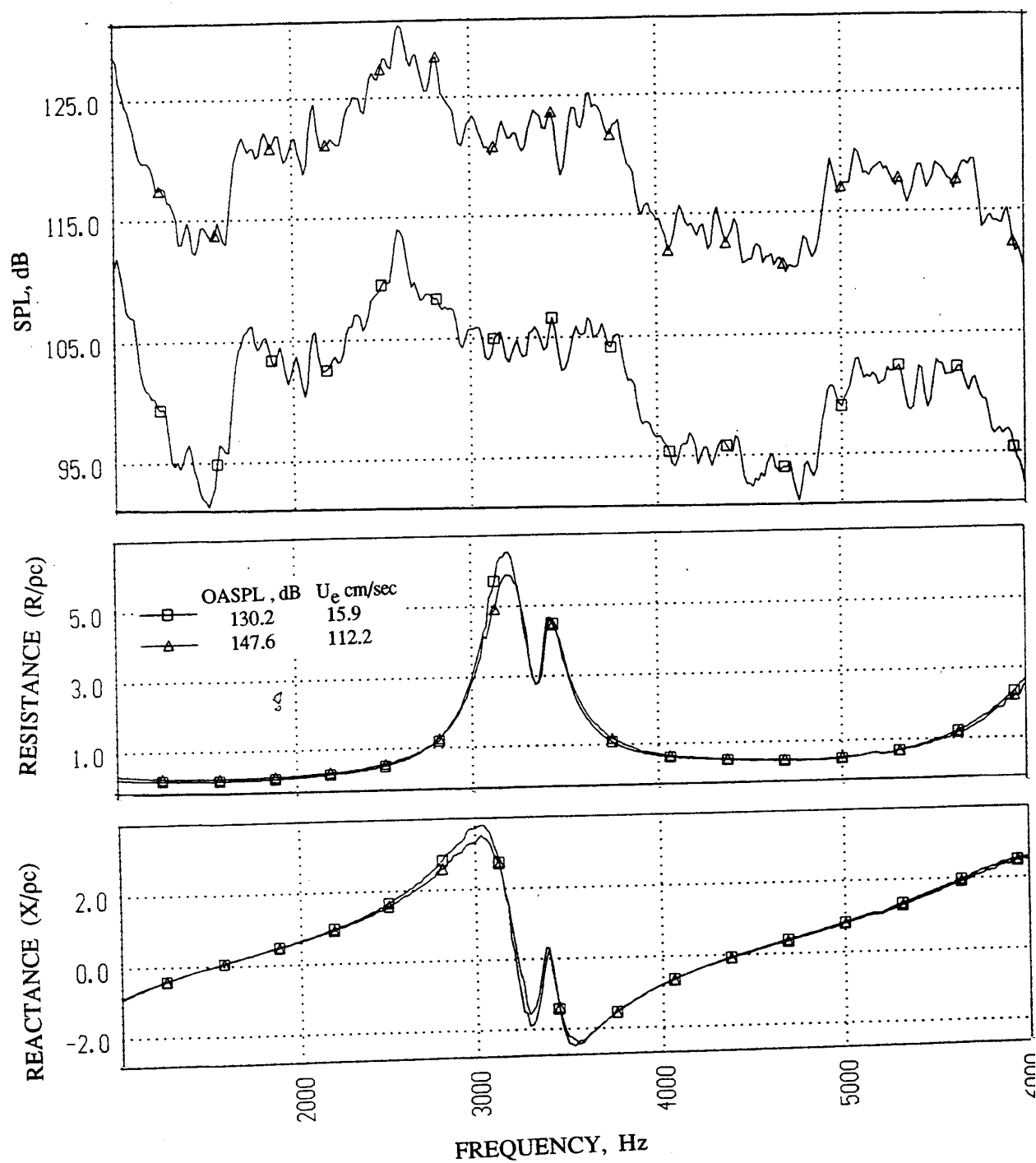


Figure 181. Sound Pressure level and corresponding normal impedance spectra at two OASPL levels for 1.25" diameter and 2"-deep silicon carbide sample of 20 ppi.

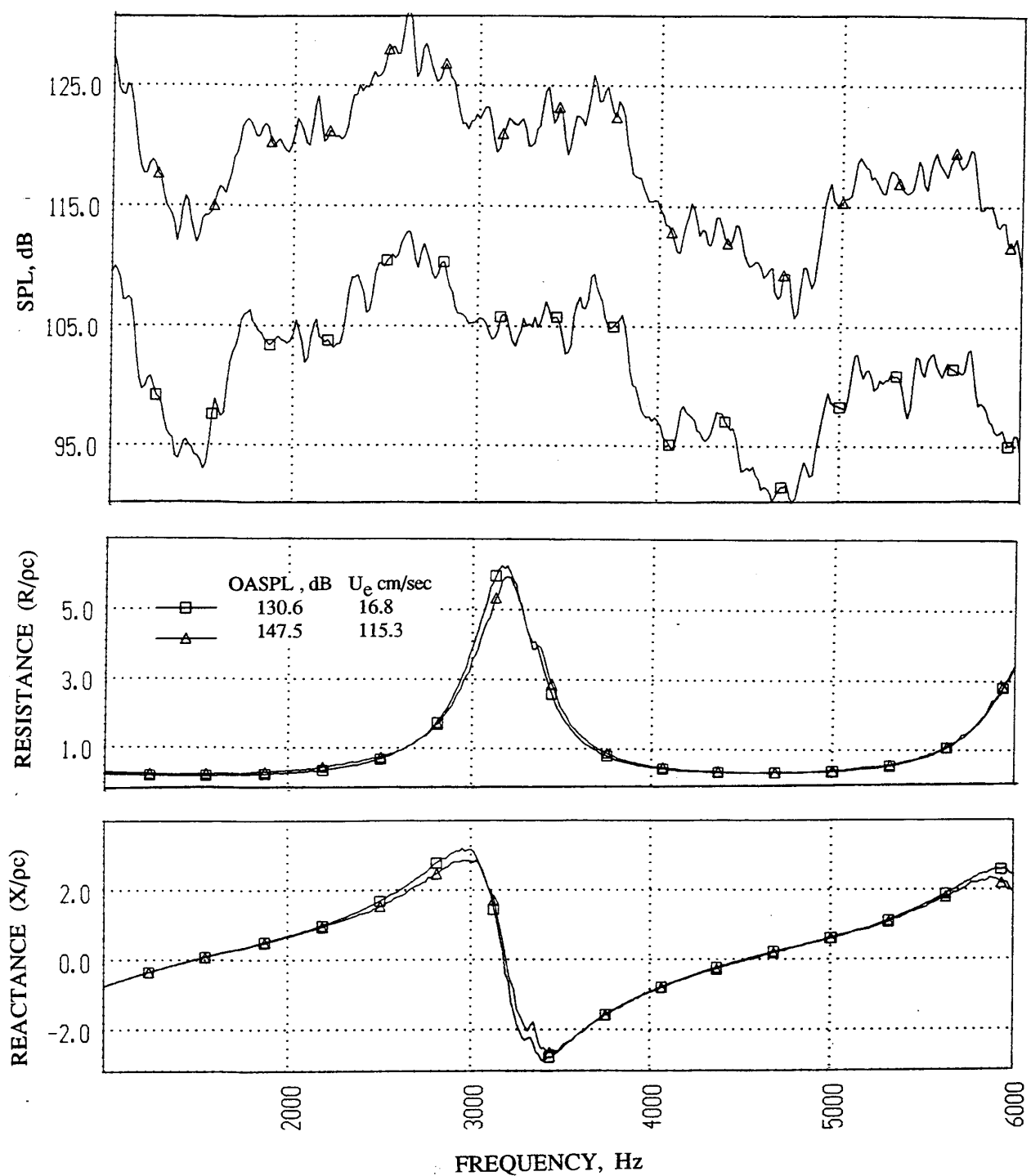


Figure 182. Sound Pressure level and corresponding normal impedance spectra at two OASPL levels for 1.25" diameter and 2"-deep silicon carbide sample of 45 ppi.

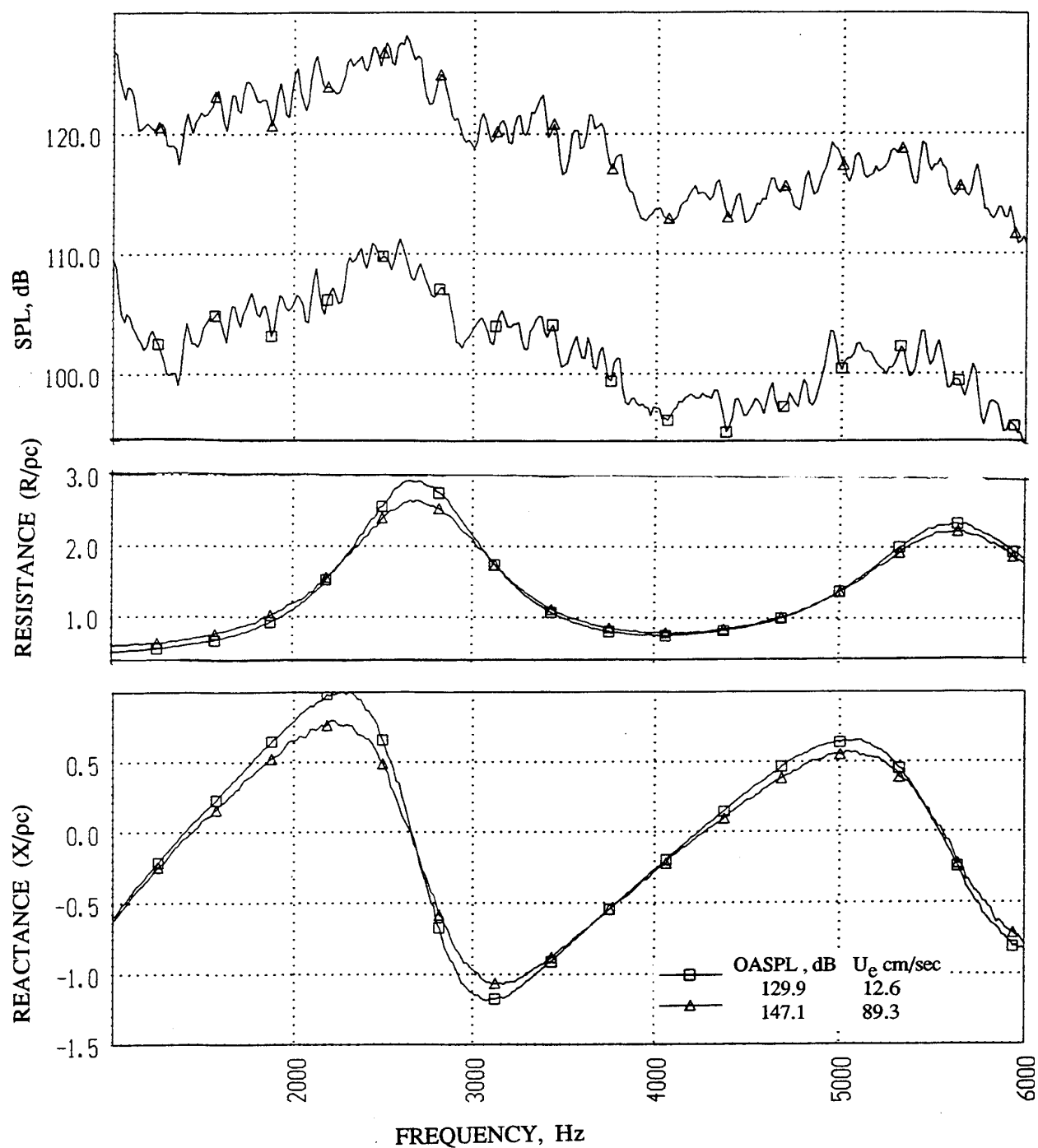


Figure 183. Sound Pressure level and corresponding normal impedance spectra at two OASPL levels for 1.25" diameter and 2"-deep silicon carbide sample of 65 ppi.

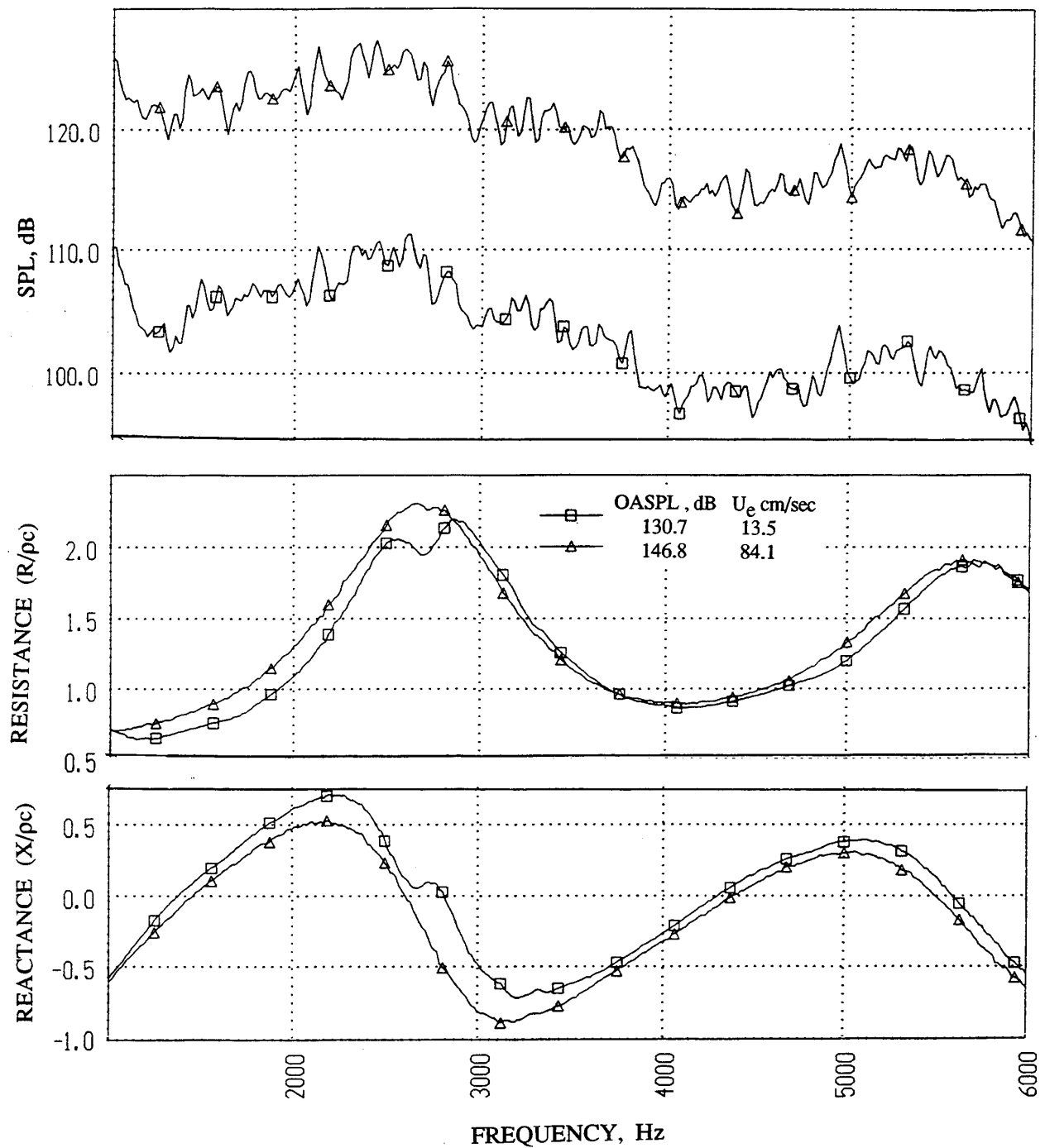


Figure 184. Sound Pressure level and corresponding normal impedance spectra at two OASPL levels for 1.25" diameter and 2"-deep silicon carbide sample of 80 ppi.

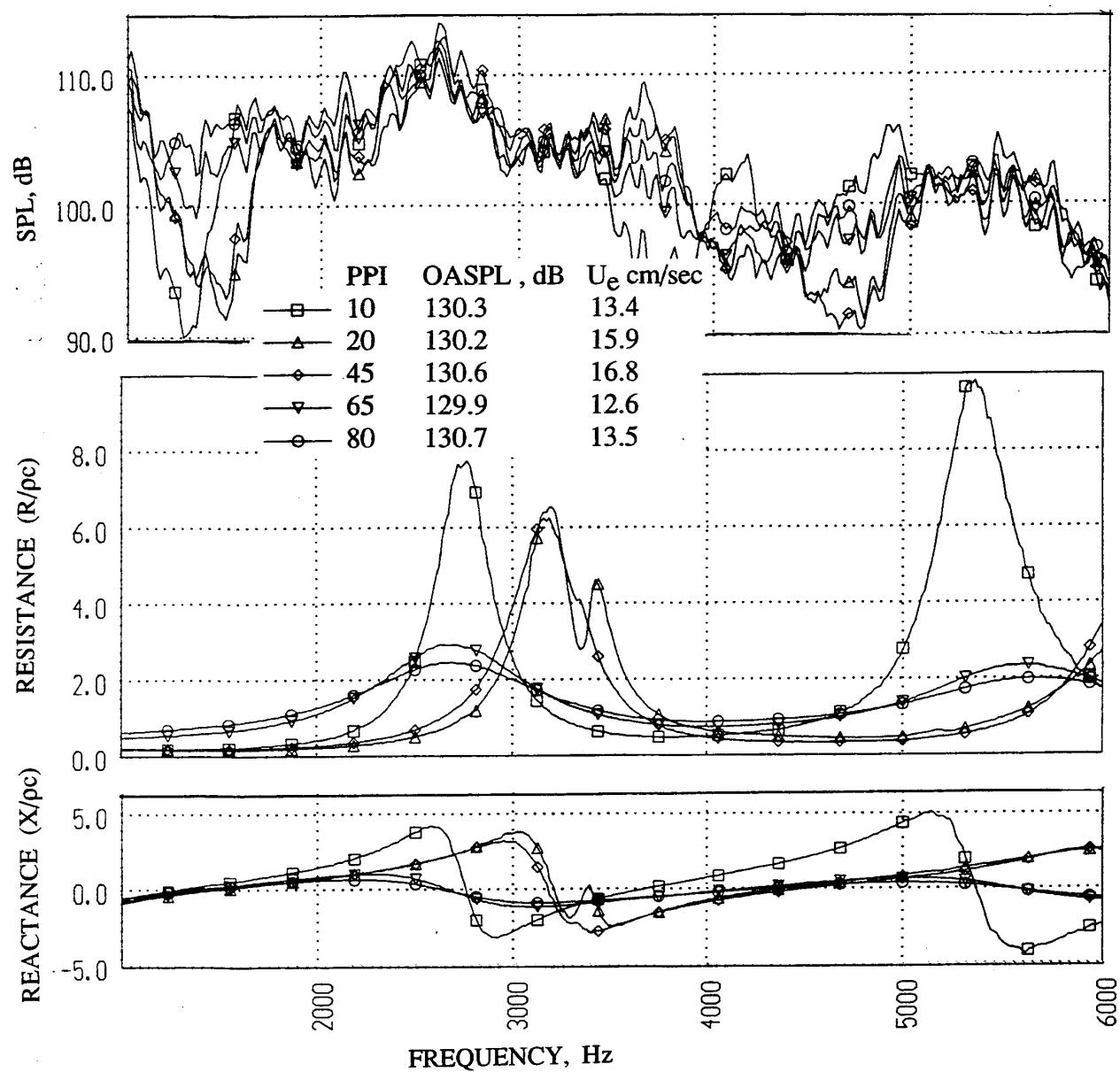


Figure 185. Sound Pressure level and corresponding normal impedance spectra for high porosity 1.25" diameter and 2"-deep silicon carbide samples of different PPI, tested with a nominal OASPL of 130 dB.

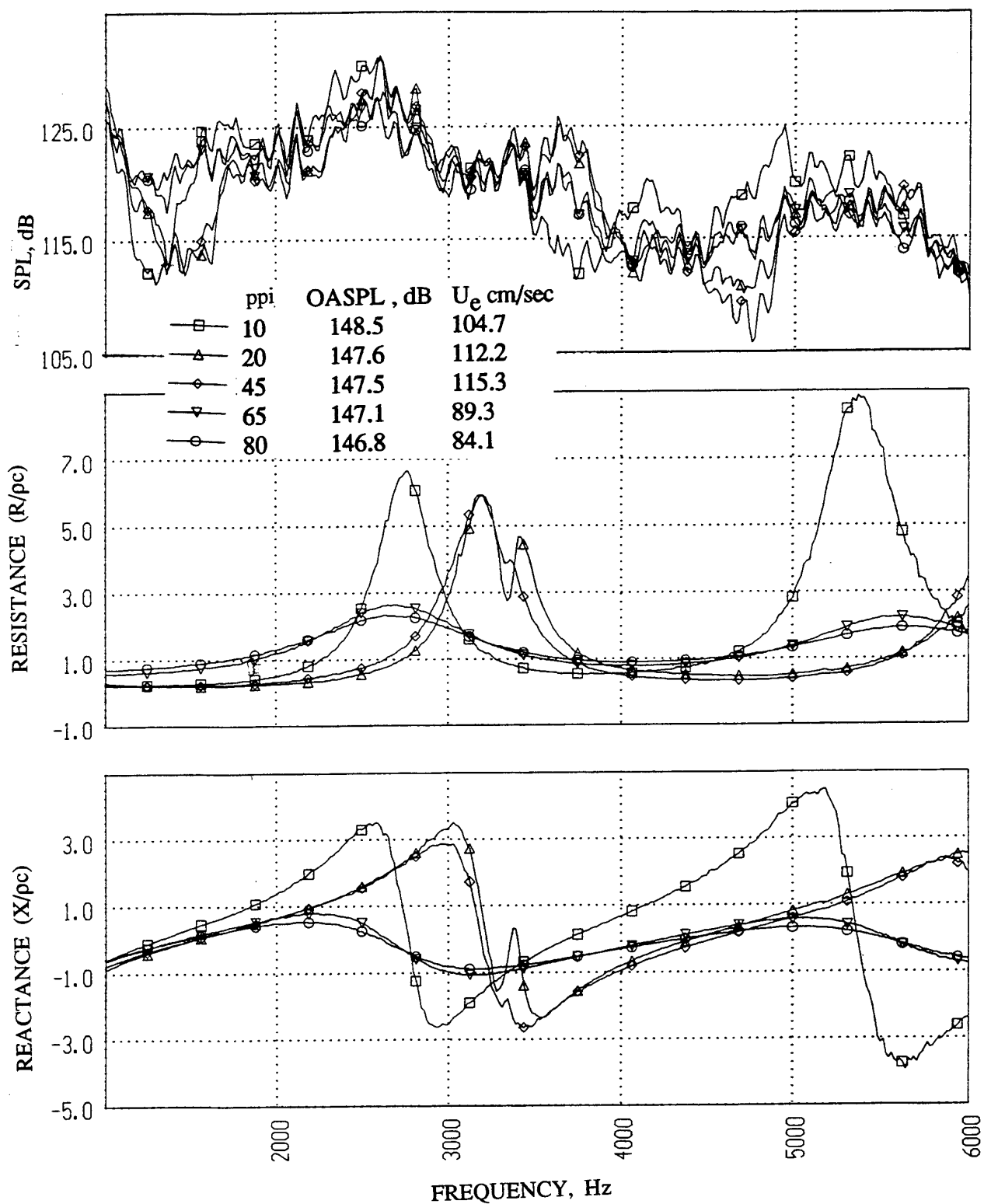


Figure 186. Sound Pressure level and corresponding normal impedance spectra for high porosity 1.25" diameter and 2"-deep silicon carbide samples of different ppi, tested with a nominal OASPL of 150 dB.

velocity is not observed. For relatively less porous samples, where very little acoustic energy is being reflected from the backplate, a very systematic particle velocity behavior is observed (will be seen later). As indicated from the individual plots, that the influence of OASPL level is small (i.e., low nonlinear effect). Hence, the impedance spectra for OASPLs of 130 and 150 dB are very much similar. Again, the influence of the backplate diminishes with increasing ppi, as observed in these summary plots.

One Inch Deep Silicon Carbide Samples: Two silicon carbide samples of 100 and 200 ppi were tested and the individual results are presented in Figures 187 and 188. The influence of acoustic excitation intensity is relatively small on the impedance levels. Comparison of impedance spectra between the samples of 100 and 200 ppi for nominal OASPL of 130 and 150 dB are shown in Figures 189 and 190, respectively. The resistance levels are higher for 200 ppi sample for most of the frequency range. The particle velocity, as expected, decreases with decreasing porosity (i.e., increasing ppi).

Half Inch Deep Low Porosity Silicon Carbide Samples: Five silicon carbide samples of 400, 500, 600, 800, and 1000 ppi were tested and the individual results are presented in Figures 191 through 195. The influence of acoustic excitation intensity is somewhat significant on the impedance levels for the samples with 400 and 500 ppi. For the higher ppi samples the effect of excitation intensity has insignificant influence on the impedance levels. Comparison of impedance spectra between the samples of different ppi for nominal OASPL of 130 and 150 dB are shown in Figures 196 and 197, respectively. The specific resistance monotonically increases with ppi for the entire frequency range. A reverse trend is observed for specific reactance. The particle velocity, as expected, decreases with decreasing porosity (i.e., increasing ppi).

5.6.2 Bulk Panels with Linear Facesheets for Flow Duct Tests

Bulk Material Panels : The basic sandwich construction of a bulk absorber panel, as illustrated in Figure 74, consists of a low resistance linear facesheet bonded to one side and a rigid non-porous backplate bonded to the other side of a bulk-filled honeycomb layer of specified thickness. Since, the tests were planned for room temperature conditions, carbon foam instead of Silicon Carbide of different ppi are used in these panels. As listed in Table 19, for three panels the bulk material is inserted into the honeycomb cells and the fourth one is just a slab of bulk material without any partition. Linear facesheets of 5 Rayls are used for the three bulk filled panels and a facesheet of 15 Rayls is used for the slab panel configuration. A higher resistive facesheet is used for the slab configuration to compensate the additional

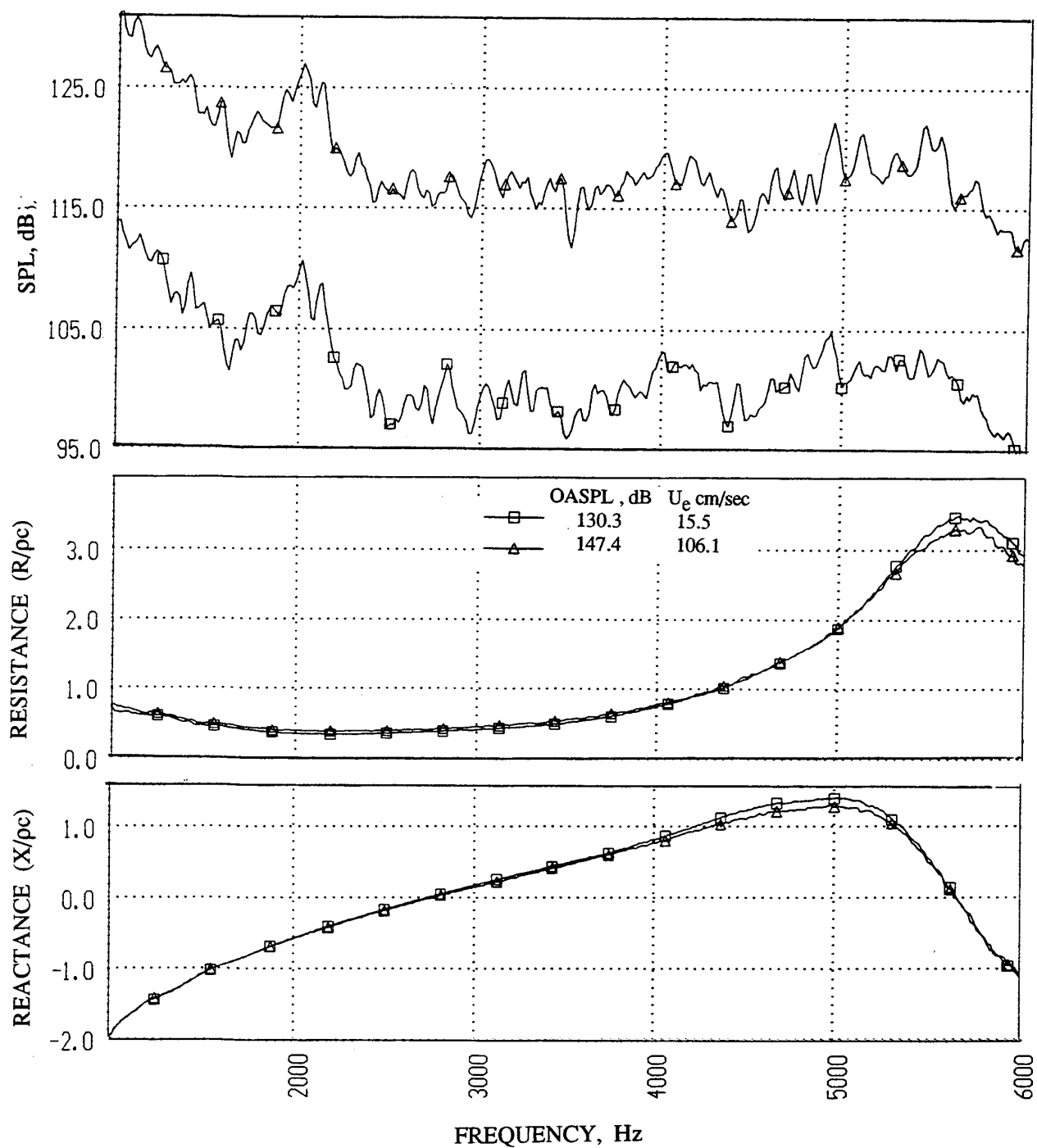


Figure 187. Sound Pressure level and corresponding normal impedance spectra at two OASPL levels for 1.25" diameter and 1"-deep silicon carbide sample of 100 ppi.

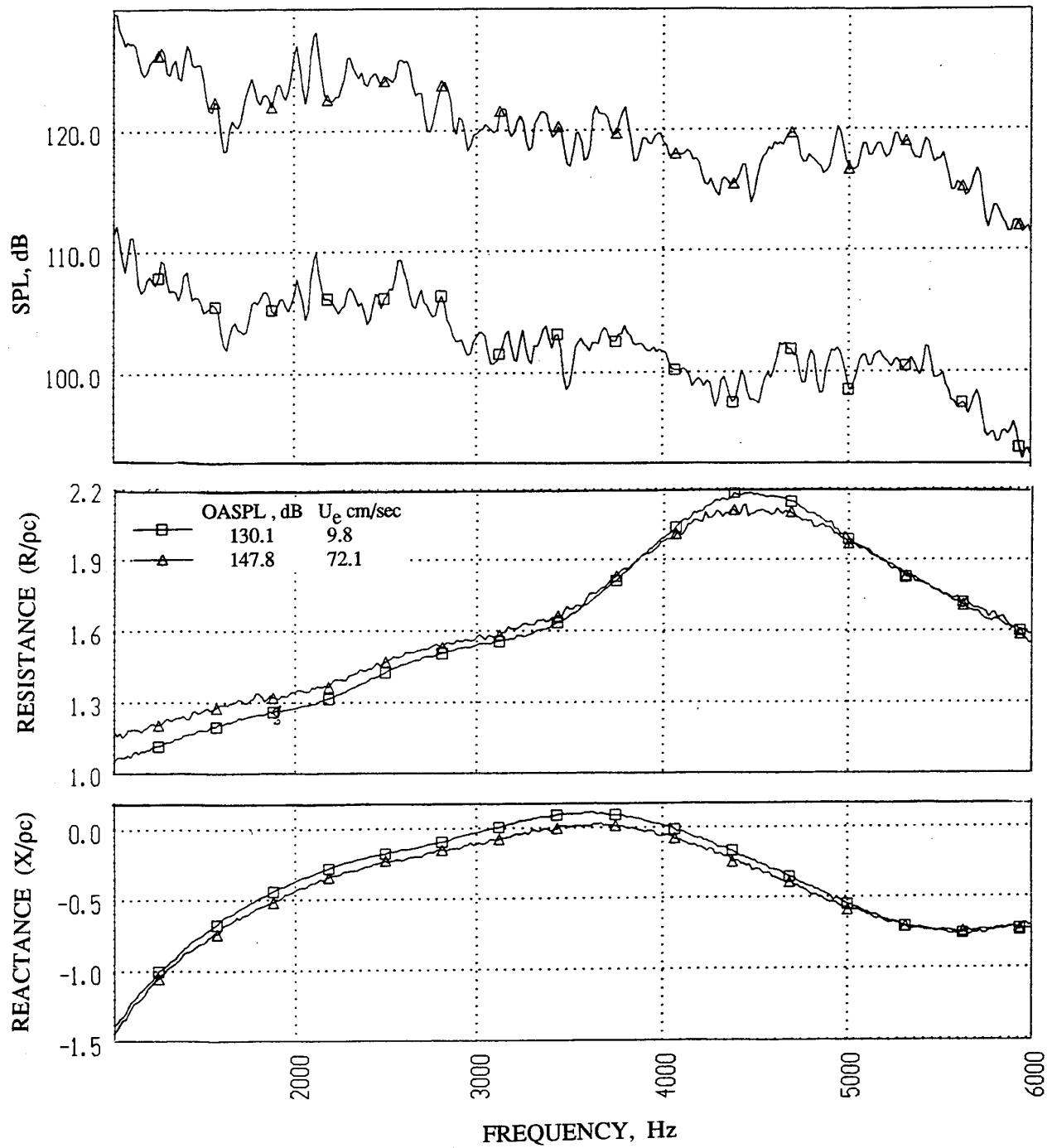


Figure 188. Sound Pressure level and corresponding normal impedance spectra at two OASPL levels for 1.25" diameter and 1"-deep silicon carbide sample of 200 ppi.

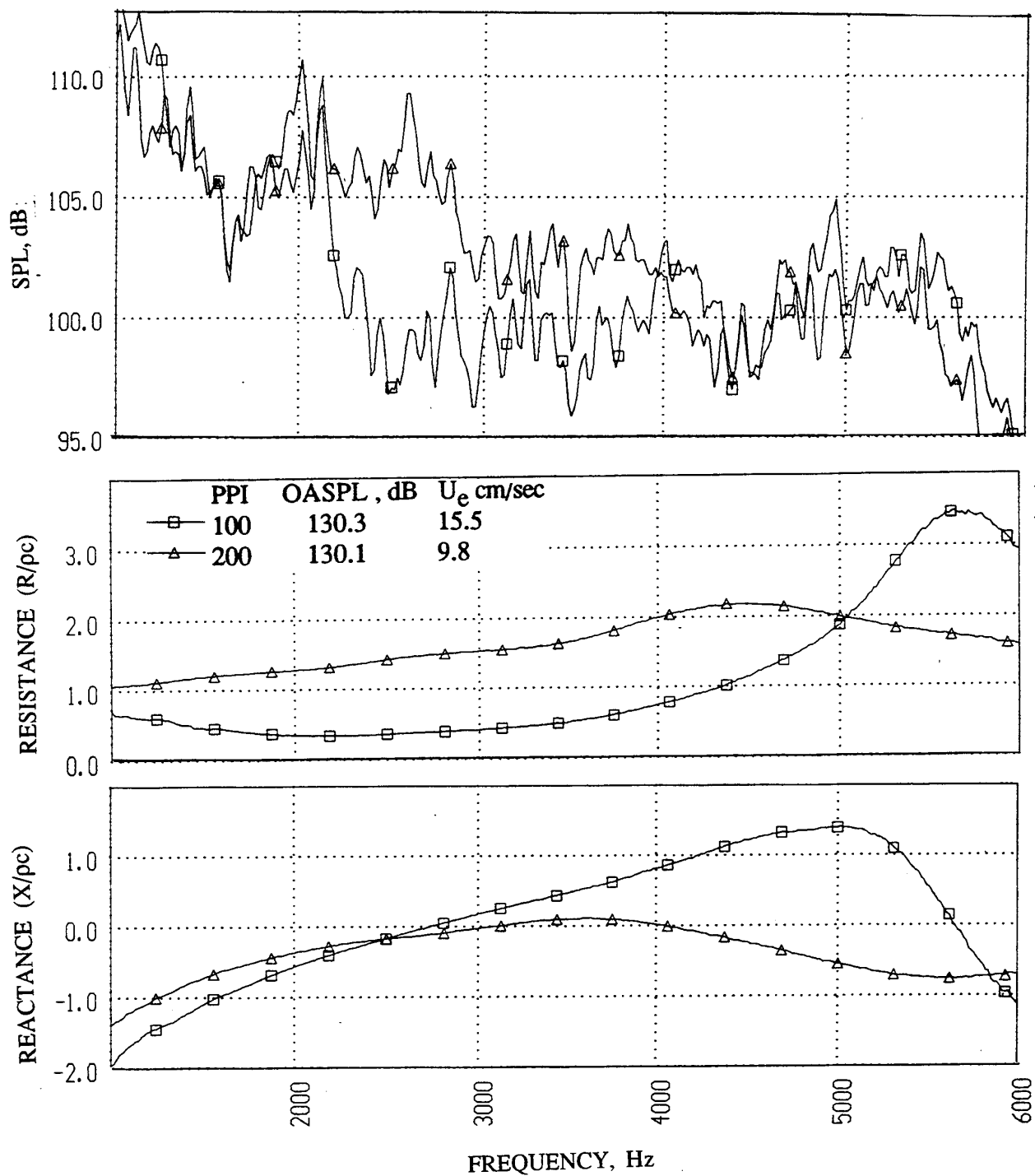


Figure 189. Sound Pressure level and corresponding normal impedance spectra for medium porosity 1.25" diameter and 1"-deep silicon carbide samples of different PPI, tested with a nominal OASPL of 130 dB.

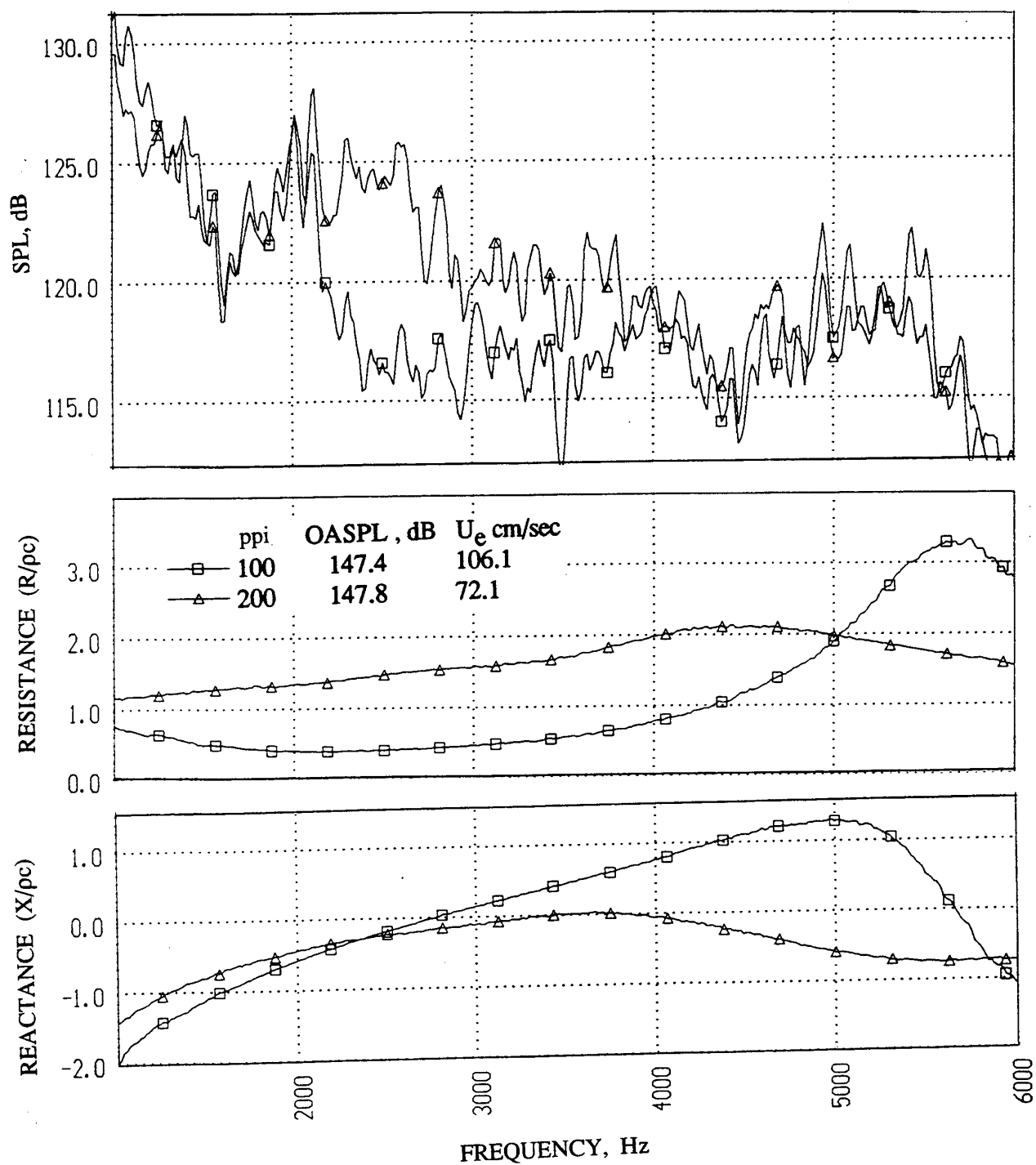


Figure 190. Sound Pressure level and corresponding normal impedance spectra for medium porosity 1.25" diameter and 1"-deep silicon carbide samples of different ppi., tested with a nominal OASPL of 150 dB.

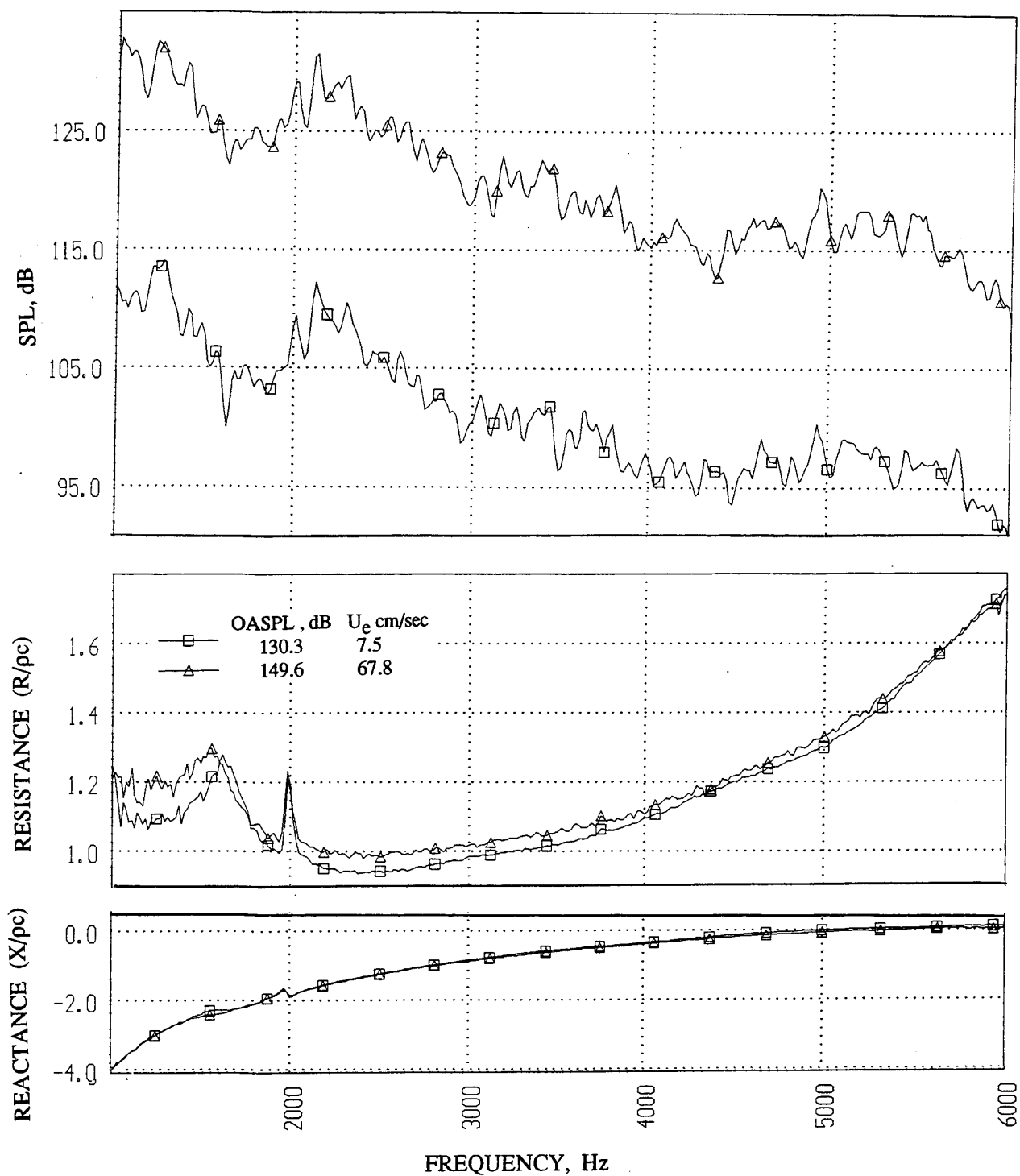


Figure 191. Sound Pressure level and corresponding normal impedance spectra at two OASPL levels for 1.25" diameter and 0.5"-deep silicon carbide sample of 400 ppi.

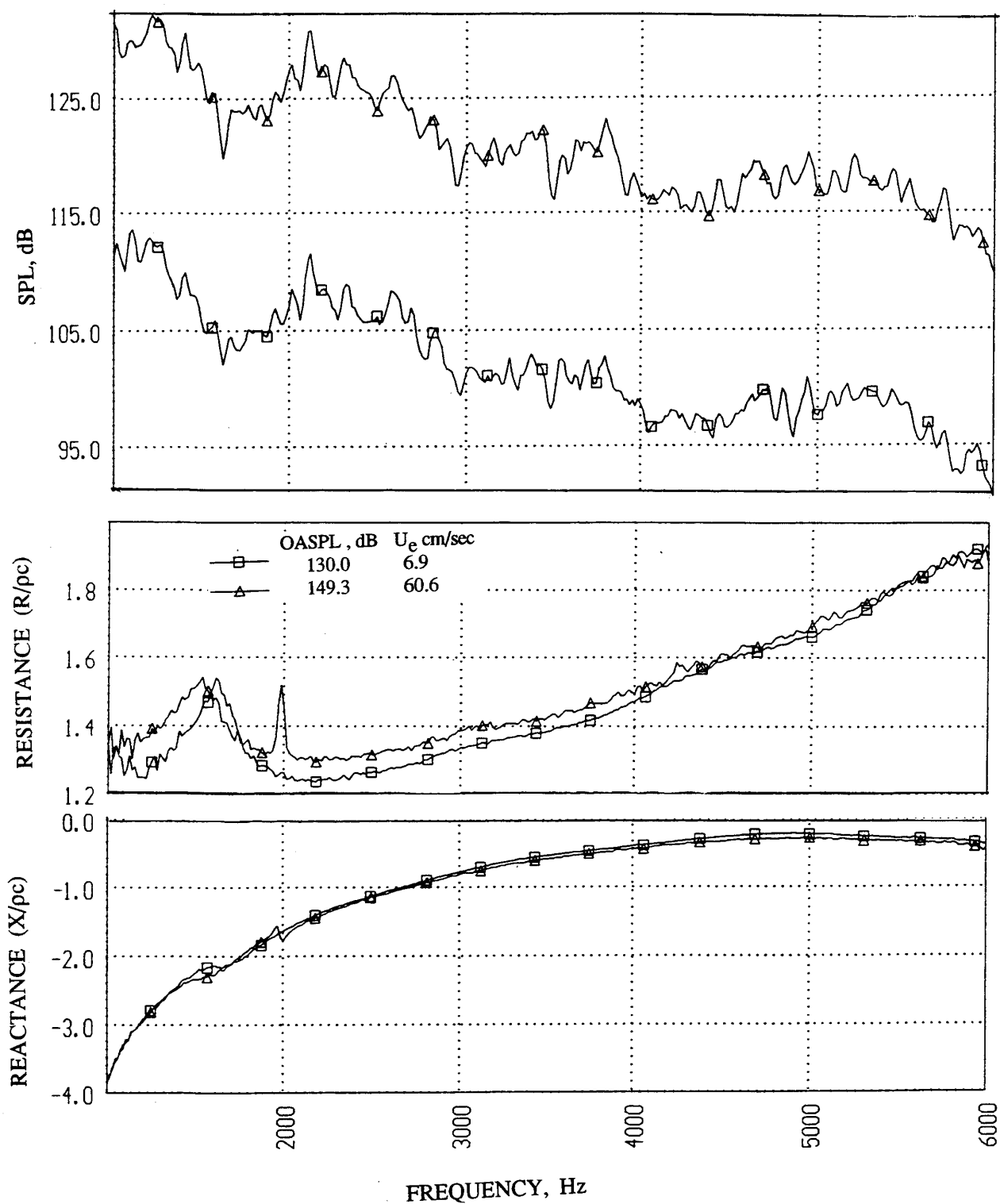


Figure 192. Sound Pressure level and corresponding normal impedance spectra at two OASPL levels for 1.25" diameter and 0.5"-deep silicon carbide sample of 500 ppi.

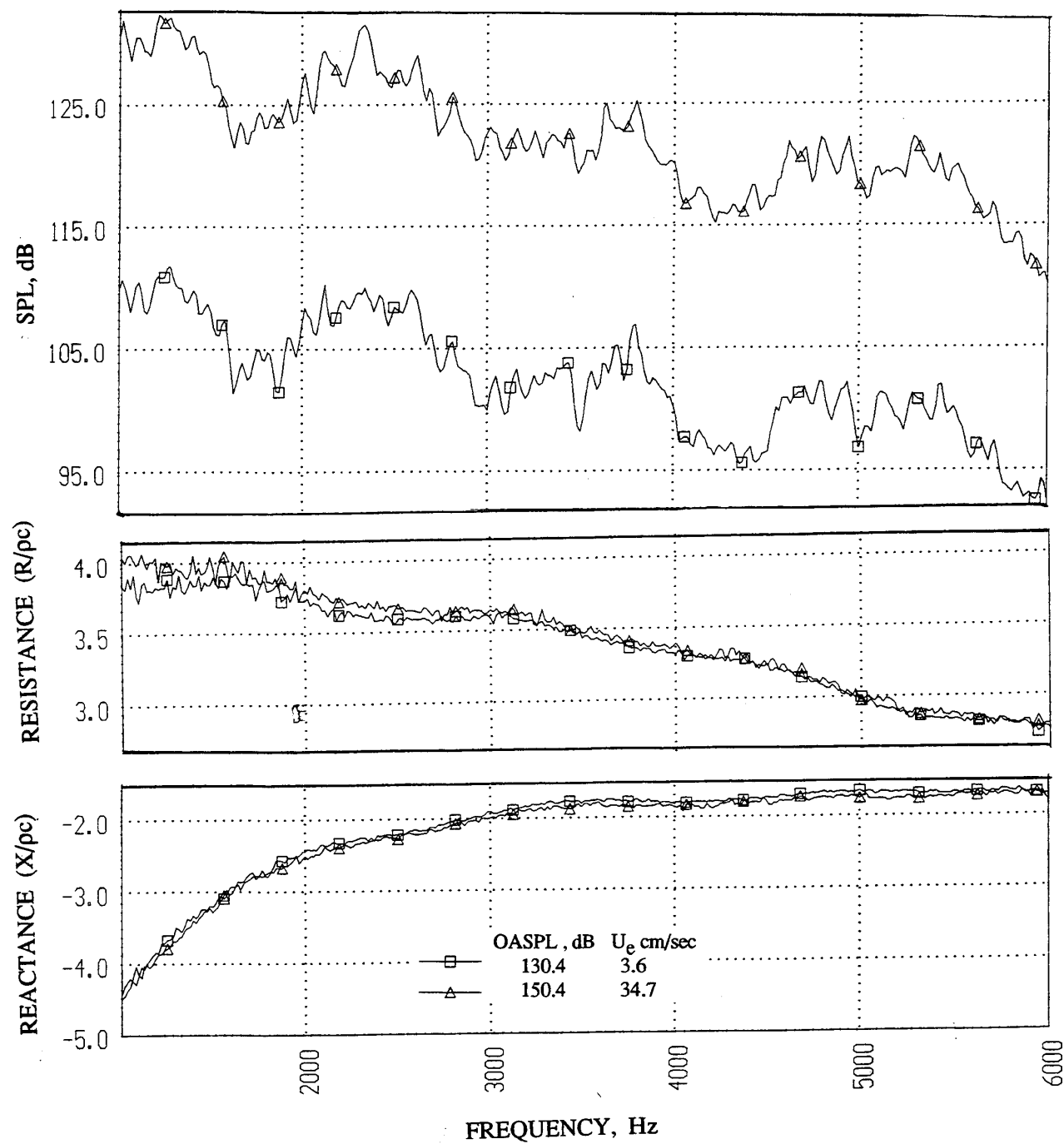


Figure 193. Sound Pressure level and corresponding normal impedance spectra at two OASPL levels for 1.25" diameter and 0.5"-deep silicon carbide sample of 600 ppi.

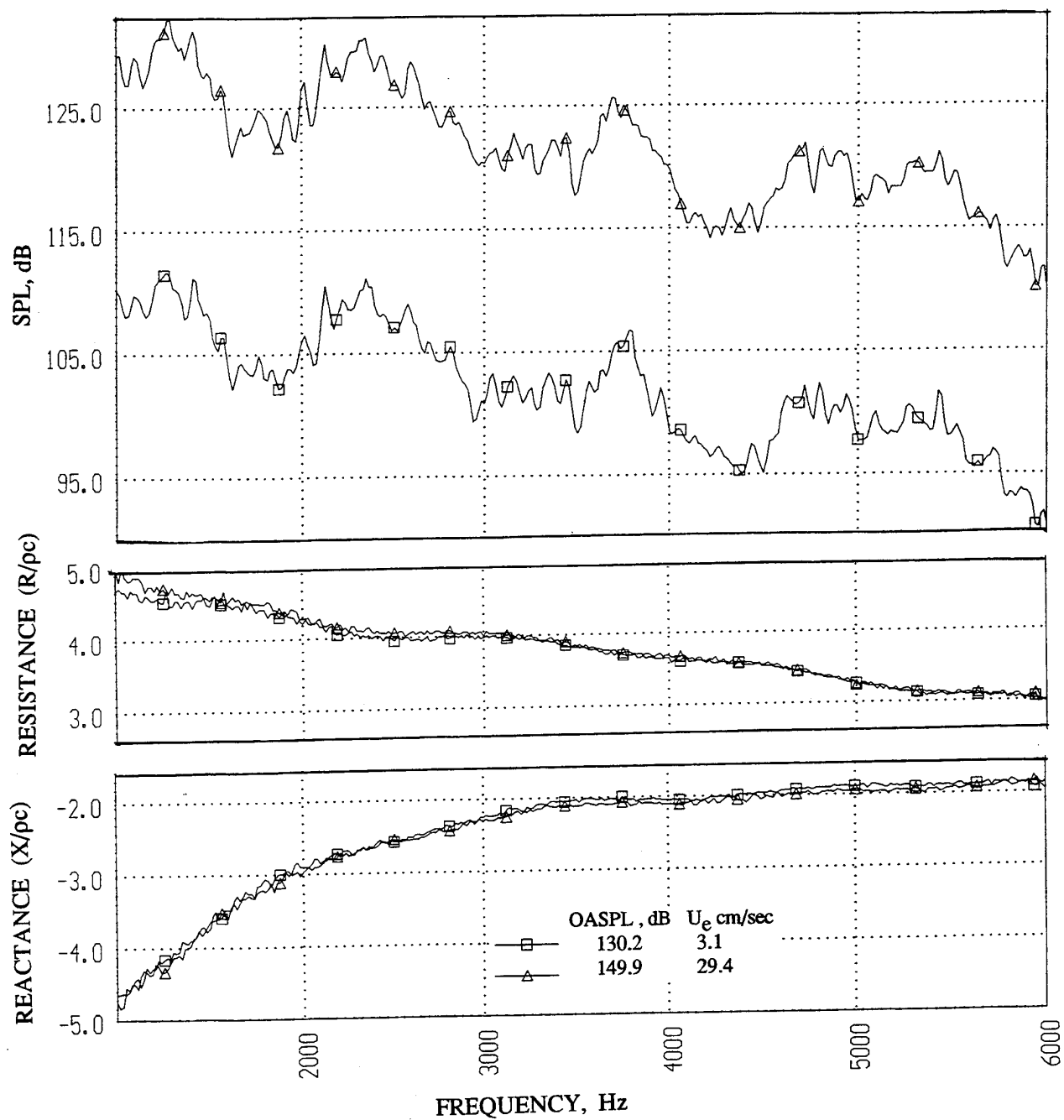


Figure 194. Sound Pressure level and corresponding normal impedance spectra at two OASPL levels for 1.25" diameter and 0.5"-deep silicon carbide sample of 800 ppi.

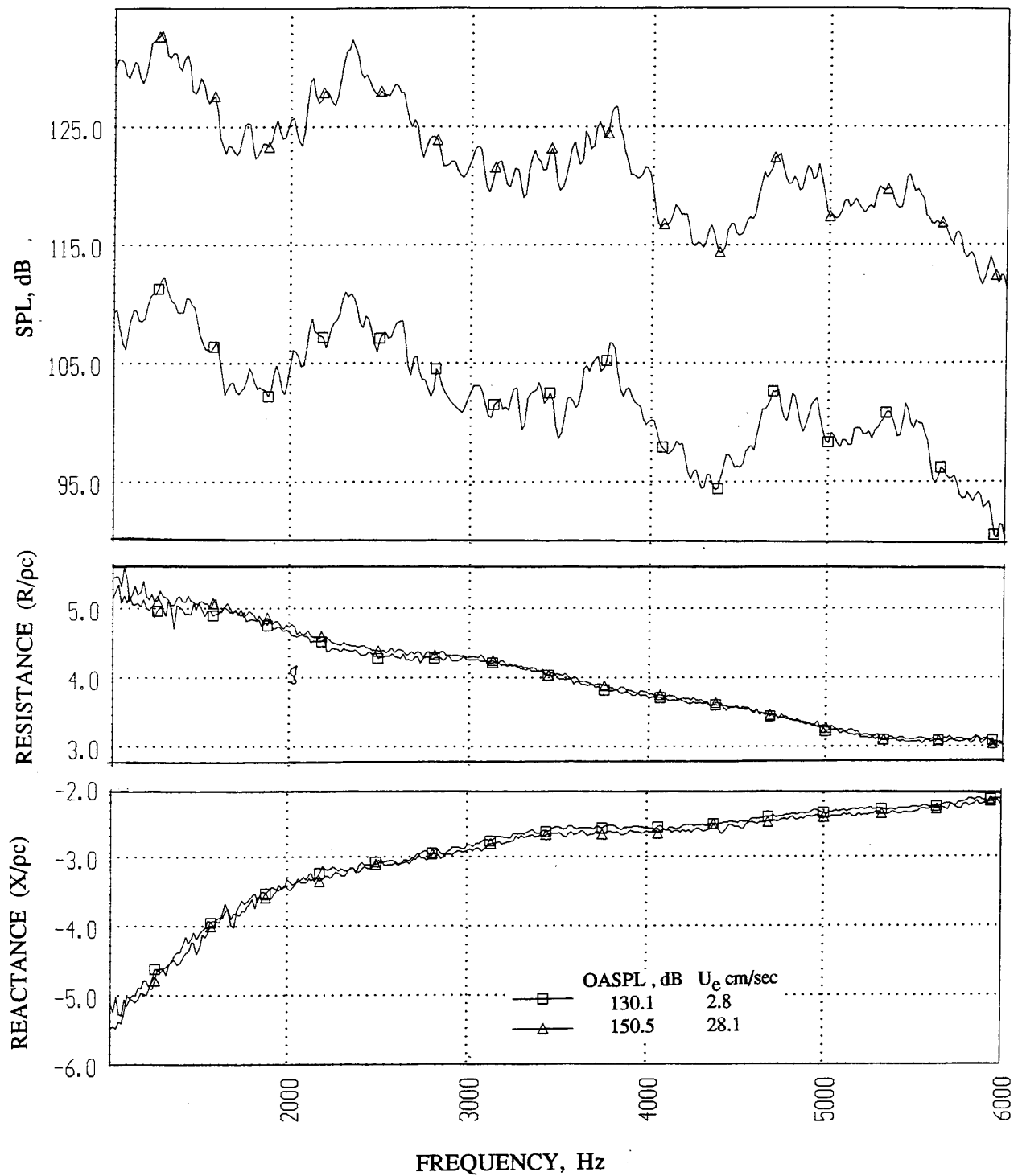


Figure 195. Sound Pressure level and corresponding normal impedance spectra at two OASPL levels for 1.25" diameter and 0.5"-deep silicon carbide sample of 1000 ppi.

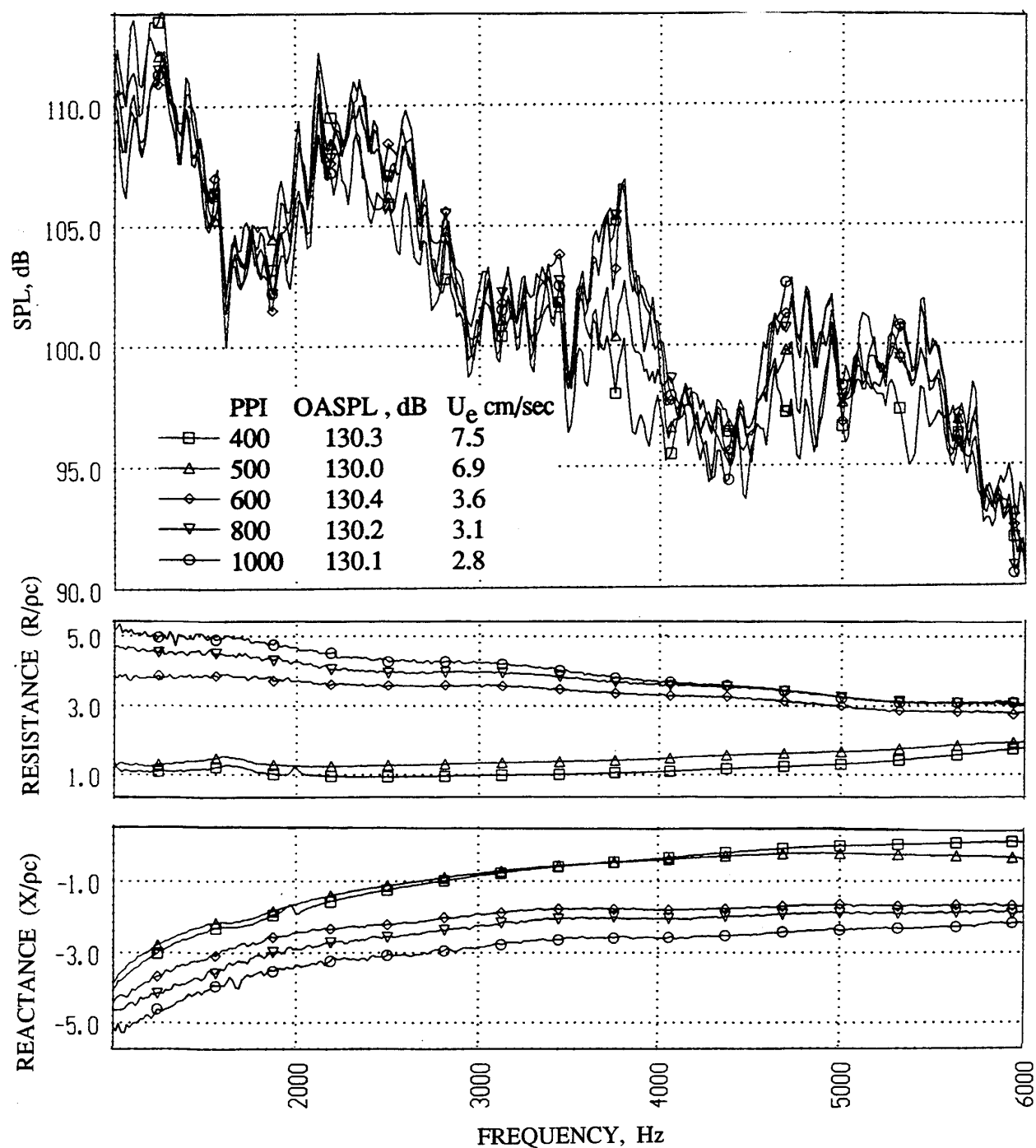


Figure 196. Sound Pressure level and corresponding normal impedance spectra for low porosity 1.25" diameter and 0.5"-deep silicon carbide samples of different PPI, tested with a nominal OASPL of 130 dB.

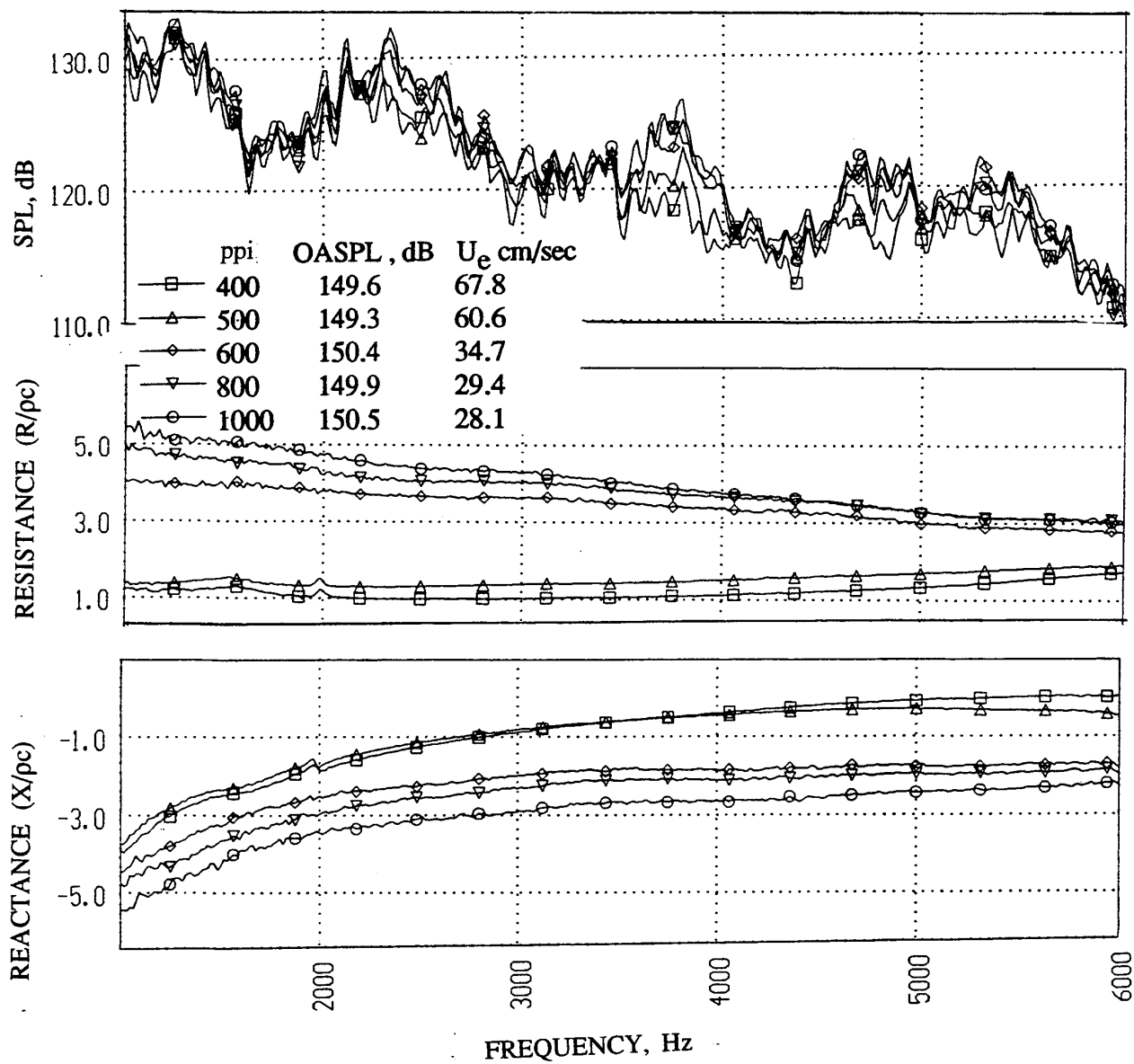


Figure 197. Sound Pressure level and corresponding normal impedance spectra for low porosity 1.25" diameter and 0.5"-deep silicon carbide samples of different ppi, tested with a nominal OASPL of 150 dB.

Table 19. Geometrical Properties and File Names for Normal Impedance and Insertion Loss Data for Carbon Foam-filled SDOF Type Panels with Linear Facesheets, 0.40" deep, 3/8" size Honeycomb Structure of 0.003" thick wall.

Panel Config. #	Sample # for DC Flow & Normal Impedance Tests with Honeycomb and facesheet	Sample # without facesheet for DC Flow & Normal Impedance Tests no Honeycomb	Bulk ppi & (Resistivity Rayls/cm)	Facesheet Nominal Resistivity, R100 in Rayls	Normal Impedance File @ 150 dB OASPL	Normal Impedance File @ 158 dB OASPL	Normal Impedance File @ 130 dB OASPL no facesheet & no Honeycomb	Normal Impedance File @ 150 dB OASPL no facesheet & no Honeycomb	Normal Impedance File @ 158 dB OASPL no facesheet & no Honeycomb	Insertion Loss 1/3-Octave Band Data Files	Insertion Loss Narrowband Data Files
3.1	3.5	3.8	400 (150)	5	wbs35.smt	wbs35h.smt	3-8-130.dat	3-8-150.dat	wbs38h.smt	tlwbs3-1.dat	rwbs3-1.smt
3.2	3.6	3.9	200 (40)	5	wbs36.smt	wbs36h.smt	3-9-130.dat	3-9-150.dat	wbs39h.smt	tlwbs3-2.dat	rwbs3-2.smt
3.3	3.7	3.10	500 (300)	5	wbs37.smt	wbs37h.smt	3-10-130.dat	3-10-150.dat		tlwbs3-3.dat	rwbs3-3.smt
3.4*			400 (150)	15	wbs34.smt	wbs34h.smt				tlwbs3-4.dat	rwbs3-4.smt

Note: 1. Panel Config #: Panels of 12"x5" Treated area tested for Insertion Loss Measurement in a Flow Duct of 4" height with one side treated (i.e., the duct height becomes 8"). For panel 3.4 there was no honeycomb structure.
2. Sample # - Samples for DC Flow Resistance & Normal Impedance Tests, identical to the corresponding panel geometry (for DC flow resistance backplates not used).

resistance provided by the blockage due to honeycomb and its bonding process for the bulk-filled configurations.

DC Flow Resistance: The facesheet characteristics are specified by its nonlinear factor $NLF_{150/20}$, DC flow resistance R_{100} , thickness, and porosity. Bulk material DC flow resistivity is the DC flow resistance of a bulk material for a given thickness, divided by the thickness. The R_{100} and $NFL_{150/20}$ are defined in the same manner as those for the linear facesheet. The $NFL_{150/20}$ is assumed to be negligible for most bulk materials. Hence, the bulk material is characterized by its resistivity R_{100} only.

Samples of the same designs as listed in Table 19 are fabricated for DC flow resistance and normal impedance tests. A separate set of test samples of the three different bulk materials (listed in Table 19) is prepared for DC flow and normal impedance tests.

Normal Impedance: Normal impedance are measured for the 0.4"-deep 200, 400, and 500 ppi samples using low and high frequency apparatus. Low frequency normal impedance results for 200, 400, and 500 pp samples are presented in Figures 198 through 200, respectively. The influence of acoustic excitation intensity is insignificant on the impedance levels for these samples. Comparison of impedance spectra between the samples of different ppi for nominal OASPLs of 130 and 150 dB are shown in Figures 201 and 202, respectively. The specific resistance monotonically increases with ppi for the entire frequency range, whereas, the reactance levels remain the same with respect to ppi. The particle velocity decreases by small amount with decreasing porosity (i.e., increasing ppi). Specific resistance values for these samples lie between 0.5 and 1.5, whereas, the goal is 1.5 to 2.0. Similarly, the specific reactance levels being between -3.0 to 0 do not meet the requirement for most frequencies.

The influence of acoustic excitation level on the normal impedance, measured in the high frequency impedance tube, for the linear facesheets, the carbon foam alone, carbon foam with facesheet, and carbon foam-filled honeycomb with facesheet is shown in Figures 203 through 205. In general, the nonlinear effects due to excitation level on normal impedance are negligible, except for 500 ppi carbon foam (see Figure 205 (b)). The effect of facesheet resistivity on normal impedance of the bulk is demonstrated in Figures 206 and 207. The resistance as well as the reactance for the facesheet increase with its resistivity (see Figure 206 (a)). For 200 ppi carbon foam, the resistance and reactance increase due to the addition of the facesheet (see Figure 206(b)). For 400-ppi carbon foam the resistance at higher frequencies (above about 8 kHz) decreases with facesheet (see Figure 207 (a)). The normal impedance for 400 ppi carbon foam with 15 Rayls' facesheet is compared with 400 ppi carbon foam-filled

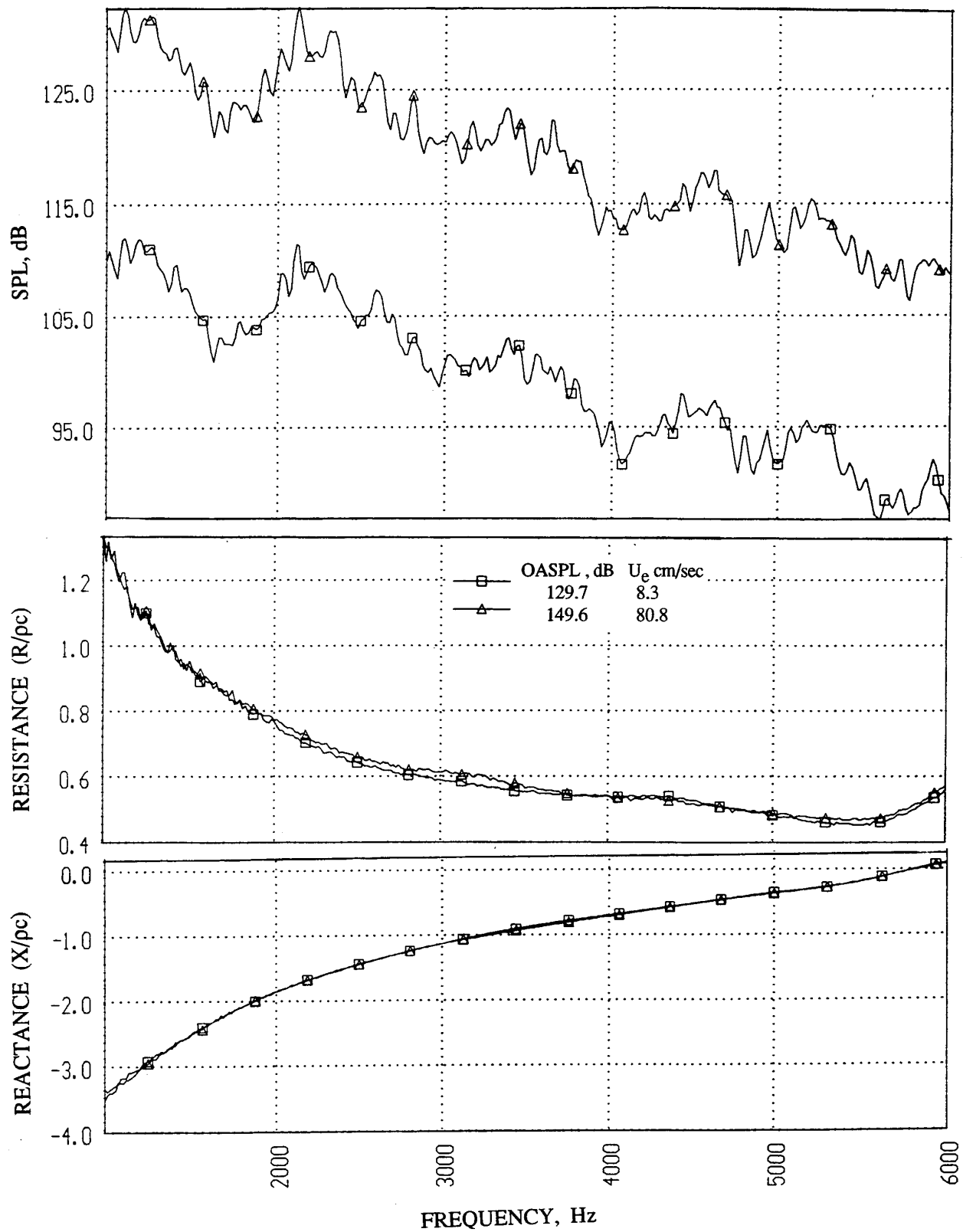


Figure 198. Sound Pressure level and corresponding normal impedance spectra at two OASPL levels for 1.25" diameter and 0.4"-deep carbon foam sample of 200 PPI.

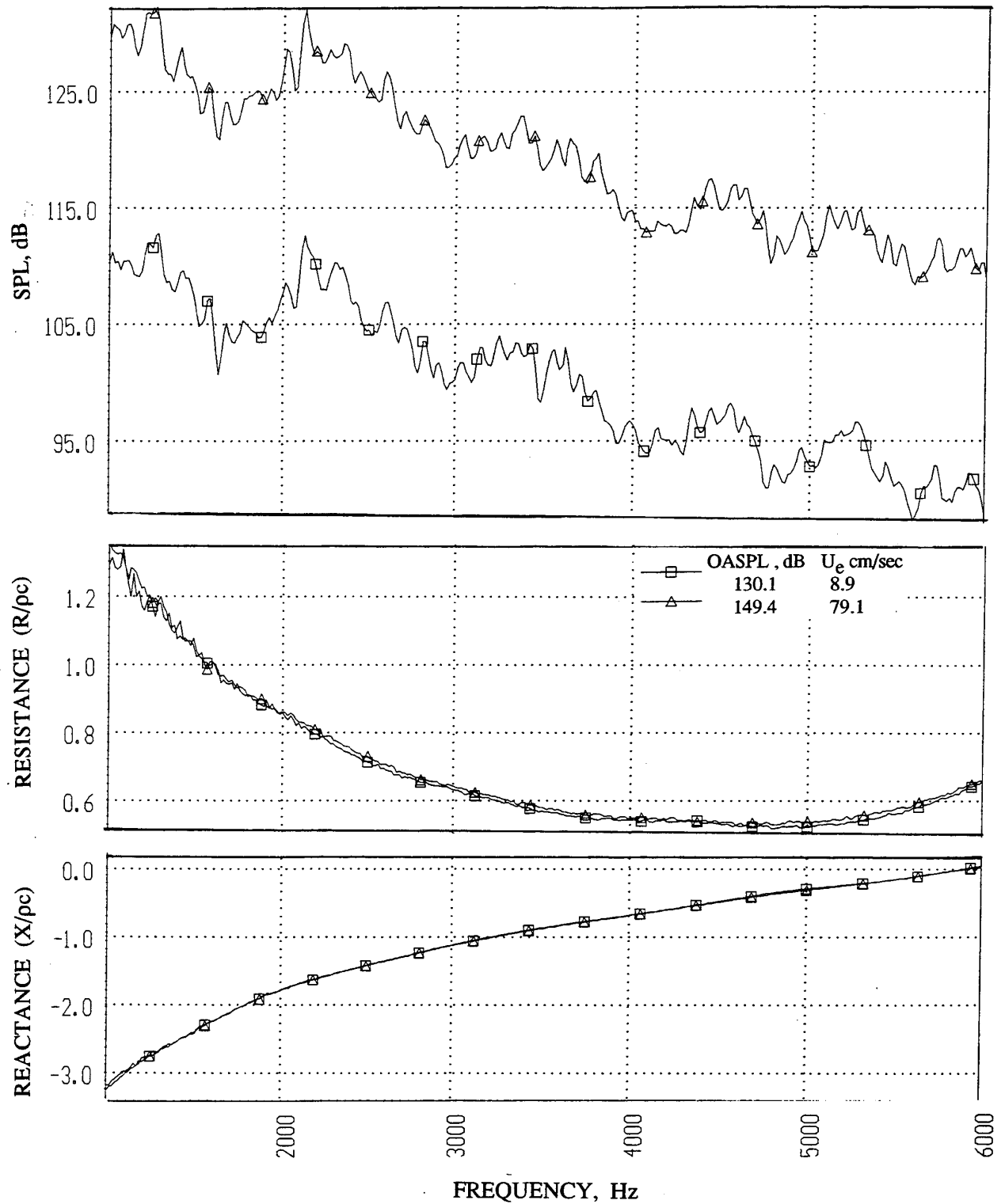


Figure 199. Sound Pressure level and corresponding normal impedance spectra at two OASPL levels for 1.25" diameter and 0.4"-deep carbon foam sample of 400 PPI.

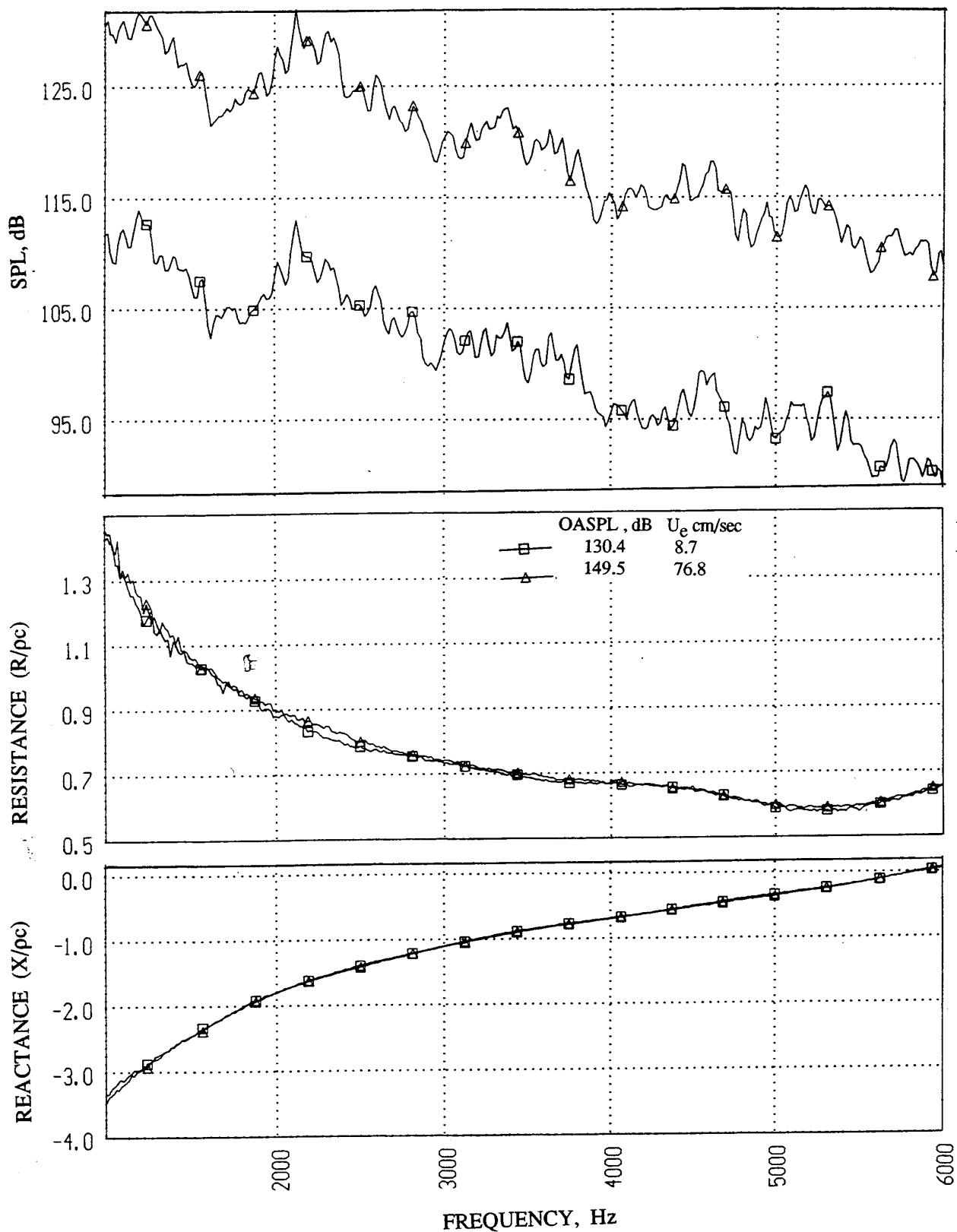


Figure 200. Sound Pressure level and corresponding normal impedance spectra at two OASPL levels for 1.25" diameter and 0.4"-deep carbon foam sample of 500 PPI.

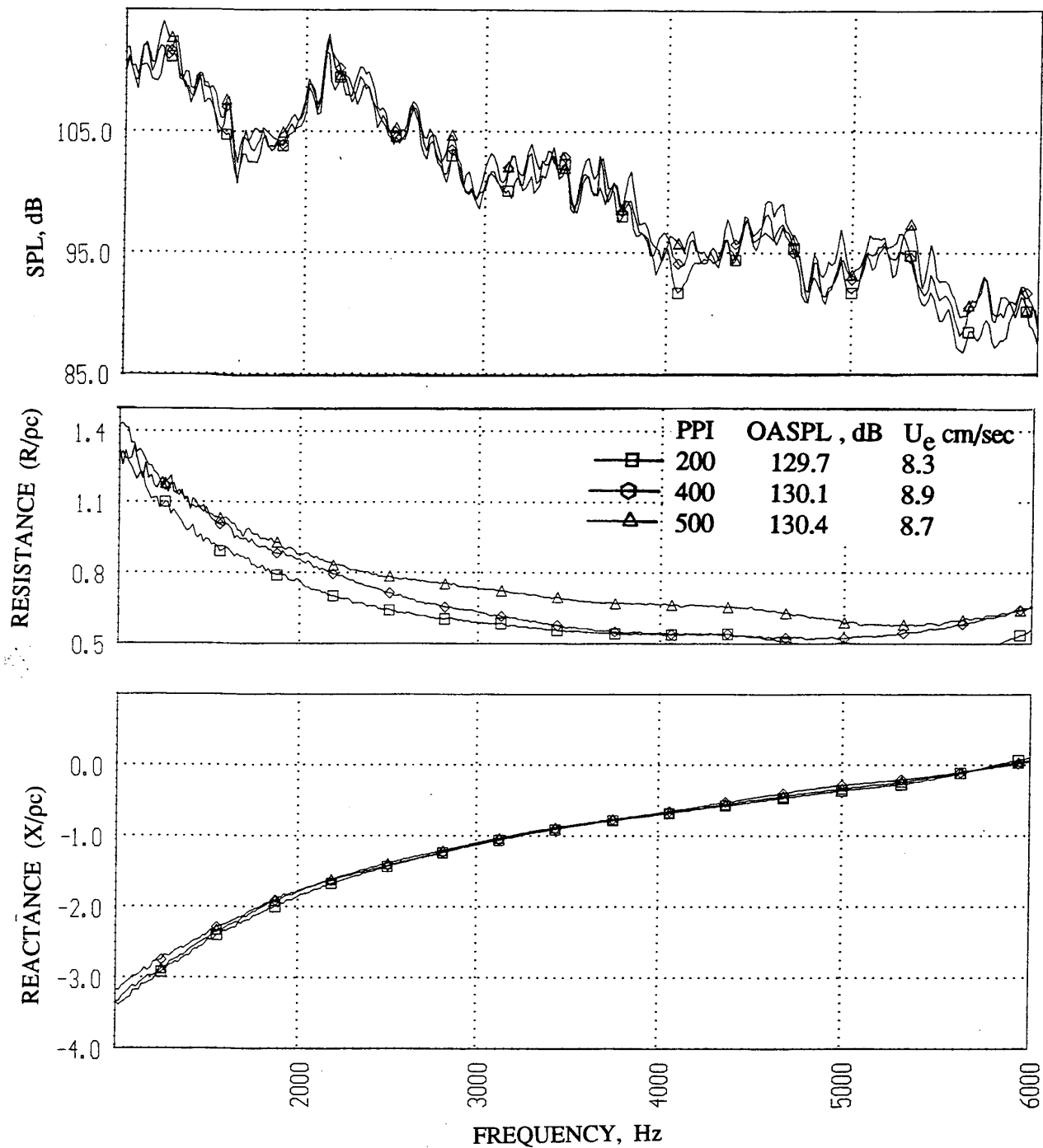


Figure 201. Sound Pressure level and corresponding normal impedance spectra for 1.25" diameter and 0.4"-deep carbon foam samples of different PPI, tested with a nominal OASPL of 130 dB.

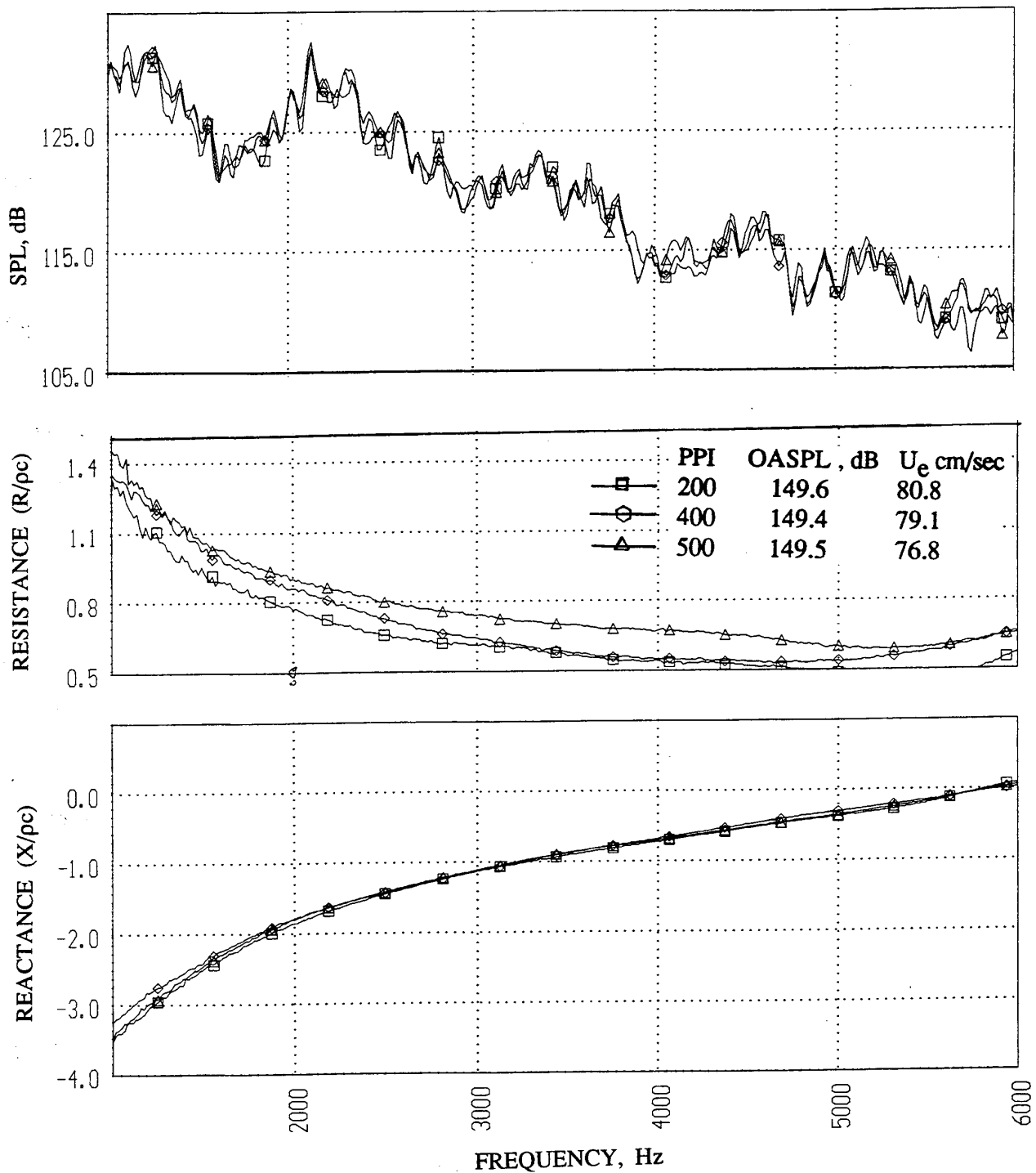


Figure 202. Sound Pressure level and corresponding normal impedance spectra for 1.25" diameter and 0.4"-deep carbon foam samples of different PPI, tested with a nominal OASPL of 150 dB..

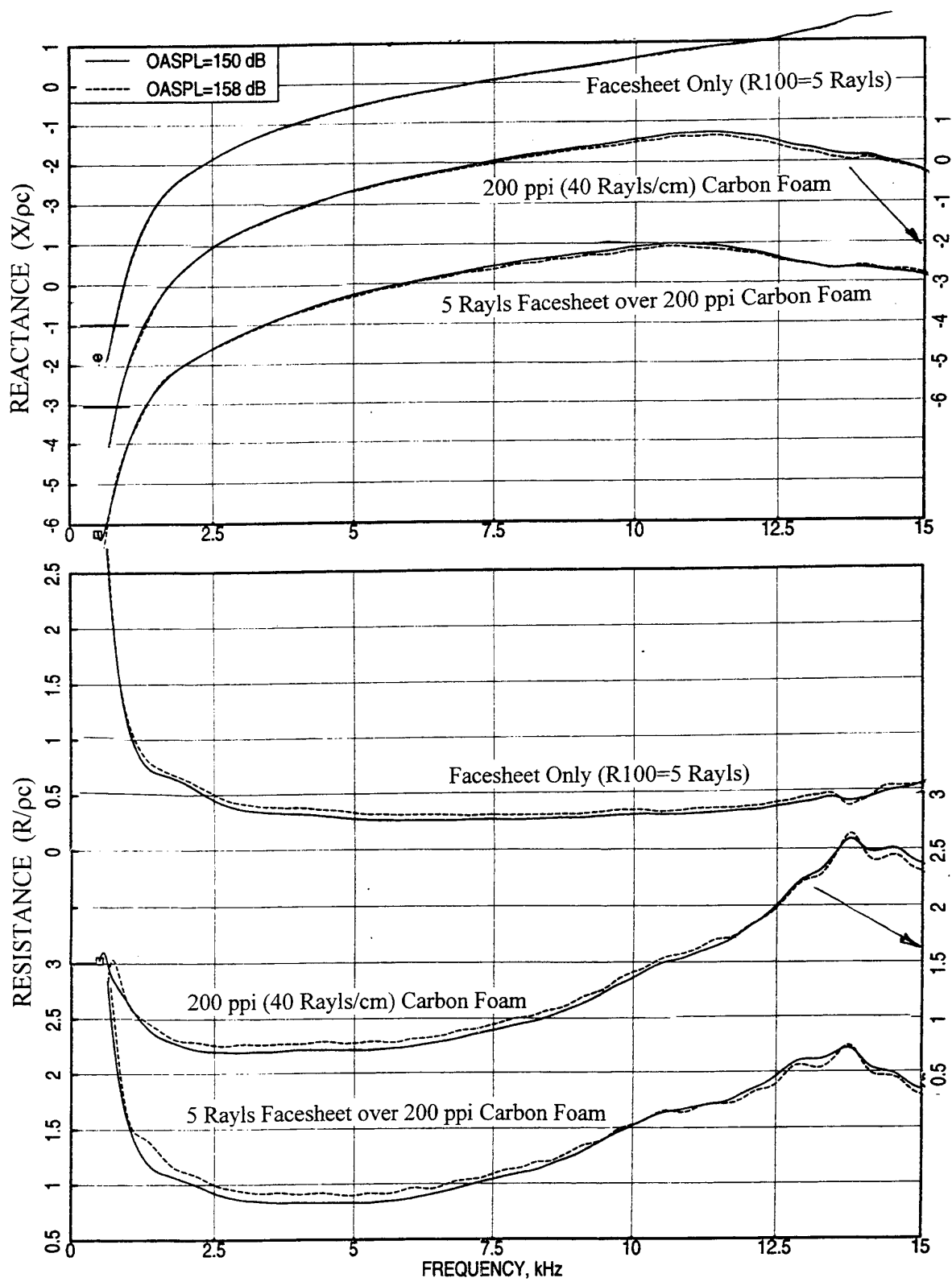


Figure 203. Effect of excitation level on normal impedance spectra for 0.4" deep samples with linear facesheet (for facesheet only configuration a 0.4" back cavity is placed).

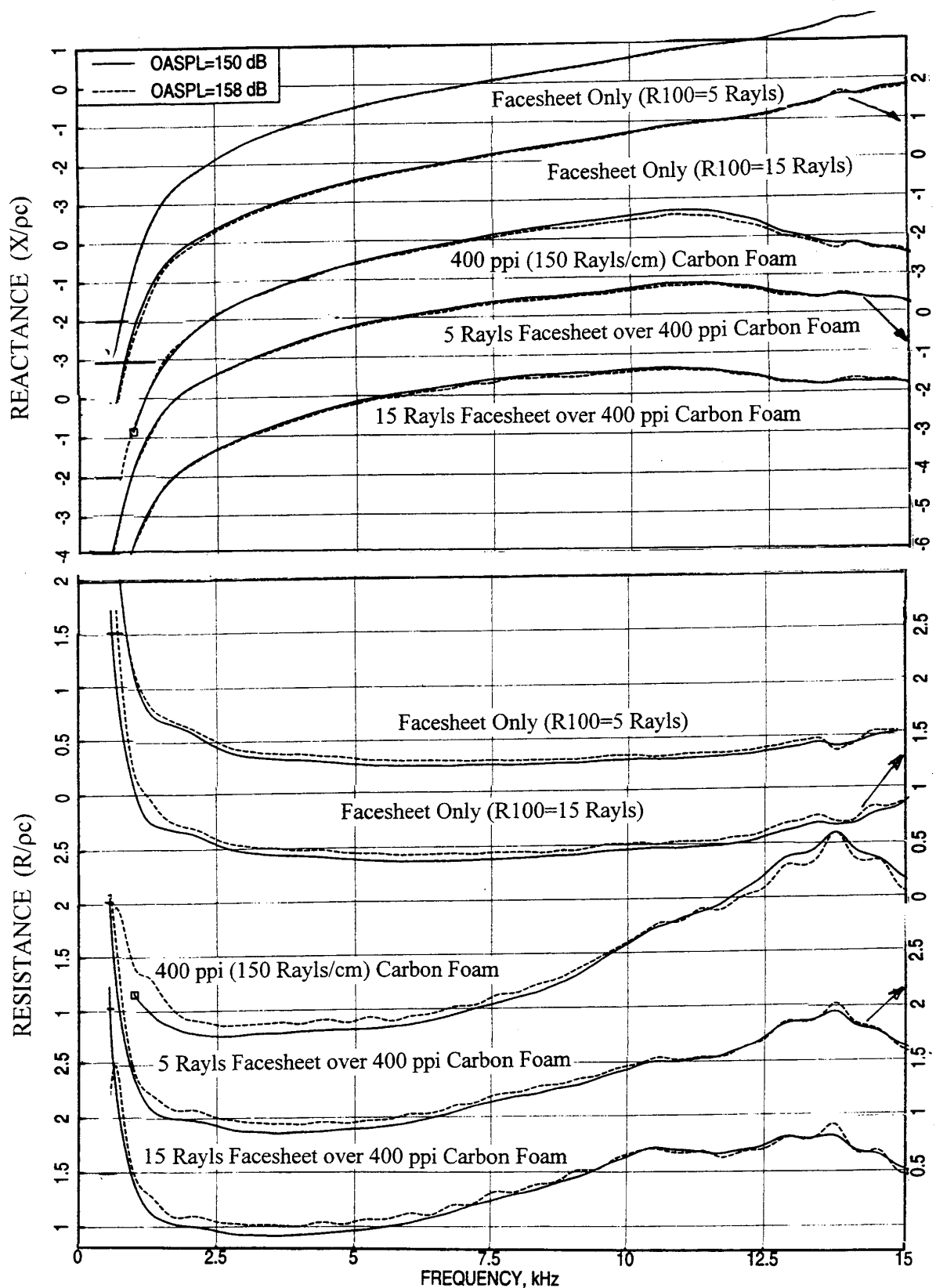


Figure 204. Effect of excitation level on normal impedance spectra for 0.4" deep samples with linear facesheet (for facesheet only configuration a 0.4" back cavity is placed).

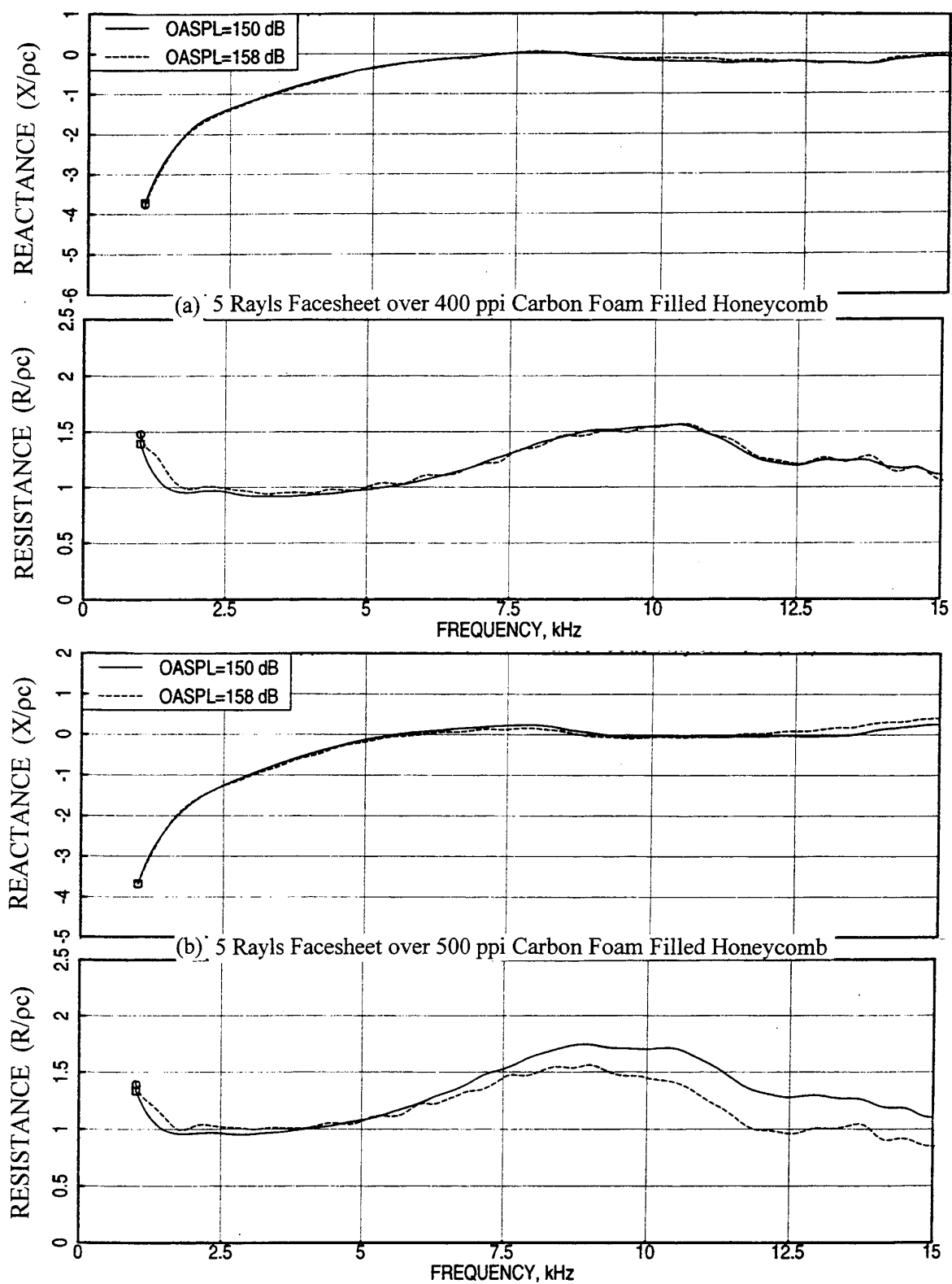


Figure 205. Effect of excitation level on normal impedance spectra for 0.4" deep bulk-filled SDOF type samples with linear facesheets of 5 Rayls.

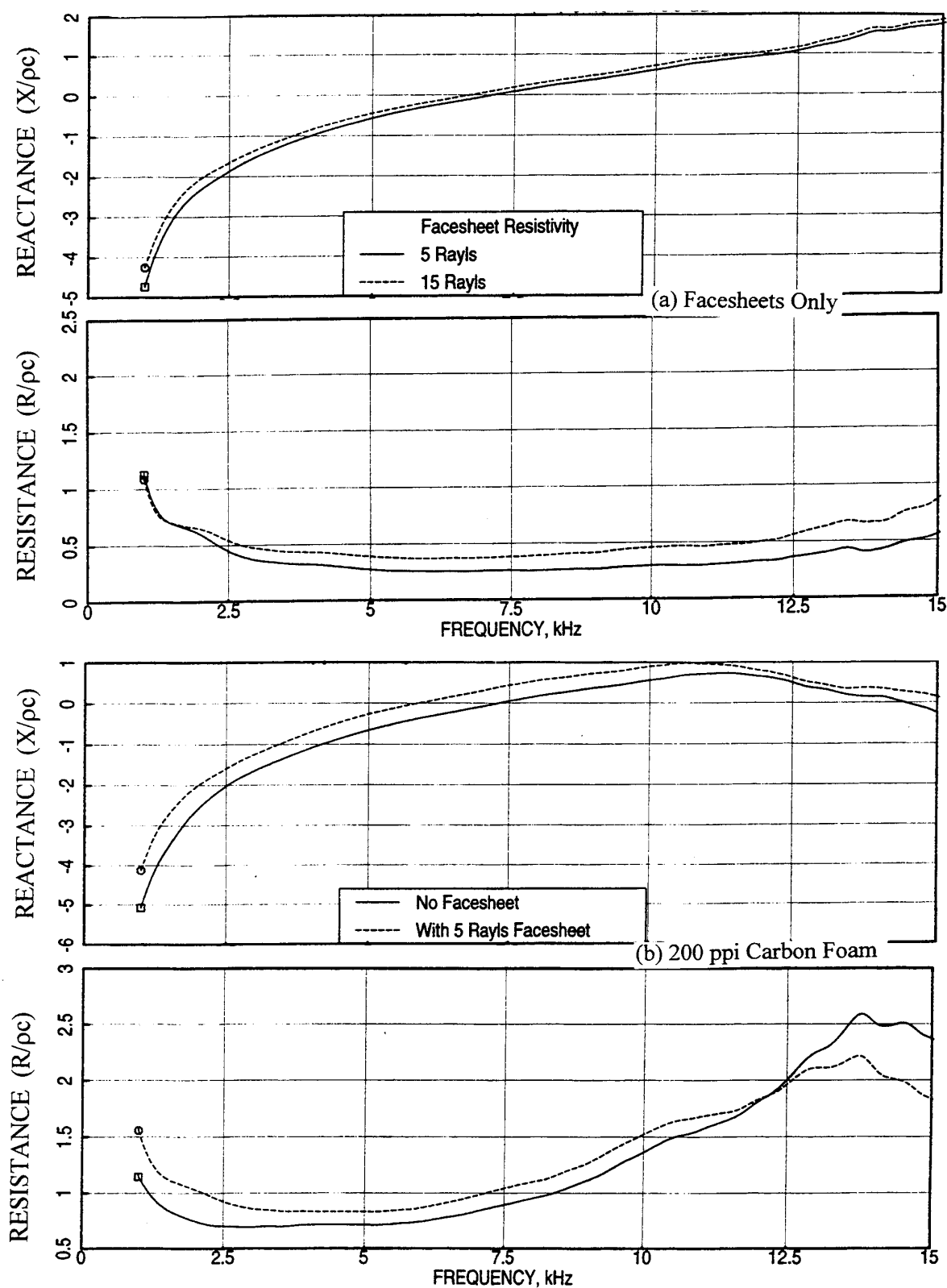


Figure 206. Effect of facesheet resistivity on normal impedance spectra for 0.4" deep samples with and without 200 ppi Carbon Foam.

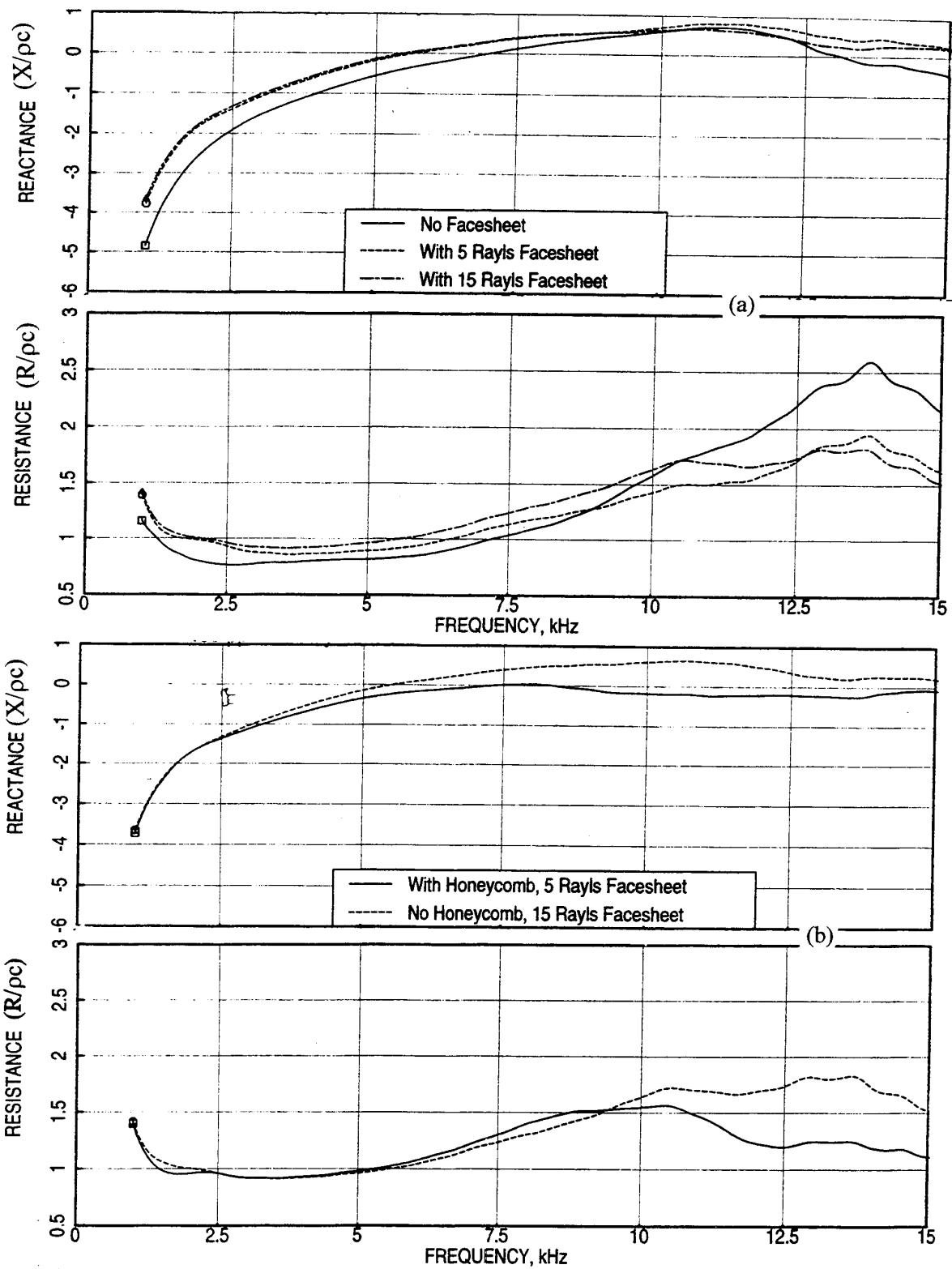


Figure 207. Effect of facesheet resistivity on normal impedance spectra for 0.4" deep 400 ppi carbon foam with linear facesheet.

sample with 5 Rayls' facesheet in Figure 207 (b). The reactance above 3 to 4 kHz and resistance at frequencies above 10 kHz are higher for bulk-filled configuration compared to bulk only with 15 Rayls' facesheet. Comparison of impedance spectra between the samples of different ppi with facesheet of 5 Rayls for nominal OASPL 150 dB is shown in Figure 208. The specific resistance monotonically increases with ppi for frequencies below 10 kHz.

Boundary Layer Results: The effect of bulk resistivity on boundary layer profiles and skin friction coefficients for three different carbon foam-filled panels with linear facesheet of 5 Rayls resistivity are shown in Figure 209. The boundary layer becomes more turbulent with decreasing bulk resistivity. The skin friction increases slightly with decreasing bulk resistivity. The velocity profiles and skin friction coefficients for a bulk filled honeycomb panel are compared with an extended reaction type panel with the same bulk material in Figure 210. The friction coefficient seems to be lower for extended reaction type panel.

Insertion Loss Results: Figure 211 shows the effect of grazing flow Mach number on insertion loss spectra for three different carbon foam-filled panels with linear facesheet of 5 Rayls resistivity. Figure 212 shows the effect of bulk resistivity on insertion loss spectra for carbon foam-filled panels with linear facesheet of 5 Rayls at different grazing flow Mach numbers. Influence of grazing flow on insertion loss spectra for 400 ppi carbon foam panels, with and without honeycomb, is shown in Figures 213 and 214. Panel with carbon slab (no honeycomb) shows relatively higher acoustic suppression.

5.7 Acoustic Characteristics of 2DOF Type Panels with Linear Facesheets and Septums:

2DOF Panels: A single 1/3-scale 2DOF type panel with linear facesheet and septum (set #4) is designed (see Figure 79). The design parameters for this panel are listed in Table 4. In addition, two variable depth 2DOF panels (set #6), shown in Figure 81, are also designed. The basic sandwich construction of these types of panels is described in section 4. Samples of the same designs are also fabricated for DC flow resistance (without any backplate) and normal impedance tests. Partial constructions of these samples, either with facesheet or with septum are also fabricated for DC flow resistance and normal impedance tests. These samples are also listed in Table 20 along with their DC flow characteristics.

5.7.1 Normal Impedance:

Two Linear Variable Depth Septum Panel (i.e., Set #6) samples, designs, I and II (see Figure 215), consisting of a linear material facesheet, linear material septum, and a double

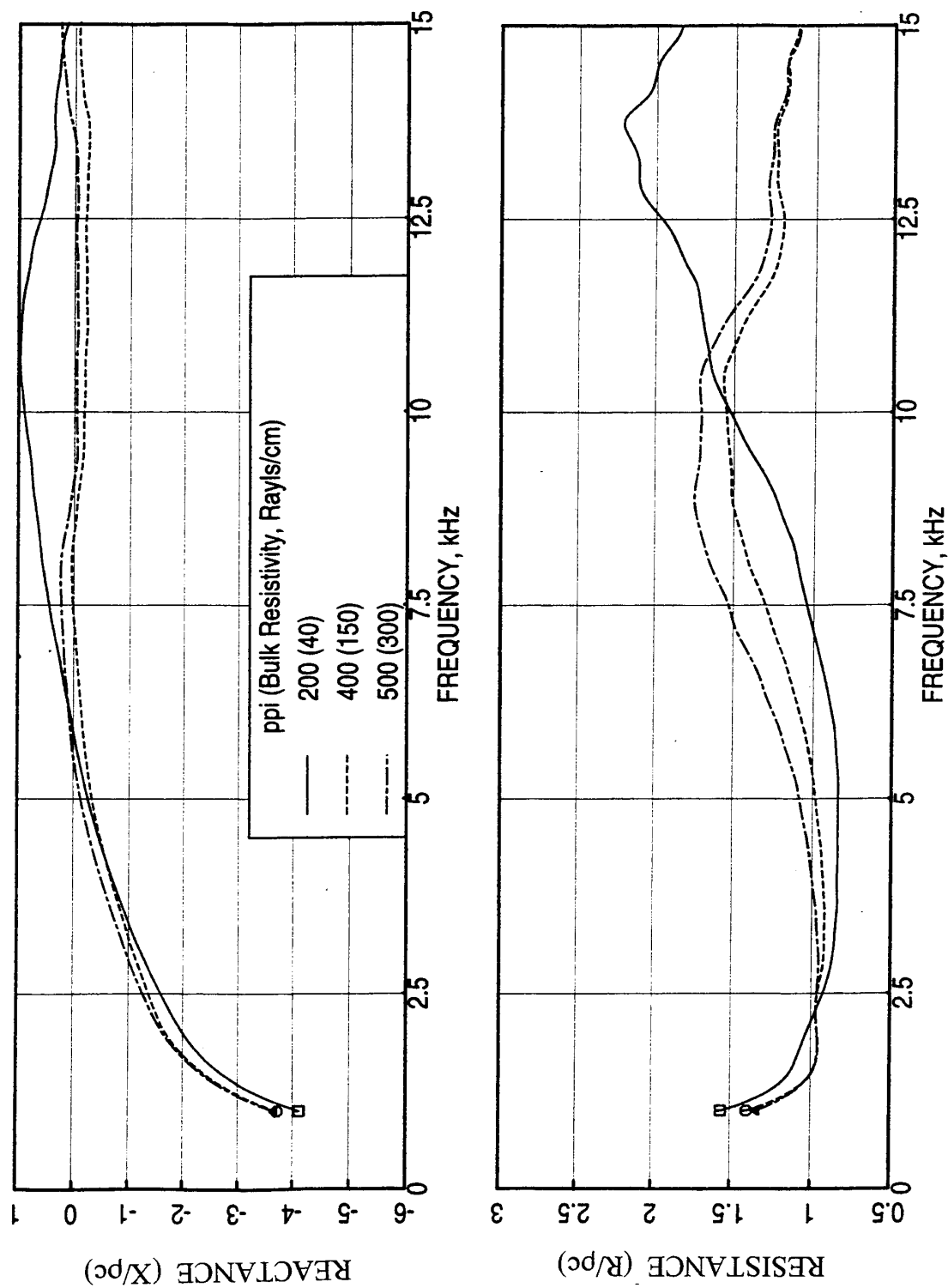


Figure 208. Effect of bulk resistivity on normal impedance spectra for 0.4" deep carbon foam-filled SDOF type samples with linear facesheets of 5 Rayls.

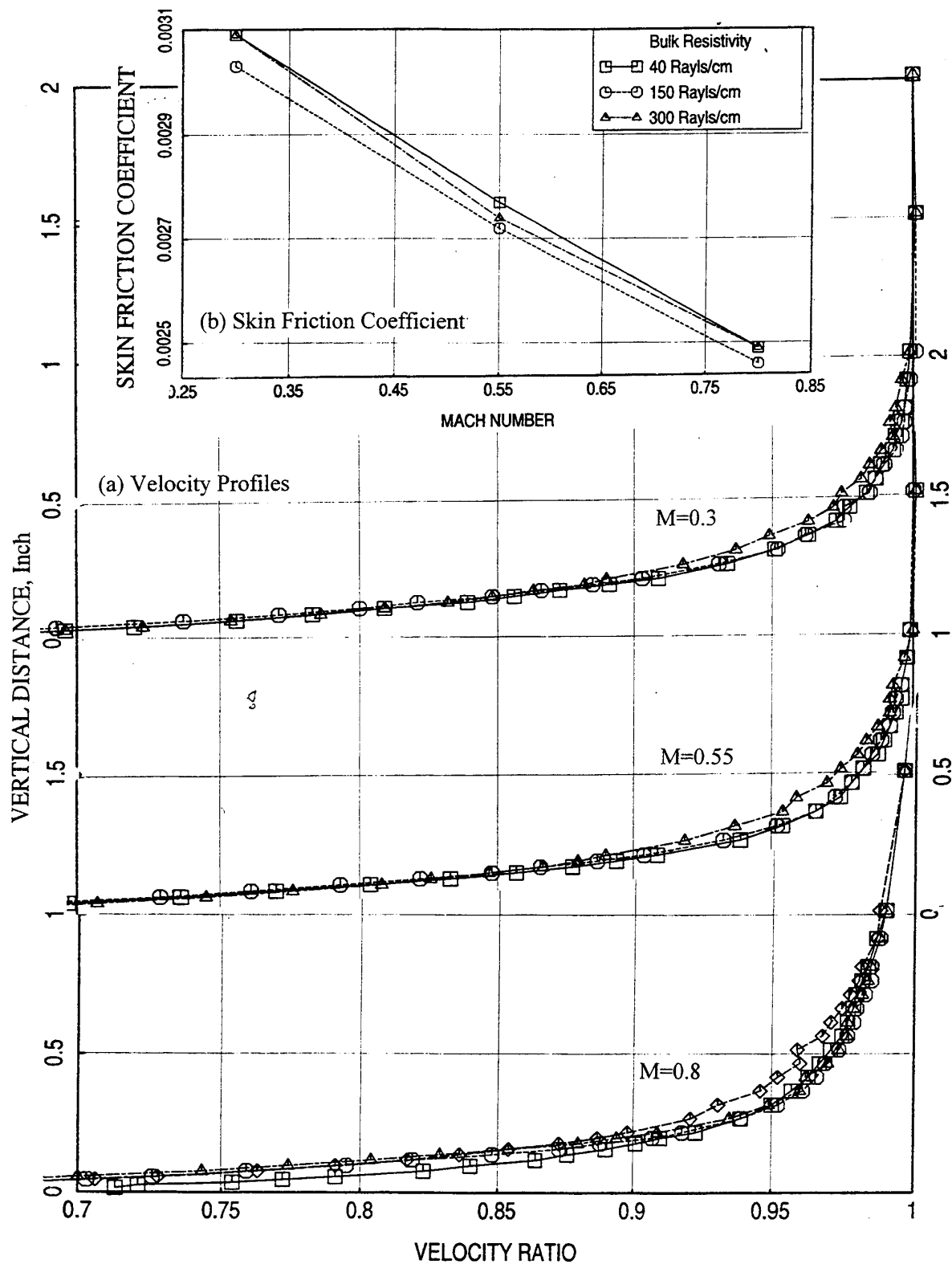


Figure 209. Effect of bulk resistivity on (a) velocity profile in the flow duct and (b) local skin friction coefficient for bulkfilled 0.4-deep SDOF type panels with linear facesheets of 5 Rayls resistivity.

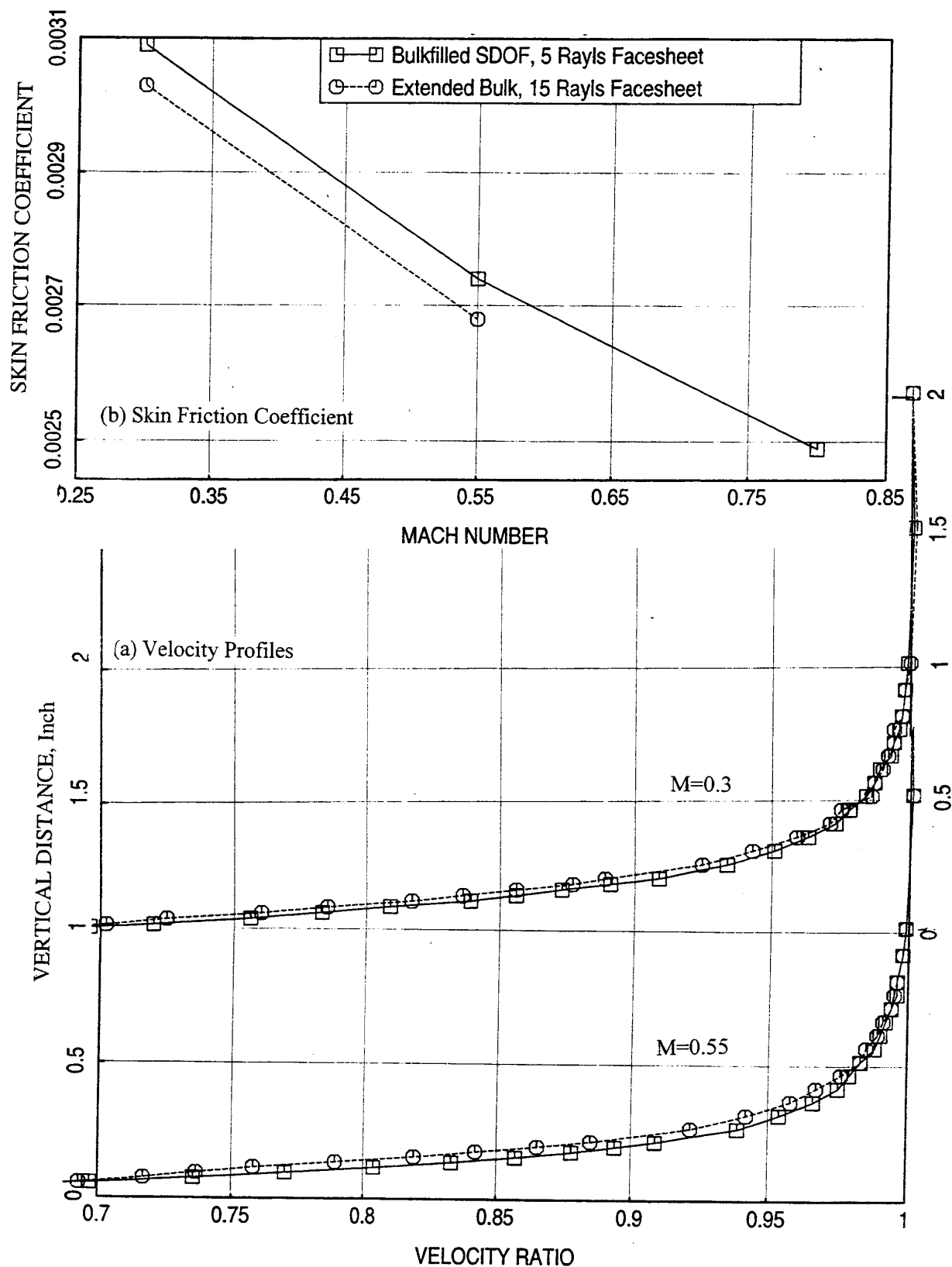


Figure 210. Comparison of (a) velocity profile in the flow duct and (b) local skin friction coefficient between 400 ppi carbon foam-filled SDOF type panel with linear facesheet of 5 Rayls and extended 400 ppi carbon foam panel with linear facesheet of 15 Rayls.

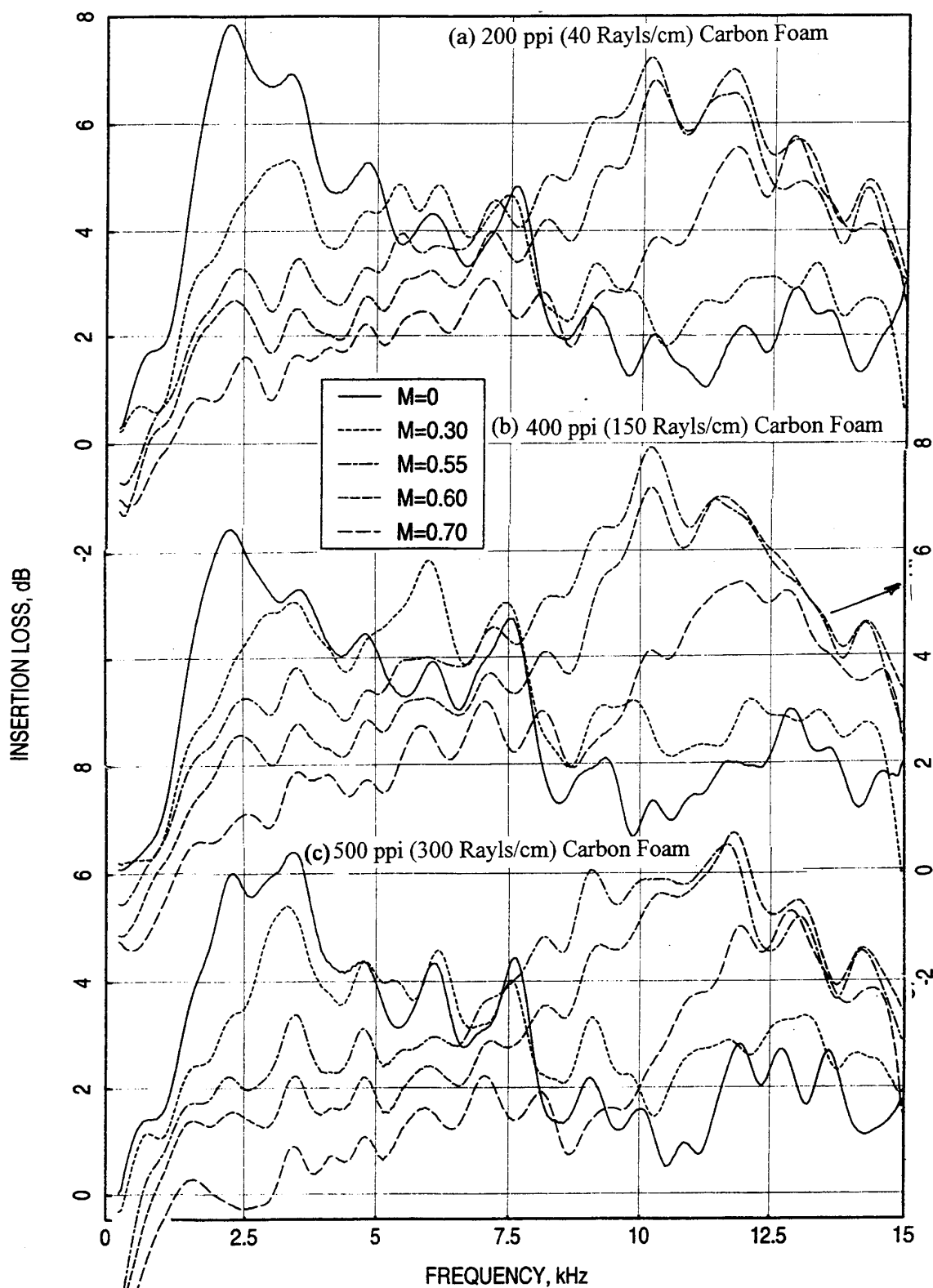


Figure 211. Influence of grazing flow Mach number on insertion loss spectra for carbon foam-filled SDOF type panels with linear facesheet of 5 Rayls, mounted on one side of the 4"-high flow duct for different bulk resistivities, $D=0.40''$.

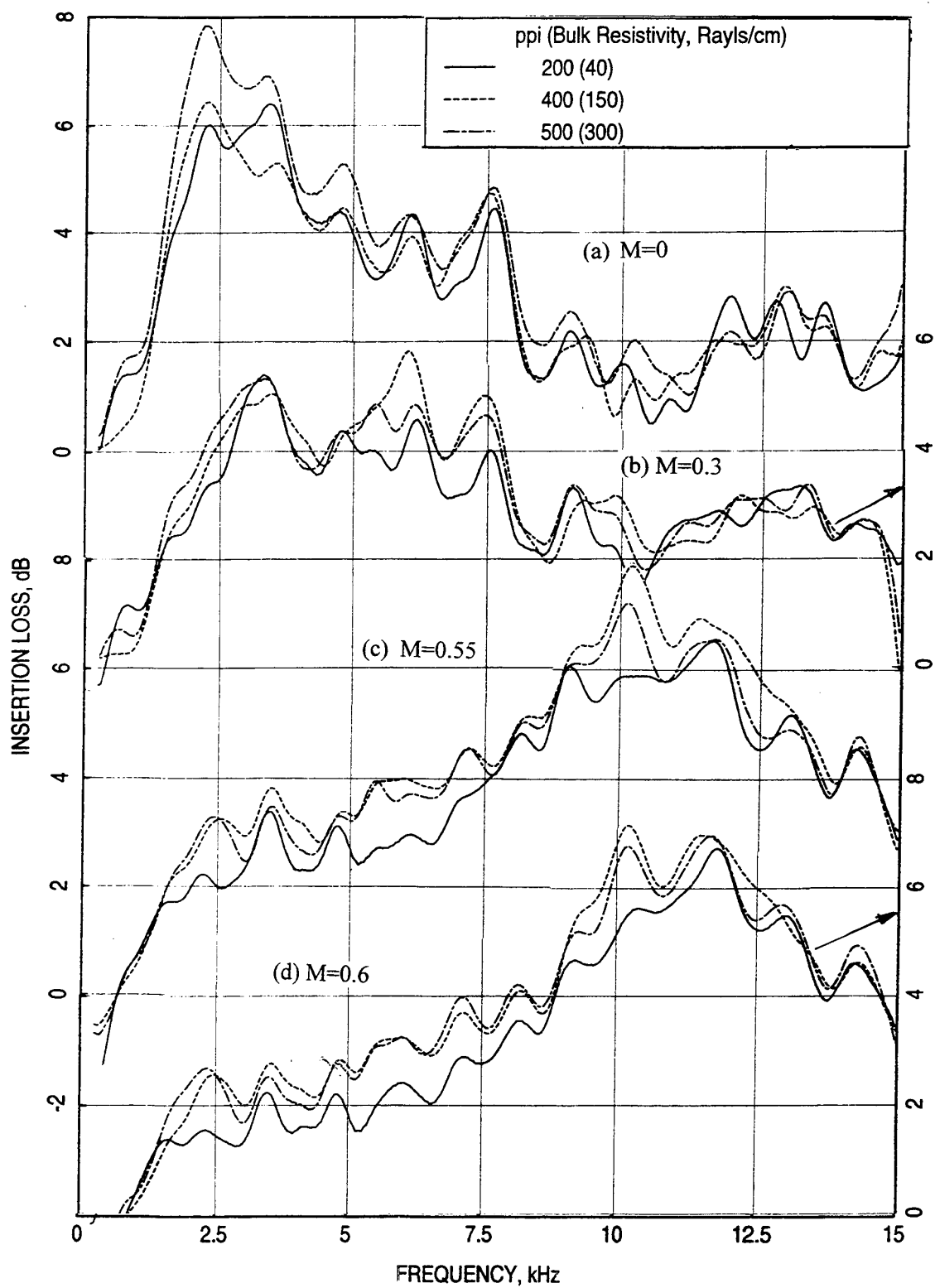


Figure 212. Effect of bulk resistivity (R100) on insertion loss spectra for carbon foam-filled SDOF type panels with linear facesheet of 5 Rayls at different grazing flow Mach numbers (M), mounted on one side of the 4"-high flow duct; $D=0.40"$.

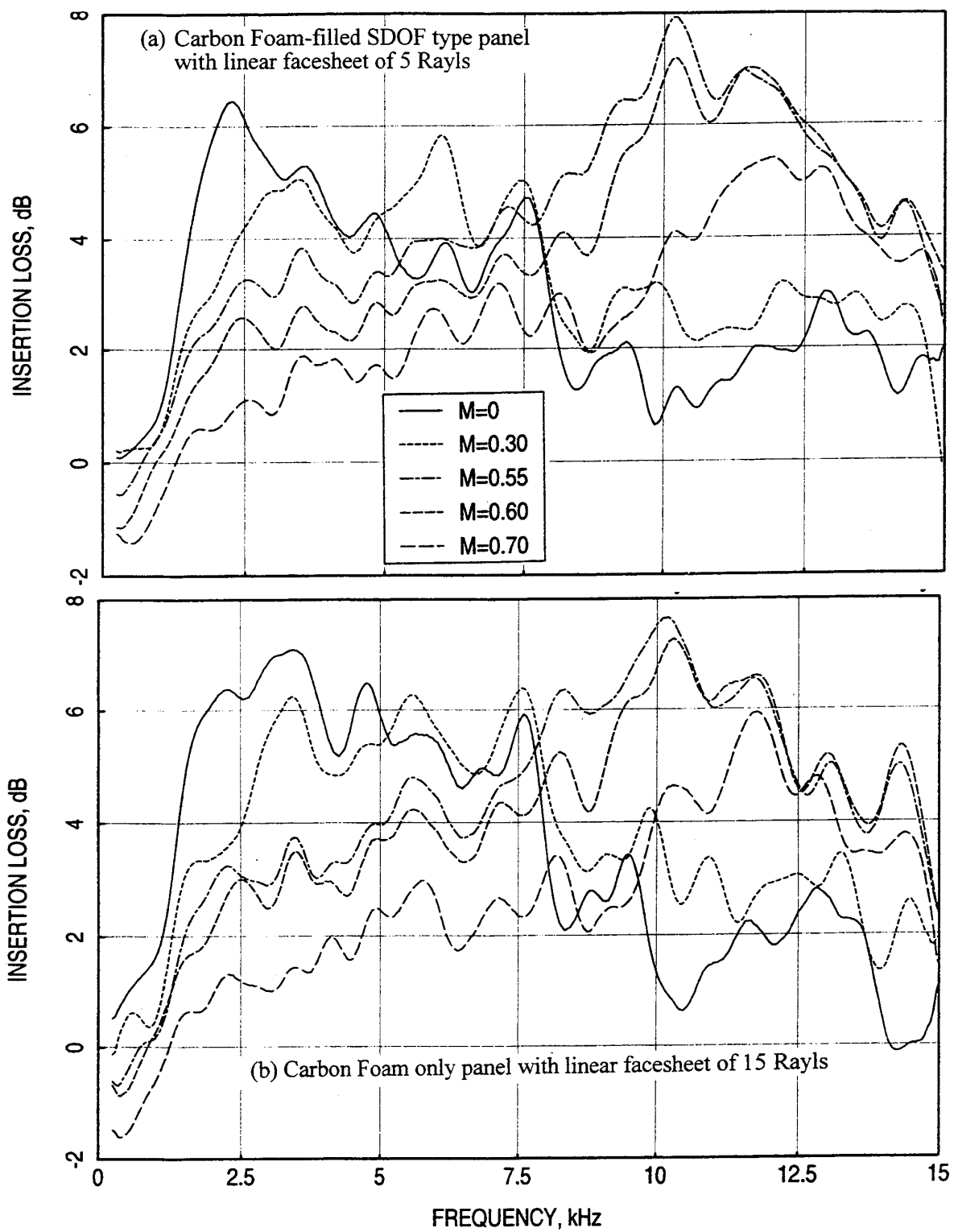


Figure 213. Influence of grazing flow Mach number on insertion loss spectra for 400 ppi (150 Rayls/cm) carbon foam panels with linear facesheets, $D=0.40''$.

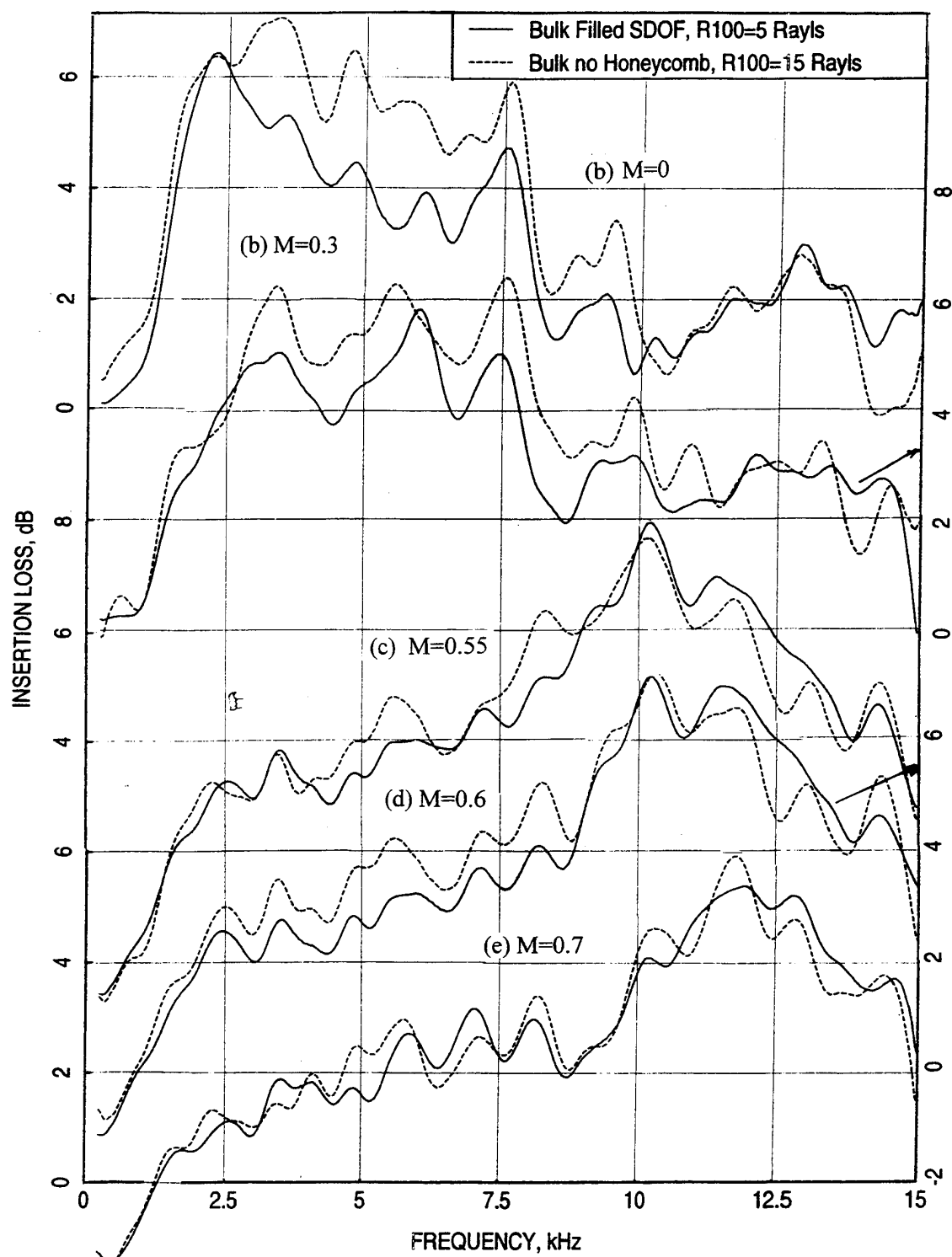
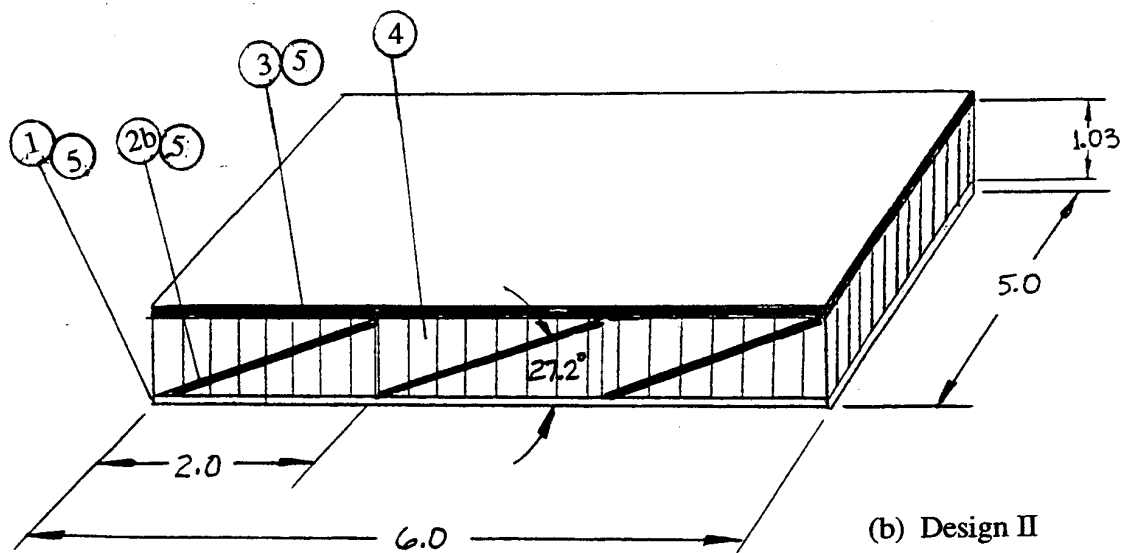
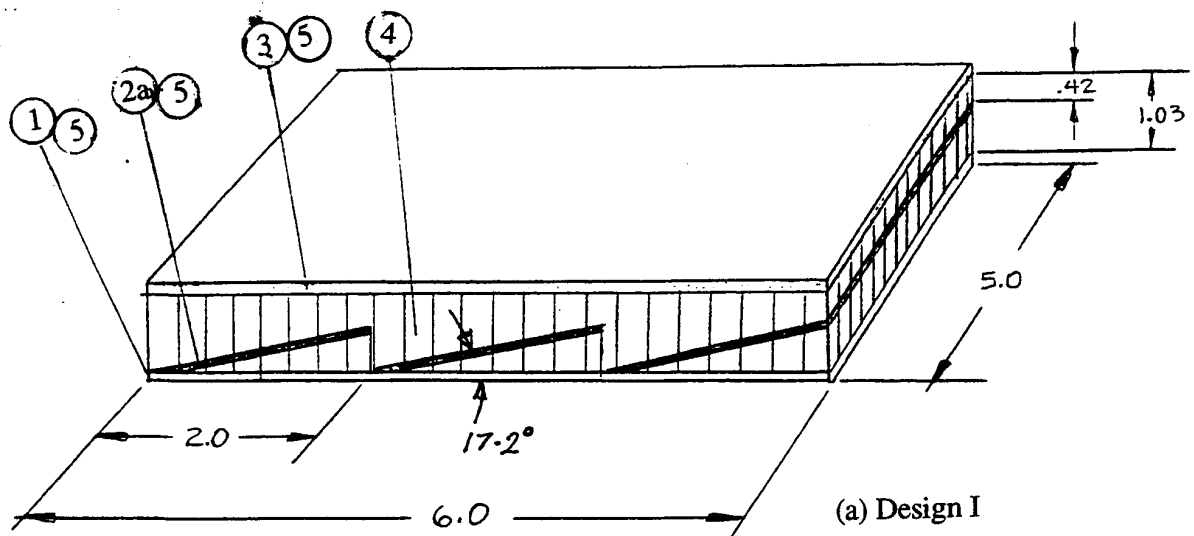


Figure 214. Comparison of insertion loss spectra between 400 ppi carbon foam-filled SDOF type panel with linear facesheet of 5 Rayls and extended 400 ppi carbon foam panel with linear facesheet of 15 Rayls at different grazing flow Mach numbers (M), mounted on one side of the 4"-high flow duct; $D=0.40$ ".



1. Aluminum Alloy of 0.25" thick
- 2a. Felt Metal, 280 Rayls
- 2b. Felt Metal, 180 Rayls
3. Felt Metal, 10 Rayls
4. Honeycomb
5. Film Adhesive

Figure 215. Variable depth 2DOF type samples with linear faceplate and septum for impedance tube test.

Table 20. DC Flow Resistace Parameters for 2DOF panel Components

Component Description	Nominal R_{100} , Rayls	A Rayls	B Rayls/cm	R_{100} Rayls	NLF (R_{150}/R_{20})
Conventional 2DOF Wiremesh Septum with Honeycomb	90	87.13	0.13	100.48	1.19
Conventional 2DOF Linear Facesheet	40	37.76	0.03	40.30	1.09
Variable Depth 2DOF, Design I Septum	280	340	0.6	400	1.2
Variable Depth 2DOF, Design II Septum	180	325	0.40	366	1.16
Variable Depth 2DOF Linear Facesheet with Honeycomb	10	8.088	0.0191	10	1.29

honeycomb backing cut at an angle are fabricated for normal impedance tests. These samples are of 5"x6" rectangular shape. Samples of 1.25" diameter are cut from these samples for the test. Figure 216 shows the normal impedance spectra for the panel design I evaluated at two OASPL levels. The excitation level does not effect the reactance. However, the resistance shows some amount of variation due to excitation level, that the resistance increases with excitation level for frequencies above 1000 Hz. Similar results for the panel design II are shown in Figure 217. In this case, resistance and reactance are slightly effected by the excitation level. Figure 218 shows comparison of normal impedance spectra between the two panel designs. Design I exhibits lower resistance but higher reactance compared to design II for the entire frequency range. This is a combined effect of the septum resistivity and its inclination.

5.7.2 Boundary Layer Results:

The boundary layer profiles for the panels are shown in Figure 219. Boundary layer parameters (i.e., local friction coefficient, displacement thickness, etc.) are evaluated and listed in Table 15. The velocity profiles seem to be fully developed at this location and the boundary layer thicknesses are relatively higher, especially for $M=0.8$. The velocity profiles at $M=0.8$ seems to be significantly different for the variable depth panels compared to SDOF and conventional 2DOF panels. The boundary layer profiles and skin friction coefficients for the conventional 2DOF and variable depth 2DOF panels are compared with those of SDOF panel with linear facesheet Figure 220. The skin friction coefficients are relatively lower for the variable depth panels compared to the conventional ones.

5.7.3 Insertion Loss Results :

Effect of Grazing Flow: Figure 221 shows the insertion loss spectra at different grazing flow Mach numbers for the conventional and the two variable depth 2DOF panels. The data files for these configurations are as follows;

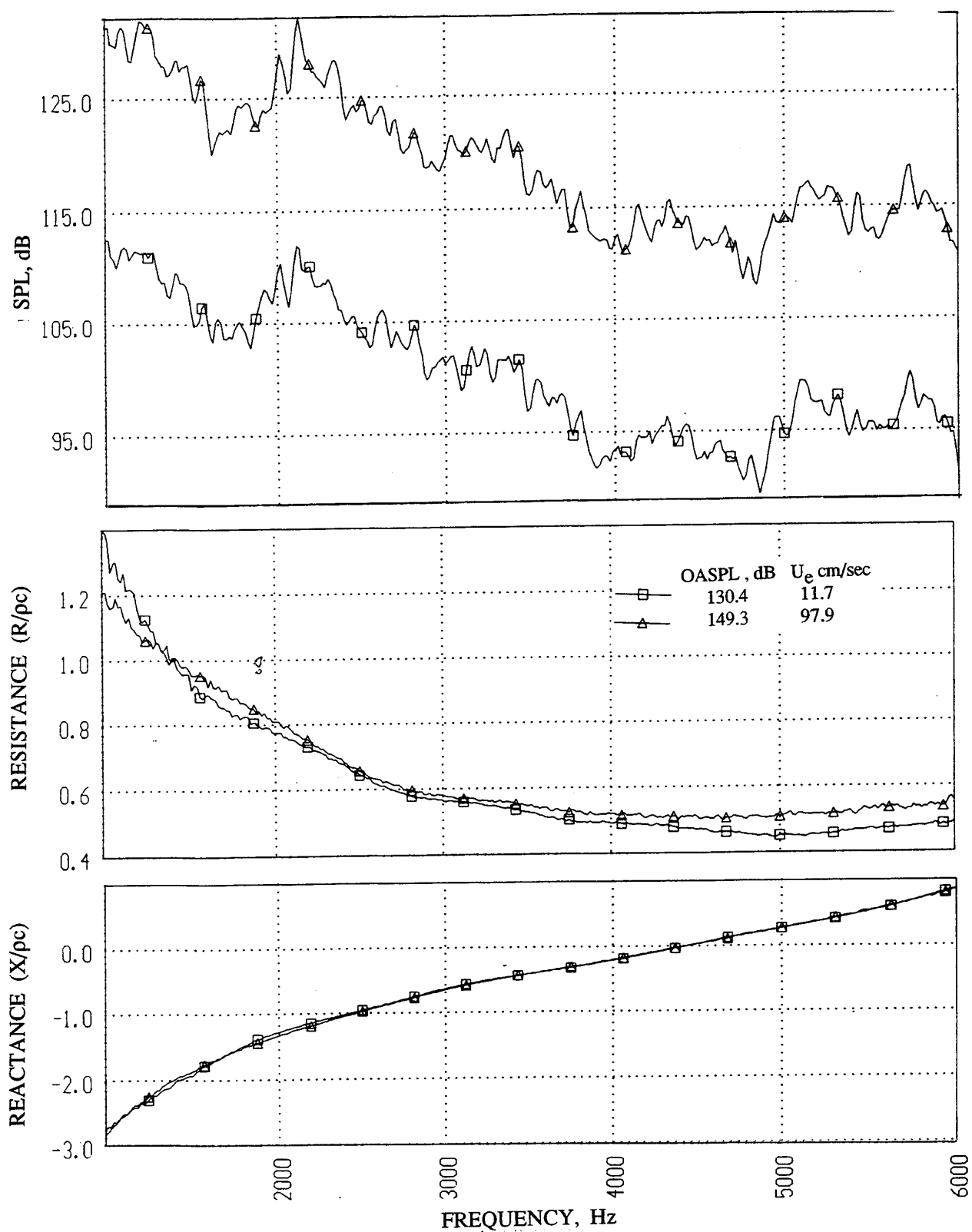


Figure 216. Sound Pressure level and corresponding normal impedance spectra at two OASPL levels for variable depth 2DOF type design I sample.

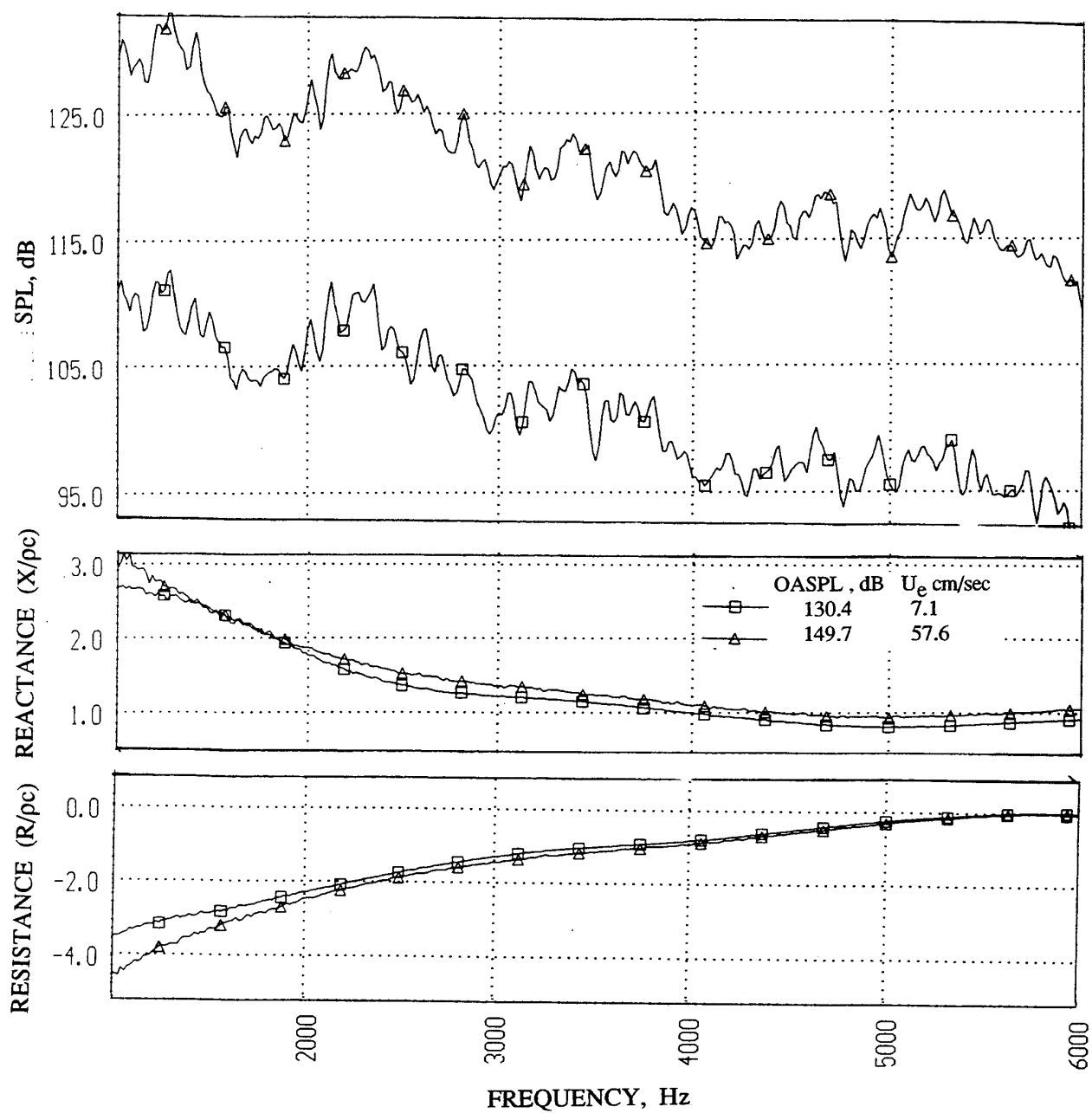


Figure 217. Sound Pressure level and corresponding normal impedance spectra at two OASPL levels for variable depth 2DOF type design II sample.

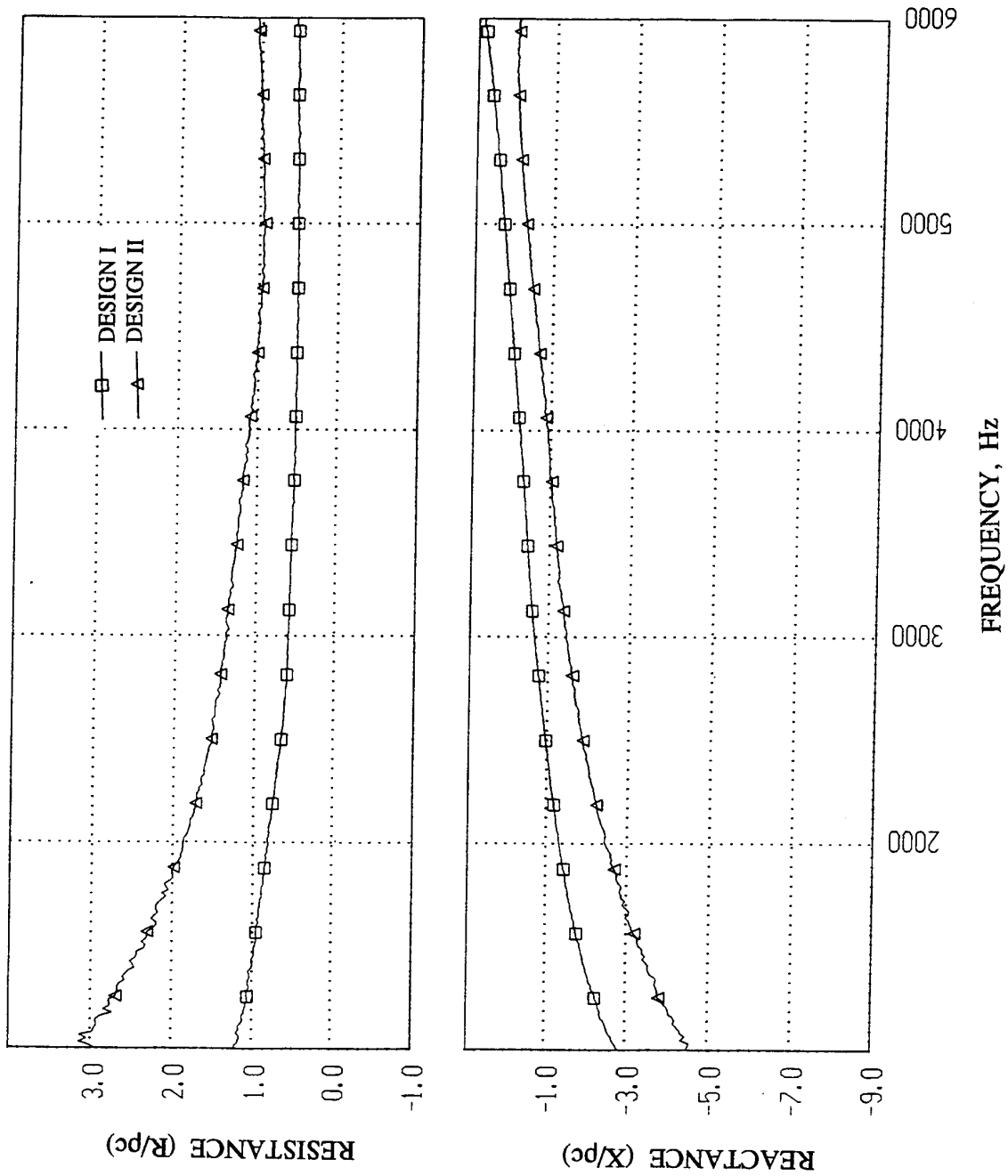


Figure 218. Comparison of normal impedance spectra between the two variable depth 2DOF type designs, tested with a nominal OASPL of 150 dB.

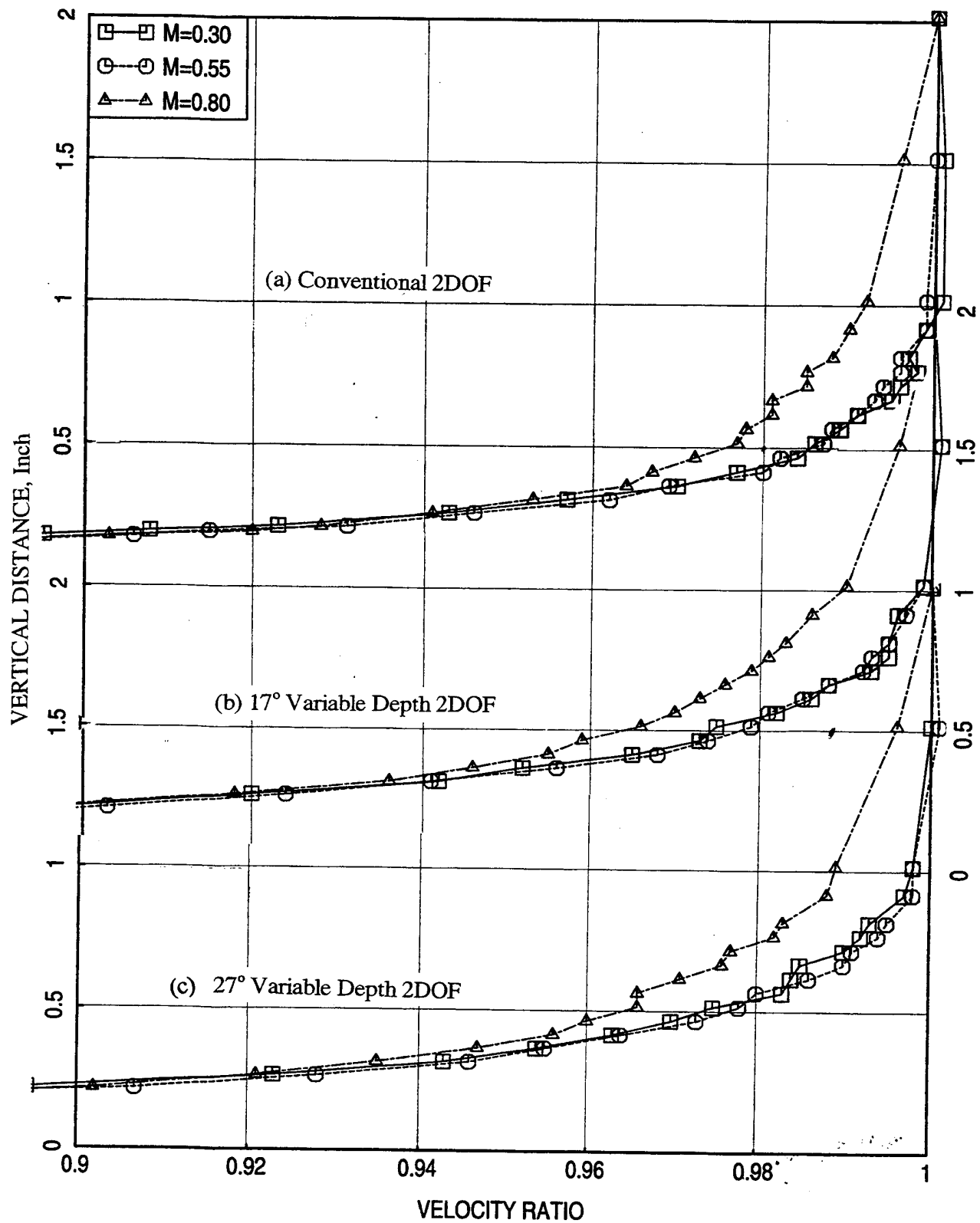


Figure 219. Influence of grazing flow Mach number (M) on velocity profiles in the flow duct for a conventional and two variable depth 2DOF panels with linear facesheets and septum.

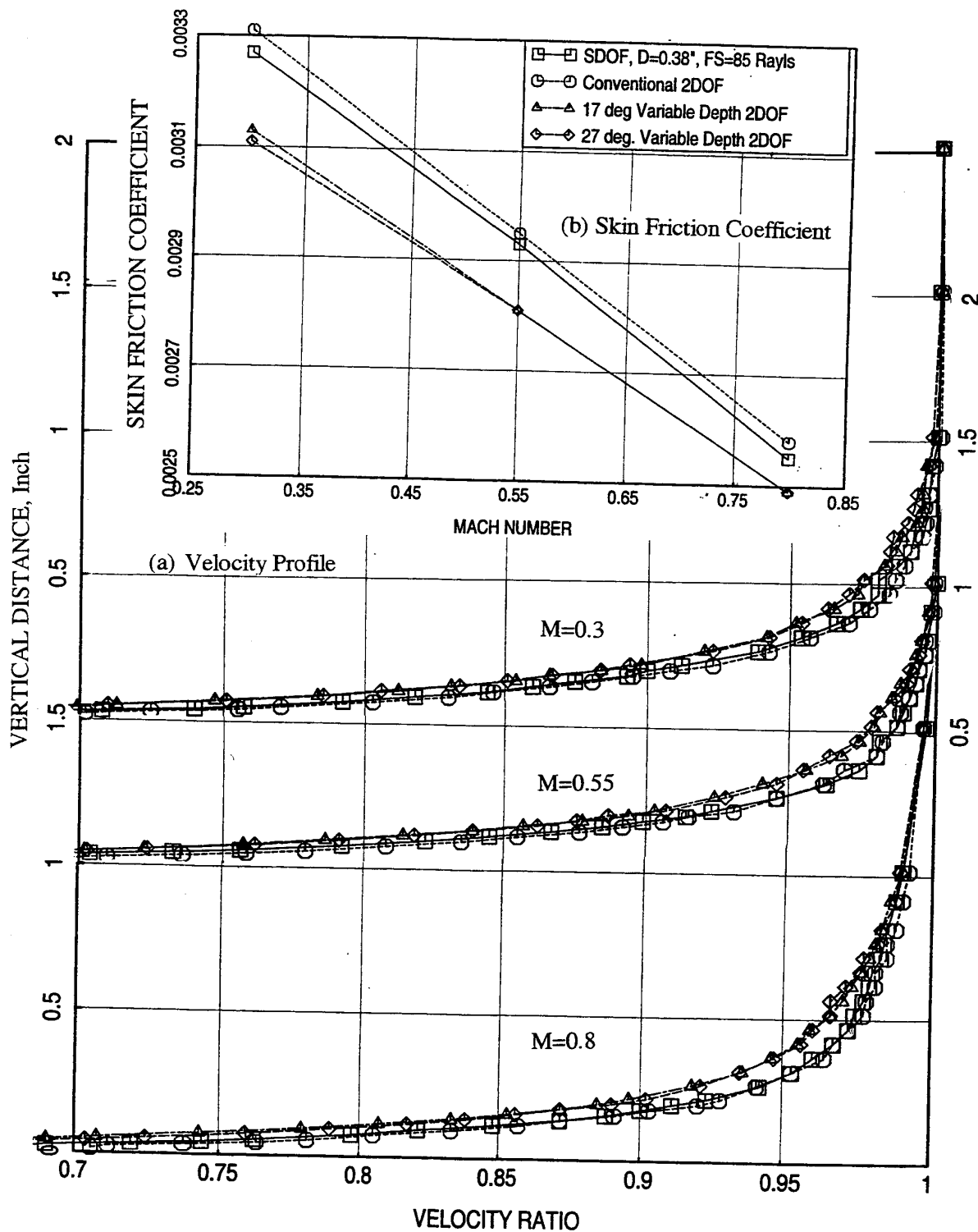


Figure 220. Comparison of (a) velocity profiles in the flow duct and (b) local skin friction coefficients between three different 2DOF panels with linear facesheet and septum and an SDOF panel with linear facesheet.

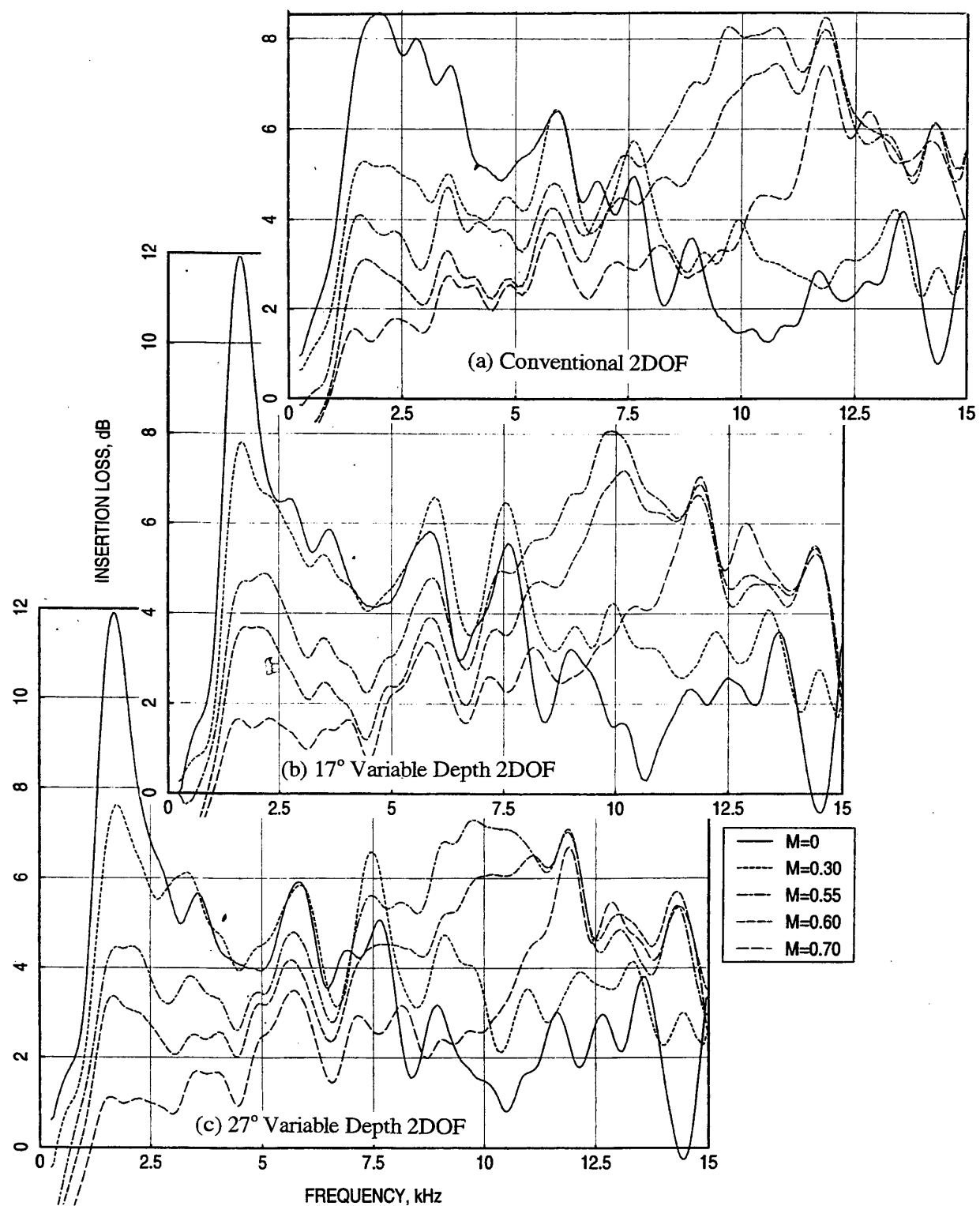


Figure 221. Influence of grazing flow Mach number (M) on insertion loss spectra for a conventional and two variable depth 2DOF 1/3-scale panels ($\eta=3.4$) with linear facesheets and septum, measured in a 4"- high (H) flow duct, mounted on one side.

Table 21. Geometrical Properties and File Names for Insertion Loss Data for 2DOF Type Panels with Linear Facesheets and septums.

Panel Configuration -Description	Insertion Loss 1/3-Octave Band Data Files	Insertion Loss Narrowband Data Files
4.1 – Conventional 2DOF Panel	ttwbs4-1.dat	rrwbs4-1.smt
6.1 – Variable Depth 2DOF Panel, Design I	Ttwbs6-1.dat	Rrwbs6-1.smt
6.1 – Variable Depth 2DOF Panel, Design I	Ttwbs6-1.dat	Rrwbs6-1.smt

Insertion loss decreases at lower frequencies and increases at higher frequencies with flow. The insertion loss is significantly higher at frequencies between 8 to 13 kHz at Mach numbers 0.55 and 0.6. This is expected, since the panels are designed to give higher acoustic suppression at higher flow conditions and since the panels are of 1/3-size the occurrence of higher acoustic suppressions are at the expected frequency range. The insertion loss spectra for the conventional and the variable depth 2DOF panels are compared at various flow conditions in Figure 222. At lower Mach numbers (0 & 0.3) the insertion loss is relatively higher for the variable depth panels at lower frequencies below 2 kHz. and is comparable at higher frequencies. Insertion loss levels are comparable for all the 2DOF panels at higher flow conditions.

The insertion loss spectrum for the conventional 2DOF panel is compared to that for a 1"-deep SDOF panel with perforated facesheet at various flow conditions (see Figure 223). The depths of these panels are comparable. The performance of the SDOF panel is significantly poor compared to the 2DOF panel, except for lower frequencies. The insertion loss results for the conventional 2DOF panel are further compared with those for an SDOF panel with linear facesheet of same scale (i.e., 1/3-scale) in Figure 224. The performance of the 2DOF panel seems to be slightly better compared to the SDOF panel.

Finally, the insertion loss spectra for 1/3-scale panels of different designs with comparable impedance spectra are compared in Figure 225. Clearly, the SDOF panel with perforated facesheet is the poorest performer among these panels. The SDOF panel with linear facesheet and bulk absorber with linear facesheet are comparable with the 2DOF panel at most frequencies. Clearly, the 2DOF panel is slightly better than the other comparable panel designs.

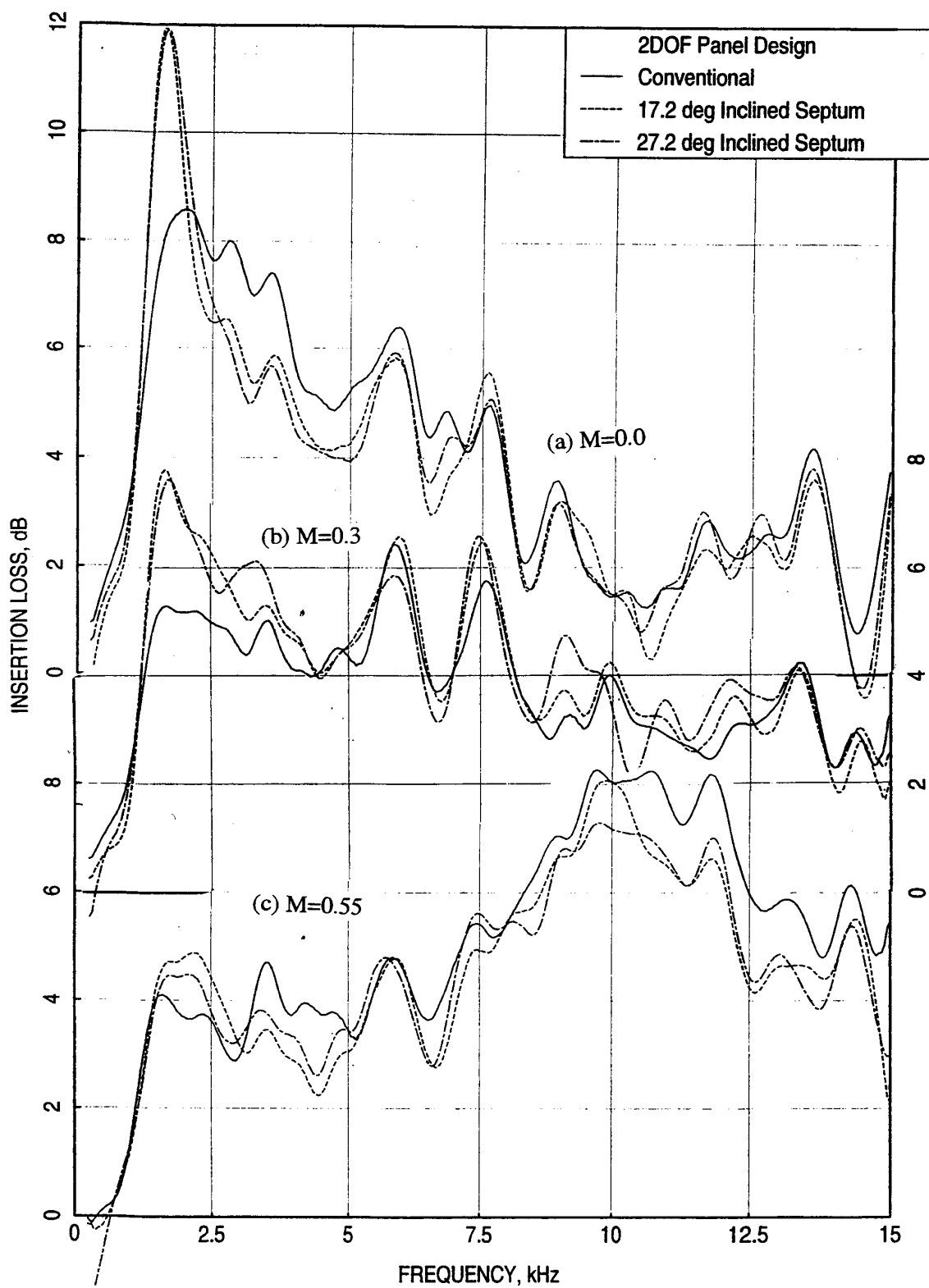


Figure 222. Comparison of insertion loss spectra between a conventional and two variable depth 2DOF 1/3-scale panels ($\eta=3.4$) with linear facesheets and septum, measured in a 4"-high (H) flow duct, mounted on one side.

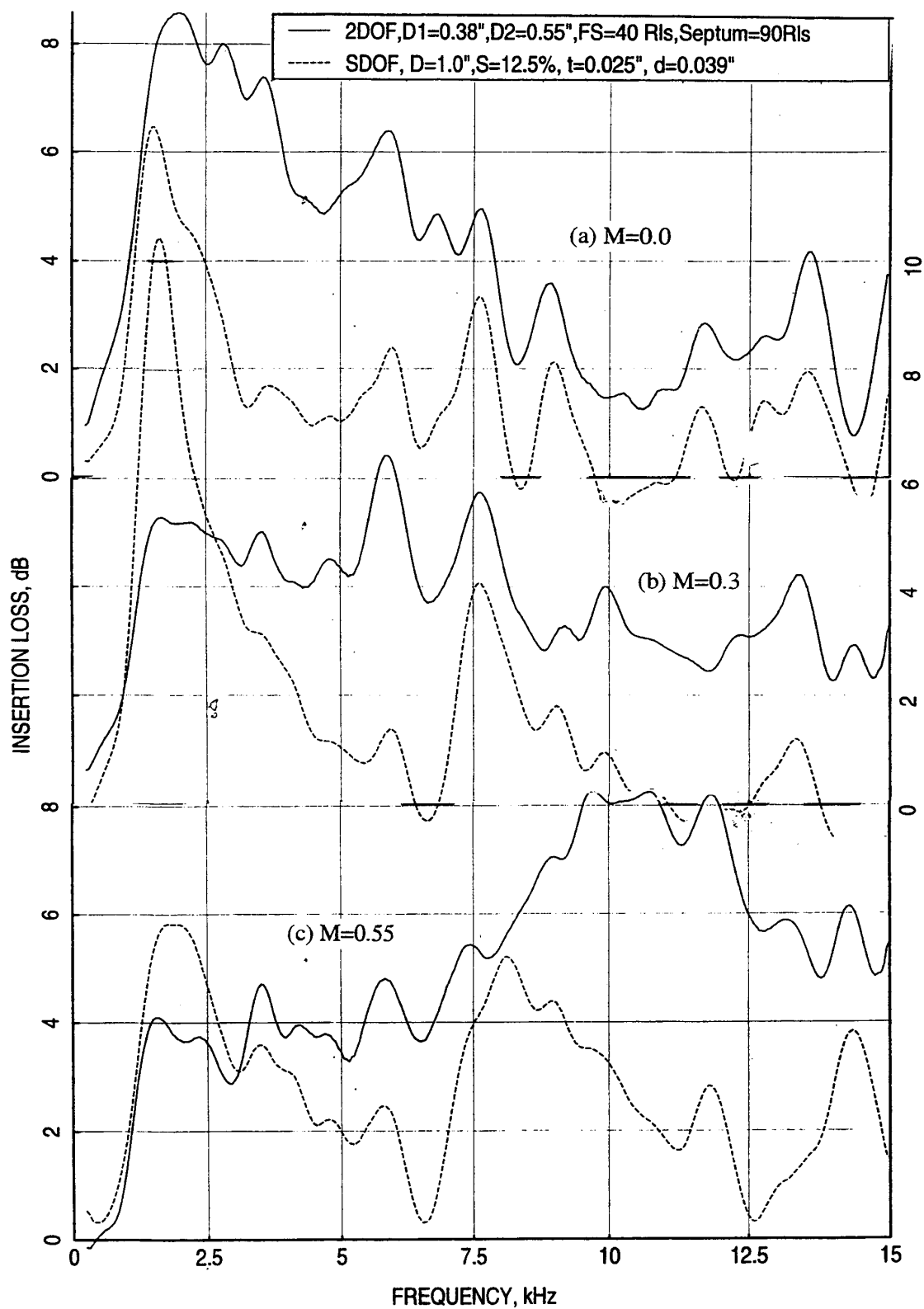


Figure 223. Comparison of insertion loss spectra between a conventional 2DOF panel with linear facesheet and septum and an 1"-deep SDOF panel with perforated facesheet, measured in a 4"-high (H) flow duct, mounted on one side.

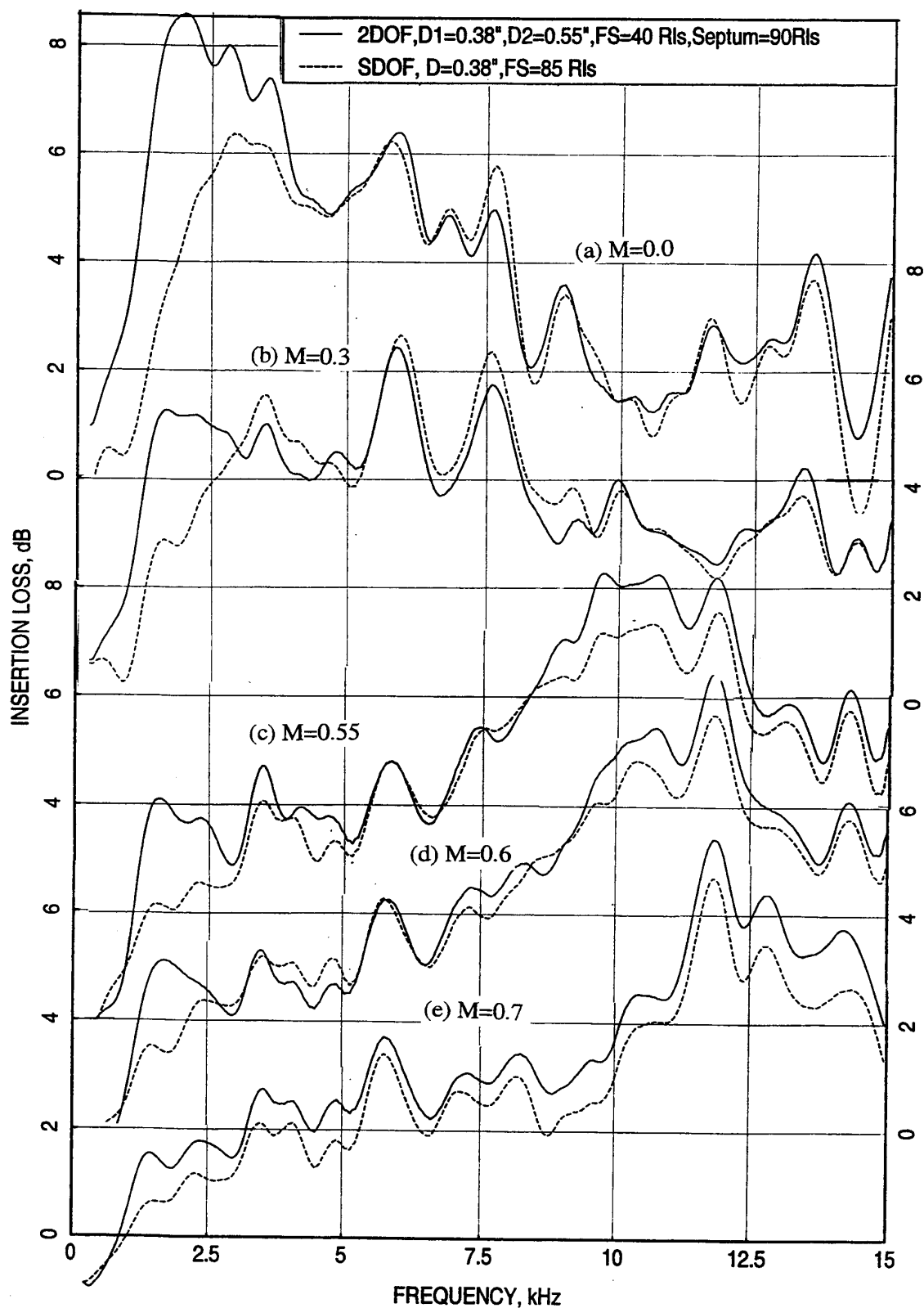


Figure 224. Comparison of insertion loss spectra between a conventional 2DOF and an SDOF 1/3-scale panels ($\eta=3.4$) with linear facesheets and septum, measured in a 4"-high (H) flow duct, mounted on one side.

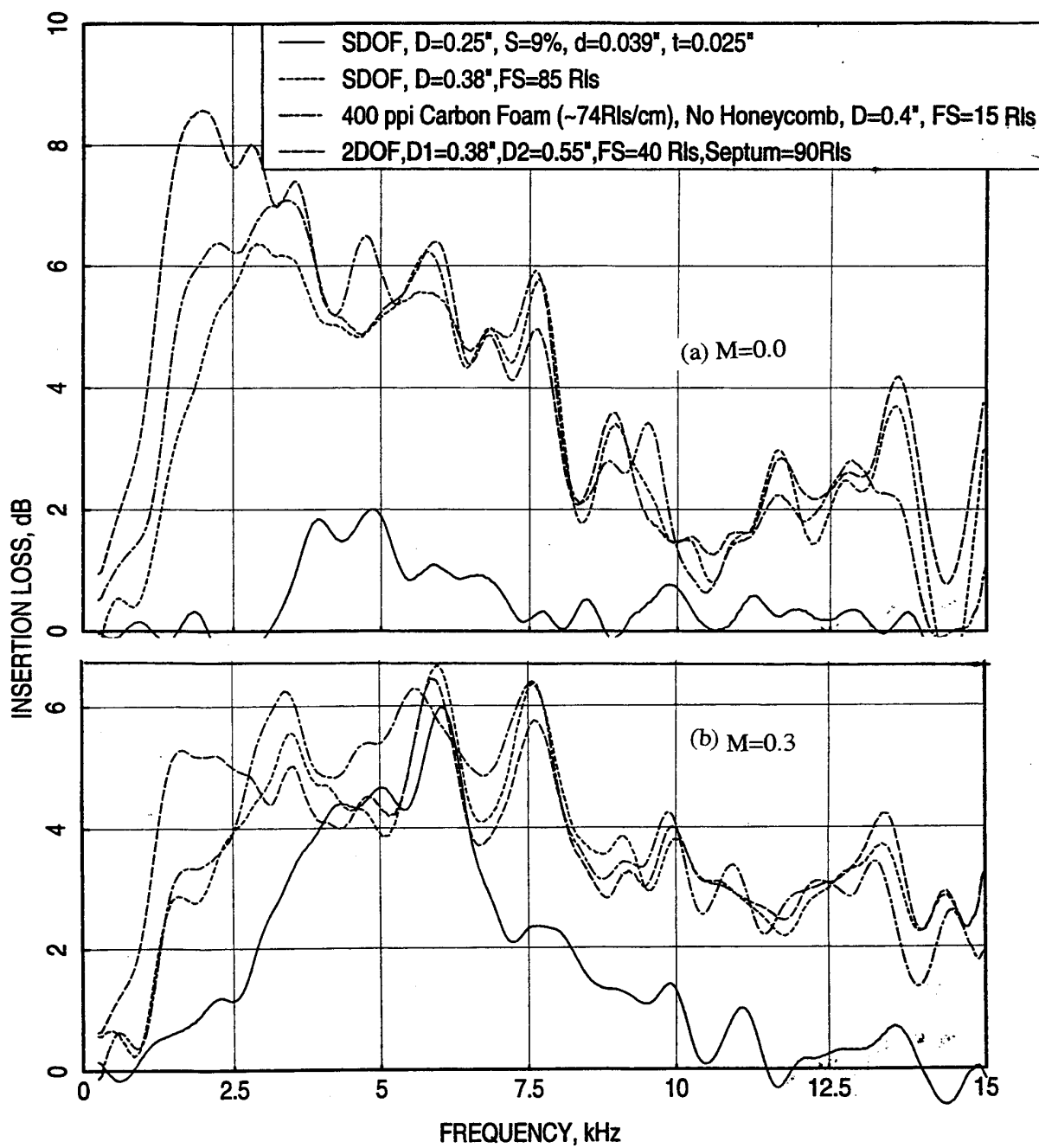


Figure 225. Comparison of insertion loss spectra for four different 1/3-scale panels ($\eta=3.4$) measured in a 4"- high (H) flow duct, mounted on one side (continued).

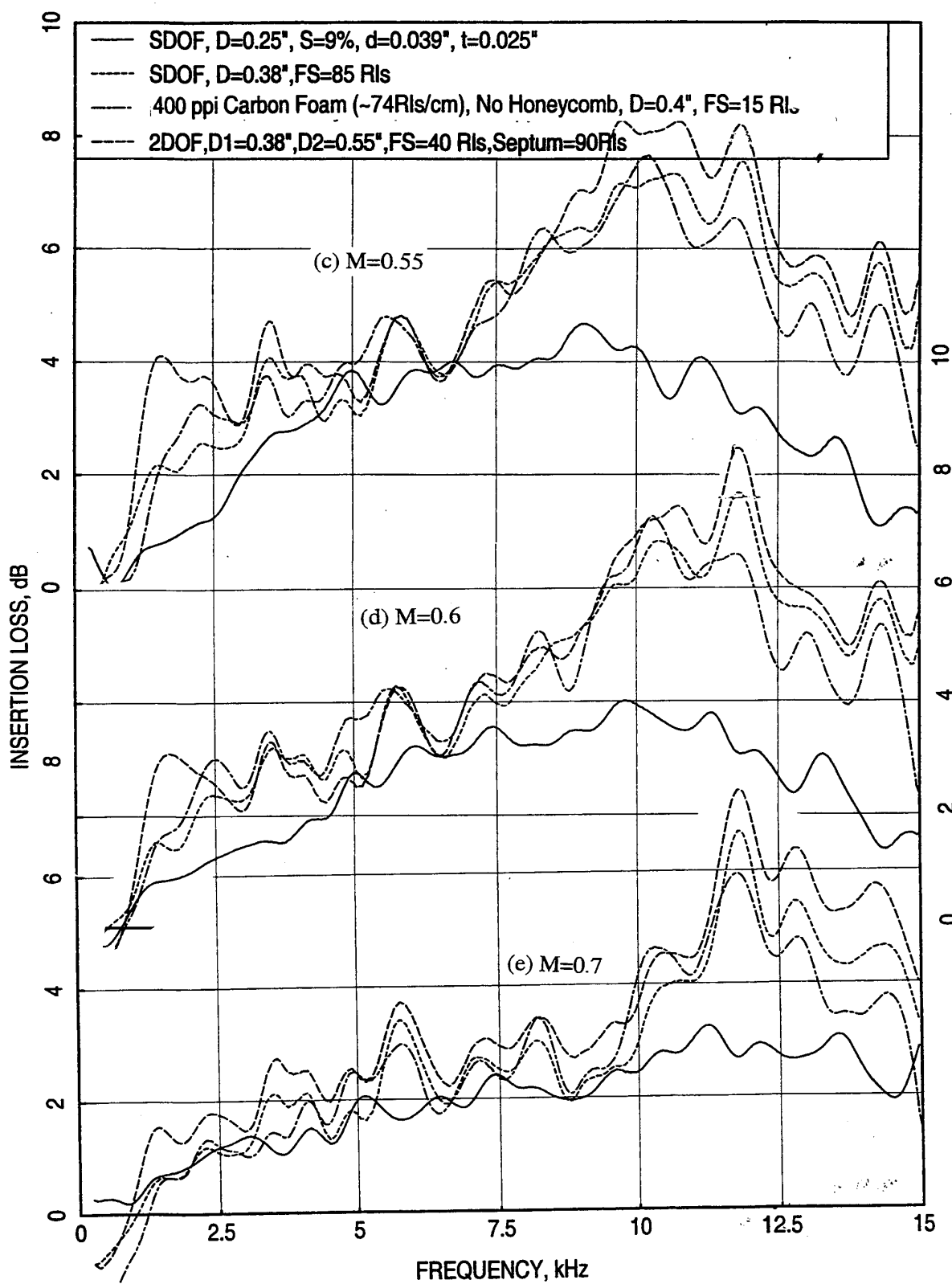


Figure 225. Comparison of insertion loss spectra for four different 1/3-scale panels ($\eta=3.4$) measured in a 4"- high (H) flow duct, mounted on one side (concluded).

6.0 DATA CORRELATION

Development of correlation to predict normal impedance for any desired acoustic treatment and acoustic suppression due to the treatment applied to an ejector utilizing the laboratory test results are important output of the liner technology program. The normal impedance and acoustic suppression predictions involve correlation of the DC flow resistance and physical properties of a liner at room temperature with its normal impedance at a desired temperature and flow condition and a correlation between the normal impedance and the insertion loss of the liner accounting for liner scaling utilizing the laboratory test results presented in this report.

While the laboratory tests are pursued to achieve this goal utilizing acoustic excitation from drivers at room temperature and moderately heated conditions, it is necessary to validate the results (i.e., correlation) for realistic acoustic and aerothermodynamic conditions. Therefore, an 8-lobed GEN 1 mixer-ejector with $SAR=4.9$, $MAR=0.97$, and $A_8=8.33 \text{ in}^2$ (see Figures 226 and 227), with different liner designs, are tested at NASA Glenn anechoic freejet facility (i.e., NATR). The ejector was treated by various SDOF and bulk absorber type liners with perforated facesheets. For SDOF type liners the honeycomb depth (D) and facesheet properties (i.e., porosity σ , thickness t , and hole diameter d) were varied. For bulk absorbers the type of bulk, the bulk depth (D), and the facesheet properties (i.e., porosity σ and thickness t) were varied. Stone's noise prediction method is utilized to extract the internal noise component from the measured farfield acoustic data for this mixer-ejector with different liners and at different aerothermodynamic conditions. Based on the hardwall and the treated configurations the ΔPWL of internal noise component is derived using the internal component of PWL . The DC flow resistance and the normal impedance for the bulk absorber liners are measured at GEAE at room temperature conditions. These results are utilized to develop/validate the DC flow resistance/normal impedance correlation and insertion loss/normal impedance correlation. For SDOF type liners the physical properties of the honeycomb and the facesheets are utilized to estimate their normal impedance. Relevant results showing the impact of various liner designs on DC flow resistance, normal impedance, and internal component of farfield noise (i.e., in terms of internal components of PWL and ΔPWL) are presented reference 28 (see GE97-160-N). The correlation schemes for normal impedance and acoustic suppression are outlined as follows:

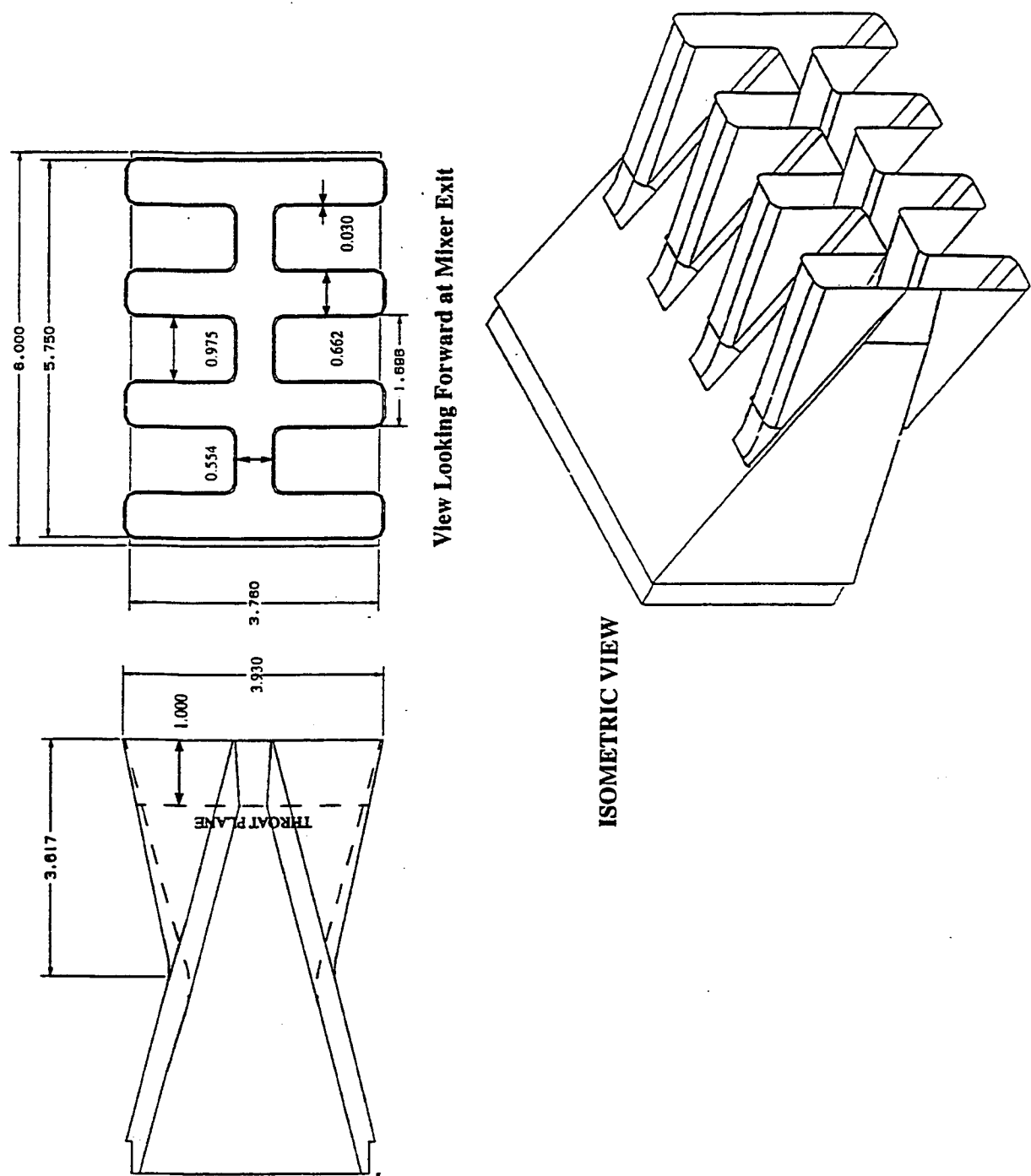


Figure 226. Geometry of a 8-lobed 2D Vortical Mixer Nozzle (All Dimensions in inches).

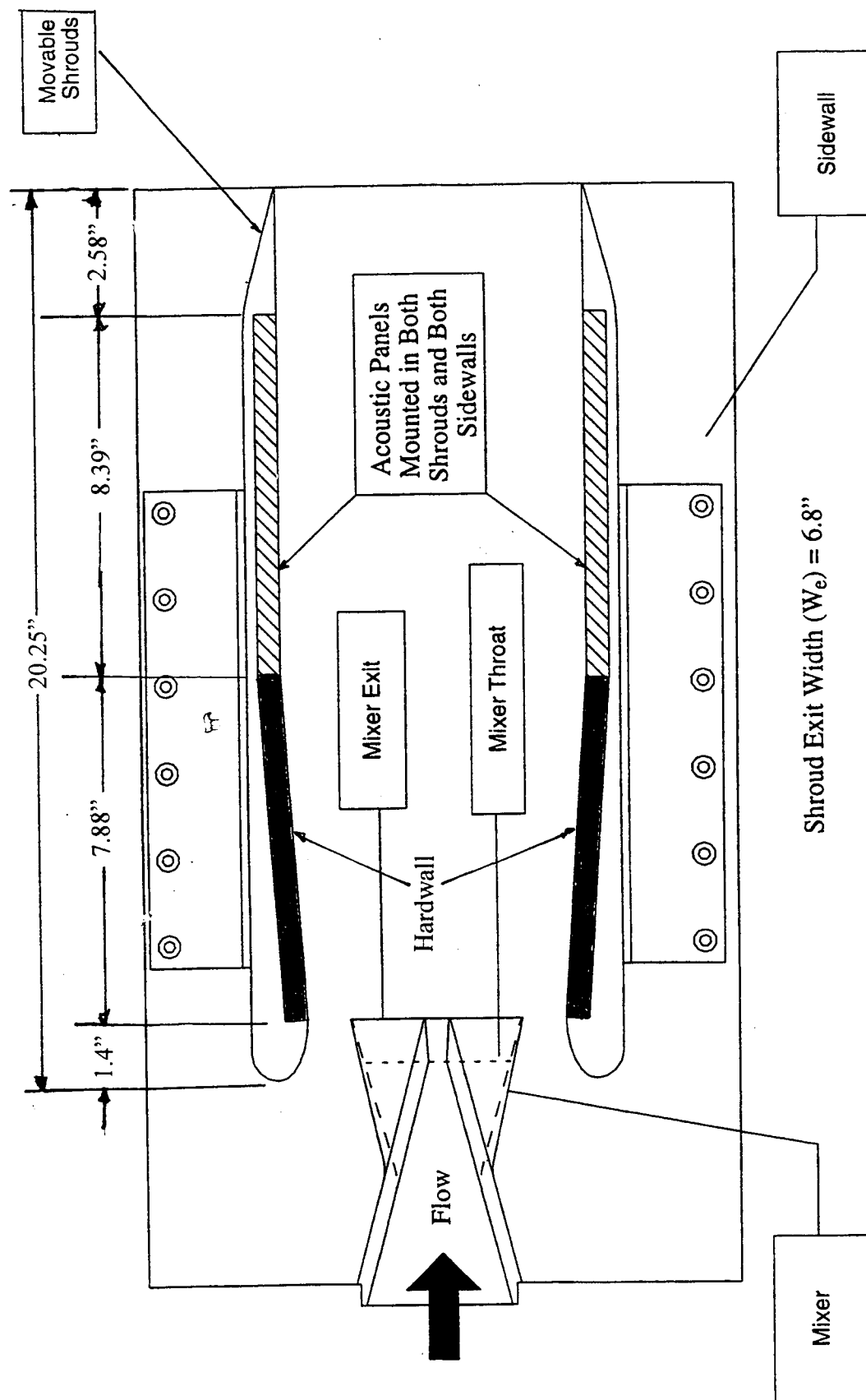


Figure 227. Acoustic treatment for the 8-lobed 2D vortical mixer-ejector nozzle for NATR tests, SAR=4.9, MAR=0.97.

6.1 Insertion Loss - Normal Impedance Correlation

Following acoustic properties of various liner panels are measured:

1. DC Flow Resistance for Perforated Facesheets, Linear Facesheets, Bulk Materials, and Liner Panels at Room Temperature - $(R_{DC})_{AMB}$
 2. DC Flow Resistance for Facesheets and Bulk Materials at High Temperatures - $(R_{DC})_T$
 3. Normal Impedance of Facesheets, Bulk materials, and Liner Panels at Room Temperature- Z_0
 4. In-Situ Impedance for SDOF type Liners with Grazing Flow at Room Temperature - Z_F
 5. DC Flow Resistance for Liner Panels with Grazing Flow at Room Temperature - $(R_{DC})_F$
 6. Insertion Loss for Liner Panels with Grazing Flow at Room Temperature - IL
- Correlate Z_0 with $(R_{DC})_{AMB}$ and validate with existing relationship
 - Correlate $(R_{DC})_T$ with $(R_{DC})_{AMB}$ to account for the temperature effect on normal impedance and insertion loss
 - Correlate Z_F with Z_0 and validate with existing grazing flow relationships
 - Correlate IL with Z_F for different Liner Types (i.e., SDOF with Perforated and Linear Facesheets, Bulk with Linear Facesheet, and Bulk-filled Honeycomb with Linear facesheet) accounting for Grazing Flow and Temperature in a Functional Form -

$$IL = F(Z_F, M, T, \omega)$$

Where, M, T, and ω being the Grazing Flow Mach Number, Flow Temperature, and Angular Frequency (i.e., $2\pi f$, f being the frequency in Hz/sec)

6.2 Validation/Improvement of Insertion Loss - Normal Impedance Correlation

Following Acoustic Properties of Liner Panels Designed and Fabricated for the Gen 1 Mixer-Ejector :

1. DC Flow Resistance for Perforated Facesheets, Bulk Materials, and Bulk with perforated facesheets at Room Temperature - $(R_{DC})_{AMB}$
2. Normal Impedance of Perforated Facesheets, Bulk materials, and Bulk with perforated facesheets at Room Temperature- Z_0
3. Farfield Acoustic Spectral Directivities in an Anechoic Chamber (at NASA's NATR Facility) for the Mixer-Ejector with the Ejector being Treated with various Liner Designs as well as with hard wall at different flow and temperature conditions - $(SPL(\theta, f))_F$

Following steps are taken to compute the acoustic suppression in terms of internal PWL difference between hardwall and treated configurations:

1. Utilize Stone's Model to Extract Internal Noise Component in the Farfield from Measured $(SPL(\theta, f))_F - (SPL(\theta, f))_{FI}$
2. Utilize a Radiation Condition at the Ejector Exit and Convert $(SPL(\theta, f))_{FI}$ Spectral Directivities in to the Ejector internal PWL spectra - $(PWL)_I$
3. Compute Ejector Insertion Loss (acoustic suppression) spectra by taking a difference of $(PWL)_I$ between Hardwall and Treated configurations - IL

- Validate/Improve the insertion loss-impedance correlation using IL with Z_F for different Liners accounting for Ejector Flow Mach number and Temperature in a Functional Form-

$$IL = F(Z_F, M, T, \omega)$$

The data correlation to predict normal impedance and acoustic suppression are developed by Dr. E. J. Rice, as a consultant to GEAE. The predictions made by the correlation agree reasonably well with the data. The correlation process and the data comparisons are presented in a separate report (Ref. 29). Due to the limitations imposed by the measured data the prediction models are not as versatile as expected. In addition, the laboratory data used in this correlation are mostly for SDOF type liner designs. Thus, the prediction models are still to be improved for bulk absorber type liners utilizing the more extensive data base acquired under liner technology program in Phase 2.

7.0 CONCLUSIONS, CONCERNS, AND RECOMMENDATIONS

7.1 Conclusions:

7.1.1 Conclusions on DC Flow and Normal Impedance Tube Test Results:

- The similarity principle to normalize DC flow resistance and the approach velocity with respect to viscosity and temperature is applicable for perforated sheets and silicon Carbide bulk materials.
- DC flow resistance for perforated sheets increases with decreasing porosity and with decreasing thickness.
- Normal impedance for perforated sheets increases with decreasing porosity and with increasing thickness.
- Normal resistance for perforated sheets decreases with decreasing hole diameter. However, the normal reactance decreases with decreasing hole diameter first and then increases by further decrease of hole diameter.
- The nonlinearity of normal impedance due to excitation level for perforated sheets is relatively higher for normal resistance compared to normal reactance. Nonlinearity increases with decreasing porosity, increasing hole diameter, and increasing thickness.
- For SDOF type liner with linear facesheets the normal impedance increases with increasing resistivity of the facesheet.
- DC flow resistance for Silicon Carbide bulk material increases with pores/inch.
- For Silicon Carbide bulk normal resistance increases and normal reactance decreases with increasing pores/inch. For very low pores/inch the cavity influence is dominant on normal impedance levels.

7.1.2 Conclusions on Flow Duct Test Results:

- DC flow resistance increases with increasing grazing flow Mach number for SDOF type liners with perforated facesheets.
- In-situ resistance increases significantly with increasing grazing flow Mach number. In-situ reactance decreases slightly with increasing grazing flow Mach number.
- At measurement location the boundary layer profiles are fully developed and the boundary layer thicknesses are relatively higher compared to hardwall. Boundary layer becomes more turbulent with increasing facesheet porosity.
- Local skin friction coefficient decreases with increasing grazing flow and increases with increasing porosity.
- Insertion loss for every panel increases with flow Mach number, as the panels are designed to give maximum suppression at higher Mach number. However, with further increase of grazing flow Mach number, the insertion loss decreases.

- Insertion loss spectra for different panels, designed for different duct heights, are of same shape when plotted against nondimensional frequency, confirming the scaling principle.
- For SDOF type panels insertion loss peak increases with decreasing porosity at no flow condition. The effect diminishes with flow. Higher hole diameter helps suppress more acoustic energy at no flow condition. The trend is reversed with flow. Acoustic suppression seems to be higher for thick facesheets.
- Insertion loss seems to be higher for the bulk absorber without honeycomb compared to honeycomb filled bulk absorber.
- Insertion loss is highest for 2DOF panel with linear facesheet and septum compared to SDOF and bulk filled panels. However, the insertion loss spectrum for SDOF panel with linear facesheet and bulk absorbers are very close to that of 2DOF panel.

7.1.3 Conclusions on Gen 1 Mixer-Ejector Test Results (Acoustic Suppression, Δ PWL):

- Δ PWL increases with increasing flight velocity at higher nozzle aerothermodynamic conditions. The effect is negligible at lower nozzle aerothermodynamic conditions.
- Δ PWL increases with decreasing nozzle aerothermodynamic condition.
- Δ PWL increases with decreasing ppi for SiC at takeoff condition. Similar effect is also observed with decreasing density for HTP material.
- Δ PWL increases with increasing facesheet porosity for bulk absorber liners.
- Δ PWL increases with increasing facesheet thickness for bulk absorber liners.
- Δ PWL increases with increasing facesheet porosity SDOF type liners.
- Effect of facesheet thickness and hole diameter on acoustic suppression is negligible for SDOF type liners.
- Bulk absorber type liners perform better compared to SDOF type liners with perforated facesheet in acoustic suppression.

7.1.4 Conclusions on Normal Impedance and Acoustic Suppression Correlation:

- Extensive acoustic impedance modeling of several material types is performed. The existing models for acoustic impedance are modified. The models can be improved for higher frequency range and for other parameters when more such data is available.
- The insertion loss modeling of the duct suppressor connecting two reverberation chambers is achieved. The results are reasonably good but could be improved. At present stage of development it would be risky to use this model to predict optimum configurations.
- The acoustic suppression modeling of Gen. 1 mixer-ejector is achieved with reasonably good agreement with the data. The model is very fundamental and probably worth improving.

7.2 Concerns and Recommendations:

- Is a linear addition (lumped) of individual impedances of a bulk sample and a perforated facesheet same as the impedance of the combined configuration? This is a valid liner

design concern. Limited amount of study, done under the current phase (see Appendix D), indicates that the lumped impedance of individual component is not true, especially at higher frequency. The study is limited to frequencies up to 6000 Hz. and includes a few liner samples. Thus, it is recommended that the scope of this study should be extended to higher frequency range and should include variety of bulk and facesheet samples.

- Is a bulk sample acoustically homogeneous along its depth? Again, the study described in Appendix D indicates that 200 ppi Silicon Carbide seems to be acoustically nonhomogeneous along its depth. The current study is limited to one bulk material and confined to 6000 Hz range. It is strongly recommended that more bulk sample of different varieties should be used for this type of study.
- Are the acoustic properties of a perforated sheet same on both surfaces? This is basically a manufacturing issue. If the holes are uniform through the thickness of the sheet the impedance ought to be the same for both sides. This should also be looked into in detail.
- Emphasis is given to SDOF type panels in Phase I study. Since, the focus has been shifted towards bulk absorbers as the prime candidate for HSCT application, the experimental study should be extended to include different bulk panels in Phase II.
- Grazing flow and temperature effects on normal impedance are not adequately evaluated. This must be a major focus in the subsequent study to evaluate these effects on varieties of panels, especially bulk absorbers, up to 20 kHz frequency range.
- Insertion loss measurements using reverberant flow duct are made for a limited number of panels, especially for SDOF types. The emphasis must be put to test bulk absorber panels with different bulk materials with facesheets of widely varying parameters.
- Acoustic suppression, extracted from model scale mixer-ejector test data, is limited to Gen. 1 model only. It is absolutely essential that the acoustic suppression is evaluated for more realistic mixer-ejector models of different scale.
- The correlation effort for normal impedance and acoustic suppression prediction must be extended to include more data, especially for bulk absorbers and for different mixer-ejector models.

APPENDIX A

ANALYTICAL BACKGROUND FOR MODAL ANALYSIS METHOD

Governing Wave equation: The equation governing the propagation of sound in an ejector environment must account not only for the interaction of the sound field with the ejector surface treatment but also with the non-uniformities of the mean flow, mean temperature and mean density of the fluid arising from the mixing of hot and cold regions of the ejector. Such an equation may be derived from the linearized forms of mass and momentum continuity equations and making use of the compressible adiabatic relationship between density and pressure. In deriving such an equation following assumptions regarding the mean properties of the fluid are necessary (see Figure A1);

- 1) The fluid is bounded by a rectangular ejector of a given aspect ratio L_x/L_y .
- 2) The axial direction of the mean flow is in the z-direction.
- 3) The high-speed hot flow through the mixing chutes and slow entrained cold flow are stacked along the y-direction.
- 4) The major variations of the mean flow and the mean temperature are along the y-coordinate, but may also be a function of x, especially near the boundary of the ejector.
- 5) The variations of the mean flow and mean temperature along the z-coordinate (flow direction) is small relative to the variations along x and y coordinates and, therefore, its interaction with the sound field may be neglected.

Thus, the Mean Axial Velocity \bar{u}_z , the Mean Density $\bar{\rho}$, the Mean Temperature \bar{T} , and the Speed of Sound c (i.e., $c^2 = \gamma R \bar{T}$) are all assumed to be functions of x and y, only. Speed of sound c is based on a reference temperature. It can be shown (Ref. 30) that the governing wave equation, in the environment described above, may be written in the form:

$$\frac{\partial^2 p}{\partial x^2} + ([2K/\{1-MK\}]) \frac{\partial M}{\partial x} - [1/\bar{\rho}] \frac{\partial \bar{\rho}}{\partial x} \frac{\partial p}{\partial x} + \frac{\partial^2 p}{\partial y^2} + ([2K/\{1-MK\}]) \frac{\partial M}{\partial y} - [1/\bar{\rho}] \frac{\partial \bar{\rho}}{\partial y} \frac{\partial p}{\partial y} + \frac{\partial^2 p}{\partial z^2} - [1/c^2] D^2 p / Dt^2 = 0 \quad (A1)$$

Where: p = compressible adiabatic perturbation pressure associated with the sound pressure field, a function of (x,y,z,t),

$M = \bar{u}_z(x,y)/c(x,y)$ = local axial Mach number, a function of (x,y),

$K = \beta/k$ = normalized axial wave number,

β = axial wave number whose evaluation is the objective of the analysis,

$k = \omega/c$ = absolute wave number of the sound field.

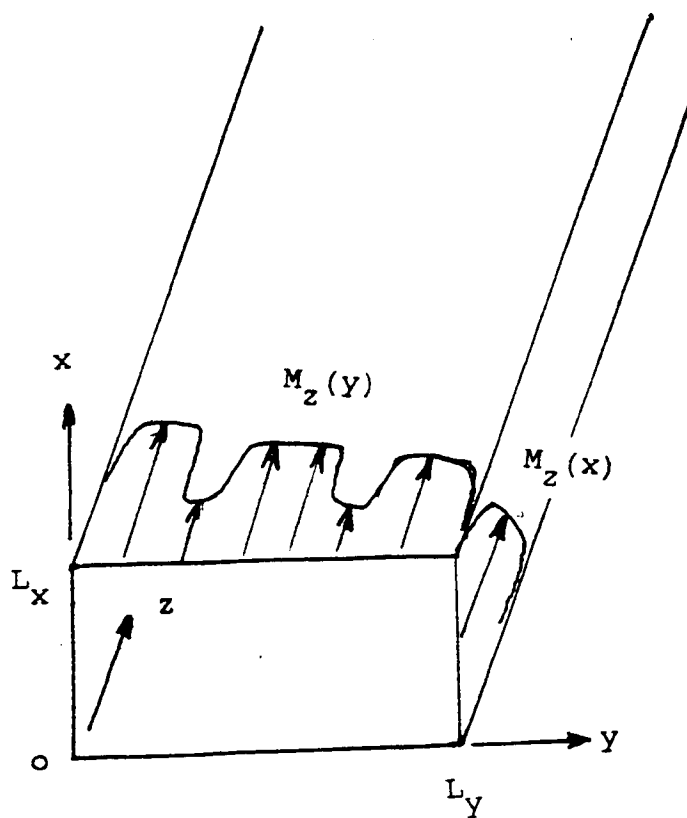


Figure A1. Mean axial flow in an ejector.

Equation (A1) reduces to the well known convected wave equation in a homogeneous fluid if the two terms multiplying the $\partial p/\partial y$ and $\partial p/\partial x$ are suppressed. Solutions for p are sought in the form (Ref. 31):

$$p(x,y,z,t) = A F(x,y) e^{j(\omega t - \beta z)} \quad (A2)$$

that satisfy the governing Equation (A1) and the wall boundary conditions that are discussed later. In this equation A is the pressure amplitude and $F(x,y)$ is the spatial pressure distribution function. If Equation (A2) is substituted in equation (A1) one obtains;

$$\begin{aligned} \frac{\partial^2 F}{\partial y^2} + ([2K/\{1-MK\}]) \frac{\partial M}{\partial y} - \{1/\bar{\rho}\} \frac{\partial \bar{\rho}}{\partial y} \frac{\partial F}{\partial y} + k^2[(1-MK)^2 - K^2] F = \\ -[\frac{\partial^2 F}{\partial x^2} + ([2K/\{1-MK\}]) \frac{\partial M}{\partial x} - \{1/\bar{\rho}\} \frac{\partial \bar{\rho}}{\partial x} \frac{\partial F}{\partial x}] \end{aligned} \quad (A3)$$

Let the right hand side of Equation (A3) be denoted as $k_x^2 F$, k_x being the equivalent wave number along x . Then Equation (A3) is split into two coupled equations;

$$d^2 F/dy^2 + ([2K/\{1-MK\}]) dM/dy - \{1/\bar{\rho}\} d\bar{\rho}/dy dF/dy + k^2[(1-MK)^2 - K^2 - k_x^2/k^2] F = 0 \quad (A4)$$

$$\text{and } d^2 F/dx^2 + ([2K/\{1-MK\}]) dM/dx - \{1/\bar{\rho}\} d\bar{\rho}/dx dF/dx + k_x^2 F = 0 \quad (A5)$$

with the coupling coefficient k_x^2 occurring in both equations.

The objective now is to solve for K , the normalized axial wave vector so that both Equations (A4) and (A5) are satisfied. For treated walls, K and k_x are complex. For rigid walls, K is either purely real or purely imaginary corresponding to cut off modes. Several values of K can be formed to satisfy the governing wave equation and the boundary conditions. Each value corresponds to a mode of propagation and therefore a mode of carrying acoustic energy. The extent to which every one mode is excited depends on the spatial amplitude and phase distribution of the source. In the absence of detailed knowledge of a source one may assume an equal or a mode weighted modal amplitude distribution for pressure or for the energy. Thus a general form for the acoustic pressure field of equation (A2) may be rewritten in the following form;

$$p(x,y,z,\omega) = \sum_m \sum_n A_{mn} F_{mn}(x,y) e^{j(\omega t - \beta_{mn} z)} = \sum_m \sum_n p_{mn} \quad (A6)$$

The corresponding expression for the acoustic particle velocity in the z -direction may be derived from the axial component of the linearized axial momentum equation and may also be written in the following form;

$$\bar{\rho} c u_z(x, y, z, \omega) = \sum_m \sum_n A_{mn} F_{mn}(x, y) Q_{mn} e^{j(\omega t - \beta_{mn} z)} = \bar{\rho} c \sum_m \sum_n u_{mn} \quad (A7)$$

$$\text{Where, } Q_{mn} = [(\beta_{mn}/k)/(1-M[(\beta_{mn}/k)]] \quad (A8)$$

The modal acoustic intensity in the axial direction, following the arguments of Morfey (Ref. 32), Cantrell and Hart (Ref. 33), and Tester (Ref. 34), may be written in the following form;

$$I_{zmn}(x, y, z, \omega) = \text{Re}[(1+M^2) p_{mn} u_{mn}^* + M\{p_{mn} p_{mn}^*/(\bar{\rho} c) + \bar{\rho} c u_{mn} u_{mn}^*\}]/2 \quad (A9)$$

Expressing the modal axial particle velocity u_{mn} in terms of modal pressure p_{mn} and the modal admittance Q_{mn} , the axial modal acoustic intensity may be simplified to

$$I_{zmn}(x, y, z, \omega) = p_{mn} p_{mn}^* \text{Re}[Q_{mn}^*(1+M^2+M Q_{mn})+M]/(2 \bar{\rho} c)$$

The modal acoustic energy flux in the z direction can be written as;

$$E_{mn}(\omega, z) = \int \int_{x, y} I_{zmn}(x, y, z, \omega) dx dy = A_{mn} A_{mn}^* \Omega_{mn} e^{j(\beta_{mn} - \beta_{mn}^*)z}$$

Where,

$$\Omega_{mn} = \text{Re}[Q_{mn}^*(1+M^2+M Q_{mn})+M] F_{mn}(x, y) F_{mn}^*(x, y) dx dy$$

Since $\beta = \beta_r + j\alpha$ and $\beta^* = \beta_r - j\alpha$, $\beta - \beta^* = 2j\alpha$

$$\text{Hence, } E_{mn}(\omega, z) = A_{mn} A_{mn}^* \Omega_{mn} e^{-2\alpha_{mn} z} \quad (A10)$$

Finally, the total axial acoustic energy flux may be written as;

$$E(\omega, z) = \sum_m \sum_n E_{mn}(\omega, 0) e^{-2\alpha_{mn} z} \quad (A11)$$

Where, $E_{mn}(\omega, 0) = A_{mn} A_{mn}^* \Omega_{mn}$. All parameters with * are the complex conjugate of the respective parameters.

Numerical Integration: To utilize Equation (A11) to estimate the acoustic energy carried by different modes it is necessary to evaluate the value of α , which can be obtained by solving Equations (A4) and (A5) to evaluate the normalized wave-vector K (i.e., $K = \{\beta_r + j\alpha\}/k$). Equations (A4) and (A5) are ordinary differential equations with variable coefficients which are functions of the differential coordinates and of the unknown normalized wave-vector K . Fourth order Runge Kutta integration scheme is used to integrate either or both the equations depending upon application of the analysis to general or simplified cases. This is described in detail in reference 31. For example, if the mean flow and mean temperature in the x-direction

were uniform, Equation (A5) need not be integrated and may be replaced by an analytic solution. Further, if walls at $x=0$ and $x=L_x$ were rigid, k_x takes on simple values such as $(n\pi/L_x)$ with n corresponding to mode order in the x -direction. Equation (A4) may then be integrated numerically to yield the normalized axial wave-vector K after satisfying boundary conditions at $y=0$ and $y=L_y$.

If the mean flow and the mean temperature along y were uniform, further simplification in the analysis are possible, that Equation (A11) could also be expressed analytically.

Boundary Conditions at the Walls: In obtaining numerical solutions for the general Equations (A4) and (A5), these equations are first cast in the form;

$$\begin{Bmatrix} p \\ p' \end{Bmatrix} = [A] \begin{Bmatrix} p \\ p' \end{Bmatrix} \quad (A12)$$

Where the prime refers to derivative with respect to x or y and matrix A contains the coefficients of the governing Equations (A4) or (A5). A numerical solution is obtained in the form (Ref. 31),

$$\begin{Bmatrix} p \\ p' \end{Bmatrix}_n = [T] \begin{Bmatrix} p \\ p' \end{Bmatrix}_0 \quad (A13)$$

Where $[T]$ is a transferred matrix and relates the pressure p and its derivative p' on one wall in terms of those on the opposite wall. The boundary conditions are imposed by expressing p' and p separately and then taking their ratio, as follows;

$$p'_n = (T_{21} + T_{22} \{p'_0/p_0\}) p_0$$

$$p_n = (T_{11} + T_{12} \{p'_0/p_0\}) p_0$$

Then,

$$\frac{p'_n}{p_n} = \frac{(T_{21} + T_{22} \{p'_0/p_0\}) p_0}{(T_{11} + T_{12} \{p'_0/p_0\}) p_0} \quad (A14)$$

(p'_0/p_0) may be expressed as the admittance on one wall and (p'_n/p_n) as the admittance on the opposite wall. Equation (A14) expresses the boundary condition equation that must be met for Equation (A2) to be the valid solution of Equation (A1).

Initial guessed values for K , the normalized axial wave-vector (assuming hard walls) are used in matrix A . Matrix T is evaluated following numerical integration and the left side of Equation (A14) is evaluated in terms of the input admittances and the coefficients of the transferred matrix. Equation (A2) becomes a solution of Equation (A1), once the transferred matrix is evaluated and minimized. The computer program (for Ejector Acoustics) accepts input as defined earlier in the main text, and contains all the necessary subroutines to carry out the numerical integrations. Suitable complex minimization routines using method of steepest decent allow evaluation of the complex propagation constants associated with each mode and the associated mode shapes. These are then used in Equation (A11) to evaluate the acoustic suppression performance of the treated ejector.

APPENDIX B

UNDERSTANDING OF INSERTION LOSS RESULTS MEASURED BY GEAE'S FLOW-DUCT FACILITY

Flow Duct Facility : The flow duct facility, schematically illustrated in Figure 47 of the main text, is used to evaluate acoustic suppression in terms of insertion loss in the presence of grazing flow for treatment panels. The duct cross section is 4 inches x 5 inches, and treatment panels of sizes of 5 inches x 12 inches are used either on one side or on two opposing sides of the duct for the current program. The flow Mach number is varied from 0 to about 0.8. The acoustic excitation is provided by four 100-watt Altec drivers. The acoustic energy flux measurements are made by flush-mounted transducer arrays upstream and downstream of the treatment panel.

Suppression Measurements: The acoustic suppression is the suppression of forward traveling acoustic energy, in terms of Δ PWL (i.e., change in sound power level), for each panel. The most accurate method to do this is to perform modal decomposition of the pressure patterns at two planes upstream and two planes downstream of the treatment section (see Figure 47). The two-plane measurement allows the forward traveling and backward traveling energy to be analytically separated. The modal patterns of first 10 modes, including the plane wave mode, for a rectangular duct is schematically shown in Figure B1. The number of sensors required for the modal measurement at a plane is one more than the number of cut-on modes at a given frequency. The number of sensors is limited to 10 per plane (see Figure 47(b)) in the current set-up. This will permit the measurement up to the frequency at which the 9th mode becomes cut on, which is about 4060 Hz without flow and about 2440 Hz with a grazing flow of Mach number 0.8. While the data is acquired by 40 transducers, which can be used for modal analysis, the output of 8 upstream and 8 down stream microphones are used on-line to estimate the insertion loss by using a less accurate p^2 estimate of the energy flux. Transducers located at 1, 4, 6, and 9, and at 11, 14, 16, and 19 (see Figure 47(b)) from upstream planes and similar locations from downstream planes are utilized for insertion loss estimation.

For the p^2 method, the insertion loss is expressed as the difference between the sum of the squared pressure amplitudes averaged over the sensor measurements at the upstream and downstream transducer planes. Insertion loss in terms of Δ dB is expressed below.

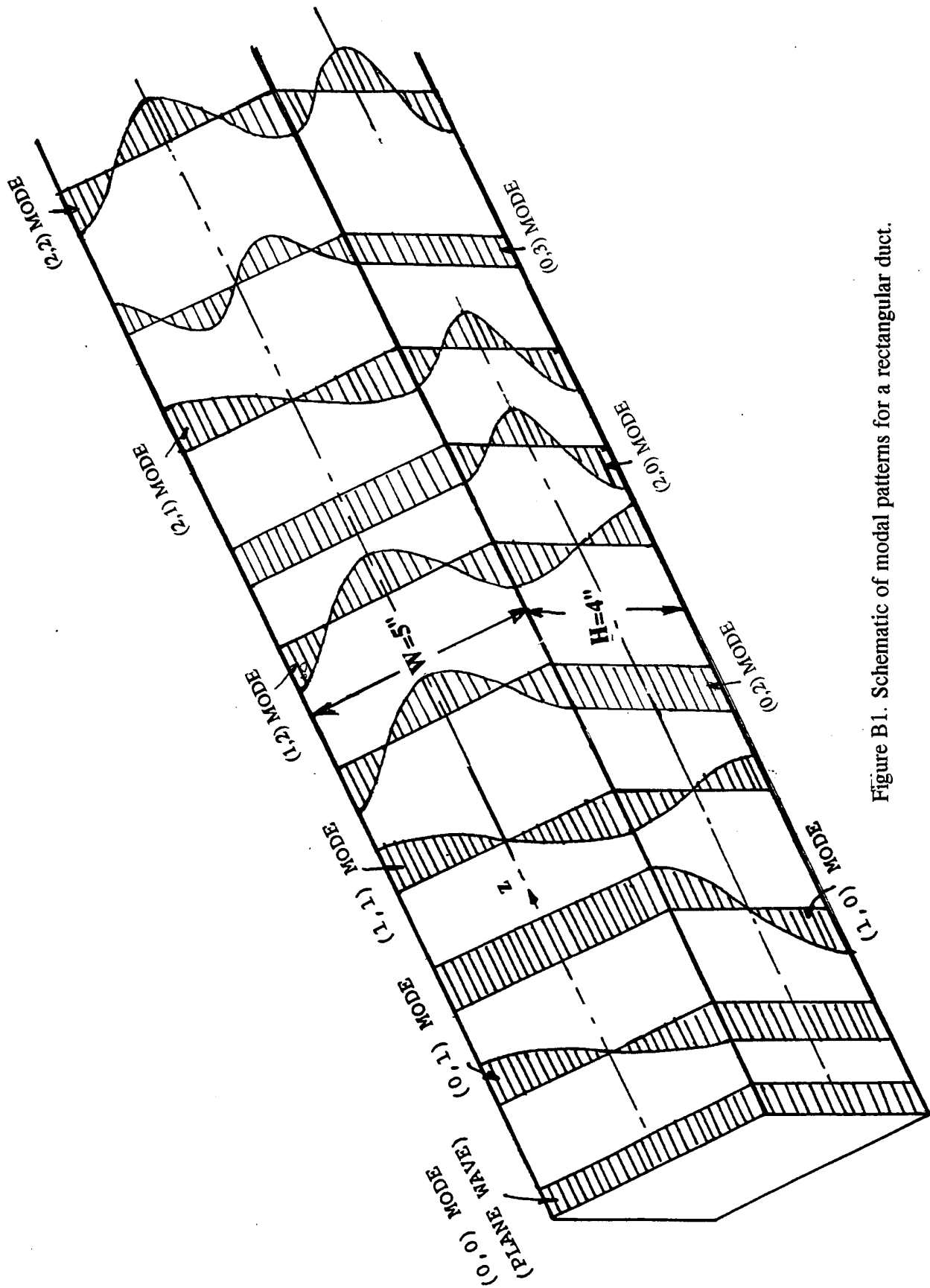


Figure B1. Schematic of modal patterns for a rectangular duct.

$$\Delta \text{dB} = 10 \log_{10} \left[\frac{1}{N} \sum_{i=1}^{i=N} p_{ui}^2 \right] - 10 \log_{10} \left[\frac{1}{N} \sum_{i=1}^{i=N} p_{di}^2 \right]$$

where, p_{ui} is the pressure measured at the i^{th} upstream microphone, p_{di} is the pressure measured at the i^{th} downstream microphone, and N is the number of microphones per plane. The insertion loss expressed above is normalized with respect to a hard wall panel to reduce possible inaccuracies associated with this process.

Experimental Results of Discrete Frequency Excitation: Several panels of different designs are tested in the flow duct facility. Acoustic insertion loss for three 1"-thick SDOF type panels are evaluated at different grazing flow Mach numbers at a number of discrete frequencies and are shown in Figure B2. The results fail to exhibit systematic trends with respect to frequency and grazing flow Mach number for the entire frequency range. There is some concern regarding the accuracy of these data, especially, due to the simplified procedure (in terms of average $\langle p^2 \rangle_{\text{avr}}$ method described before) applied to evaluate these results. However, some information can still be derived from these results. Since, these panels are 1"-deep, the tuning frequencies at which the most acoustic suppression is expected are relatively low. Based on the data of Figure B2, it appears, that the acoustic suppression for these panels is occurring at frequencies up to about 4 kHz. The randomness of insertion loss results above this frequency range is attributed to the simplified $\langle p^2 \rangle_{\text{avr}}$ procedure utilized in data evaluation. For the panels with thin facesheets (i.e., $t=0.025"$) the peak suppression seems to occur at about 3 kHz. For the 0.08"-thick facesheet panel the tuning frequency seems to be around 2 kHz and is lower than the other two panels.

Insertion loss results for the same three panels are plotted with respect to grazing flow Mach number at fixed frequencies in Figure B3. Most favorable frequency with respect to insertion loss is 3150 Hz for thin facesheet panels and 1933 Hz for the thicker panel. With respect to the grazing flow, the thin facesheet panels are more effective in suppressing the acoustic energy at higher Mach numbers (about 0.4 to 0.6), whereas, the thicker facesheet panel is less sensitive to grazing flow. The insertion loss results are compared between the three panels at fixed frequencies in Figure B4. The panel with 9% porosity seems to be most effective in suppressing acoustic energy at higher Mach numbers.

Figure B5 shows the insertion loss with respect to frequency for different grazing flow Mach numbers for a 0.7" deep SDOF type panel with perforated facesheet (see Figure B5(a)) and a 0.38" deep SDOF type panel with a linear facesheet (see Figure B5(b)). For both the cases we do not see any systematic trend in insertion loss variation with respect to frequency or Mach

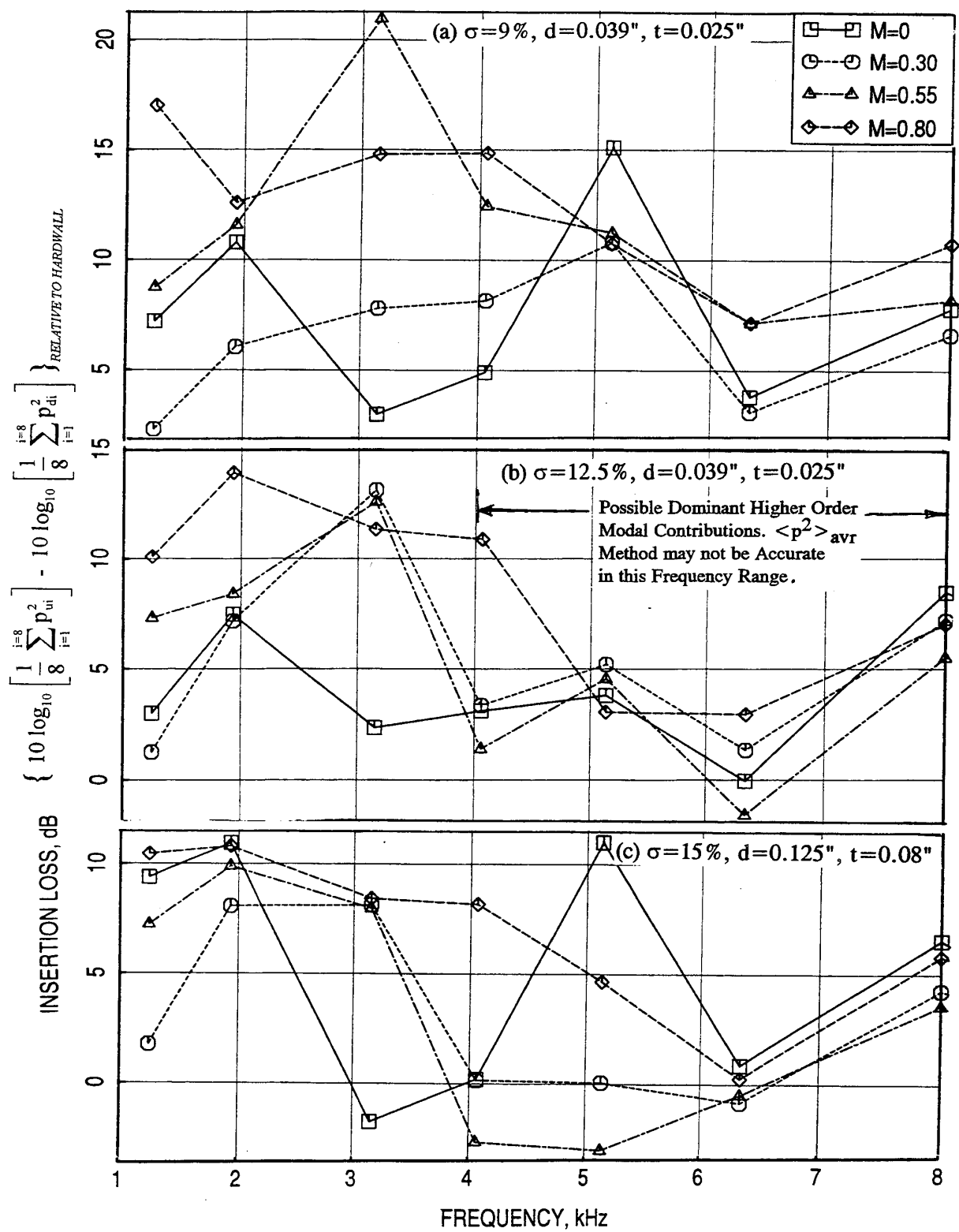


Figure B2. Effect of grazing flow Mach number (M) on insertion loss spectra for 1"-deep SDOF type panels with perforated facesheets.

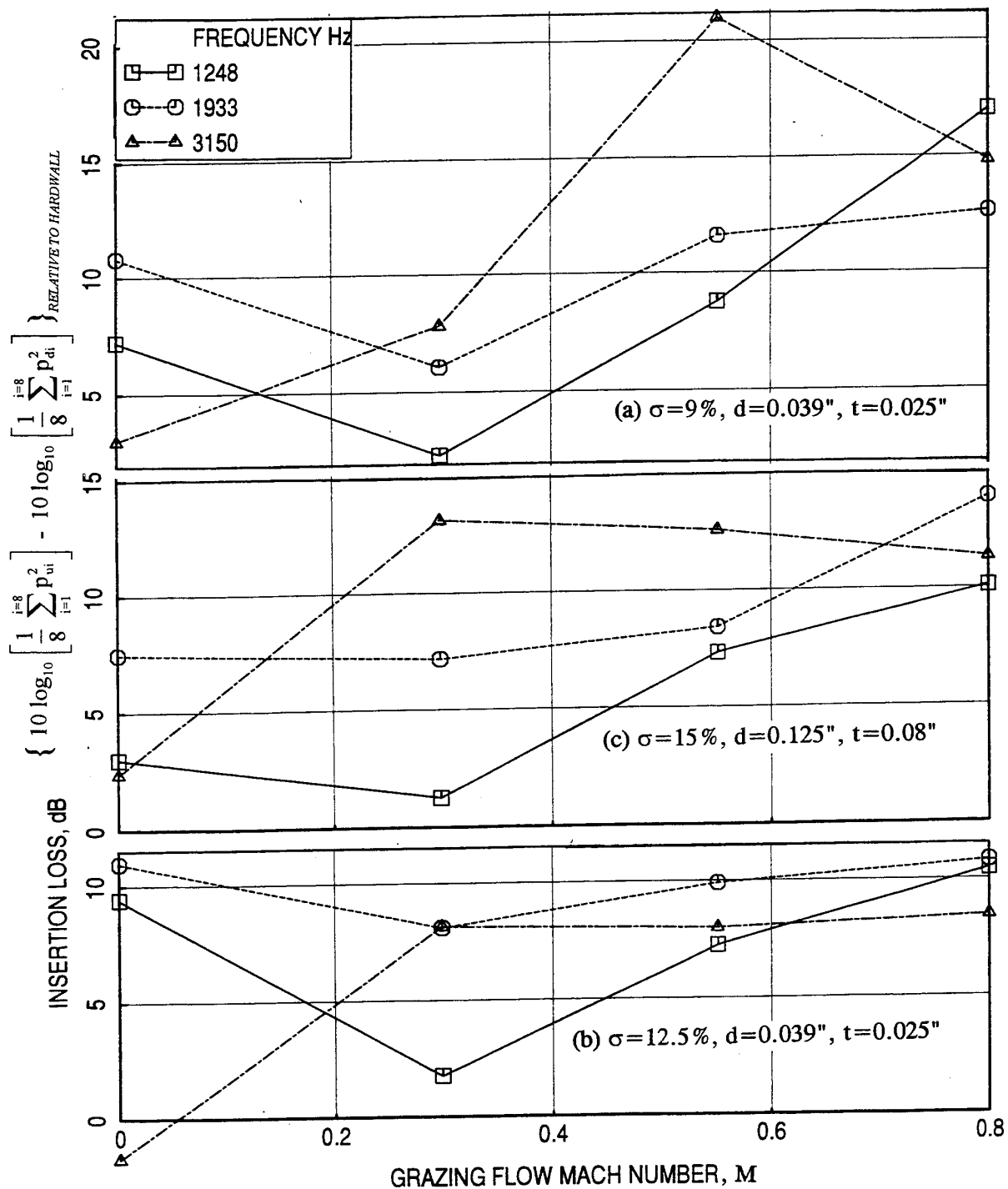


Figure B3. Effect of grazing flow Mach number (M) on insertion loss at different excitation frequencies for 1"-deep SDOF type panels with perforated facesheets.

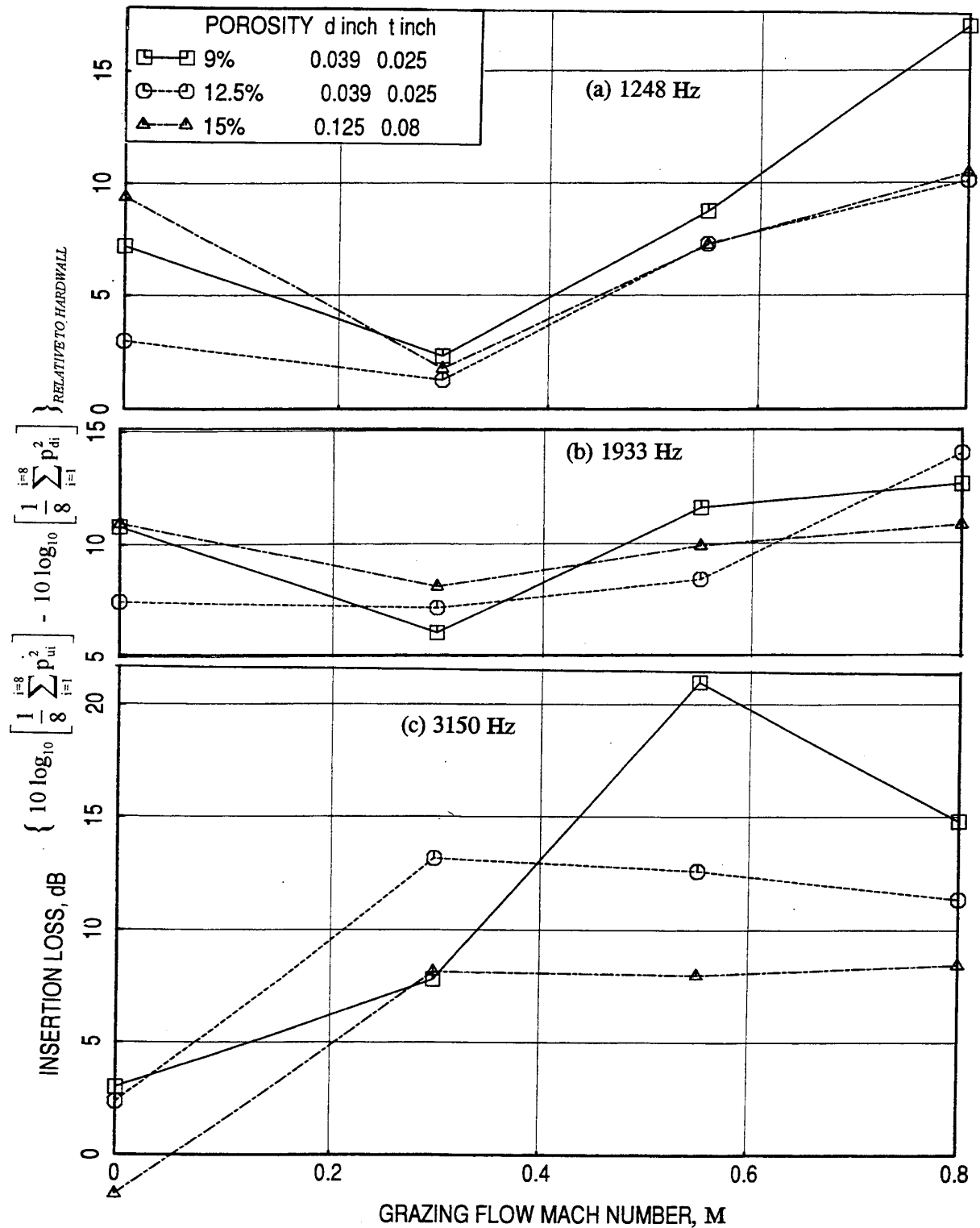


Figure B4. Effect of facesheet porosity on insertion loss as a function of grazing flow Mach number (M) at different excitation frequencies for 1"-deep SDOF type panels with perforated facesheets; d/t=1.56

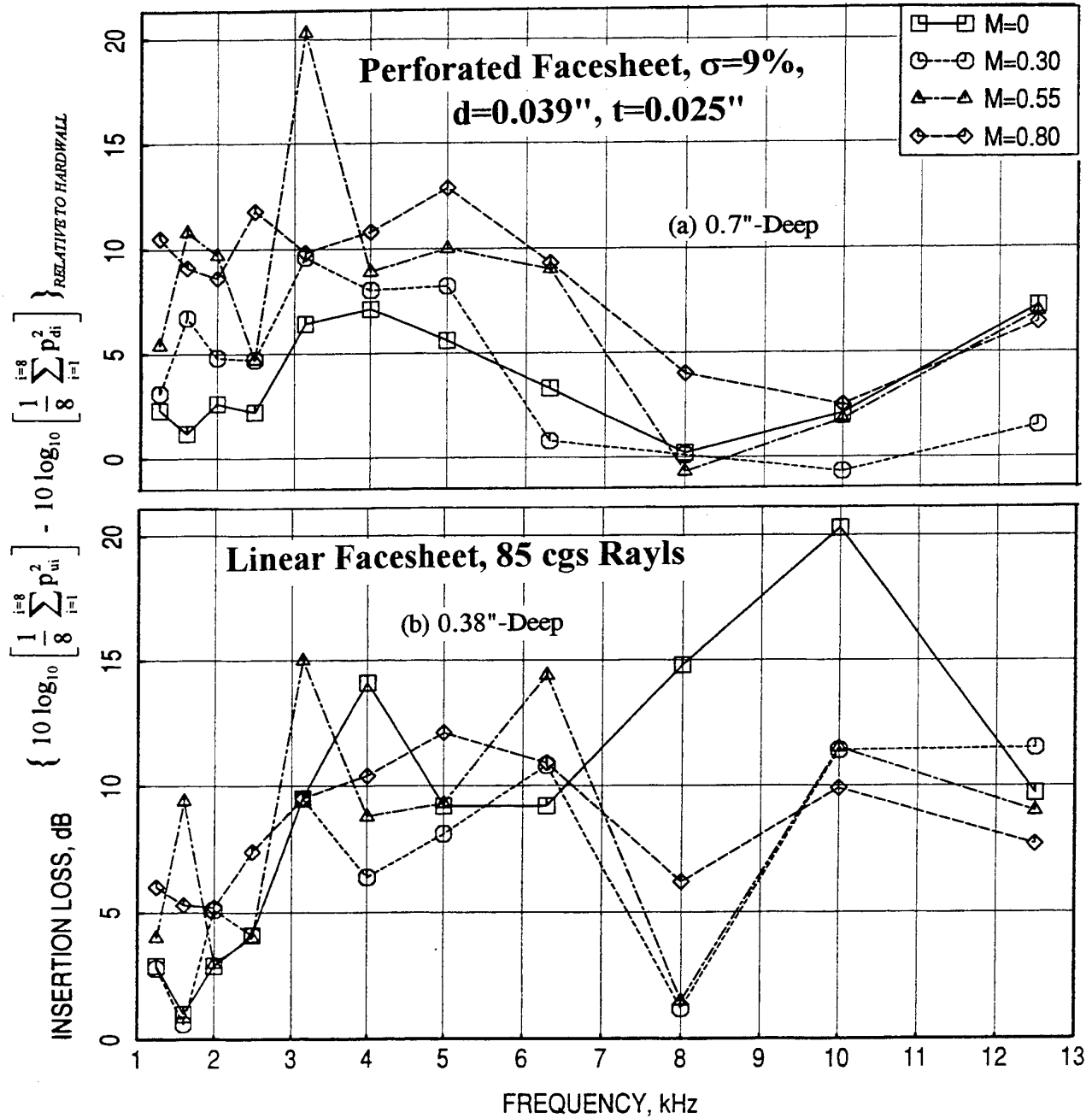


Figure B5. Insertion loss at different grazing flow Mach numbers for SDOF type liners;
 (a) 0.7" deep with a perforated facesheet, 9% porosity, $t=0.02''$, $d=0.39''$
 and (b) 0.38" deep with a linear facesheet of resistivity of 85 Rayls.

number. The general information is that the 0.7"-deep panel is effective up to about 6 kHz compared to the 0.38"-deep panel, which seems to be suppressing noise up to about 8 kHz. This is an expected trend. Insertion loss for two bulkfilled SDOF type panels with linear facesheets is shown in Figure B6. Again, we fail to see any systematic trend with respect to frequency and grazing flow Mach number, except that the acoustic suppression is limited up to about 7 kHz. The effect of bulk resistivity on insertion loss for bulkfilled SDOF type panels with the same linear facesheets is shown in Figure B7. However, there is no well-defined effect of bulk resistivity observed in these results. Figure B8 shows the insertion loss variation with respect to frequency at a number of grazing flow Mach numbers for a 2DOF type panel with linear facesheet and septum and for a 1" deep SDOF type panel with perforated facesheet. The insertion loss variation does not follow any set trend with respect to frequency and Mach number.

The SPL spectra for all 8 individual transducer locations and their average values for a bulkfilled treatment panel for upstream and downstream array positions are shown in Figures B9 and B10 for grazing flow Mach numbers of 0 and 0.55, respectively. Substantial scatter is observed in these results. The effect of grazing flow Mach number on SPL at two fixed locations (i.e., at 1 and 9) and on average SPL for upstream and downstream planes are examined in Figures B11 through B13, respectively. Again the scatter with respect to frequency and flow Mach number is significant.

Experimental Results of Impulsive Excitation: The flow duct facility to evaluate acoustic suppression in terms of insertion loss in the presence of grazing flow for treatment panels using impulse technique is schematically illustrated in Figure 51. The acoustic excitation is provided either by a single or by four 100-watt Altec driver(s). The acoustic energy flux measurements are made by flush-mounted transducer arrays upstream and downstream of the treatment panel. An impulsive acoustic source, designed and fabricated, is installed in the flow duct facility, as shown in Figure 51. The sound source is designed to generate high frequency noise from low frequency acoustic drivers. The output of four 100 watt acoustic drivers are funneled in to a 24" long converging duct of about 3" diameter through 1.125" diameter tubes, which converges to about 0.75" diameter at the other end.. This tube is then bent by 90° such that the output of the acoustic drivers exits at the center of the flow duct and subsequently reduced to 0.5" diameter through a straight 0.5" diameter tube of about 12" long. In this system, use is made of the fact that for a fixed acoustic power level, the intensity of the sound wave increases as the cross-sectional area of the duct decreases. In turn, a strong non-linear effect is obtained. Thus, the contraction ratio of the tube carrying the acoustic

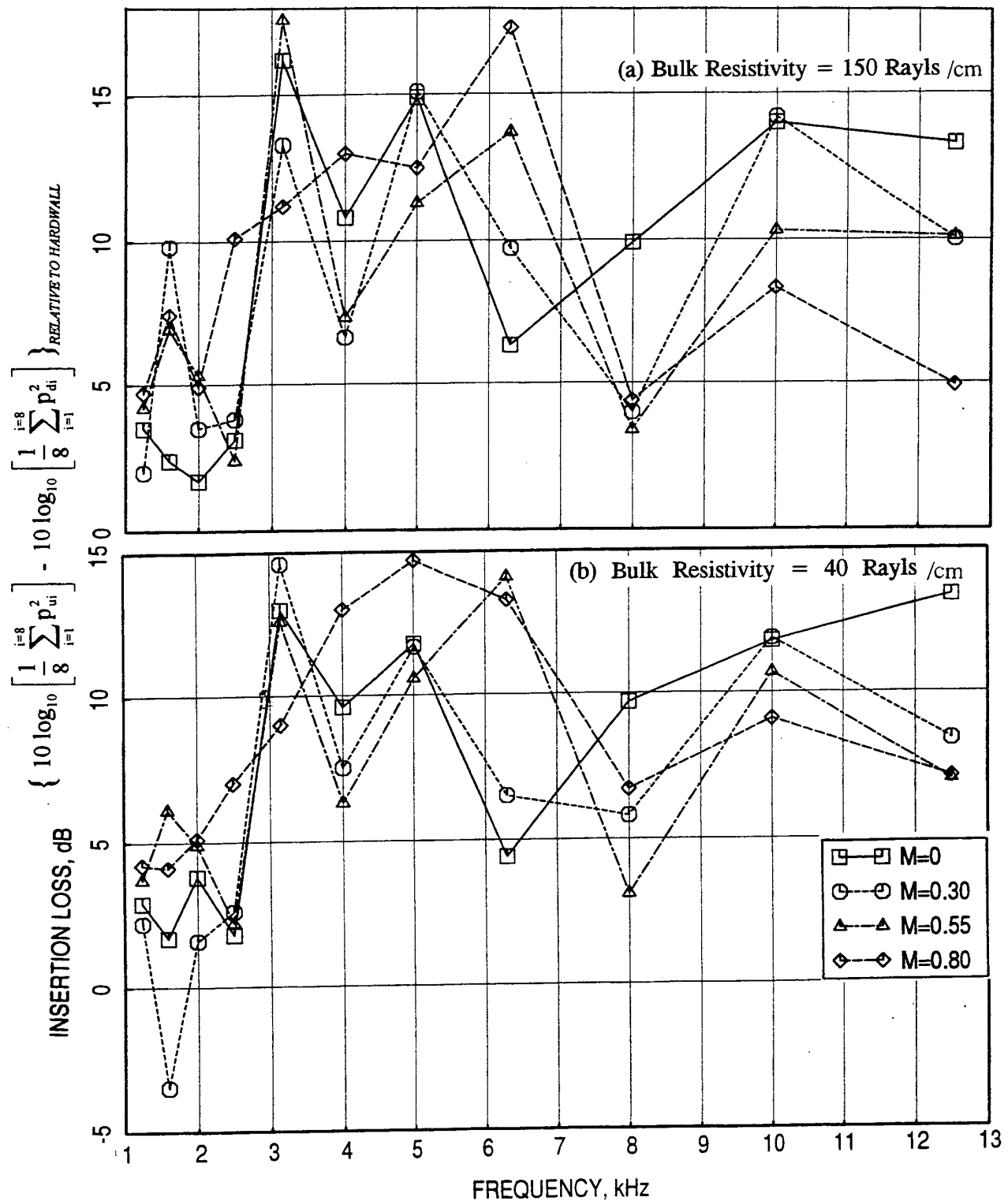


Figure B6. Insertion loss at different grazing flow Mach numbers for bulkfilled SDOF type liners with linear facesheets of resistivity of 5 Rayls and with bulk resistivity of (a) 150 and (b) 40 Rayls/cm.

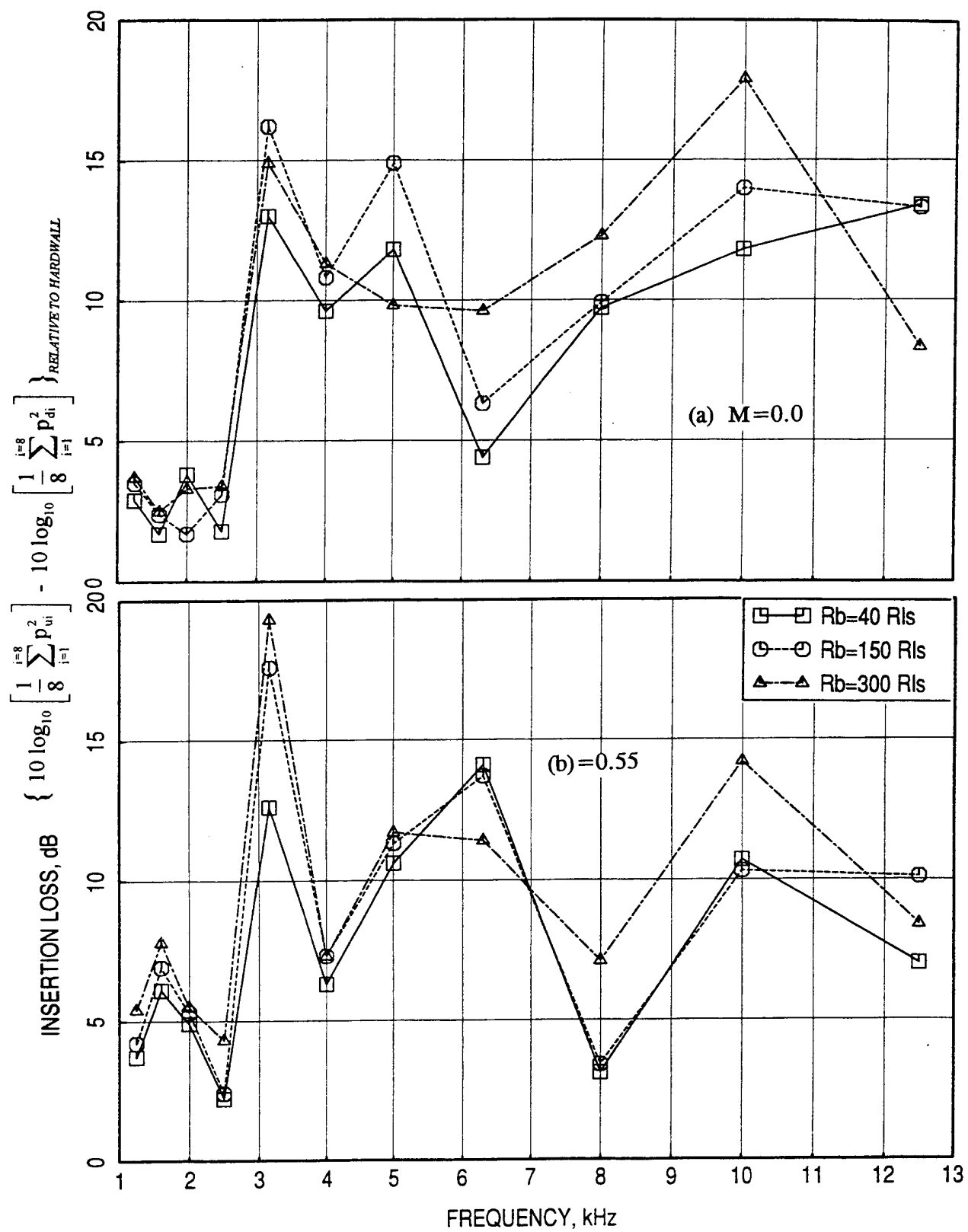


Figure B7. Effect of bulk resistivity on insertion loss for a bulkfilled SDOF type liner with linear facesheets of resistivity of 5 Rayls; (a) $M=0.0$ and (b) $M=0.55$.

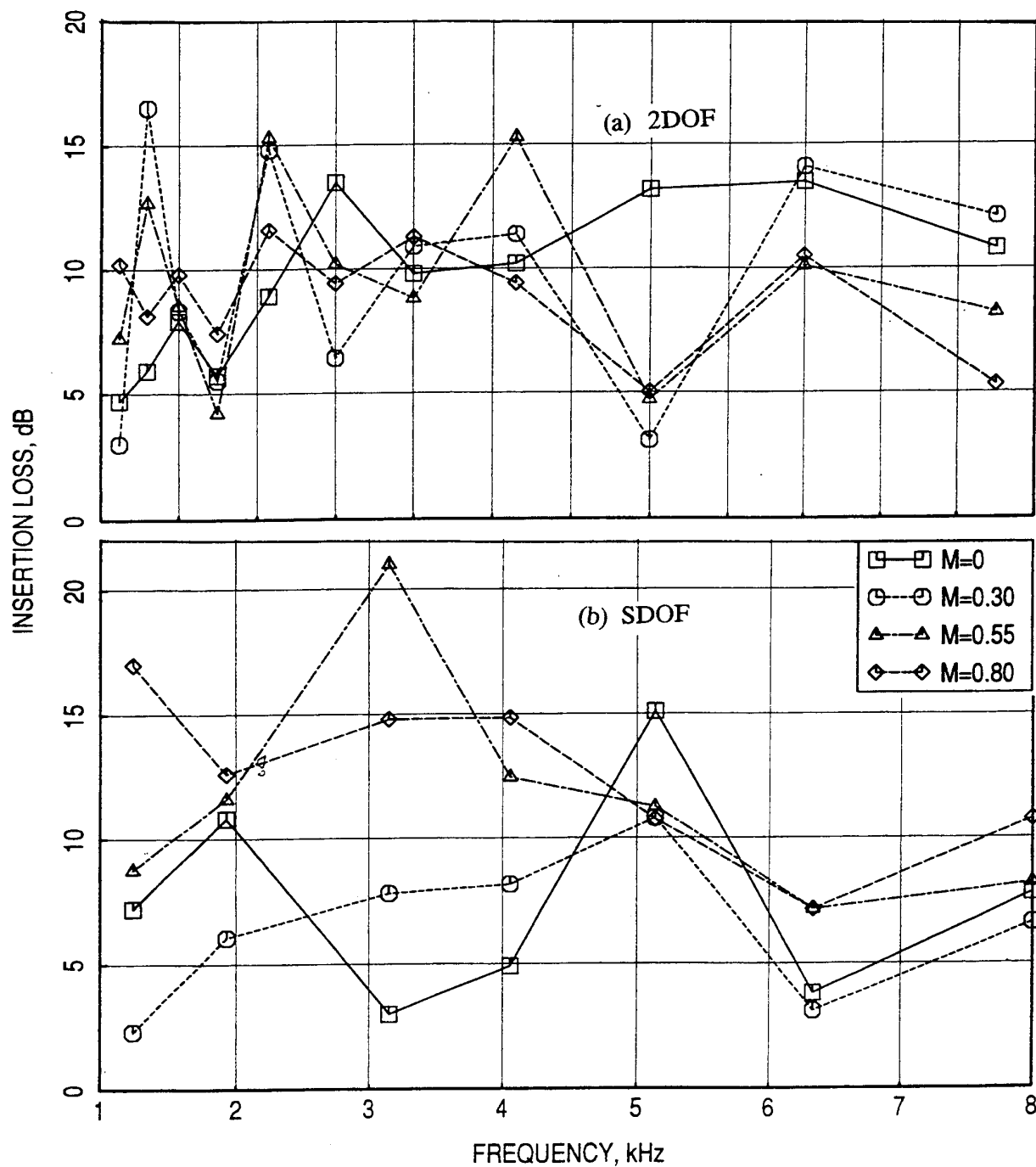


Figure B8. Insertion loss at different grazing flow Mach numbers for (a) a 2DOF type liner, upper cavity depth=0.3", lower cavity depth=0.55", linear facesheet and septum resistivities of 40 and 90 Rayls; and (b) a 1" deep SDOF type liner with perforated facesheet, 9% porosity, $t=0.025"$, $d=0.39"$.

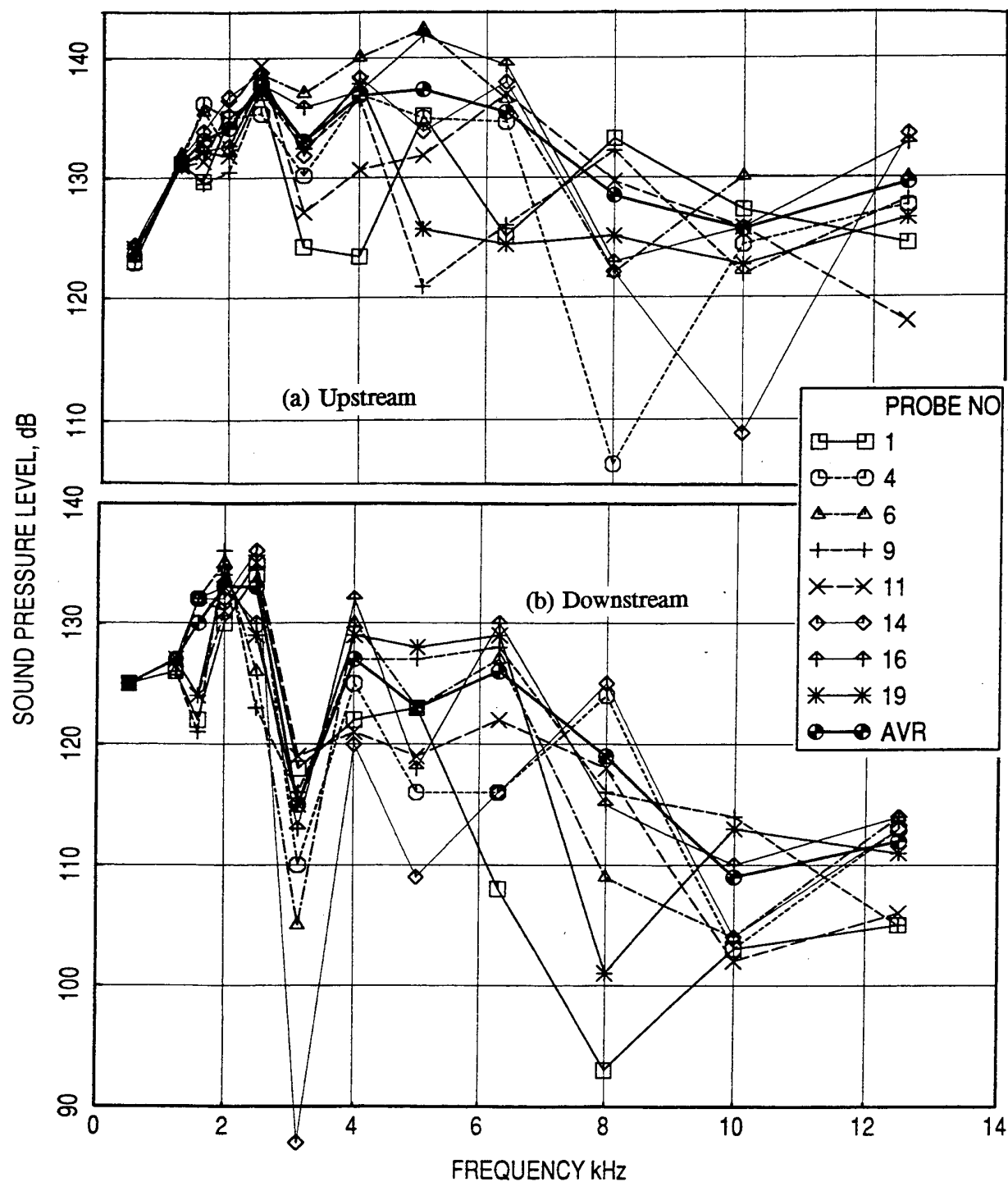


Figure B9. SPL spectra at various probe locations and their average value for a bulkfilled SDOF type liner with linear facesheet of resistivity of 5 Rayls and bulk resistivity of 150 Rayls at (a) upstream and (b) downstream planes; $M=0.0$.

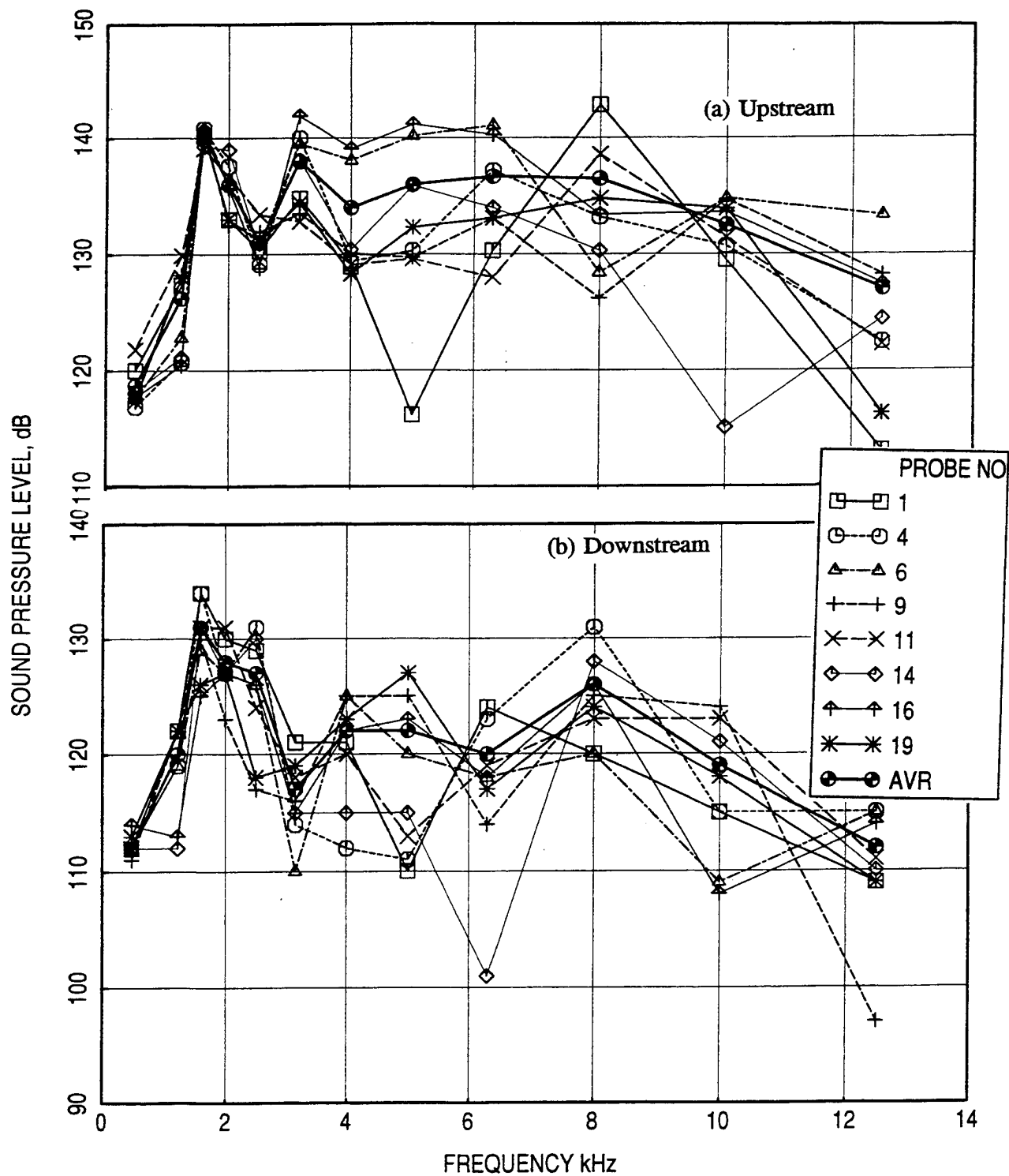


Figure B10. SPL spectra at various probe locations and their average value for a bulkfilled SDOF type liner with linear facesheet of resistivity of 5 Rayls and bulk resistivity of 150 Rayls at (a) upstream and (b) downstream planes; $M=0.55$.

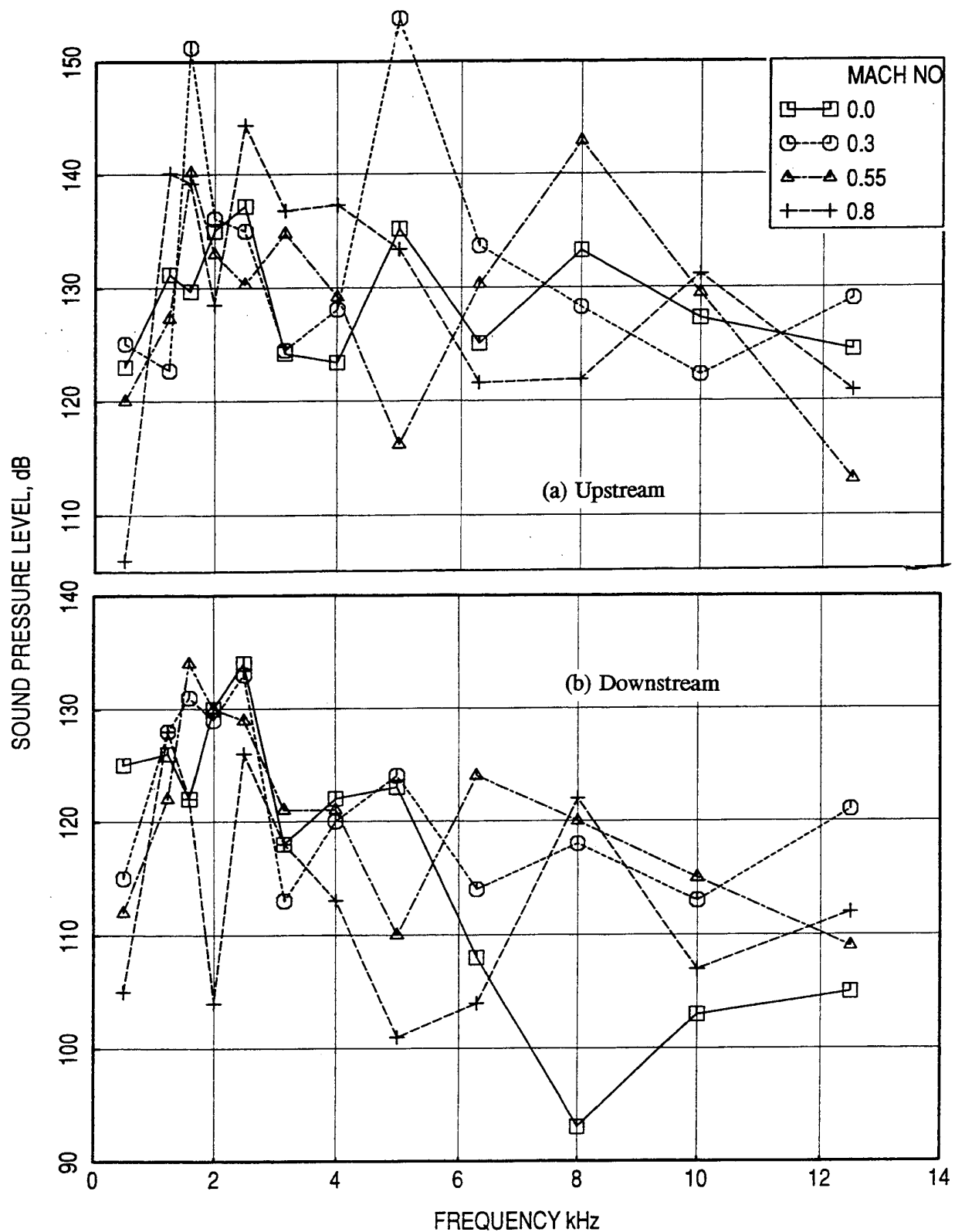


Figure B11. SPL spectra at probe location #1 for different grazing flow Mach numbers for a bulkfilled SDOF type liner with linear facesheet of resistivity of 5 Rayls and bulk resistivity of 150 Rayls at (a) upstream and (b) downstream planes.

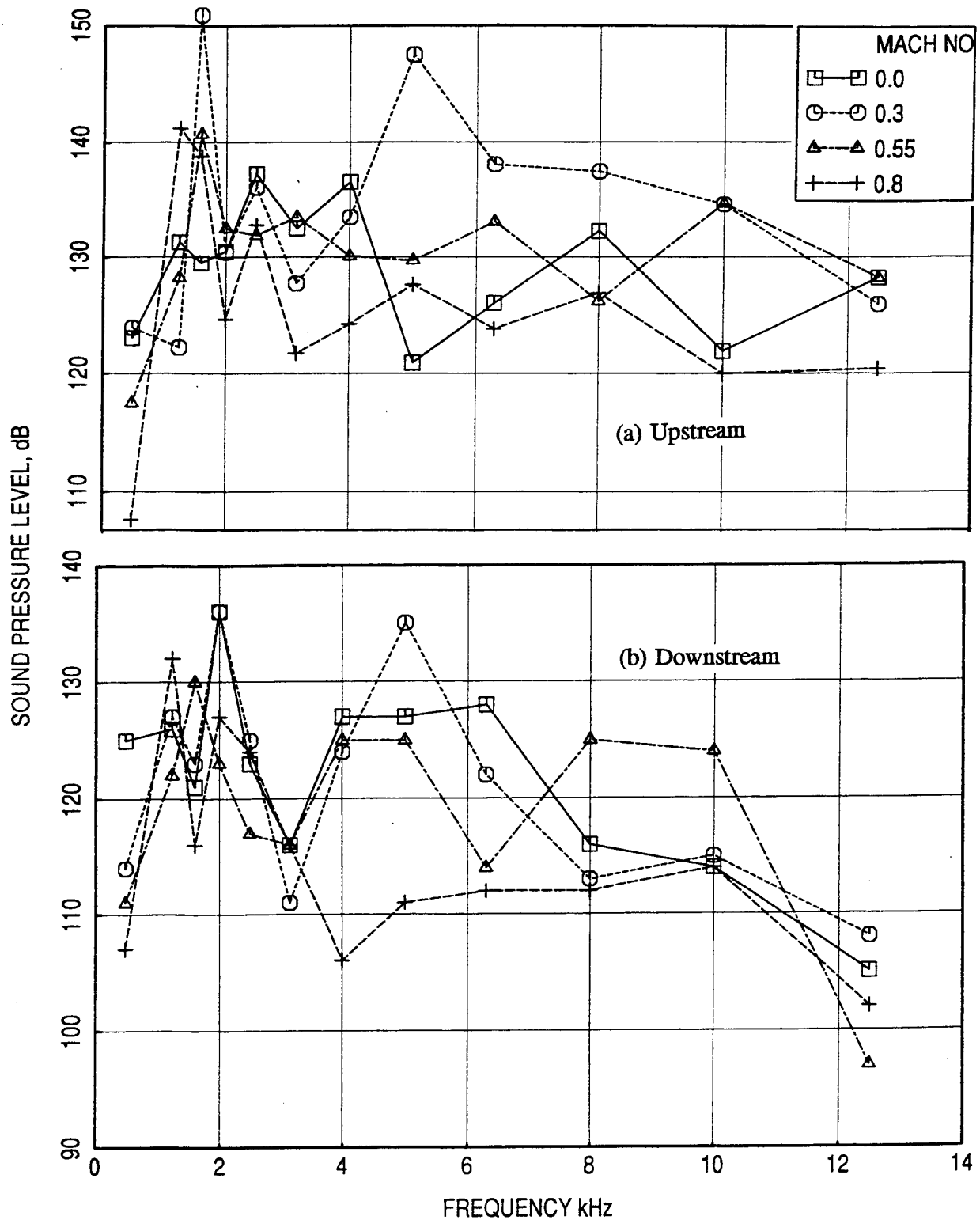


Figure B12. SPL spectra at probe location #9 for different grazing flow Mach numbers for a bulkfilled SDOF type liner with linear facesheet of resistivity of 5 Rayls and bulk resistivity of 150 Rayls at (a) upstream and (b) downstream planes.

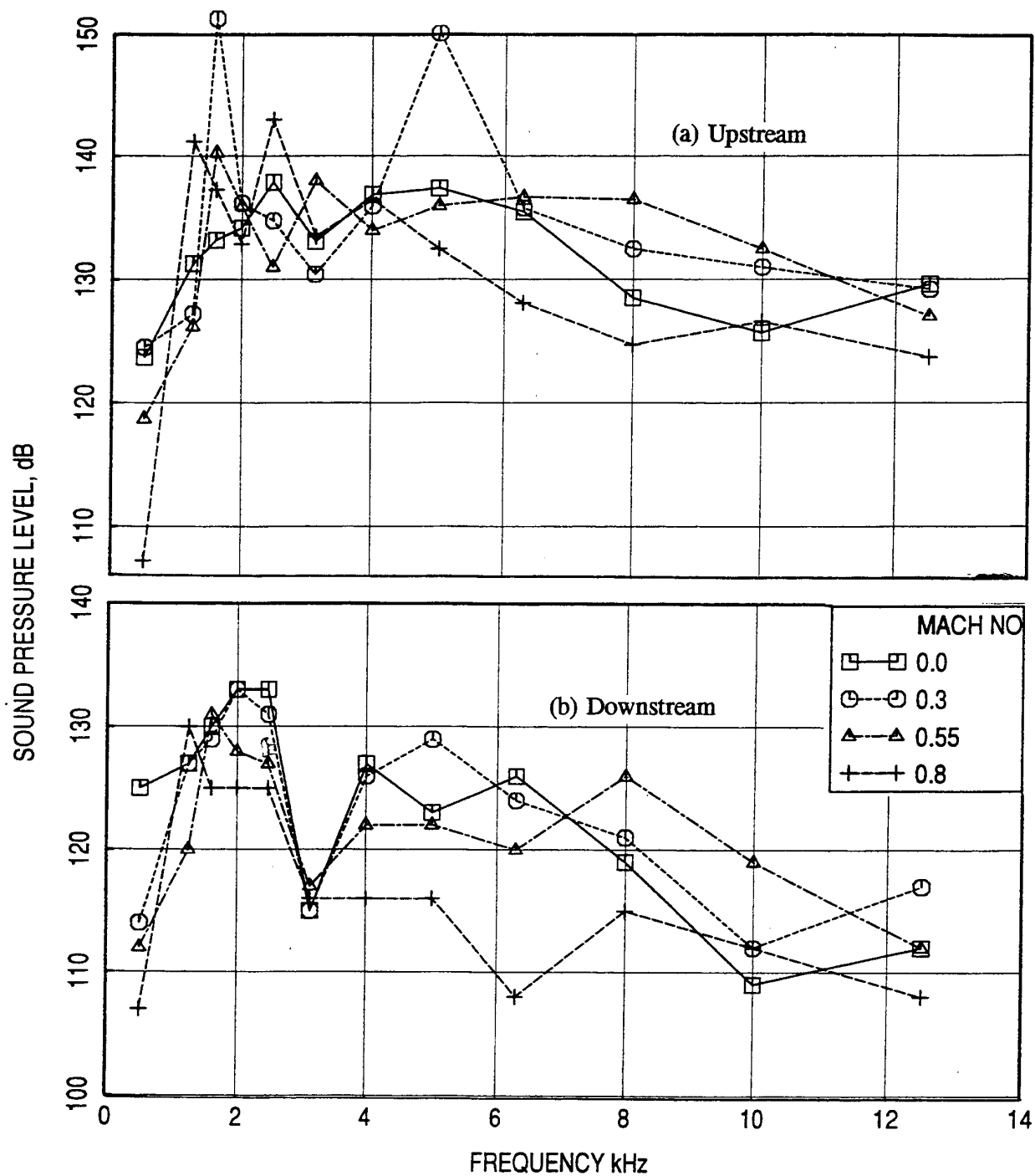


Figure B13. Average SPL spectra for different grazing flow Mach numbers for a bulkfilled SDOF type liner with linear facesheet of resistivity of 5 Rayls and bulk resistivity of 150 Rayls at (a) upstream and (b) downstream planes.

signal broadens the frequency range due to non-linear effect. This is further enhanced by the nonlinear propagation of the high intensity sound wave in the 0.5" diameter tube. Certain amount of insulation is applied on the flow duct wall at the sound source exit to absorb the reflections, which may not coalesce during the propagation of the pulse.

For the present study rectangular pulses of about 300 to 400 μ s wide and with a peak level of 20 to 60 volt, generated 10/sec, are used to excite the acoustic drivers. In the presence of high velocity flow, it becomes extremely difficult to isolate the pulse from dominant broadband flow noise. In this situation a time domain signal averaging technique is used to recover the pulse from the flow noise. If a sufficient number of individual pulse records, separated by an adequate time period, are averaged, the contribution from the flow-associated random fluctuations are averaged to zero, thus enabling recovery of the pulse time history. A synchronizing signal is used to find the start of each record. The simple summation process increases the signal-to-noise ratio because the noise, which is not coherent with the synchronizing signal, averages toward zero with an increasing number of samples. The signal averaging, illustrated in Figure 52, involves the generation of a train of pulses from the acoustic driver system using a pulse generator. The acoustic pulse train contaminated with flow noise is measured by the transducers and is fed to a signal analyzer in real time. The analyzer is simultaneously triggered by the same electronic signal used to excite the acoustic driver system. Thus the pulse is recovered applying a large number of averaging.

When a positive or negative pulse propagating in a tube as a one-dimensional wave exits out to a three-dimensional field (i.e., in to the wider flow duct in this case) the pulse shape changes. The three-dimensional pulse contains a main compression pulse similar to the pulse in the source tube followed by a lower amplitude rarefaction pulse. A typical impulsive signal measured by one of the flow duct upstream transducer is shown in Figure B14 for no flow condition. The main pulse consists of a prominent negative pulse followed by a positive pulse, as expected. The subsequent chain of pulses is the reflections from duct ends and other surfaces. The frequency content of the pulse depends on slope of the leading edge of the main pulse. The slope of the pulse leading edge of Figure B14 is very steep and hence very broad frequency content is expected in this pulse. However, we see a major problem that a second pulse appears slightly downstream of the first before its completion. Hence, this would cause destructive and additive interference in the spectral content and this effect would be different for different measurement locations.

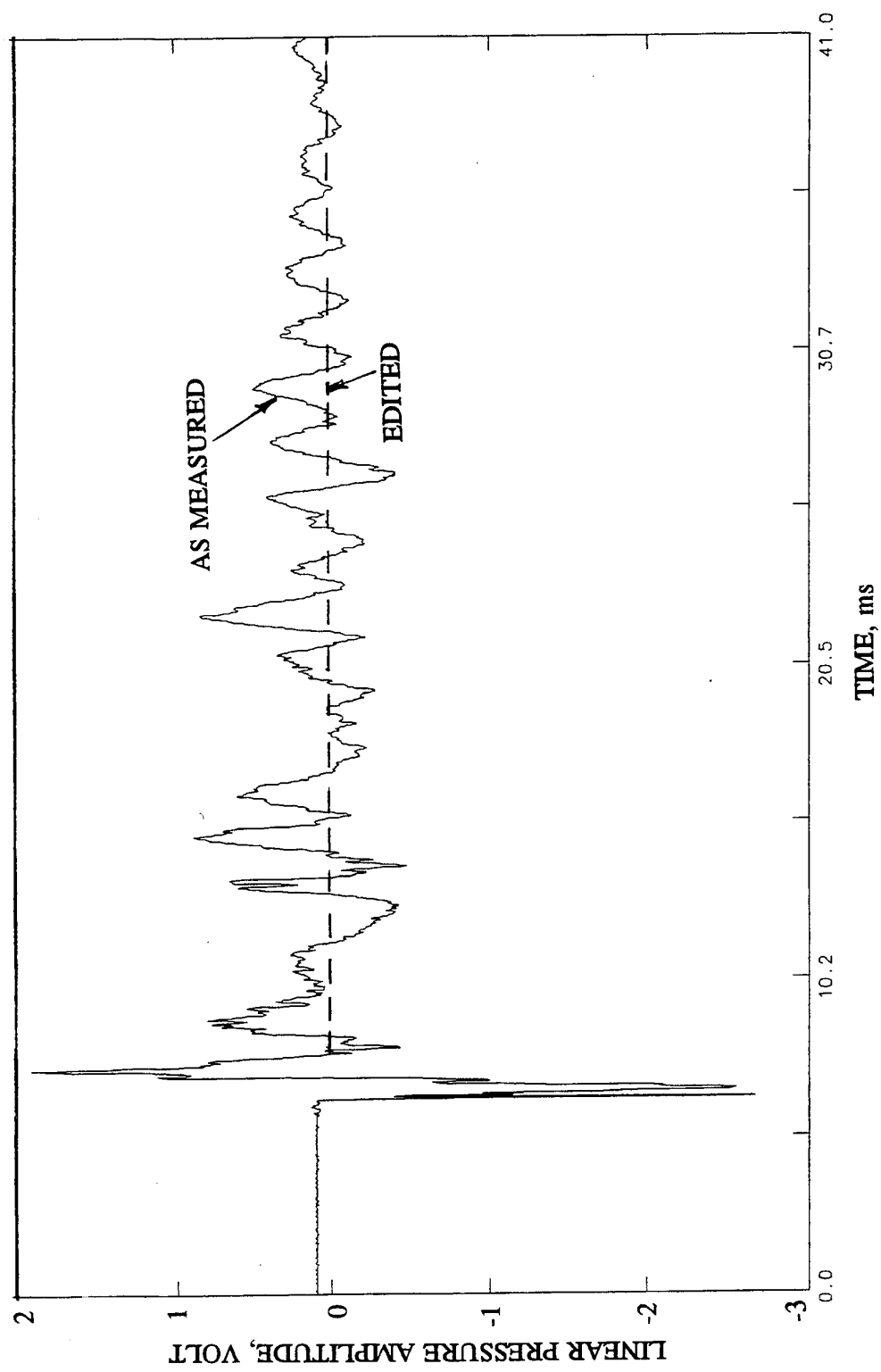


Figure B14. A typical impulsive signal measured by an upstream transducer and its edited form; excitation pulse level=44 volts and width=300 μ s, flow Mach number=0.

The origin of the second pulse, which did not coalesce with the direct one, is due to the reflections close to the source exit. The insulation provided to absorb such reflections is not adequate due to the lack of its absorbing capability and its extent downstream of the source exit. However, we will examine the characteristics of this imperfect pulse to see if we can come out with a method to estimate the insertion loss of panels by using this pulse. In the impulse technique an editing process is utilized to remove the unwanted portions of the signals from the total signal time history. The editing process is shown in Figure B14 by dotted line. Figure B15 shows the sound pressure level spectrum of the time domain signal of Figure B14, with and without editing. Editing is necessary to correctly account for the main propagating signal without including any reflections.

Based on the above discussion of the uncoalesced pulse, we can see its effect on the spectral distribution of Figure B15, that instead of a linearly varying SPL spectrum, peaks and troughs are present. This behavior would not be consistent with respect to different locations, especially, between upstream and downstream transducers, which are separated by about 54".

Next, the effect peak level of excitation pulse on the output signal is examined in Figures B16 and B17. The pulse amplitude (see Figure B16) as well as SPL levels (see Figure B17) increase with increasing pulse voltage. The effect of signal averaging is examined for pulses in the presence of flow with Mach number 0.15 in Figures B18 and B19. It can be seen that the higher number of averages reduces more amount of background noise, since the signal-to-noise ratio improvement is proportional to the square root of the number of averages. Finally, the impact of excitation pulse width is shown in Figure B20 for a flow Mach number of 0.4. Signal-to-noise ratio is improved because of increased pulse strength due to wider pulse width.

Tests are conducted to evaluate the insertion loss for the hard wall and an SDOF type panel at a number of flow Mach numbers using the impulse method. The initial data acquisition process for impulse test method involved a number of steps. A computer program called DIGIT was used to acquire time domain data on a disc. Then another program, CREDIT, was used to average the stored data in time domain and edit the averaged data, one channel at a time. Finally, FFT analysis of the edited signal was performed by a third program called FRAN. The disc I/O rate and demultiplexing large amount of data from sixteen pressure transducer channels were extremely time consuming. In addition, the process of time domain averaging, editing, and FFT analysis, one channel at a time, was also very time consuming.

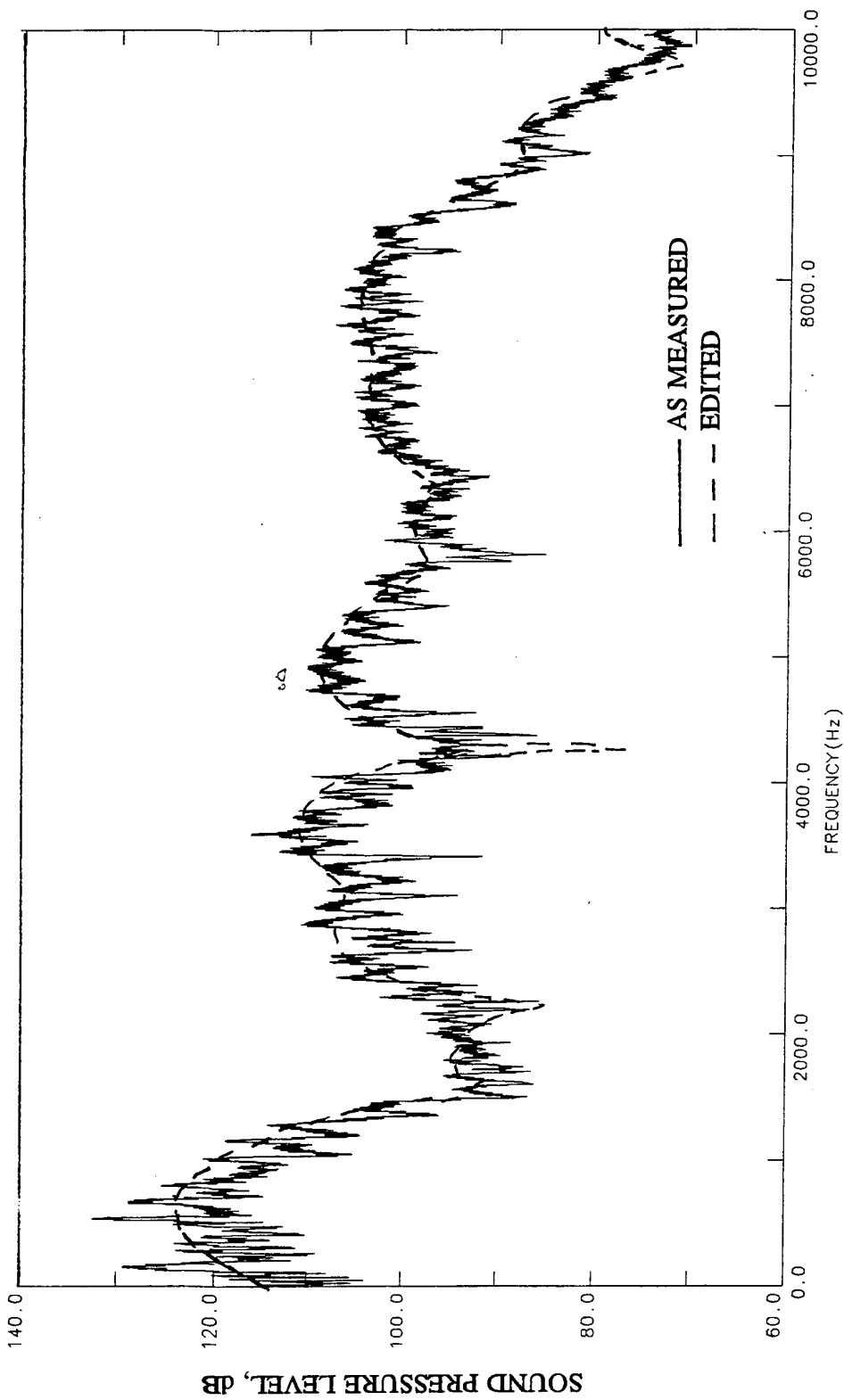


Figure B15. Effect of editing on sound pressure level spectrum for an impulsive signal measured by an upstream transducer; excitation pulse level=44 volts and width=300 μ s, flow Mach number=0.

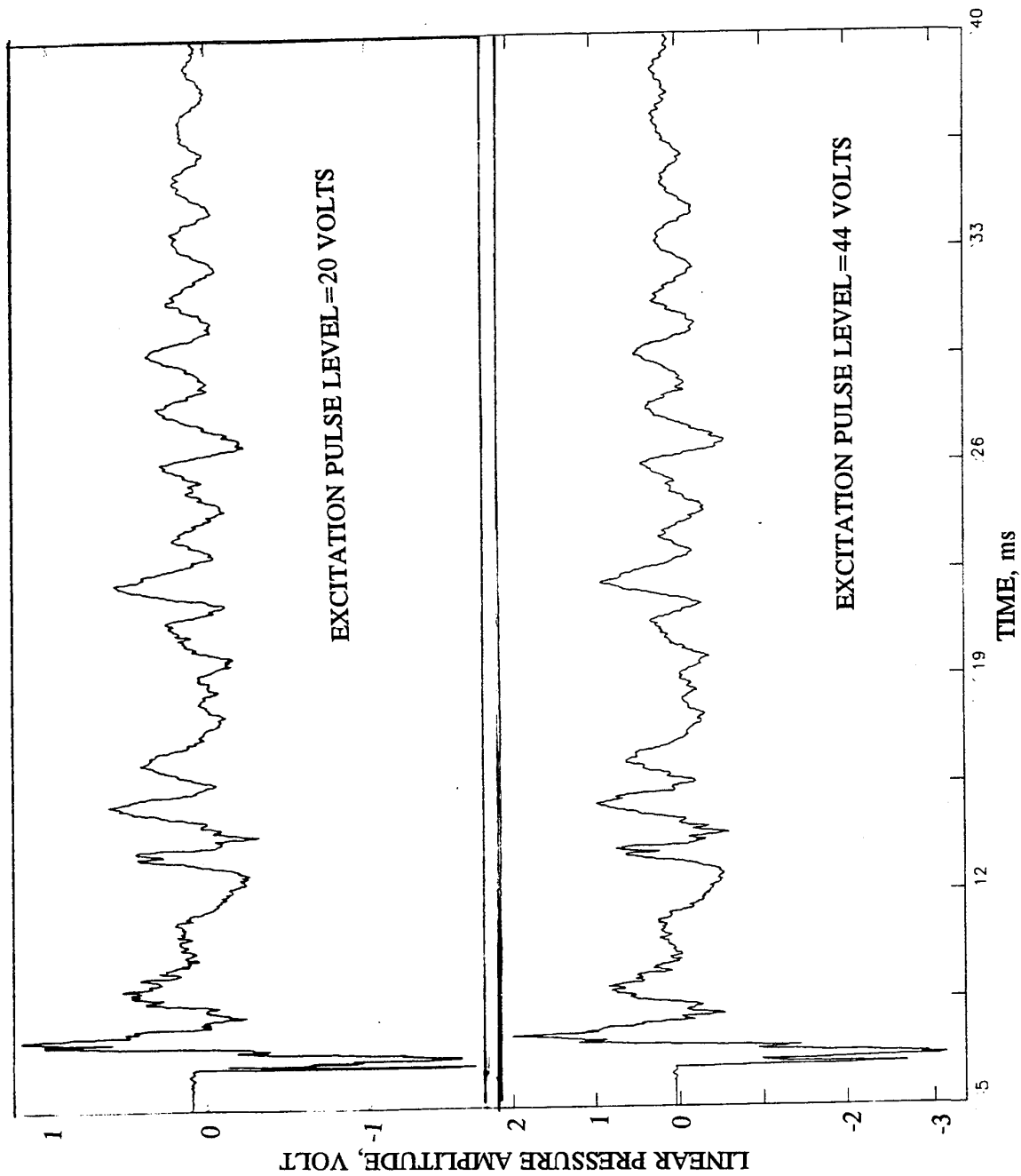


Figure B16. Effect of excitation level on time domain impulsive signal measured by an upstream transducer; excitation pulse width=300 μ s, flow Mach number=0.

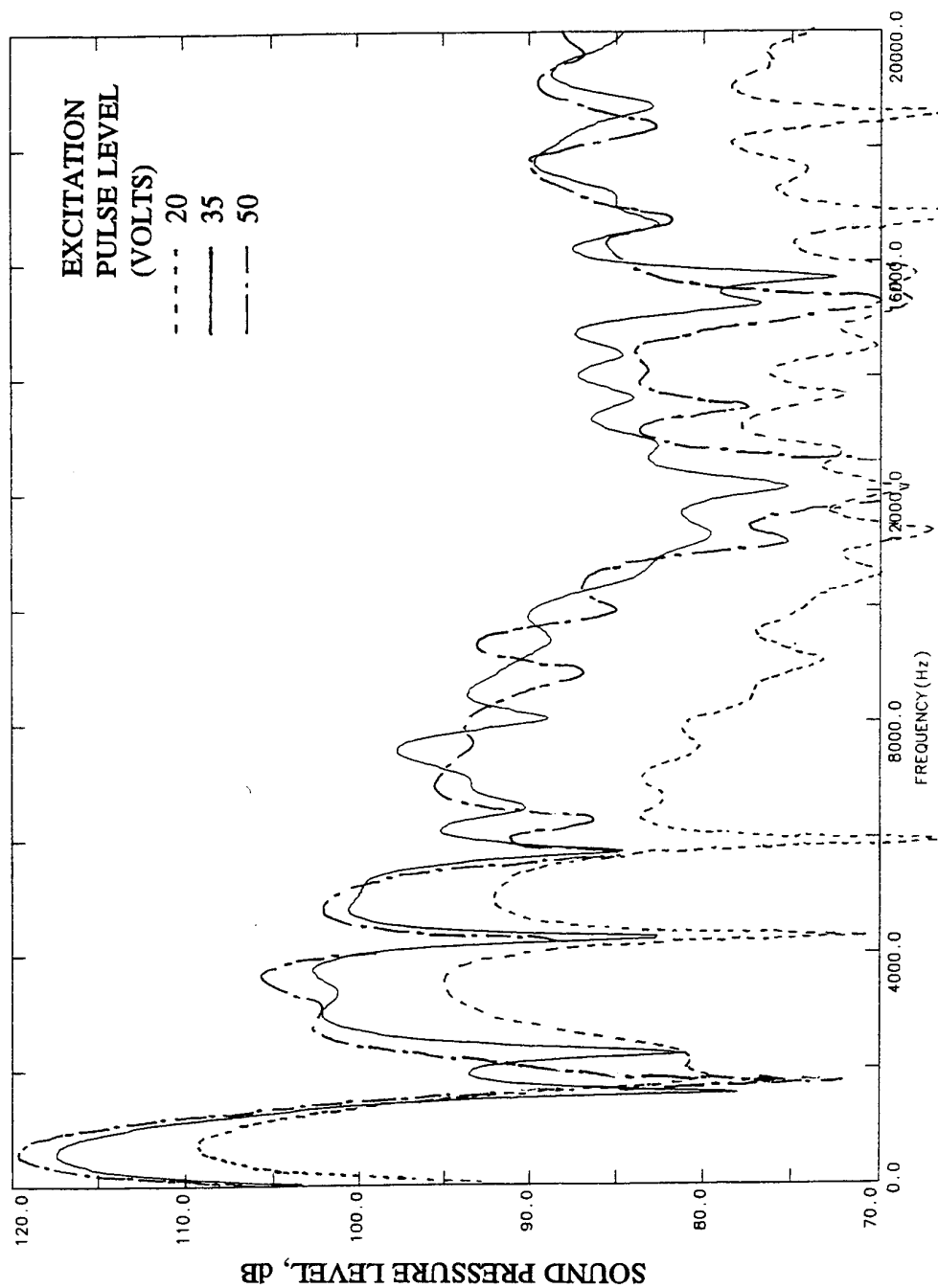


Figure B17. Effect of excitation level on sound pressure level spectrum for impulsive signals measured by an upstream transducer; excitation pulse width=300 μ s, flow Mach number=0.

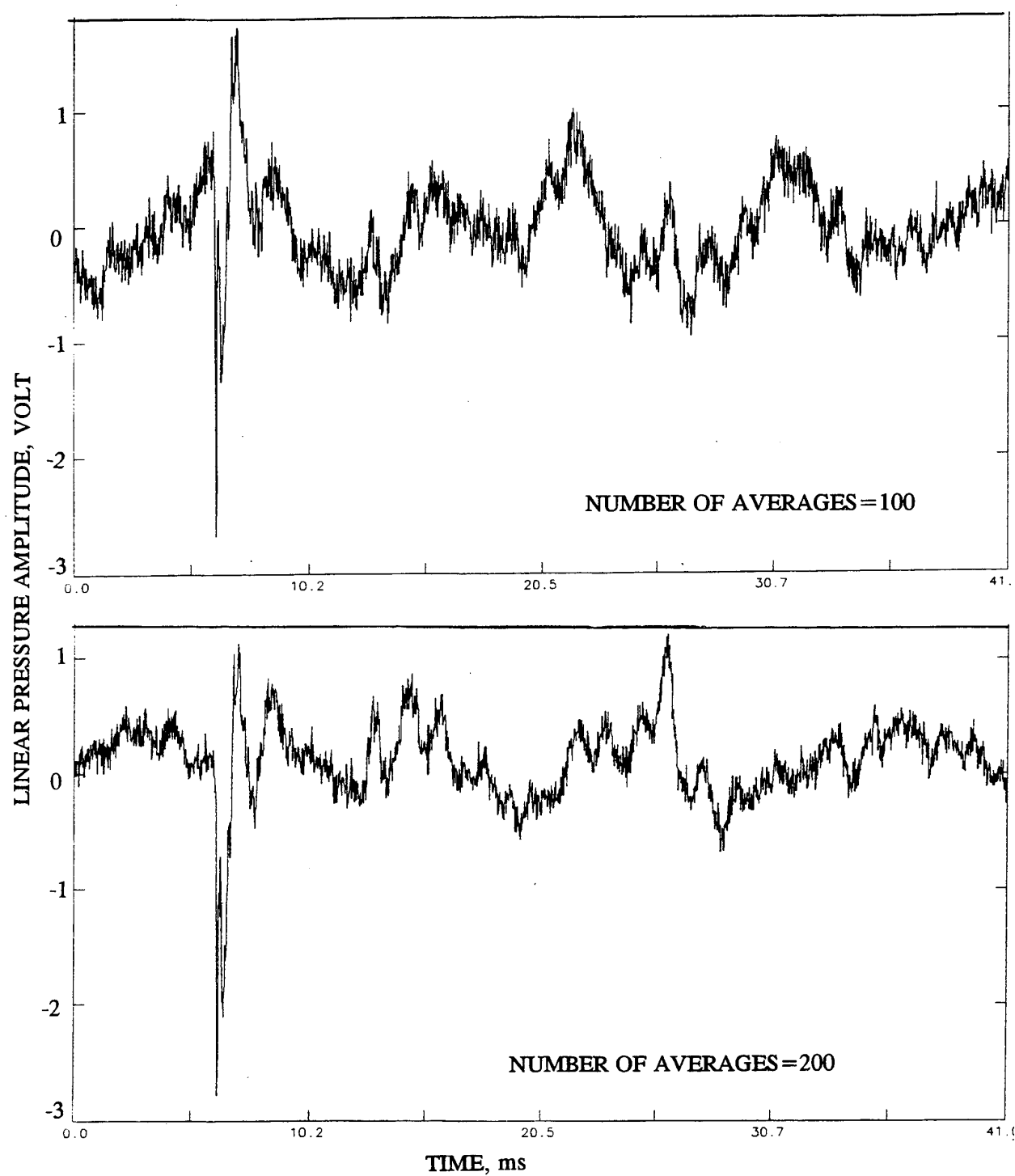


Figure B18. Effect of number of time domain averages on impulsive signals measured by an upstream transducer; excitation pulse level=44 volts and width=300 μ s, flow Mach number=0.15.

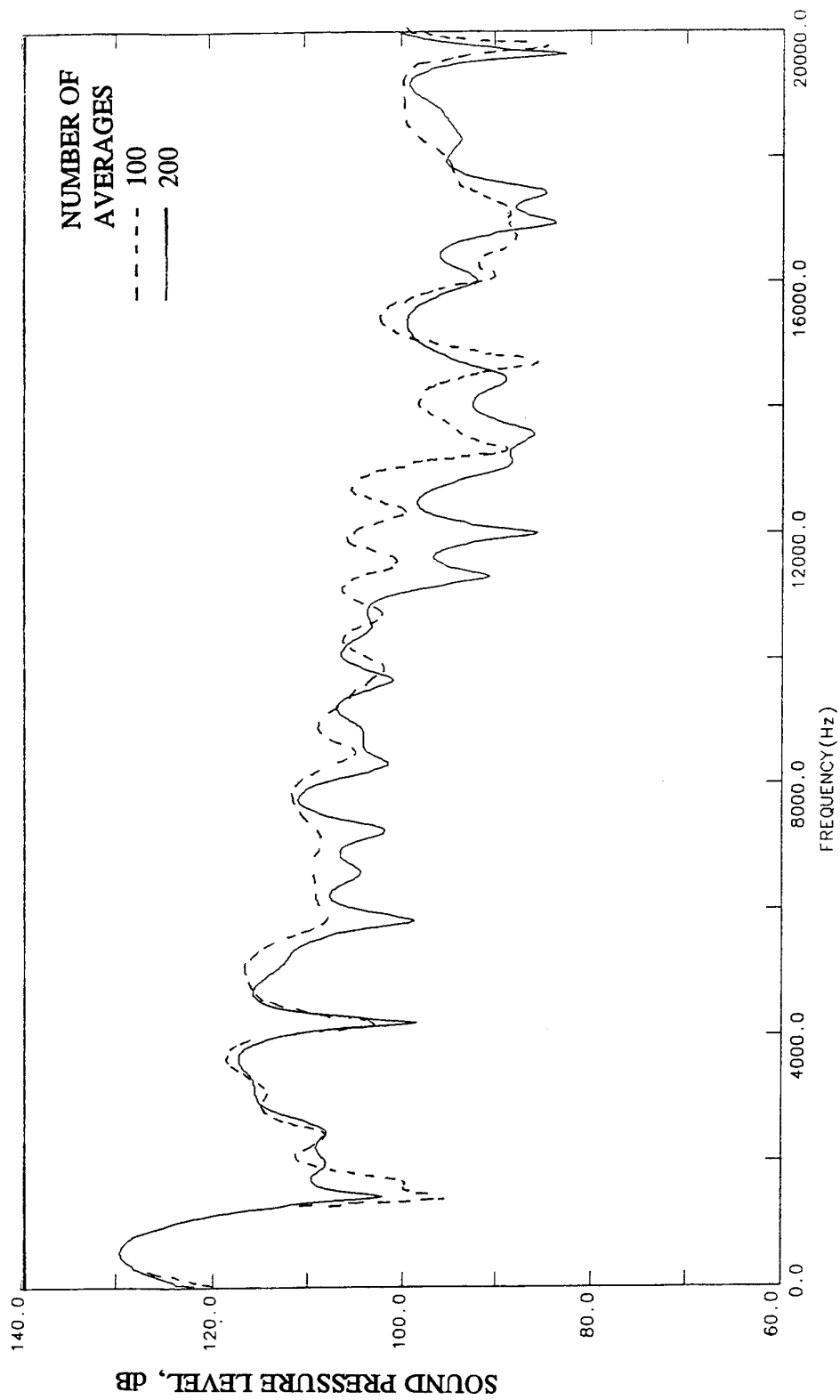


Figure B19. Effect of number of time domain averages on sound pressure level spectrum for impulsive signals measured by an upstream transducer; excitation pulse level=44 volts and width=300 μ s, flow Mach number=0.15.

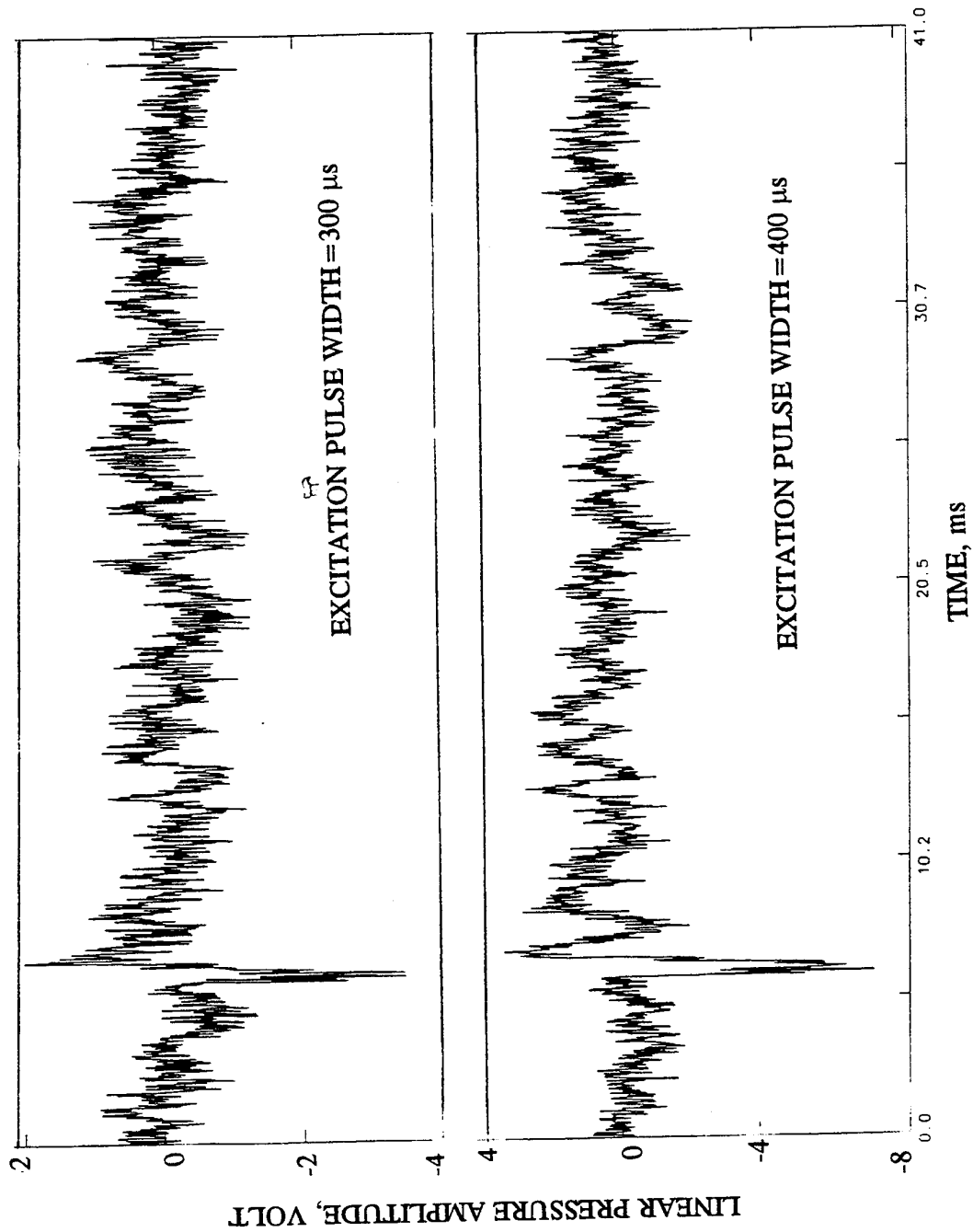


Figure B20. Effect of excitation pulse width on time domain impulsive signal measured by an upstream transducer; excitation pulse level=60 volts, flow Mach number=0.4, number of time domain averages=1000.

To minimize the time cycle for each test a customized software program is developed to perform real-time data averaging, editing, and FFT analysis for all the channels simultaneously without transferring the digitized transducer output to the disc. This process reduces the analysis time by order of magnitude compared to the initial analysis cycle.

Figure B21 shows the averaged time domain data with and without editing and the sound pressure level spectrum of the edited signal for a single transducer in the upstream plane for hard wall configuration at a flow Mach number of 0.4. Similar results for a downstream transducer are shown in Figure B22. The sound pressure level spectra for upstream plane and downstream plane transducers are averaged over 8 transducers for the corresponding planes and are shown in Figure B23(a). Since the time histories obtained in the flow duct are not single pulses, their FFT outputs are not smooth. These SPL spectra contain SPL dips. Finally, the insertion loss spectrum, the difference between upstream and downstream averaged sound pressure level spectra, is shown in Figure B23(b). It should be noted that the results corresponding to SPL dips are inaccurate.

Similar results are obtained for a 0.7" deep SDOF type panel with a 9% porous 0.02" thick face sheet with 0.039" diameter holes, bonded to a 3/8" wide honeycomb structure. These results are shown in Figures B24 through B26.

While, it is expected that the insertion loss for hard wall configuration should be zeros, we observe significant insertion loss at frequencies above 8000 Hz. This could be due to a number of reasons, namely, the problem associated with the pulse characteristics and the inaccuracy in energy flux measurement due to the presence of higher order modes. The hard wall insertion loss may be used as the no loss level and a relative value may be calculated for any liner panel as the actual insertion loss. The insertion loss for the panel, as shown in Figure B26(b), is more or less of the same levels as those for the hard wall. Hence, a relative value of insertion loss for the panel compared to the hard wall is insignificant. The possible problems in this technique are basically the same as those speculated for discrete frequency excitation. An additional problem in this method is caused generated pulse, which was not a single pulse as required.

Concerns and Possible Problems: Based on the insertion loss results presented in this appendix, it became an important issue to examine the validity of the insertion loss measurement techniques. It is essential to examine the following assumptions made in evaluating the insertion loss results, which might not be justified;

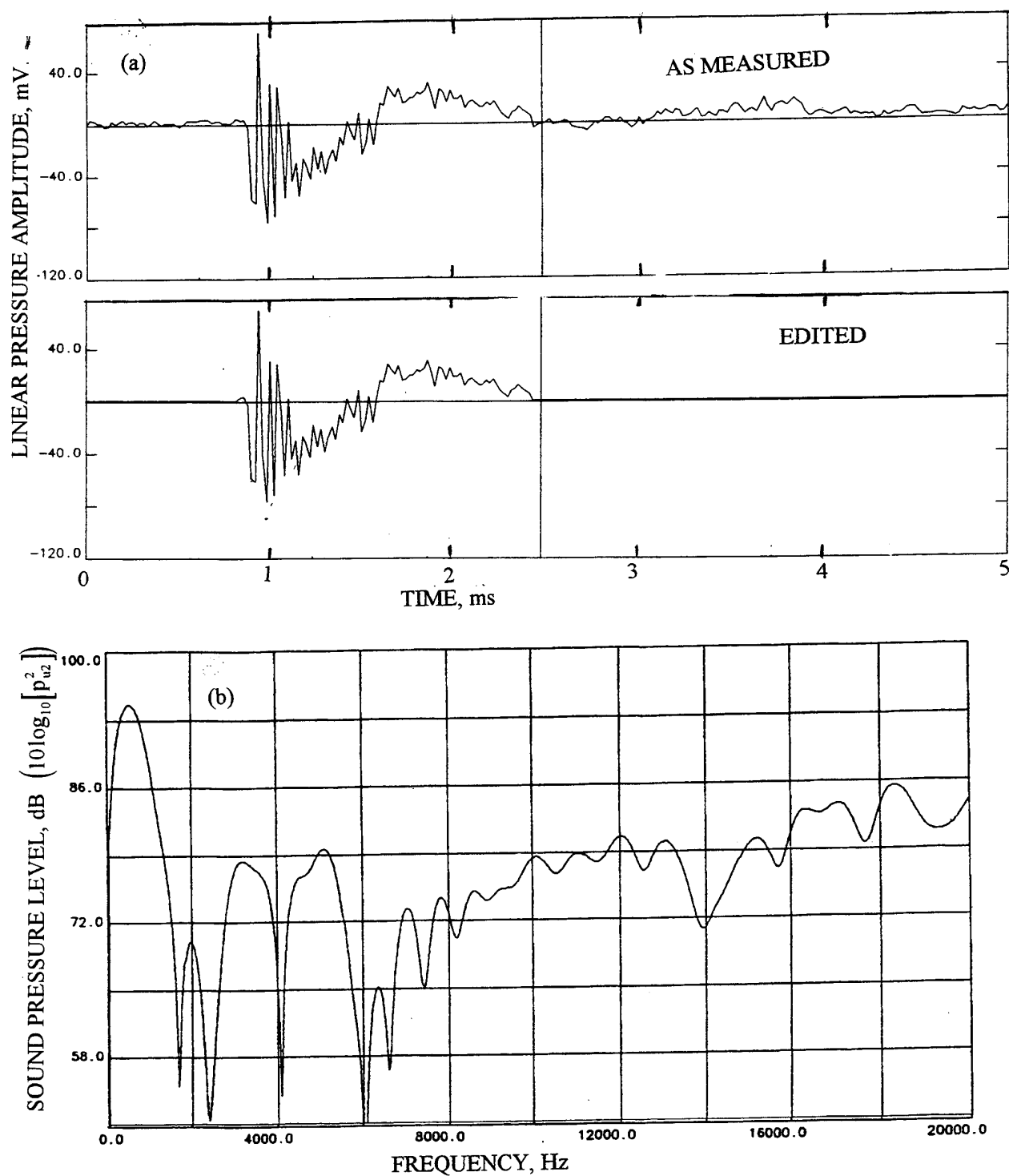


Figure B21. (a) An impulsive signal measured by an upstream transducer after 4000 averages and (b) its sound pressure level in the flow duct with hard wall configuration; excitation pulse level=60 volts and width=400 μ s, flow Mach number=0.4.

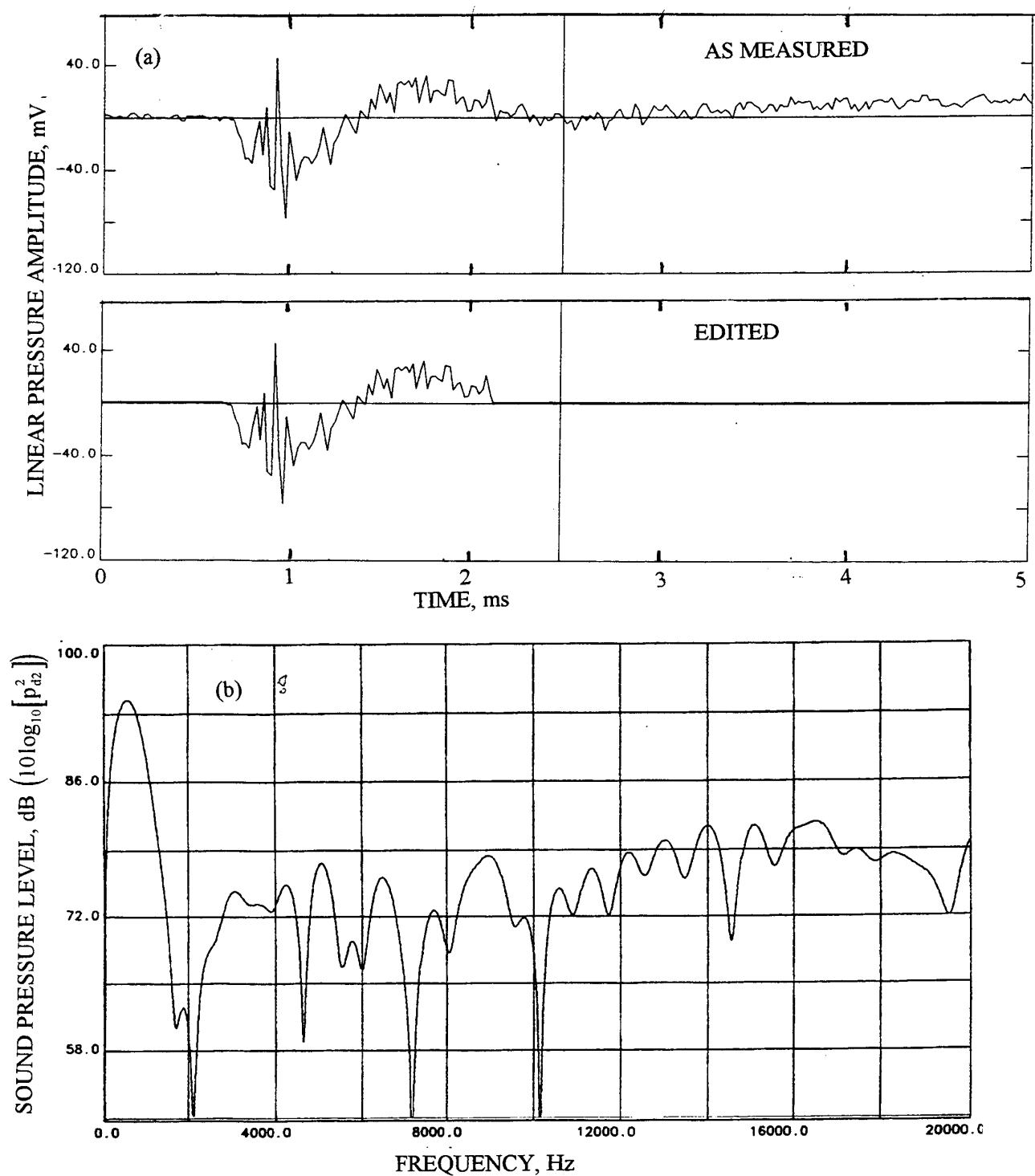


Figure B22. (a) An impulsive signal measured by a downstream transducer after 4000 averages and (b) its sound pressure level in the flow duct with hard wall configuration; excitation pulse level=60 volts and width=400 μ s, flow Mach number=0.4.

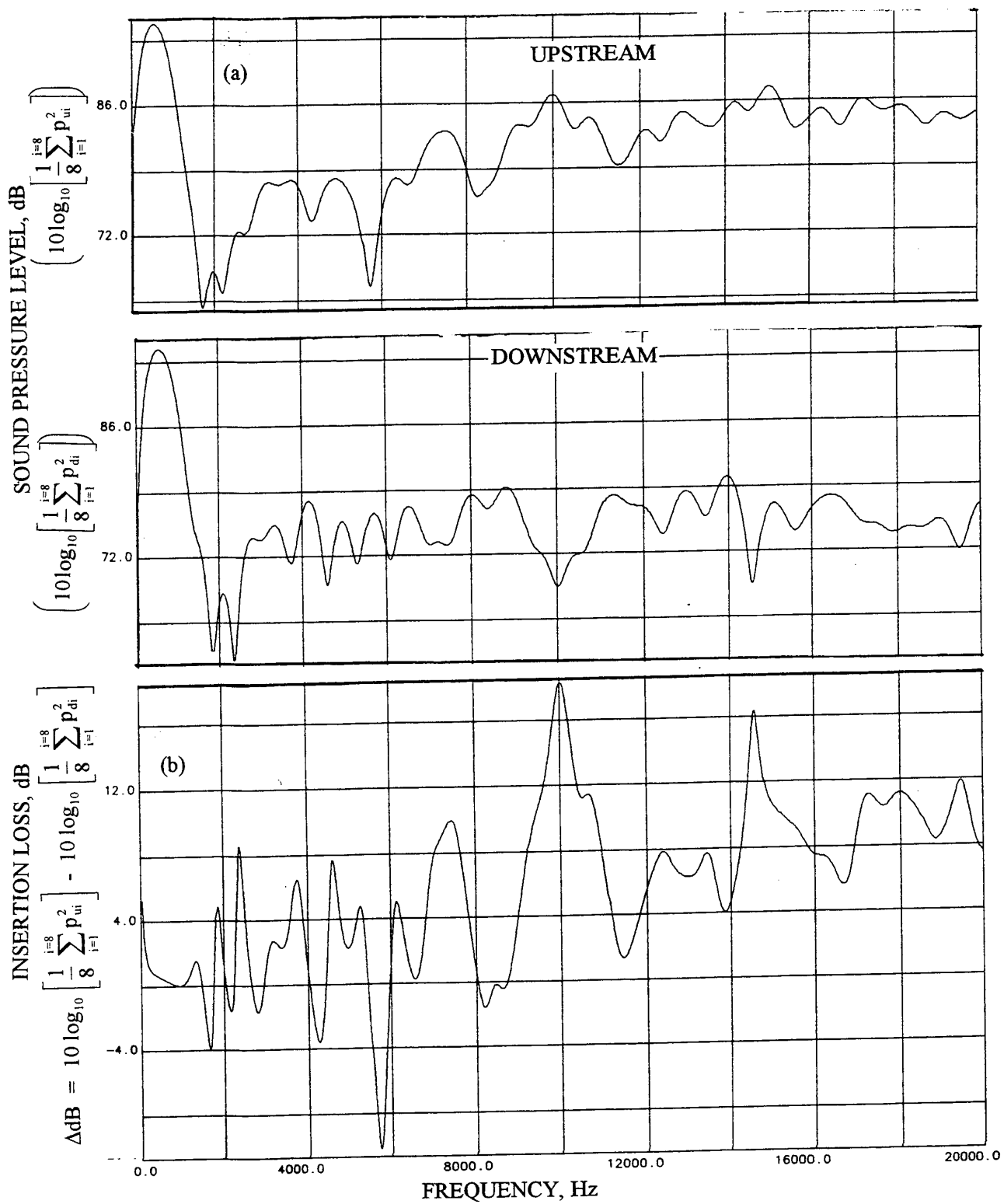


Figure B23. (a) Average sound pressure levels of upstream and downstream measurements and (b) the insertion loss for hard wall configuration of the flow duct; excitation pulse level=60 volts and width=400 μ s, flow Mach number=0.4.

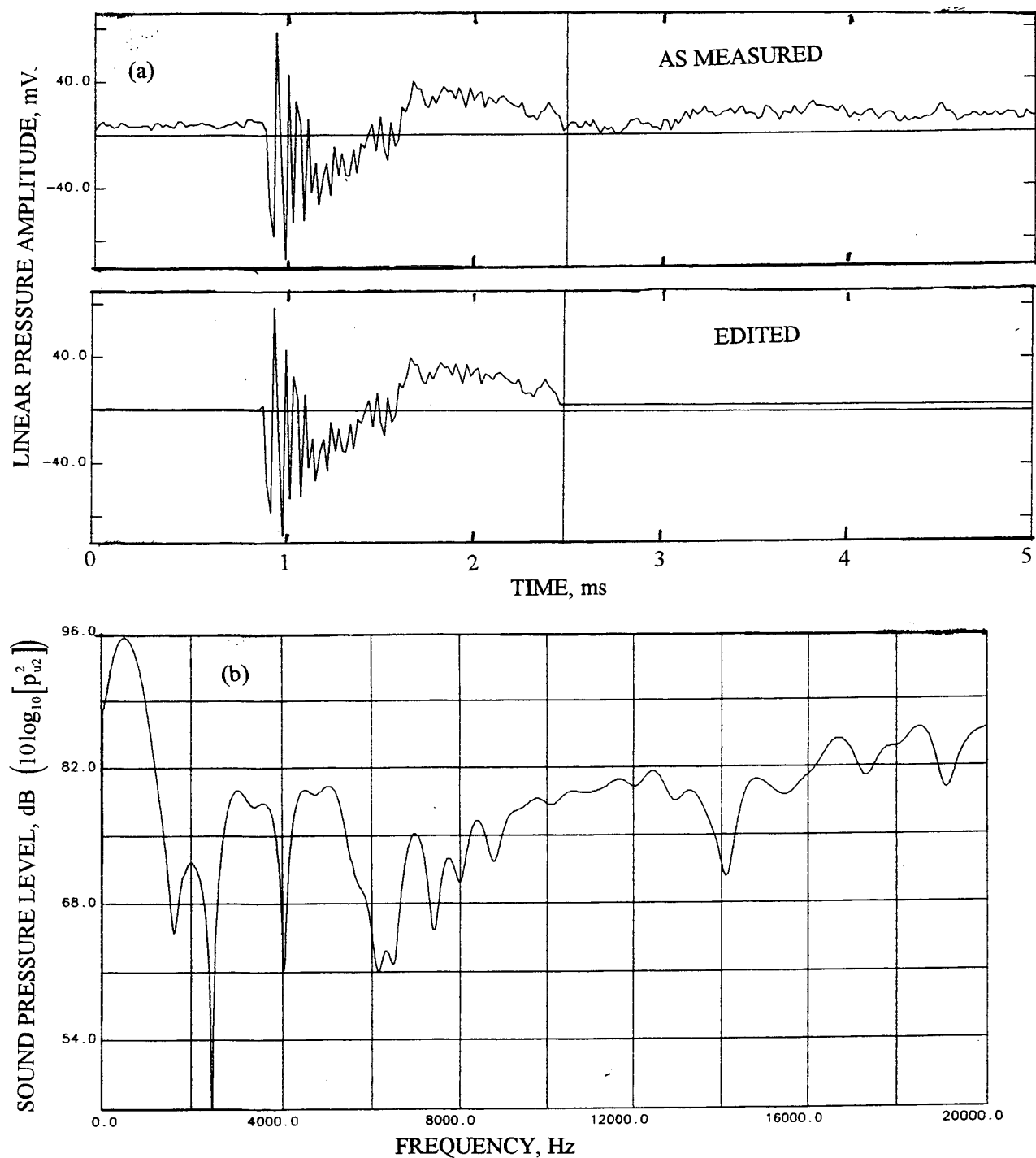


Figure B24. (a) An impulsive signal measured by an upstream transducer after 4000 averages and (b) its sound pressure level in the flow duct for a 0.7" deep SDOF type panel with a 9% porous face sheet (0.02" thick and 0.039" hole diameter) and 3/8" wide honeycomb structure; excitation pulse level=60 volts and width=400 μ s, flow Mach number=0.4.

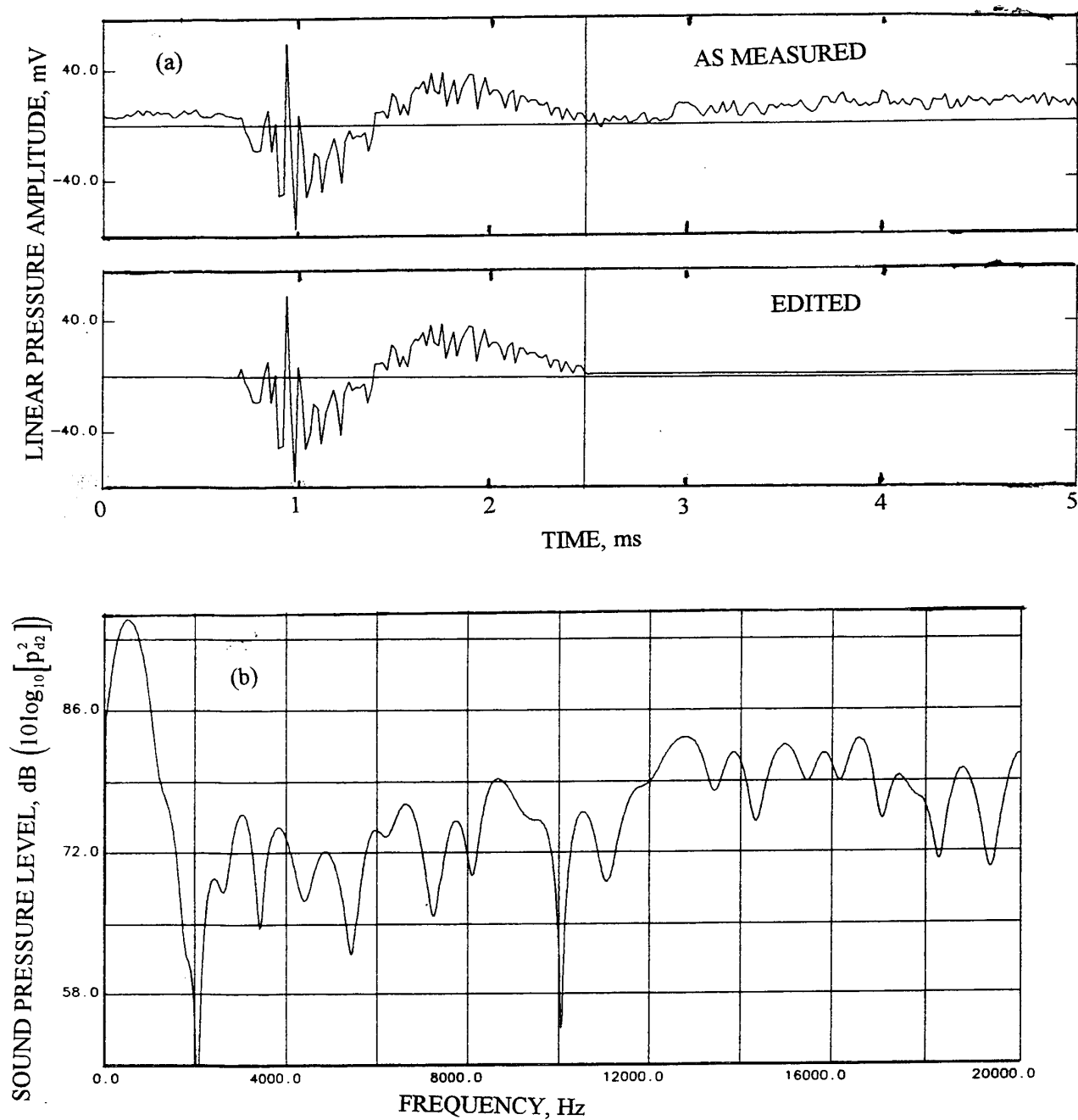


Figure B25. (a) An impulsive signal measured by a downstream transducer after 4000 averages and (b) its sound pressure level in the flow duct for a 0.7" deep SDOF type panel with a 9% porous face sheet (0.02" thick and 0.039" hole diameter) and 3/8" wide honeycomb structure; excitation pulse level=60 volts and width=400 μ s, flow Mach number=0.4.

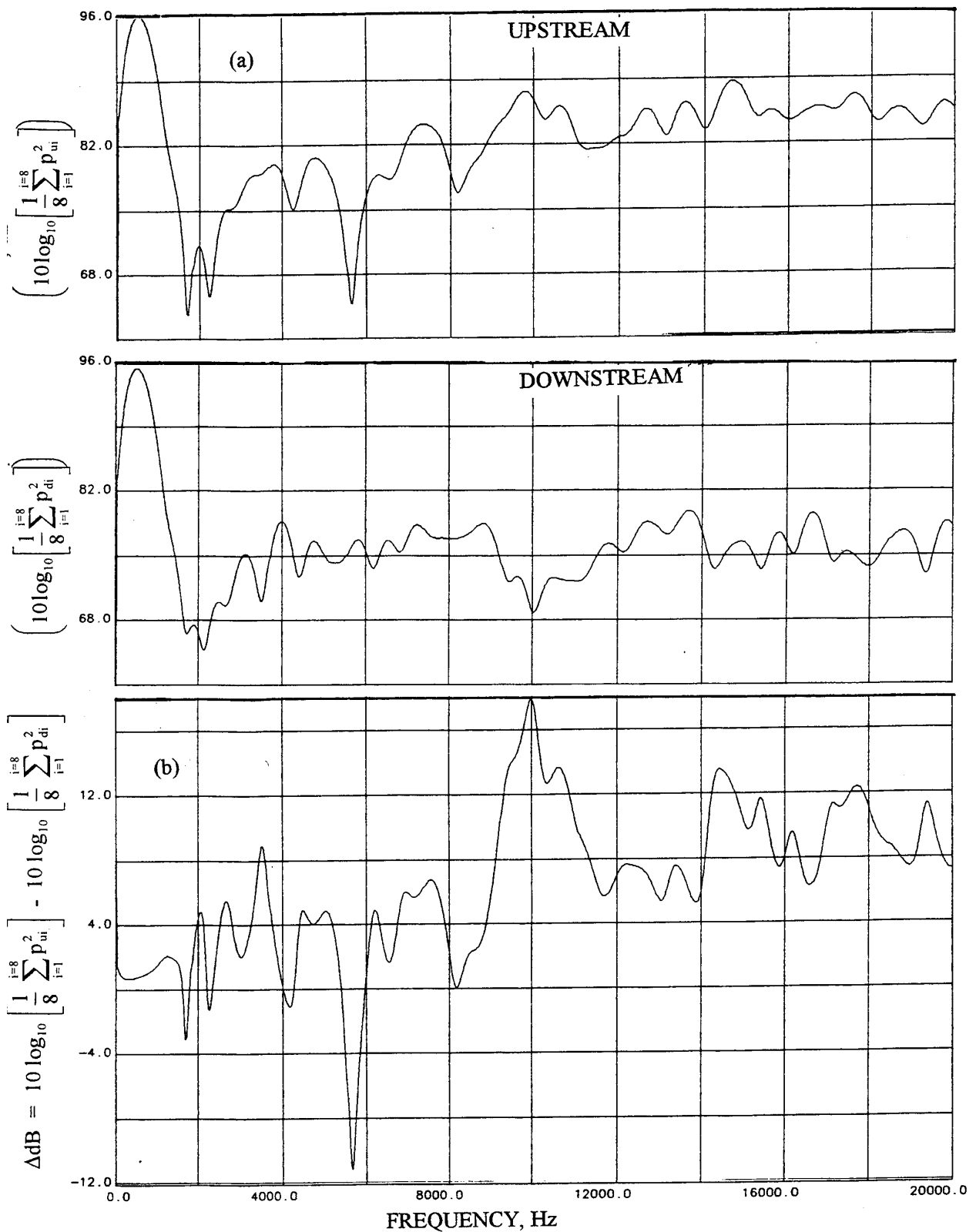


Figure B26. (a) Average sound pressure levels of upstream and downstream measurements and (b) the insertion loss in the flow duct for a 0.7" deep SDOF type panel with a 9% porous face sheet (0.02" thick and 0.039" hole diameter) and 3/8" wide honeycomb structure; excitation pulse level=60 volts and width=400 μ s, flow Mach number=0.4.

1. Reflections: It is assumed that the reflections from the terminations and discontinuities are insignificant to cause a strong standing wave in the duct for discrete frequency excitation. For impulse technique, it is assumed that the reflections are separated out in time from the main pulse, which did not happen.

2. Nonlinear Propagation: Distortions of the propagating waves of reasonably high amplitudes are assumed to be insignificant even though the upstream and downstream measurement locations are 54" apart.

3. Influence of Higher Order Modes: Influence of higher order propagating modes is ignored. If their influence is significant, they can cause strong standing wave patterns in the duct even without reflections and they will introduce SPL variations in the xy plane (at fixed axial location), as observed in experimental data of Figures B9 and B10.

Let us examine the effects on insertion loss if the above assumptions are not valid.

1. Termination Reflections and Nonlinear Propagation: Let us examine the effect of reflections and nonlinear propagation of sound waves on insertion loss as qualitatively demonstrated in Figure B27. The sound emanating from the source would propagate upstream (i.e., P_{iu} , the upstream propagating incident wave) and downstream (i.e., P_{id} , the downstream propagating incident wave). The possible termination reflections are P_{rd} (downstream propagating reflected wave due to P_{iu}) and P_{ru} (upstream propagating reflected wave due to P_{id}).

A very simplistic approach is considered, in which the influences of higher orders modes are ignored. With this assumption, if there is no termination reflection one will find a constant amplitude propagating wave (zero dB, as shown in Figure B27) for hard wall configuration. This is the idealized situation that with acoustic panel installed in the flow duct, the insertion loss evaluation process will give accurate result. However, this is rarely possible in actual situation.

Assuming finite reflections from both terminations, a standing wave will be formed upstream of the sound source due to P_{rd} and P_{iu} . However, P_{rd} will not form any standing wave downstream of the sound source with P_{id} , since P_{rd} and P_{id} are propagating in the same direction. However, a strong standing wave is likely to be formed due to upstream propagating reflection P_{ru} from the exhaust termination. This is shown in Figure B27 as the standing wave (amplitude) with the same maxima and minima along the length of the tube. If an acoustic panel is put on the flow duct then a different standing wave of same maxima and minima will

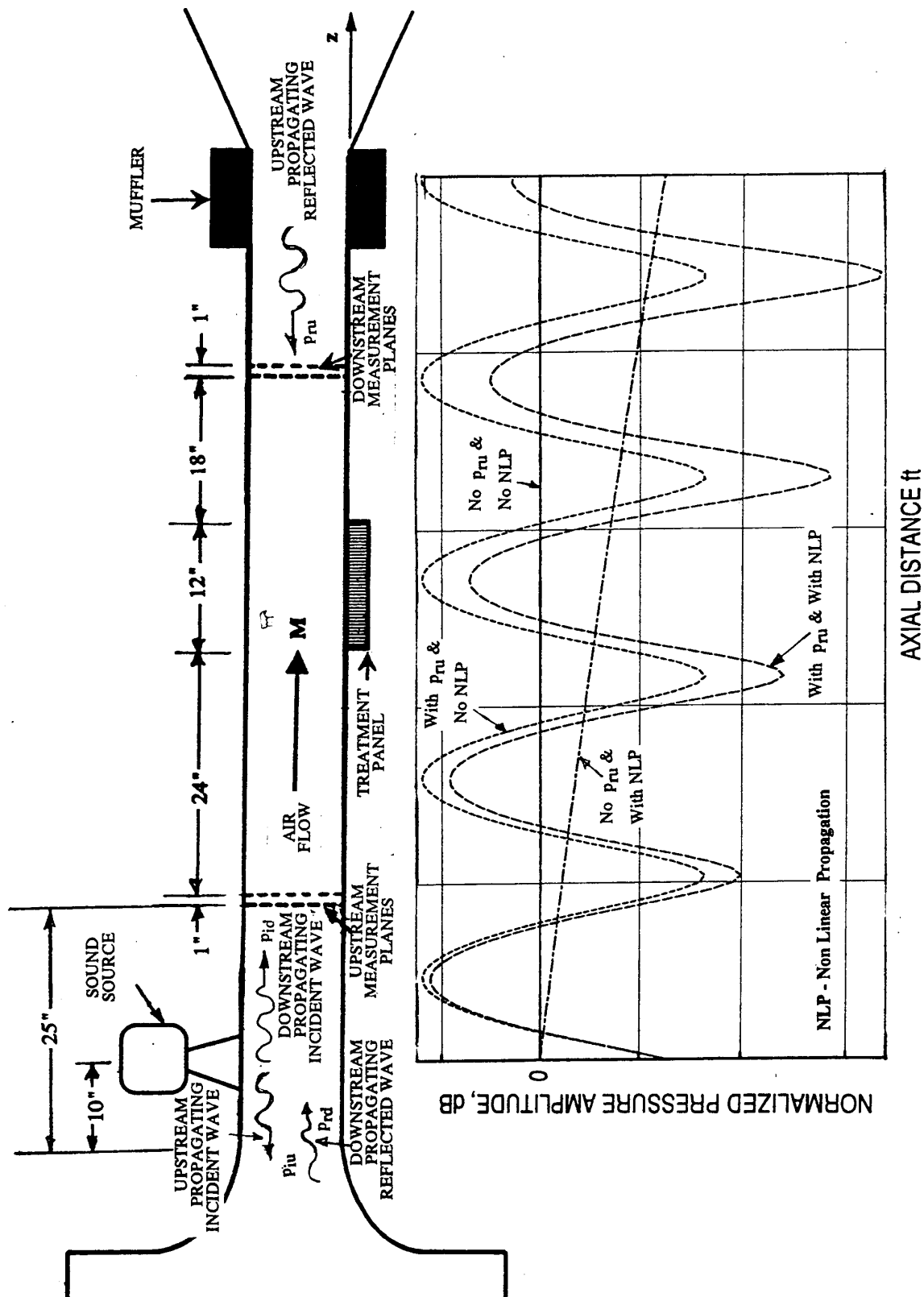


Figure B27. Effect of reflections and nonlinear wave propagation on axial distribution of pressure amplitudes in a duct with hard walls.

be seen down stream of the acoustic panel. If the maxima fall at both upstream and downstream transducer locations, then a reasonable insertion loss can be evaluated. One may argue that the normalization process with respect to hard wall should be able to compensate for this error. However, the standing wave for hard wall and with acoustic panel may not be identical with respect to their maxima and minima locations. If the transducer location(s) falls near the minima of the standing wave, then slight difference in standing wave position between hard wall and treated configurations will introduce significant error.

When a high amplitude wave propagates in a duct the waveform is distorted and at the extreme situation an N-wave is formed. The distorted wave contains a number of higher harmonics, while the amplitude of fundamental frequency is lowered down. Significant amplitude drop is possible even without any real absorption when a large propagation distance is considered. This is shown in Figure B27 in the absence of any reflection, which is a gradually decaying propagating wave.

If the nonlinear propagation is combined with termination reflection a decaying standing wave is formed (see Figure B27). In this case, the error due to reflection as well as due to wave distortion will contaminate the actual acoustic suppression.

The effect of reflection is further examined quantitatively by plotting the amplitude of the following equation with respect to axial distance (z) without any grazing flow;

$$P/A = \exp(ikz) + |\sigma| \exp\{-i(kz - \phi)\}$$

$$= \{\cos(kz) + |\sigma| \cos(kz - \phi)\} + i \{\sin(kz) - |\sigma| \sin(kz - \phi)\}$$

where; $P = A \exp(ikz) + B \exp\{-i(kz - \phi)\}$

$B/A = \sigma = |\sigma| \exp(i\phi)$ - Reflection coefficient

$k = 2\pi f/c$, f being the frequency in Hertz and c being the speed of sound

Following reflection coefficient is assumed:

$$\sigma = \{10^{(-0.5f/1000)}\} \exp[i\{(1-f/300) + 1\}90] \text{ for } f < 3000 \text{ Hz}$$

$$= \{10^{(-0.5f/1000)}\} \exp[i90] \text{ for } f > 3000 \text{ Hz}$$

Based on the above expression the reflection coefficient amplitudes become 0.316, 0.1, and 0.01 and phases become 150°, 120°, and 90° for frequencies 1000, 2000, and 3000 Hz, respectively.

Figure B28 shows the effect of the reflection from downstream termination. The standing wave amplitude for 1000 Hz gives a 6-dB variation between maxima and minima. Since the reflection coefficient amplitudes are lowered substantially for higher frequencies (i.e., 10% for 2000 Hz and 1% for 3000 Hz) the standing wave amplitude variations between maxima and minima are also relatively smaller at these frequencies. If the measurement locations do not fall at or near standing wave maxima the insertion loss estimation could be highly erroneous, as appeared from these results.

The nonlinear propagation of a wave is modeled by allowing a 10% amplitude decay per foot (i.e., $|P/A| = [1 - 0.1z]$) in the standing wave equation. The axial amplitude distributions are evaluated with and without any termination reflection and are plotted in Figure B29. Figure 29(a) shows the axial amplitude decay in the absence of any termination reflection. It is apparent that a decay of about 5 dB is possible within an axial distance of about 4.5 feet. Figure B29(b) shows the amplitude distributions, accounting for nonlinear propagation and downstream termination reflection. Again, the uncertainty in insertion loss measurement due to standing wave formation and amplitude decay due to nonlinear propagation is apparent from this figure.

2. Influence of Higher Order Modes: With acoustic excitation higher order modes are likely to be generated and cut-on in the flow duct. Figure B1 illustrates a few modes, as they would appear in a rectangular duct. In this situation, even if the termination reflection were absent, one would observe a standing wave type amplitude distribution caused by higher order modes, which are of different amplitudes and would propagate at different phase speeds. In addition, the effect of higher order modes makes the sound pressure levels different at different transducer locations, even at the same axial cross sectional plane. These effects are qualitatively examined by Dr. R. Kraft for a simplified situation, assuming the presence of only three vertical modes (i.e., (1,0), (2,0), and (3,0)) in addition to plane wave mode. The treatment impedance of $Z/pc = 1.0 - 1.0i$ with a grazing flow Mach number of 0.5 are used in this analysis. Results for 4000 Hz are presented.

In the analysis p^2 sum (i.e., $\sum p^2$) is calculated for 8 upstream and 8 downstream transducers, whose locations are shown in Figure B30(a). Upstream $\sum p^2$ distribution is computed over a 24" range from $z = -18"$ to $z = 6"$, the treatment being started at $z = 6"$ and the source being at $z = 0$, as shown in Figure B30(b). Effects of mode reflections off the leading edge of the treatment panel are included in the $\sum p^2$ distribution. The downstream $\sum p^2$ distribution is extended over 24" from the treatment panel trailing edge, as shown in Figure B30(b).

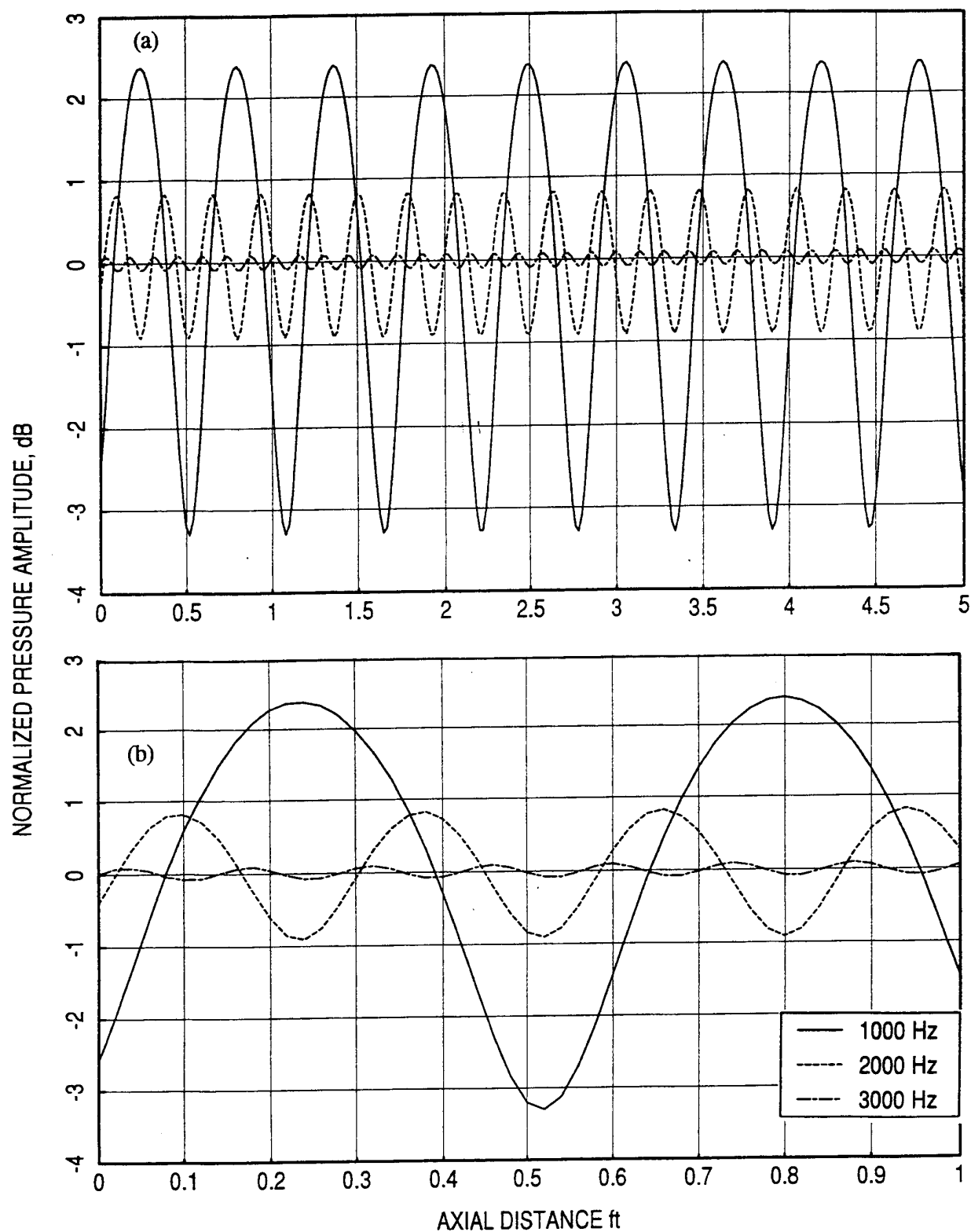


Figure B28. Effect of reflection on axial distribution of pressure amplitudes in a duct with hard walls at different frequencies; (a) Distributed over 5' and (b) Distributed over 1'.

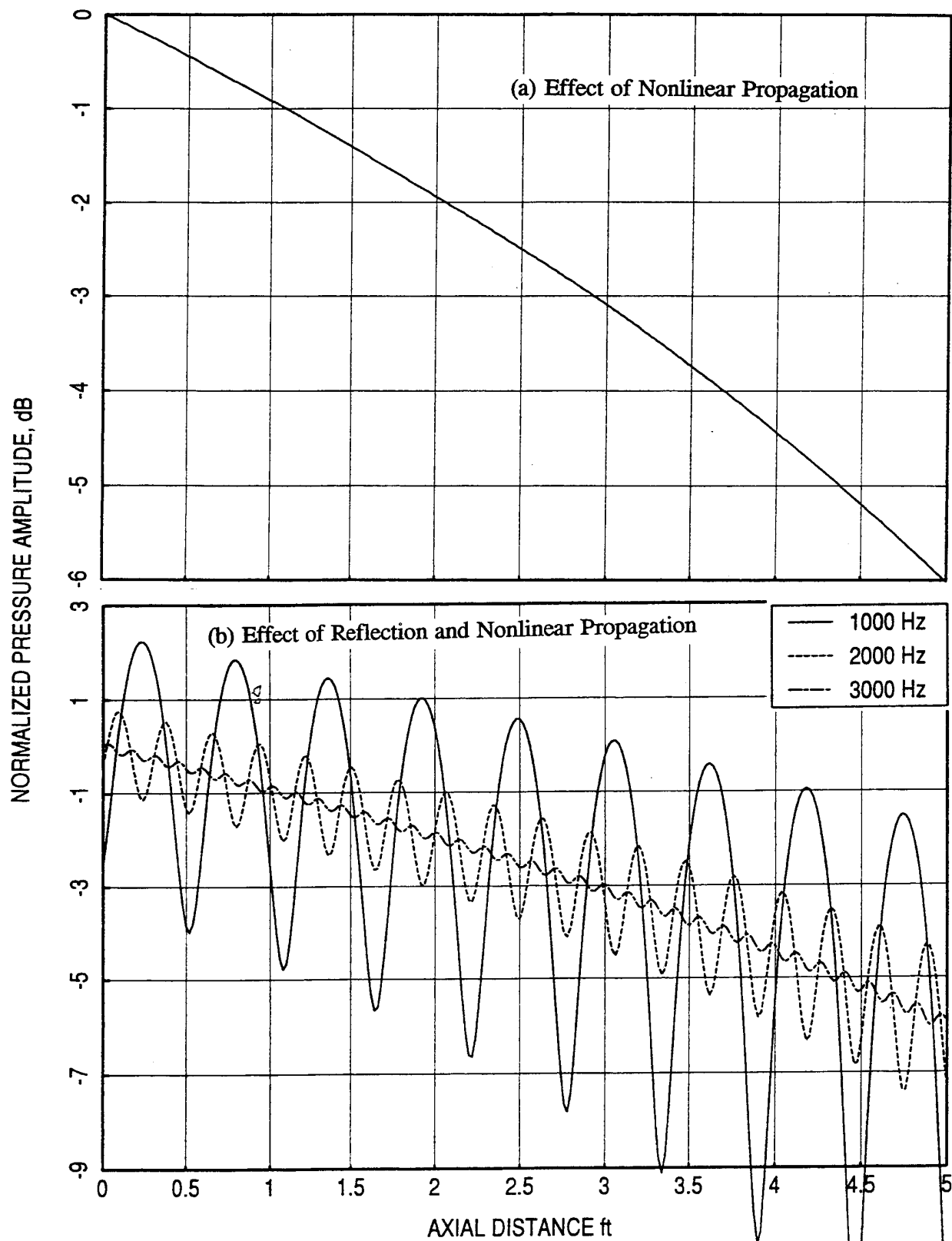


Figure B29. Effect of (a) nonlinear wave propagation and (b) combined effects of nonlinear wave propagation and reflection on axial distributions of pressure amplitudes in a duct with hard walls at different frequencies.

Figure B31 shows the axial distributions of Σp^2 for upstream and downstream of the treatment panel. Figure B31(b) shows the downstream Σp^2 distributions without and with termination reflections. A 5% termination reflection for each mode is included for the Σp^2 distribution.

From Figure B31, it is noted that the Σp^2 varies in level with axial position of the sensor location both upstream and downstream over a range of several dB. This variation is caused primarily not by interference of reflected waves, but by constructive and destructive interference of waves propagating in the forward direction. These forward propagating modes have different axial phase velocities (axial wavelengths) that cause the interference. At least two modes must be present in roughly similar magnitude to obtain this effect, no variation would be found in the case where only one mode were propagating.

Depending on where the upstream and downstream sensor arrays happen to be located the difference of upstream Σp^2 and downstream Σp^2 may be different from the actual ΔPWL . In this case, the maximum difference (max. level upstream minus min. level downstream) would be 7.5-dB suppression. The minimum difference (min. level upstream minus max. level downstream) would be 2.3-dB suppression. The exact suppression is 3.3 dB, which is not comparable to the levels evaluated for two extreme cases. Thus, the errors indicated by this particular case can be considered to be potentially quite large, depending on sensor array location.

To illustrate the SPL differences between the transducer locations in an array, the axial distribution of SPL for transducers at locations 1 and 9 (see Figure B30(a)) are evaluated and shown in Figure B32 for upstream and downstream of the treatment panel.. These results automatically cover the variation between the transducers with the same xy locations on both arrays separated by 1" (i.e., for locations 11 and 19, respectively). Since, the cross modes (i.e., along y) are not included in this analysis the axial SPL variations at locations 1 and 4, and 9 and 6 will be identical. Hence, the axial SPL variations at location 1 and 9 are adequate for all 8 transducer locations. As can be seen in Figure B32, the axial distributions between these two locations are substantially different, especially when minima of one location falls near the maxima of the other.

It is important to note that this is only one case out of a choice of many possibilities. Since the mode content for the duct measurement is not known, it is impossible to use this method as a correction to the test data; it is limited to use simply as an indicator of possible error in the

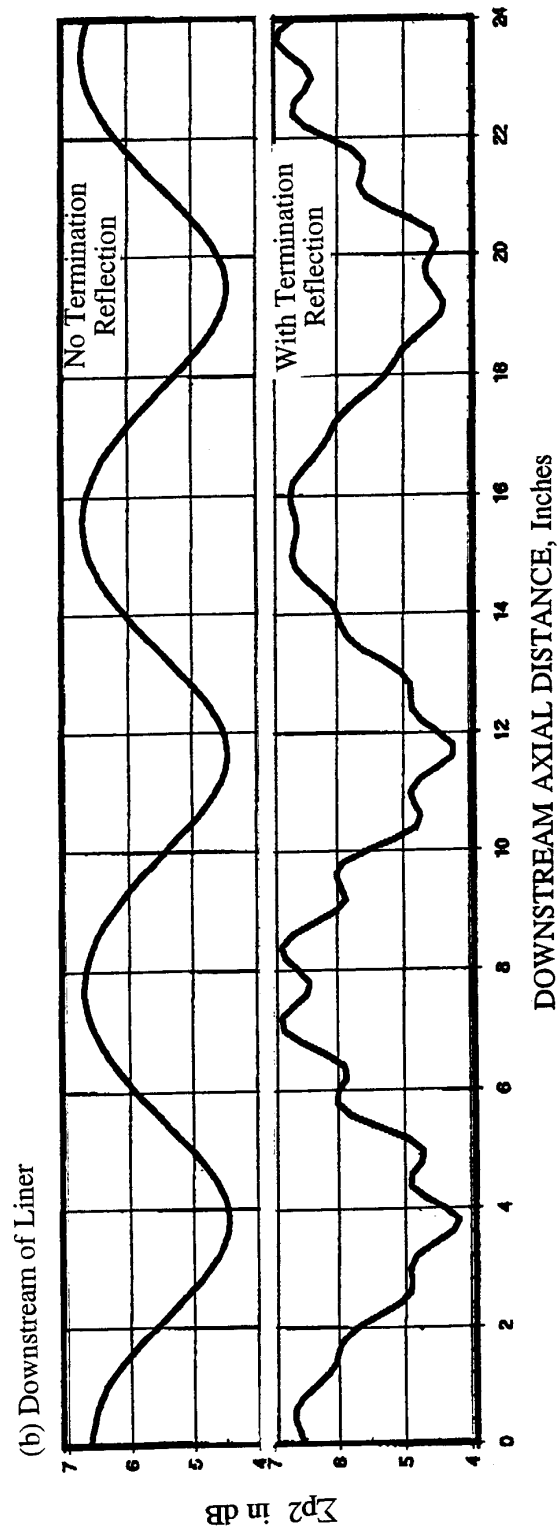
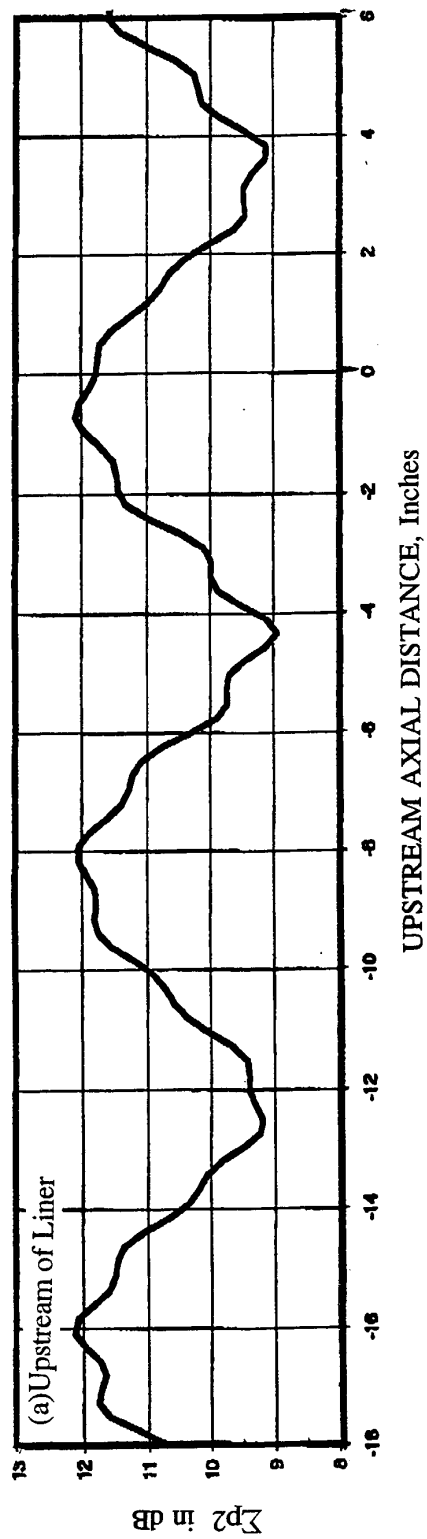


Figure B31. Axial distribution of Σp^2 amplitude at (a) the upstream and (b) the downstream of the liner at 4000Hz., accounting for three vertical cut-on modes; $M=0.5$.

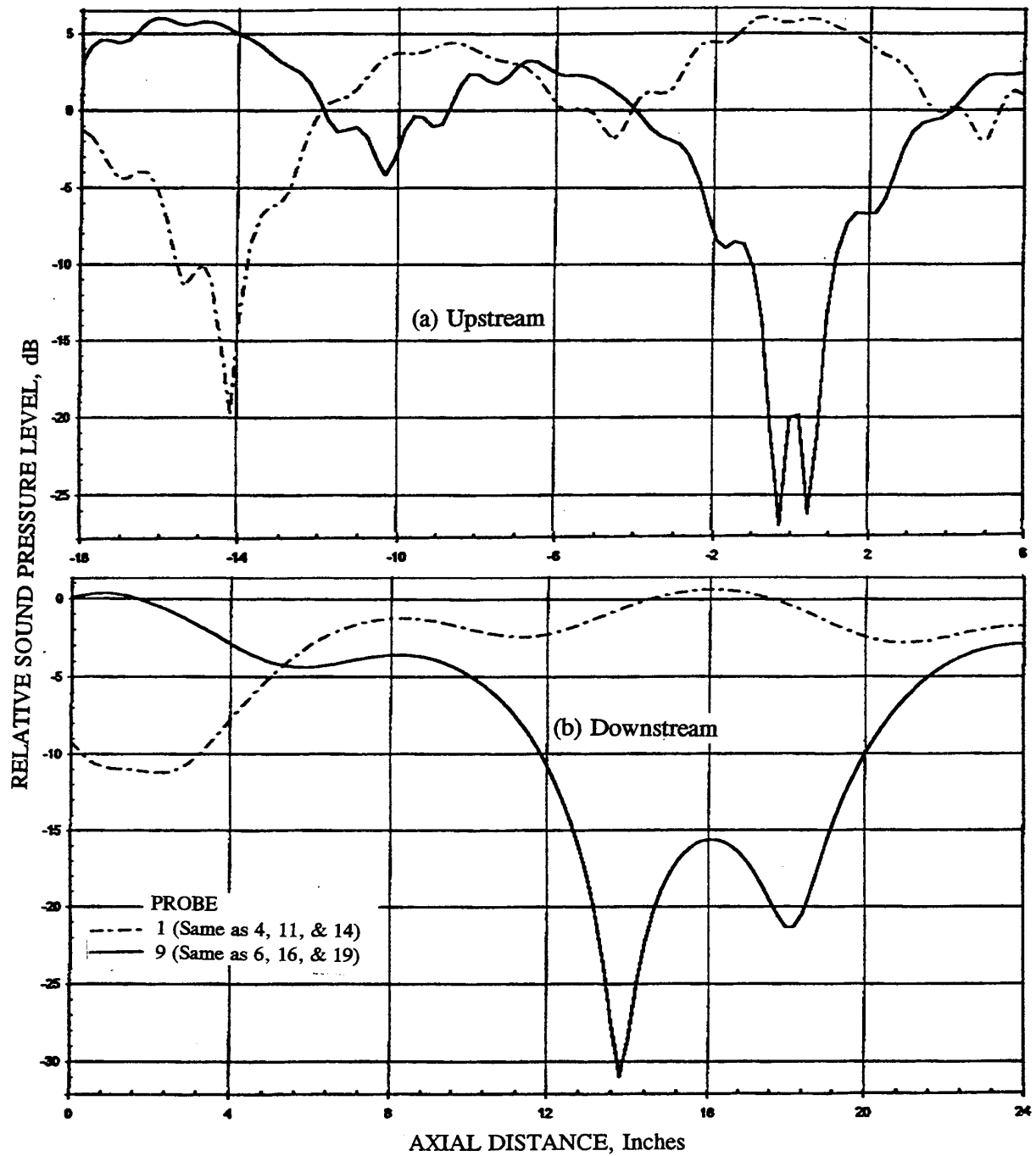


Figure B32. Axial distribution of pressure amplitude at two probe locations at (a) upstream and (b) downstream (no reflection) of the liner at 4000 Hz., accounting for three vertical cut-on modes, $M=0.5$.

measurement. Different results are expected at different frequencies, for different liners, and with different mode content.

Possible Solutions: The following solutions may be applied to evaluate the insertion loss accurately by flow duct tests;

1. Modal Decomposition Method: Currently 40 transducers are used to measure sound pressure levels at two upstream and two downstream planes with respect to the acoustic liner. In this configuration, the first 9 cut-on modes can be evaluated and the insertion loss thus evaluated will be reliable up to maximum frequencies of 4060 Hz, 3880 Hz, 3390 Hz, and 2440 Hz with grazing flow Mach numbers of 0, 0.3, 0.55, and 0.80, respectively. These frequencies would be much lower than the frequencies of interest. However, if the higher order cut-on modes above 9 are less dominant, then the current set of test data can be made useful even at higher frequencies. To examine the difference between the insertion loss computed by P^2 method and by modal analysis the flow duct data is analyzed by both the methods for an SDOF panel (1"-deep, $\sigma=8\%$, $d=0.039"$, $t=0.025"$) and plotted in Figure B33. This is further plotted in Figure B34 at individual Mach numbers. Clearly, the agreement between the two sets of data is poor. In addition, the modal analysis results still exhibit certain amount of randomness.

For better understanding and for proper utilization of modal analysis, more number of transducers may be used at each plane. The location of these transducers can be selectively chosen on the basis of analytical model to minimize their numbers. In addition, if it is established that the reflections are less dominant, that there are no strong standing waves in the duct, then transducers may be used only at one plane, both upstream and downstream of the panel. However, it seems impractical to adapt this process for the current test program.

2. Minimized Influence of Reflections and Nonlinear Propagation: If reflections are dominant and causing strong standing waves in the duct, then the excitation frequencies should be selected, such that the measurement planes would lie close to the standing wave maxima. Lower amplitude excitation should be used and the measurement planes should be brought closer to the leading and trailing edges of the liner if nonlinearity is contributing to the error.

To evaluate the presence of various effects, namely, dominant higher order modes, strong reflections, and wave distortion due to nonlinear propagation it is necessary to survey the acoustic field in the duct with and without flow. This is performed by mounting 40

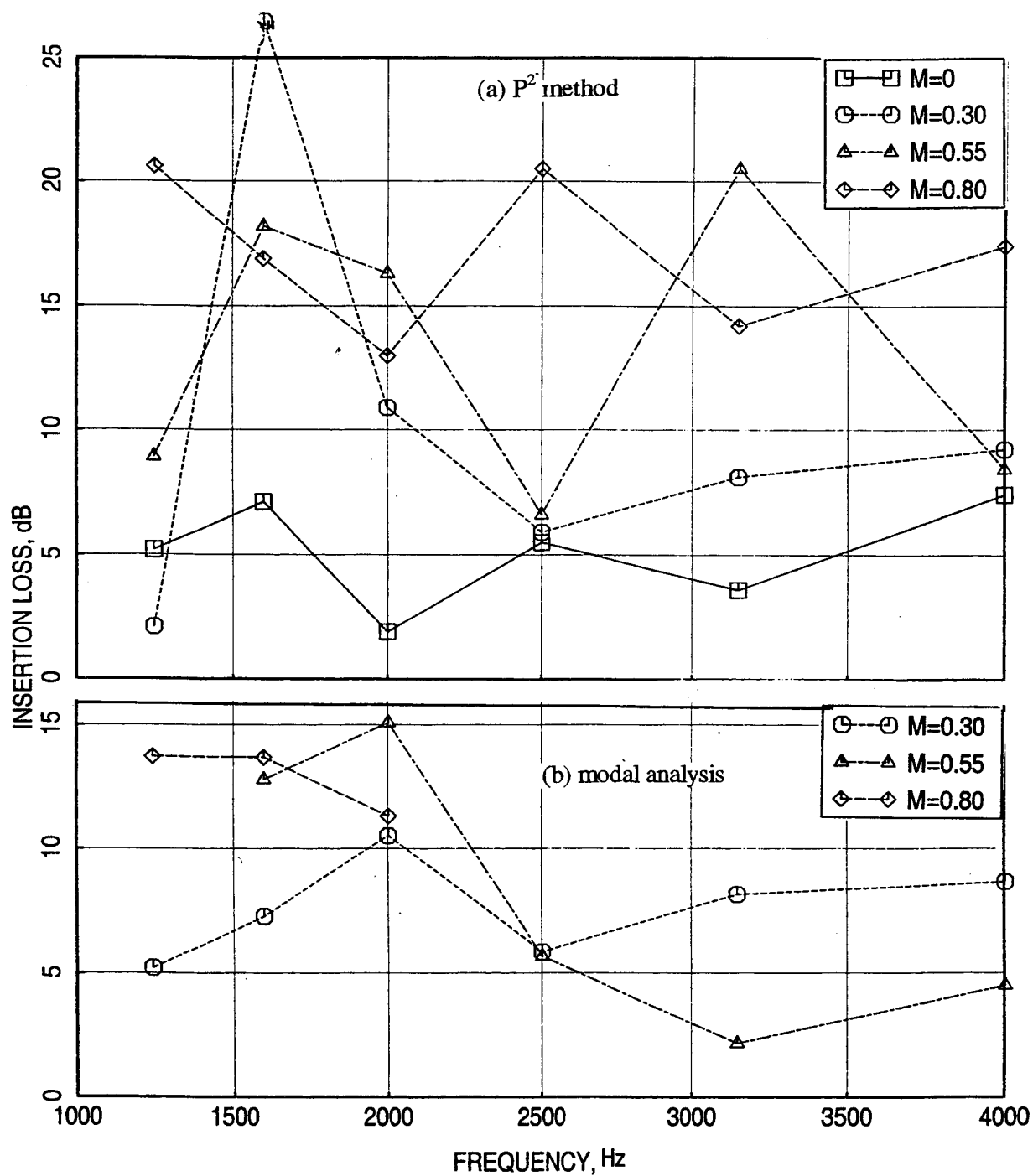


Figure B33. Insertion loss (a) by P² method and (b) by modal analysis at different grazing flow Mach numbers (M) for an 1"-deep SDOF type liner with a perforated facesheet of 8% porosity, $d=0.039$ ", $t=0.025$ ".

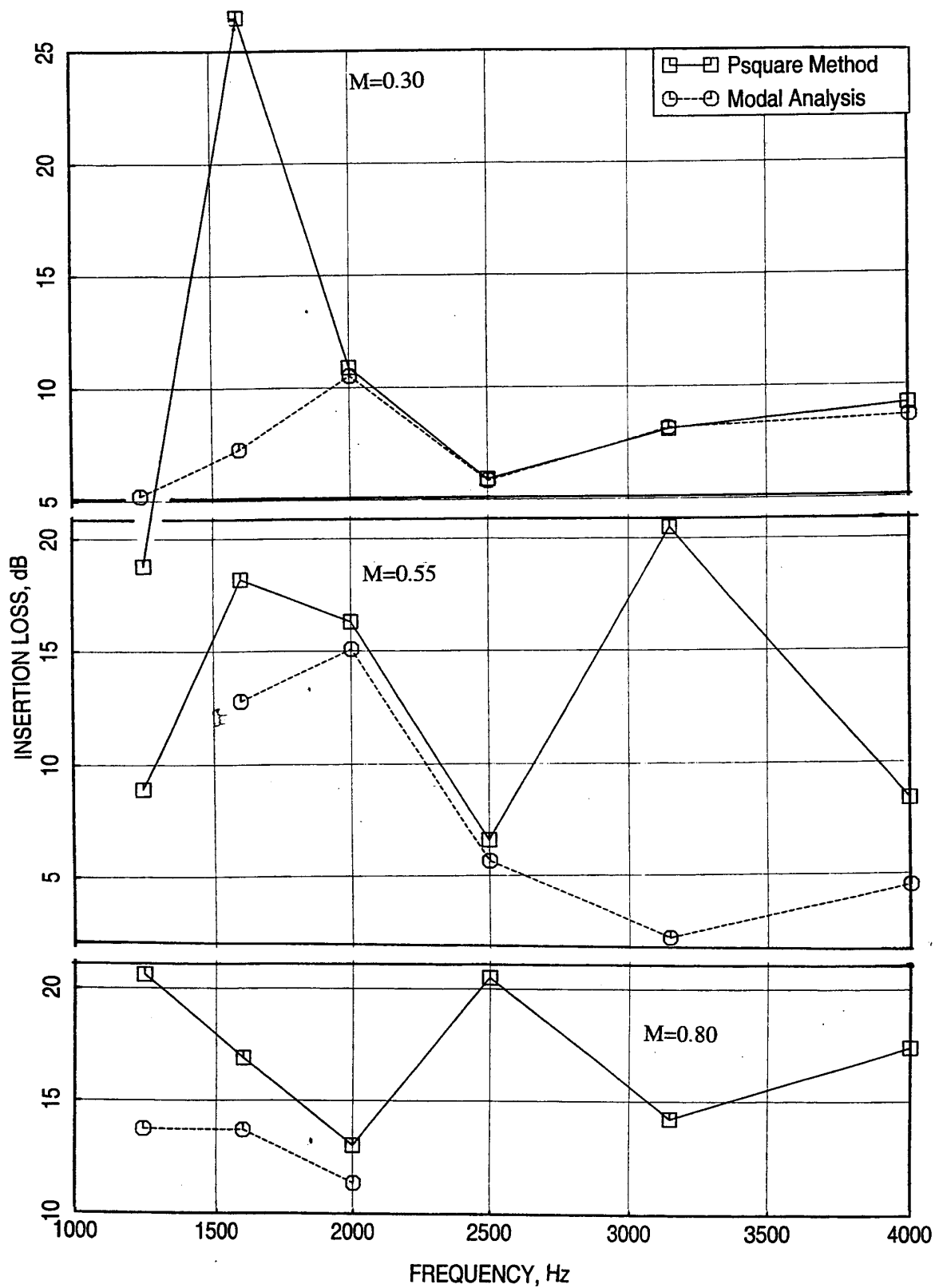


Figure B34. Comparison of insertion loss by P^2 method and by modal analysis at different grazing flow Mach numbers (M) for an 1"-deep SDOF type liner with a perforated facesheet of 8% porosity, $d=0.039$ ", $t=0.025$ ".

transducers axially along different z locations (see Figure B35) at the centerline of the upper wall (opposite to the treatment side). In this arrangement transducers are closely mounted at the upstream and downstream planes, where 10 transducers were installed for insertion loss evaluation. Measurements are made at these transducer locations with and without acoustic liner needs to establish the similarity of the sound fields.

The axial variation of linear magnitude and phase at different excitation frequencies are compared between hardwall and treated configurations in Figures B36 and 37. The amplitudes and phases are relative to the transducer 1 output. Axial variation of the soundfield within an inch is significant near the insertion loss evaluation planes. This becomes worse at higher frequencies. In addition, strong standing wave pattern is clearly existing in the flow duct. Thus, the P^2 method is likely to introduce significant error. Indication of insertion loss is observed across the test section, where the treatment is mounted. This is further demonstrated in Figure B38 by comparing the axial variation of sound pressure level (dB) between the hardwall and treated configurations. Insertion loss seems to be insignificant at lower and higher frequencies. However, significant acoustic suppression is observed at mid frequencies (i.e., between 1000 to 4000 Hz). Figure B39 shows the axial variation of relative insertion loss amplitude for $M=0$ and $M=0.55$.

With these results appropriate steps can be applied to obtain meaningful insertion loss information from flow duct tests. However, this effort needs significant effort in detail survey measurements and development of intuitive ways to evaluate insertion loss from these measurements. Thus, it was not pursued for the current laboratory program.

3. Reverberant Termination to the Flow Duct: Another approach, which gives reasonably accurate insertion loss by p^2 method, is the addition of reverberant terminations at both ends of the flow duct. In this arrangement, the excitation sound is generated in an upstream reverberant chamber by placing acoustic drivers of different sizes in different orientations. This chamber is attached to the flow duct through a gradual contraction. Grazing flow air passes through this chamber. The upstream acoustic energy is measured by mounting transducers in this chamber. Due to the Reverberant characteristics of the sound field, the measurement in the chamber accounts adequately the acoustic energy flux, which propagates through the duct and avoids the problem of nonuniformity of acoustic field in the duct due to higher order modes. Similarly, the duct exhausts in to another reverberation chamber, where the acoustic energy is measured by several transducers. Hence more reliable insertion loss is obtained in this approach.

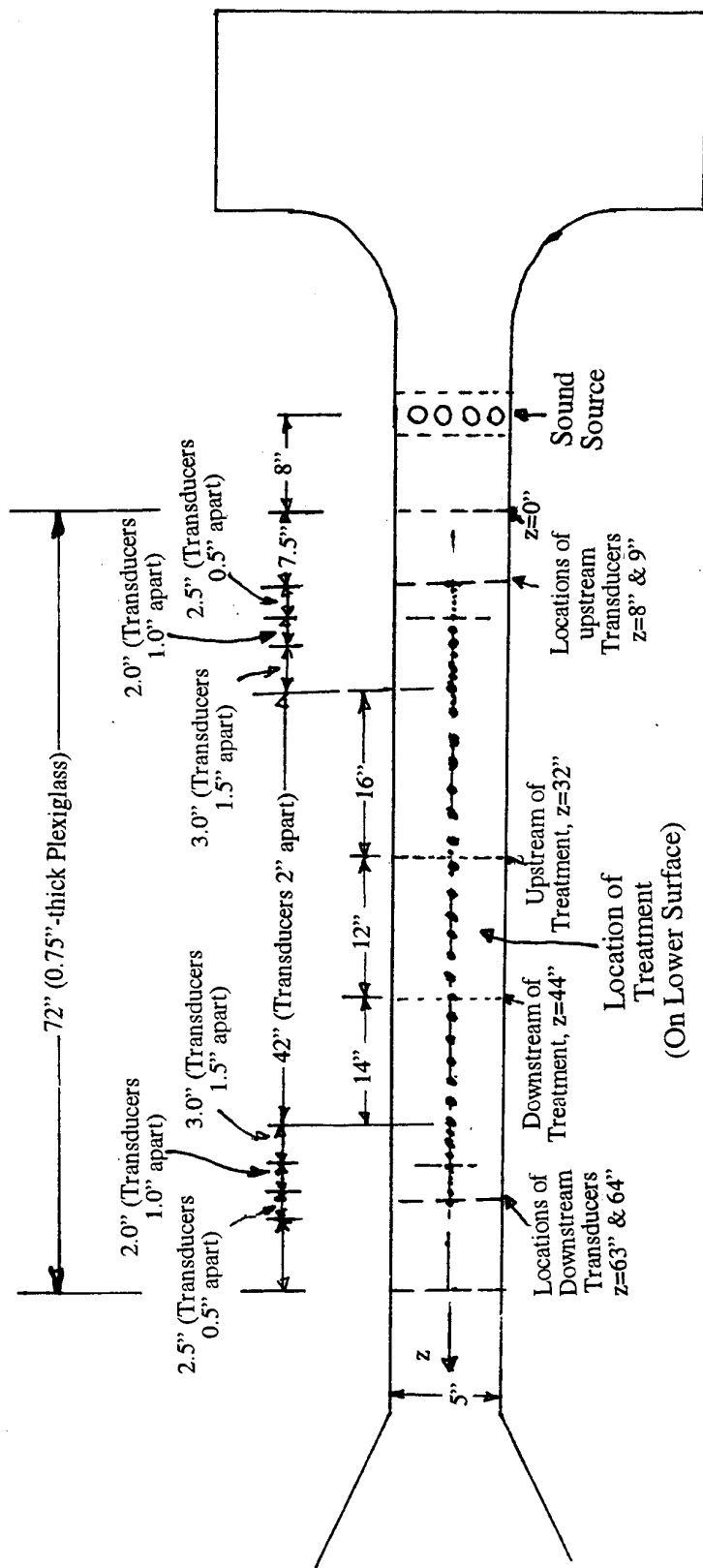


Figure B35. Schematic of the flow duct apparatus with axially mounted transducers (on the opposite side of the treatment panel).

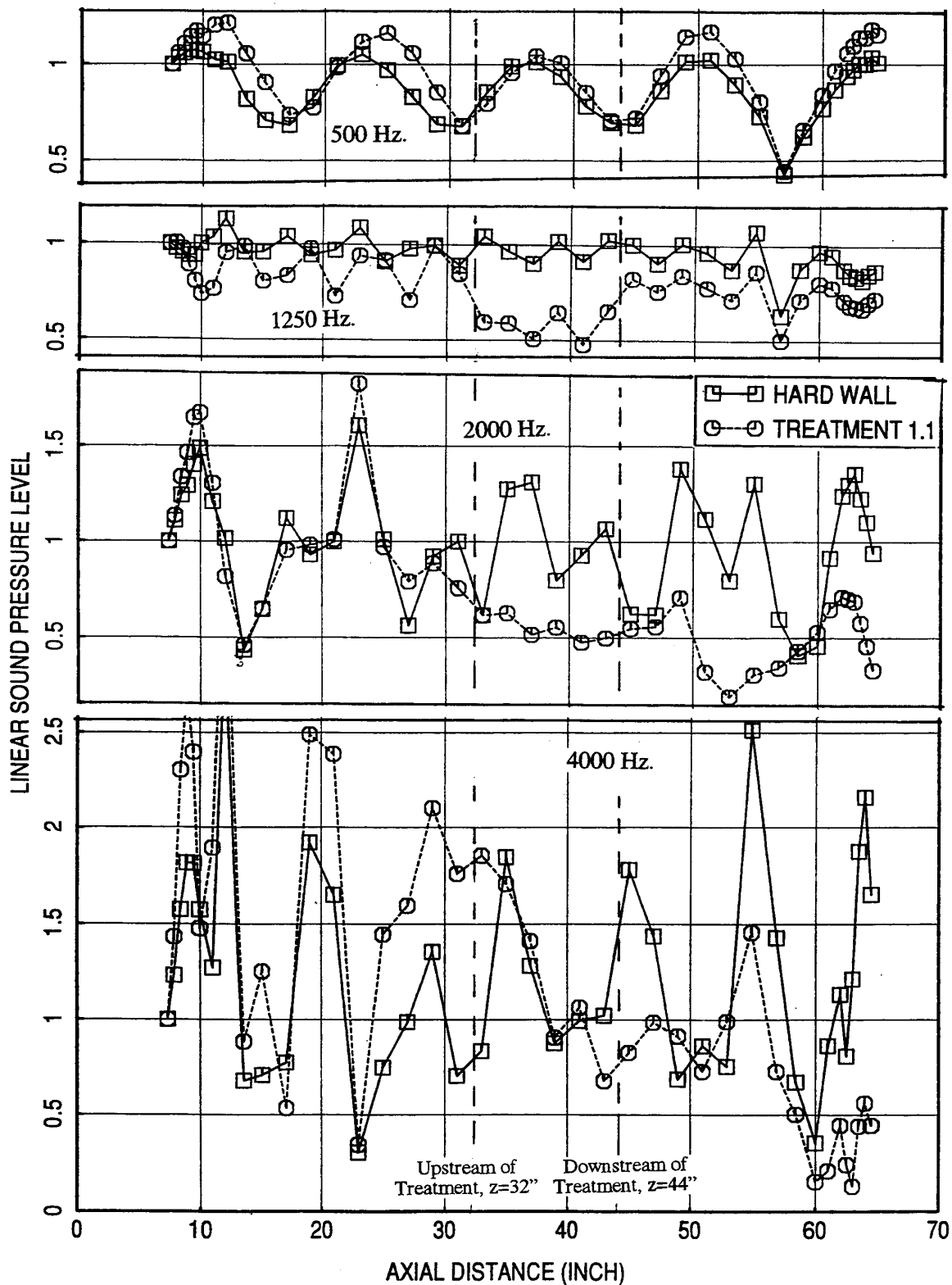


Figure B36. Axial distribution of relative linear sound pressure level at different frequencies for a hardwall compared to an SDOF type 0.7"-deep treatment panel with perforated facesheet; $\sigma=9\%$, $d=0.039$ ", $t=0.02$ ".

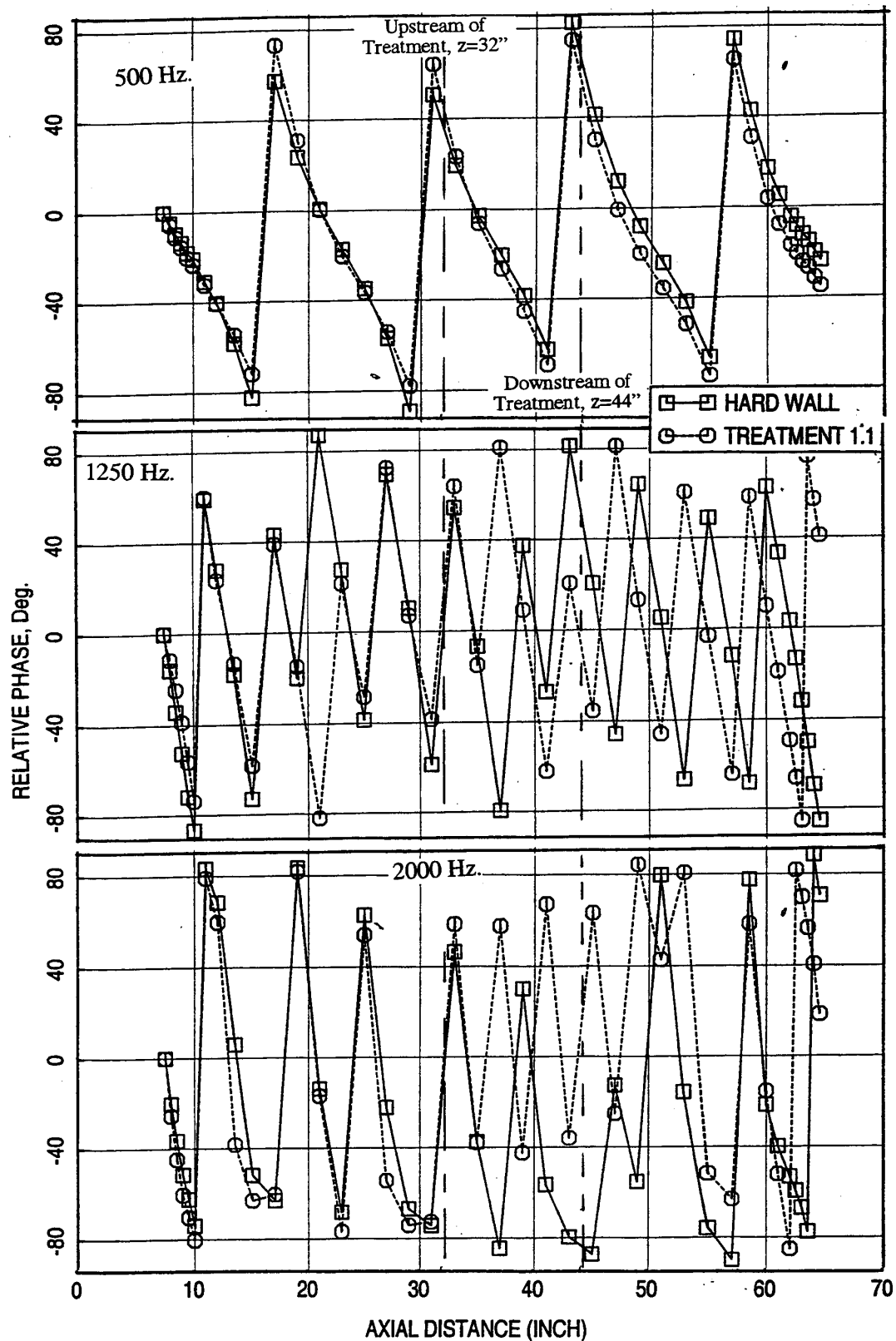


Figure B37. Axial distribution of relative phase at different frequencies for a hard wall compared to an SDOF type 0.7"-deep treatment panel with perforated facesheet; $\sigma = 9\%$, $d = 0.039''$, $t = 0.02''$.

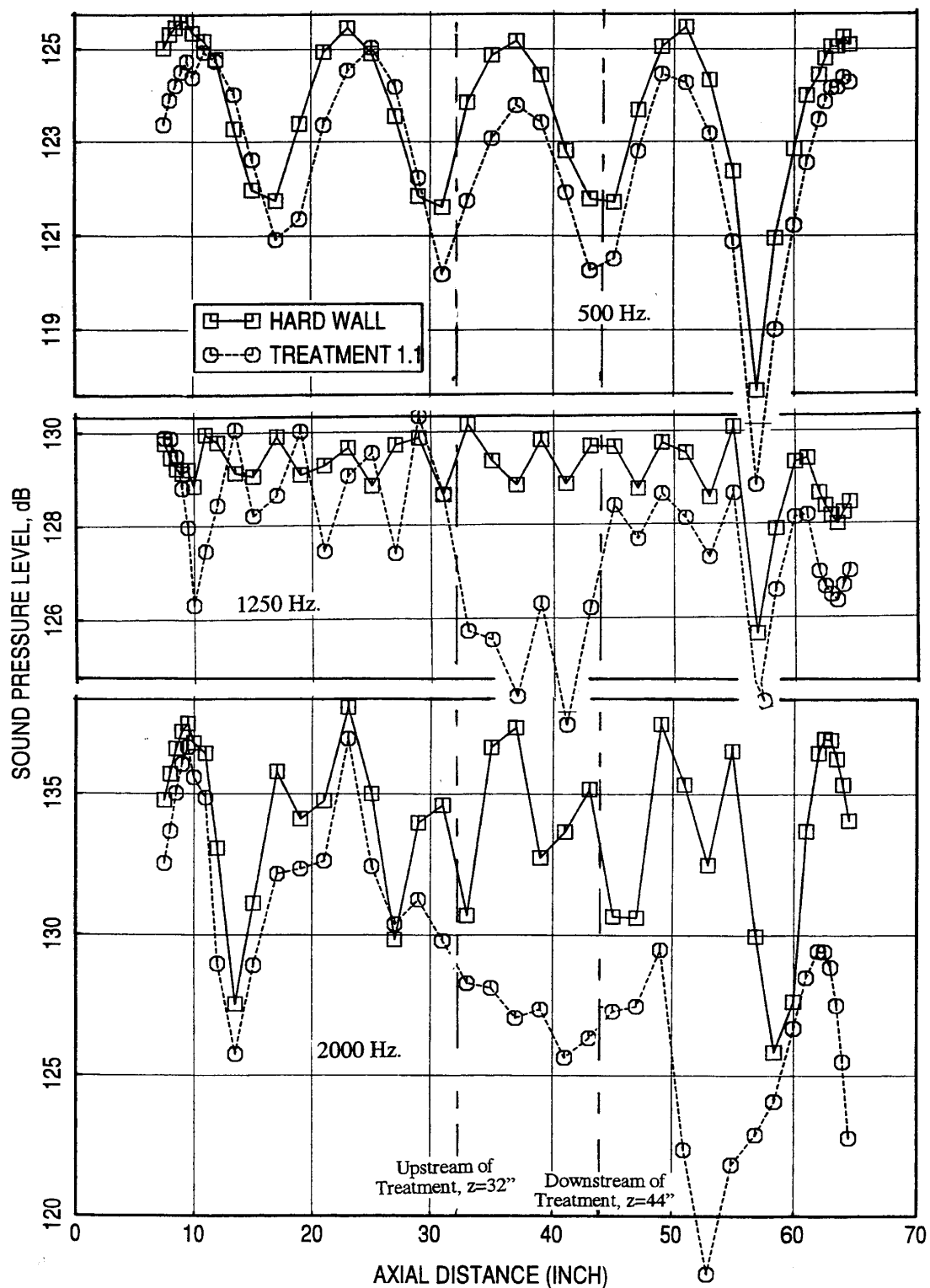


Figure B38. Axial distribution of sound pressure level (dB) at different frequencies for a hardwall compared to an SDOF type 0.7''-deep treatment panel with perforated facesheet ; $\sigma=9\%$, $d=0.039''$, $t=0.02''$ (continued).

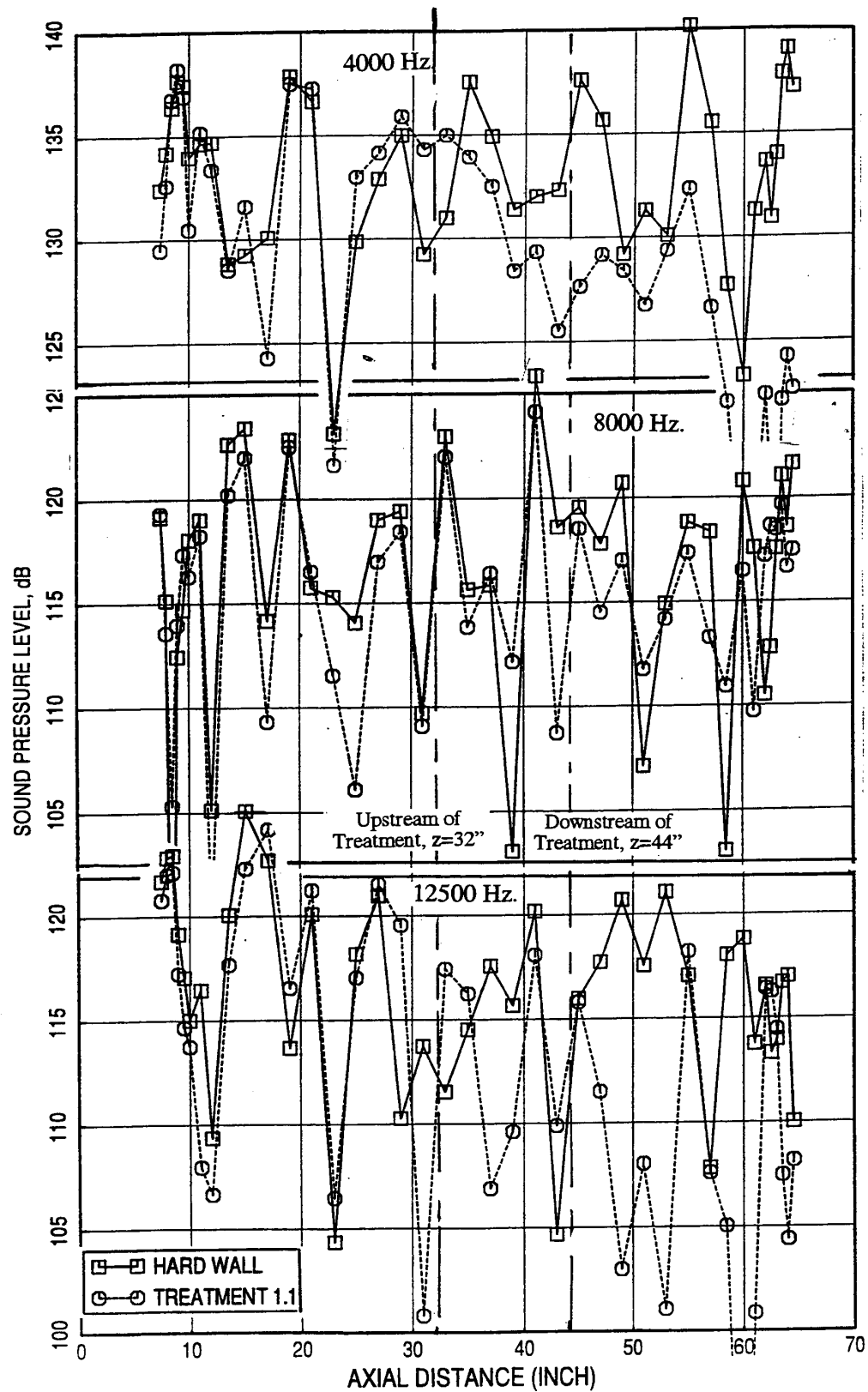


Figure B38. Axial distribution of sound pressure level (dB) at different frequencies for a hardwall compared to an SDOF type 0.7''-deep treatment panel with perforated facesheet ; $\sigma=9\%$, $d=0.039''$, $t=0.02''$ (concluded).

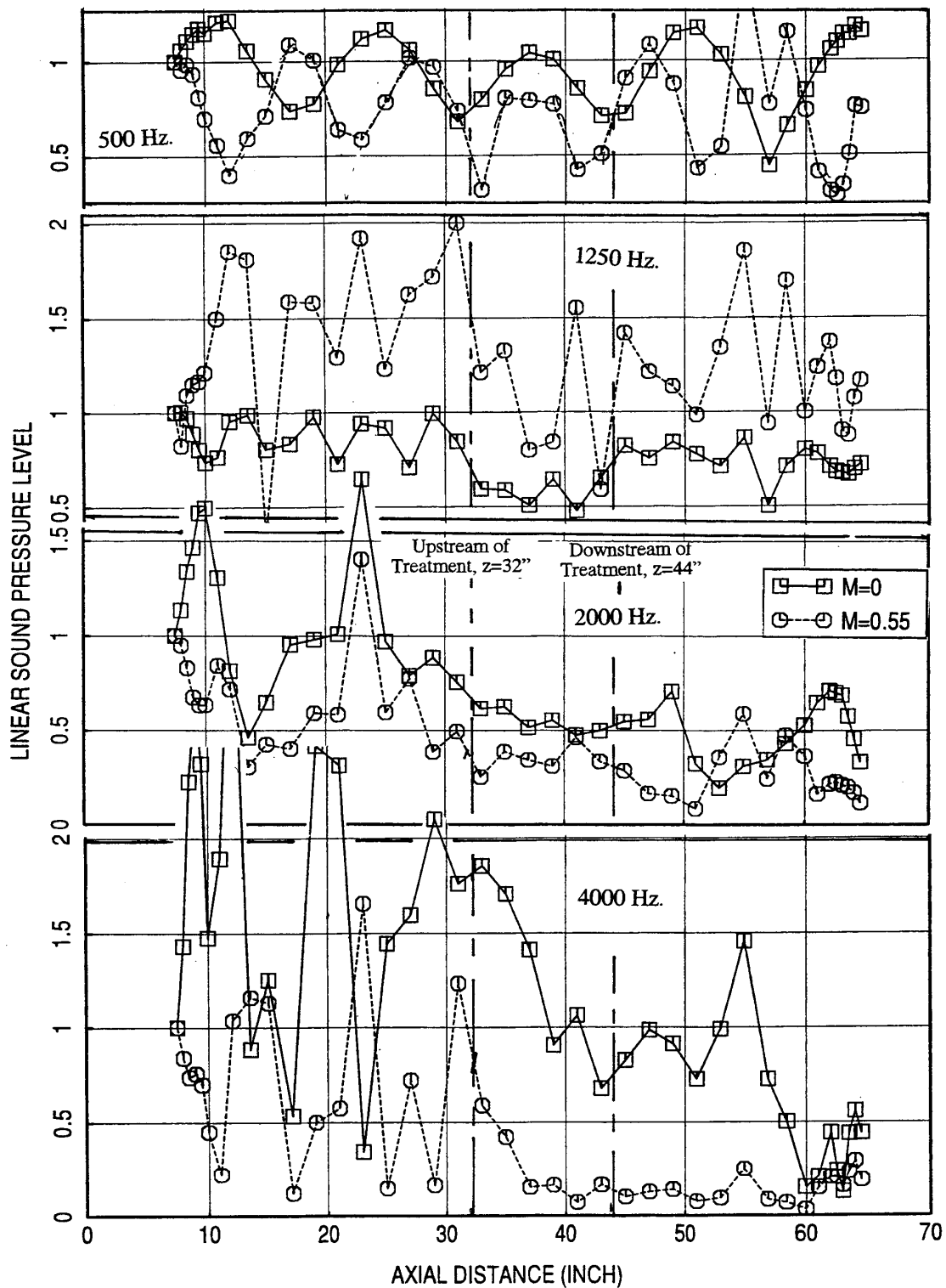


Figure B39. Axial distribution of relative linear sound pressure level at different frequencies at 0 and 0.55 grazing flow Mach numbers for an SDOF type 0.7"-deep treatment panel with perforated facesheet; $\sigma=9\%$, $d=0.039$ ", $t=0.02$ ".

Typical insertion loss results obtained by Rohr Inc. in their flow duct (see Figure 54), which is equipped with reverberation chambers, are shown in Figure B40. Insertion loss results for two SDOF type panels of 1" and 0.2" deep with 24"x5.5" size and with 60 Rayls linear facesheets are shown in Figure B40. The effect of grazing Mach number is clearly evident in these results. The 1" panel gives more suppression at the tuning frequency of about 1250 Hz, whereas, the 0.2" panel tunes at a much higher frequency of about 4000 to 5000 Hz with much lower suppression. Based on these and other results obtained from this facility it is decided that the insertion loss measurements would be made at Rohr Inc., instead of developing the GEAE flow duct facility for this purpose.

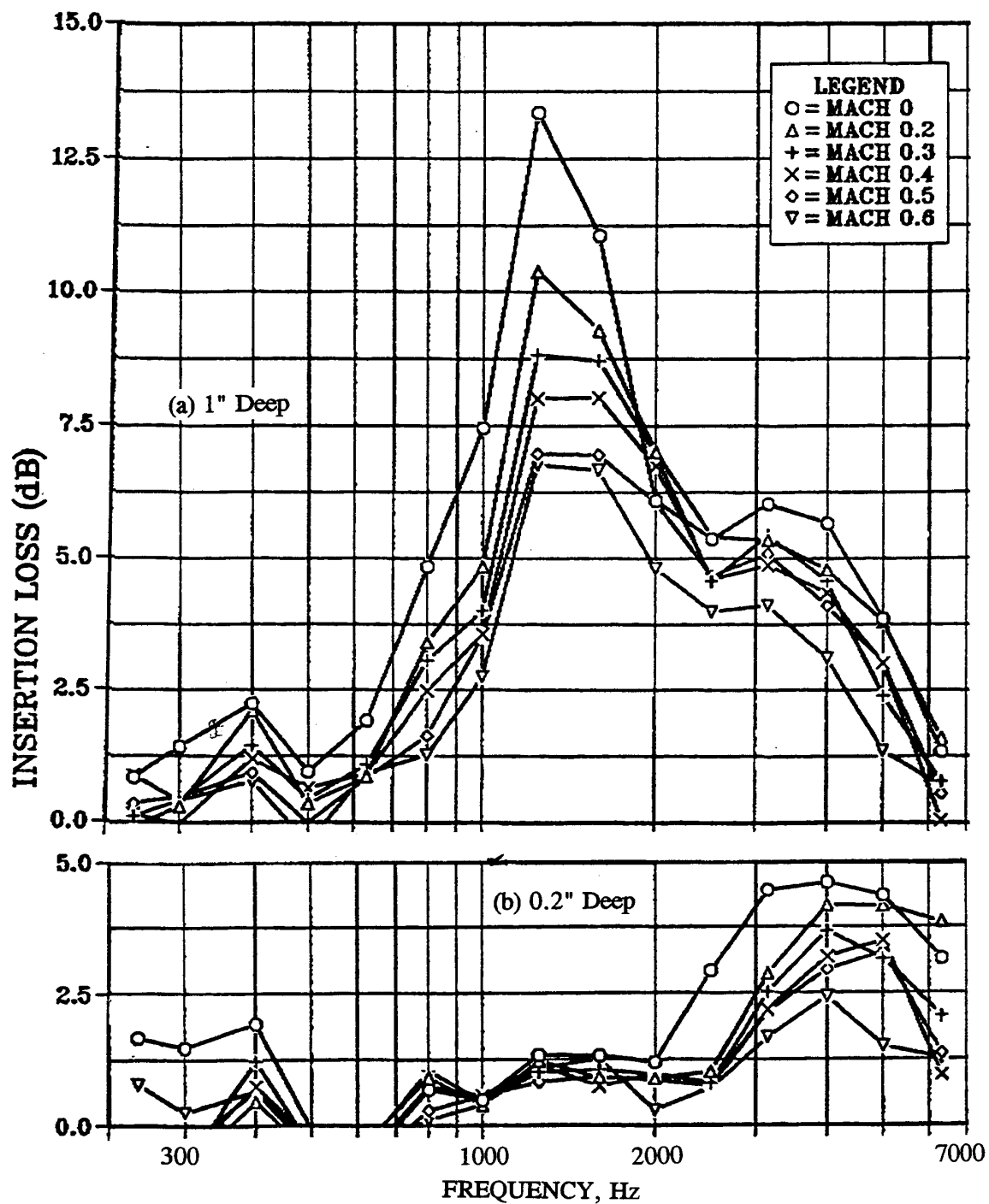


Figure B40. Insertion loss spectra at different grazing flow Mach numbers for SDOF type liners, (a) 1" deep and (b) 0.2" deep, with linear facesheets of resistivity of 60 Rayls, measured in a flow duct with reverberation terminations (Courtesy of Rohr Inc.)

APPENDIX C

A SCREENING STUDY FOR CERAMIC MATRIX COMPOSITE MATERIALS FOR HSCT EJECTOR LINER

Lightweight ceramic materials are candidates for acoustic liners for HSCT ejectors. Ceramic bulk absorbers and honeycombs are evaluated under the HSCT Ejector Liner Acoustic Technology Development Program with close coordination with EPM program. Test samples of various compositions and processes have been obtained from a wide variety of suppliers and are listed in Table C1. All these samples are used to select the ones suitable for HSCT application.

General Process Descriptions for Fabrication :

Ceramic Bulk Absorbers: These materials are divided according to their macrostructure and processing into four groups, namely, Chemical Vapor Infiltration (CVI) foams, Slurry Infiltrated Foams, Fibrous Ceramics, and Microsphere Composites, and can be used as bulk absorbing materials for acoustic liners. The macrostructure of these ceramic foam processes are shown in Figure C1 and general processing descriptions for fabrication are briefly described below:

- 1. Chemical Vapor Infiltration (CVI) Foams** - Formed by chemical vapor infiltration of organic open cell foam perform. A polyurethane foam billet having the desired macrostructure (pore size) is used as a precursor. The polymer foam is resin impregnated and the resin is subsequently crosslinked. The foam is then pyrolyzed to form a carbon skeleton. After machining the billet to near-net shape, the individual ligaments are coated using chemical vapor deposition/infiltration by the forced thermal gradient technique to produce the ceramic end product. The macrostructure of these types of foams is illustrated in Figure C1. These materials are typically SiC and may have oxidation problems. They have excellent specific compressive strengths and very low densities are achievable. However, the fabrication costs are very high.
- 2. Slurry Infiltration (SI) Foams** - Formed by slurry (ceramic particulate) infiltration of an organic open cell perform. The process begins with a polyurethane foam piece of the desired macrostructure. The polymer foam is cut to the appropriate size and shape for the application. In the next stage, the filaments or struts of the polyurethane are coated with the ceramic slurry and the excess slurry is squeezed out. Moisture is removed either by convection or microwave drying. Next, the piece is fired to volatilize the organic

Table C1. Ceramic Acoustic Materials Supplied to the Advanced Liner Program

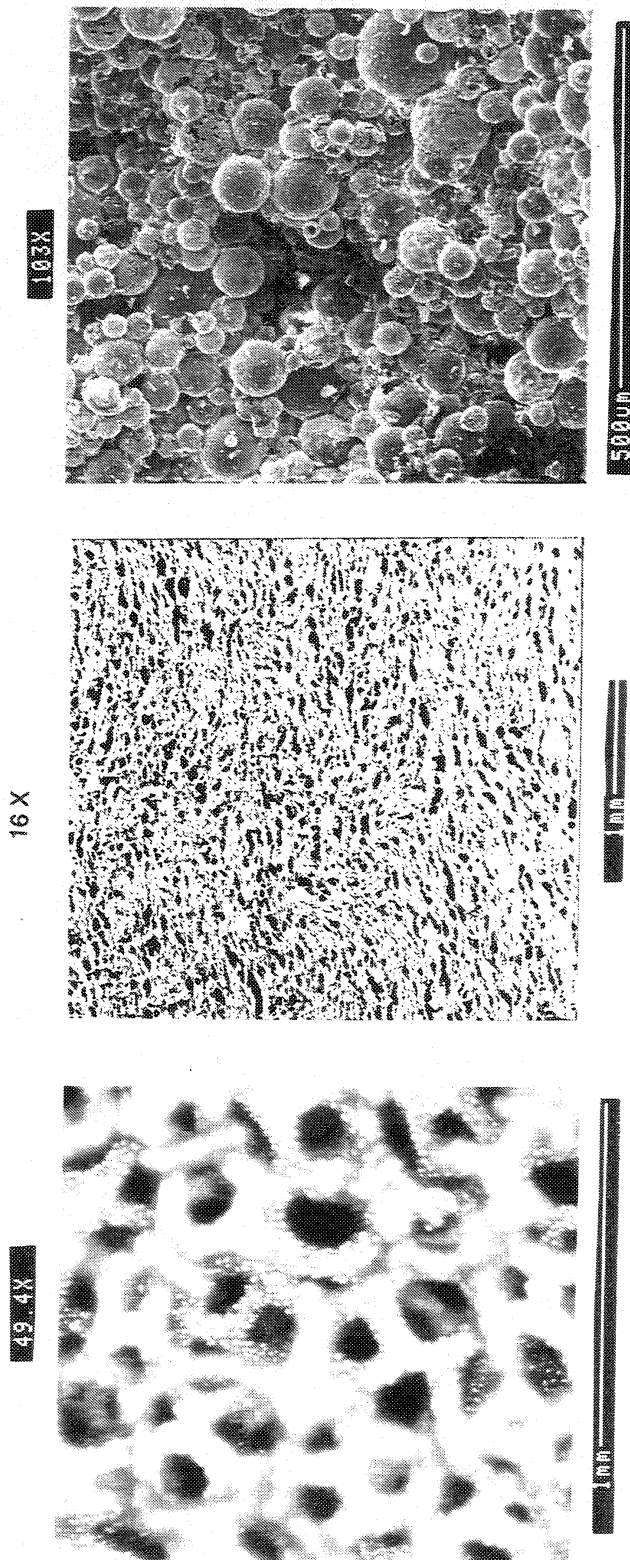
Sample No	Sample Type	Company	Process	Composition	Porosity	Density (lb/ft ³)	Depth	Cross Section	Cell Geometry TYPE / CROSS SECTION
1	Cellular Cube	Corning	Extrusion	Cordierite	64 cpi	21	3"	5 9/10" x 5 7/8"	Square 12/100" x 12/100"
2	Cellular Cylinder	Corning	Extrusion	Cordierite	350 cpi	25	3 1/2"	3" diameter	Square 5/100" x 5/100"
3	Cellular Ellipse	Corning	Extrusion	Cordierite	400 cpi	27	3 1/4"	6 5/8" x 3 1/8"	Square 5/100" x 5/100"
4	Cellular Ellipse	Corning	Extrusion	Cordierite	470 cpi	25	6"	4 3/4" x 3 1/8"	Square 5/100" x 5/100"
5	Porous Brick	Hi Tech Ceramics	Slurry Infiltration	Alumina	65 ppi	68	15/16"	5 1/5" x 5 1/5"	
6	Porous Brick	Selee	Slurry Infiltration	Alumina	10 ppi	36	7/8"	3" x 3"	
7	Porous Brick	Selee	Slurry Infiltration	Mullite	20 ppi	32	7/8"	3" x 2 7/8"	
8	Porous Brick	Selee	Slurry Infiltration	Mullite	10 ppi	21	9/10"	3" x 3"	
9	Porous Brick	Selee	Slurry Infiltration	SiC	20 ppi	44	1"	5 1/10" dia.	
10	Porous Brick	Selee	Slurry Infiltration	Ca,Mg,PSZ	30 ppi	89	3/8"	3" x 3"	
11	Porous Brick	Selee	Slurry Infiltration	Mg-PSZ	30 ppi	53	15/16"	3" x 3"	
12	Porous Brick	Selee	Slurry Infiltration	Alumina	30 ppi	40	9/10"	3" x 3"	
13	Porous Brick	Selee	Slurry Infiltration	Mg-PSZ	15 ppi	56	1"	3" x 3"	
14	Porous Brick	Selee	Slurry Infiltration	Mg-PSZ	10 ppi	53	1"	3" x 3"	
15	Porous Cylinder	Selee	Slurry Infiltration	Mg-PSZ	35 ppi	80	3/8"	2 3/10" dia.	
16	Porous Cylinder	Selee	Slurry Infiltration	Cordierite	30 ppi	41	1/2"	2 7/8" dia.	
17	Porous Cylinder	Selee	Slurry Infiltration	Mg-PSZ	65 ppi	62	2/5"	2 1/5" dia.	
18	Porous Brick	Astromet	Slurry Infiltration	ZTA (T2)	30 ppi	39	9/10"	3" x 3"	
19	Porous Brick	Astromet	Slurry Infiltration	ZTA (T2)	10 ppi	37	9/10"	2 9/10" x 2 9/10"	
20	Porous Brick	Astromet	Slurry Infiltration	ZTA (T2)	15 ppi	38	9/10"	2 9/10" x 2 9/10"	
21	Porous Brick	Astromet	Slurry Infiltration	Ca-PSZ	10 ppi	42	7/8"	2 7/10" x 2 7/10"	
22	Porous Brick	Astromet	Slurry Infiltration	Ca-PSZ	30 ppi	42	7/8"	2 7/10" x 2 7/10"	
23	Cellular Brick	Corning	Extrusion	Cordierite	300 cpi	26	3 7/16"	5 9/10" x 5 9/10"	Square 1/8" x 1/8"
24	Porous Cylinder	Ultramet	CVI	SiC	100 ppi	40	17/32"	5 9/10" diam.	
25	Porous Cylinder	Ultramet	CVI	SiC	20 ppi	20	1"	5 3/8" diam.	
26	Porous Cylinder	Ultramet	CVI	SiC	60 ppi	8	1/2"	5 7/16" diam.	
27	Porous Cylinder	Amercom	CVI	SiC	60 ppi	12	1 1/5"	2 1/4" diam.	
28	Porous Cylinder	Amercom	CVI	SiC	80 ppi	24	1 3/8"	2 1/4" diam.	
29	Porous Cylinder	Amercom	CVI	SiC	10 ppi	18	3/4"	2 1/4" diam.	
30	Porous Brick	Amercom	CVI	SiC	10 ppi	27	1 1/8"	3 1/5" x 1 1/4"	
31	Porous Cylinder	Amercom	CVI	SiC	30 ppi	26	1 1/10"	2 3/10 diam.	
32	Porous Sheet	ERG	Resin Impregnation	Vitreous Carbon	10 ppi	4	1/4"	3 7/16" x 1 1/2"	
33	Porous Sheet	ERG	Resin Impregnation	Vitreous Carbon	20 ppi	4	1/4"	3 7/16" x 1 1/2"	

Table C1.1. Ceramic Acoustic Materials Supplied to the Advanced Liner Program

Sample No	Sample Type	Company	Process	Composition	Porosity	Density (lb/ft ³)	Depth	Cross Section	Cell Geometry TYPE / CROSS SECTION
34	Porous Sheet	ERG	Resin Impregnation	Vitreous Carbon	30 ppi	4	1/4"	3 7/16" x 1 1/2"	
35	Porous Sheet	ERG	Resin Impregnation	Vitreous Carbon	45 ppi	4	1/4"	3 7/16" x 1 1/2"	
36	Porous Sheet	ERG	Resin Impregnation	Vitreous Carbon	80 ppi	4	1/4"	3 7/16" x 1 1/2"	
37	Porous Sheet	ERG	Resin Impregnation	Vitreous Carbon	100 ppi	4	1/4"	3 7/16" x 1 1/2"	
38	Porous Cylinder	3M	Poly. Cure/CVD	Alumina/SiC	N/A	44	5/8"	2 7/10" diam.	
39	Porous Cylinder	3M	Poly. Cure/CVD	Alumina/SiC	N/A	46	5/8"	2 7/10" diam.	
40	Porous Cylinder	3M	Poly. Cure/CVD	Alumina/SiC	N/A	71	7/10"	2 7/10" diam.	
41	Porous Brick	DuPont Lanxide	DIMOX	SiC(p)/Alumina	10 ppi	33	1 1/16"	4" x 3 9/10"	
42	Cellular Brick	DuPont Lanxide	DIMOX	SiC(p)/Alumina	1.25 cpi	39	1"	7 1/10" x 3 3/4"	Honeycomb 3/4" x 3/8"
43	Cellular Brick	DuPont Lanxide	DIMOX	SiC(p)/Alumina	0.75 cpi	35	1 1/10"	12" x 9 1/2"	Honeycomb 4/5" x 3/5"
44	Cellular Brick	DuPont Lanxide	DIMOX	SiC(p)/Alumina	1.8 cpi		1"	11 1/2" x 10"	
45	Cellular Brick	DuPont Lanxide	DIMOX	SiC(p)/Alumina	2.5 cpi		1"	16" x 16"	
46	Cellular Brick	DuPont Lanxide	DIMOX	SiC(p)/Alumina	4 cpi		1"	16" x 13"	
47	Porous Brick	Boeing	Vac. Form/Sol-Gel	Oxide Fibers	N/A	22	1/2"	2 1/20" x 3 2/16"	
48	Porous Brick	Boeing	Vac. Form/Sol-Gel	Oxide Fibers/SiC Whiskers	N/A	21	5 1/16"	3 1/10" x 2 2/10"	
49	Porous Brick	Boeing	Vac. Form/Sol-Gel	Oxide Fibers	N/A	17	1 4/10"	3 5/16" x 5 7/16"	
50	Porous Brick	Boeing	Vac. Form/Sol-Gel	Oxide Fibers/SiC Whiskers	N/A	21	1 7/16"	4" x 4 1/16"	
51	Porous Cylinder	Westinghouse	Vac. Form/Sol-Gel	Oxide Fibers	N/A	14	2 5/16"	2" diam.	
52	Porous Cylinder	Westinghouse	Vac. Form/Sol-Gel	Oxide Fibers	N/A	14	2 5/16"	2" diam.	
53	Porous Brick	MDTI	Vac Form/Sintering	Aluminoborosilica Fibers	N/A	16	1/2"	3 1/4" x 3 1/4"	
54	Porous Brick	MDTI	Vac Form/Sintering	Aluminoborosilica Fibers	N/A	16	1/2"	3" x 3"	
55	Porous Brick	MDTI	Vac Form/Sintering	Aluminoborosilica Fibers	N/A	16	1/2"	3" x 3"	
56	Porous Brick	GEAE	Hydro-gel	Alumina-Silica	N/A	24	1 1/4"	4 1/16" x 4 3/16"	
57	Porous Brick	GEAE	Hydro-gel	Alumina-Silica	N/A	20	15/16"	3 1/10" x 2 15/16"	
58	Porous Sheet	ICI	Fiber Blanket	Alumina Fiber	N/A	5			
59	Porous Cylinder	3M	Poly. Cure/CVD	Alumina-Silica	N/A		1"	2 1/8" diam	
60	Porous Cylinder	3M	Poly. Cure/CVD	Alumina-Silica	N/A		1"	2 1/8" diam.	

NOTE: Sample 57 is a "sandwich" structure with 0.12"-thick
and 20% porous face sheets on both surfaces

cpi - cells per square inch
ppi - pores per inch
density - lb/cu.ft.



**CVI (Chemical Vapor Infiltration)
and Slurry Infiltration Foams**

Fibrous Ceramics

**Hollow
Microsphere
Composites**

Figure C1. Macrostructure of ceramic bulk absorber materials.

constituents including the entire polyurethane structure, and as the temperature is increased, sintering of the remaining ceramic occurs. The macrostructure is similar to CVI foams as shown in Figure C1. These foams can be made in a wide range of compositions and shapes. In comparison to CVI foams, they are less expensive, but are higher in density and have low specific compressive strengths.

3. **Fibrous Ceramics (Vacuum Forming/Sol-gel and Vacuum Forming/ Sintering Processes)** - Ceramic fibers are dispersed in an aqueous slurry using a high shear mixing technique. The slurry is cast onto a porous tool under vacuum to remove the excess water and produce felt (fiber mat). The felt is dried further. The resulting fiber mat may be used as a flexible blanket absorber or it may be infiltrated with a 'sol'. The felt is then fired in a high temperature furnace to densify the 'sol' matrix (if used), or to sinter/fuse the fibers together (if a 'sol' matrix is not used). Figure C1 shows the macrostructure of a typical fibrous ceramic. These materials can be made in wide range of compositions and sizes. They have a wide density range and medium fabrication cost.
4. **Microsphere Composites (Castable Hydrogel and Polymer Cure/CVD Processes)** - An aqueous suspension containing refractory microspheres with an organic (phenolic) or inorganic (glass frit/acid) binding phase, whiskers or short fibers optional, is prepared and then casted into a mold of desired shape. The green article is gelled or cured, respectively, and subsequently dried slowly to remove excess water. Next, the material is treated at high temperatures to vitrify the inorganic binder, or processed in a gas phase reactor to infiltrate a ceramic phase if an organic bonding agent is used initially. The macrostructure of a typical microsphere composite is shown in Figure C1. These composites can be fabricated in a wide range of compositions and shapes. These materials are in the early stages of development, and further characterization is required.

Honeycombs: Formed by several different processes, similar to those described above for ceramic foams, with the potential for producing a continuous fiber-reinforced material. Honeycombs can be used for locally reacting single-degree-of-freedom or two-degree-of-freedom type liners. The cells can be configured by size and depth to attenuate acoustic energy for different frequency ranges.

Normal Impedance Results: The ceramic composite samples obtained from various suppliers are tested in the GEAE Acoustic Laboratory to evaluate the normal impedance spectra of these materials, which are used for initial screening process to select suitable liner materials. As an initial means to compare the acoustic characteristics of different samples, the

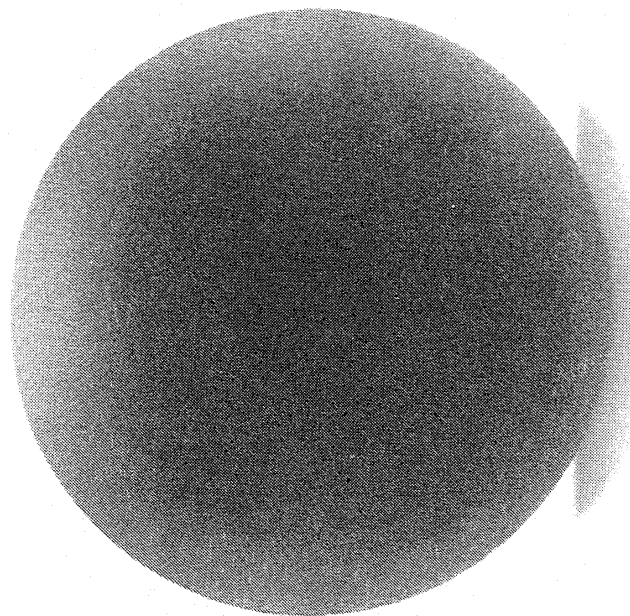
conventional plunker apparatus with a 1.25-inch diameter tube is used to measure the normal impedance spectra up to about 6000 Hz. These measurements are conducted at different broadband noise excitation sound pressure levels to identify the nonlinear behavior of these materials. All the tests are performed at the room temperature and pressure conditions.

The plunker impedance measurement system is a nondestructive system based on the impedance tube principle. As in the impedance tube, the sound field consists of plane waves reflected from the 'test sample' surface combining with the incident sound waves. However, in this case, some sound leakage may occur, which may introduce some amount of inaccuracy in the result. However, for initial study this measurement system is quite adequate. Our design impedance goal for ejector liners is set, that the specific resistance and reactance values should lie within 1.5 to 2.0 and -0.5 to 0.0, respectively, for the entire frequency range. Very few samples have impedance spectra, which meet these criteria. Samples with impedance values relatively closer to the above mention impedance goal are described in this report.

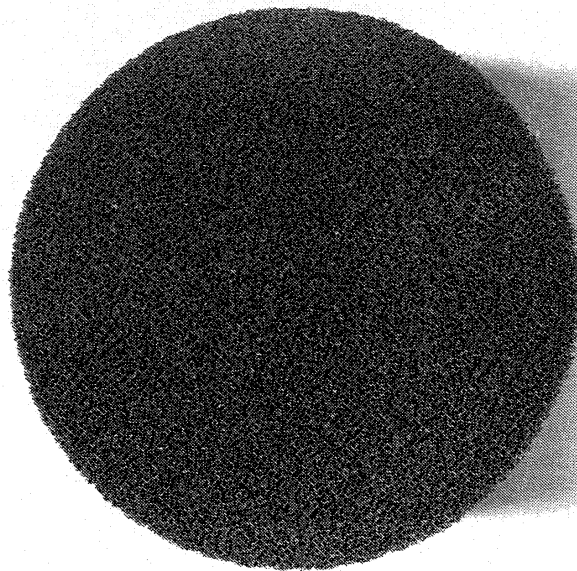
Ceramic Bulk Absorbers: Measured normal impedance spectra for a few samples from each of the four groups of ceramic foams are described below.

1. **CVI Foams** - Figure C2 shows the photograph of two CVI samples, #24 and #27, with 100 and 60 ppi, respectively. The measured normalized impedance spectra of these samples and another sample (i.e., sample #25) are plotted in Figure C3 to indicate the effect of sample density on their acoustic characteristics. The sample with higher density seems to have higher resistance, but lower reactance levels compared to the samples with lower density. However, these samples seem to meet the impedance requirement very closely for HSCT liner purposes.
2. **Slurry Infiltration Foams** - Photograph of two typical Slurry Infiltration foam samples, #5 and 19, with 65 and 10 ppi, respectively, are shown in Figure C4. To examine the nonlinear behavior of ceramic foam the normalized impedance spectra for sample #5 are measured with three different broadband excitation levels and the results are compared in Figure C5. Small amount of nonlinearity is observed at lower frequencies, where the resistance and reactance values decrease with increasing OASPL. This effect is further examined for sample #17 in Figure C6, which indicates insignificant nonlinear effect. Since, both these samples are of equal density and ppi, the composition seems to be the reason for their difference in nonlinear behavior. The measured normalized impedance spectra of three SI samples with different density are

CHEMICAL VAPOR INFILTRATION (CVI)
SIC



SAMPLE #24



SAMPLE #27

Figure C2. Photographic views of two Chemical Vapor Infiltration (CVI) ceramic composites.

SIC MATERIAL, OASPL=152 dB

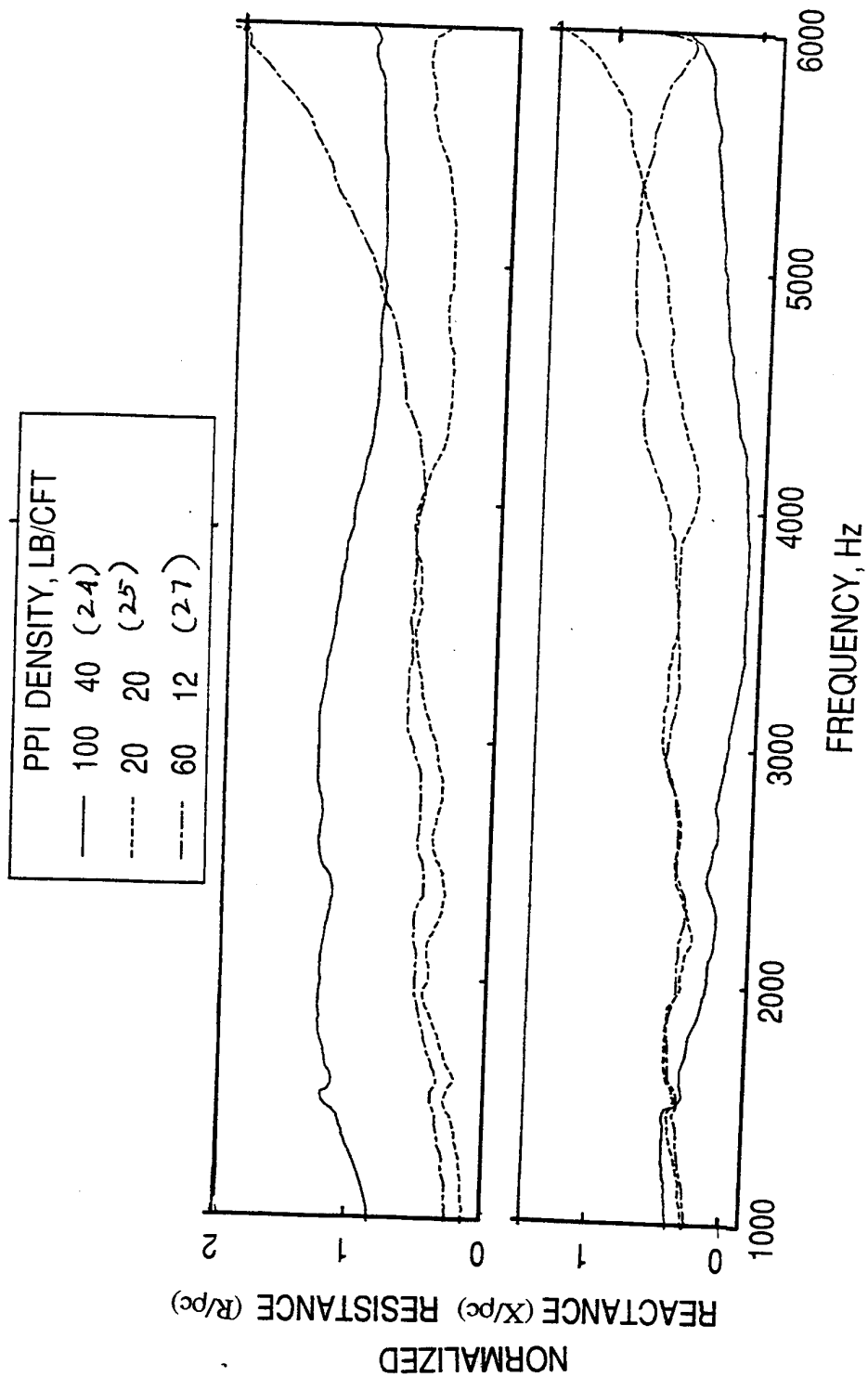
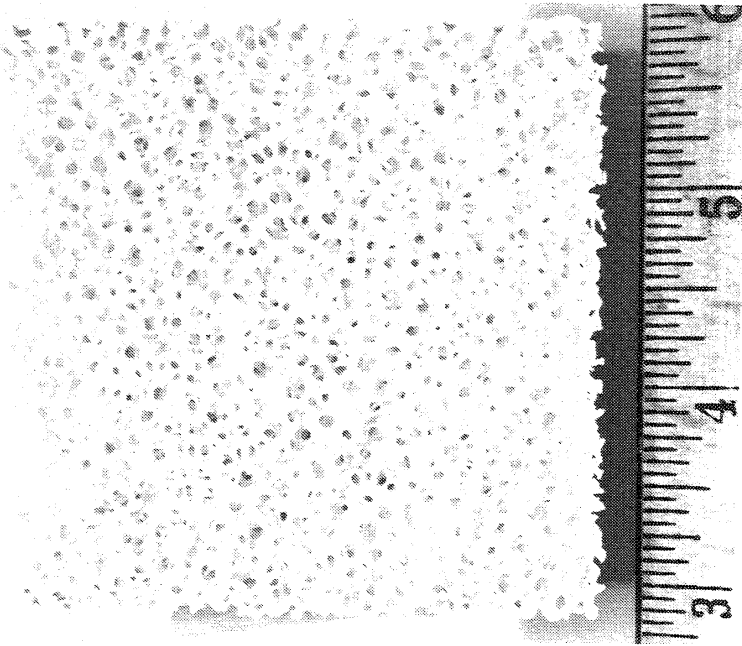
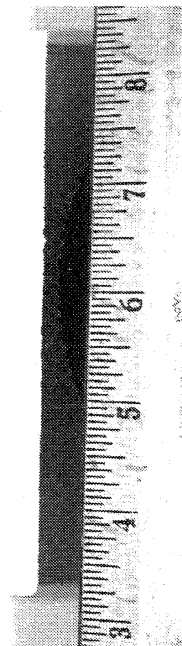


Figure C3. Effect of density on measured impedance spectra for SIC materials.

SLURRY INFILTRATION FOAM



ZTA (T2)
SAMPLE #19



ALUMINA
SAMPLE #5

Figure C4. Photographic views of two Slurry Infiltration (SI) ceramic foam samples.

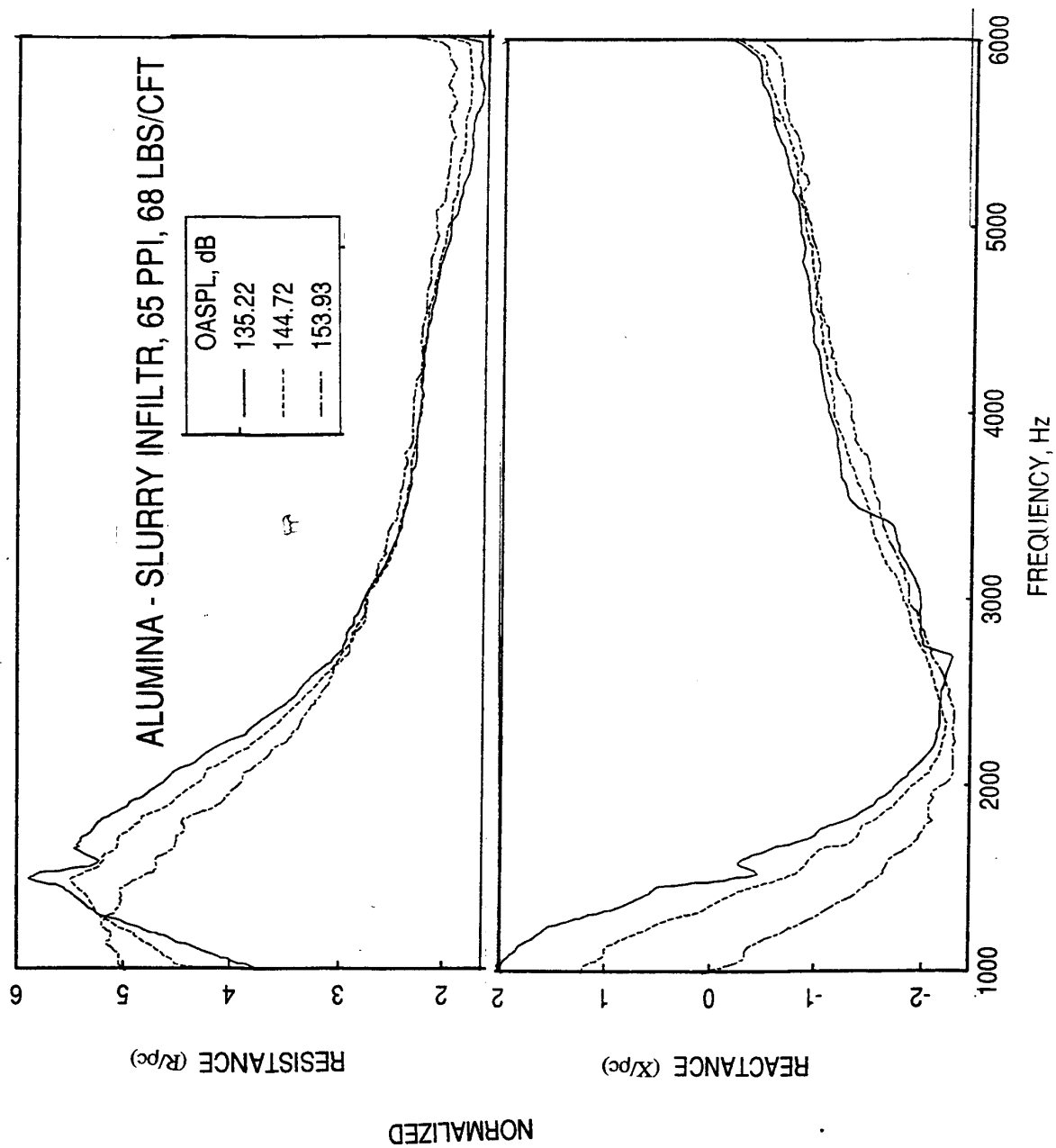


Figure C5. Effect of excitation sound pressure level on measured impedance spectra for an Alumina - slurry infiltration composite (sample #5).

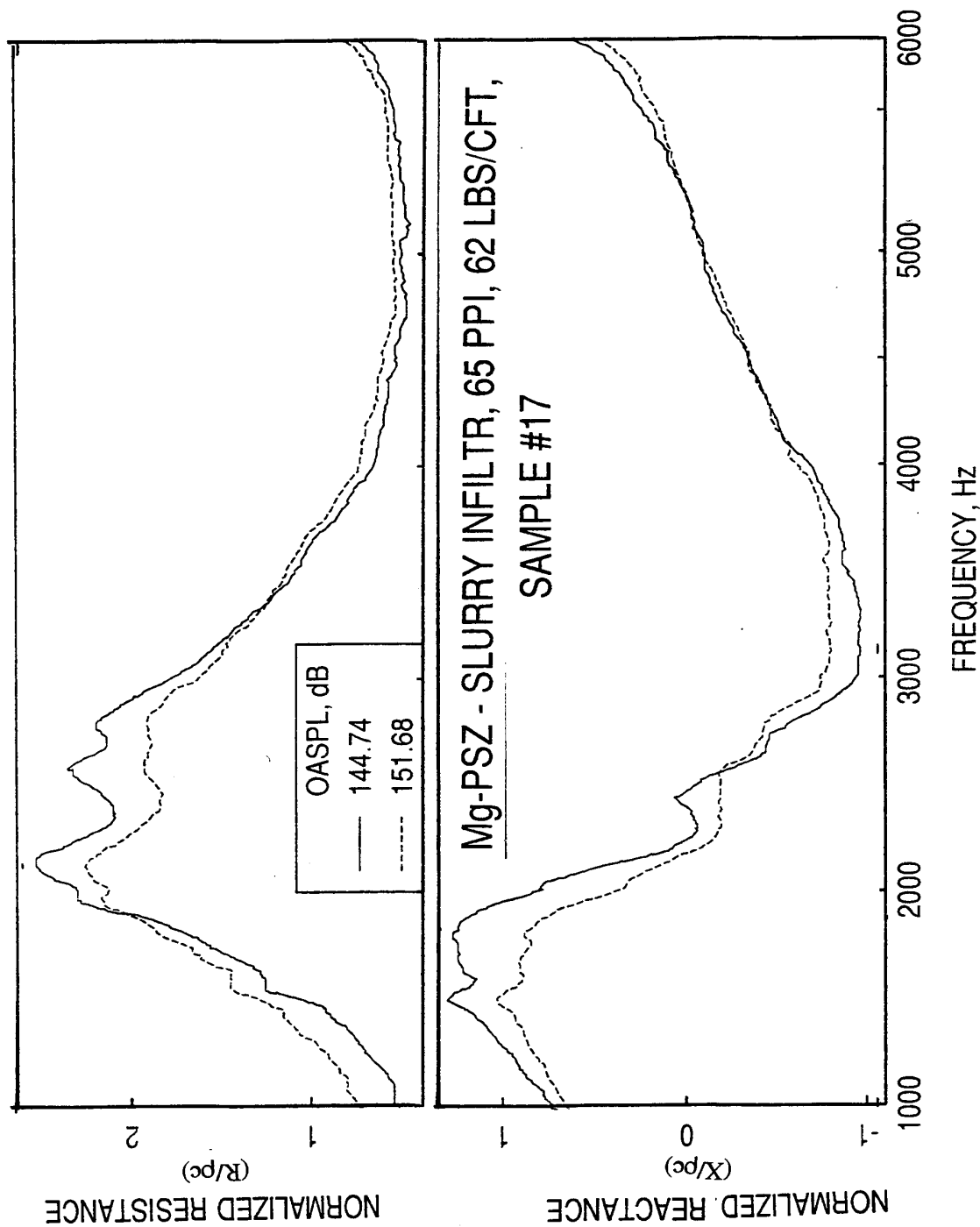


Figure C6. Effect of excitation sound pressure level on measured impedance spectra for an Mg-PSZ - slurry infiltration composite (sample #17).

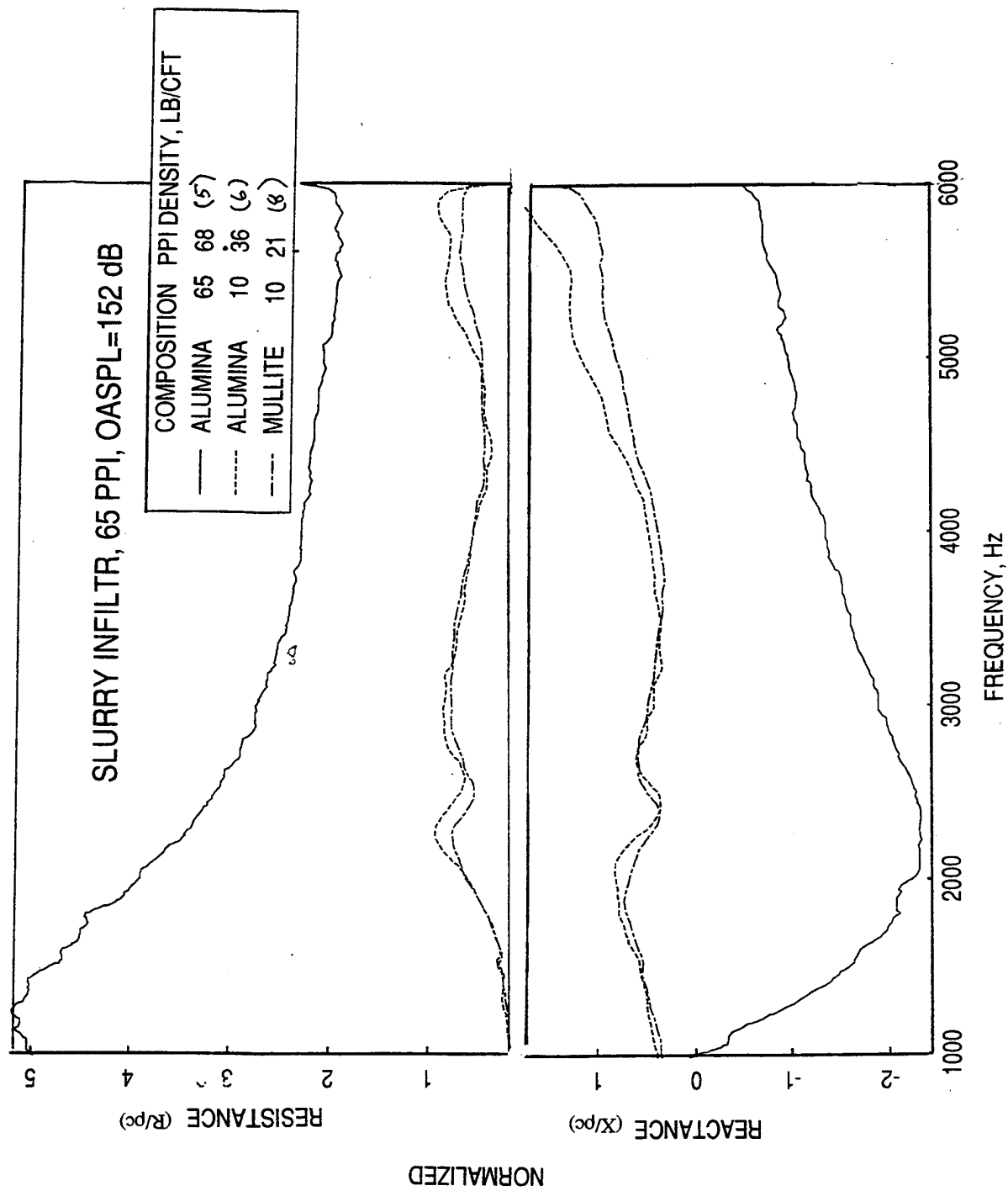


Figure C7. Effect of density on measured impedance spectra for Slurry Infiltration Foam materials.

plotted in Figure C7. Again, the sample with higher density seems to have higher resistance, but lower reactance levels compared to the samples with lower density. Figure C8 is another impedance plot for four other SI samples, which have desired impedance criteria for HSCT liner.

3. **Fibrous Ceramics (Vacuum Forming/Sol-gel and Vacuum Forming/ Sintering Processes)** - Figure C9 shows the photographic views of two fibrous ceramic samples with different process and composition. We received more than one samples of same property under this category. That allowed us to examine the effect of two different samples of same property on their acoustic impedance. Figures B10 and B11 are devoted for this purpose. As can be observed, some differences are noticed between the two sets of results (scales are magnified to see the effect). Normalized impedance spectra between two fibrous ceramic samples with different densities are plotted in Figure C12. However, any conclusion on the basis of density is not possible in this case, since the depth of these two samples is widely different.
4. **Microsphere Composites (Castable Hydrogel and Polymer Cure/CVD Processes)** - A limited number of microsphere composites are obtained. Figure C13 is a photographic view of two of the samples of this category. Impedance results for most of the samples are not shown here, since they have very high resistance levels. Measured normalized impedance spectra for a sample with relatively lower resistance measured at two different excitation levels are shown in Figure C14. This type of composites exhibits some amount of nonlinear behavior.

Honeycombs: Impedance values for honeycomb samples can not be used directly to identify their effectiveness, since the actual liner using honeycomb (i.e., honeycomb with appropriate face sheet for an SDOF type liner) would have entirely different impedance spectra compared to those for the bare honeycomb samples. However, these impedance spectra can be used to design appropriate facesheets, such that the final liners would have desired impedance spectra.

Figure C15 shows the photographs of a few typical ceramic cellular (honeycomb) samples tested in the GEAE Acoustic Laboratory. Figure C16 is the measured normalized impedance spectra for a 3"-deep ceramic honeycomb (sample #1) with 64 cells per square inch (0.12" square cells). As expected, we observe resistance peaks and corresponding change in sign of reactance at certain frequencies. These are the anti-resonating frequencies based on the depth of the honeycomb cell. The resonance frequency corresponds to the mid-point of two successive anti-resonance frequencies and it also coincides with zero reactance. For this

SLURRY INFILTR, OASPL=152 dB

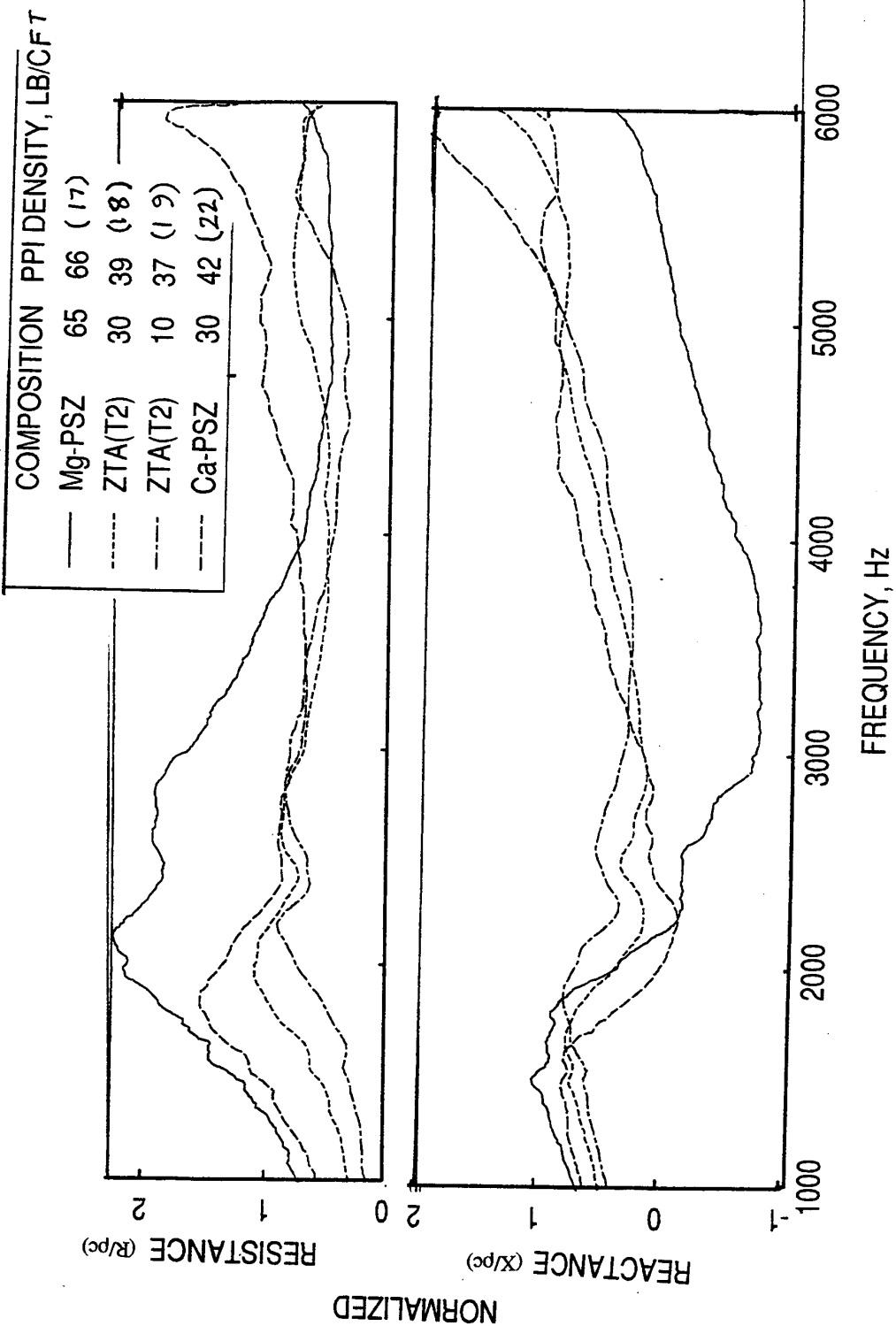
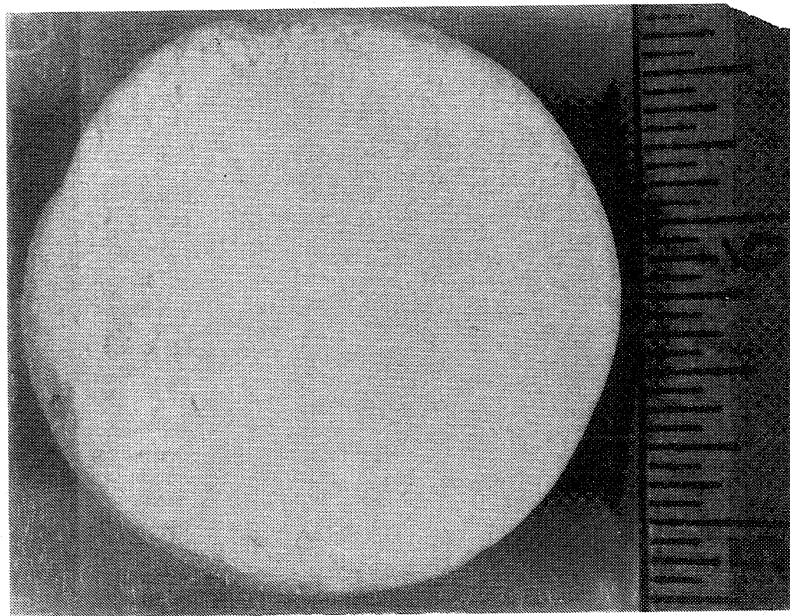
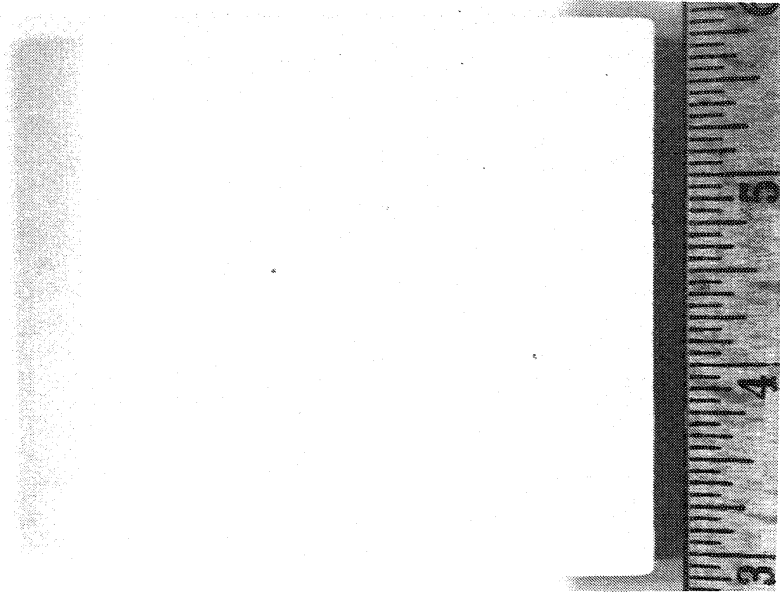


Figure C8. Effect of density on measured impedance spectra for Slurry Infiltration Foam materials.

FIBROUS CERAMICS AS BULK ABSORBER



VACUUM FORMING/SOL-GEL
OXIDE FIBERS
SAMPLE #52



VACUUM FORMING/SINTERING
ALUMINO BOROSILICA FIBER
SAMPLE #55

Figure C9. Photographic views of two Fibrous Ceramic samples.

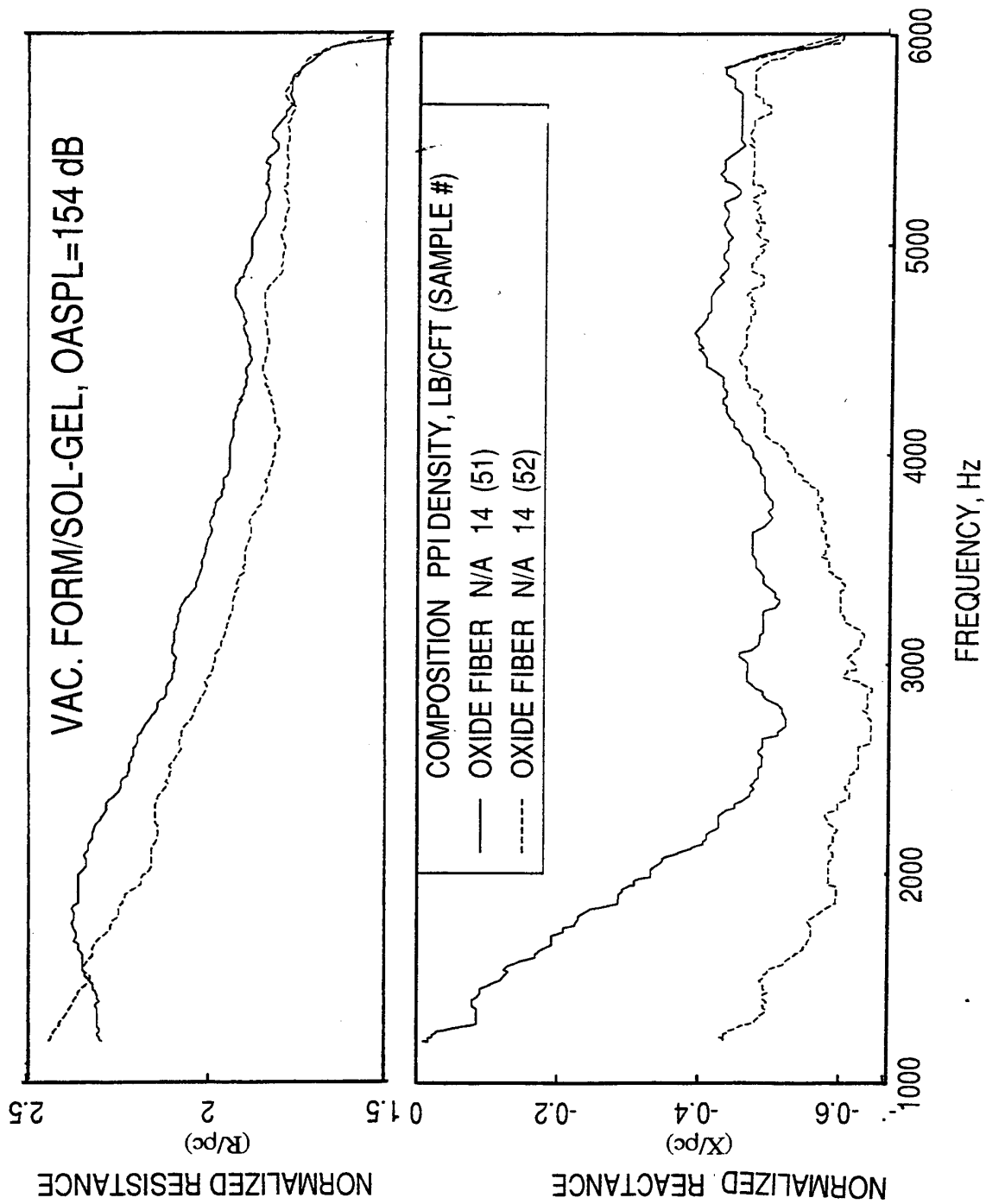


Figure C10. Effect of two different Fibrous Ceramic samples of same property on their acoustic impedance.

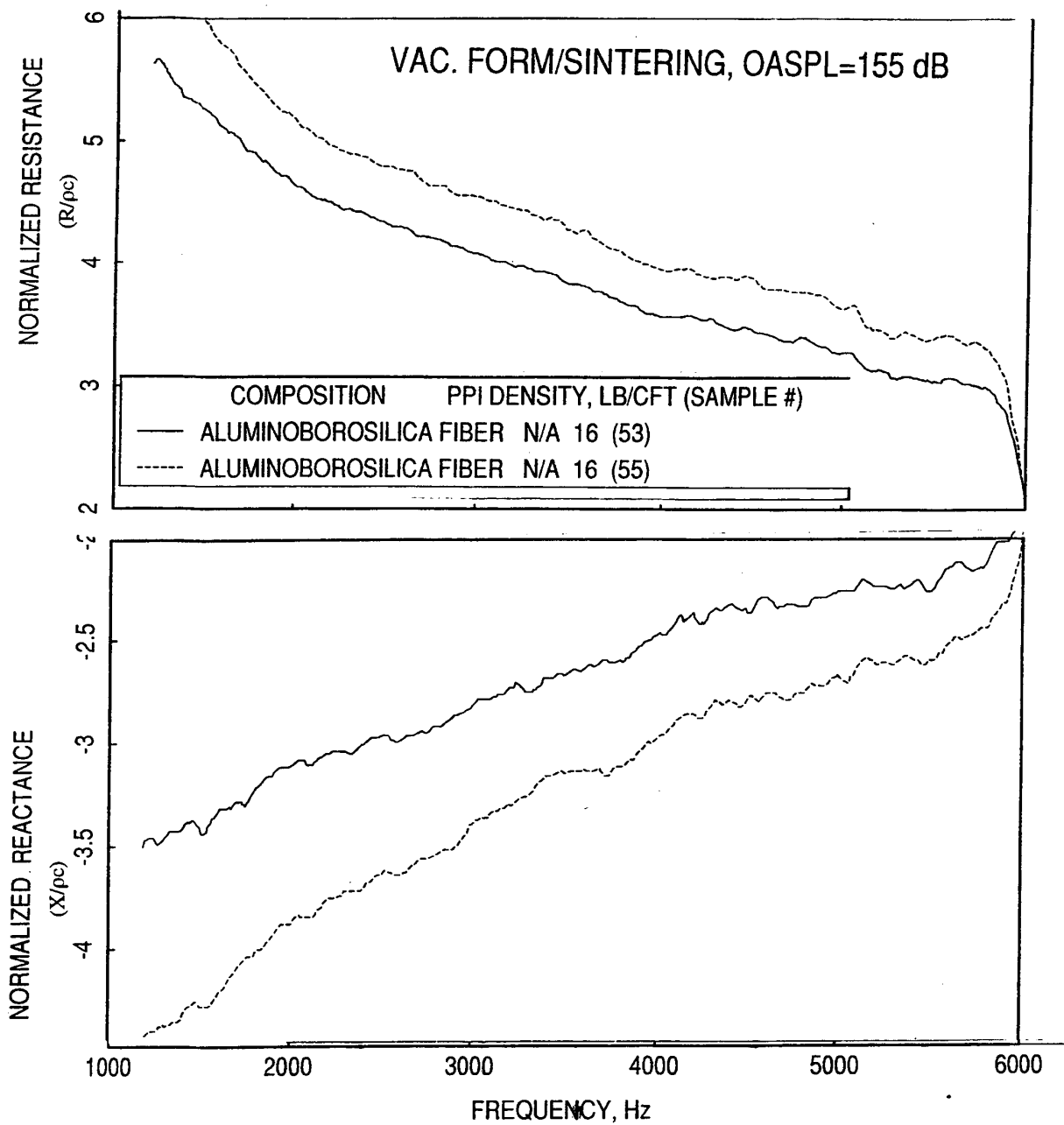


Figure C11. Effect of two different Fibrous Ceramic samples of same property on their acoustic impedance.

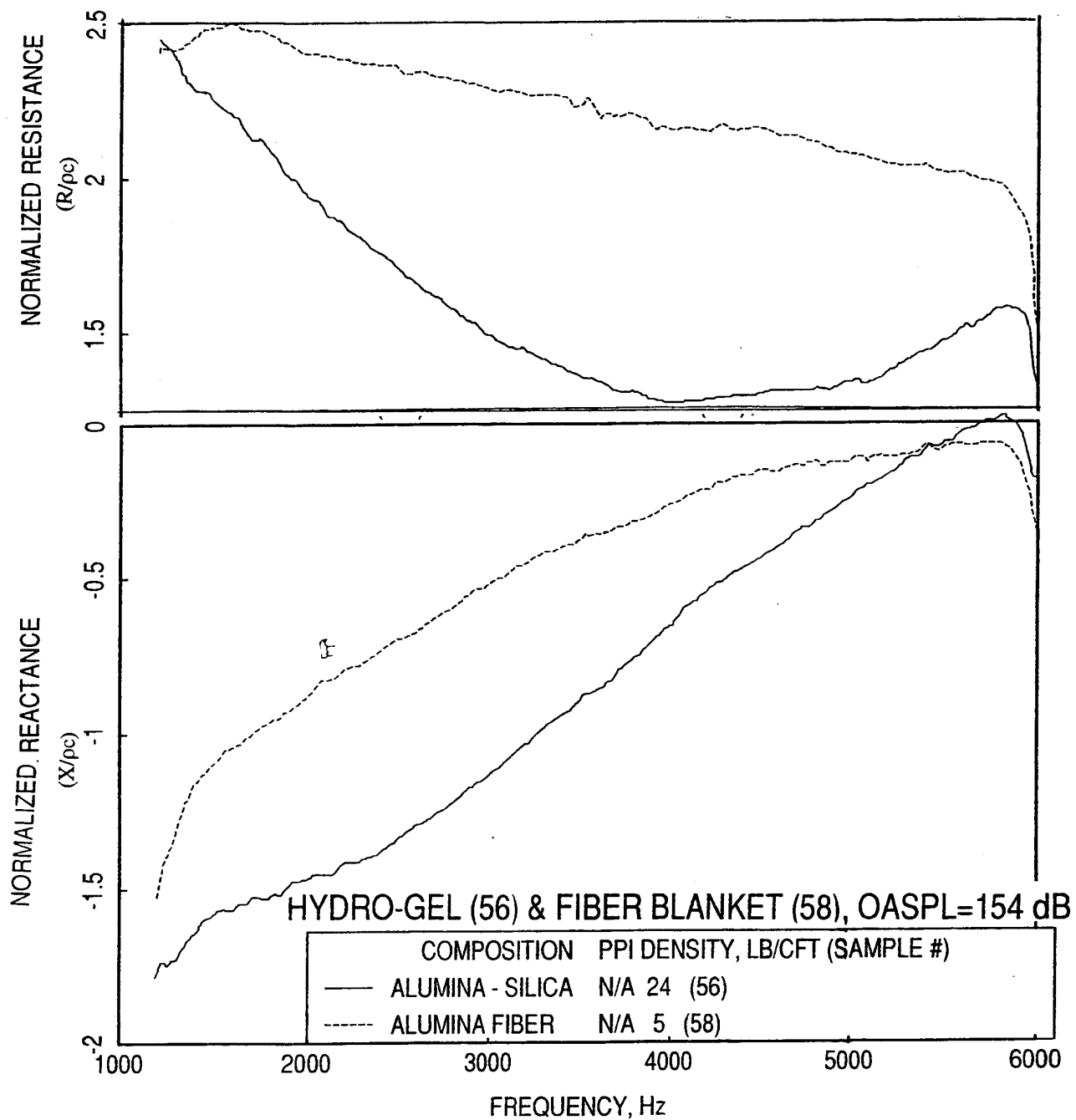
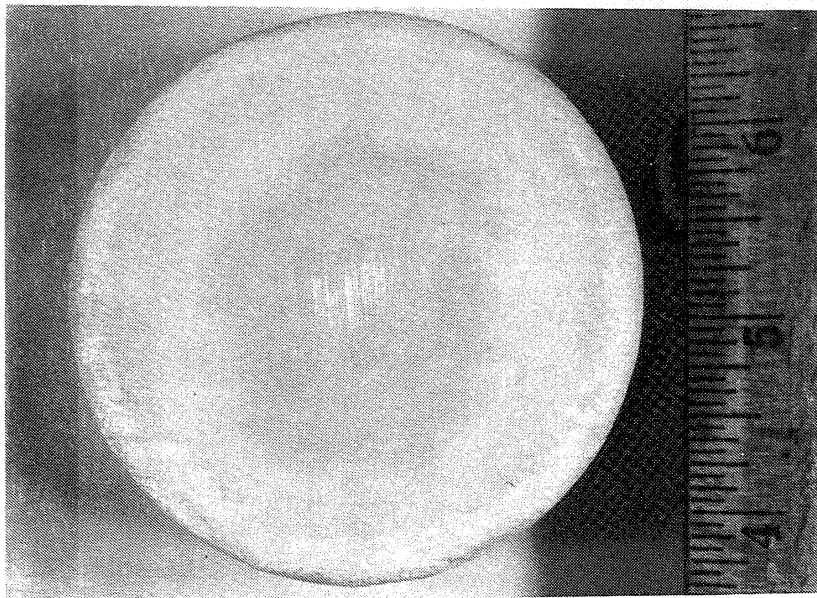
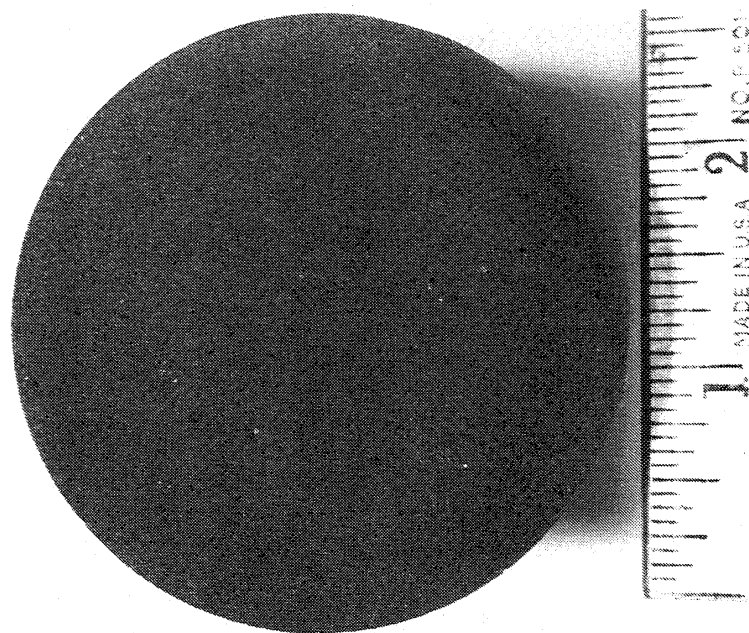


Figure C12. Effect of density on measured impedance spectra for Fibrous Ceramic materials.

MICROSPHERE COMPOSITES AS BULK ABSORBER



**HYDROGEL PROCESS
ALUMINA-SILICA
SAMPLE #56**



**POLYMER CURE/CVD PROCESS
ALUMINA/S/C
SAMPLE #38**

Figure C13. Photographic views of two Microsphere composite samples.

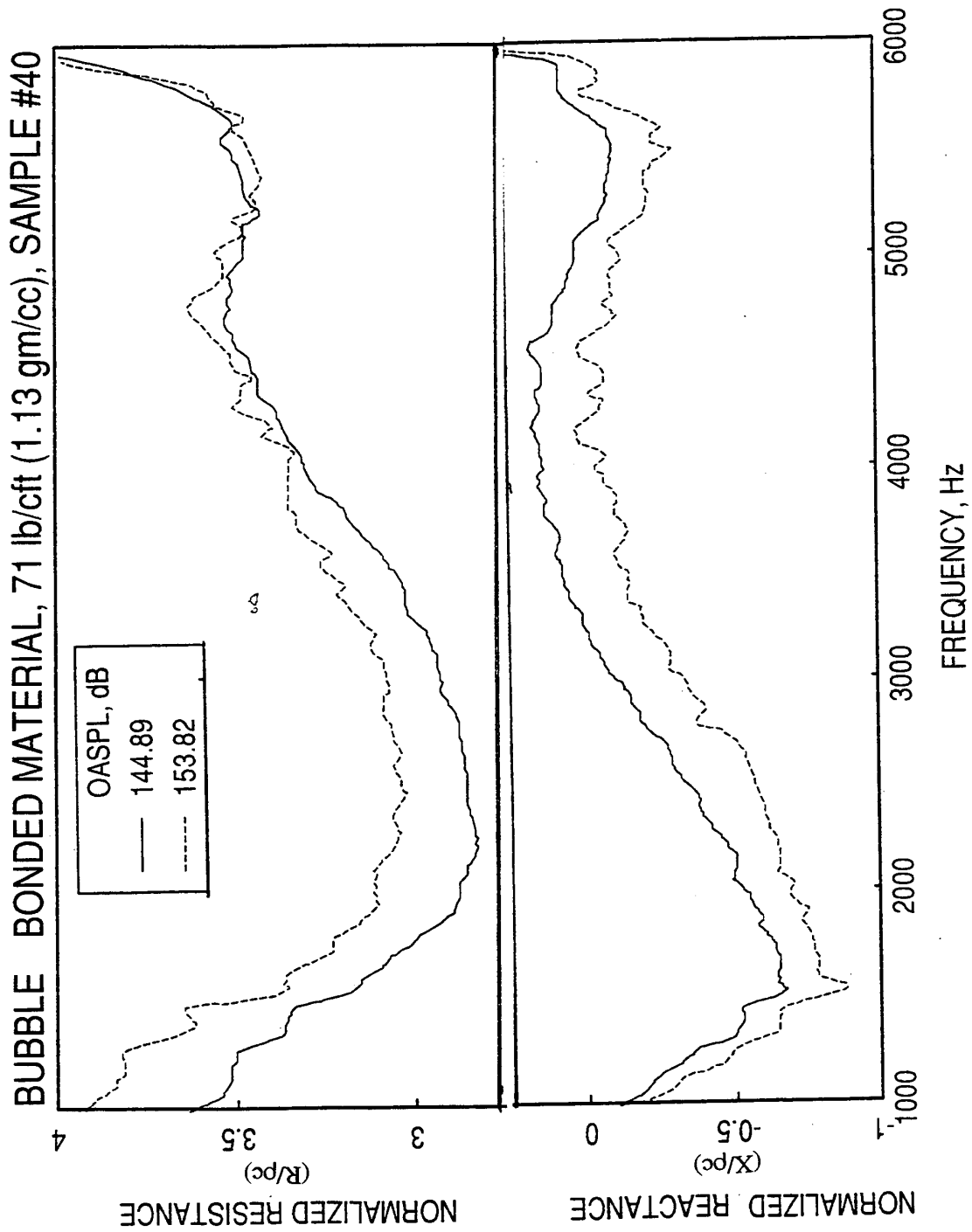
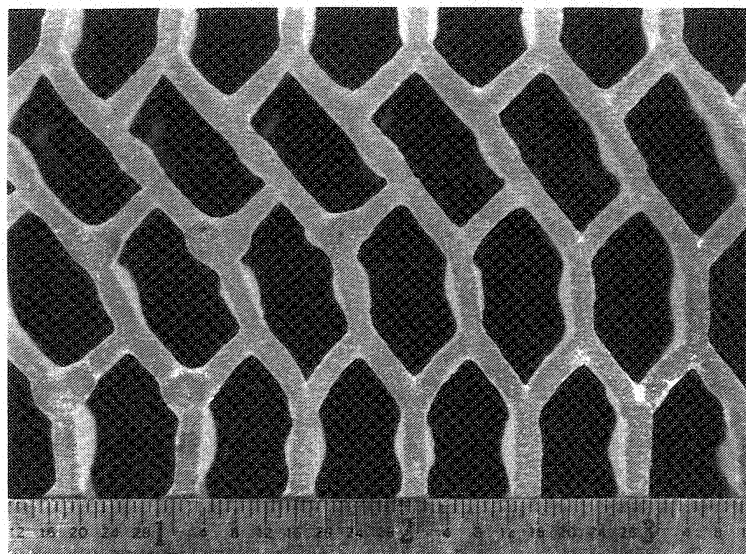
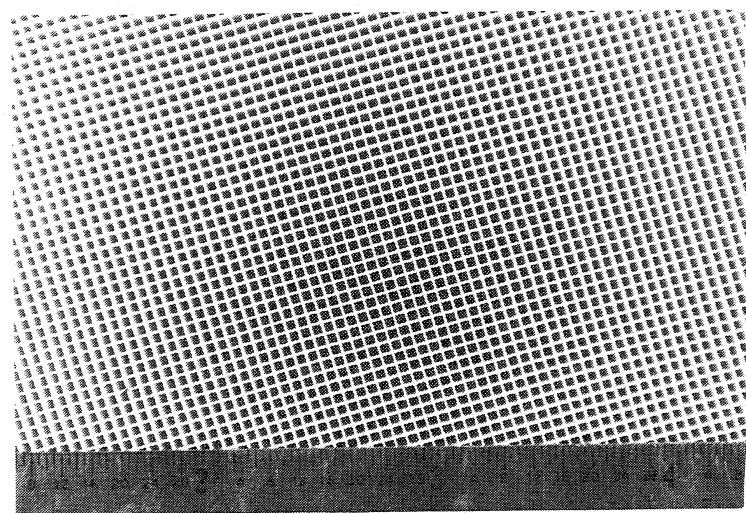


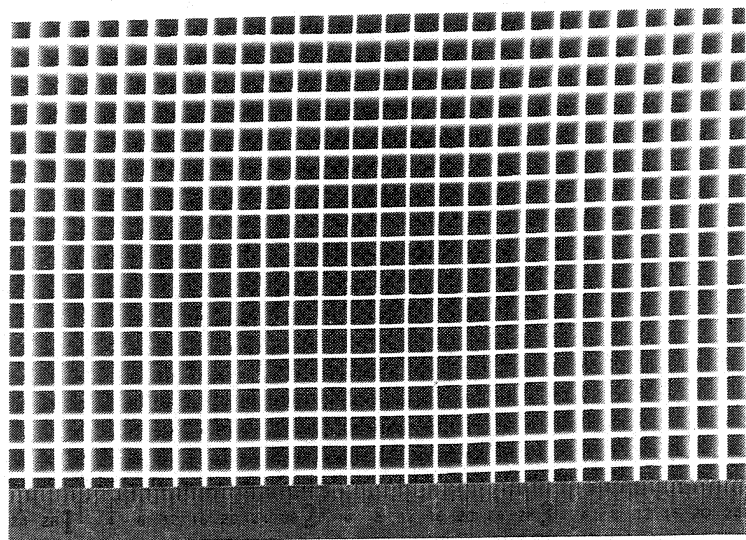
Figure C14. Effect of excitation sound pressure level on measured impedance spectra for a bubble bonded Microsphere Composite (sample #40).



DIMOX PROCESS
SiC () / ALUMINA
0.75"x0.375"-HONEYCOMB CELL
SAMPLE #42



EXTRUSION PROCESS
CORDIERITE
0.05" SQUARE CELL SECTION (400 cpi)
SAMPLE #3



EXTRUSION PROCESS
CORDIERITE
0.12" SQUARE CELL SECTION (64cpi)
SAMPLE #1

Figure C15. Photographic views of three cellular (honeycomb) samples.

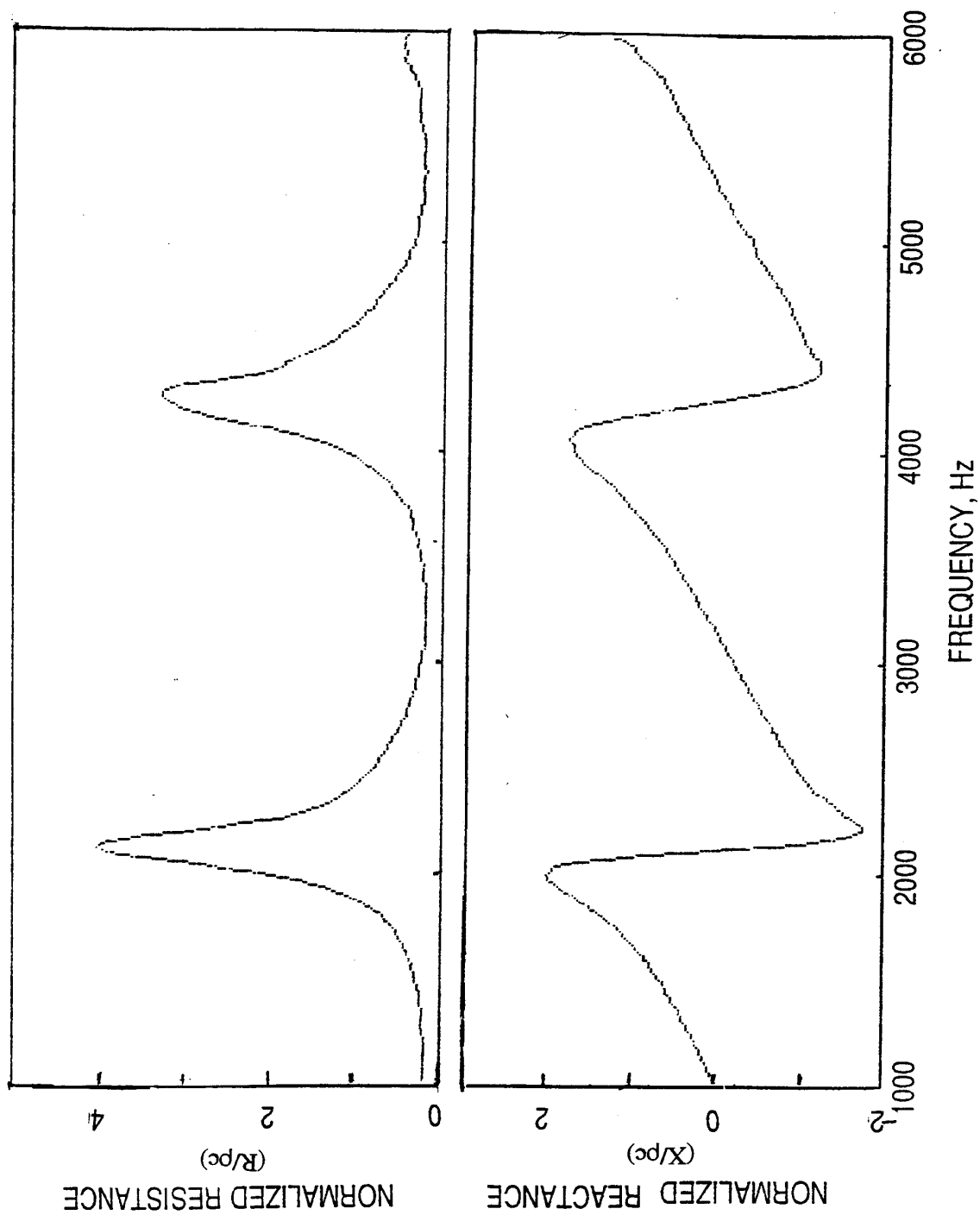


Figure C16. Measured impedance spectra for a cellular brick (sample #1) with 3"-deep 0.12"-square cells.

sample the first resonance frequency is about 1150 Hz and the interval between successive resonances is about 4310 Hz. The interval between the successive resonance frequencies does not depend on the cell size. However, the first resonance frequency changes with the cell size, as illustrated in Figure C17, which is the measured normalized impedance spectra for another 3.25"-deep ceramic honeycomb (sample #3) sample with 400 cells per square inch (i.e., 0.05" square cells). The first resonance frequency for this sample is about 800 Hz (not shown in the figure) and the interval between successive resonances is about 3720 Hz. The interval between two successive resonance frequencies is slightly different (lower) compared to that of Figure C16, but the location of first resonance is quite different. Next, the measured normalized impedance spectra for a 6"-deep honeycomb sample (sample #4) with the same cell size (i.e., 0.05" square cell) of sample #3 are plotted in Figure C18. The frequency step between two successive resonance frequencies is about 2060 Hz, which is much smaller compared to those of Figures C16 and C17, due to the higher cell depth.

Conclusions: Based on the screening studies silicon carbide (SiC) foams prepared by chemical vapor infiltration process seem to have the potential for HSCT liner application. Thus, silicon carbide foams of varying ppi and densities are procured for rigorous laboratory and model-scale mixer-ejector tests.

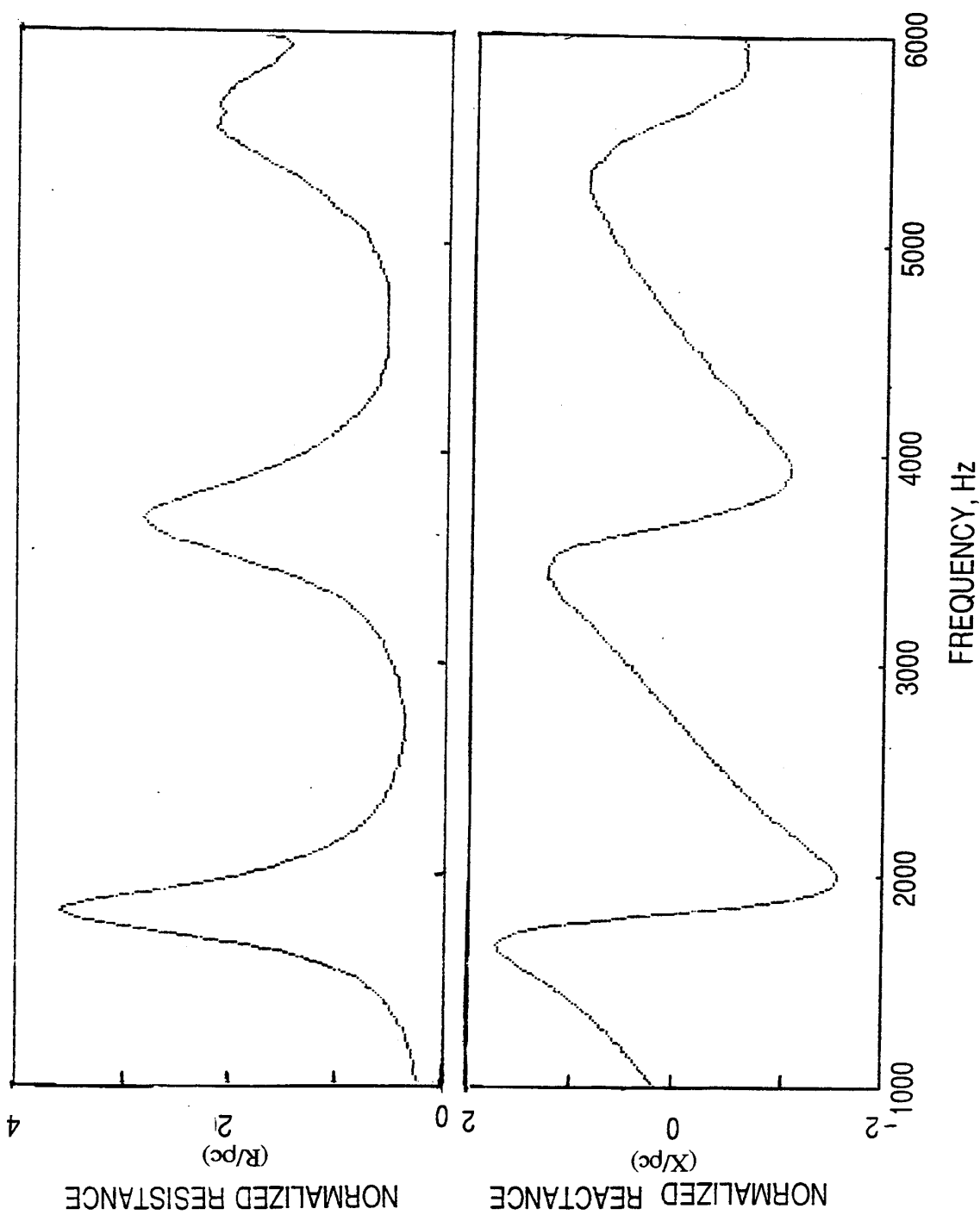


Figure C17. Measured impedance spectra for a cellular ellipse (sample #3) with 3.25" - deep 0.05" -square cells.

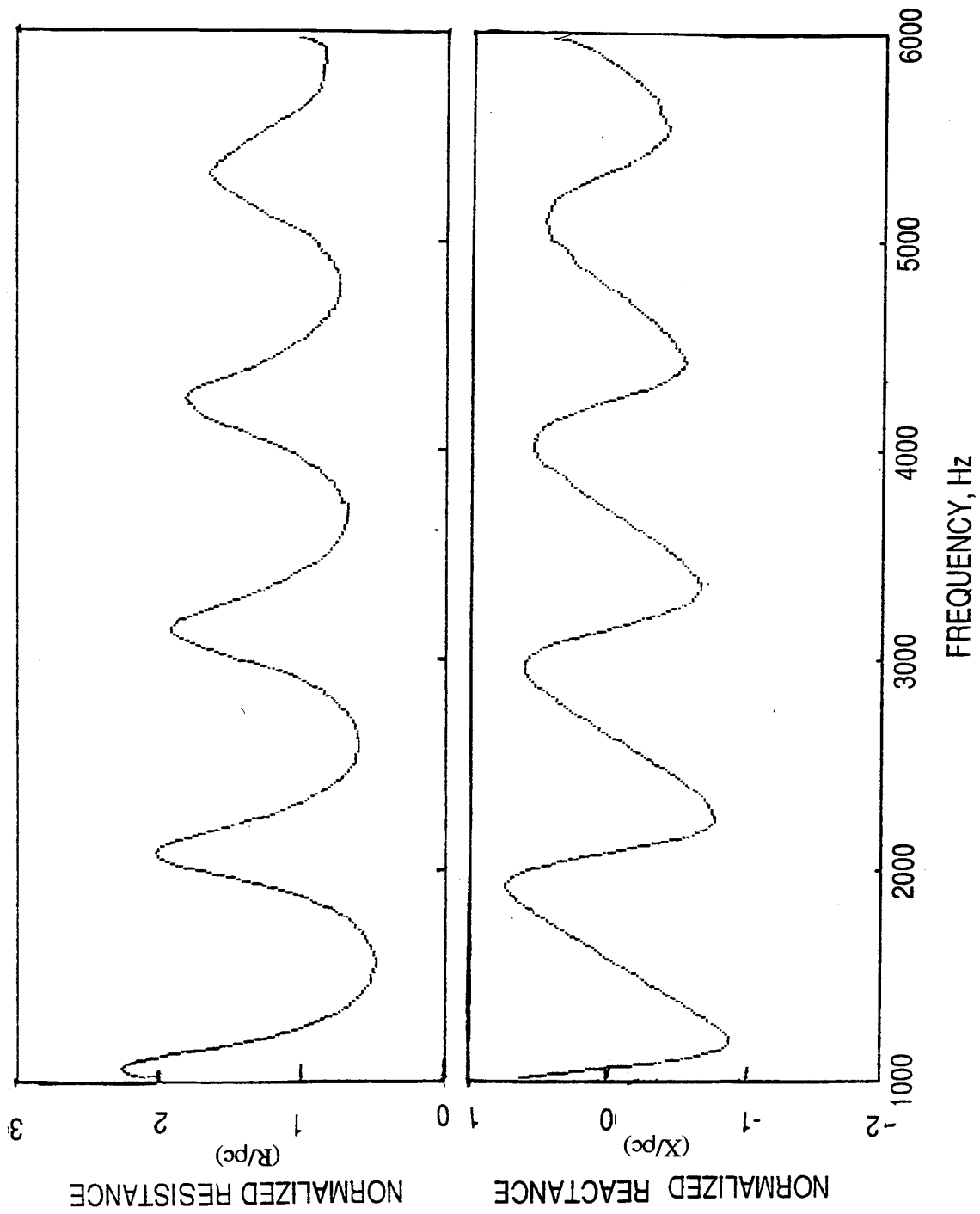


Figure C18. Measured impedance spectra for a cellular ellipse (sample #4) with 6"-deep 0.05"-square cells.

APPENDIX D

ACOUSTIC CHARACTERISTICS OF BULK MATERIALS WITH FACESHEETS

Impedance tube and DC flow tests are conducted for a few bulk material and perforated plate samples and their combinations to evaluate the effect of bulk thickness and the effect of perforated facesheet porosity on the normal impedance and DC flow resistance of the samples.

Effect of Perforated Facesheet Porosity on Normal Impedance and DC Flow Resistance of a Bulk Sample with the Facesheet: The acoustic panels used in the model scale HSCT mixer-ejector nozzles during acoustic tests contain bulk material with a 37% porous facesheet. The normal impedance for these panels meets the optimum criteria for most of the frequency range. Currently, there is a concern regarding the manufacturability of such highly (i.e., 37%) porous facesheets out of CMC materials, which are the likely candidates for HSCT nozzle liners. Impedance and DC flow tests are conducted for four facesheet samples of different porosity, provided by P&W, with and without a 200 ppi silicon carbide 1"-deep bulk material sample to evaluate their impedance characteristics.

Two facesheet samples have 60° stagger hole pattern, whereas, the other two have 90° stagger hole pattern. The porosity is different for each sample. The physical parameters for these samples are described in Figures D1 and D2. The thickness and the hole diameter are the same for all four samples. A one-inch deep cavity is used behind the perforated facesheet samples for normal impedance tube tests. Figure D3 shows the normal resistance and reactance spectra for the cavity alone and the cavity with the facesheets. Both the resistance and the reactance increase with decreasing porosity of the facesheets. The first anti-resonance frequency of the one-inch deep cavity is about 1800 Hz at room temperature. Therefore, the second anti-resonance appears at about 5400 Hz. At these frequencies we observe distinct spikes on resistance spectrum. It should be noted that the corresponding frequencies with facesheets are lower compared to those for the cavity alone and they seem to decrease with decreasing facesheet porosity. The equivalent depth of the cavity with facesheet becomes higher and hence the anti-resonance frequencies decrease slightly. The impact of anti-resonance frequencies is insignificant on reactance spectra.

It is well established that the normal impedance of a cavity with a facesheet (i.e., lumped impedance) is the linear combination of the individual normal impedance of the cavity and the facesheet evaluated individually. Hence, the cavity alone impedance values are subtracted from those for the cavity with facesheet combinations to evaluate the impedance of facesheet samples alone. These spectra are plotted in Figure D4. Again, the normal impedance increases

60° STAGGER PATTERN (i.e., $\theta = 60^\circ$)

h = Vertical distance between two rows of holes

d_h = Distance between centers along a row = $2h/\tan(\theta)$

d_s = Slant distance between centers along a row = $h/\sin(\theta)$

For $\theta = 60^\circ$, $d_h = d_s = h/0.866$

d = Hole diameter = $3/32"$ (0.093")

t = Plate thickness = $0.05"$ ~ $0.063"$

A_H = Area of each hole = $\pi d^2/4 = 6.903 \times 10^{-3}$ sq"

SAMPLE # 1

No of holes per row = 21

No of rows = 15

No of holes in $3.7" \times 1.89"$ (6.993 sq") area = 280

Open Area for 280 holes = $280 \times 6.903 \times 10^{-3} = 1.933$ sq"

Porosity = % of open area = $1.933 \times 100 / 6.993 = 27.6$ %

Vertical distance between rows = $h = 0.1356"$

Distance between centers = $d_h = d_s = 0.156"$

SAMPLE # 2

No of holes per row = 18

No of rows = 13

No of holes in $3.68" \times 1.77"$ (6.514 sq") area = 210

Open Area for 280 holes = $210 \times 6.903 \times 10^{-3} = 1.4496$ sq"

Porosity = % of open area = $1.4496 \times 100 / 6.514 = 22.25$ %

Vertical distance between rows = $h = 0.1476"$

Distance between centers = $d_h = d_s = 0.17"$

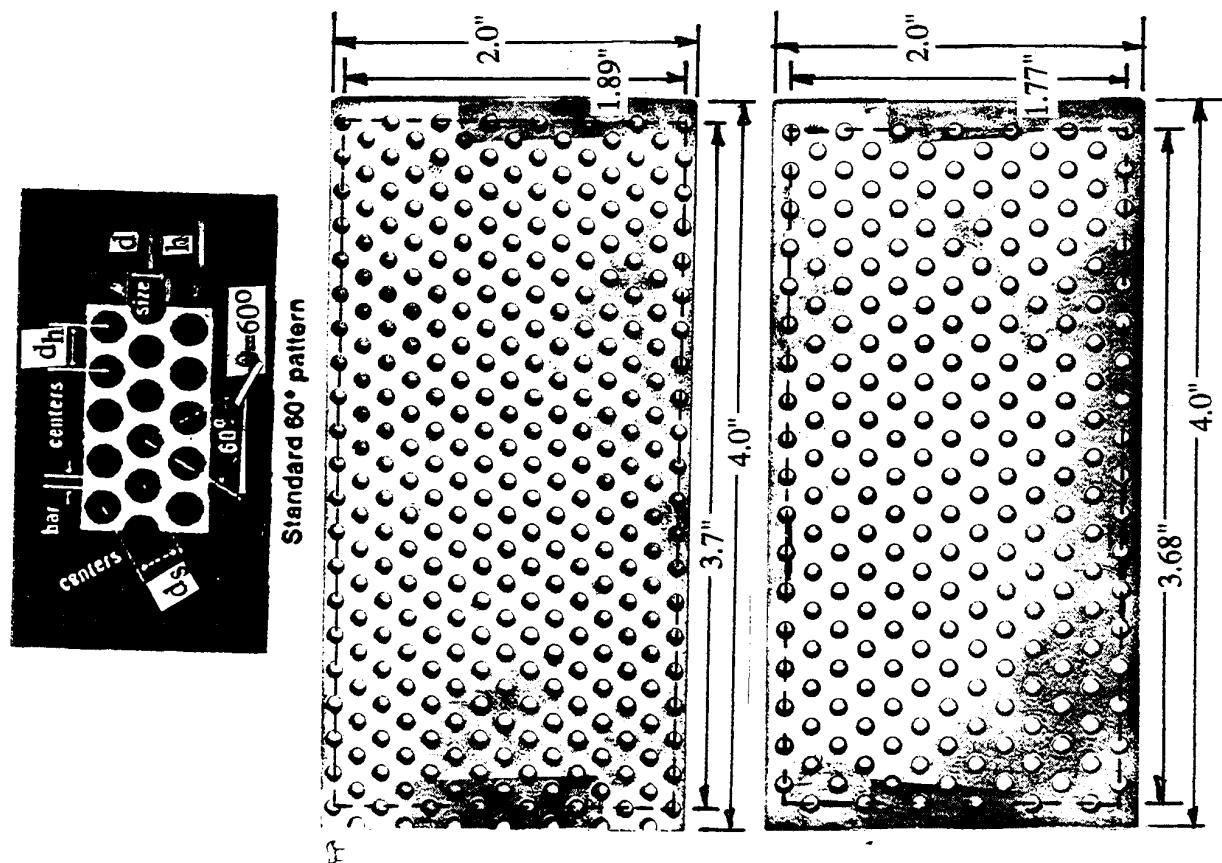


Figure D1. Physical parameters for two perforated sheets of different porosity with 60° hole stagger pattern.

90° STAGGER PATTERN (i.e., $\theta=45^\circ$)

h = Vertical distance between two rows of holes

d_h = Distance between centers along a row = $2h/\tan(\theta)$

d_s = Slant distance between centers along a row = $h/\sin(\theta)$

For $\theta=45^\circ$, $d_h = 2h$, $d_s = h/0.707$

d = Hole diameter = $3/32$ " (0.093")

t = Plate thickness = 0.05" \sim 0.063"

A_H = Area of each hole = $\pi d^2/4 = 6.903 \times 10^{-3}$ sq"

SAMPLE # 3

No of holes per row = 17

No of rows = 17

No of holes in 3.465"x1.693" (5.866 sq") area = 264

Open Area for 280 holes = $264 \times 6.903 \times 10^{-3} = 1.8224$ sq"

Porosity = % of open area = $1.8224 \times 100 / 5.866 = 31.0$ %

Vertical distance between rows = $h = 0.1055$ "

Horizontal distance between centers = $d_h = 0.211$ "

Slant distance between centers = $d_s = 0.1496$ "

SAMPLE # 4

No of holes per row = 19

No of rows = 20

No of holes in 3.465"x1.81" (6.272 sq") area = 351.5

Open Area for 280 holes = $351.5 \times 6.903 \times 10^{-3} = 2.426$ sq"

Porosity = % of open area = $2.426 \times 100 / 6.272 = 38.7$ %

Vertical distance between rows = $h = 0.0955$ "

Horizontal distance between centers = $d_h = 0.191$ "

Slant distance between centers = $d_s = 0.1348$ "

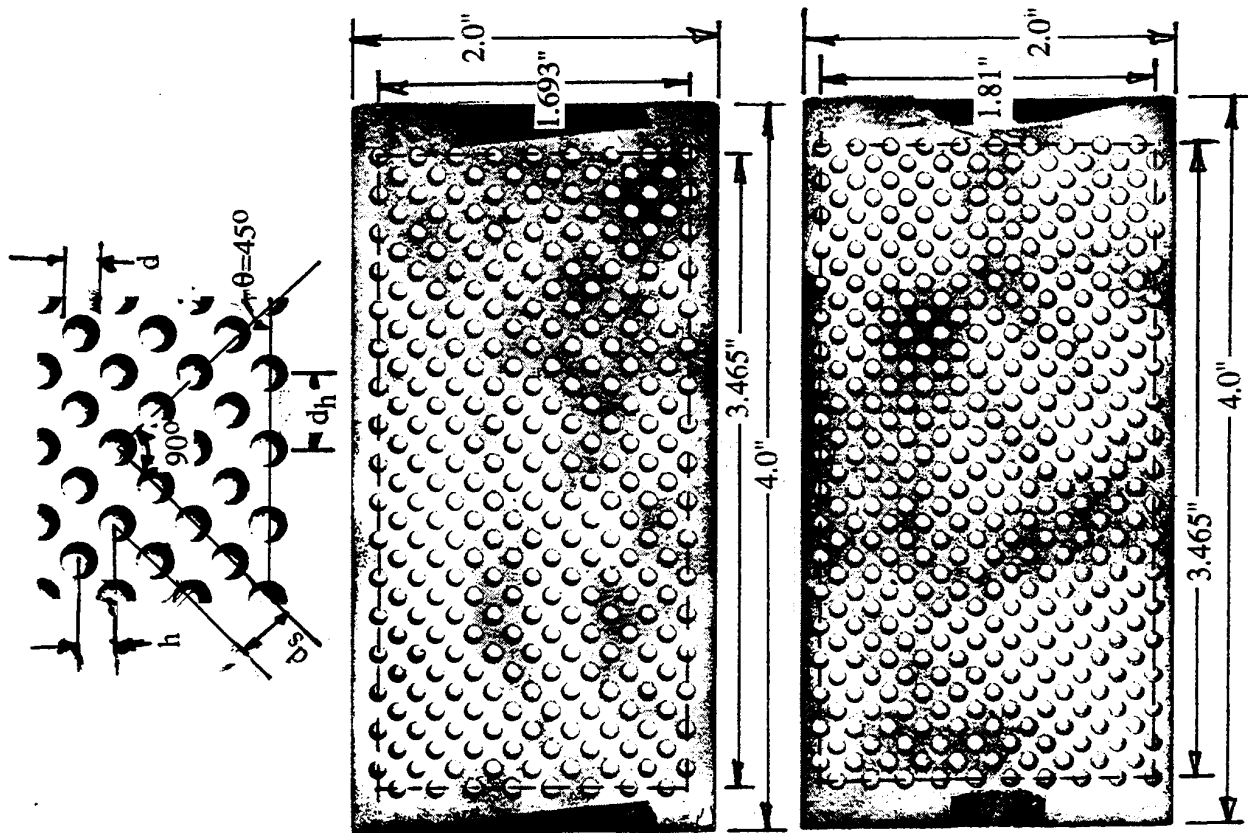


Figure D2. Physical parameters for two perforated sheets of different porosity with 90° hole stagger pattern.

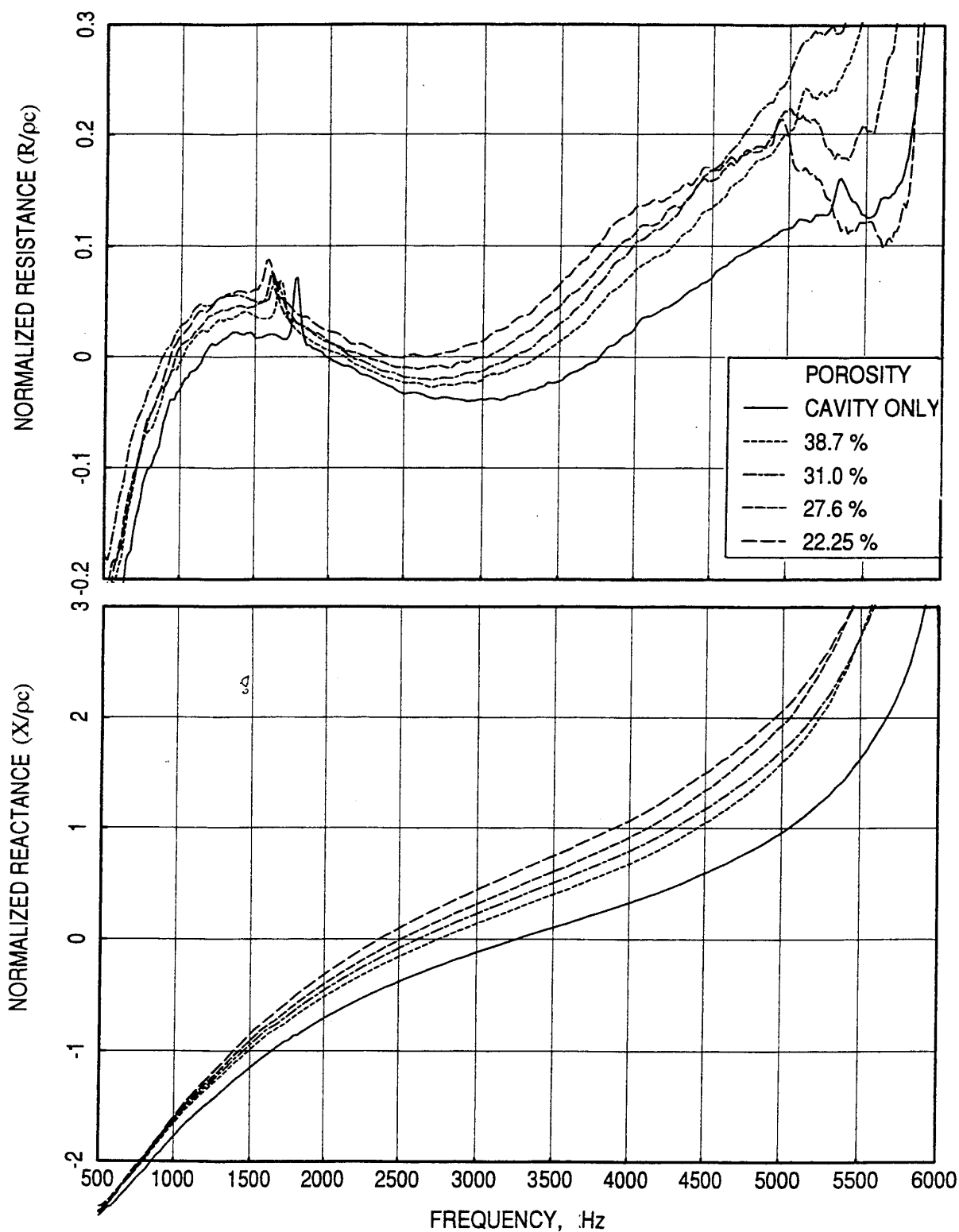


Figure D3. Normal impedance spectra of a 1"-deep cavity and the cavity with perforated facesheets of different porosity; nominal broadband excitation OASPL = 140 dB.

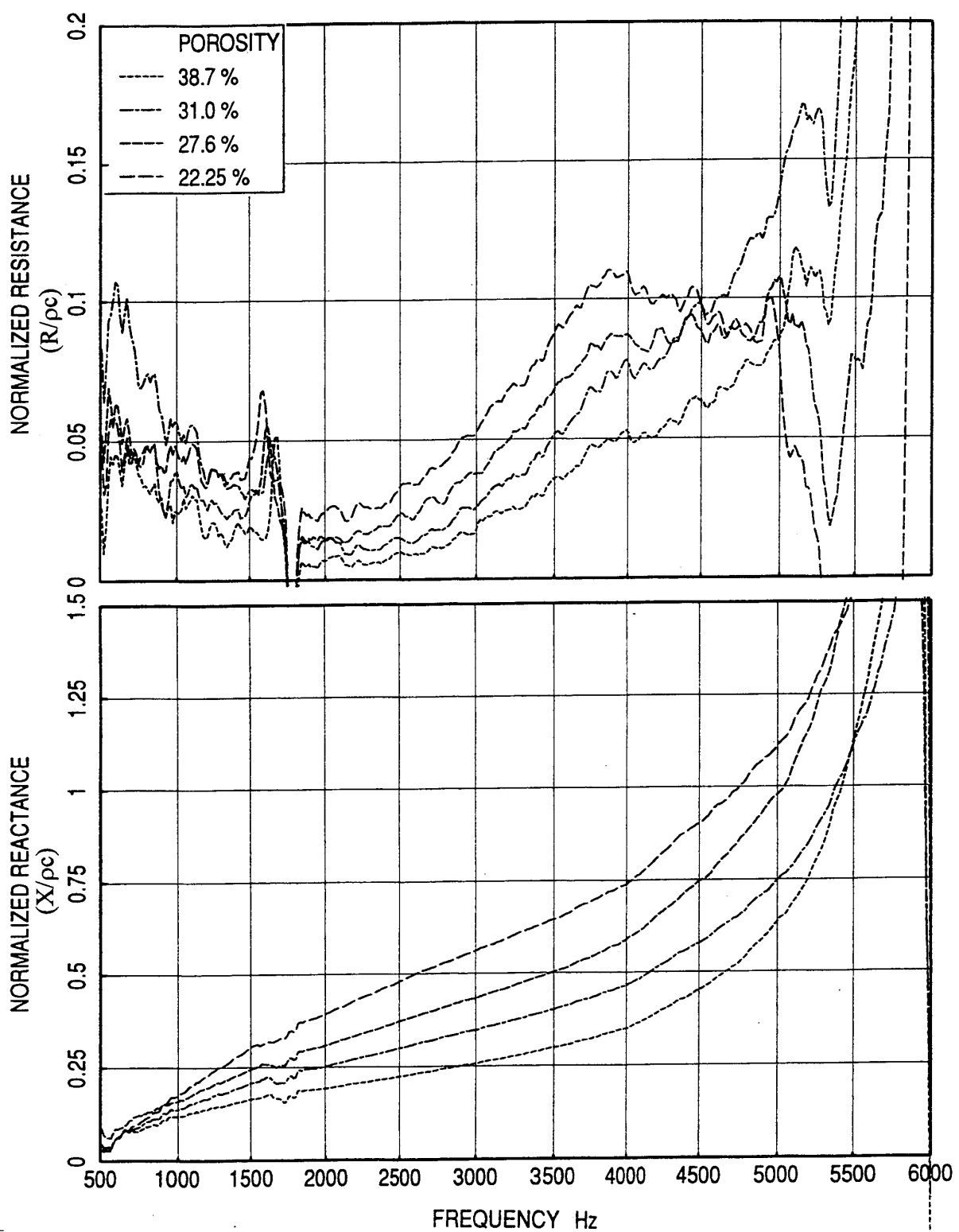


Figure D4. Normal impedance spectra for perforated facesheets of different porosity; nominal broadband excitation OASPL =140 dB.

with decreasing facesheet porosity. The resistance spectra show positive and negative spikes close to the anti-resonance frequencies. This is mostly due to the non-coincidence of anti-resonance frequencies for the cavity-facesheet combination compared to the cavity alone configuration. More accurate results could be obtained by measuring the impedance of the cavity and cavity-facesheet combination simultaneously (Ref. 27).

Next, the normal impedance spectra for the 1"-deep silicon carbide sample with and without the facesheets are measured and plotted in Figure D5. While the reactance spectra clearly indicate that the normalized reactance values are higher for the bulk with facesheet configurations compared to bulk material alone and that the values increase with decreasing facesheet porosity, the resistance spectra do not show such trends at higher frequencies. At lower frequencies the resistance changes due to the facesheets are minimal. At higher frequencies, the resistance values increase due to facesheet with decreasing porosity, similar to reactance characteristics for two facesheet combinations, for which the porosities are lower (i.e. 27.6% and 22.25%) and their hole pattern are staggered by 60°. For 90° stagger pattern facesheets the trend is reversed. It appears that the **lumped resistance due to the bulk and the facesheet is not a linear sum of their individual values.**

To examine the lumped impedance characteristics of the bulk with facesheets, the individual normal impedance of the facesheets, as evaluated and shown in Figure D4, are added to the normal impedance of the bulk alone configuration. The resulted normal impedance spectra are shown in Figure D6, which are qualitatively similar to the lumped impedance spectra of Figure D5, especially for reactance case. The lumped (i.e., combined measurement) resistance and reactance spectra are compared with the linearly added spectra in Figures D7 and D8, respectively. The agreement between the lumped and added levels is very good at lower frequencies. At higher frequencies, the added impedance levels are higher compared to the lumped values, especially for facesheets of higher porosity. In general, linear addition of individual impedance for bulk and perforates may give reasonable impedance for screening purpose, especially at lower frequencies.

DC flow resistance for each of the four facesheets is measured at the room temperature conditions. The DC flow resistance values depend on the direction of flow with respect to the facesheet surface. Hence, the DC flow resistance is measured by mounting the sample both ways and a mean is calculated. Figure D9 shows the average DC flow resistance with respect to the flow velocity. As expected, the DC flow resistance increases with decreasing porosity.

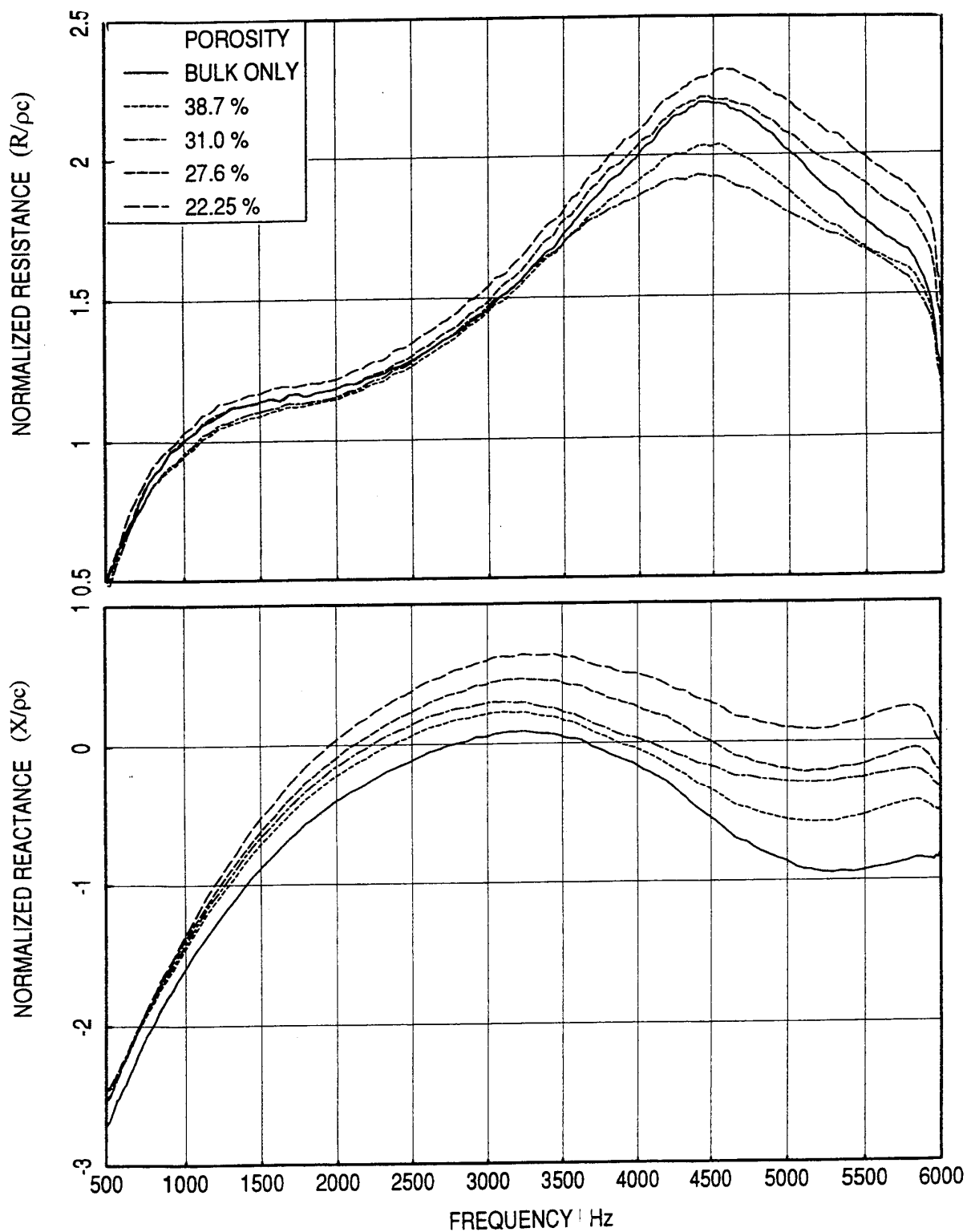


Figure D5. Normal impedance spectra of a 1"-deep silicon carbide bulk material with 200 ppi and the same bulk material with perforated facesheets of different porosity; nominal broadband excitation OASPL = 140 dB.

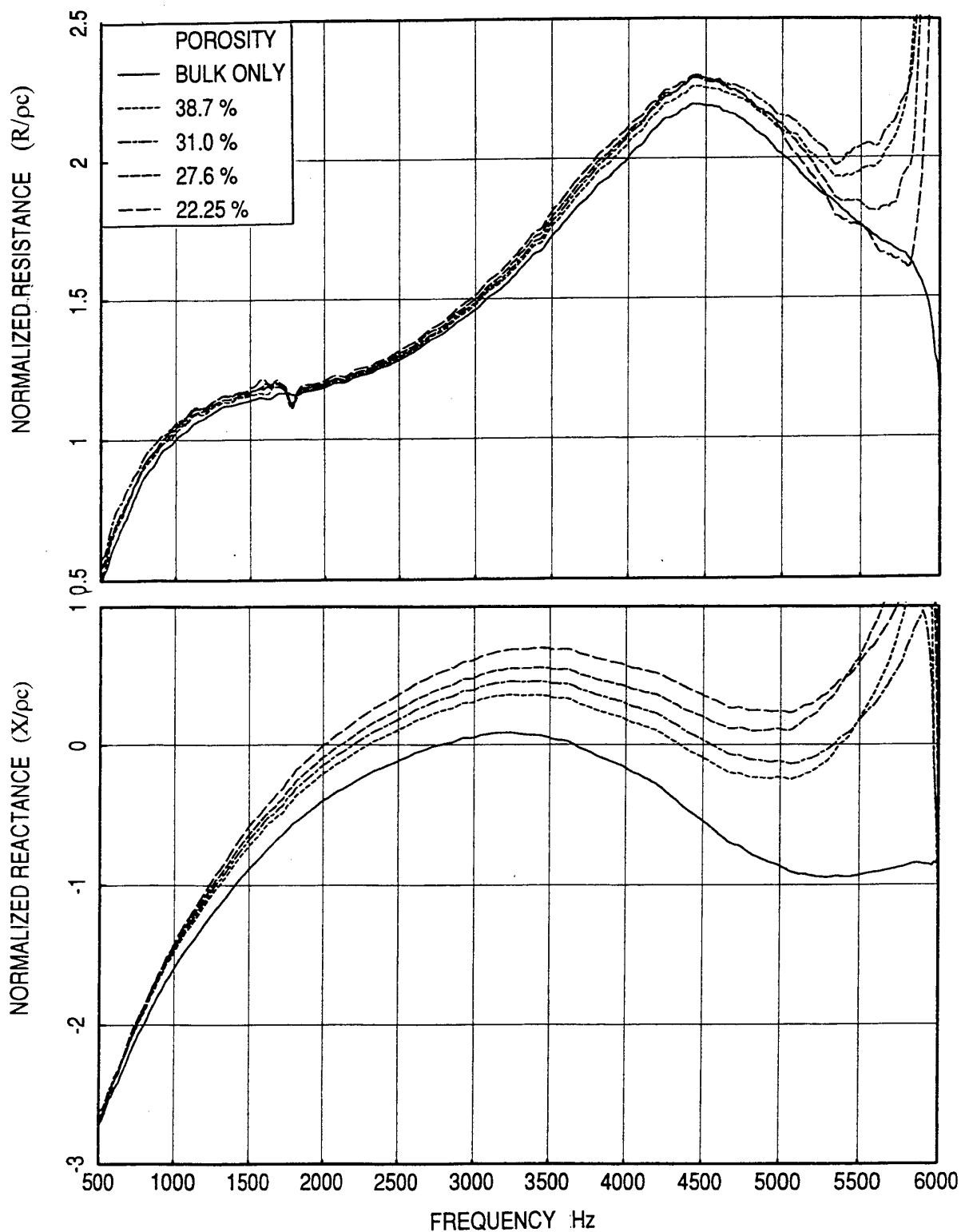


Figure D6. Normal impedance spectra of a 1"-deep silicon carbide bulk material with 200 ppi and the lumped normal impedance spectra of the same bulk material and perforated facesheets of different porosity; nominal broadband excitation OASPL = 140 dB.

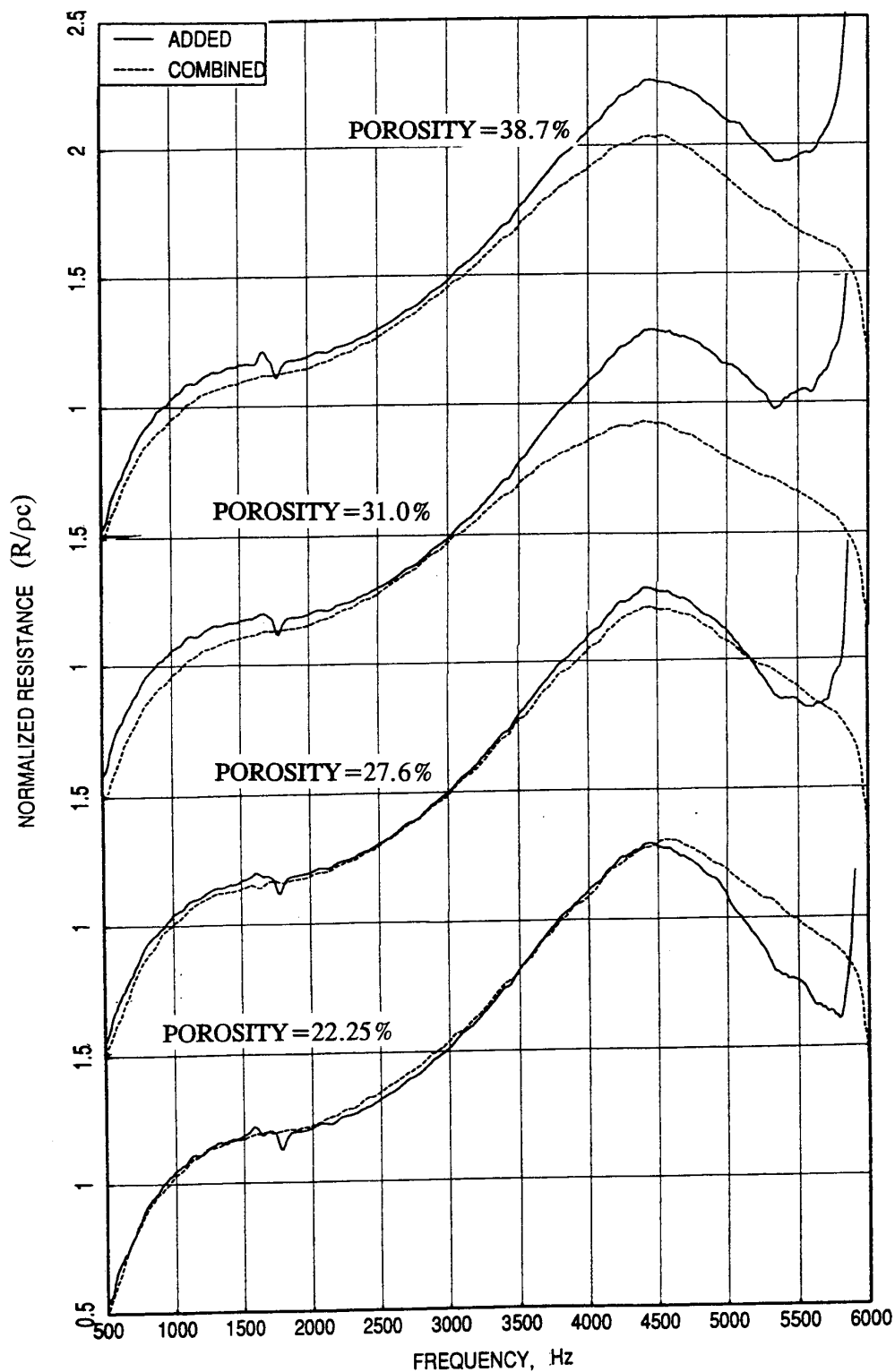


Figure D7. Comparison between the normal resistance spectrum for a 1"-deep silicon carbide bulk material (200 ppi) with perforated facesheet and the lumped normal resistance spectrum of the same bulk material and the perforated facesheet; nominal broadband excitation OASPL = 140 dB.

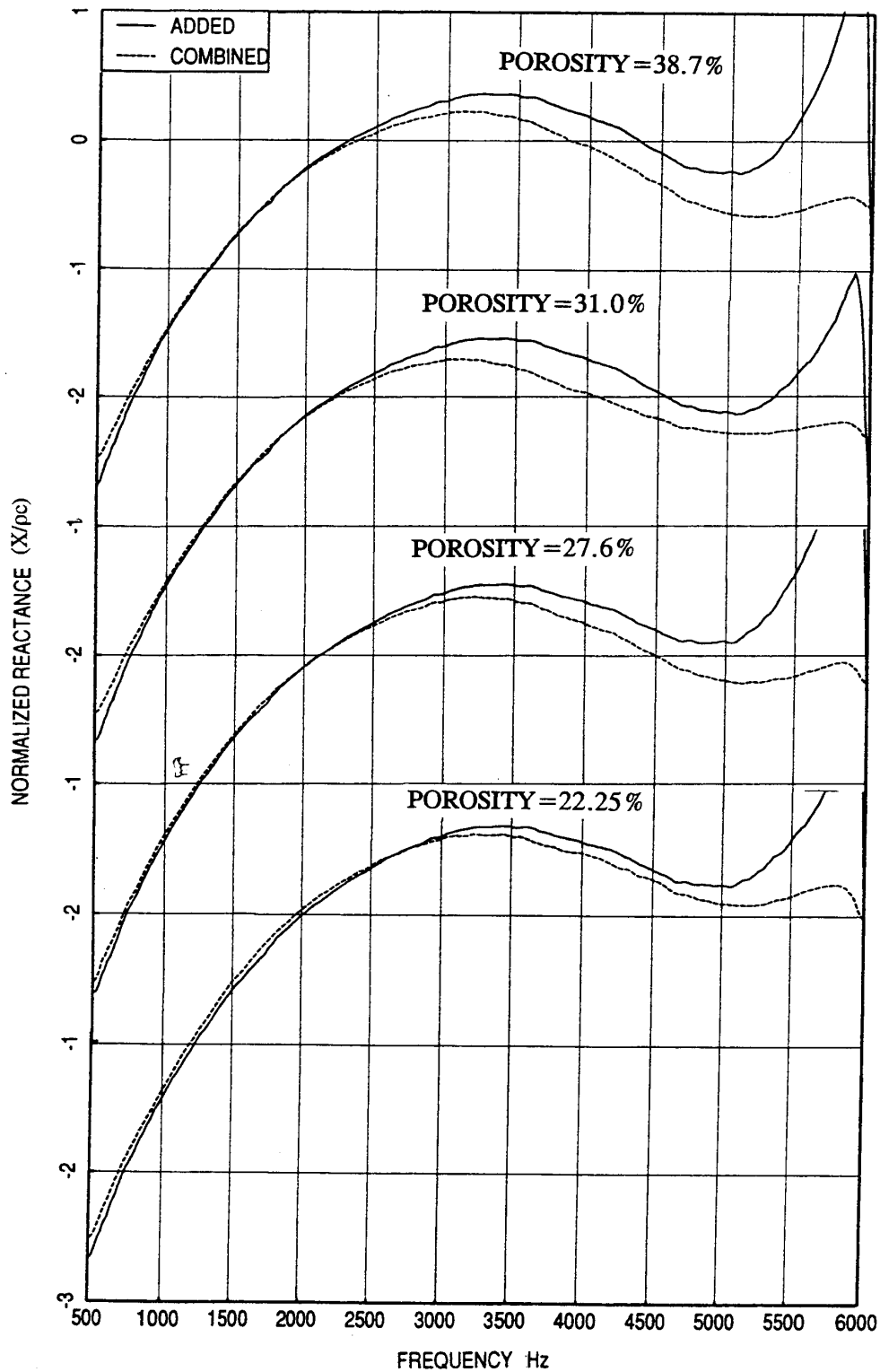


Figure D8. Comparison between the normal reactance spectrum for a 1"-deep silicon carbide bulk material (200 ppi) with perforated facesheet and the lumped normal reactance spectrum of the same bulk material and the perforated facesheet; nominal broadband excitation OASPL = 140 dB.

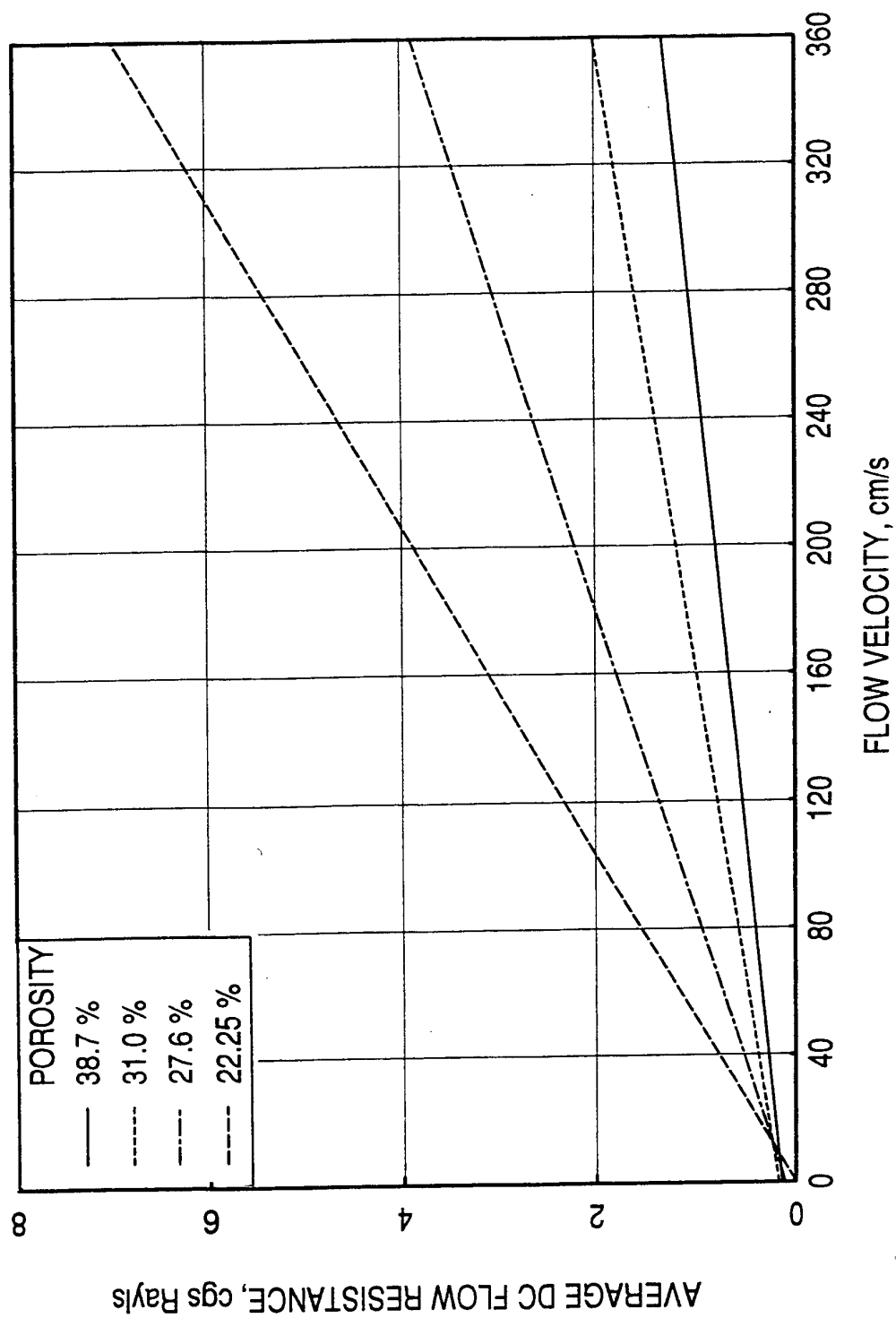


Figure D9. Effect of porosity on DC flow resistance for perforated plates..

Effect of Bulk Depth on Normal Impedance and DC Flow Resistance: Another concern regarding acoustic liner designs for scale model HSCT exhaust nozzle is the impedance characteristics of bulk material with respect to their depth. Based on Delany and Bazley (Ref. 6) the impedance level increases with increasing bulk material depth. However, the simplified model used in Ref. 6 does not predict the impedance spectra accurately, especially for complex materials. Hence, tests are conducted by measuring the normal impedance spectra for three 200-ppi silicon carbide bulk material samples of different depths. Two different levels of broadband noise excitations are utilized in these tests. Figures D10 and D11 show the impedance spectra for these samples for nominal OASPL of 150 dB and 130 dB, respectively. For both cases the impedance levels increase with increasing sample depth, except for 1" deep sample at higher frequencies. The discrepancy may have been caused by the non-homogeneous nature of the bulk materials with respect to their depths.

Figure D12 shows the DC flow resistance per unit depth (i.e., cm) with respect to flow velocity for 200 ppi silicon carbide bulk evaluated using samples of different depths. While, it is expected that the DC flow resistance per unit depth derived from samples of different depths of a homogeneous bulk material should be the same, the results of Figure D12 do not show this trend. While, the DC flow resistance levels derived from 1" and 0.64" deep samples are reasonably closer to each other, those values for 0.3"-deep sample are significantly different. The possible reason could be the non-homogeneous character of the bulk material. The samples of 0.64" and 0.3" are prepared from a sample of 1" deep material. It is possible that the process utilized to manufacture this sample might have caused a porosity gradation along the depth, such that the 0.3" sample comes out from higher porous side compared to 0.64" sample, while the average porosity is being exhibited by the 1"-deep sample.

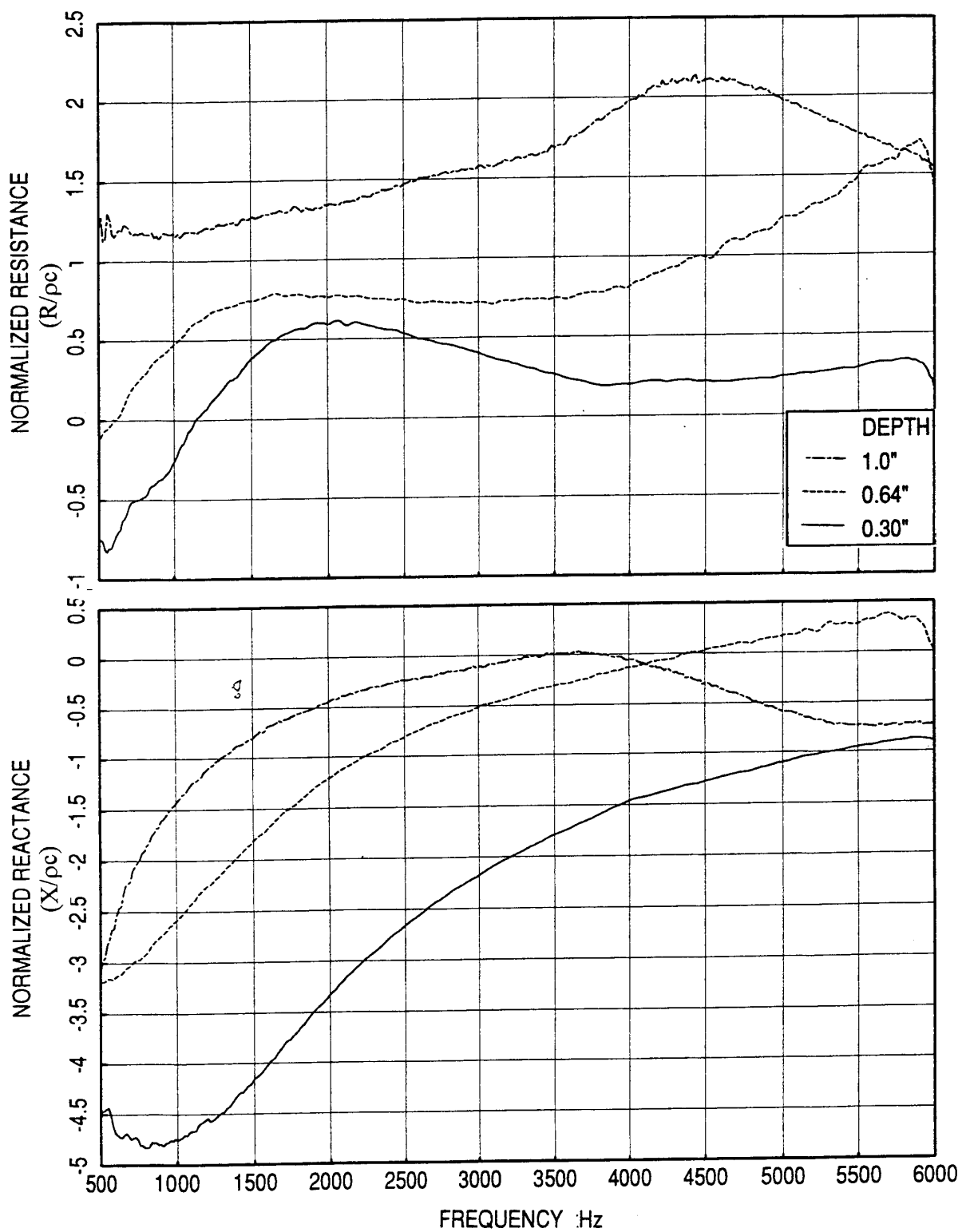


Figure D10. Effect of depth on normal impedance spectra for silicon carbide bulk material with 200 ppi; nominal broadband excitation OASPL = 150 dB.

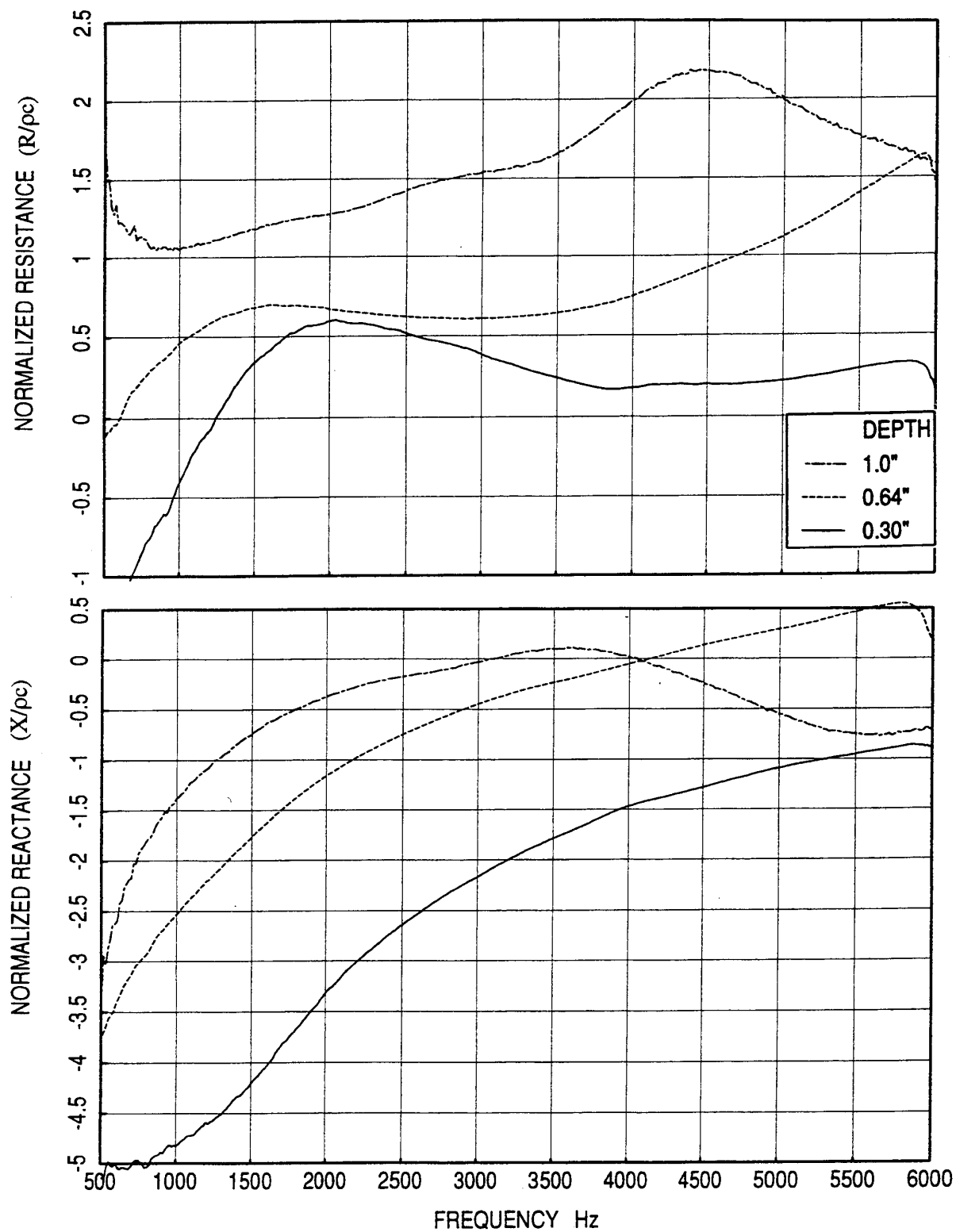


Figure D11. Effect of depth on normal impedance spectra for silicon carbide bulk material with 200 ppi; nominal broadband excitation OASPL = 130 dB.

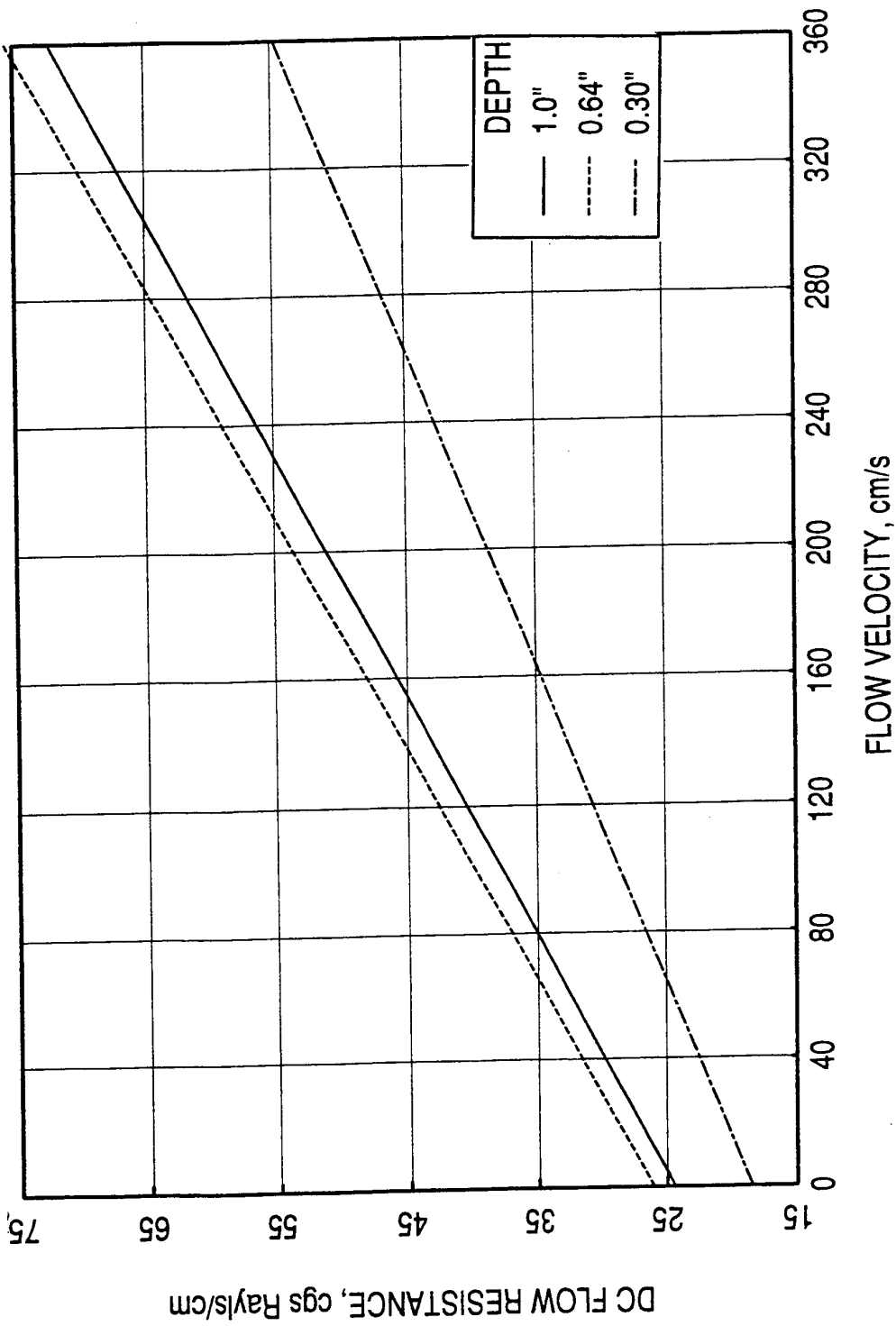


Figure D12. Effect of sample depth on DC flow resistance per unit depth for silicon carbide bulk material with 200 ppi.

REFERENCES

1. Brausch, J. F, Motsinger, R. E., and Hoerst, D. J., "Simulated Flight Acoustic Investigation of Treated Ejector Effectiveness on Advanced Mechanical Suppressors for High Velocity Jet Noise Reduction.", NASA CR 4019, 1986.
2. Brausch, J. F and Hoerst, D. J., "Simulated Flight Acoustic Investigation of Treated Ejector Effectiveness on Advanced Mechanical Suppressors for High Velocity Jet Noise Reduction - Comprehensive Data Report, Volume II - Laser Velocimeter, Aerodynamic Instrumentation, and Shadowgraph Data.", GEAE Report - R85AEB517, NASA CR 175103, 1985.
3. Motsinger, R. E., and Kraft, R. E., "Design and Performance of Duct Acoustic Treatment", in "Aeroacoustics of Flight Vehicles : Theory and Practice - Volume 2: Noise Control" NASA reference Publication 1258, Vol 2, WRDC TR 90-3052.
4. Liepmann, H. W. and Roshko, A., "Elements of Gas Dynamics." Wiley, New York, 1956.
5. Zorumski, W. E. and Tester, B. J., "Prediction of the Acoustic Impedance of Duct Liners." NASA TM X-73951, 1976.
6. Delany, M. E. and Bazley, E. N., "Acoustical Properties of Fibrous Absorbent Materials." Applied Acoustics, 3 (2), pp. 105-116, 1970.
7. Morse, P. M. and Ingard, K. U. "Theoretical Acoustics" New York, McGraw-Hill, 1968.
8. Motsinger, R.E., Kraft, R.E., Zwick, J.W., Vukelich, S.I., Minner, G.L., and Baumeister, K.J., "Optimization of Suppression for Two-Element Treatment Liners for Turbomachinery Exhaust Ducts", NASA CR-134997, April, 1976.
9. Syed, A. A. and Lewis, D. L., "The Measurement of Acoustic Suppressions in a Flow Duct using an Energy Flux Measurement Technique", AIAA 90-3949, 1990.
10. Hermann Schlichting, "Boundary-Layer Theory", McGraw Hill Book Company, 1979.
11. Bobba, C. R. and Lahti, D. J., "Least Squares Fit to Turbulent Boundary Layer Data Conforming to Law of the Wall and Law of the Wake Profiles", General Electric Technical Memorandum 80-299, 1980.
12. Coles, D. E. and Hirst, E. A., "Computation of Turbulent Boundary Layers", AFOOR - IFS - Stanford Conference, 1968.
13. Dean, P. D., "An In-Situ Method of Wall Impedance Measurement in Flow Ducts", Journal of Sound and Vibration, 34(1), 97-130, 1974.
14. Salikuddin, M., Dean, P. D., Plumlee, H. E. Jr. and Ahuja, K. K., "An Impulse Test Technique with Application to Acoustic Measurements", JSV 70, 487-501, 1980.

15. Salikuddin, M., Ahuja, K. K., & Brown, W. H., "An Improved Impulse Method for Studies on Acoustic Transmission in Flow Ducts with use of Signal Synthesis and Averaging of Acoustic Pulses", JSV 94, 33-61, 1984.
16. Ahuja, K. K. and Salikuddin, M. "Acoustic Power Dissipation on Radiation through Duct Terminations Experiments". JSV 91, 479-502, 1983.
17. Salikuddin, M. and Mungur, P., "Acoustic Radiation Impedance of Duct-Nozzle System", JSV 86, 497-522, 1983.
18. Salikuddin, M. "Acoustic Behavior of Orifice Plates and Perforated Plates with Reference to Low Frequency Sound Absorption", JSV 139, 361-381, 1990.
19. Salikuddin, M. and Brown, W. H., "Non-Linear Effects in Finite Amplitude Wave Propagation through Orifice Plate and Perforated Plate Terminations" JSV 139, 383-405, 1990.
20. Salikuddin, M. and Brown, W. H., "Non-Linear Effects in Finite Amplitude Wave Propagation through Ducts and Nozzles" JSV 106, 71-106, 1986.
21. Salikuddin, M. and Brown, W. H., "Non-Linear Effects in Finite Amplitude Wave Propagation through Ducts and Nozzles" JSV 106, 71-106, 1986.
22. Singh, R. and Katra, T. "Development of an Impulse Technique for Measurement of Muffler Characteristics", JSV 56, 279-298, 1989.
23. Handler, R. A., "Experimental Investigation of Acoustic Pulse Propagation in Nearly Choked Ducts", AIAA 7th Aeroacoustics Conference Paper No. 81-1964, 1981.
24. Davies, J. C. and Mulholland, K. A., "An Impulse Method for Measuring Normal Impedance at Oblique Incidence", JSV 67, 135-149, 1979.
25. Davies, J. C. and Gibbs, B. M. "The Oblique Incidence Measurement of Transmission Loss by an Impulse Method" JSV 74, 381-393, 1981.
26. To, C. W. S. and Doige, A. G., "The Application of a Transient Testing Method to the Determination of Acoustic Properties of Unknown Systems", JSV 74, 545-554, 1980.
27. Salikuddin, M., Syed, A. A., and Mungur, P., "Acoustic Characteristics of Perforated Sheets with Throughflow in High Intensity Noise Environment." Journal of Sound and Vibration, 1993.
28. Salikuddin, M., "Farfield Acoustic Characteristics of an 8-Lobed Vortical Mixer-Ejector Nozzle, Treated with Various SDOF and Bulk Absorber Type Liners, for Insertion Loss/Normal Impedance Correlation Development." 1997, HSR/CPC Program Coordination Memo No: GE97-160-N, NAS3-27235.

29. Rice, E. J., "Semi-Empirical Correlation between Liner Insertion Loss and Normal Impedance – HSR Related Duct and Mixer-Ejector." 1999, HSR/CPC Program Coordination Memo No: GE99-008-N, NAS3-27235.
30. Kapur, A and Mungur, P., "On the propagation of sound in a rectangular duct with gradients of mean flow and of mean temperature in both transverse directions." 1982, J. Sound Vib. Vol 23, p.401-404.
31. Mungur, P and Plumblee, H.E. "Propagation and attenuation of sound in a soft walled annular duct containing a sheared flow." 1969, NASA SP 207, p.305-327:.
32. Morfey, C. L. "Acoustic energy in non-uniform flow." 1971, J. Sound Vib. Vol 14, p.159-170.
33. Cantrel, R. H. and Hart, R. W. "Interaction between sound and flow." 1964, JASA Vol 36, p.697-706.
34. Tester, B. J., "Acoustic energy flow in lined ducts containing plug flow." 1973, J. Sound Vib. Vol 28, p.205-215.

REPORT DOCUMENTATION PAGE			Form Approved OMB No. 0704-0188	
Public reporting burden for this collection of information is estimated to average 1 hour per response, including the time for reviewing instructions, searching existing data sources, gathering and maintaining the data needed, and completing and reviewing the collection of information. Send comments regarding this burden estimate or any other aspect of this collection of information, including suggestions for reducing this burden, to Washington Headquarters Services, Directorate for Information Operations and Reports, 1215 Jefferson Davis Highway, Suite 1204, Arlington, VA 22202-4302, and to the Office of Management and Budget, Paperwork Reduction Project (0704-0188), Washington, DC 20503.				
1. AGENCY USE ONLY (Leave blank)		2. REPORT DATE September 2006		3. REPORT TYPE AND DATES COVERED Final Contractor Report
4. TITLE AND SUBTITLE Acoustic Characteristics of Various Treatment Panel Designs for HSCT Ejector Liner Acoustic Technology Development Program			5. FUNDING NUMBERS WBS 984754.02.07.03.04.01 NAS3-27235	
6. AUTHOR(S) M. Salikuddin, R.E. Kraft, A.A. Syed, D.D. Vu, P. Mungur, L.E. Langenbrunner, and R.K. Majjigi				
7. PERFORMING ORGANIZATION NAME(S) AND ADDRESS(ES) General Electric Aircraft Engines One Neumann Way Cincinnati, Ohio 45215-1915			8. PERFORMING ORGANIZATION REPORT NUMBER E-15678	
9. SPONSORING/MONITORING AGENCY NAME(S) AND ADDRESS(ES) National Aeronautics and Space Administration Washington, DC 20546-0001			10. SPONSORING/MONITORING AGENCY REPORT NUMBER NASA CR-2006-214399	
11. SUPPLEMENTARY NOTES Project manager, Clayton L. Meyers, Aeronautics Division, NASA Glenn Research Center, organization code PRV, 216-433-3882.				
12a. DISTRIBUTION/AVAILABILITY STATEMENT Unclassified - Unlimited Subject Category: 07 Available electronically at http://gltrs.grc.nasa.gov This publication is available from the NASA Center for AeroSpace Information, 301-621-0390.			12b. DISTRIBUTION CODE	
13. ABSTRACT (Maximum 200 words) The objectives of the initial effort (Phase I) of HSR Liner Technology Program, the selection of promising liner concepts, design and fabrication of these concepts for laboratory tests, testing these liners in the laboratory by using impedance tube and flow ducts, and developing empirical impedance/suppression correlation, are successfully completed. Acoustic and aerodynamic criteria for the liner design are established. Based on these criteria several liners are designed. The liner concepts designed and fabricated include Single-Degree-of-Freedom (SDOF), Two-Degree-of-Freedom (2DOF), and Bulk Absorber. Two types of SDOF treatment are fabricated, one with a perforated type face plate and the other with a wiremesh (woven) type faceplate. In addition, special configurations of these concepts are also included in the design. Several treatment panels are designed for parametric study. In these panels the facesheets of different porosity, hole diameter, and sheet thickness are utilized. Several deep panels (i.e., 1 in. deep) are designed and instrumented to measure DC flow resistance and insitu impedance in the presence of grazing flow. Basic components of these panels (i.e., facesheets, bulk materials, etc.) are also procured and tested. The results include DC flow resistance, normal impedance, and insertion loss.				
14. SUBJECT TERMS Propulsion systems (aircraft)			15. NUMBER OF PAGES 429	
			16. PRICE CODE	
17. SECURITY CLASSIFICATION OF REPORT Unclassified	18. SECURITY CLASSIFICATION OF THIS PAGE Unclassified	19. SECURITY CLASSIFICATION OF ABSTRACT Unclassified	20. LIMITATION OF ABSTRACT	

